



Mohammad Aghazadeh Meshgi, MSc

**Synthesis of Indium and Germanium Nanoparticles and
Germanium Nanowires
&
Synthesis of Oligosilanes Containing Hypervalent Silicon Atom**

DOCTORAL THESIS

to achieve the university degree of
Doktor der technischen Wissenschaften
submitted to

Graz University of Technology

Supervisor

Prof. Dr. Christoph Marschner

Institute of Inorganic Chemistry

AFFIDAVIT

I declare that I have authored this thesis independently, that I have not used other than the declared sources/resources, and that I have explicitly indicated all material which has been quoted either literally or by content from the sources used. The text document uploaded to TUGRAZonline is identical to the present doctoral thesis.

Date

Signature

This work was financed by the Austrian Science Foundation (Fonds zur Förderung der Wissenschaftlichen Forschung) firstly via the project “Polygermanium Chemistry” (P-22678) and afterwards by project “Hypercoordinated Silanes” (P-26417) and was carried out from August 2012 to December 2015 at the Institute of Inorganic Chemistry, Graz University of Technology.

Acknowledgment

Here I would like to thank my advisor Professor Dr. Christoph Marschner for his scientific as well as financial supports during my work as PhD student at Graz University of Technology. It was a great pleasure and chance for me to perform my research under his supervision, while having my own independency during work. His high level of knowledge and patience was a great opportunity for me as a materials engineer to gradually improve my knowledge of chemistry and reach to my early dream. The dream to raise my knowledge in the field of nanomaterial synthesis for electronic applications while, improving my knowledge of chemistry. In fact, his patience, special educational method, geniality and sense of humor, precise advice and full support even in case of failures, had profound effects on my personality and raised my perseverance, independence and self-confidence and was the reason for my success during my PhD.

I would like to thank his wife and colleague, Dr. Judith Baumgartner for her precise work regarding interpretation of all crystallographic data of my research as well as her hospitality during various banquets in their home and villa.

I have to especially thank my mother Giti Faroughi, my father Hassan Aghazadeh Meshgi and my sister Mahzad Aghazadeh Meshgi for their emotional support during my hard times and particularly in case of failures while performing my research.

For all advice, help and collaboration during my work in laboratory I would like to thank my colleagues Filippo Stella, Malgorzata Walewska, Rainer Zitz, Dr. Johann Hlina and Dr. Andreas Wallner.

I would like to thank Dr. Peter Poelt for precise scrutiny of my nano-materials via electron microscope and his interest on the results of my research.

Also it was a great opportunity to collaborate with my Russian colleagues Dr. Kirill V. Zaitsev, Dr. Sergey S. Karlov and Prof. Galina S. Zaitseva to prepare different types of oligosilanes containing hypervalent silicon atom.

Moreover I would like to thank all individuals who helped me to analyze my samples directly or indirectly as follows: Prof. Gregor Trimmel (TGA analysis), Prof. Hansjoerg Weber (NMR spectroscopy), Dr. Brigitte Bitschnau (X-ray powder diffraction), Dr. Ilse Letofsky-Papst (TEM microscope), Dr. Manfred Kriechbaum (SAXS analysis), Dr. Christian Gspan (SAED analysis), Ms. Josefine Hobisch (TGA analysis), Prof. Torsten Mayr (Dynamic light scattering), Ms. Elisabeth Scheucher (Dynamic light scattering), Ms. Karin Bartl (EI/MS), Ms. Astrid Falk (GC-MS) and Ms. Monika Filzwieser (Elemental analysis).

Finally I would like to thank Austrian Fonds zur Förderung der wissenschaftlichen Forschung (FWF) for financial support via the projects P-22678 and P-26417.

Abbreviations

AAO	Anodic aluminum oxide
CVD	Chemical vapor deposition
DLS	Dynamic light scattering
DMF	Dimethylformamide
DPG	Diphenylgermane
DSC	Differential scanning calorimetry
ec-LLS	Electrochemical liquid-liquid-solid
EDS	Energy dispersive X-ray spectroscopy
EG	Ethylene glycol
HMDS	Hexamethyldisilazane
HRTEM	High-resolution transmission electron microscope
MBE	Molecular beam epitaxy
NBG	<i>n</i> -Butylgermane
NMR	Nuclear magnetic resonance
OMVPE	Organometallic vapor phase epitaxy
PDDF	Pair-distance distribution functions
PVP	Polyvinyl pyrrolidone
SAED	Selected area electron diffraction
SAXS	Small angle X-ray scattering
SFLS	Supercritical fluid-liquid-solid
SLS	Solution-liquid-solid
Squalane	2,6,10,15,19,23-Hexamethyltetracosane
Squalene	2,6,10,15,19,23-Hexamethyltetracosane-2,6,10,14,18,22-hexaene
SVG	Solvent vapor growth
TBG	Tetrabutylgermane
TBP	Tri- <i>n</i> -butylphosphine
TCG	Trichlorogermane
TEG	Tetraethylgermane
TEM	Transmission electron microscope
TGA	Thermogravimetric analysis
TOP	Tri- <i>n</i> -octylphosphine
TOPO	Tri- <i>n</i> -octylphosphine oxide
VLS	Vapor-liquid-solid
XRD	X-ray diffraction

1 Table of contents

1	Introduction	20
1.1	Nanoparticles	20
1.1.1	Synthesis of germanium nanoparticles	20
1.1.1.1	Thermal decomposition of germanium precursors	20
1.1.1.2	Reduction of germanium halide	20
1.1.1.3	Metathesis reactions of germanium Zintl salts	21
1.1.2	Synthesis of indium nanoparticles	21
1.1.3	Size and morphology characterization methods	22
1.1.3.1	Transmission electron microscope	22
1.1.3.2	Dynamic light scattering	23
1.1.3.3	Small angle X-ray scattering	23
1.2	Germanium nanowires	25
1.2.1	Different synthesis methods	25
1.2.1.1	Solution phase methods	25
1.2.1.1.1	Supercritical fluid-liquid-solid (SFLS)	28
1.2.1.1.2	Colloidal route	29
1.2.1.1.3	Solvent vapor growth (SVG)	30
1.2.1.2	Gas phase methods	30
1.2.1.2.1	Chemical Vapor Deposition	30
1.2.1.2.2	Laser Ablation	30
1.2.1.2.3	Molecular beam epitaxy	31
1.2.1.3	Electrochemical method	32
1.2.1.3.1	Electrochemical liquid-liquid-solid (ec-LLS)	32
1.2.2	Non-catalytic growth of germanium nanowires	32
1.2.2.1	Germanium nanowires grown without catalysts	32
1.2.2.2	Template method	34
1.2.3	Dopants of germanium nanowires	34
1.2.4	Defect formation in germanium nanowires	35
1.2.4.1	Solvent effect	35
1.2.4.2	Seed effects	36
1.3	Polysilylsilatranes	38
1.3.1	Polysilanes	38
1.3.1.1	Electron delocalization in polysilanes	38
1.3.1.2	UV-vis absorption of polysilanes	39
1.3.2	Atranes and silatranes	39
1.3.3	Other compounds containing a pentacoordinated silicon atom	40
1.3.3.1	Silatranes with different types of ligands	40
1.3.3.2	Silocanes	41
1.3.4	Synthetic strategies of silatranes	42
1.3.4.1	Synthesis from alkoxy silane	42
1.3.4.2	Synthesis from chlorosilane	43
1.3.5	Reactivity of silatranes	43
2	Synthesis of new oligosilylgermanes	46
2.1	Oligosilylgermane compounds containing germanium-hydrogen bonds:	46
2.1.1	Synthesis of pentakis(trimethylsilyl)digermane (1)	46
2.1.2	Synthesis of 1,1,2,2-tetrakis(trimethylsilyl)digermane (8)	47

2.1.3	Synthesis of bis(trimethylsilyl)[tris(trimethylsilyl)silyl]germane (11)	48
2.1.4	Synthesis of bis(trimethylsilyl)pentamethyldisilanylgermane (14)	48
2.2	Synthesis of other oligosilylsilanes and -germanes:	49
2.2.1	Synthesis of (pentamethyldisilyl)tris(trimethylsilyl)germane (16)	49
2.2.2	Synthesis of bis(trimethylsilyl)pentamethyldisilanylgermyl-potassium.18-crown-6 (15)	49
2.2.3	Synthesis of (<i>tert</i> -butyldiphenylsilyl)tris(trimethylsilyl)germane (26).....	50
2.2.4	Synthesis of 1-(<i>tert</i> -butyl)-3,3,3-trimethyl-1,1-diphenyl-2,2-bis(trimethylsilyl)trisilane (27)	52
2.2.5	Synthesis of ((<i>tert</i> -butyldiphenylsilyl)bis(trimethylsilyl)germyl)potassium.18-crown-6 (30).....	52
2.2.6	Synthesis of 2- <i>tert</i> -butyl-2,2-diphenyl-1,1-bis(trimethylsilyl)disilanyl)potassium.18-crown-6 (31)	54
2.3	Conclusion.....	57
3	TGA and DSC investigation of oligosilylgermanes	59
3.1	[Tris(trimethylsilyl)silyl]trimethylgermane (33)	59
3.2	Tetrakis(trimethylsilyl)germane (34)	59
3.3	Hexakis(trimethylsilyl)digermane (6)	59
3.4	Pentakis(trimethylsilyl)digermane (1).....	60
3.5	Conclusion.....	60
4	Colloidal synthesis of germanium nanoparticles	64
4.1	Germanium nanoparticles synthesis with tris(trimethylsilyl)germane (3) in presence of dicobalt octacarbonyl.....	64
4.1.1	In <i>n</i> -heptane with precursor to dicobalt octacarbonyl ratio 20:1 at 90 °C.....	64
4.1.2	In <i>n</i> -heptane with precursor to dicobalt octacarbonyl ratio 20:1 at 142 °C	64
4.1.3	In <i>n</i> -dodecane with precursor to dicobalt octacarbonyl ratio 20:1 at 142 °C in presence of TOPO	67
4.1.4	In <i>n</i> -dodecane with precursor to dicobalt octacarbonyl ratio 20:4 at 142 °C in presence of TOPO	70
4.1.5	In <i>p</i> -xylene with precursor to dicobalt octacarbonyl ratio 20:1 at 142 °C in the presence of TOPO ...	73
4.2	Germanium nanoparticles synthesis with tris(trimethylsilyl)germane precursor without dicobalt octacarbonyl.....	76
4.2.1	In <i>n</i> -dodecane without dicobalt octacarbonyl at 142 °C in presence of TOPO	76
4.2.2	In <i>n</i> -hexadecane without dicobalt octacarbonyl at 252 °C in presence of TOPO and oleylamine.....	77
4.3	Conclusion.....	79
5	Colloidal synthesis of indium nanoparticles	82
5.1	Synthesis of indium nanoparticles in polar medium followed by phase transfer to a non-polar medium.....	82
5.1.1	Indium nanoparticles capped tri- <i>n</i> -butylphosphine	82
5.1.2	Indium nanoparticles capped tri- <i>n</i> -butylphosphine phase transfer reaction.....	86
5.1.3	FT-IR confirmation of ligand exchange during phase transfer reaction	88
5.2	One step synthesis of indium nanoparticles in a non-polar medium	90
5.2.1	Simultaneous phase transfer and ripening method	90
5.2.2	Small-angle X-ray scattering (SAXS) analysis of colloidal solution of indium nanoparticles.....	93
5.3	Conclusion.....	95
6	Colloidal synthesis of germanium nanowires	97
6.1	Synthesis of germanium nanowires at 180 °C.....	98
6.1.1	In the presence of TOPO	98
6.2	Synthesis of germanium nanowires at 300 °C	102

6.2.1	In the presence of TOPO or oleylamine	102
6.3	Synthesis of germanium nanowires at 350 °C	107
6.3.1	In the presence of oleylamine	107
6.3.2	In pure oleylamine	109
6.3.3	In a mixture of oleylamine and TOPO	110
6.4	Synthesis of germanium nanowires at 380 °C	111
6.4.1	In the presence of TOPO	111
6.5	Conclusion.....	111
7	Oligosilanylsilatrane	114
7.1	Synthesis of primary silatrane units.....	114
7.1.1	Synthesis of 1-chlorosilatrane (40)	114
7.1.2	Synthesis of phenylsilatrane (41).....	114
7.1.3	Synthesis of 1-bromosilatrane (42)	115
7.1.4	Synthesis of 1-silatranyltriflate (43).....	116
7.2	Synthesis of oligosilanylsilatrane.....	116
7.2.1	Synthesis of tris(trimethylsilyl)silatranylsilane (44)	116
7.2.2	Synthesis of bis(trimethylsilyl)methylsilatranylsilane (55)	125
7.2.3	Synthesis of bis(trimethylsilyl)ethylsilatranylsilane (57).....	125
7.2.4	Synthesis of bis(trimethylsilyl)phenylsilatranylsilane (60).....	127
7.2.5	Synthesis of (<i>tert</i> -butyldimethylsilyl)bis(trimethylsilyl)silatranylsilane (62)	130
7.2.6	Synthesis of bis(trimethylsilyl)isopropylsilatranylsilane (65).....	131
7.2.7	Synthesis of 1,1-bis(trimethylsilyl)-1-silatranyl-pentamethyltrisilane (67)	131
7.2.8	Synthesis of bis(trimethylsilyl)silatranylsilane (70)	133
7.2.9	Synthesis of disilatranyl-bis(trimethylsilyl)silane (72).....	135
7.2.10	Synthesis of 2-silatranyl-2,5,5-tris(trimethylsilyl)decamethylhexasilane (75)	135
7.2.11	Synthesis of 2,5-disilatranyl-2,5-bis(trimethylsilyl)decamethylhexasilane (77).....	137
7.2.12	Synthesis of <i>cis/trans</i> 1,4-disilatranyl-1,4-bis(trimethylsilyl)octamethylcyclohexasilane (80).....	138
7.2.13	Protonation of tris(trimethylsilyl)silatranylsilane (44) with trifluoromethanesulfonic acid.....	142
7.3	Synthesis of silatranylsilylanions.....	144
7.3.1	Synthesis of bis(trimethylsilyl)silatranylsilylpotassium.18-crown-6 (73)	144
7.3.2	Synthesis of trimethylsilylphenylsilatranylsilylpotassium.18-crown-6 (87)	145
7.3.3	Synthesis of (<i>tert</i> -butyldimethylsilyl)(trimethylsilyl)silatranylsilylpotassium.18-crown-6 (88).....	147
7.3.4	Synthesis of trimethylsilylmethylsilatranylsilylpotassium.18-crown-6 (90).....	147
7.3.5	Synthesis of trimethylsilylethylsilatranylsilylpotassium.18-crown-6 (93)	149
7.3.6	Synthesis of 2,5-disilatranyl-decamethylhexasilyl-2,5-dipotassium.18-crown-6 (96)	149
7.4	Transmetallation reactions	151
7.4.1	Synthesis of bis[bis(trimethylsilyl)silatranylsilyl]zinc (98).....	151
7.4.2	Synthesis of dicyclopentadienyl[bis(trimethylsilyl)silatranylsilyl]hafniumchloride (99).....	153
7.4.3	Synthesis of dicyclopentadienyl[bis(trimethylsilyl)silatranylsilyl]zirconiumchloride (71)	155
7.5	Conclusion.....	155
8	Oligosilanylsilatrane with other types of ligands	158
8.1	Synthesis of primary silatrane units.....	158
8.1.1	Synthesis of aminotris(phenyl-2'-oxy)silylchloride (130).....	158
8.1.2	Synthesis of aminotris(-3',5'-dimethylbenzyl-2'-oxy)silylchloride (132).....	160
8.2	Synthesis of oligosilanylsilatrane.....	161

8.2.1	Synthesis of 1,1,1-aminotris(phenyl-2'-oxy)-2,2-bis(trimethylsilyl)trimethyltrisilane (135)	161
8.2.2	Synthesis of 1,1,1-aminotris(-3',5'-dimethylbenzyl-2'-oxy)-(4''-tris(trimethylsilyl)silyl)butanyloxysilane (139)	163
8.2.3	Synthesis of 1,1,1-aminotris(-3',5'-dimethylbenzyl-2'-oxy)-2,2-bis(trimethylsilyl)trimethyltrisilane (141)	165
8.3	Conclusion.....	167
9	Oligosilanylsilocanes	169
9.1	Synthesis of primary silocane unites.....	169
9.1.1	Synthesis of MeN(CH ₂ CH ₂ O) ₂ SiMeCl (104).....	169
9.1.2	Synthesis of (MeO) ₂ Si(OCH ₂ CH ₂) ₂ NMe (106)	169
9.1.3	Synthesis of Cl ₂ Si(OCH ₂ CH ₂) ₂ NMe (107)	171
9.2	Synthesis of oligosilanylsilocanes	172
9.2.1	Synthesis of 2'-(2',6'-dimethyl-1',3',6',2'-dioxasilocanyl)-tris(trimethylsilyl)silane (110)	172
9.2.2	Synthesis of 1,4-bis-2'-(2',6'-dimethyl-1',3',6',2'-dioxasilocanyl)-1,1,4,4-tetrakis(trimethylsilyl)tetramethyltetrasilane (112)	172
9.2.3	Synthesis of [(Me ₃ Si) ₃ Si] ₂ Si(OCH ₂ CH ₂) ₂ NMe (116)	174
9.2.4	Synthesis of [(Me ₃ Si) ₃ Ge] ₂ Si(OCH ₂ CH ₂) ₂ NMe (117)	175
9.3	Synthesis of silocanylsilylanions.....	178
9.3.1	Synthesis of 2'-(2',6'-dimethyl-1',3',6',2'-dioxasilocanyl)bis(trimethylsilyl)silanylpotassium.18-crown-6 (113).....	178
9.4	Conclusion.....	178
10	Synthesis of methoxysilanes	180
10.1	Synthesis of tris(trimethylsilyl)[trimethoxysilyl]silane (160).....	180
10.2	Synthesis of bis(trimethylsilyl)[trimethoxysilyl]silylpotassium.18-crown-6 (161)	180
10.3	Synthesis of 2,5-bis(trimethoxysilyl)-2,5-bis(trimethylsilyl)decamethylhexasilane (162).....	181
10.4	Conclusion.....	183
11	UV-Vis study of oligosilanes containing a hypervalent silicon atom	185
11.1	Oligosilanes containing a silatranyl substituent.....	185
11.2	Cyclohexasilane containing silatranyl substituent	186
11.3	Oligosilane containing silocanyl substituent.....	187
11.4	Conclusion.....	188
12	Experimental section.....	190
12.1	General Experimental	190
12.1.1	Chemical substances.....	190
12.2	Analytical methods.....	191
12.2.1	Nuclear magnetic resonance (NMR) spectroscopy.....	191
12.2.2	Gas chromatography.....	191
12.2.3	Mass spectroscopy.....	191
12.2.4	Direct insertion electron impact mass spectrometry (DI-EI)	191
12.2.5	Transmission electron microscope (TEM)	191
12.2.6	Scanning electron microscope (SEM)	191
12.2.7	Dynamic light scattering (DLS) analysis	192

12.2.8	X-ray crystal structure analysis	192
12.2.9	X-ray powder diffraction (XRD) analysis.....	192
12.2.10	Thermogravimetric analysis (TGA)	192
12.2.11	UV-Visible spectroscopy	192
12.2.12	Elemental analysis.....	192
12.2.13	Fourier-transform infrared spectroscopy (FT-IR)	192
12.2.14	Small angle X-ray scattering (SAXS)	193
12.2.15	Melting point.....	193
12.3	Other equipment	193
12.3.1	Tube furnace	193
12.3.2	Centrifuge.....	193
12.4	Synthesis of chemical compounds	194
12.4.1	Pentakis(trimethylsilyl)digermane (1)	194
12.4.2	1,1,2,2-Tetrakis(trimethylsilyl)digermane (8)	195
12.4.3	Bis(trimethylsilyl)[tris(trimethylsilyl)silyl]germane (11)	196
12.4.4	Bis(trimethylsilyl)pentamethyldisilanylgermane (14).....	197
12.4.5	(Pentamethyldisilanyl)tris(trimethylsilyl)germane (16).....	198
12.4.6	Bis(trimethylsilyl)pentamethyldisilanylgermyl-potassium.18-crown-6 (15).....	199
12.4.7	(<i>tert</i> -Butyldiphenylsilyl)tris(trimethylsilyl)germane (26)	200
12.4.8	1-(<i>tert</i> -Butyl)-3,3,3-trimethyl-1,1-diphenyl-2,2-bis(trimethylsilyl)trisilane (27)	201
12.4.9	((<i>tert</i> -Butyldiphenylsilyl)bis(trimethylsilyl)germyl)potassium.18-crown-6 (30)	202
12.4.10	2- <i>tert</i> -Butyl-2,2-diphenyl-1,1-bis(trimethylsilyl)disilanyl)potassium.18-crown-6 (31).....	203
12.5	Synthesis of oligosilanylsilatranes	204
12.5.1	Synthesis of N(CH ₂ CH ₂ OSiMe ₃) ₃ (39)	204
12.5.2	1-Chlorosilatrane ⁷⁷ (40).....	205
12.5.3	Phenylsilatrane ^{77,79} (41)	206
12.5.4	1-Bromosilatrane ¹¹⁰ (42).....	207
12.5.5	1-Silatranyltriflate (43).....	208
12.5.6	Tris(trimethylsilyl)silatranylsilane (44)	209
12.5.7	Bis(trimethylsilyl)methylsilatranylsilane (55)	211
12.5.8	Bis(trimethylsilyl)ethylsilatranylsilane (57)	212
12.5.9	Bis(trimethylsilyl)phenylsilatranylsilane (60)	213
12.5.10	(<i>tert</i> -Butyldimethylsilyl)bis(trimethylsilyl)silatranylsilane (62).....	214
12.5.11	Bis(trimethylsilyl)isopropylsilatranylsilane (65)	215
12.5.12	1,1-Bis(trimethylsilyl)-1-silatranyl-pentamethyltrisilane (67).....	216
12.5.13	Bis(trimethylsilyl)silatranylsilane (70).....	217
12.5.14	Disilatranyl-bis(trimethylsilyl)silane (72)	218
12.5.15	2-Silatranyl-2,5,5-tris(trimethylsilyl)decamethylhexasilane (75)	219
12.5.16	2,5-Disilatranyl-2,5-bis(trimethylsilyl)decamethylhexasilane (77).....	220
12.5.17	<i>cis/trans</i> 1,4-Disilatranyl-1,4-bis(trimethylsilyl)octamethylcyclohexasilane (80)	221
12.5.18	Protonated tris(trimethylsilyl)silatranylsilane (44) with trifluoromethanesulfonic acid	223
12.5.19	Bis(trimethylsilyl)silatranylsilylpotassium.18-crown-6 (73).....	224
12.5.20	Trimethylsilylphenylsilatranylsilylpotassium.18-crown-6 (87)	225
12.5.21	(<i>tert</i> -Butyldimethylsilyl)(trimethylsilyl)silatranylsilylpotassium.18-crown-6 (88)	226
12.5.22	Trimethylsilylmethylsilatranylsilylpotassium.18-crown-6 (90).....	227
12.5.23	Trimethylsilylethylsilatranylsilylpotassium.18-crown-6 (93)	228
12.5.24	2,5-Disilatranyl-decamethylhexasilyl-2,5-dipotassium.18-crown-6 (96)	229
12.5.25	Bis[bis(trimethylsilyl)silatranylsilanyl]zinc (98)	230
12.5.26	Dicyclopentadienyl[bis(trimethylsilyl)silatranylsilyl]hafniumchloride (99).....	231

12.5.27	Dicyclopentadienyl[bis(trimethylsilyl)silatranylsilyl]zirconiumchloride (71)	232
12.6	Synthesis of oligosilanyl silatranes with other types of ligands	233
12.6.1	Tris(2-methoxyphenyl)amine ⁷⁰	233
12.6.2	Tris(2-hydroxyphenyl)amine ⁷⁰ (131)	234
12.6.3	Aminotris(phenyl-2'-oxy)silylchloride ⁷⁰ (130)	235
12.6.4	Tris(2-hydroxy-4,6-dimethylbenzyl)amine ⁷¹	236
12.6.5	Aminotris(-3',5'-dimethylbenzyl-2'-oxy)silylmethoxide ⁷¹ (133)	237
12.6.6	Aminotris(-3',5'-dimethylbenzyl-2'-oxy)silylchloride (132)	238
12.6.7	1,1,1-Aminotris(phenyl-2'-oxy)-2,2-bis(trimethylsilyl)trimethyltrisilane (135)	239
12.6.8	1,1,1-Aminotris(-3',5'-dimethylbenzyl-2'-oxy)-(4''-tris(trimethylsilyl)silyl)butanyloxysilane (139)	240
12.6.9	1,1,1-Aminotris(-3',5'-dimethylbenzyl-2'-oxy)-2,2-bis(trimethylsilyl)trimethyltrisilane (141)	241
12.7	Synthesis of oligosilanyl silocanes	243
12.7.1	Synthesis of MeN(CH ₂ CH ₂ O) ₂ SiMeCl (104)	243
12.7.2	(MeO) ₂ Si(OCH ₂ CH ₂) ₂ NMe (106)	244
12.7.3	Cl ₂ Si(OCH ₂ CH ₂) ₂ NMe (107)	245
12.7.4	2'-(2',6'-dimethyl-1',3',6',2'-dioxasilocanyl)-tris(trimethylsilyl)silane (110)	246
12.7.5	1,4-Bis-2'-(2',6'-dimethyl-1',3',6',2'-dioxasilocanyl)-1,1,4,4-tetrakis(trimethylsilyl)tetramethyltetrasilane (112)	247
12.7.6	[(Me ₃ Si) ₃ Si] ₂ Si(OCH ₂ CH ₂) ₂ NMe (116)	248
12.7.7	[(Me ₃ Si) ₃ Ge] ₂ Si(OCH ₂ CH ₂) ₂ NMe (117)	249
12.7.8	2'-(2',6'-dimethyl-1',3',6',2'-dioxasilocanyl)bis(trimethylsilyl)silanylpotassium.18-crown-6 (113)	250
12.8	Synthesis of methoxysilanes	251
12.8.1	Tris(trimethylsilyl)[trimethoxysilyl]silane (160)	251
12.8.2	Bis(trimethylsilyl)[trimethoxysilyl]silylpotassium.18-crown-6 (161)	253
12.8.3	2,5-Bis(trimethoxysilyl)-2,5-bis(trimethylsilyl)decamethylhexasilane (162)	254
12.9	Nanomaterials' synthesis	255
12.9.1	Synthesis of germanium nanoparticles	255
12.9.1.1	In <i>n</i> -heptane with precursor to dicobalt octacarbonyl ratio 20:1 at 90 °C	255
12.9.1.2	In <i>n</i> -heptane with precursor to dicobalt octacarbonyl ratio 20:1 at 142 °C	255
12.9.1.3	In <i>n</i> -dodecane with precursor to dicobalt octacarbonyl ratio 20:1 at 142 °C in presence of TOPO	255
12.9.1.4	In <i>n</i> -dodecane with precursor to dicobalt octacarbonyl ratio 20:4 at 142 °C in presence of TOPO	255
12.9.1.5	In <i>p</i> -xylene with precursor to dicobalt octacarbonyl ratio 20:1 at 142 °C in presence of TOPO	255
12.9.1.6	In <i>n</i> -dodecane without dicobalt octacarbonyl at 142 °C in presence of TOPO	256
12.9.1.7	In <i>n</i> -hexadecane without dicobalt octacarbonyl at 252 °C in presence of TOPO and oleylamine	256
12.9.2	Synthesis of indium nanoparticles	256
12.9.2.1	Indium nanoparticles capped tri- <i>n</i> -butylphosphine	256
12.9.2.2	Indium nanoparticles capped tri- <i>n</i> -butylphosphine phase transfer to the mixture of <i>n</i> -dodecane and oleylamine	257
12.9.2.3	Indium nanoparticles simultaneous phase transfer and ripening method	257
12.9.2.4	Indium nanoparticles simultaneous phase transfer and ripening method in presence of diphenylamine or 1-phenylethylamine	257
12.9.3	Synthesis of germanium nanowires with 1,1,2,2-tetrakis(trimethylsilyl)digermane (8) precursor	258
12.9.3.1	Germanium nanowires synthesis at 180 °C in <i>n</i> -dodecane in presence of TOPO	258
12.9.3.2	Germanium nanowires synthesis at 300 °C in <i>n</i> -hexadecane in presence of TOPO	258
12.9.3.3	Germanium nanowires synthesis at 300 °C in <i>n</i> -hexadecane in presence of oleylamine	258
12.9.3.4	Germanium nanowires synthesis at 350 °C in presence of oleylamine	259
12.9.3.5	Germanium nanowires synthesis at 380 °C in squalane in presence of TOPO	260
12.10	Preparation of analytical samples of nanomaterials	261

12.10.1	Germanium nanoparticles separation from solution for SEM analysis	261
12.10.2	Indium nanoparticles sample preparation for TEM analysis	261
12.10.3	Indium nanoparticles capped ligands sample preparation for FT-IR spectroscopy.....	261
12.10.4	Germanium nanowires separation from solution for SEM and TEM analysis	262
13	References	263
14	Appendix.....	268
14.1	X-ray crystallographic tables	268
14.1.1	(<i>tert</i> -Butyldiphenylsilyl)tris(trimethylsilyl)germane (26)	268
14.1.2	1-(<i>tert</i> -Butyl)-3,3,3-trimethyl-1,1-diphenyl-2,2-bis(trimethylsilyl)trisilane (27)	269
14.1.3	((<i>tert</i> -Butyldiphenylsilyl)bis(trimethylsilyl)germyl)potassium.18-crown-6 (30)	270
14.1.4	2- <i>tert</i> -Butyl-2,2-diphenyl-1,1-bis(trimethylsilyl)disilanyl)potassium.18-crown-6 (31)	271
14.1.5	Tris(trimethylsilyl)silatranysilane (44)	272
14.1.6	Bis(trimethylsilyl)methylsilatranysilane (55)	273
14.1.7	Bis(trimethylsilyl)ethylsilatranysilane (57)	274
14.1.8	Bis(trimethylsilyl)phenylsilatranysilane (60)	275
14.1.9	(<i>tert</i> -Butyldimethylsilyl)bis(trimethylsilyl)silatranysilane (62).....	276
14.1.10	Bis(trimethylsilyl)silatranysilane (70).....	277
14.1.11	Disilatranyl-bis(trimethylsilyl)silane (72)	278
14.1.12	2,5-Disilatranyl-2,5-tris(trimethylsilyl)decamethylhexasilane (77)	279
14.1.13	<i>trans</i> -1,4-Disilatranyl-1,4-bis(trimethylsilyl)octamethylcyclohexasilane (<i>trans</i> -80).....	280
14.1.14	<i>cis</i> -1,4-Disilatranyl-1,4-bis(trimethylsilyl)octamethylcyclohexasilane (<i>cis</i> -80)	281
14.1.15	Protonated tris(trimethylsilyl)silatranysilane (44) with Trifluoromethanesulfonic acid	282
14.1.16	Bis(trimethylsilyl)silatranysilyl)potassium.18-crown-6 (73).....	283
14.1.17	Trimethylsilylphenylsilatranysilyl)potassium.18-crown-6 (87)	284
14.1.18	(<i>tert</i> -Butyldimethylsilyl)(trimethylsilyl)silatranysilyl)potassium.18-crown-6 (88)	285
14.1.19	Bis[bis(trimethylsilyl)silatranysilanyl]zinc (98)	286
14.1.20	Dicyclopentadienyl[bis(trimethylsilyl)silatranysilyl]hafniumchloride (99)	287
14.1.21	MeN(CH ₂ CH ₂ O) ₂ SiMeCl (104)	288
14.1.22	1,4-bis-2'-(2',6'-dimethyl-1',3',6',2'-dioxazasilocanyl)-1,1,4,4-tetrakis(trimethylsilyl)tetramethyltetrasilane (112)	289
14.1.23	[(Me ₃ Si) ₃ Si] ₂ Si(OCH ₂ CH ₂) ₂ NMe (116)	290
14.1.24	[(Me ₃ Si) ₃ Ge] ₂ Si(OCH ₂ CH ₂) ₂ NMe (117)	291
14.1.25	Aminotris(phenyl-2'-oxy)silylchloride (130)	292
14.1.26	1,1,1-Aminotris(phenyl-2'-oxy)-2,2-bis(trimethylsilyl)trimethyltrisilane (135)	293
14.1.27	1,1,1-Aminotris(-3',5'-dimethylbenzyl-2'-oxy)-(4''-tris(trimethylsilyl)silyl)butanyloxysilane (139)	294
14.1.28	1,1,1-Aminotris(-3',5'-dimethylbenzyl-2'-oxy)-2,2-bis(trimethylsilyl)trimethyltrisilane (141)	295
14.1.29	Bis(trimethylsilyl)[trimethoxysilyl)silyl)potassium.18-crown-6 (161)	296
14.2	Curriculum Vitae	297

Table of figures:

Figure 1-1. SAED pattern of a) single crystal grain of Co-Fe alloy¹⁵, b) polycrystalline and c) amorphous Al₂O₃.¹⁶22

Figure 1-2. PDDF histogram of nanoparticles with different shapes. Globular particles with bell shaped PDDF. Cylindrical particles with small overshoot and a linear tail in the PDDF. Lamellar particles PDDF resembles to the globular PDDF, but the curvature at small r-values is different.¹⁹24

Figure 1-3. The PDDFs of core-shell particles. Depending on the $\Delta\rho$, different PDDFs can be obtained.¹⁹24

Figure 1-4. "The aggregate of two subunits make a PDDF which can be recognized by a second peak."¹⁹24

Figure 1-5. 'Illustration of two possible DPG decomposition routes leading to Au-seeded Ge nanowire growth: (a) homogeneous and (b) heterogeneous DPG decomposition.'²¹26

Figure 1-6. Ge⁰ forms from GeI₂ in presence of trioctylphosphine at higher temperatures in contrast to ambient temperature. Germanium nanowire forms due to incorporation of Ge⁰ atoms into bismuth nanocrystal.²²26

Figure 1-7. Gold-germanium phase diagram with a eutectic point at around 28 % germanium at 361 °C.²⁹27

Figure 1-8. Bismuth-germanium phase diagram with a eutectic point close to 100% bismuth at 271 °C.³⁰28

Figure 1-9. Apparatus for nanowire synthesis with supercritical fluid-liquid-solid technique.²³29

Figure 1-10. a) Schematic illustration of colloidal synthesis of semiconductor nanowires, seeding agents and as synthesized germanium/silicon nanowires are both inside a high boiling point solvent by decomposition of germanium/silicon containing precursor. b) Schematic illustration of solvent-vapor-growth of germanium nanowires, substrate containing seeding agent incorporated in a vapor phase of a high boiling point solvent which carries germanium/silicon containing precursor.²⁷29

Figure 1-11. 'Schematic illustration of wire growth process: (a) substrate after Au deposition by vacuum evaporation; (b) Au-alloy clusters formed by annealing the substrate; (c) nanocylinder wires grown from Au-alloy clusters during CVD.'³⁹31

Figure 1-12. '(a) Proposed description of the formation of crystalline Ge at Hg electrodes by ec-LLS: (1) HGeO₃⁻ (aq) is reduced at the Hg electrode surface; (2) Ge is dissolved into the Hg electrode; (3) the resultant Ge-Hg amalgam reaches the saturation point, after which Ge crystallites (denoted as cubes) precipitate within the Hg pool; (4) the initial Ge crystallites serve as subsequent crystallization centers that produce polycrystalline aggregates. (b) SEM micrograph of an angled view of the top of a Ge filament film section (scale bar: 500 nm). (c) Proposed scheme for Ge filament growth. An initial dense layer of larger Ge particles provides nucleation points for unidirectional spherulitic filament growth. New extensions to the filament length occur within the Ge-Hg amalgam at the bottom of the film.'⁴³33

Figure 1-13. 'Schematic depiction of ec-LLS process for Ge nanowire electrodeposition at an indium nanoparticle electrode on an inert conductive substrate.'⁴⁴33

Figure 1-14. 'Ge droplets penetrate the pores of the AAOs and crystallize upon cooling yielding germanium nanowires. Excess GeO₂ and AAO templates are etched away in 15% H₃PO₄ solution and freestanding germanium nanowires.'⁴⁷34

Figure 1-15. 'The schematic depicts the five different types of NWs discussed; IA: straight, defect free NWs, IB: laterally faulted NWs, IC: longitudinally faulted NWs, II: angular NWs and III: more complex, wormlike kinked NWs.'⁵⁴36

Figure 1-16. 'TEM image showing two nanowire-seed regions with brightness contrast at locations of the stacking faults along their axes in both silver seeds and germanium nanowires due to twinning. The inset shows the interface between the seed particle with steps, which influences the Ge lattice of the growing nanowire.'⁵⁵37

Figure 1-17. 'Raman spectra revealing the defect distributions for nanowires grown with different seeds, based on mismatches with the phonon confinement model (blue line) fitted curves. ¹²⁵	37
Figure 1-18. "Orbitals and resonance integrals included in the Ladder C model." ¹⁵⁹	39
Figure 2-1. Crystal structure of (tris(trimethylsilyl)(<i>tert</i> -butyldiphenylsilyl)germane (26)	51
Figure 2-2. Crystal structure of 1-(<i>tert</i> -butyl)-3,3,3-trimethyl-1,1-diphenyl-2,2-bis(trimethylsilyl)trisilane (27) ...	53
Figure 2-3. Crystal structure of ((<i>tert</i> -butyldiphenylsilyl)bis(trimethylsilyl)germyl)potassium.18-crown-6 (30) ...	55
Figure 2-4. Crystal structure of 2- <i>tert</i> -butyl-2,2-diphenyl-1,1-bis(trimethylsilyl)disilanyl)potassium.18-crown-6 (31)	56
Figure 3-1. TGA and DSC diagram of [tris(trimethylsilyl)silyl]trimethylgermane (33)	60
Figure 3-2. TGA and DSC diagram of tetrakis(trimethylsilyl)germane (34)	61
Figure 3-3. TGA and DSC diagram of hexakis(trimethylsilyl)digermane (6)	61
Figure 3-4. TGA and DSC diagram of pentakis(trimethylsilyl)digermane (1)	62
Figure 3-5. Comparison of the thermogravimetric analysis of oligosilylgermane 33 , 34 , 6 and 1	62
Figure 4-1. ²⁹ Si NMR spectrum with D ₂ O lock of reaction between tris(trimethylsilyl)germane (3) and dicobalt octacarbonyl after 3 days at 90 °C. The peak at -6.1 ppm relates to tris(trimethylsilyl)germane (3)	65
Figure 4-2. ²⁹ Si NMR spectrum with D ₂ O lock of reaction between tris(trimethylsilyl)germane (3) and dicobalt octacarbonyl (20:1 molar ratio) after 24 hours at 142 °C. The peak at -6.1 ppm which relates to tris(trimethylsilyl)germane (3) shows that most of the precursor has been consumed	65
Figure 4-3. SEM images of black residue obtained from the reaction of tris(trimethylsilyl)germane (3) with dicobalt octacarbonyl (20:1 molar ratio) in <i>n</i> -heptane at 142 °C. a) sample contains spherical particles as well as sheet like structures. b and c) spherical particles are mainly sub 1 μm. d) an isolated sub 2 μm particle	66
Figure 4-4. ²⁹ Si NMR spectrum with D ₂ O lock of reaction between tris(trimethylsilyl)germane (3) and dicobalt octacarbonyl (20:1 molar ratio) at 142 °C in <i>n</i> -dodecane in presence of TOPO. The peak at -6.1 ppm relates to tris(trimethylsilyl)germane (3) and peak at 6.9 ppm relates to hexamethyldisiloxane. a) After 24 hours. b) After 48 hours	68
Figure 4-5. SEM images of spherical particles obtained from the reaction of tris(trimethylsilyl)germane (3) with dicobalt octacarbonyl (20:1 molar ratio) in <i>n</i> -dodecane in presence of TOPO at 142 °C. Sample contains mainly spherical particles with diameter close to 1 μm beside particles with nanometer scale	69
Figure 4-6. ²⁹ Si NMR spectrum with D ₂ O lock of reaction between tris(trimethylsilyl)germane (3) and dicobalt octacarbonyl (20:4 molar ratio) at 142 °C in <i>n</i> -dodecane in presence of TOPO. The peak at -6.1 ppm relates to tris(trimethylsilyl)germane (3) and peak at 6.9 ppm relates to hexamethyldisiloxane. a) After 24 hours. b) After 48 hours	71
Figure 4-7. SEM images of spherical particles obtained from the reaction of tris(trimethylsilyl)germane (3) with dicobalt octacarbonyl (20:4 molar ratio) in <i>n</i> -dodecane in presence of TOPO at 142 °C. Sample contains sub 3 μm particles	72
Figure 4-8. ²⁹ Si NMR spectrum with D ₂ O lock of reaction between tris(trimethylsilyl)germane (3) and dicobalt octacarbonyl (20:1 molar ratio) at 142 °C in <i>p</i> -xylene in presence of TOPO. The peak at -6.5 ppm relates to tris(trimethylsilyl)germane (3) and peak at 6.9 ppm relates to hexamethyldisiloxane. a) After 24 hours. b) After 6 days	74
Figure 4-9. SEM images of spherical particles obtained from the reaction of tris(trimethylsilyl)germane (3) with dicobalt octacarbonyl (20:1 molar ratio) in <i>p</i> -xylene in presence of TOPO at 142 °C. Sample contains both sub 1	

µm spherical particles and very fine nanoscale particles. d) Z-contrast image shows brighter microscale particles composed of heavier elements in comparison to darker nanoscale particles.75

Figure 4-10. ²⁹Si NMR spectrum with D₂O lock of thermal decomposition reaction of tris(trimethylsilyl)germane (**3**) at 142 °C in *n*-dodecane in presence of TOPO after 48 hours. The peak at -6.1 ppm relates to tris(trimethylsilyl)germane (**3**) and peak at 6.9 ppm relates to hexamethyldisiloxane. a)76

Figure 4-11. SEM images of nanoparticles obtained from the thermal decomposition of tris(trimethylsilyl)germane (**3**) without dicobalt octacarbonyl in *n*-dodecane in presence of TOPO at 142 °C. Sample contains irregular sub 500 nm particles as well as very fine nanoparticles.77

Figure 4-12. Colloidal solution of germanium nanoparticles as synthesized from tris(trimethylsilyl)germane (**3**) in presence of TOPO and oleylamine after 20 minutes heating at 252 °C.....78

Figure 4-13. ²⁹Si NMR spectrum of colloidal solution of germanium nanoparticles synthesized from tris(trimethylsilyl)germane (**3**) in presence of TOPO and oleylamine after 20 minutes heating at 252 °C. (D₂O lock).78

Figure 4-14. DLS number distribution of colloidal solution of germanium nanoparticles as synthesized from tris(trimethylsilyl)germane (**3**) in presence of TOPO and oleylamine after 20 minutes heating at 252 °C.....79

Figure 5-1. DLS analysis of Indium nanoparticles capped TBP with different InCl₃ concentration in DMF. Down is InCl₃ concentration related to each sample.83

Figure 5-2. Relation between InCl₃ concentration in DMF and mean particle size diameter measured by DLS technique. Numbers on the left side of the squares show mean particle size.84

Figure 5-3. a) Bright filed TEM image of indium nanoparticles of sample C.....84

Figure 5-4. Fast Fourier transformation of two particles shows faint rings and dots which is a sign for partial crystallinity of particles, a) Particle 1 in Figure 5-3b, b) Particle 2 in Figure 5-3b.85

Figure 5-5. SAED patterns of two indium nanoparticles in Figure 5-3 show amorphous structures.85

Figure 5-6. X-ray diffraction pattern of indium nanoparticles. A large peak at the beginning of XRD pattern shows amorphous structure of nanoparticles. Due to weakness of peaks it is not possible to determine the crystalline compound(s). The peak at 30 degree could relate to indium oxide caused by surface oxidation during sample transfer to XRD instrument.86

Figure 5-7. a) Indium nanoparticles in DMF at the bottom of vial, the top transparent solution is a mixture of dodecane and oleylamine,87

Figure 5-8. DLS number distribution of: Blue curve) indium nanoparticles after phase transfer to *n*-dodecane/oleylamine mixture with average diameter of 14 nm. Green curve) as prepared indium nanoparticles in DMF with average diameter of 8 nm.87

Figure 5-9. FT-IR spectra red line) Indium nanoparticles capped TBP, blue line) pure TBP.89

Figure 5-10. FT-IR spectra red line) Indium nanoparticles after phase transfer with sign of oleylamine,89

Figure 5-11. DLS intensity distribution of colloidal solution of indium nanoparticles with *n*-dodecane/oleylamine mixture. Blue line relates to as synthesized sample. Red line relates to the same sample after 7 days. Although as synthesized nanoparticles are mono-dispersed without any sign of agglomeration but sign of agglomeration appears in old sample.92

Figure 5-12. DLS intensity distribution of colloidal solution of indium nanoparticles with *n*-dodecane/oleylamine-diphenylamine mixture. Blue line relates to as synthesized sample. Red line relates to the same sample after 70 days. Nanoparticles are mono-dispersed without any sign of agglomeration in both as synthesized and old sample.92

Figure 5-13. FT-IR spectra (red line) pure oleylamine, (violet line) indium nanoparticles from *n*-dodecane/oleylamine-diphenylamine, (blue line) indium nanoparticles from *n*-dodecane/oleylamine, (green line) pure TBP93

Figure 5-14. Distance distribution function $p(r)$ of as synthesized colloidal solution of indium nanoparticles. Red line: indium nanoparticles in presence of oleylamine/diphenylamine. Blue line: indium nanoparticles in presence of oleylamine. Green line: monodispersed sample with symmetrical bell shaped histogram. Sample with oleylamine/diphenylamine has a more narrow distance distribution and contains sub 10 nm particles, compared to sub 12 nm particles in the sample with only oleylamine.....94

Figure 6-1. Indium-germanium phase diagram with a eutectic point at 99.98% indium at 156 °C.¹⁰⁶97

Figure 6-2. SEM image of indium catalyzed germanium nanowires synthesized at 180 °C in presence of TOPO with a polydispersed colloidal solution of indium nanoparticles. a) High yield of germanium nanowires. b) The spheres on tip of nanowires are indium nanoparticles. Due to polydispersity of colloidal solution of indium nanoparticles, numerous fine germanium nanowires have covered larger nanowires.....99

Figure 6-3. Bright field TEM images of germanium nanowires synthesized at 180 °C shows worm-like nanowires.99

Figure 6-4. High resolution TEM images showing atomic planes and crystalline structure of germanium nanowires however due to crystalline faults they do not have a well-ordered crystalline structure.100

Figure 6-5. EDS analysis of indium catalyzed germanium nanowires synthesized at 180 °C (signals for Cu, Co, Fe and C relates to the TEM grid). a) Germanium nanowire. b) Indium nanoparticle at the tip of germanium nanowire.....101

Figure 6-6. Bright field TEM image of indium catalyzed germanium nanowires synthesized at 300 °C in presence of TOPO. Nanowires are curly and highly twisted.103

Figure 6-7. High resolution TEM images of indium catalyzed germanium nanowires synthesized at 300 °C in presence of TOPO, showing atomic planes and crystalline structure of germanium nanowires; however, due to crystalline faults they do not have a well-ordered crystalline structure.103

Figure 6-8. SEM image of indium catalyzed germanium nanowires synthesized at 300 °C in presence of oleylamine. More straight nanowires are present in this sample in comparison to the sample synthesized in presence of TOPO.104

Figure 6-9. Bright field TEM image of indium catalyzed germanium nanowires synthesized at 300 °C in presence of oleylamine.....104

Figure 6-10. a) Bright field TEM image, b) SAED pattern, c) Dark field TEM image of same germanium nanowire. d) Bright field TEM image, e) SAED pattern, f) Dark field TEM image of another germanium nanowire. Although germanium nanowires are crystalline, numerous planar defects (stacking faults) exists parallel to the nanowires axis. g) dark field TEM image of a germanium nanowire and h) related SAED pattern of the nanowire with [001] zone axis.105

Figure 6-11. a & b) dark field TEM images of a germanium nanowire with different Bragg conditions. c) Overlay results of a (green) & b (red) shows presence of planar defects (stacking faults) in the structure.106

Figure 6-12. SEM image of indium catalyzed germanium nanowires synthesized at 350 °C in presence of oleylamine. a) Irregular and coagulated germanium nanoparticles along with a few number of curly germanium nanowires present in the sample. b) Spherical micro scale particles.....107

Figure 6-13. SEM image of indium catalyzed germanium nanowires synthesized at 350 °C in presence of oleylamine. a) EDS analysis of table 6-3 relates to the red box. b) Presence of spherical microscale germanium particles among nanowires. c, d) high yield of germanium nanowires.108

Figure 6-14. SEM image of indium catalyzed germanium nanowires synthesized at 350 °C in pure oleylamine. a) Presence of some spherical microscale particles among nanowires. b) Some of germanium nanowires are straight.	109
Figure 6-15. SEM image of indium catalyzed germanium nanowires synthesized at 350 °C in a mixture of oleylamine and TOPO. a) A large number of spherical microscale particles of germanium were formed in presence of TOPO. b) A few number of germanium nanowires are in between of spherical microscale particles of germanium.	110
Figure 6-16. SEM image of indium catalyzed germanium nanowires synthesized at 380 °C in squalane in presence of TOPO. Instead of germanium nanowires, agglomerated germanium nanoparticles were formed.	111
Figure 7-1. a) ²⁹ Si NMR, b) ¹ H NMR spectrum of reaction between tris(trimethylsilyl)silylpotassium (45) and 1-chlorosilatrane (40). A mixture of tetrakis(trimethylsilyl)silane (47), tris(trimethylsilyl)silane (48) and tris(trimethylsilyl)silatranylsilane (44) was obtained. NMR is performed in toluene with D ₂ O lock.	118
Figure 7-2. a) ²⁹ Si NMR, b) ¹ H NMR spectrum of reaction between bis[tris(trimethylsilyl)silyl]magnesium (46) and 1-chlorosilatrane (40). Instead of tris(trimethylsilyl)silatranylsilane (44) just tris(trimethylsilyl)silane (48) formed. NMR is performed in toluene with D ₂ O lock.	119
Figure 7-3. a) ²⁹ Si NMR, b) ¹ H NMR spectrum of synthesis of silatrane 44 via the reaction of tris(trimethylsilyl)silylpotassium (45) and 1-bromosilatrane. The final product is a mixture of tetrakis(trimethylsilyl)silane (47), hexakis(trimethylsilyl)disilane (48) and tris(trimethylsilyl)silane(49). NMR is performed in benzene with D ₂ O lock.	120
Figure 7-4. a) ²⁹ Si NMR, b) ¹ H NMR spectrum of synthesis of silatrane 44 via the reaction of tris(trimethylsilyl)silylpotassium (45) and 1-silatranyltriplate (43). Spectrum shows mostly the target silatrane 44 with small amount of tetrakis(trimethylsilyl)silane (47). NMR is performed in CDCl ₃	122
Figure 7-5. Crystal structure of tris(trimethylsilyl)silatranylsilane (44).	124
Figure 7-6. Crystal structure of bis(trimethylsilyl)methylsilatranylsilane (55).	126
Figure 7-7. Crystal structure of bis(trimethylsilyl)ethylsilatranylsilane (57).	128
Figure 7-8. Crystal structure of bis(trimethylsilyl)phenylsilatranylsilane (60).	129
Figure 7-9. Crystal structure of (<i>tert</i> -butyldimethylsilyl)bis(trimethylsilyl)silatranylsilane (62).	132
Figure 7-10. Crystal structure of bis(trimethylsilyl)silatranylsilane (70)	134
Figure 7-11. Crystal structure of disilatranyl-bis(trimethylsilyl)silane (72).	136
Figure 7-12. Crystal structure of 2,5-disilatranyl-2,5-bis(trimethylsilyl)decamethylhexasilane (77).	139
Figure 7-13. Crystal structure of <i>trans</i> -1,4-disilatranyl-1,4-bis(trimethylsilyl)octamethylcyclohexasilane (<i>trans</i> - 80). The ring is engaging a chair conformation.	140
Figure 7-14. Crystal structure of <i>cis</i> -1,4-disilatranyl-1,4-bis(trimethylsilyl)octamethylcyclohexasilane (<i>cis</i> - 80) with a twisted boat conformation of the six membered ring.	141
Figure 7-15. Crystal structure of Protonated tris(trimethylsilyl)silatranylsilane (44) with trifluoromethanesulfonic acid.	143
Figure 7-16. Crystal structure of bis(trimethylsilyl)silatranyl silyl potassium.18-crown-6 (73).	146
Figure 7-17. Crystal structure of trimethylsilylphenylsilatranyl silyl potassium.18-crown-6 (87)	148
Figure 7-18. Crystal structure (<i>tert</i> -butyldimethylsilyl)(trimethylsilyl)silatranyl silyl potassium.18-crown-6 (88)	150

Figure 7-19. Crystal structure of bis[bis(trimethylsilyl)silatranylsilanyl]zinc (98).....	152
Figure 7-20. Crystal structure of dicyclopentadienyl[bis(trimethylsilyl)silatranylsilyl]hafniumchloride (99)	154
Figure 8-1. Crystal structure of aminotris(phenyl-2'-oxy)silylchloride (130)	159
Figure 8-2. Crystal structure of tris(2-hydroxy-4,6-dimethylbenzyl)amine. hydrogenchloride (134)	160
Figure 8-3. Crystal structure of 1,1,1-aminotris(phenyl-2'-oxy)-2,2-bis(trimethylsilyl)trimethyltrisilane (135) ..	162
Figure 8-4. Crystal structure of N[CH ₂ (Me ₂ C ₆ H ₂)O] ₃ SiOCH ₂ CH ₂ CH ₂ CH ₂ Si(SiMe ₃) ₃ (139).....	164
Figure 8-5. Crystal structure of 1,1,1-aminotris(-3',5'-dimethylbenzyl-2'-oxy)-2,2-bis(trimethylsilyl)trimethyltrisilane (141).....	166
Figure 9-1. Crystal structure of MeClSi(OCH ₂ CH ₂) ₂ NMe (104).....	170
Figure 9-2. Crystal structure of 1,4-bis-2'-(2',6'-dimethyl-1',3',6',2'-dioxazasilocanyl)-1,1,4,4-tetrakis(trimethylsilyl)tetramethyltetrasilane (112)	173
Figure 9-3. Crystal structure of [(Me ₃ Si) ₃ Si] ₂ Si(OCH ₂ CH ₂) ₂ NMe (116).....	176
Figure 9-4. Crystal structure of [(Me ₃ Si) ₃ Ge] ₂ Si(OCH ₂ CH ₂) ₂ NMe (117)	177
Figure 10-1. Crystal structure of bis(trimethylsilyl)[trimethoxysilyl]silylpotassium.18-crown-6 (161).....	182
Figure 11-1. UV.Vis spectra of different oligosilanes with SiMe ₃ , silatranyl and methoxy substituents.....	185
Figure 11-2. UV.Vis spectra of cyclohexasilanes with SiMe ₃ and silatranyl substituents.	186
Figure 11-3. UV.Vis spectra of different oligosilanes with silocanyl substituent.	187

Chapter 1

Introduction

1 Introduction

1.1 Nanoparticles

1.1.1 Synthesis of germanium nanoparticles

1.1.1.1 Thermal decomposition of germanium precursors

Synthesis of germanium nanoparticles by thermal decomposition of a germanium containing precursor occurs in heated high boiling solvents. For example, Zaitseva et al.¹ have reported synthesis of germanium nanocrystals by thermal decomposition of different germanium precursors like tetraethylgermane (TEG), tetrabutylgermane (TBG) and trichlorogermane (TCG) in high boiling solvents like tri-*n*-octylamine, squalene and octacosane. Below 360 °C only amorphous germanium nanoparticles were reported; however at 410 °C in squalene with TCG as precursor, depending on the synthesis time, narrow size distribution germanium nanoparticles with mean particle diameter of 4 and 6 nm were synthesized. Nanoparticles with mean size diameter of 5 nm were reported by TEG in octacosane at 425 °C. In contrast to TCG and TEG, nanoparticles with wide size distribution and mean particle diameter of 9 nm were obtained with TBG.¹

Schaak and co-workers have reported also synthesis of crystalline germanium nanoparticles with GeI₄ as precursor in presence of oleic acid and hexamethyldisilazane (HMDS) in oleylamine at 260 °C in reflux condition.² A series of different experiments revealed the key variables that were important for formation of Ge nanocrystals. It was found that both oleic acid and HMDS were important parameters for formation of mono-dispersed crystalline nanoparticles. Without HMDS, formation of amorphous and without oleic acid, formation of agglomerated nanoparticles has been reported.²

1.1.1.2 Reduction of germanium halide

Kauzlarich and co-workers³ have reported synthesis of butyl-capped germanium nanoparticles with mean particle size of 4 nm via reaction of GeCl₄ with sodium naphthalenide in glyme at room temperature, followed by addition of *n*-BuMgCl to produce alkyl-terminated nanoparticles. It was found that an organic polymeric side product containing germanium also formed during the reaction. Upon removal of the organic side product by heat treatment in vacuum, undesirable transformation of initial crystalline nanoparticles to amorphous nanoparticles occurred above 300 °C; however further heat treatment above 561 °C resulted in phase transfer of amorphous nanoparticles again to crystalline nanoparticles. Upon heat treatment above 561 °C particles growth to approximately 8 nm in diameter was observed.³

In a different approach Heath and co-workers⁴ have reported reaction of various germanium halides mixtures with an ultrafine NaK alloy dispersion in heptane (prepared by ultrasonication of liquid NaK alloy) under inert atmosphere in order to obtain amorphous germanium nanoparticles.⁴ Further heat treatment of the amorphous product in a sealed pressure vessel at 270 °C for 24-48 h under nitrogen, gave crystalline germanium nanoparticles. Depending on reagents and amount of them, Ge nanocrystals with approximately 6, 10 and 20 nm in diameter were obtained.⁴

1.1.1.3 Metathesis reactions of germanium Zintl salts

Kauzlarich and co-workers⁵ have reported the metathesis reaction that occurs between GeCl₄ and Zintl salts such as magnesium germanide (Mg₂Ge), sodium germanide (NaGe) and potassium germanide (KGe) in reflux condition, for synthesis of colloidal solution of crystalline Ge nanoparticles. Upon refluxing GeCl₄ and different Zintl salts in glyme solvents for different period of time depending on solvent type, Ge nanocrystals with diameters between 2 and 10 nm were formed. It was found that the type of solvent and the amount of reagents directly affects the particles diameter.⁵

1.1.2 Synthesis of indium nanoparticles

Synthesis of nanoparticles with reduction method is rapid and feasible even at low temperatures. Moreover it is possible to produce mixture of several elements or alloy by simultaneous reduction of two or even more metal salts.⁶ Despite the advantages, final particle size distribution of the product is highly dependent on various parameters such as reductant,⁷ solvent and surfactant type.⁸

Average size of nanoparticles synthesized by reduction mechanism is highly dependent on reaction driving force. In case of copper nanoparticles the average size of nanoparticles decreases by increase in the reaction driving force. During the redox process two half-cell reactions were taken place. One cell is the reduction of copper ion to metallic copper or specifically copper nanoparticles and another cell is the oxidation of reductant. According to reverse relation between driving force (electromotive force) and particle size, type of reductant affects the particles diameter, therefore by choosing the right reductant smaller particles can be obtained.⁷

Copper nanoparticles synthesis in water and ethylene glycol (EG) as polar solvents in presence of polyvinyl pyrrolidone (PVP) as polymeric capping agent were studied. Copper nanoparticles synthesized in water had a wide size distribution and were not stable for a long time due to oxidation and formation of copper oxide (I), but in contrast those particles which were synthesized in EG had a narrow size distribution and smaller mean particle size and were fairly stable even after 22 days. PVP as a polymeric capping agent had a profound effect on reducing particle size, and any increase in the amount of PVP, directly decreased particle size of the product.⁸

Tilley and co-workers have reported synthesis of indium nanoparticles via reduction of indium salt with LiBH₄ (Equation 1-1).⁹ It is argued that the electromotive force for the reaction of anhydrous indium(III) chloride with LiBH₄ is sufficient for formation of fine indium nanoparticles.⁹



(Equation 1-1)

In this study isobutylamine as solvent and three different capping ligands - tri-*n*-octylphosphine (TOP), tri-*n*-octylphosphine oxide (TOPO) and oleylamine - were used and indium nanoparticles with diameter less than 10 nm were synthesized at 70 °C under reflux condition.

In contrast to sub-10 nm indium nanoparticles in isobutylamine, highly faceted indium polyhedral structures with sizes varying between 20 nm to several micrometers depending on the ratio between indium(III) chloride and TOPO were obtained in N,N-diethylaniline.⁹

In another study indium nanoparticles capped oleylamine synthesized at 100 °C in reflux condition in diethylene glycol were transferred to pentane or dodecane by Hammarberg et al.¹⁰ According to the TEM image of the transferred nanoparticles, the particles were non-agglomerated with diameters between 10 to 12 nm, however in contrast to TEM results, DLS analysis of transferred nanoparticles demonstrated mean particle size of 18 nm with presence of some particles around 40 nm.¹⁰

1.1.3 Size and morphology characterization methods

1.1.3.1 Transmission electron microscope

Transmission electron microscope (TEM) as a powerful instrument has emerged to study the structure of materials and it has a unique capability to provide morphological information, crystallographic data, and chemical composition on a very small scale.¹¹

High-resolution transmission electron microscope (HRTEM) is one of the most powerful analytical instruments used for characterization of nanomaterials which provides information in atomic scale and it is an essential instrument for nanotechnology.¹²

HRTEM imaging of nanoparticles has several important advantages. Firstly, the actual particle size and morphology can be observed. Secondly, the whole crystal structure including, crystal defects, lattice mismatch and atomic planes can be imaged.¹³

Moreover, selected area electron diffraction (SAED) as a diffraction technique in HRTEM can be used to characterize crystal structure and identify crystal defects. In principle, SAED is similar to X-ray powder diffraction, but areas much smaller in size can be analyzed by SAED in comparison to X-ray powder diffraction.¹⁴ According to SAED pattern of a sample, it is easily possible to differentiate between amorphous, single crystal and polycrystalline materials and even an isolated nanostructure. Figure 1-1 shows SAED pattern of different materials with amorphous or crystalline structure.

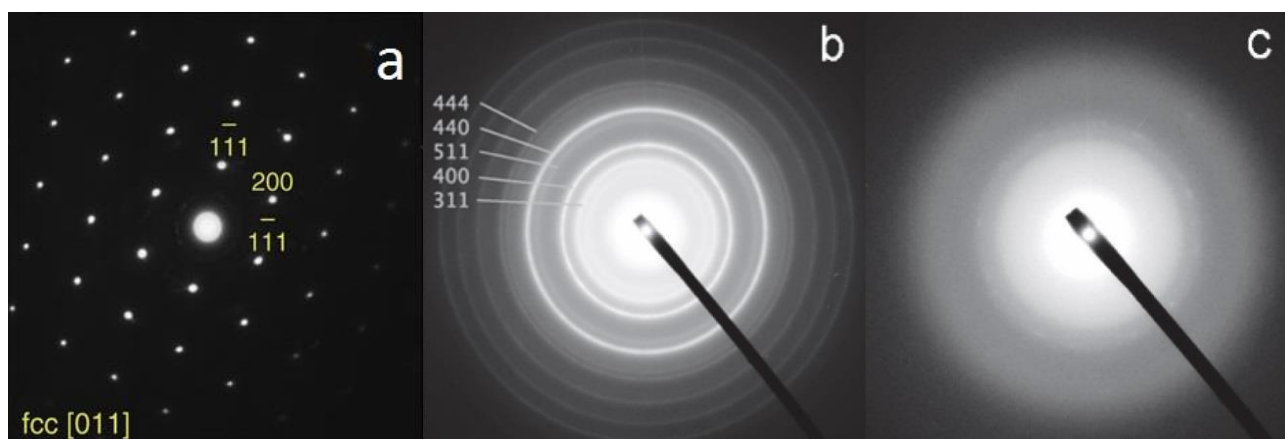


Figure 1-1. SAED pattern of a) single crystal grain of Co-Fe alloy¹⁵, b) polycrystalline and c) amorphous Al₂O₃.¹⁶

1.1.3.2 Dynamic light scattering

Although imaging a sample with HRTEM provides direct estimate of size, morphology and texture in high resolution, in case of nanoparticles it is important to count a large number of particles from several images in a time consuming procedure, in order to obtain a complete statistical average. Electron microscopy can be employed only for analysis of dry specimens. This means that colloidal solutions can be examined only after solvent evaporation which may affect the native structure of colloids, as they are prone to aggregation during solvent evaporation. To solve mentioned problems a nondestructive technique named as dynamic light scattering (DLS) has emerged for particle size characterization of colloidal solutions, especially in the nanoscale range.¹⁷

In practice, suspended nanoparticles in a liquid are constantly moving. The nanoparticles are floating in liquid due to Brownian motion. Brownian motion for floating nanoparticles is the constant movement of nanoparticles due to the permanent collision of the molecules of the liquid. A very important feature of the Brownian motion is that large particles move slowly and small particles move more quickly. DLS technique uses this significant characteristic of the Brownian motion to determine the size of particles. When the red laser beam shines on the moving particles, each particle scatters the beam depending on its own characteristics and velocity. Finally the scattered light from the particles is collected by a photodiode (detector) for further analysis.¹⁸

DLS has the capability to provide averaged estimate of particle size from a large number of particles in colloidal solutions. Moreover, it can measure a wide range of particle sizes in the submicron range in a very short period of time.¹⁷

1.1.3.3 Small angle X-ray scattering

Small angle X-ray scattering (SAXS) is a nondestructive analytical method to determine the averaged particle size and the shape of particles in solution. In general, X-rays are sent to the colloidal solution of particles, and then the result of nanoparticles interaction with beam will be sent out from each particle as a signal. Therefore, the average structure of all particles within the colloidal solution can be determined. The SAXS technique is accurate for particles approximately below 30 nm without the need for special sample preparation.¹⁹

Depending on the particles structure different types of histograms named as “pair-distance distribution functions” (PDDF) can be observed. In practice, different histograms of distances inside the particles can be found. Globular particles form a bell shaped histogram with a symmetrical peak. Cylindrical particles form a small overshoot and linear tail in the PDDF histogram and lamellar particles form a histogram which is similar to the globular PDDF histogram, but the curvature at small r-values is slightly different (Figure 1-2). In general, the r-value at the decay point of histogram to zero indicates the largest distance that can be found inside the particle.¹⁹ Inhomogeneous (or core-shell) particles form a different PDDF histogram because the histogram is weighted by unequal ($\Delta\rho$) values that are connected by each distance. Thus, all distances that crosses the border from positive to negative $\Delta\rho$ -values count negative which produces a dip in the histogram (Figure 1-3). According to Figure 1-4 PDDF histogram of samples containing aggregated particles show two peaks but in contrast to the second peak in the PDDF histogram of core-shell particles, the second peak in samples with aggregation is smaller.¹⁹

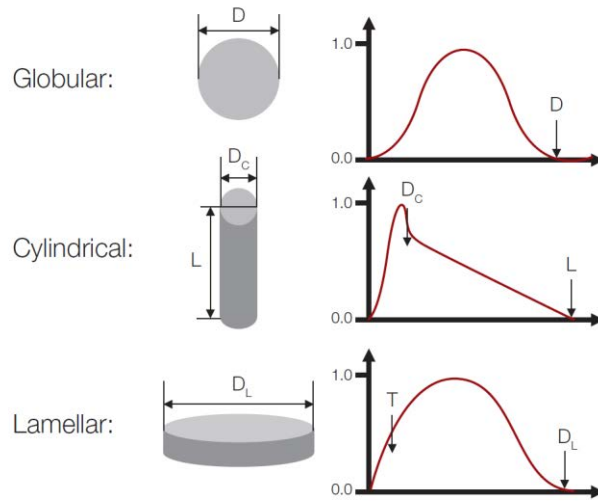


Figure 1-2. PDDF histogram of nanoparticles with different shapes. Globular particles with bell shaped PDDF. Cylindrical particles with small overshoot and a linear tail in the PDDF. Lamellar particles PDDF resembles to the globular PDDF, but the curvature at small r -values is different.¹⁹

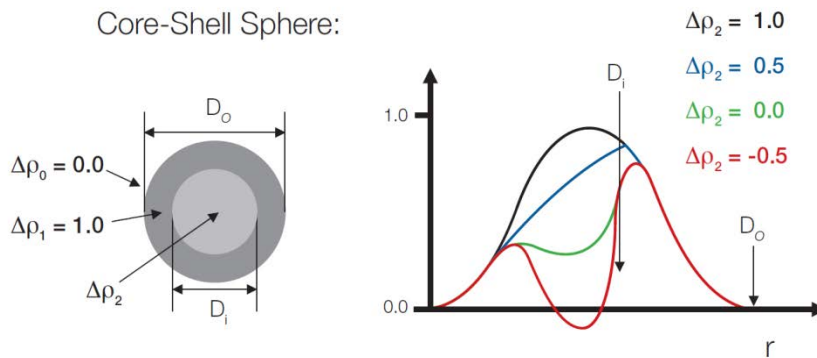


Figure 1-3. The PDDFs of core-shell particles. Depending on the $\Delta\rho$, different PDDFs can be obtained.¹⁹

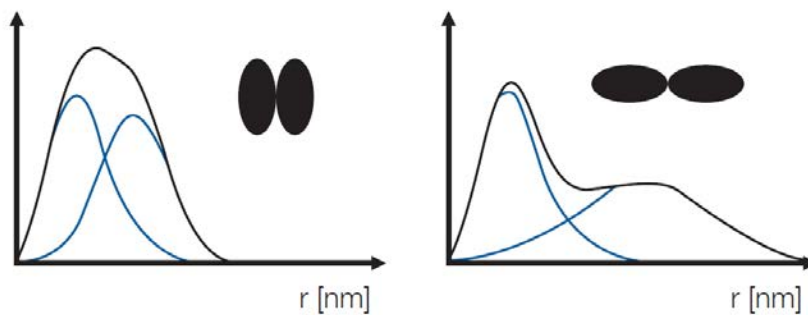


Figure 1-4. "The aggregate of two subunits make a PDDF which can be recognized by a second peak."¹⁹

1.2 Germanium nanowires

1.2.1 Different synthesis methods

Mechanism involving synthesis of germanium nanowires with seeding agents is based on initially decomposition of precursor molecules containing germanium atoms and formation of reactive Ge^0 species, followed by diffusion of reactive Ge^0 species into seeding agents or nanocrystals and formation of an alloy nanocrystal. Once the eutectic condition of the alloy nanocrystal is reached, it becomes a molten droplet due to the lower melting point of the eutectic point of binary-phase systems. While the diffusion of reactive Ge^0 species continues into the molten droplet, supersaturation of germanium in the molten droplet and as a result precipitation of germanium and nucleation and growth of a crystalline nanowire from the molten droplet occurs.²⁰ Depending on the presence of the precursor in solution phase or gas phase the synthetic method divides into two different categories involving solution or gas phase method, respectively.

1.2.1.1 Solution phase methods

The solution-liquid-solid (SLS) mechanism in the first step is based on dissolution and decomposition of a precursor containing germanium atom in a solution phase. Depending on the precursor type different decomposition reactions can take place.

Diphenylgermane (DPG) is a precursor which is widely used for synthesis of germanium nanowires. Decomposition of DPG in absence of Au nanocrystals is very slow and no one would consider DPG as an appropriate precursor for SLS synthesis of Ge nanowires. However, when Au nanocrystals are introduced into the reaction, the reaction mixture turns immediately black due to the fast formation of Ge^0 . In fact Au nanocrystals have an important role on fast decomposition of DPG and formation of reactive Ge^0 species at high temperatures.²¹

Figure 1-5 shows the two possible reaction mechanisms between DPG and Au nanocrystals. In a homogeneous DPG decomposition mechanism, DPG would first redistribute to germane (GeH_4) without intervention of Au nanocrystal and then the formed GeH_4 would decompose to Ge^0 that diffuses to the Au nanocrystal.²¹

In one possible heterogeneous decomposition mechanism, disproportion decomposition of DPG to Ge^0 will occur by adsorption of DPG on the surface of Au nanocrystal. Another possible heterogeneous reaction mechanism might be adsorption of GeH_4 from solution, followed by hydrogen desorption and then Ge^0 diffusion into the seed. A third possibility for heterogeneous mechanism might be rearrangement of DPG to GeH_4 by adsorption of DPG on the surface of Au nanocrystal, followed by decomposition of GeH_4 to Ge^0 .²¹

GeI_2 is another type of precursor which is used for SLS synthesis of germanium nanowires in presence of bismuth nanoparticles. Figure 1-6 shows the possible pathway for formation of Ge^0 from GeI_2 . In presence of TOP at elevated temperatures two molecules of GeI_2 are generating one GeI_4 and one reactive Ge^0 . In contrast to decomposition of DPG which is likely depending on Au nanocrystals, formation of Ge^0 from GeI_2 occurs without intervention of bismuth nanocrystals. Finally due to germanium diffusion into bismuth nanocrystals, germanium nanowires nucleate and grow.²²

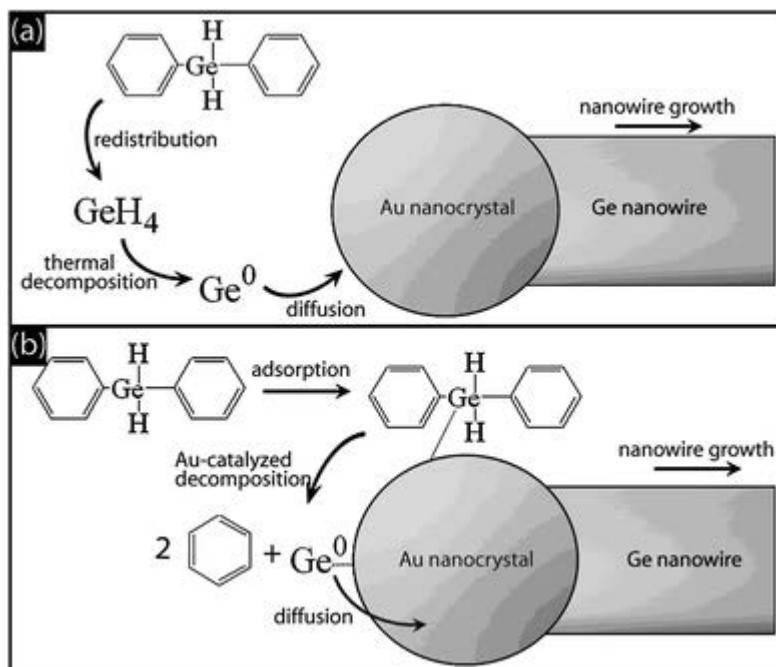


Figure 1-5. 'Illustration of two possible DPG decomposition routes leading to Au-seeded Ge nanowire growth: (a) homogeneous and (b) heterogeneous DPG decomposition.'²¹

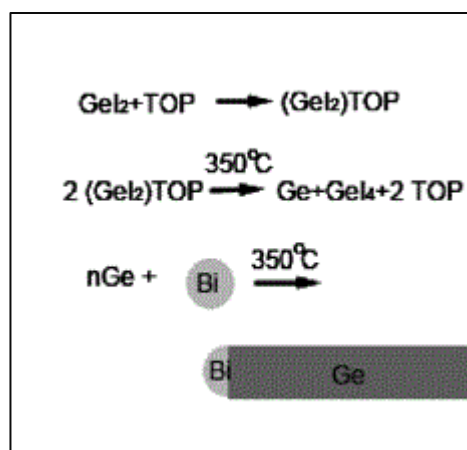


Figure 1-6. Ge^0 forms from GeI_2 in presence of trioctylphosphine at higher temperatures in contrast to ambient temperature. Germanium nanowire forms due to incorporation of Ge^0 atoms into bismuth nanocrystal.²²

Second step in the solution-liquid-solid mechanism is the formation of liquid droplets of metal nanocrystals-germanium. Different types of metal nanocrystals like Au,^{23,24} Ag,²⁵ Bi,²⁶ and Sn²⁷ as seeding agents for synthesis of germanium nanowires have been reported by different research groups. Seeding nanocrystals play an important role in precursor decomposition as well as catalyzing nanowire growth.²⁸ Beside melting point, a key factor for selection of a suitable seeding nanocrystal relates to its solvating abilities.²⁸ This phenomenon could be comprehend from binary phase diagram of germanium-seeding nanocrystal.²³ The binary phase

diagram of germanium-gold shown in Figure 1-7 displays the coexistence of a liquid solution with solid Ge above the eutectic point at 28 % Ge and a temperature of 361 °C.²⁹ Similarly binary phase diagram of germanium-bismuth shown in Figure 1-8 displays a eutectic point close to the melting point of bulk bismuth.³⁰

The general mechanism involves Ge dissolution into seeding agent to form an alloy at the initial step, then the alloy becomes a liquid droplet under continues diffusion of Ge into the initial alloy. At a certain point a further increase in the Ge concentration in the liquid droplet leads to supersaturation, precipitation, and finally axial growth of a germanium nanowire.^{24,28}

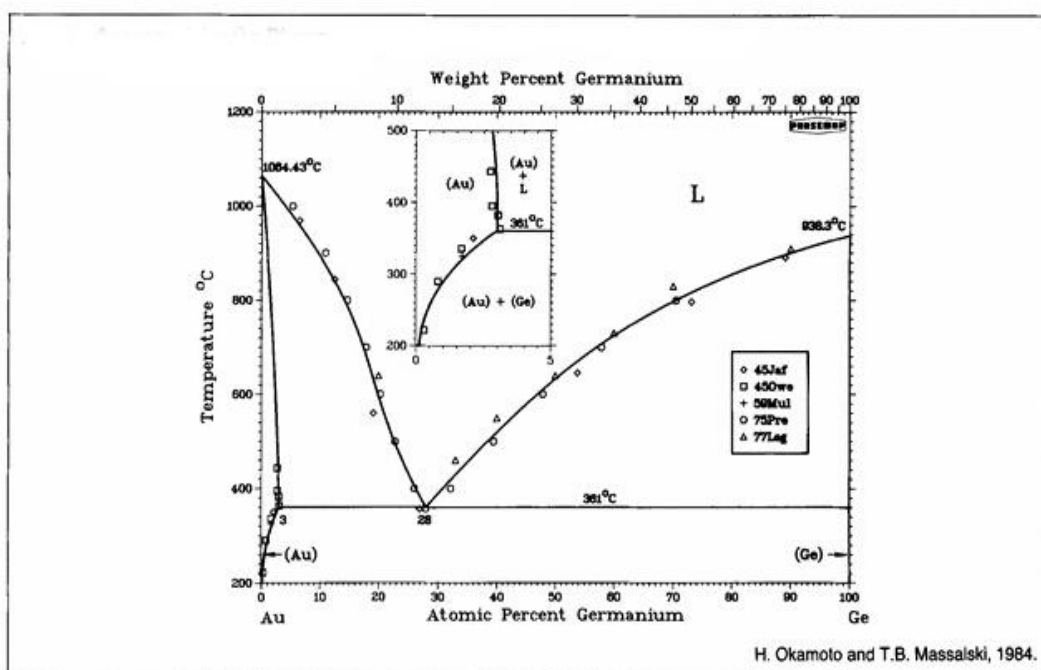


Figure 1-7. Gold-germanium phase diagram with a eutectic point at around 28 % germanium at 361 °C.²⁹

Although precursor containing germanium and seeding nanocrystals are common reagents in most synthesis methods, but synthesis environment possesses a significant effect on the quality and characteristics of nanowires.

Dispersed Au nanocrystals in solution can produce free floating nanowires with higher output than surface growth methods. The solution phase mechanism provides rational tunability of the synthesis parameters, like concentration of precursor and seeding nanocrystals, while providing a required synthesis temperature and high precursor feeding and diffusion rate for the reaction.²³

Capping ligands such as TOPO²⁶ and TOP²² are widely used in the solution synthesis of germanium nanowires to prevent the aggregation of nanowires. The presence of capping ligands on the surface of germanium nanowires causes chemical surface passivation and improves colloidal dispersibility of nanowires.²²

In general, mass production of nanomaterials is feasible with solution synthesis methods at lower cost without the need for high vacuum complex systems,²⁷ and in particular in case of Ge

nanowires, in addition to the mentioned reasons, easy tunability of the synthesis parameters and high diffusion rate environment have led to the formation of high yields of nanowires.³¹

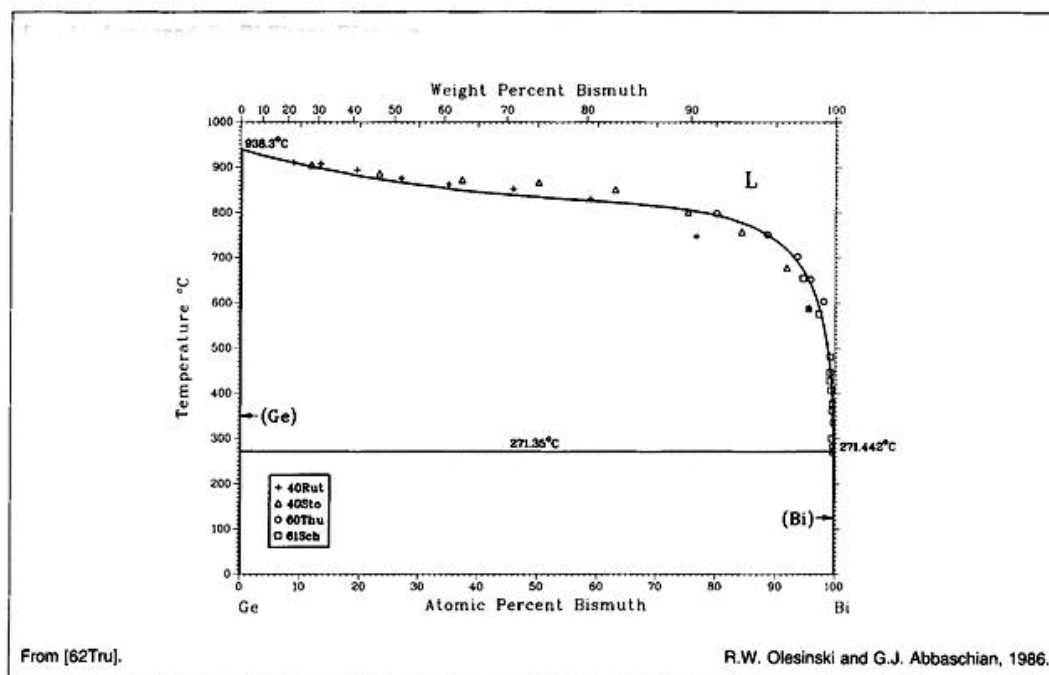


Figure 1-8. Bismuth-germanium phase diagram with a eutectic point close to 100% bismuth at 271 °C.³⁰

The solution based growth technique can be categorized into three different routes such as supercritical-fluid-liquid-solid (SFLS), colloidal and solvent-vapor-growth (SVG) routs. These techniques are different mainly because of the growth medium.²⁷

1.2.1.1.1 Supercritical fluid-liquid-solid (SFLS)

Holmes et al.³² for the first time have reported synthesis of crystalline nanowires in hexane, heated and pressurized above its critical point with alkanethiol-coated gold nanocrystals as seeding agent.³² The main necessity for the use of SFLS solvents can be explained by the fact that most organic solvents have boiling points lower than 300 °C, which is not sufficient to thermally decompose DPG or other types of precursor. In SFLS reactions, the solvent is heated above its boiling point to form a supercritical phase. In fact, SFLS media have special characters such as high solubilizing capability and special state which is between a liquid and a gas and finally facilitating temperatures which are necessary for nanowire formation.²⁷ In this synthesis technique, the pressure is prepared by the HPLC pump in the reaction vessel made of stainless steel, followed by injection of seeding agent and precursor in a low boiling solvent such as cyclohexane.²³ This technique affords a tunable synthesis of high quality and defect free crystalline germanium nanowires with high yields.³³ Figure 1-9 provides a schematic view of a system containing HPLC pump suitable for SFLS synthesis of germanium nanowires.

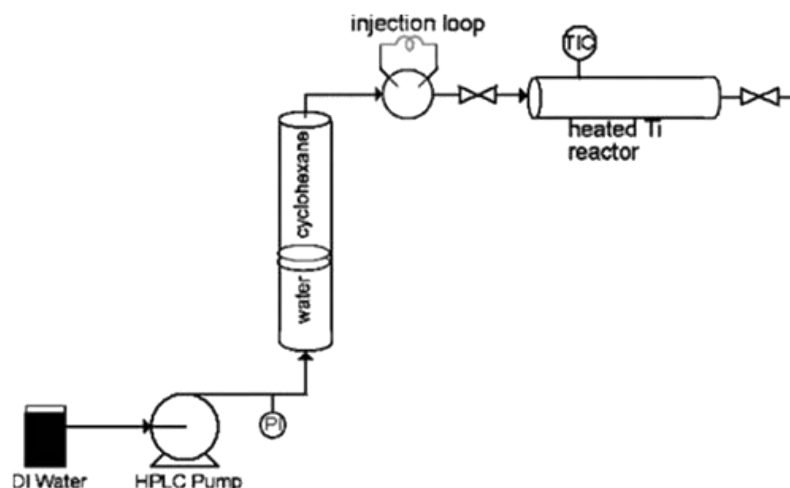


Figure 1-9. Apparatus for nanowire synthesis with supercritical fluid-liquid-solid technique.²³

1.2.1.1.2 Colloidal route

High boiling point media (above 400 °C) enables synthesis of high quality nanowires with an appropriate yield in systems with atmospheric pressure.²⁷ Synthesis of germanium nanorods with bismuth nanocrystals as seeding agent at 350 °C and synthesis of germanium nanowires with gold nanocrystals at 380 °C in both squalane and squalene as high boiling media has reported by Chockla et al.^{21,26} These appropriate high boiling organic solvents allow the previously realized obstacles to formation of crystalline nanowire in systems with atmospheric pressure to be overcome.²⁷ Thus production of nanowires with this method in mass quantities suitable for industrial applications such as printed electronics and nanowire/polymer composites is feasible.²¹ Figure 1-10a shows schematic process of colloidal synthesis of germanium nanowires.

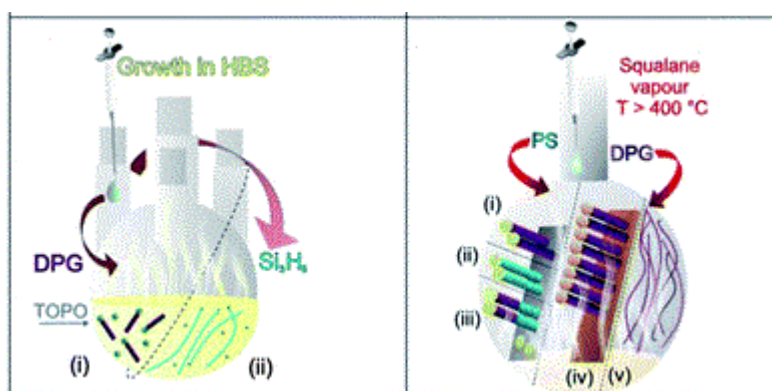


Figure 1-10. a) Schematic illustration of colloidal synthesis of semiconductor nanowires, seeding agents and as synthesized germanium/silicon nanowires are both inside a high boiling point solvent by decomposition of germanium/silicon containing precursor. b) Schematic illustration of solvent-vapor-growth of germanium nanowires, substrate containing seeding agent incorporated in a vapor phase of a high boiling point solvent which carries germanium/silicon containing precursor.²⁷

1.2.1.1.3 Solvent vapor growth (SVG)

Although high yield synthesis of germanium nanowires with high boiling point media has been reported successfully, it is not appropriate for direct growth of nanowires from a substrate. Due to that Ryan and co-workers²⁷ exploited the vapor phase of a high boiling point media for nanowire growth. In practice, in the vapor phase of a high boiling point media such as squalane or squalene related to the synthesis temperature (between 400 °C to 460 °C depending on the solvent), a wide variety of seeding agents and substrates can be incorporated.²⁷ Figure 1-10b shows schematic process of solvent-vapor-growth of germanium nanowires. In general, in solution phase methods due to the easy tunability of the synthesis parameters and high diffusion rate, mass production of Ge nanowires is possible.³¹

1.2.1.2 Gas phase methods

1.2.1.2.1 Chemical Vapor Deposition

Simply, chemical vapor deposition (CVD) involves deposition of a thin film via chemical reactions on a surface of a heated object in a closed chamber. In this technique the precursor presents in the gas phase and the chemical reactions responsible for formation of the thin film occur on or near the surface of the heated object.³⁴

GeH₄ is one of the most common precursors in the CVD synthesis of germanium nanowires,³⁵ meanwhile GeCl₄ is another type of precursor suitable for CVD synthesis of germanium nanowires.³⁶ Depending on the type of molecules used in the deposition process, different derivatives of CVD terminology exists such as metal-organic chemical vapor deposition (MOCVD) or organometallic chemical vapor deposition (OMCVD).³⁴

Similar to solution base methods, synthesis of nanowires in gas phase with CVD method via vapor-liquid-solid (VLS) mechanism, is based on formation of Ge-metal nanocrystal eutectic alloy.³⁷ The general VLS mechanism involves dissolution of reactive Ge species into a nanocrystal seed to form an alloy at the initial step, then under continuous Ge dissolution the alloy becomes a liquid droplet, at a certain point when the high concentration of Ge leads to formation of a supersaturated liquid droplet, precipitation and axial growth of a Ge nanowire from liquid droplet occurs.²⁴ According to the large number of studies the VLS mechanism dominates the axial growth of Ge nanowires.³⁷ Figure 1-11 shows a schematic illustration of the growth of nanowires by CVD-VLS method using gold nanocrystals.

Although CVD method has been widely used in the synthesis of semiconductor materials, it has some disadvantageous. In a standard CVD-VLS synthetic process, stationary seeding agents on the surface of a substrate, limit the nanowire growth on the surface. The limited number of metal catalysts in the reactor reduces the amount of producible nanowires and increases precursor waste. In addition, the processing equipment with expensive and sophisticated gas installations, high-vacuum equipment, bubblers vaporizers, and secure observation instruments increases the cost of the production.³¹

1.2.1.2.2 Laser Ablation

Lieber and co-workers²⁰ have developed a procedure utilizing laser ablation to produce semiconductor nanowires which has been proven as a successful but sophisticated method for production of germanium nanowires.³⁸ In practice, a pulsed laser shines onto a target that

contains both precursor and seeding agents. As a result of ablation, nanocrystals of alloys that contain atoms of both precursor and seed form. Then nanowires grow from these nanocrystals via VLS mechanism.²⁰

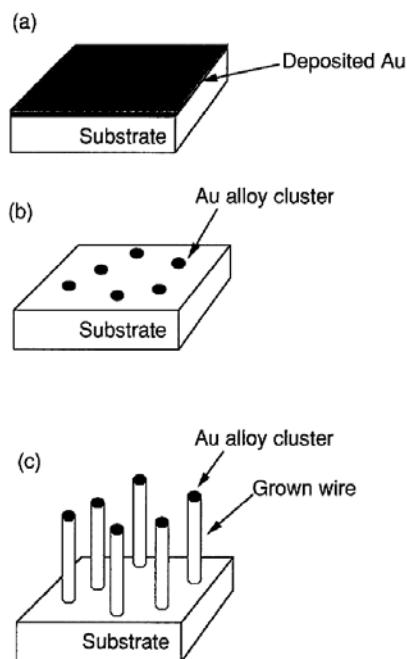


Figure 1-11. Schematic illustration of wire growth process: (a) substrate after Au deposition by vacuum evaporation; (b) Au-alloy clusters formed by annealing the substrate; (c) nanocylinder wires grown from Au-alloy clusters during CVD.³⁹

For instance the synthesis of germanium nanowires with this technique was accomplished by utilization of $\text{Ge}_{0.9}\text{Fe}_{0.1}$ alloy at a reaction temperature of 820 °C. It was found that the germanium nanowires have diameters between 3 to 9 nm and a twinning of Ge (111) plane.²⁰ Lee et al.⁴⁰ have reported synthesis of germanium nanowires with laser ablation technique, where the target was a mixture of Ge and GeO_2 instead of a metal containing target. Mechanism involving growth of germanium nanowires with a mixture of Ge and GeO_2 target was explained with the deposition of substoichiometric germanium oxide and subsequent phase separation into Ge and GeO_2 . Although the presence of GeO_2 facilitates the formation of nanowires, single crystalline germanium nanowires were covered with a thick layer of amorphous GeO_2 .⁴⁰

1.2.1.2.3 Molecular beam epitaxy

Molecular beam epitaxy (MBE) is a process where the formation of pure and highly crystalline materials occurs on a crystalline substrate in a very slow rate under high or ultra-high vacuum via continuous supply of reactive species prepared by molecular or atomic beams. With this technique the deposited layer(s) has (have) the same crystalline structure as the substrate or a structure with a similar symmetry and slight lattice parameter difference. The beams in MBE

have high thermal energy and are generated by evaporation or sublimation of appropriate materials. With MBE precise control over doping level is possible. Moreover formation of materials with different chemical composition profile along specific growth direction is feasible.⁴¹

For the first time, Omi et al.⁴² have reported synthesis of germanium nanowires by MBE. In their approach a Si (113) substrate was used for deposition of germanium vapor and formation of self-assembled Ge nanowires along the crystal orientation of the substrate. Germanium nanowires prepared with this method were constrained on Si (113) surfaces and were not single-crystalline.⁴²

1.2.1.3 Electrochemical method

1.2.1.3.1 Electrochemical liquid-liquid-solid (ec-LLS)

Maldonado and co-workers have reported synthesis of polycrystalline germanium filaments resembling germanium nanowires from an aqueous solution at ambient temperature. This method is based on electrodeposition of germanium from aqueous solution of GeO₂ followed by dissolution into a liquid Hg electrode, saturation of the liquid alloy, and precipitation as polycrystalline germanium resembling germanium nanowires.⁴³ Figure 1-12 shows the proposed mechanism for the formation of germanium filaments.

In another experiment indium nanoparticles were deposited on a conductive support such as n-type silicon or copper which is inactive toward germanium electrodeposition and used instead of the liquid Hg electrode for the ec-LLS synthesis of germanium nanowires.⁴⁴ Figure 1-13 shows this schematic ec-LLS process for germanium nanowire electrodeposition on indium nanoparticle. Due to the presence of discrete indium nanoparticles instead of the Hg pool, individual germanium nanowires instead of germanium filaments are formed. According to HRTEM study polycrystalline germanium nanowires were grown with this technique.⁴⁴

1.2.2 Non-catalytic growth of germanium nanowires

1.2.2.1 Germanium nanowires grown without catalysts

Formation and growth of germanium nanowires occurs without any seeding agents in a procedure known as self-seeding mechanism based on VLS mechanism. The self-seeding mechanism is based on the overlap and interaction between two Ge moieties at the initial step of growth which provides a suitable condition for the subsequent nanowire growth. One Ge moiety acts as a seed for another one to be incorporated into the germanium nanowire.³⁵

Holmes and co-workers reported the synthesis of germanium nanowires with self-seeding mechanism via SFLS method using oligosilylgermane precursors.^{45,46} In one approach using hexakis(trimethylsilyl)digermane as a precursor the synthesis of germanium nanowires with an amorphous silicon shell in supercritical toluene with a diameter as small as 4 nm has been reported.⁴⁵ In another approach as precursor 1,2-bis[tris(trimethylsilyl)germyl]-tetramethyl-disilane (Ge:Si/1:4), hexakis(trimethylsilyl)digermane (Ge:Si/1:3), bis[tris(trimethylsilyl)germyl]dimethylgermane (Ge:Si/1:2) or equal mixture of diphenylsilane and DPG (Ge:Si/1:1) were used and the result was the synthesis of germanium nanowires with or without an amorphous silicon shell.⁴⁶ It has been concluded that the final diameter of the

germanium nanowires depends on the ease of the liberation of germanium atoms and the Ge:Si ratio in these four different precursors.⁴⁶

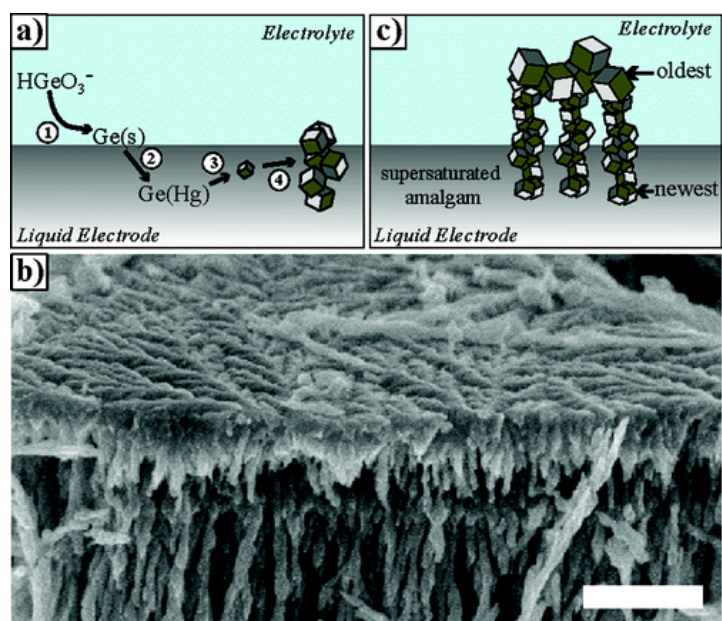


Figure 1-12. (a) Proposed description of the formation of crystalline Ge at Hg electrodes by ec-LLS: (1) HGeO_3^- (aq) is reduced at the Hg electrode surface; (2) Ge is dissolved into the Hg electrode; (3) the resultant Ge-Hg amalgam reaches the saturation point, after which Ge crystallites (denoted as cubes) precipitate within the Hg pool; (4) the initial Ge crystallites serve as subsequent crystallization centers that produce polycrystalline aggregates. (b) SEM micrograph of an angled view of the top of a Ge filament film section (scale bar: 500 nm). (c) Proposed scheme for Ge filament growth. An initial dense layer of larger Ge particles provides nucleation points for unidirectional spherulitic filament growth. New extensions to the filament length occur within the Ge-Hg amalgam at the bottom of the film.⁴³

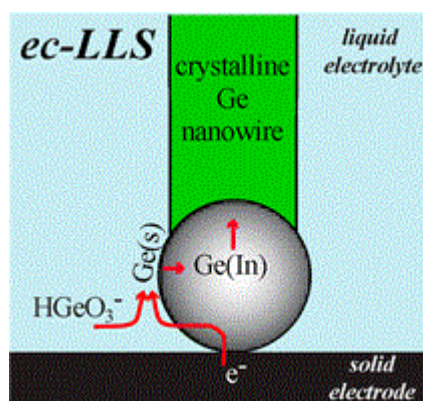


Figure 1-13. Schematic depiction of ec-LLS process for Ge nanowire electrodeposition at an indium nanoparticle electrode on an inert conductive substrate.⁴⁴

1.2.2.2 Template method

The template method is known to be a general route for the synthesis of nanomaterials. Porous materials like silicon oxide and anodic aluminum oxide (AAO) or hollow carbon nanotubes are among the appropriate templates for the growth of germanium nanowires with polycrystalline structure. Utilization of Germanium nanowires formed by this method is along with difficulties due to random orientation of germanium nanowires inside the porous materials. Further purification and assembling procedures need to be performed on nanowires to make them functional for electronic application.³⁵

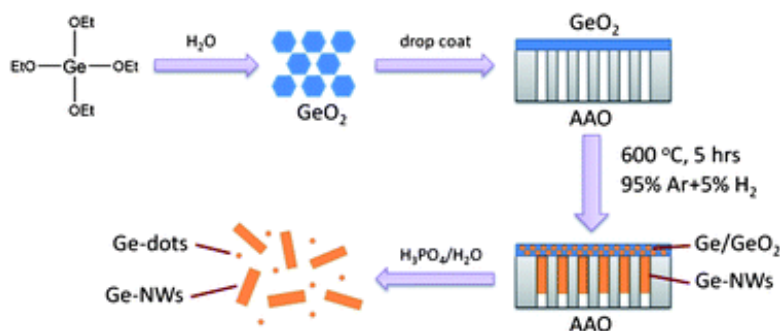


Figure 1-14. 'Ge droplets penetrate the pores of the AAOs and crystallize upon cooling yielding germanium nanowires. Excess GeO₂ and AAO templates are etched away in 15% H₃PO₄ solution and freestanding germanium nanowires.⁴⁷

Veinot and co-workers⁴⁷ have reported a template assisted synthesis of germanium nanowires using AAO templates with different pore size and a sol-gel derived GeO₂ precursor to prepare germanium nanowires via thermal heating in a slightly reducing atmosphere at 600 °C. Liberation of germanium nanowires from AAO template were performed by dissolution of the template in a diluted H₃PO₄ solution. Depending on the pore size of the template germanium nanowires with diameters from 300 nm to 40 nm were synthesized.⁴⁷ Figure 1-14 provides a schematic synthesis of germanium nanowires via the template assisted mechanism.

1.2.3 Dopants of germanium nanowires

The physical, chemical, and morphological properties of nanowires define their optical properties. Several parameters affect the emission and absorption properties and in general electronic characteristics of semiconductor nanomaterials among which are length, diameter, composition, doping level, defect concentration, crystal structure growth direction, and nature of facets.⁴⁸

For doping purposes, Group III (p-Ge) and Group V (n-Ge) are the most important elements. Acceptor elements such as boron, aluminum, gallium and indium are suitable elements for production of p-type germanium semiconductors. The maximum solid solubility of indium in germanium is $\sim 4 \times 10^{18} \text{ cm}^{-3}$ which is lower than for gallium, aluminum or boron. In contrast donor elements such as phosphorous, arsenic and antimony are suitable elements for production of n-type germanium semiconductors.⁴⁹

Diffusion of dopants beside solid solubility of them is another important factor as dopants depending on their size tend to diffuse out of the germanium matrix. Although donors with negative charge have large ionic size, they become positively charged on giving up their electrons to the germanium matrix and thus diffuse much more rapidly than the acceptors which in germanium matrix become negatively charged.⁵⁰

1.2.4 Defect formation in germanium nanowires

Beside shape, size and composition which characterizing nanowires, recently, polytype has appeared as another important aspect of research. Polytypes give the opportunity to engineer crystalline structure of nanowires and expand range of electronic and optoelectronic properties of them.⁵¹ It is reported that polytype generation has relation to primary formation of kinks.^{51,52} In simple terms formation of planar defects concomitant with nanowire kinking is the origin of the polytype.⁵¹

According to Morris J.W. in 'Defects in crystals' the most common planar defects in nanowires are stacking faults which are categorized in three different types as follow:⁵³

- i) 'Extrinsic stacking fault is one that can be created by inserting an extra plane of atoms into the structure. In the ...ABC|B|ABC... pattern, the plane marked |B| is an extrinsic stacking fault.
- ii) Intrinsic stacking fault is one that can be created by removing a plane of atoms. In the sequence ...ABC||BCABC.. the defect marked || corresponds to a missing A-plane, and is hence an intrinsic stacking fault.
- iii) Twin boundary is a surface that separates two volumes of crystal that are mirror images of one another. In the sequence ...ABCAB|C|BACBA... the plane marked C is a twin boundary; on either side the crystal has a perfect FCC structure, but the two FCC lattices are mirror images of one another across the twin plane.⁵³

1.2.4.1 Solvent effect

Ryan and co-workers⁵⁴ have studied the effect of high boiling point solvents and synthesis temperature on the morphology of non-seeded germanium nanowires and types of crystal defects in their structure. The syntheses were based on thermal decomposition of DPG in squalene at 420 °C or squalane at 420 °C and 450 °C. Formation of mainly straight and defect free germanium nanowires in squalene at 420 °C has been reported; however, in squalane at the same temperature defected and worm-like germanium nanowires has been observed. Even more crystalline defects have been reported in squalane at 450 °C.⁵⁴

Figure 1-15 provides schematic illustration of different types of crystal defects that has been reported on this research. In general single crystal (IA) nanowires, longitudinal (IC) and lateral containing stacking faulted (IB) nanowires are mostly forming in squalene; however, angular faulted (II) and more complex faulted (III, worm like) nanowires are mostly forming in squalane at 450 °C. It is found that lateral and longitudinal stacking faults are related to faulting on the closest packed plane (111) for nanowires with $\langle 111 \rangle$ and $\langle 11\bar{2} \rangle$ growth directions, respectively. Nanowires containing kink and wormlike nanowires are different, and

interplay between preferred nanowire growth direction and defect orientation is responsible for shape and morphology of these nanowires.⁵⁴

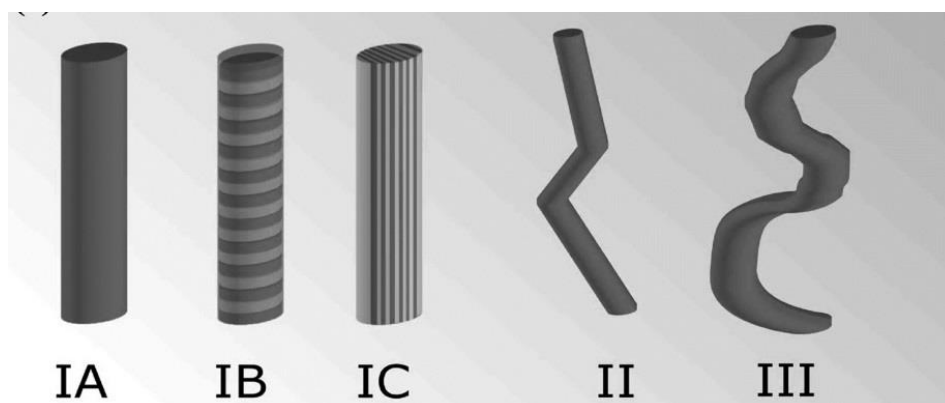


Figure 1-15. 'The schematic depicts the five different types of NWs discussed; IA: straight, defect free NWs, IB: laterally faulted NWs, IC: longitudinally faulted NWs, II: angular NWs and III: more complex, wormlike kinked NWs.'⁵⁴

1.2.4.2 Seed effects

Holmes and co-workers⁵⁵ have reported the transfer of defects from metallic-seed to seeded germanium nanowire. In their approach germanium nanowires were synthesized by supercritical fluid-solid-solid (SFSS) mechanism using DPG precursor and Ag nanoparticles as seeding agent. Although the initial mean diameter of Ag nanocrystals was approximately 6 nm with few amount of defects, subsequent anneal in supercritical conditions at the nanowire growth temperature (~ 400 °C) caused fusion of nanoparticles and increased the amount of twinning defects in coagulated particles. Germanium nanowires were seeded from mentioned coagulated Ag particles were mostly grown along $\langle 111 \rangle$ and $\langle 112 \rangle$ direction with $\{111\}$ twinning defects along their axis. According to TEM images these twinning planes have roots in Ag nanoparticles which confirm twinning transfer from seeds to germanium nanowires (Figure 1-16).⁵⁵

In another approach bimetallic alloy seeds of $\text{Au}_x\text{Ag}_{1-x}$ were used to study the effect of alloy seeds on characteristics and defect density of germanium nanowires. In this case twin planes $\{111\}$ were grown along $\langle 112 \rangle$ axis of germanium nanowires,²⁵ similar to the study which pure Ag seeds were used.

Figure 1-17 displays the micro-Raman spectra of germanium nanowires seeded with alloyed $\text{Ag}_{0.50}\text{Au}_{0.50}$ and $\text{Ag}_{0.75}\text{Au}_{0.25}$ and pure Ag seeds. 'The high density of twin boundaries in the $\text{Ag}_{0.75}\text{Au}_{0.25}$ seeded nanowires, over the entire diameter range, along with a large number of twinned nanowires decreases the effective phonon confinement length resulting in a red-shifted asymmetrical and broadened Raman peak.' The most major peak broadening and a red shift of the phonon mode in the Raman spectra of the $\text{Ag}_{0.75}\text{Au}_{0.25}$ -seeded nanowires in comparison to sample synthesized with $\text{Ag}_{0.50}\text{Au}_{0.50}$ and pure Ag seeds, shows the high density of twinning in $\text{Ag}_{0.75}\text{Au}_{0.25}$ -seeded nanowires. According to this study alloy seeds with various chemical compositions provide overall adjustment over twin formation in the germanium nanowires.²⁵

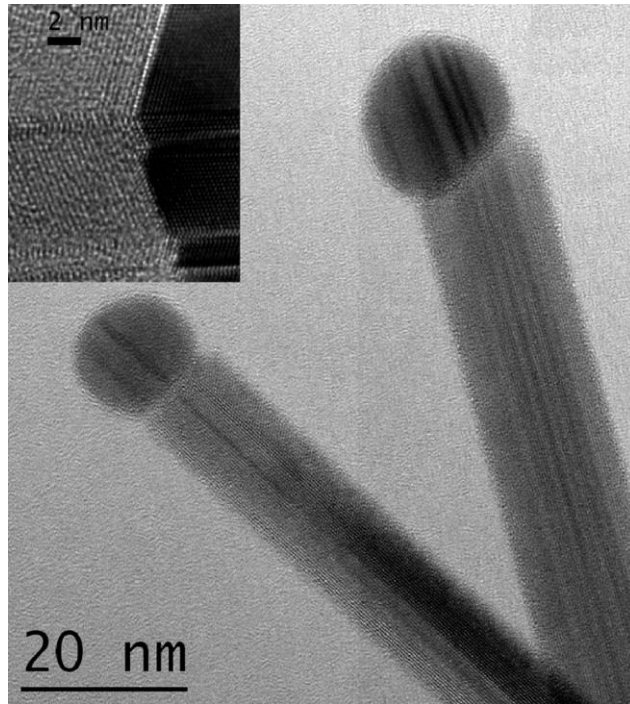


Figure 1-16. TEM image showing two nanowire-seed regions with brightness contrast at locations of the stacking faults along their axes in both silver seeds and germanium nanowires due to twinning. The inset shows the interface between the seed particle with steps, which influences the Ge lattice of the growing nanowire.⁵⁵

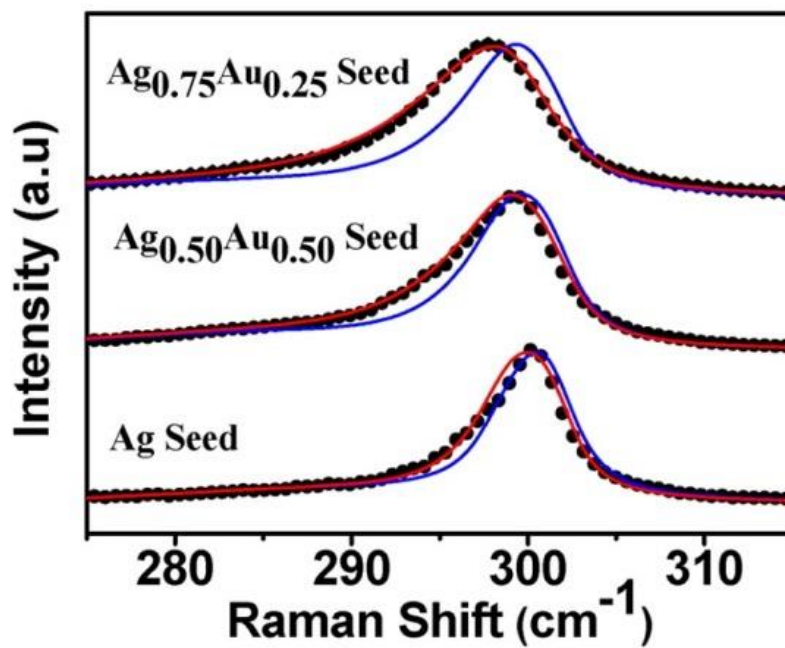
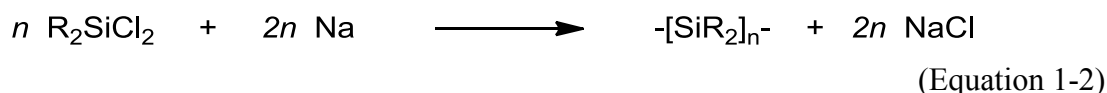


Figure 1-17. Raman spectra revealing the defect distributions for nanowires grown with different seeds, based on mismatches with the phonon confinement model (blue line) fitted curves.²⁵

1.3 Polysilylsilatrane

1.3.1 Polysilanes

The First polysilane derivatives were reported by Kipping⁵⁶ in 1921 by heating diphenylsilicon dichloride with sodium via procedure known as Wurtz-type coupling (Equation 1-2). It was reported that these crystalline silicohydrocarbons with general formula of $\text{Si}_n\text{Ph}_{2n}$ are soluble in all ordinary solvents and do not melt below 300 °C.⁵⁶



Up to the 1980s efforts have been made for the synthesis and characterization of different polysilanes but to some extent with limited success. Since 1980s the modern era in the field of substituted polysilanes began with the synthesis of soluble homo- and copolymers.⁵⁷

In the 1980s Wesson and Williams⁵⁸ reported the synthesis of random polymerization of mixtures of dimethyldichlorosilane with ethylmethyldichlorosilane or methylpropyldichlorosilane with sodium metal dechlorination. The molecular weight of these copolymers was reported in the range of 25,000 to 50,000 without any significant trends against composition or other experimental variables.⁵⁸

In another approach West and co-workers⁵⁷ reported synthesis of polysilastirene by two various methylphenyldichlorosilane and dimethyldichlorosilane monomers. Depending on the ratio of precursors, soluble polymers in common organic media with molecular weights above 1,000,000 were afforded.⁵⁷

1.3.1.1 Electron delocalization in polysilanes

σ -Bond electron delocalization is known as an important characteristic of polysilanes.⁵⁹ Michl and co-workers⁶⁰ contributed computational studies such as Ladder C and Sandorfy C models on the ground-state and lowest excited singlet potential energy surfaces of short linear permethylated oligosilanes to recognize the effect of *anti* and *gauche* conformations.⁶⁰ According to Ladder C model which uses simplified version of Hückel theory and only considers molecular orbitals of σ symmetry and $\sigma\sigma^*$ excited states, three types of orbital interaction exists in polysilanes.⁶⁰ The primary σ -interaction (β_{prim}) exists between orbitals of two adjacent silicon atoms pointing at each other, the second one is geminal interaction (β_{gem}) and it exists between orbitals of the same silicon atom, and the third one is the vicinal interaction (β_{vic}) which is mostly responsible for conformational σ -bond electron delocalization and it exists between orbitals of two adjacent silicon atoms pointing away from each other (Figure 1-18).⁵⁹ In general upon increasing the polysilane chain length an increase in the energy level of HOMO and an equal decrease in the energy level of LUMO occurs. Thus the orbital energy shift due to elongation of chain length, causes a red shift of the $\sigma\sigma^*$ excitation energy.⁶¹

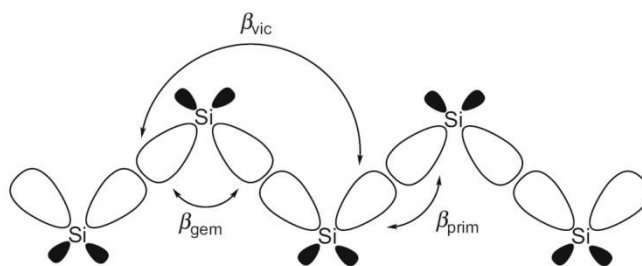


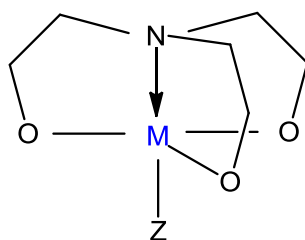
Figure 1-18. "Orbitals and resonance integrals included in the Ladder C model."⁵⁹

1.3.1.2 UV-vis absorption of polysilanes

In early studies it was reported that the special spectral properties of hexaphenyldisilane was related to an interaction between the phenyl groups. However Gilman for the first time in 1964 reported that the unique UV absorption properties of permethylated polysilanes relates to the polysilane backbone and not to the substituents.⁶² Later this unique phenomenon was attributed to $\sigma\sigma^*$ transitions within the polysilane chain.⁶³ Moreover, it was found that, upon elongation of the polysilane chain, σ -bond electron delocalization occurs within the silicon backbone, similar to π -electron delocalization in polyenes upon chain extension.⁶³ Indeed, it is impossible to ignore substituent effects on polysilane properties and its related effects on UV absorption spectra, when different organic functional groups such as alkyl or aryl or even atoms such as oxygen or nitrogen with lone pairs of electrons are linked to polysilane chain.^{57,64,65} However, it is difficult to differentiate between direct effects of the substituents induced by electronic properties of them, from conformational change generated by indirect effects of the substituents, on spectral properties of the polysilane chain.⁵⁷ In general the $\sigma\sigma^*$ excitation energy decreases significantly upon elongation of the polysilane chain and causes a bathochromic shift in UV absorption spectra,⁶¹ while it increases upon twisting from *trans* to *gauche* conformation and causes a hypsochromic shift in UV absorption spectra.⁶⁰

1.3.2 Atranes and silatranes

Mikhail Grigorievich Voronkov has proposed the term "atrane" for the first time in 1966 and he has named different atranes with regard to the central **M** element as silatrane (**M**=silicon), boratrane (**M**=boron), alumatrane (**M**=aluminum). Silatranes are containing a nitrogen-silicon dative bond which forms a stable coordinated complex between the alkoxy silane and the tertiary amine (Scheme 1-1).⁶⁶



Scheme 1-1. General structure of atrane molecules.

Gordon and co-workers have stated that 'an important observation regarding the structural characteristics of these compounds is the relationship between the Si-Z and Si-N distances: A longer Si-Z bond length (implying a weaker Si-Z bonding interaction) generally results in a shorter Si-N distance (suggesting a stronger Si-N bonding interaction). This is consistent with the notion that the axial bonding in pentacoordinated compounds may be described in terms of three-center four-electron (3c4e) bonding.'⁶⁷

The silatrane has a distorted trigonal bipyramidal structure at the silicon atom with three planer oxygen atoms. As a result of nitrogen lone pair donation to the silicon atom, the nitrogen points to silicon atom and forms a four coordinated tetrahedron.⁶⁸

According to X-ray studies of silatranes with (Z= H, halogen, aryl, alkyl and O) the Si-N distance ranges from 2.05 to 2.20 Å which is significantly shorter than the sum of the van der Waals radii of silicon and nitrogen with 3.5 Å and is slightly longer than the typical single Si-N bond distance with approximately 1.7 to 1.8 Å. In the gas phase the Si-N distance increases which confirms a weaker Si-N interaction in gas phase.⁶⁸

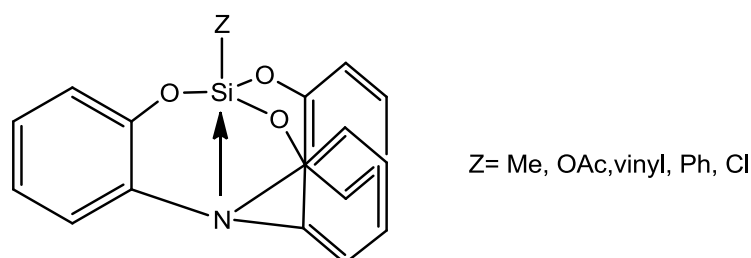
High flexibility of trigonal bipyramidal structure of silatranes along the Si-N dative bond reflects the nature of Si-N bonding. In fact Si-N bonding is not a covalent bonding; nor is it based on intermolecular charge transfer.⁶⁹

To explain the nature of Si-N bonding Ortiz and co-workers⁶⁹ have stated that: 'The electrostatic nature of Si-N bonding is confirmed by the invariance of the atomic charges with respect to Si-N distance, by the linear character of the ground state dipole moment function, and by the high sensitivity of the ionization energies of the nitrogen lone pair and Si-Z levels with respect to the Si-N separation. As the Si-N distance grows, the binding energies of the nitrogen lone pair electrons decrease, while those of the Si-Z ionization energy increase. These trends in ionization energies can be explained by changes in the local positive electrostatic potentials near the nitrogen lone pair and the Si-Z bond. These results show that Si-N bonding is mainly electrostatic.'⁶⁹

1.3.3 Other compounds containing a pentacoordinated silicon atom

1.3.3.1 Silatranes with different types of ligands

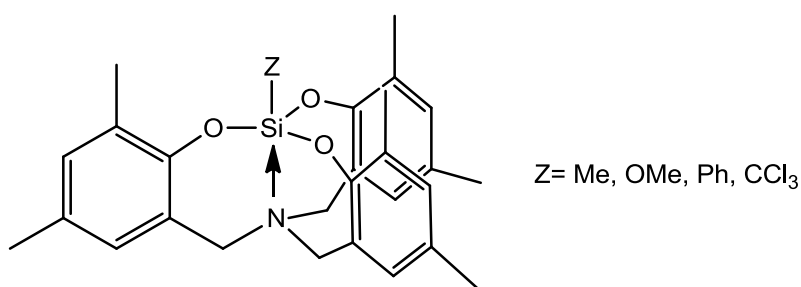
Frye and co-workers⁷⁰ have reported synthesis of tris(2-hydroxyphenyl)amine as an appropriate chelating agent in reactions with different organyltrichlorosilanes and SiCl₄ to synthesize various pentacoordinated derivatives of ZSi(OC₆H₄)₃N (Z= Me, OAc, vinyl, Ph, Cl) (Scheme 1-2).⁷⁰



Scheme 1-2. A silatrane with a tris(2-hydroxyphenyl)amine ligand.

Holmes and co-workers⁷¹ have reported the synthesis of a series of silatranes $N[\text{CH}_2(\text{Me}_2\text{C}_6\text{H}_2)\text{O}]_3\text{SiZ}$ ($Z = \text{Me}, \text{OMe}, \text{Ph}, \text{CCl}_3$) which were prepared by reaction of tris(2-hydroxy-4,6-dimethylbenzyl)amine as an appropriate chelating agent with different organosilanes (Scheme 1-3). The substituent group on the silicon atom highly influences the Si-N interaction and due to that various Si-N distances from 2.745 Å for Me to 2.025 Å for CCl_3 have been reported.⁷¹

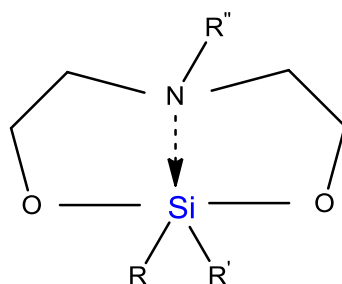
All the synthesized silatranes were characterized by NMR spectroscopy and single crystal X-ray crystallography. In presence of an electron withdrawing Z substituent an upfield shift in ^{29}Si NMR was observed, indicated the more acidic nature of the silatrane and shorter Si-N bond distance. However, the increase in electron donating capability of Z substituent resulted in downfield shifts in ^{29}Si NMR and an increase in Si-N bond distance. It is concluded that in six-membered tricyclic silatranes the effect of Z substituents on Si-N interaction is greater in comparison to five-membered tricyclic silatranes.⁷²



Scheme 1-3. Silatrane synthesized by tris(2-hydroxy-4,6-dimethylbenzyl) amine ligand.

1.3.3.2 Silocanes

Silocanes with bidentate chelating ligands and a pentacoordinated silicon atom are another type of compounds with hypervalent silicon atom suitable for stereochemical interconversion studies.⁷³ Structures of these molecules contain different derivatives of dialkanolamine with a silicon atom with or without transannular Si-N interaction depending on the substituents on silicon and nitrogen (Scheme 1-4). This Si-N interaction in silocanes is weaker than that in silatranes.⁷⁴



Scheme 1-4. General structure of silocane molecule.

X-ray studies have been reported by Lukevics and co-workers⁷⁵ on four different silocanes with different substituents on silicon and nitrogen atoms with general formula of $R_2Si(OCH_2CH_2)NR'$ (Table 1-1).⁷⁵

Table 1-1. X-ray interatomic measurements for Si-N distances for different silocanes.

R	R'	Si-N distance (Å)
C ₆ H ₅	CH ₃	2.68
C ₆ H ₅	(CH ₃) ₃ C	3.16
CH ₃	C ₆ H ₅	3.19
C ₆ H ₅	C ₆ H ₅	3.08

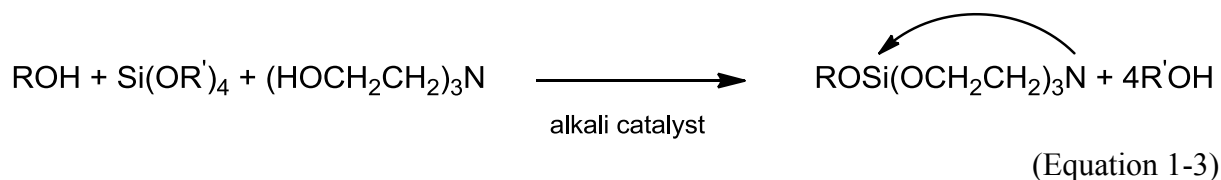
The data represents that the Si-N interaction in this group of compounds is highly influenced by the substituent on the silicon and nitrogen atom. The effect can be either due to electronic properties or steric effects of the substituents.⁷⁵

1.3.4 Synthetic strategies of silatranes

Voronkov and co-workers⁷² have reported synthesis of silatranes in 1963 and since then different strategies have been proposed and developed for the synthesis of these group of compounds containing pentacoordinated silicon atom.⁷²

1.3.4.1 Synthesis from alkoxy silane

This early method involved transesterification of alkoxy silane with triethanolamine or substituted triethanolamine in a corresponding alcohol as solvent in the presence of an alkaline catalyst (an alkali metal hydroxide) which catalyzed the reaction and increased the yield of the final product (Equation 1-3). Finally to obtain the product, the corresponding alcohol (methanol, ethanol, etc.) was distilled off the reaction mixture.⁶⁶



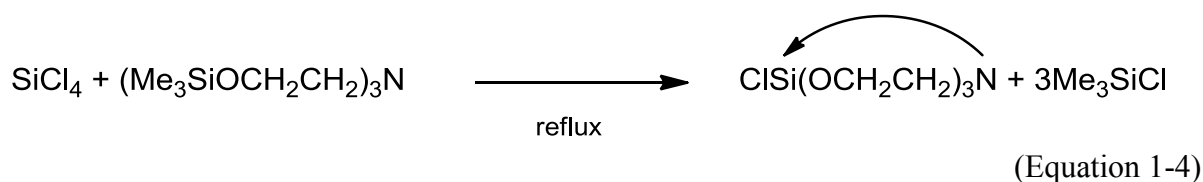
Beside alkali metal hydroxides, transesterification reaction has also been reported in the presence of other catalytic compounds such as tetraethylammonium fluoride hydrate.⁷¹

Depending on the substituted ligand in alkoxy silane, transesterification reaction can proceed without catalyst but with appropriate yield.⁷² Karlov et al.⁷⁶ have reported transesterification reaction between $(MeO)_3SiC\equiv CPh$ and trialkanolamine at room temperature in methanol and formation of corresponding silatrane with more than 54% yield.⁷⁶

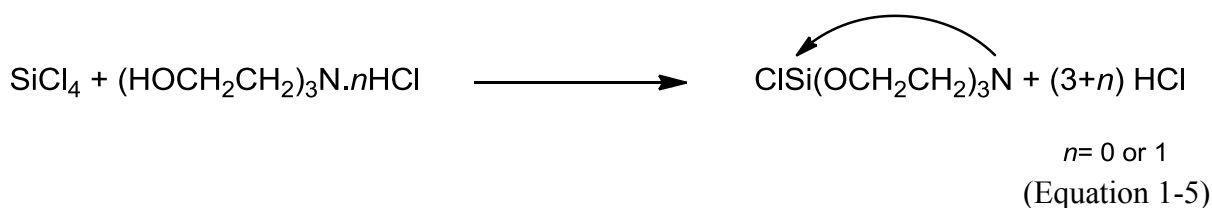
1.3.4.2 Synthesis from chlorosilane

Voronkov and co-workers have reported series of different reactions concerning synthesis of 1-chlorosilatrane, among which two methods are based on use of SiCl_4 .⁷⁷

I) Reaction of tetrachlorosilane with tris(2-trimethylsiloxyethyl)amine (Equation 1-4):⁷⁸

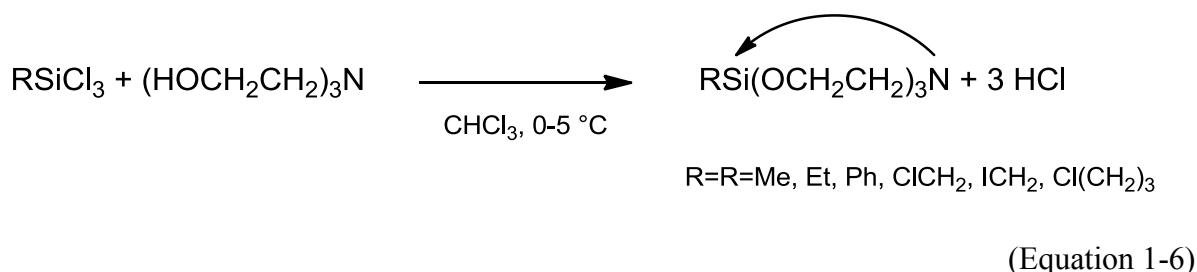


II) reaction of triethanolamine or its hydrochloride (chloroprotatrane) with tetrachlorosilane (Equation 1-5):⁷⁷



Beside the synthesis of 1-chlorosilatrane with SiCl_4 , Frey et al.⁷⁰ have reported also synthesis of chloro(2,2',2''-nitriлотриphenoxy)silane from reaction of tetrachlorosilane and 2,2',2''-nitriлотриphenol under reflux condition in n-butylether.⁷⁰

Voronkov and co-workers⁷⁹ have reported synthesis of different organylsilatranes $\text{RSi}(\text{OCH}_2\text{CH}_2)_3\text{N}$ ($\text{R} = \text{Me, Et, Ph, ClCH}_2, \text{ICH}_2, \text{Cl}(\text{CH}_2)_3$) by reaction of trialkanolamine with the corresponding organyltrichlorosilane in chloroform at 0-5 °C followed by distillation of chloroform and hydrogen chloride off the reaction flask (Equation 1-6).⁷⁹



1.3.5 Reactivity of silatranes

The reactivity of 1-iodosilatrane toward $(\text{Me}_3\text{Si})_2\text{O}$, $\text{RC}\equiv\text{CH}$, ROR' , MeCO_2Et and $\text{RR}'\text{Hg}$ was studied by Voronkov in 1982 and it was reported to be a reactive electrophile.⁸⁰ In contrast to 1-iodosilatrane, 1-chlorosilatrane has very low reactivity with nucleophiles. The low reactivity of 1-chlorosilatrane is associated with its unusual geometry. Firstly, the backside attack is

impossible because of steric reasons, secondly the Si-Cl bond cleavage by side attack is also inadequate due to the absence of angular strain and due to the slightly short Si-Cl bond length of 2.12 Å.⁸¹

Strong nucleophiles such as *n*-BuLi were found to react with 1-chlorosilatrane and 1-bromosilatrane to give, after reduction with LiAlH₄, tri-*n*-butylsilane as the main product; even in presence of excess *n*-BuLi. It was also found that *n*-Bu₃SiCl did not form during the reaction before reduction with LiAlH₄. Low yield of *n*-Bu₄Si from the reaction of 1-chlorosilatrane with excess of *n*-BuLi after a prolonged reaction, showed that *n*-butylsilatrane is not obtained during the reaction and instead Si-O bond is cleaved instead of Si-Cl bond, similar to reactions involved *n*-BuLi and chloroalkoxysilanes.⁸¹

In contrast to 1-chlorosilatrane, 1-haloalkylsilatrane has a reactive halogen atom which reacts easily with different nucleophiles.⁸²

n-BuLi attack has been reported mainly on Si-O bond in vinylsilatrane at 20 °C, but in contrast addition of ^tBuLi to vinylsilatrane involves only addition to the C=C bond at -78 °C, with no attack to the Si-O bond.⁸¹

Beside halogens as leaving groups of silatrane, triflate as a new promising leaving group of germatrane has been reported by Karlov et al.⁸³ Recently, Zaitsev et al.⁸⁴ have reported reaction of (Me₃Si)₃GeK.THF with 1-germatranyltriflate with 34% yield of the end product.⁸⁴

Chapter 2

Synthesis of new oligosilylgermanes

2 Synthesis of new oligosilylgermanes

2.1 Oligosilylgermane compounds containing germanium-hydrogen bonds:

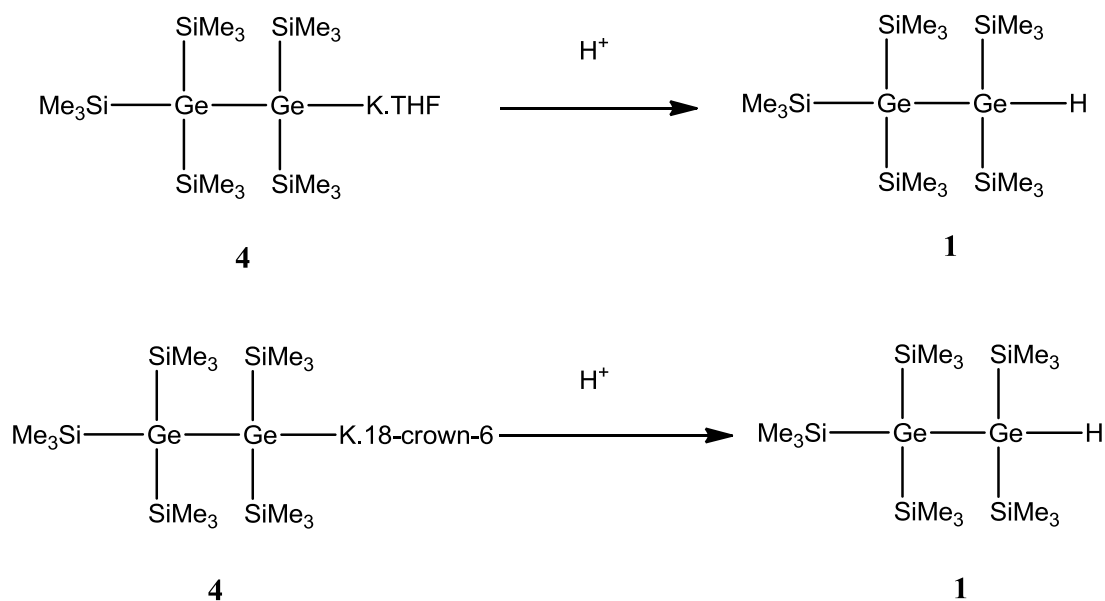
Germane (GeH_4) as a colorless gas which thermally decomposes on hot surfaces heated above $280\text{ }^\circ\text{C}$ ⁸⁵ is used in the semiconductor industry for synthesis of germanium nanowires with different epitaxial methods such as chemical beam epitaxy. As germane is known to be a toxic gas, Shenai-Khatkhate and co-workers⁸⁶ have reported other compounds containing germanium-hydrogen bond like isobutylgermane as a liquid and less hazardous precursor than germane for deposition of germanium thin films by OMVPE.⁸⁶

Recently, DPG was studied widely as another type of germanium precursor for synthesis of germanium nanowires particularly above $380\text{ }^\circ\text{C}$.²⁷ However, the higher temperatures are mostly necessary to improve the quality of nanowires and to obtain single crystalline nanowires.^{21,54}

Due to frequent application of precursors containing germanium-hydrogen bonds in the semiconductor industry, another group of precursors which can be used for the synthesis of germanium based semiconductors will be described below:

2.1.1 Synthesis of pentakis(trimethylsilyl)digermane (1)

Hydrolysis of tris(trimethylsilyl)germylpotassium (2) by aqueous sulfuric acid has been reported by Marschner et al.⁸⁷ which gave tris(trimethylsilyl)germane (3). According to this method, hydrolysis of oligosilylgermylpotassium 4⁸⁷ was carried out in a solution mixture of diethylether/aqueous sulfuric acid with 1:1 ratio (Scheme 2-1).



Scheme 2-1. Hydrolysis of oligosilylgermylpotassium (4) with aqueous sulfuric acid

Up: oligosilylgermylpotassium synthesis in THF

Down: oligosilylgermylpotassium synthesis in benzene in presence of 18-crown-6

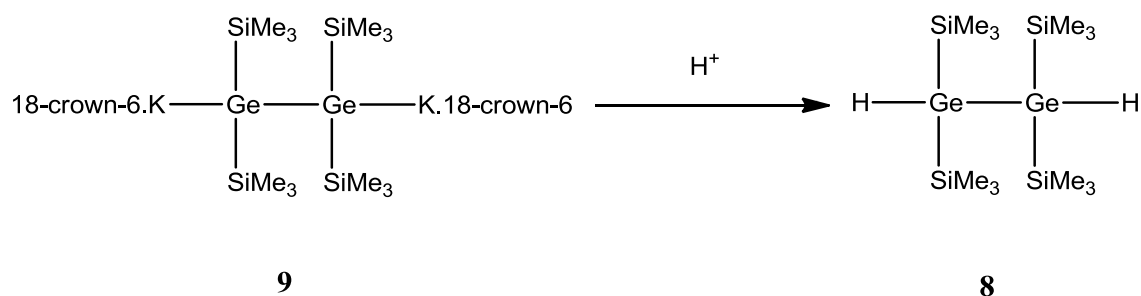
With a 1:1 mixture of diethylether/aqueous sulfuric acid a mixture of respective germanium hydride **1** and hexakis(trimethylsilyl)digermane (**6**) was obtained. The reaction was improved by changing the ratio of diethylether/aqueous sulfuric acid to 1:4. In this experiment germanium hydride **1** was obtained with only traces of germanium hydride **3** which is easily removable by sublimation at 42 °C.

Formation of oligosilylgermane **6** in the first reaction with higher volume of diethylether could be explained by low accessibility of hydrolysis agent and in contrast higher accessibility of trimethylsilyl group for oligosilylgermylpotassium **4**.

In contrast to NMR spectroscopic analysis of germanium hydride **1** which showed a pure sample, GC-Mass analysis of the same sample showed small quantity of germanium hydride **1** and high quantity of germanium hydride **3** and tetrakis(trimethylsilyl)germane (**7**). This phenomenon shows that germanium hydride **1** is not a stable compound at elevated temperatures and it decomposes to lighter compounds.

2.1.2 Synthesis of 1,1,2,2-tetrakis(trimethylsilyl)digermane (**8**)

Similar to the method reported by Marschner et al.⁸⁷ hydrolysis of tetrakis(trimethylsilyl)digermyl-1,2-dipotassium 2×18-crown-6⁸⁷ (**9**) with an ice cold solution mixture of diethylether/aqueous sulfuric acid with 1:4 ratio gave germanium dihydride **8** (Scheme 2-2).



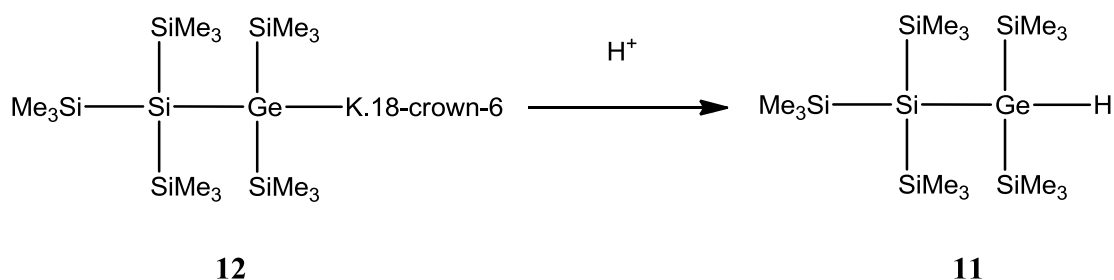
*Scheme 2-2. Hydrolysis of tetrakis(trimethylsilyl)digermyl-1,2-dipotassium 2×18-crown-6 (**15**) with aqueous sulfuric acid*

Oligosilylgermyldipotassium **9** decomposes rapidly in solution to tris(trimethylsilyl)germylpotassium. 18-crown-6 (**10**) but it is fairly stable in crystalline state. Low volume of solution during synthesis of oligosilylgermyldipotassium **9** increases the speed of crystallisation and reduces the possibility of decomposition. It is necessary to separate the red crystals of oligosilylgermyldipotassium **9** from the mother solution by decantation to remove oligosilylgermylpotassium **10** and to obtain a pure germanium dihydride **8** after hydrolysis.

The presence of small quantity of oligosilylgermylpotassium **10** after hydrolysis gave germanium hydride **3**. Sublimation of a mixture of germanium hydride **8** and **3** at 40 °C for purification of germanium hydride **8** is not possible due to very high sensitivity of germanium dihydride **8** and thermal decomposition at this temperature. Furthermore GC-Mass analysis of pure germanium dihydride **8** showed only germanium hydride **3** and oligosilylgermane **7** without any sign of germanium hydride **8**. These facts confirm higher sensitivity of germanium dihydride **8** to germanium hydride **1**.

2.1.3 Synthesis of bis(trimethylsilyl)[tris(trimethylsilyl)silyl]germane (**11**)

Hydrolysis of bis(trimethylsilyl)[tris(trimethylsilyl)silyl]germyl-potassium.18-crown-6⁸⁷ (**12**) with aqueous sulfuric acid was done similar to the literature procedure report by Marschner et al.⁸⁷ (Scheme 2-3).



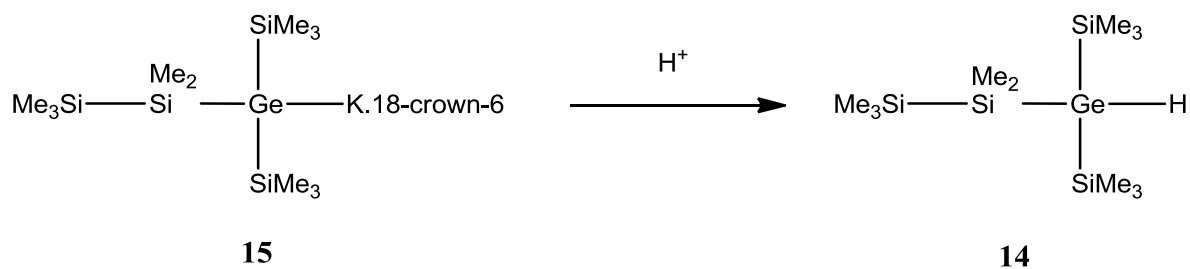
*Scheme 2-3. Hydrolysis of bis(trimethylsilyl)[tris(trimethylsilyl)silyl]germyl-potassium .18-crown-6 (**12**) with aqueous sulfuric acid*

In the GC-Mass analysis of germanium hydride **11** no sign of germanium hydride **3** or oligosilylgermane **7** was observed and only germanium hydride **11** as a single compound was observed. This fact confirms higher thermal stability of germanium hydride **11** than germanium hydride **1** and **8**.

2.1.4 Synthesis of bis(trimethylsilyl)pentamethyldisilanylgermane (**14**)

Hydrolysis of bis(trimethylsilyl)pentamethyldisilanylgermyl-potassium (**15**) with aqueous sulfuric acid was performed similar to the literature procedure report by Marschner et al.⁸⁷ (Scheme 2-4).

Similar to germanium hydride **11** in the GC-Mass analysis of germanium hydride **14** no sign of germanium hydride **3** or oligosilylgermane **7** was observed and only germanium hydride **14** as a single compound was observed. According to this GC-Mass analysis, it can be concluded that mentioned germanium hydrides containing two germanium atoms in the backbone are more sensitive to thermal decomposition than those containing only one germanium atom. Such sensitivity can be related to a weaker bond between the two germanium atoms in comparison to a germanium silicon bond present in the backbone of molecule.

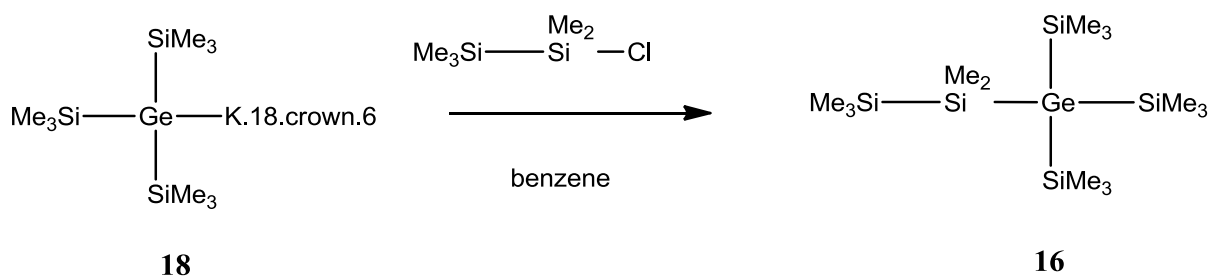


Scheme 2-4. Hydrolysis of bis(trimethylsilyl)pentamethyldisilanylgermyl-potassium.18-crown-6 (15) with aqueous sulfuric acid

2.2 Synthesis of other oligosilylsilanes and -germanes:

2.2.1 Synthesis of (pentamethyldisilyl)tris(trimethylsilyl)germane (16)

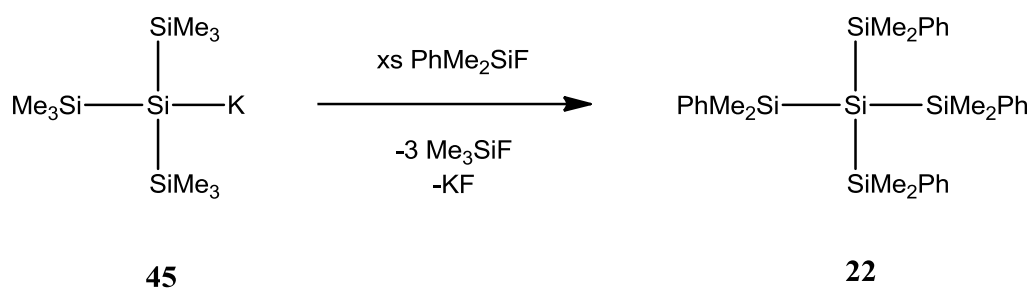
Synthesis of oligosilylgermane **16** was performed similar to the procedure for synthesis of tris(trimethylsilyl)[tris(trimethylsilyl)silyl]germane (**17**) reported by Marschner et al.⁸⁷ by reaction of chloropentamethyldisilane with tris(trimethylsilyl)germyl-potassium.18-crown-6 (**18**) at room temperature (Scheme 2-5).



Scheme 2-5. Synthesis of (pentamethyldisilyl)tris(trimethylsilyl)germane (16) by reaction of chloropentamethyldisilane with tris(trimethylsilyl)germyl-potassium.18-crown-6 (18)

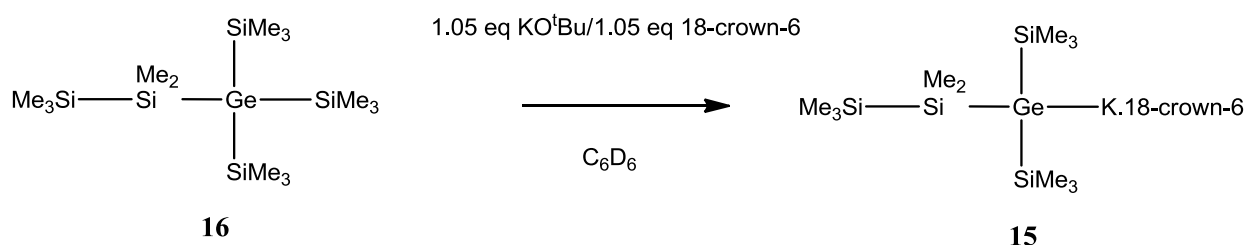
2.2.2 Synthesis of bis(trimethylsilyl)pentamethyldisilanylgermyl-potassium.18-crown-6 (15)

Exchange of all functional groups between tris(trimethylsilyl)silylpotassium (**45**) and dimethylphenylfluorosilane and finally formation of tetrakis(dimethylphenylsilyl)silane (**22**) has been reported previously by Marschner et al.⁸⁸ (Scheme 2-6). Similarly in the course of the reaction between oligosilylgermane **16** and KO^tBu in THF, due to the slow reaction rate, exchange of functional groups between oligosilylgermylpotassium **15** and the remaining of precursor occurs. Due to this, a mixture of tris(trimethylsilyl)germylpotassium (**24**) and oligosilylgermylpotassium **15** forms instead of pure oligosilylgermylpotassium **15**.



Scheme 2-6. 'Tris(trimethylsilyl)silylpotassium (45) exchange reaction of all trimethylsilyl against dimethylphenylsilyl groups terminated by potassium fluoride elimination'⁸⁸

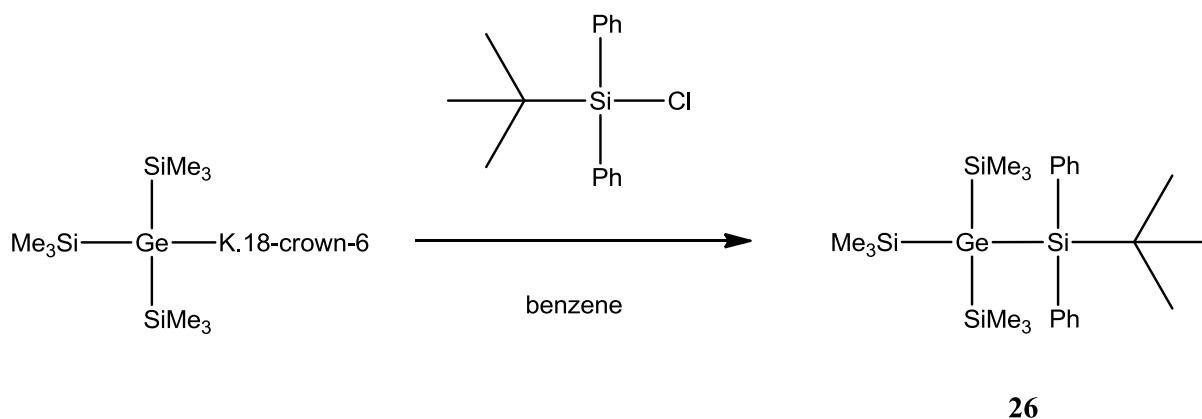
To suppress the exchange of functional groups, synthesis of oligosilylgermylpotassium **15** was performed in benzene in the presence of 18-crown-6 instead of THF (Scheme 2-7).



Scheme 2-7. Synthesis of bis(trimethylsilyl)pentamethyldisilanylgermyl-potassium. 18-crown-6 (15)

2.2.3 Synthesis of (*tert*-butyldiphenylsilyl)tris(trimethylsilyl)germane (26)

Synthesis of oligosilylgermane **26** was performed according to literature procedure reported by Marschner et al.⁸⁷ by reaction of oligosilylgermylpotassium with silylhalide at room temperature (Scheme 2-8).



Scheme 2-8. Synthesis of (*tert*-butyldiphenylsilyl)tris(trimethylsilyl)germane (26)

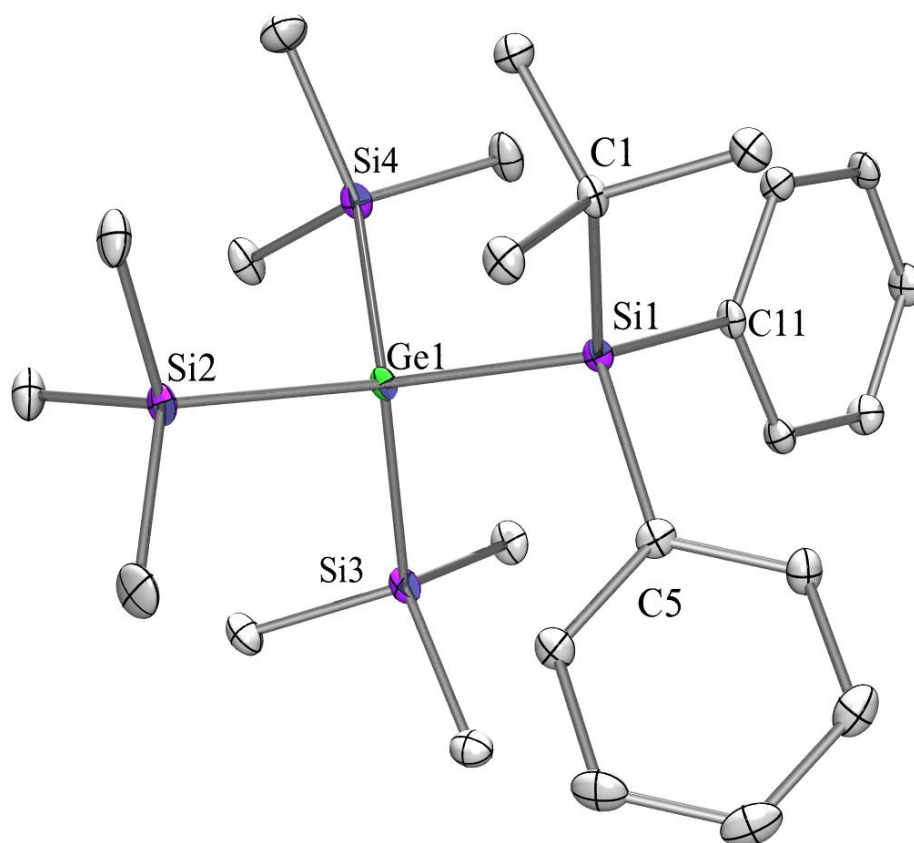


Figure 2-1. Crystal structure of (tris(trimethylsilyl)(*tert*-butyldiphenylsilyl)germane (**26**)

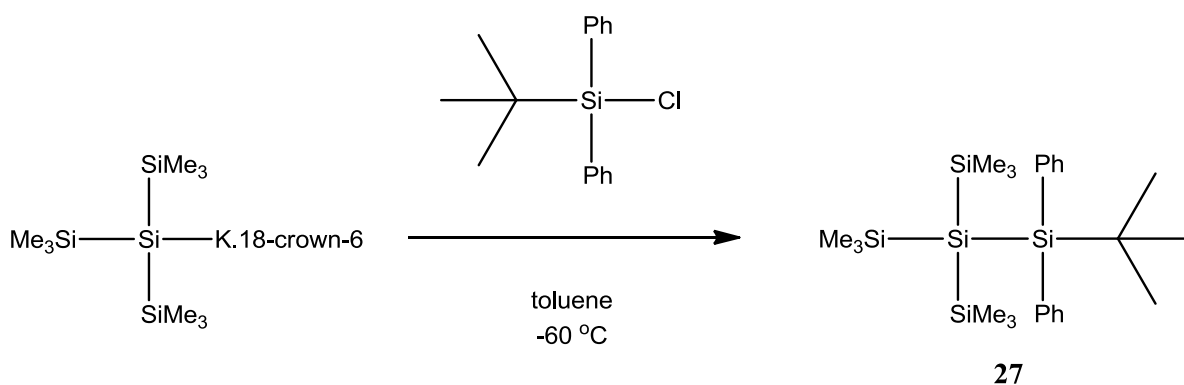
Table 2-1. Selected bond lengths and angles of (tris(trimethylsilyl)(*tert*-butyldiphenylsilyl)germane (**26**)

Bond Length	[Å]	Bond Angle	[°]
Ge(1)-Si(1)	2.4175(14)	Si(3)-Ge(1)-Si(1)	108.36(4)
Ge(1)-Si(2)	2.4108(13)	Si(4)-Ge(1)-Si(1)	111.96(5)
Ge(1)-Si(3)	2.4072(12)	C(1)-Si(1)-Ge(1)	112.91(13)
Si(1)-C(1)	1.916(4)	C(5)-Si(1)-Ge(1)	111.90(14)
Si(1)-C(11)	1.887(4)	C(11)-Si(1)-Ge(1)	107.63(14)
		C(5)-Si(1)-C(1)	106.15(17)
		Si(2)-Ge(1)-Si(1)	119.00(5)

Figure 2-1 shows the crystal structure of oligosilylgermane **26**. According to Table 2-1 the length of Ge(1)-Si(1) bond in the crystal structure of **26** is 2.4175 Å which in comparison is shorter than the Ge(1)-Si(1) bond in tris(trimethylsilyl)[tris(trimethylsilyl)silyl]germane (**17**) with 2.4256 Å.⁸⁹ This shortness in the bond length could be due to presence of less bulky phenyl groups in comparison to trimethylsilyl group.

2.2.4 Synthesis of 1-(*tert*-butyl)-3,3,3-trimethyl-1,1-diphenyl-2,2-bis(trimethylsilyl)trisilane (**27**)

Synthesis of oligosilane **27** was performed according to literature procedure, by reaction of oligosilylpotassium **20** with *tert*-butylchlorodiphenylsilane at low temperature (Scheme 2-9).⁹⁰



Scheme 2-9. Synthesis of 1-(*tert*-butyl)-3,3,3-trimethyl-1,1-diphenyl-2,2-bis(trimethylsilyl)trisilane (**27**)

Figure 2-2 shows the crystal structure of oligosilane **27**. The length of Si(1)-Si(2) bond in oligosilane **27** is 2.3827 Å which in comparison is shorter than the Si(1)-Si(1) bond in hexakis(trimethylsilyl)disilane (**49**) with 2.40 Å.⁹¹ This shortness in the bond length could be due to presence of less bulky phenyl groups in comparison to trimethylsilyl group.

2.2.5 Synthesis of ((*tert*-butyldiphenylsilyl)bis(trimethylsilyl)germyl)potassium.18-crown-6 (**30**)

To study the possibility of oligosilylgermylpotassium formation from oligosilylgermane **26** and also the shielding effect of one *tert*-butyl and two phenyl and groups at one silicon atom in the presence of a non-nucleophilic base such as potassium *tert*-butoxide, oligosilylgermane **26** was reacted with KO^tBu and 18-crown-6 in benzene (Scheme 2-10).

NMR spectroscopic analysis of oligosilylgermylpotassium **30** and GC-Mass analysis of its ethylbromide derivative confirmed that **30** forms as a pure product and KO^tBu can not attack the silicon atom of the backbone. Figure 2-3 shows the crystal structure of **30**.

According to Table 2-3 the (Ge1)-(K2) distance of **30** is 3.6214 Å which is a little bit longer than Ge-K distance of oligosilylgermyldipotassium **9** with Ge-K distances of 3.5223 Å and 3.4968 Å. Longer Ge-K distance is due to presence of a bulky *tert*-butyl and two phenyl groups which increases the stress on two trimethylsilyl groups and consequently due to steric repulsion Ge-K bond elongation occurs.

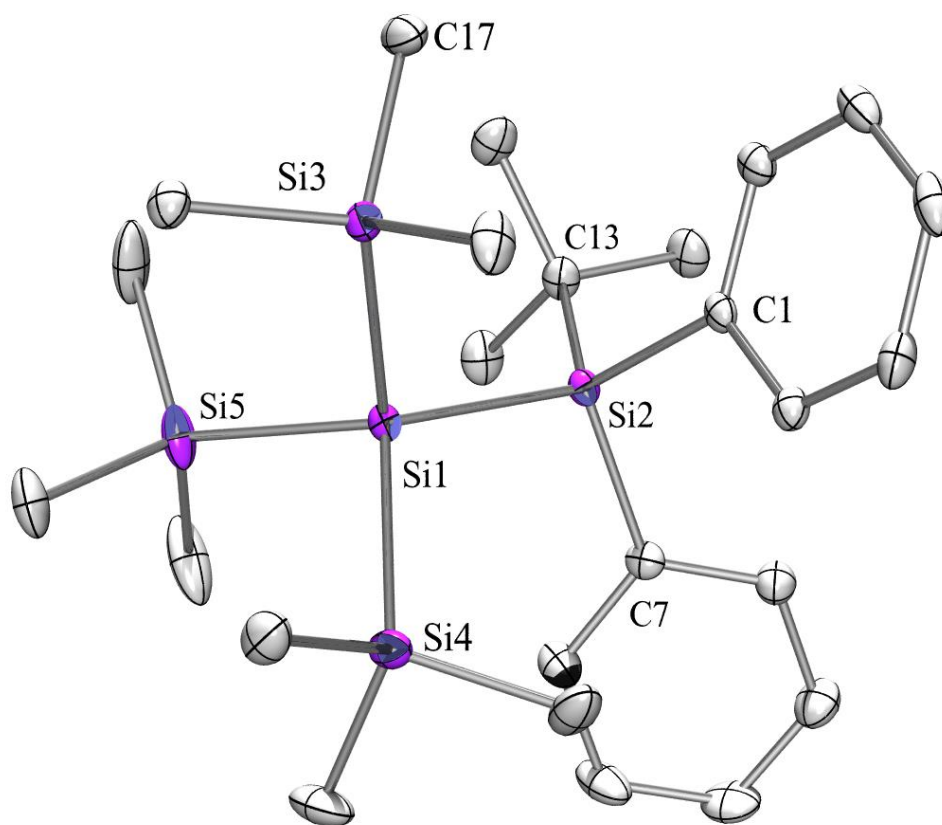
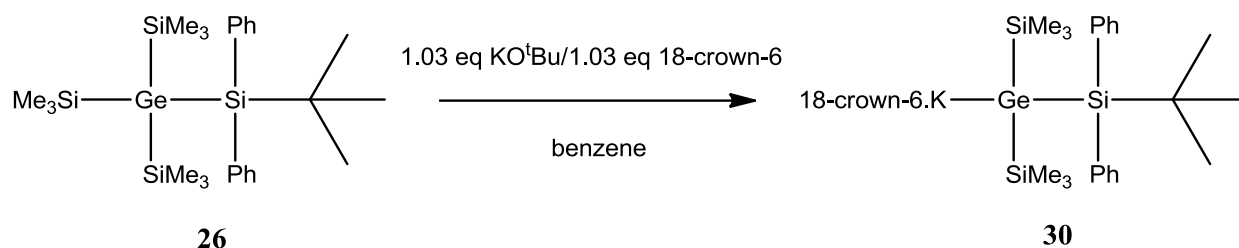


Figure 2-2. Crystal structure of 1-(*tert*-butyl)-3,3,3-trimethyl-1,1-diphenyl-2,2-bis(trimethylsilyl)trisilane (**27**)

Table 2-2. Selected bond lengths and angles of 1-(*tert*-butyl)-3,3,3-trimethyl-1,1-diphenyl-2,2-bis(trimethylsilyl)trisilane (**27**)

Bond Length	[Å]	Bond Angle	[°]
Si(1)-Si(2)	2.3827(10)	Si(4)-Si(1)-Si(2)	112.18(3)
Si(1)-Si(3)	2.3600(10)	Si(3)-Si(1)-Si(2)	108.01(3)
Si(1)-Si(5)	2.3654(10)	C(13)-Si(2)-Si(1)	115.69(8)
Si(2)-C(1)	1.898(2)	C(7)-Si(2)-Si(1)	109.80(7)
Si(2)-C(13)	1.919(2)	C(1)-Si(2)-Si(1)	106.01(7)
		C(7)-Si(2)-C(13)	105.82(10)
		Si(5)-Si(1)-Si(2)	119.85(3)

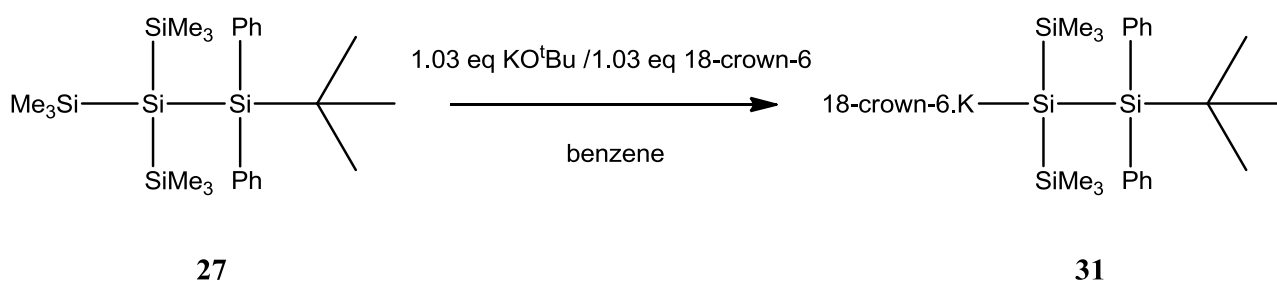
The presence of a bulky *tert*-butyl group beside two phenyl groups, makes the structure asymmetric and due to that Si(2)-Ge(1)-K(2) angle with 104.21° is smaller than Si(1)-Ge(1)-K(2) angle with 121.87°.



Scheme 2-10. Synthesis of ((*tert*-butyl-diphenylsilyl)bis(trimethylsilyl)germyl)potassium.18-crown-6 (**30**)

2.2.6 Synthesis of 2-*tert*-butyl-2,2-diphenyl-1,1-bis(trimethylsilyl)disilanyl)potassium.18-crown-6 (**31**)

Similar to previous oligosilylgermylpotassium **30**, oligosilylpotassium **31** was synthesized from the reaction of oligosilane **29** with KO^tBu and 18-crown-6 in benzene (Scheme 2-11). NMR spectroscopic analysis of oligosilylpotassium **31** and GC-Mass analysis of its ethylbromide derivative confirmed that the oligosilylpotassium **31** forms as a pure product and KO^tBu cannot attack the silicon atom in the backbone which is shielded by two phenyl and one *tert*-butyl groups. Figure 2-4 shows the crystal structure of oligosilylpotassium **31**.



Scheme 2-11. Synthesis of 2-*tert*-butyl-2,2-diphenyl-1,1-bis(trimethylsilyl)disilanyl)potassium.18-crown-6 (**31**)

The (Si1)-(K1) distance of oligosilylpotassium **31** is 3.6450 Å (Table 2-4) which is longer than Si-K distance of 1,1,3,3-tetrakis(trimethylsilyl)-2,2-dimethyltrisilyl-1,3-dipotassium (**32**) with Si-K distances of 3.5011 Å and 3.5836 Å.⁹² The longer Si-K distance is due to the presence of a bulky *tert*-butyl and two phenyl groups which increases the stress on two trimethylsilyl groups and consequently due to steric repulsion Si-K bond elongation occurs.

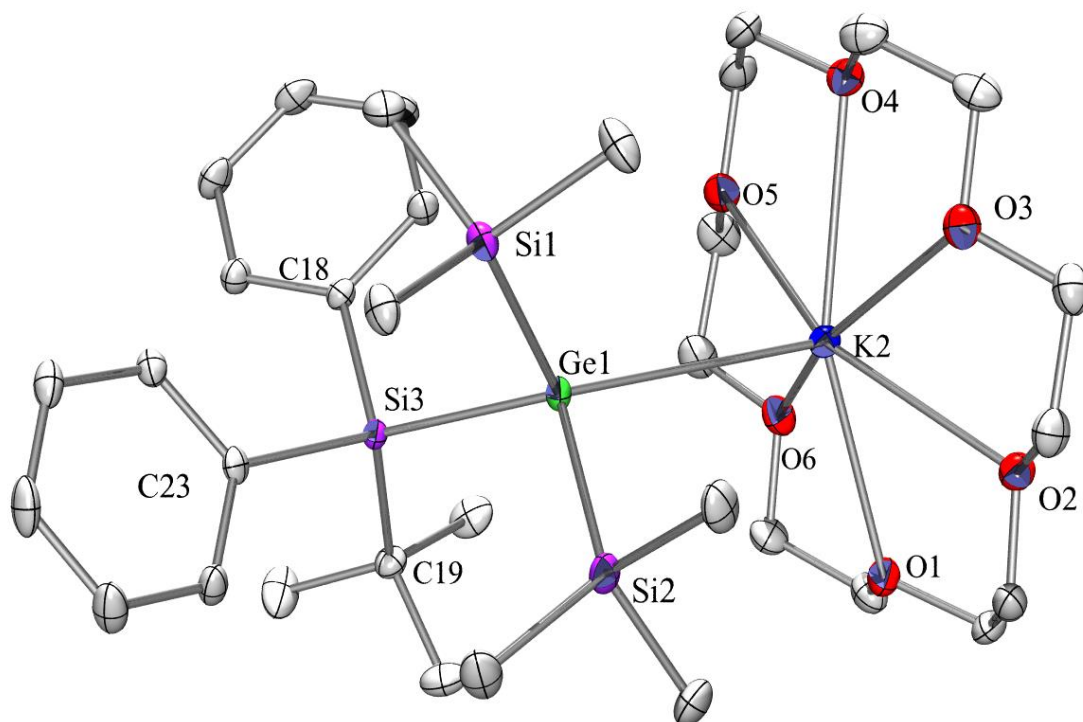


Figure 2-3. Crystal structure of ((*tert*-butyldiphenylsilyl)bis(trimethylsilyl)germyl)potassium.18-crown-6 (**30**)

Table 2-3. Selected bond lengths and angles of ((*tert*-butyldiphenylsilyl)bis(trimethylsilyl)germyl)potassium (**30**)

Bond Length	[Å]	Bond Angle	[°]
Ge(1)-Si(3)	2.3994(7)	Si(3)-Ge(1)-K(2)	124.38(2)
Ge(1)-K(2)	3.6214(10)	Si(1)-Ge(1)-K(2)	121.87(2)
Ge(1)-Si(1)	2.4038(9)	Si(2)-Ge(1)-K(2)	104.21(3)
Si(3)-C(19)	1.932(2)	C(19)-Si(3)-Ge(1)	112.38(8)
Si(3)-C(23)	1.899(2)	C(23)-Si(3)-Ge(1)	116.89(7)
		C(18)-Si(3)-Ge(1)	107.74(8)

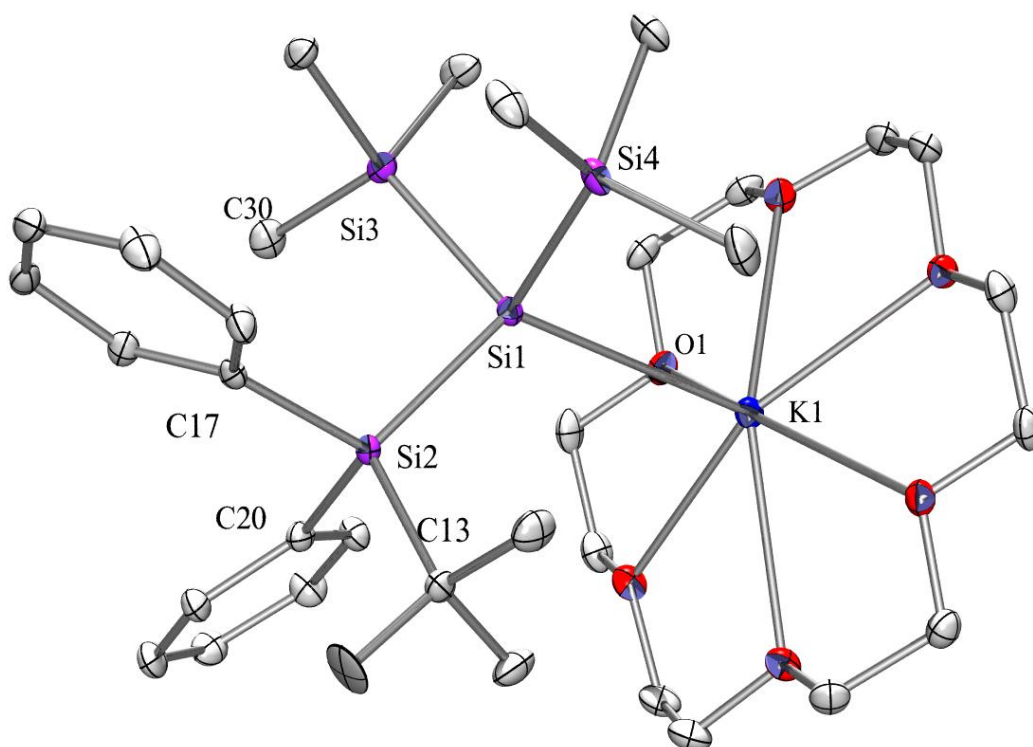


Figure 2-4. Crystal structure of 2-*tert*-butyl-2,2-diphenyl-1,1-bis(trimethylsilyl)disilanyl)potassium.18-crown-6 (**31**)

Table 2-4. Selected bond lengths and angles of 2-*tert*-butyl-2,2-diphenyl-1,1-bis(trimethylsilyl)disilanyl)potassium.18-crown-6 (**31**)

Bond Length	[Å]	Bond Angle	[°]
Si(1)-Si(2)	2.3502(9)	Si(2)-Si(1)-K(1)	123.68(3)
Si(1)-K(1)	3.6450(11)	Si(3)-Si(1)-K(1)	120.03(3)
Si(1)-Si(4)	2.3512(10)	Si(4)-Si(1)-K(1)	104.17(3)
Si(2)-C(13)	1.933(2)	C(13)-Si(2)-Si(1)	112.53(8)
Si(2)-C(17)	1.905(2)	C(17)-Si(2)-Si(1)	116.80(7)
		C(20)-Si(2)-Si(1)	108.09(8)

The presence of a bulky *tert*-butyl group beside two phenyl groups, makes the structure asymmetric and due to that Si(4)-Si(1)-K(1) angle with 104.17° is smaller than Si(3)-Si(1)-K(1) angle with 120.03°.

2.3 Conclusion

Some new oligosilylgermane compounds containing one or two weak germanium-hydrogen bonds and one or two germanium atoms in the backbone were synthesized. The synthesis of these germanium hydrides was based on the selective cleavage of one or two trimethylsilyl groups by butoxide attack and subsequently hydrolysis of the formed germylpotassium with diluted sulfuric acid. GC-Mass analysis of the germanium hydrides with two germanium atoms in the molecule's backbone showed high thermal sensitivity and their thermal decomposition to tris(trimethylsilyl)germane (**3**) and tetrakis(trimethylsilyl)germane (**7**) could be observed. However, germanium hydrides with only one germanium atom in the backbone showed higher thermal stability.

Synthesis of oligosilylgermanes containing one silicon and one germanium and oligosilanes containing two silicon atoms in the backbone with *tert*-butyl and phenyl substituents at one silicon atom were performed. It was found that in this group of compounds the attack of the butoxide occurred selective at a trimethylsilyl group and not at the silicon bearing the *tert*-butyl and two phenyl groups.

Chapter 3

TGA and DSC investigation of oligosilylgermanes

3 TGA and DSC investigation of oligosilylgermanes

CVD is one of the gas phase methods, widely used for the synthesis of germanium nanowires. In this method the precursor type can affect the final products composition, morphology and even resistivity to environmental conditions.⁴⁵ In an experiment DPG, NBG, and TEG were used as precursor for the VLS synthesis of germanium nanowires and among them, DPG exhibited the most appropriate reactivity. Although the synthesis was successful, germanium nanowires were introduced into an alkanethiol solution to passivate their surface and improve their oxidation resistance.³¹ In another approach germanium nanowires encapsulated within multi-walled carbon nanotubes were reported by CVD synthesis at 800 °C using phenyltrimethylgermane as precursor.⁹³

Oxidation resistance germanium nanowires covered with an amorphous layer of SiO_x has been reported where the germanium core diameter to the SiO_x shell thickness has a direct relation to the germanium to silicon ratio in the oligosilylgermane precursors.⁹⁴

Due to diversity of products according to precursor type, here different types of oligosilylgermanes are studied by TGA and DSC analysis to furthermore characterize the behavior of light and semi-heavy oligosilylgermanes for CVD synthesis of germanium nanowires.

3.1 [Tris(trimethylsilyl)silyl]trimethylgermane (33)

Figure 3-1 shows the thermogravimetric analysis (TGA) and differential scanning calorimetry (DSC) diagram related to oligosilylgermane **33**. According to the TGA diagram, evaporation of **33** commences from 80 °C and ends up with a negligible residue at 200 °C. The DSC diagram only shows the required heat for evaporation without any sign of decomposition or phase transition.

3.2 Tetrakis(trimethylsilyl)germane (34)

Figure 3-2 shows the TGA and DSC diagram of oligosilylgermane **34**. According to the TGA diagram, evaporation of **34** commences from 80 °C and ends up with a negligible residue at 200 °C. The DSC diagram only shows the required heat for evaporation without any sign of decomposition or phase transition. Although oligosilylgermane **33** and **34** have different chemical structures, they both have equal molecular weight and chemical composition resulting to a similar TGA and DSC diagram.

3.3 Hexakis(trimethylsilyl)digermane (6)

Figure 3-3 shows the TGA and DSC diagram of oligosilylgermane **6**. According to the TGA diagram the main mass loss which is about 92% commences from 90 °C and ends up at 305 °C. Second mass loss which is around 2% commences from 305 °C and ends up at 450 °C and final residue is around 6%.

The DSC diagram shows a weak endothermic signal around 150 °C but the main endothermic signal is observed at around 273 °C which is accompanied with one additional endothermic sharp peak at 288 °C and this could be a phase transition or a fast chemical reaction. What happens during the mass loss cannot be explained exactly, but it seems that it is not only evaporation/sublimation, there were also some reactions and/or phase transitions.

3.4 Pentakis(trimethylsilyl)digermane (1)

Due to the sensitivity of germanium hydride **1** to oxygen, the sample was transferred to an aluminium crucible inside the glove box and before analysis several holes were made in the crucible. Figure 3-4 shows the TGA and DSC diagram related to germanium hydride (**1**). According to the TGA diagram weight loss commences at 80 °C similar to previous oligosilylgermanes but in contrast to them with a slight weight loss at higher temperatures and a sharp weight loss occurs at 213 °C. Also the DSC diagram shows a very sharp peak at 213 °C means a fast heat absorption at this temperature. This phenomenon could be explained according to GC-Mass analysis of this compound by decomposition of germanium hydride **1** and formation of light germanium hydride **3**. From 213 °C till 450 °C a very smooth weight loss occurs and the final residue for **1** is around 25%. The high amount of residue could be explained by trap of material inside the aluminum crucible.

3.5 Conclusion

Figure 3-5 shows TGA analysis of different oligosilylgermanes that for comparison put together in one diagram. Oligosilylgermane **33** and **34** with different chemical structure but same molecular weight and chemical composition behaved similarly and show fast evaporation between 80 °C and 200 °C. Oligosilylgermane **6** with nearly twice the weight of the two previous compounds needs higher evaporation temperatures and its complete evaporation occurs at 300 °C. Germanium hydride **1** shows a unique behavior due to formation of germanium hydride **3** by thermal decomposition. In fact germanium hydride **1** shows a promising result for low temperature CDV synthesis of germanium nanostructures.

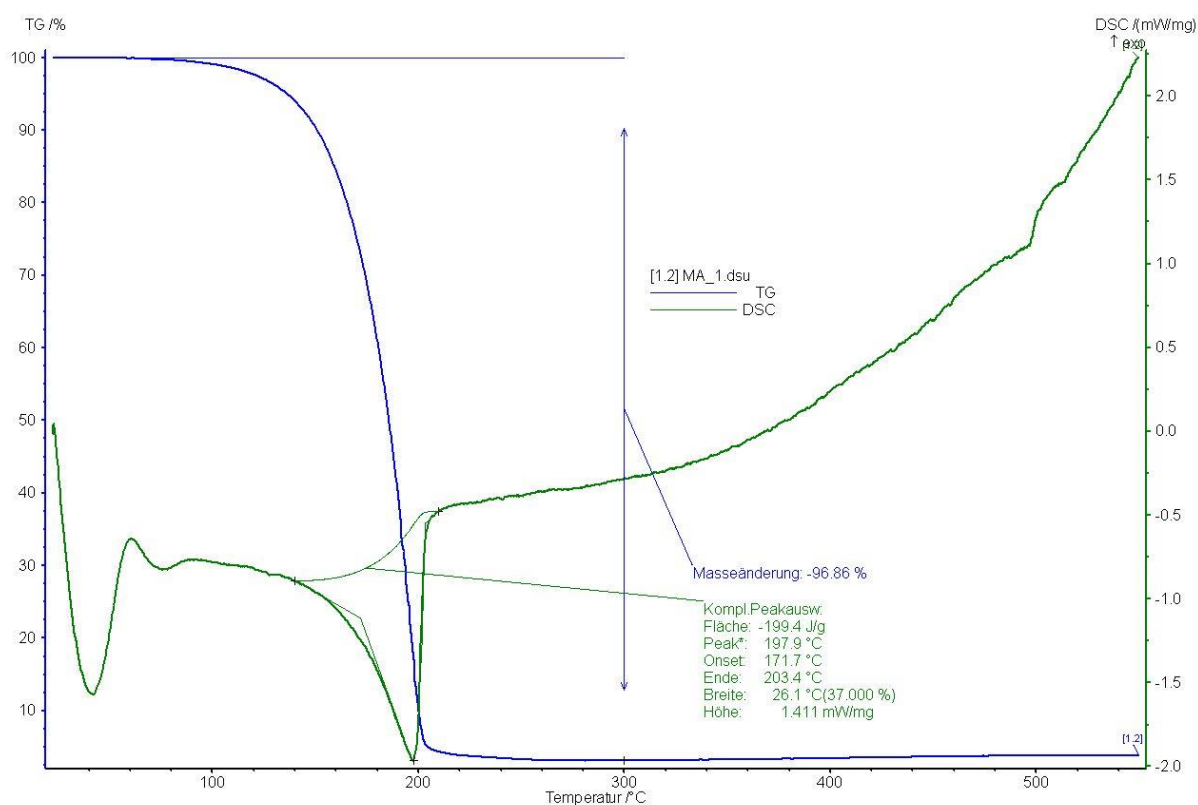


Figure 3-1. TGA and DSC diagram of [tris(trimethylsilyl)silyl]trimethylgermane (**33**).

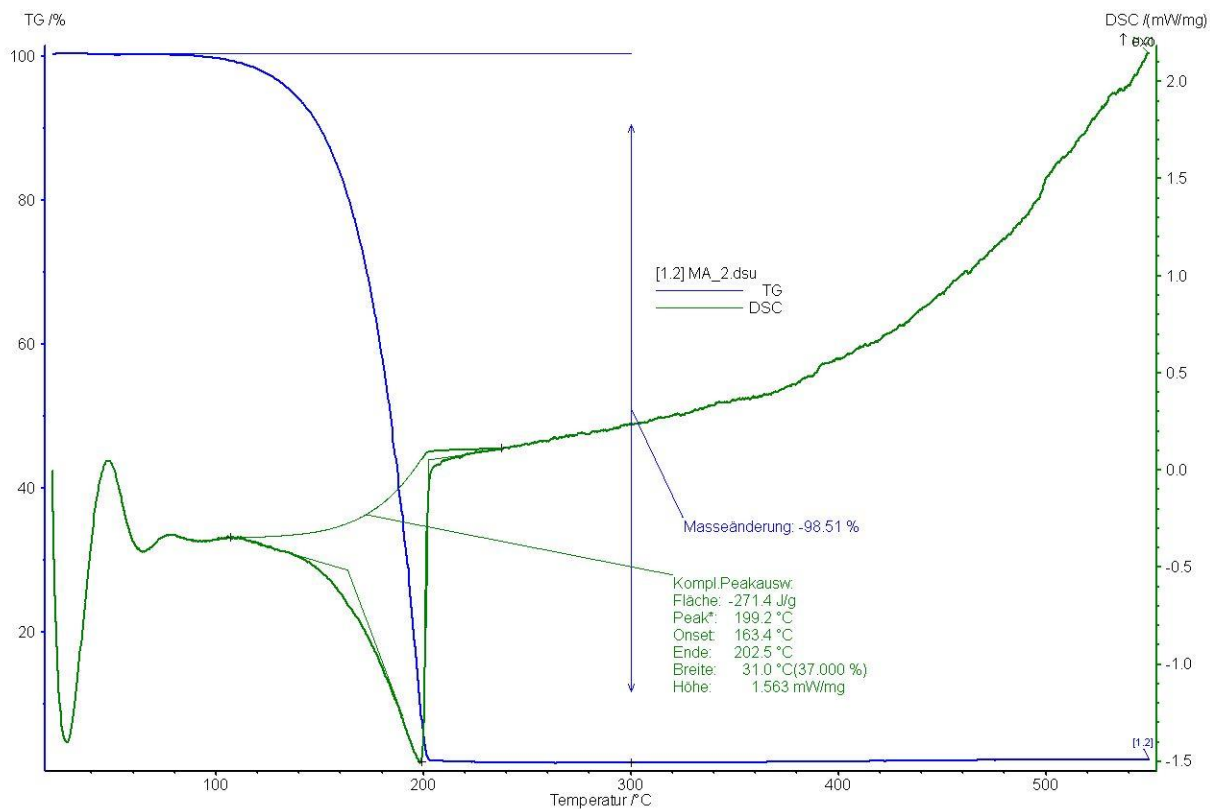


Figure 3-2. TGA and DSC diagram of tetrakis(trimethylsilyl)germane (**34**).

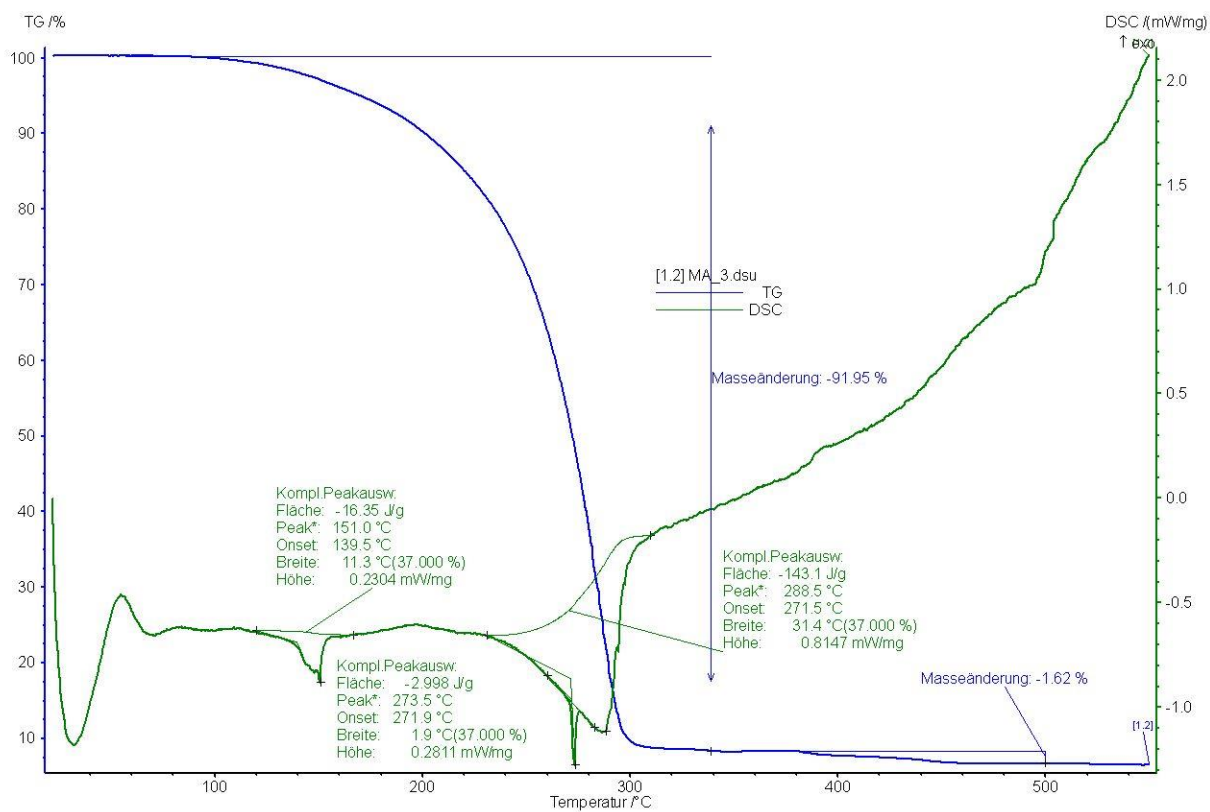


Figure 3-3. TGA and DSC diagram of hexakis(trimethylsilyl)digermane (**6**).

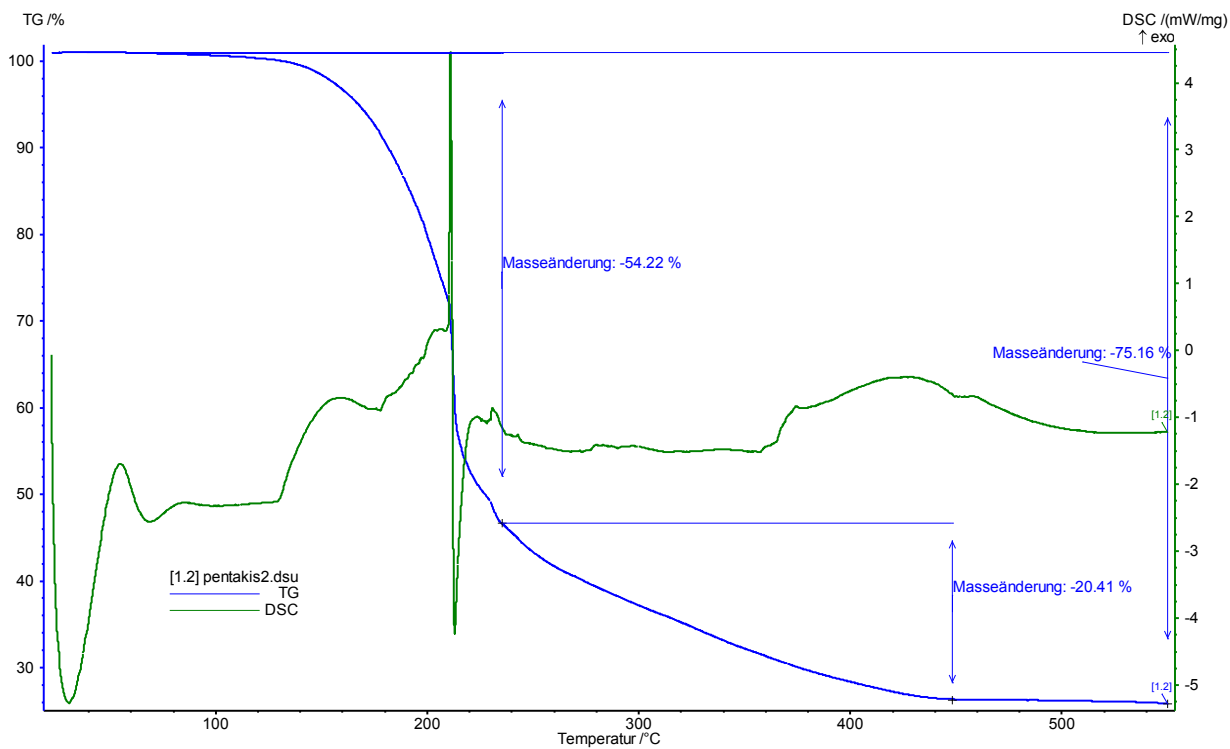


Figure 3-4. TGA and DSC diagram of pentakis(trimethylsilyl)digermane (**1**).

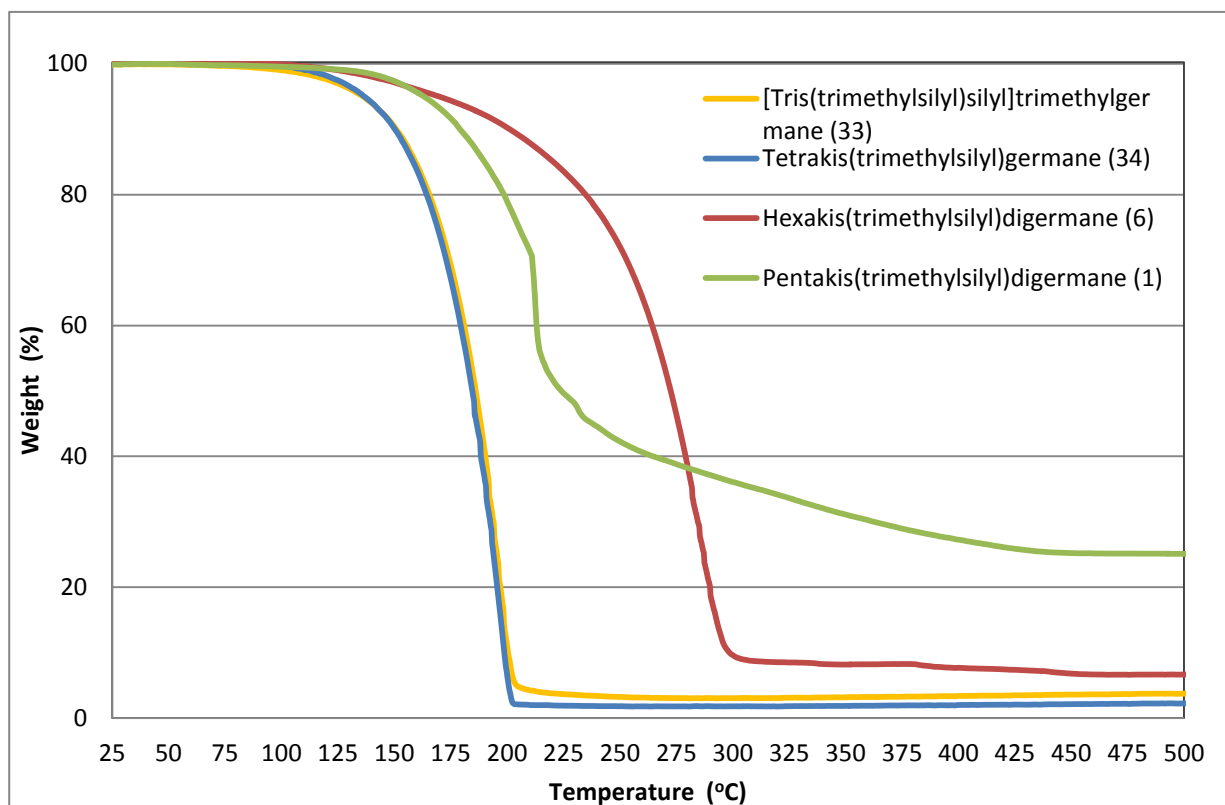


Figure 3-5. Comparison of the thermogravimetric analysis of oligosilylgermane **33**, **34**, **6** and **1**.

Chapter 4

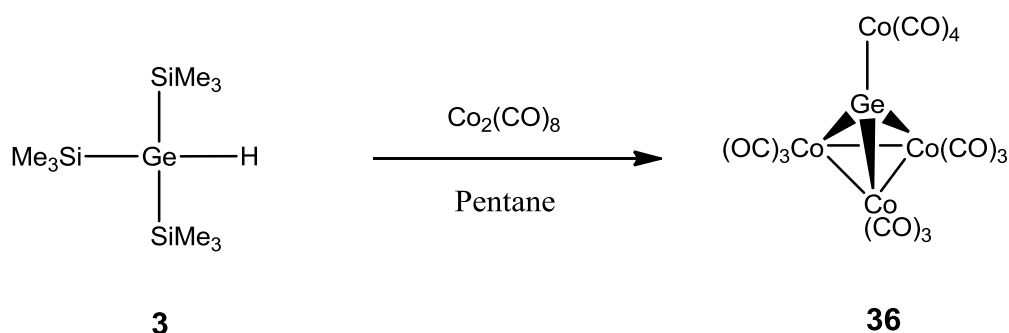
Colloidal synthesis of germanium nanoparticles

4 Colloidal synthesis of germanium nanoparticles

4.1 Germanium nanoparticles synthesis with tris(trimethylsilyl)germane (**3**) in presence of dicobalt octacarbonyl

Scheme 4-1 shows formation of tetracobalt germanium complex (**36**) by reaction of dicobalt octacarbonyl with germanium hydride **3** via a mechanism which is involving a Si-Ge bond activation in presence of cobalt reported.⁹⁵

In fact the mechanism involving Si-Ge bond activation in presence of cobalt dissociates the germanium atom of **3** and transfers it into the new complex **36**. The presence of the germanium atom in this complex could be the germanium source for the synthesis of germanium nanostructures if at higher temperatures germanium could be released from complex **36** without cobalt-carbonyl bond cleavage.



*Scheme 4-1. Formation of tetracobalt germanium complex (**36**) by reaction of dicobalt octacarbonyl with tris(trimethylsilyl)germane (**3**)*

4.1.1 In *n*-heptane with precursor to dicobalt octacarbonyl ratio 20:1 at 90 °C

Pursuing the idea of catalytic transformation of germanium hydride **3** to any types of germanium nanostructure by dicobalt octacarbonyl, germanium hydride **3** and dicobalt octacarbonyl (ratio 20:1 mole %) were dissolved in alkane solvents and heated at different temperatures in a Schlenk bomb.

Figure 4-1 shows the ²⁹Si NMR spectroscopic analysis of the reaction mixture with D₂O lock after 3 days at 90 °C in *n*-heptane. The signal at -6.1 ppm relates to germanium hydride **3** and shows that the precursor is still the main compound of the reaction mixture. Solid residue was not observed after centrifugation of the reaction mixture at 6000 rpm for 60 minutes.

4.1.2 In *n*-heptane with precursor to dicobalt octacarbonyl ratio 20:1 at 142 °C

Figure 4-2 shows ²⁹Si NMR spectroscopic analysis of the reaction mixture with D₂O lock after 24 hours at 142 °C in *n*-heptane. The height of the signal at -6.1 ppm which relates to germanium hydride **3** has decreased and new signals at -5.3 and -4.6 ppm have appeared. A black residue was obtained after centrifugation of the reaction mixture at 6000 rpm for 60 minutes which was further studied with SEM microscope.

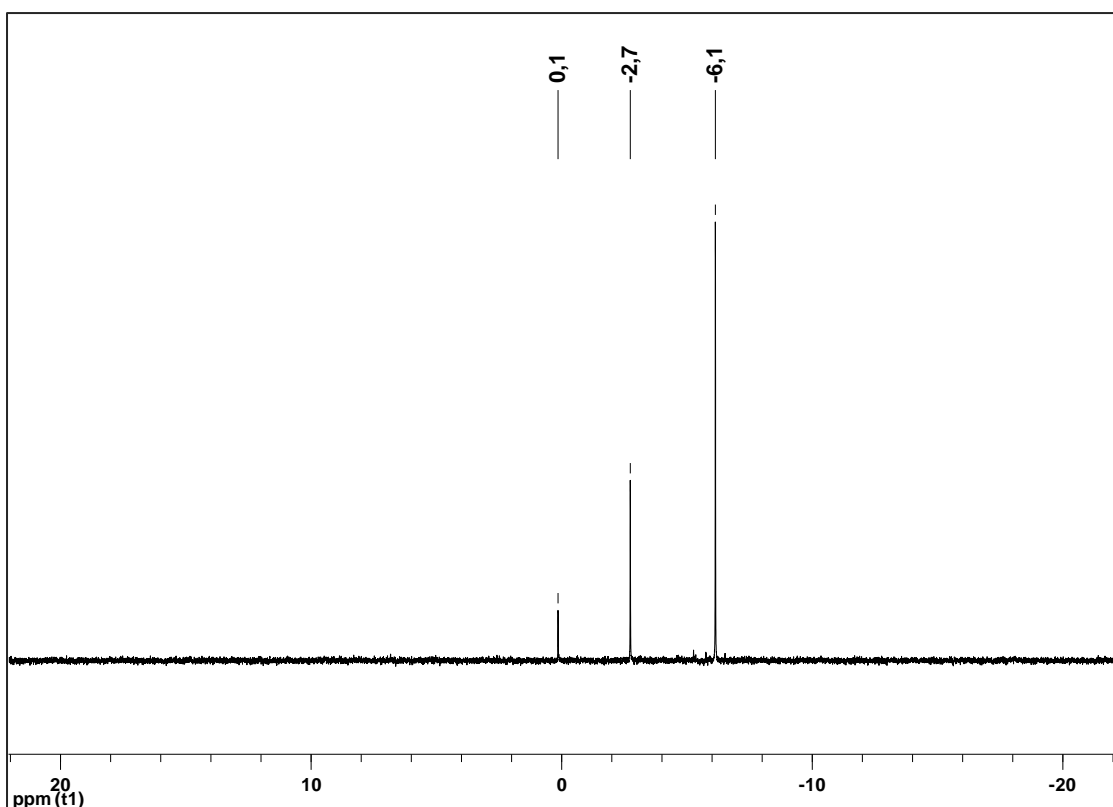


Figure 4-1. ^{29}Si NMR spectrum with D_2O lock of reaction between tris(trimethylsilyl)germane (**3**) and dicobalt octacarbonyl after 3 days at 90°C . The peak at -6.1 ppm relates to tris(trimethylsilyl)germane (**3**).

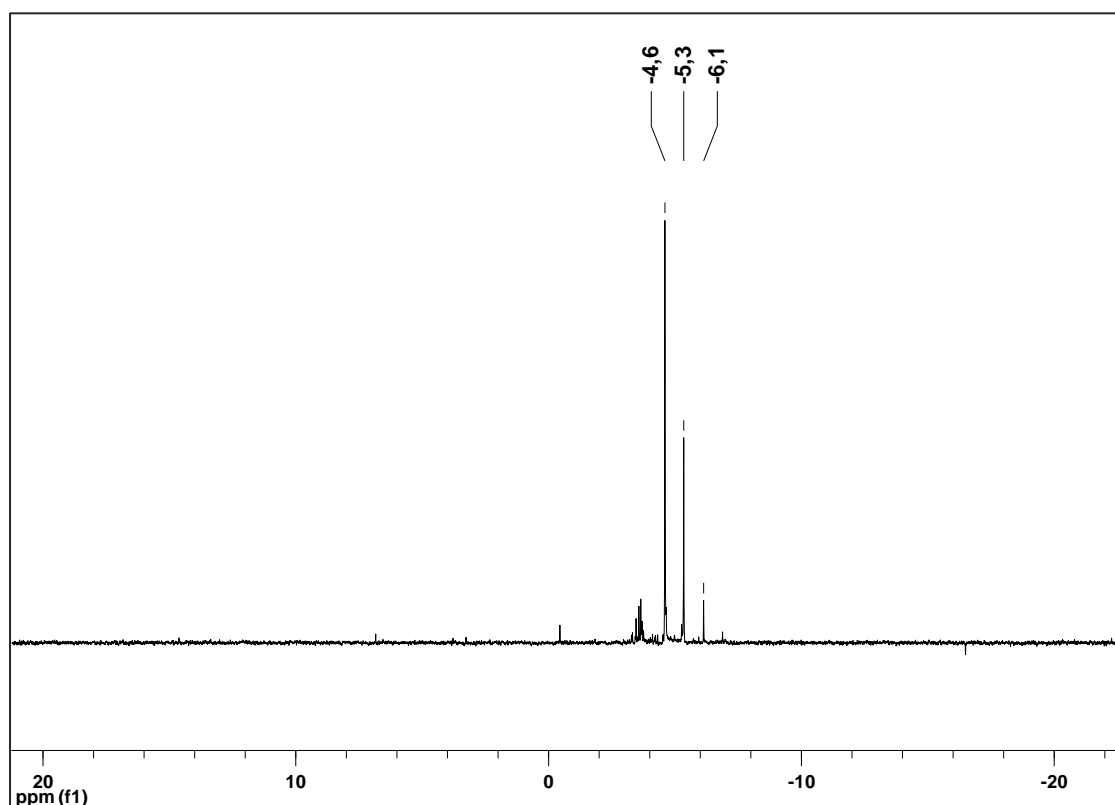


Figure 4-2. ^{29}Si NMR spectrum with D_2O lock of reaction between tris(trimethylsilyl)germane (**3**) and dicobalt octacarbonyl (20:1 molar ratio) after 24 hours at 142°C . The peak at -6.1 ppm which relates to tris(trimethylsilyl)germane (**3**) shows that most of the precursor has been consumed.

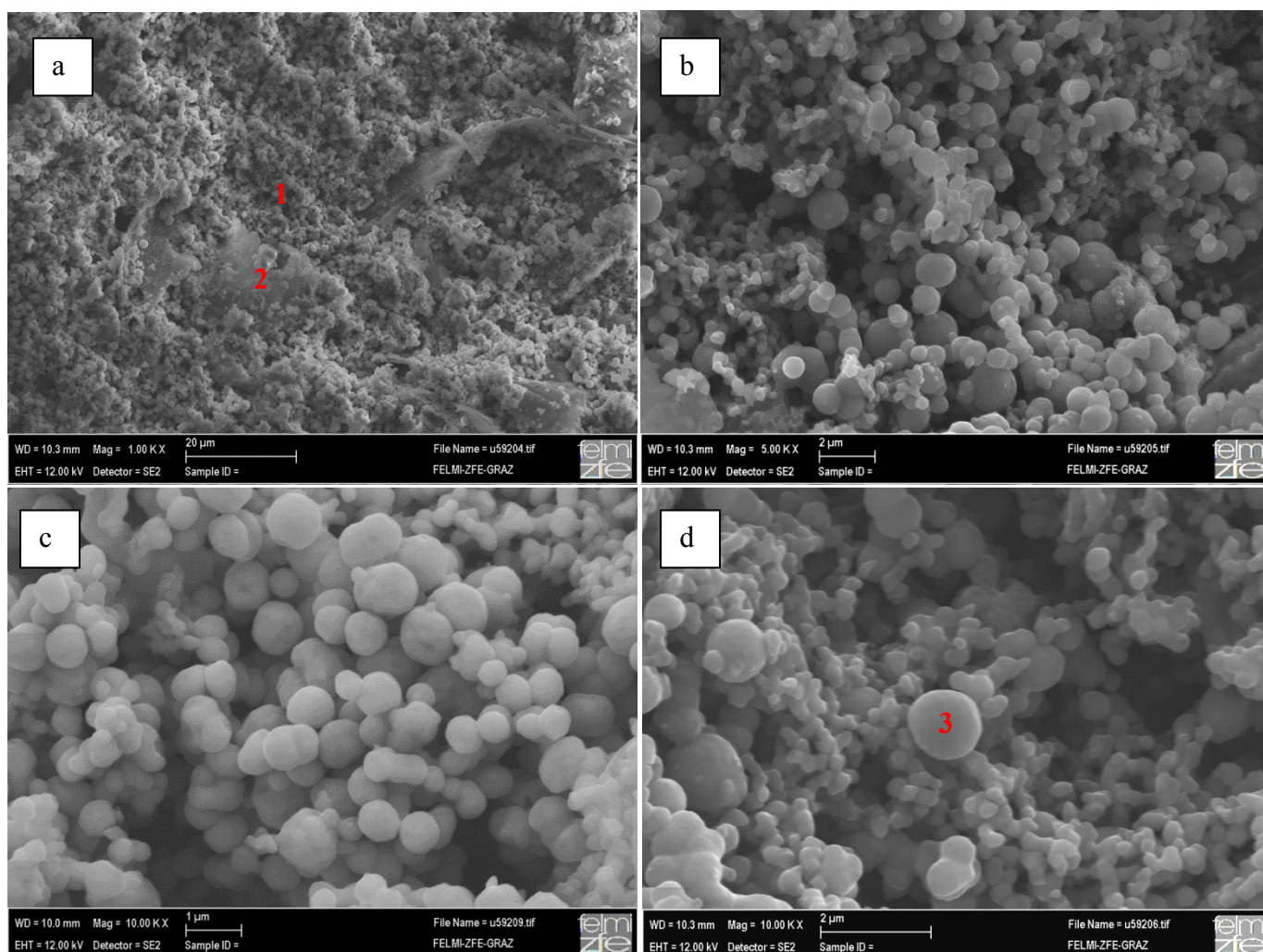


Figure 4-3. SEM images of black residue obtained from the reaction of tris(trimethylsilyl)germane (**3**) with dicobalt octacarbonyl (20:1 molar ratio) in *n*-heptane at 142 °C. a) sample contains spherical particles as well as sheet like structures. b and c) spherical particles are mainly sub 1 μm. d) an isolated sub 2 μm particle.

Table 4-1. Chemical composition comparison of spherical and sheet like structures in figure 4-3.

	Germanium (Wt %)	Cobalt (Wt %)	Silicon (Wt %)
Point 1	56.6	39.9	3.5
Point 2	41.5	55.9	2.6
Point 3	62.1	34.7	3.2

Figure 4-3 shows the SEM images of the black residue at different magnifications. The sample contains mainly spherical particles, however sheet like structures are also visible (Figure 4-3a). Spherical particles are mostly smaller than 1 μm ; however, few particles larger than 1 μm are also present in the sample.

Table 4-1 shows the chemical composition of the sample according to energy dispersive X-ray spectroscopy (EDS). It shows that both the spherical particles and the sheet like structures are mixture of germanium and cobalt. According to EDS analysis of the indicated points 1 and 2 in Figure 4-3a, the amount of germanium in a group of spherical particles in point 1 is higher than the amount of germanium in sheet like structure in point 2. According to Figure 4-3d, EDS analysis of sub 2 μm particle (indicated as point 3) shows that the amount of germanium in one spherical particle is equal to a group of spherical particles and in general is higher than the amount of germanium in sheet like structure. According to both ^{29}Si NMR spectrum of the reaction mixture in Figure 4-2 and EDS analysis of black residue in Table 4-1, silicon mostly remains in the solution and does not incorporate into the black residue.

4.1.3 In *n*-dodecane with precursor to dicobalt octacarbonyl ratio 20:1 at 142 °C in presence of TOPO

As *n*-heptane boils at 142 °C, *n*-dodecane with boiling point of 214 °C was used for this reaction. In contrast to the previous reaction, here capping ligand (TOPO) was used to prevent aggregation of nanocrystals. Also due to the inhomogeneity of the product in previous reaction and presence of both the spherical particles and the sheet like structures with different chemical composition, here the reaction was performed while stirring at 400 rpm to increase the homogeneity of the product.

For this reaction germanium hydride **3** to TOPO in a molar ratio of 1:3 and germanium hydride **3** to dicobalt octacarbonyl in a molar ratio of 20:1 was used.

Figure 4-4 shows ^{29}Si NMR spectroscopic analysis of the reaction mixture with D_2O lock. Figure 4-4a shows the reaction mixture after 24 hours and Figure 4-4b shows it after 48 hours. Again the signal at -6.1 ppm relates to germanium hydride **3**. Comparison between Figure 4-2 and 4-4 shows that the precursor consumption rate in the presence of TOPO is slower. Also due to the presence of TOPO a new signal at 6.9 ppm appears. The signal at 6.9 ppm relates to hexamethyldisiloxane.⁹⁶ Formation of hexamethyldisiloxane is due to the reaction between trimethylsilyl groups of precursor and oxygen of TOPO. After 48 hours the obtained black solution was mixed with methanol to remove the capping ligand and afterwards centrifuged at 6000 rpm for 10 minutes under nitrogen to isolate the solid product.

Figure 4-5 shows SEM images of the solid obtained after centrifugation. In presence of TOPO as a capping ligand two different types of particles were formed. The first type consists of mainly spherical particles with diameter close to 1 μm . The second type consists of very fine particles with nanometer dimensions. Although in the absence of TOPO sheet like structures as well as spherical particles with wide range of diameter are formed, in presence of TOPO mainly two different types of spherical particles are obtained. Table 4-2 shows chemical composition of the sample according to EDS analysis which relates to Figure 4-5. According to Figure 4-5a, in area 1 both micro and nanoscale particles are present.

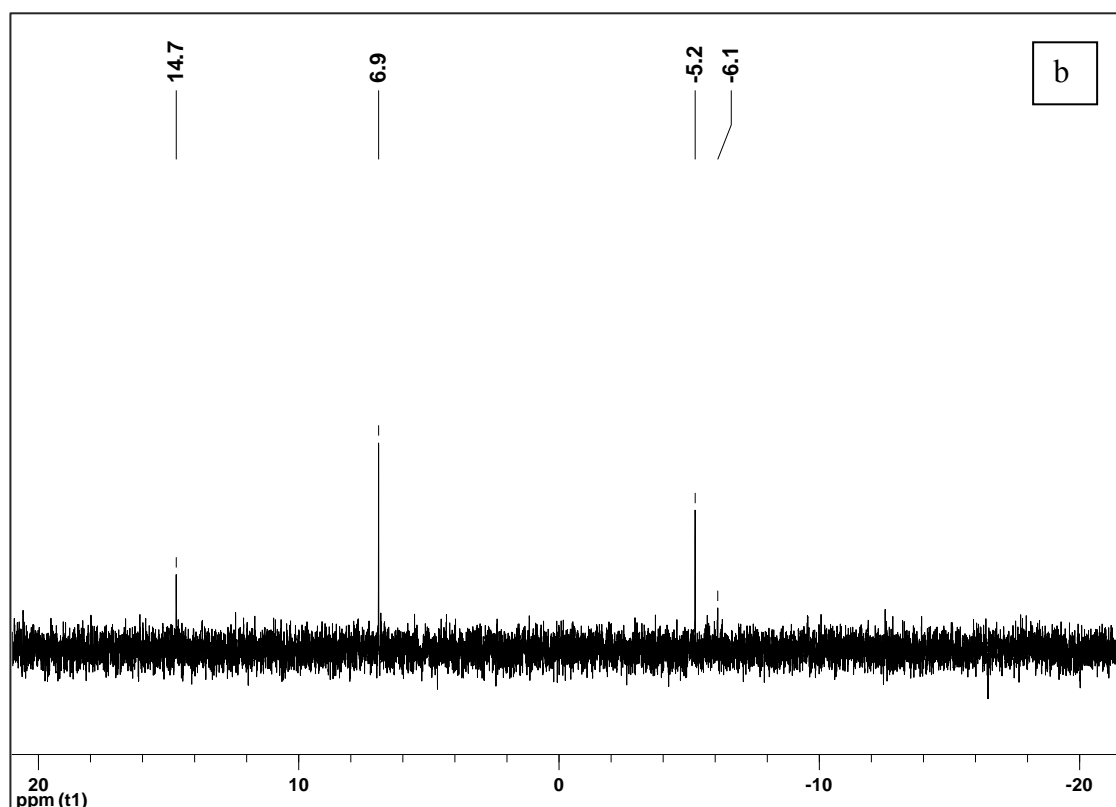
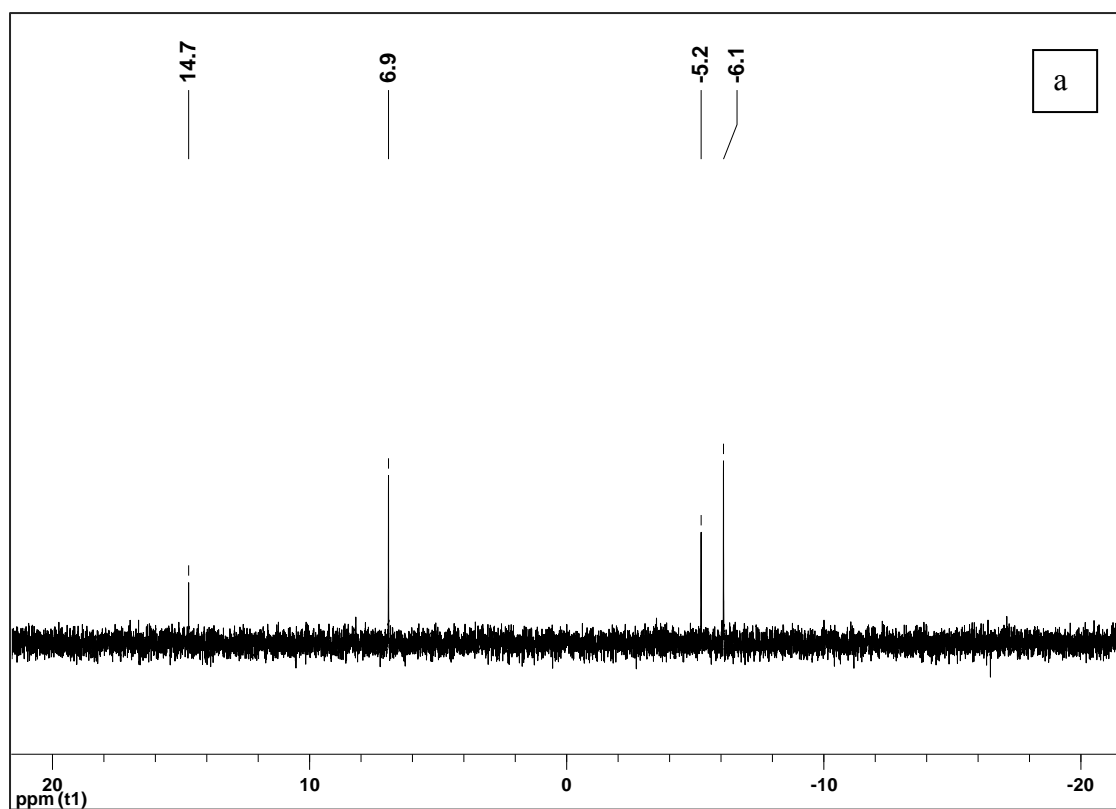


Figure 4-4. ^{29}Si NMR spectrum with D_2O lock of reaction between tris(trimethylsilyl)germane (**3**) and dicobalt octacarbonyl (20:1 molar ratio) at 142°C in *n*-dodecane in presence of TOPO. The peak at -6.1 ppm relates to tris(trimethylsilyl)germane (**3**) and peak at 6.9 ppm relates to hexamethyldisiloxane. a) After 24 hours. b) After 48 hours.

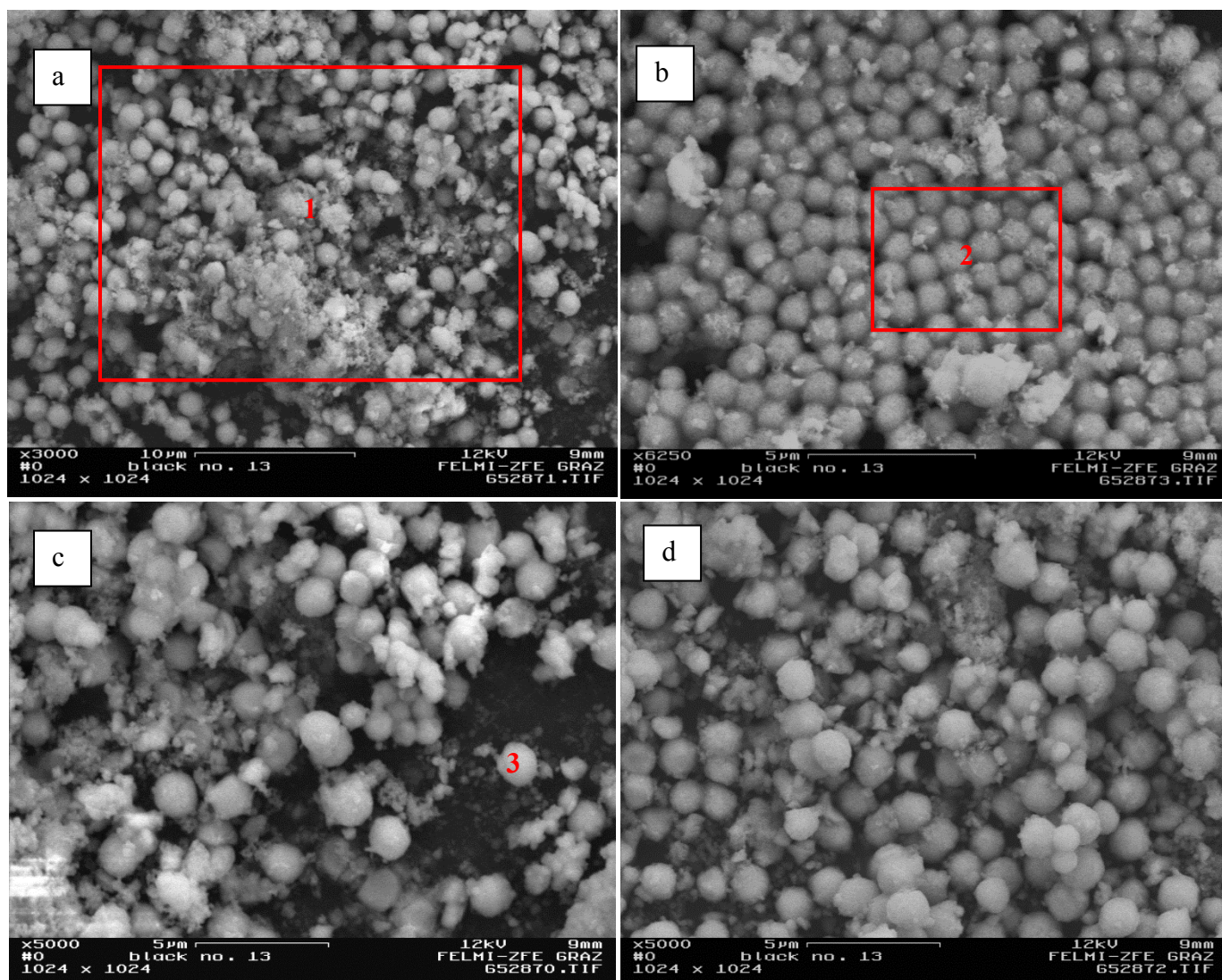


Figure 4-5. SEM images of spherical particles obtained from the reaction of tris(trimethylsilyl)germane (**3**) with dicobalt octacarbonyl (20:1 molar ratio) in *n*-dodecane in presence of TOPO at 142 °C. Sample contains mainly spherical particles with diameter close to 1 μ m beside particles with nanometer scale.

Table 4-2. Chemical composition of different areas of microscale and nanoscale particles in Figure 4-5.

	Germanium (Wt %)	Cobalt (Wt %)	Silicon (Wt %)
Area 1	82.3	12.0	5.7
Area 2	86.2	12.7	1.1
Point 3	83.1	14.0	2.9

The average chemical composition of the whole sample in area 1 is very similar to a group of microscale particles marked as area 2 in Figure 4-5b as well as one microscale particle in Figure 4-5c marked as point 3. This in fact confirms more homogeneity of the sample in comparison to the sample without TOPO and mechanical stirring. The main difference between chemical composition of microscale particles and area 1 in Figure 4-5a is the higher amount of silicon in area 1. As the quantity of silicon in microscale particles is small, this in fact has relation mainly to nanoscale particles. As the nanoscale particles are agglomerated to each other, the higher amount of silicon in nanoscale particles could be due to the residue of the solution containing hexamethyldisiloxane or other silicon containing compounds among them (^{29}Si NMR spectrum in Figure 4-4b shows different silicon containing compounds in the reaction mixture).

4.1.4 In *n*-dodecane with precursor to dicobalt octacarbonyl ratio 20:4 at 142 °C in presence of TOPO

In this reaction the molar ratio of precursor to dicobalt octacarbonyl was changed from 20:1 in the previous reaction to 20:4. The reason was to find out the effect of higher quantity of dicobalt octacarbonyl onto the particle size distribution of the final product.

Figure 4-6 shows ^{29}Si NMR spectroscopic analysis of the reaction mixture with D_2O lock. Figure 4-6a shows the reaction mixture after 24 hours and Figure 4-6b after 48 hours. Again the signal at -6.1 ppm relates to germanium hydride **3**. The presence of the precursor after 48 hours shows that higher quantity of dicobalt octacarbonyl slightly prolongs the consumption of the precursor.

After 48 hours the obtained black solution was mixed with methanol to remove the capping ligand and afterwards it was centrifuged at 6000 rpm for 10 minutes under nitrogen to isolate a solid product.

Figure 4-7 shows SEM images of the solid obtained after centrifugation. In contrast to the sample with a precursor to dicobalt octacarbonyl ratio of 20:1 with sub $1\ \mu\text{m}$ particles, here with higher amount of cobalt, the particle size increases. Figure 4-7c shows several particles with a diameter close to $3\ \mu\text{m}$. In both samples with different amount of dicobalt octacarbonyl nanoscale particles are present. Due to presence of nanoscale particles as well as particles with diameter close to $3\ \mu\text{m}$, the sample with higher amount of cobalt has wider particle size distribution.

Table 4-3 shows the chemical composition of the sample according to EDS analysis which relates to Figure 4-7a. Comparison between micro and nanoscale particles shows that higher amount of cobalt exist in microscale particles. Also comparison between microscale particles of both samples with different amount of cobalt according to Table 4-2 and 4-3 shows that by increasing the amount of dicobalt octacarbonyl the level of cobalt in microscale particles will increase dramatically which shows the direct influence of cobalt to the formation of microscale particles.

Here the amount of silicon in nanoscale particles is higher than microscale particles which similar to the previous sample could be due to the residue of the solution containing hexamethyldisiloxane or other silicon containing compounds among them (^{29}Si NMR spectrum in Figure 4-6b shows different silicon containing compounds in the reaction mixture).

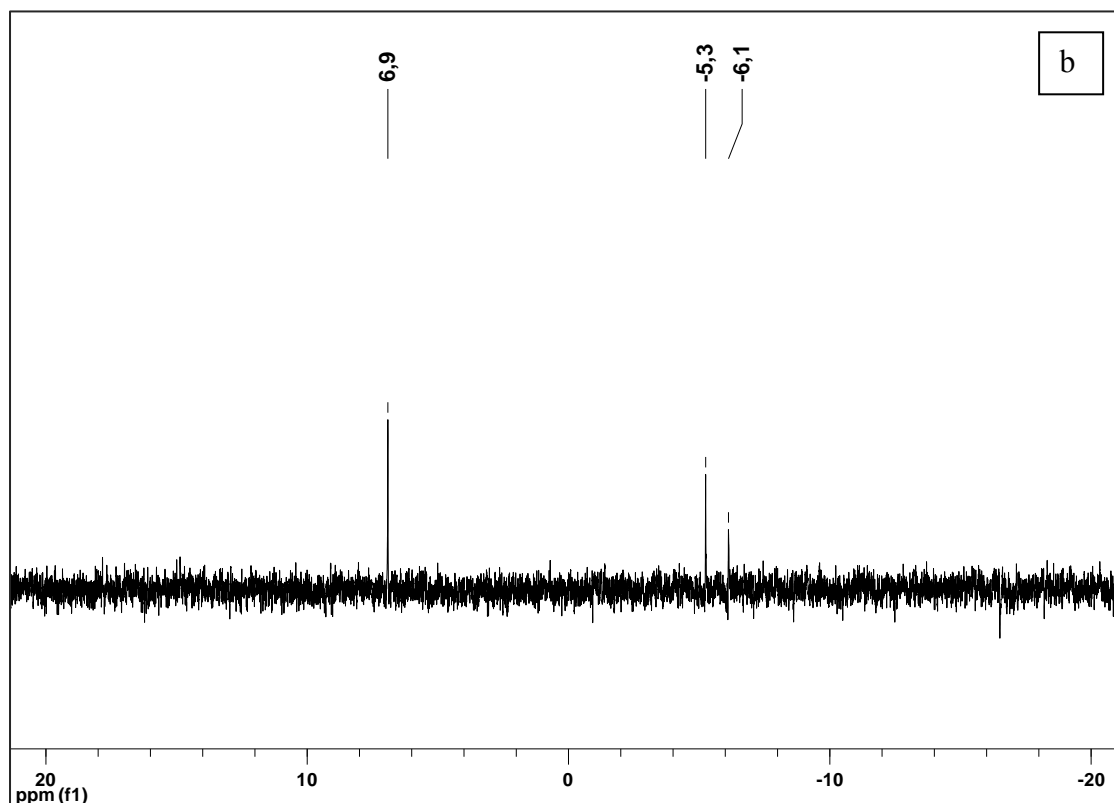
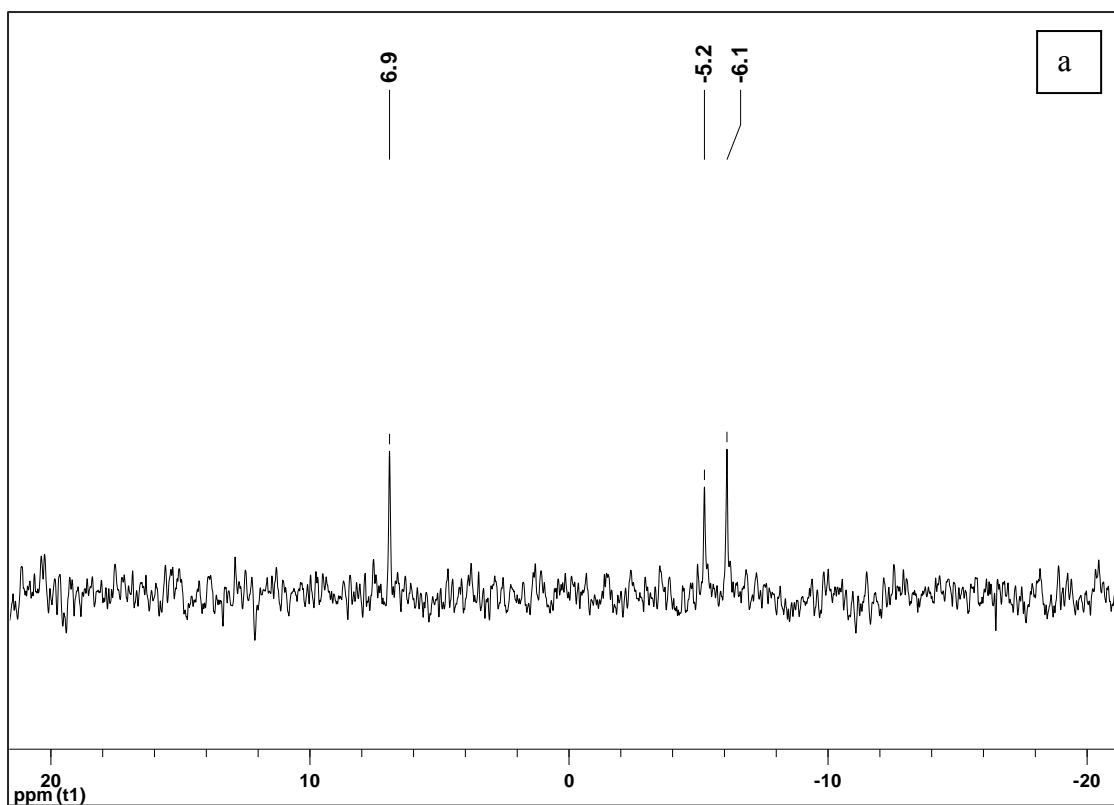


Figure 4-6. ^{29}Si NMR spectrum with D_2O lock of reaction between tris(trimethylsilyl)germane (**3**) and dicobalt octacarbonyl (20:4 molar ratio) at $142\text{ }^\circ\text{C}$ in *n*-dodecane in presence of TOPO. The peak at -6.1 ppm relates to tris(trimethylsilyl)germane (**3**) and peak at 6.9 ppm relates to hexamethyldisiloxane. a) After 24 hours. b) After 48 hours.

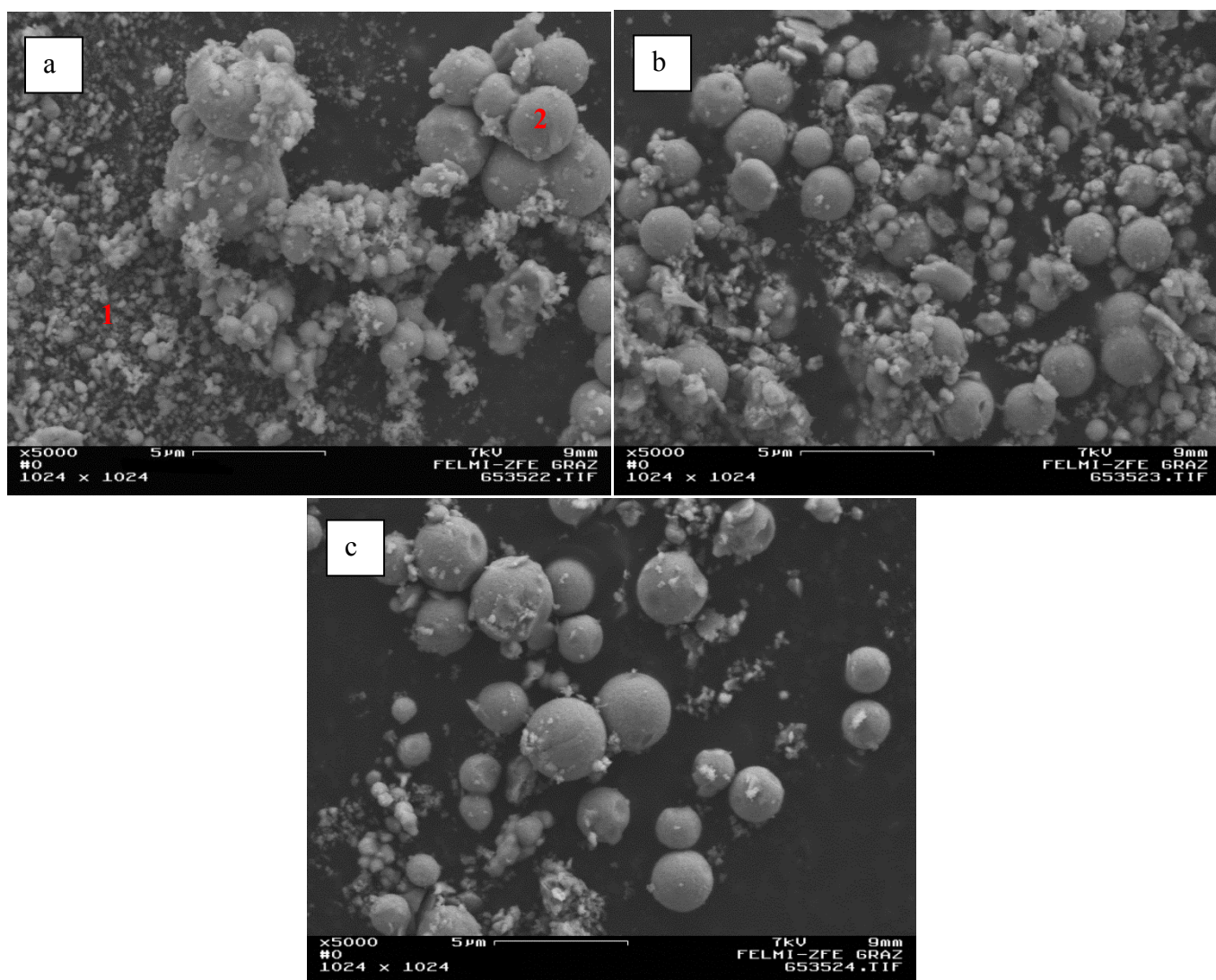


Figure 4-7. SEM images of spherical particles obtained from the reaction of tris(trimethylsilyl)germane (**3**) with dicobalt octacarbonyl (20:4 molar ratio) in *n*-dodecane in presence of TOPO at 142 °C. Sample contains sub 3 μm particles.

Table 4-3. Chemical composition of different areas of microscale and nanoscale particles in Figure 4-7a.

	Germanium (Wt %)	Cobalt (Wt %)	Silicon (Wt %)
Point 1 (nanoscale particles)	83.5	14.2	2.3
Point 2 (microscale particles)	74.5	25.0	0.6

4.1.5 In *p*-xylene with precursor to dicobalt octacarbonyl ratio 20:1 at 142 °C in the presence of TOPO

p-Xylene was used instead of *n*-dodecane to figure out the effect of the solvent onto the morphology and size distribution of particles and the other parameters were kept similar to that in section 4.1.3.

Figure 4-8 shows ²⁹Si NMR spectroscopic analysis of reaction mixture with D₂O lock. Figure 4-8a shows the reaction mixture after 24 hours and Figure 4-8b shows the reaction mixture after 6 days. Signal at -6.5 ppm relates to germanium hydride **3**. Slow consumption of precursor over 6 days which was not observed previously in case of any alkane solvents is due to *p*-xylene.

According to visual observation after 24 hours the color of the reaction mixture was black but during the next 5 days it slowly turned to black/brownish and at the end it became completely brown.

This brown solution was mixed with methanol to remove the capping ligand and centrifuged at 6000 rpm for 10 minutes under nitrogen to isolate a solid product.

Figure 4-9 shows the SEM images of the solid obtained after centrifugation. The sample contains both micro and nanoscale particles. In contrast to the samples prepared in alkanes with small amounts of nanoscale particles, here with *p*-xylene the amount of nanoscale particles is higher. According to Figure 4-9, the microscale particles are mainly sub 1 μm which is similar to the size of microscale particles of the sample in section 4.1.3. It should be considered that both samples the one with *p*-xylene and the sample in section 4.1.3 have the same amount of dicobalt octacarbonyl in the reaction mixture.

Table 4-4 shows the chemical composition of the sample according to EDS analysis which relates to Figure 4-9c. Cobalt exists mainly in microscale particles and the nanoscale particles are mainly composed of germanium. Chemical composition of microscale particles here and in section 4.1.3 according to Table 4-4 and 4-2 are similar to each other. However the amount of nanoscale particles which are composed of germanium is higher in *p*-xylene.

Figure 4.9d shows a Z-contrast image of the sample. In Z-contrast or atomic number image in SEM analysis, phases with higher atomic number appear brighter while phases with lower atomic number appear darker.⁹⁷ According to Z-contrast image, microscale particles which are brighter than nanoscale particles are made of heavier elements. The Z-contrast image is in agreement with the EDS analysis which shows cobalt exists mainly in microscale particles.

As the chemical composition of microscale particles here and in section 4.1.3 is equal to each other, it seems that initially microscale particles are forming and when the amount of cobalt decreases in the reaction mixture, formation of nanoscale particles starts which are mainly composed of germanium. This indeed is in accordance with solution's colour change from black to brown according to visual observation. Color of solutions in section 4.1.3 and 4.1.4 with alkanes as solvents were black and these samples according to SEM images composed of microscale particles. However the sample in *p*-xylene was black at the initial step and then turned to brown within 5 days. It also shows that formation of black microscale particles in the presence of cobalt is fast but the formation of nanoscale particles in the absence of cobalt is slow. Slow formation of nanoscale particles in the absence of cobalt could occur by thermal decomposition of **3** followed by the reaction of a trimethylsilyl group with the oxygen atom of TOPO to form hexamethyldisiloxane.

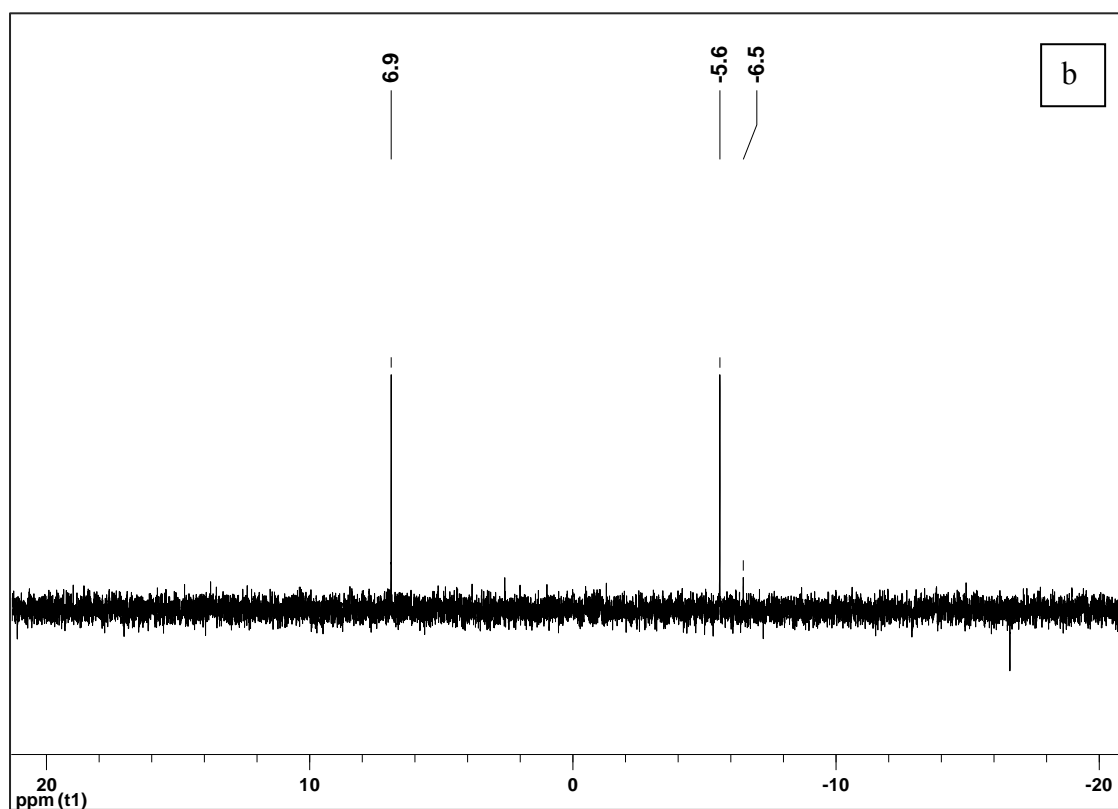
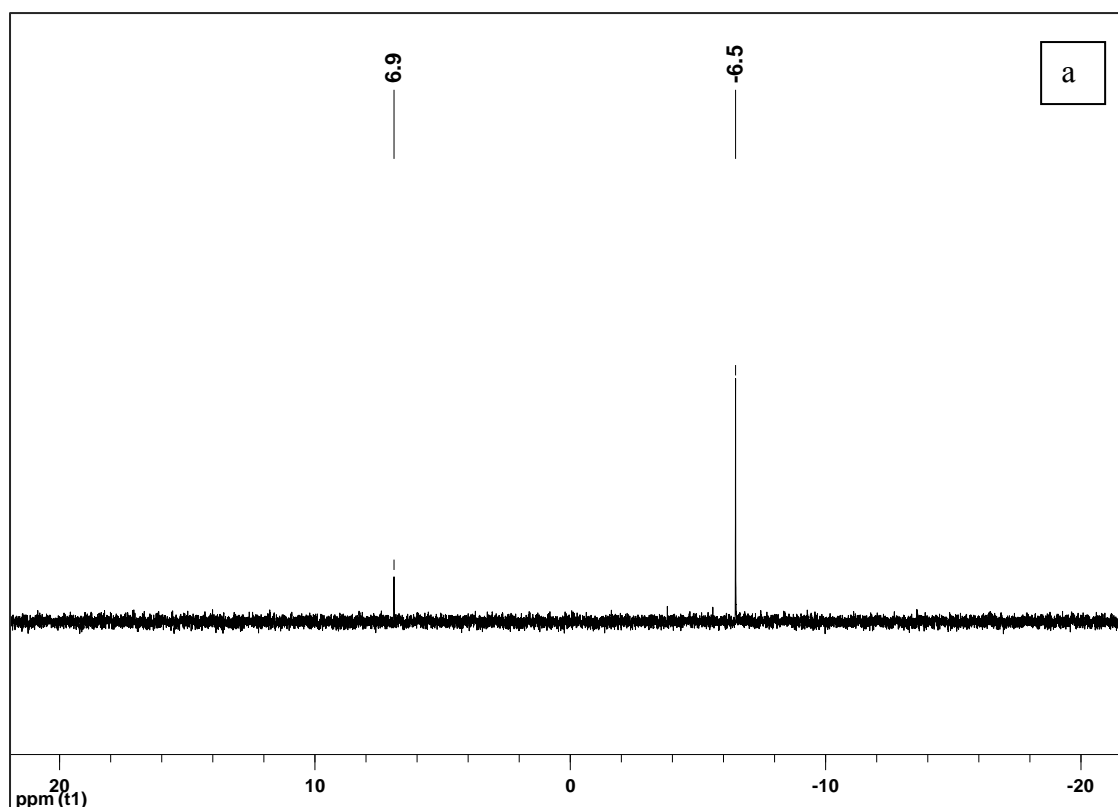


Figure 4-8. ^{29}Si NMR spectrum with D_2O lock of reaction between tris(trimethylsilyl)germane (**3**) and dicobalt octacarbonyl (20:1 molar ratio) at 142°C in *p*-xylene in presence of TOPO. The peak at -6.5 ppm relates to tris(trimethylsilyl)germane (**3**) and peak at 6.9 ppm relates to hexamethyldisiloxane. a) After 24 hours. b) After 6 days.

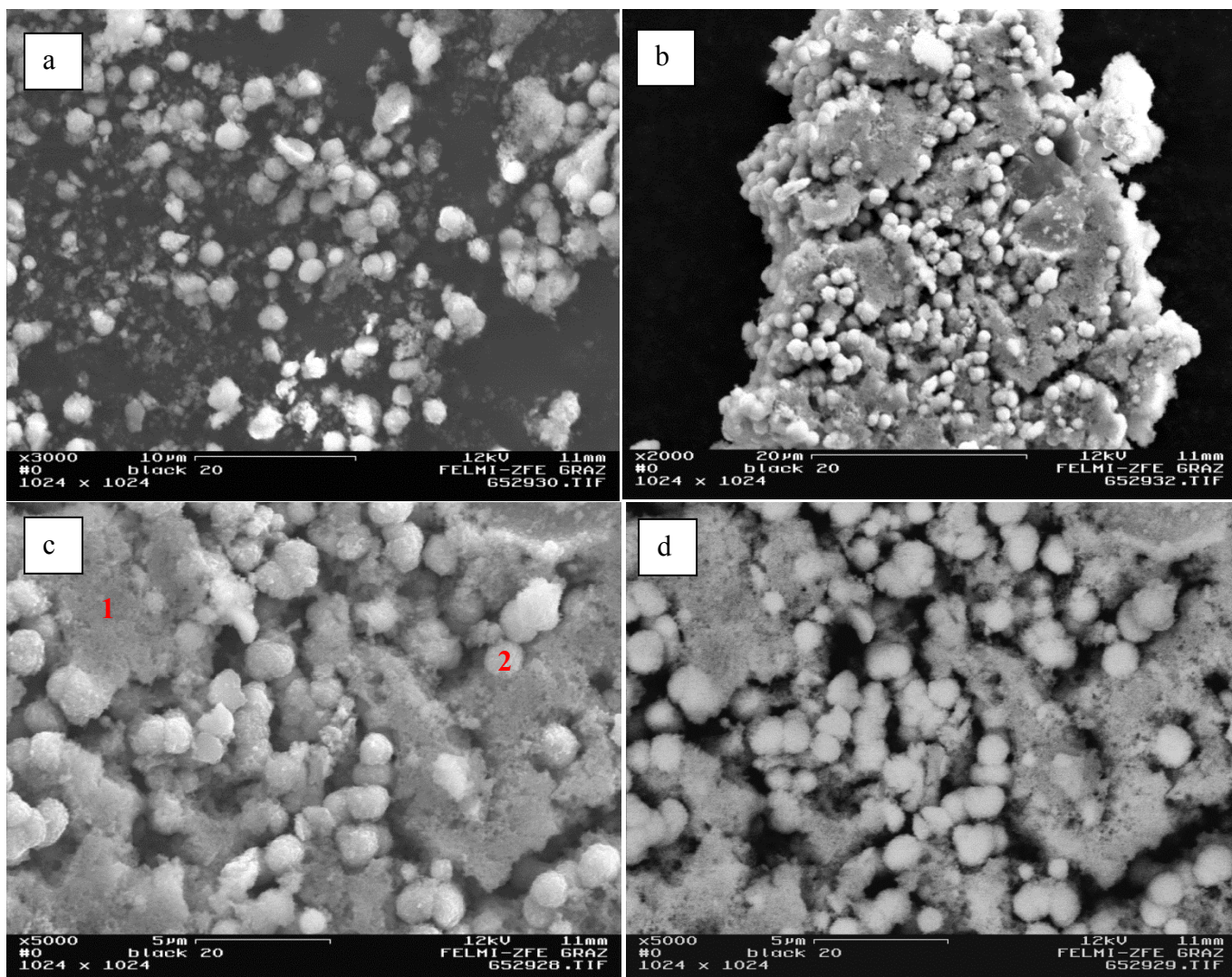


Figure 4-9. SEM images of spherical particles obtained from the reaction of tris(trimethylsilyl)germane (**3**) with dicobalt octacarbonyl (20:1 molar ratio) in *p*-xylene in presence of TOPO at 142 °C. Sample contains both sub 1 μm spherical particles and very fine nanoscale particles. d) Z-contrast image shows brighter microscale particles composed of heavier elements in comparison to darker nanoscale particles.

Table 4-4. Chemical composition of different areas of microscale and nanoscale particles in Figure 4-7c.

	Germanium (Wt %)	Cobalt (Wt %)	Silicon (Wt %)
Point 1 (nanoscale particles)	97.0	1.7	1.1
Point 2 (microscale particles)	85.1	14.6	0.3

4.2 Germanium nanoparticles synthesis with tris(trimethylsilyl)germane precursor without dicobalt octacarbonyl

4.2.1 In *n*-dodecane without dicobalt octacarbonyl at 142 °C in presence of TOPO

It was found previously that spherical microscale particles containing high level of cobalt are formed via a mechanism involving dicobalt octacarbonyl. However, nanoscale particles mainly composed of germanium were formed via thermal decomposition of precursor. To understand the effect of dicobalt octacarbonyl on the formation of spherical microscale particles, here thermal decomposition of the precursor was performed only in presence of TOPO without dicobalt octacarbonyl. Figure 4-10 shows ^{29}Si NMR spectroscopic analysis of the reaction mixture with D_2O lock after 48 hours. Signal at -6.1 ppm which relates to germanium hydride **3** displays complete consumption of precursor. Due to absence of cobalt, a brown solution was obtained instead of a black solution. The obtained brown solution was mixed with methanol to remove the capping ligand and after centrifugation at 6000 rpm for 10 minutes under nitrogen a solid product was isolated.

Figure 4-11 shows SEM images of the solid obtained after centrifugation. The sample contains very fine nanoscale particles as well as irregular sub-micron particles. Although big particles exist in the absence of dicobalt octacarbonyl but their size is smaller and their shape is completely irregular in comparison to the spherical microscale particles of those samples with dicobalt octacarbonyl.

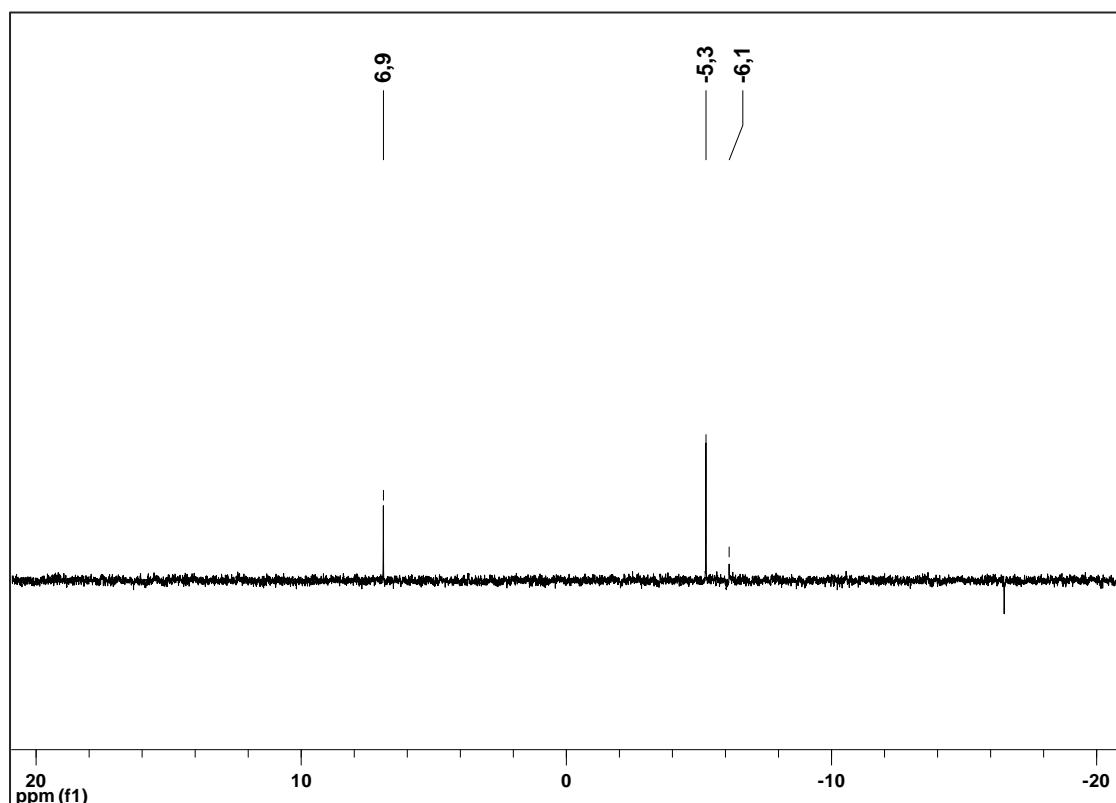


Figure 4-10. ^{29}Si NMR spectrum with D_2O lock of thermal decomposition reaction of tris(trimethylsilyl)germane (**3**) at 142 °C in *n*-dodecane in presence of TOPO after 48 hours. The peak at -6.1 ppm relates to tris(trimethylsilyl)germane (**3**) and peak at 6.9 ppm relates to hexamethyldisiloxane. a)

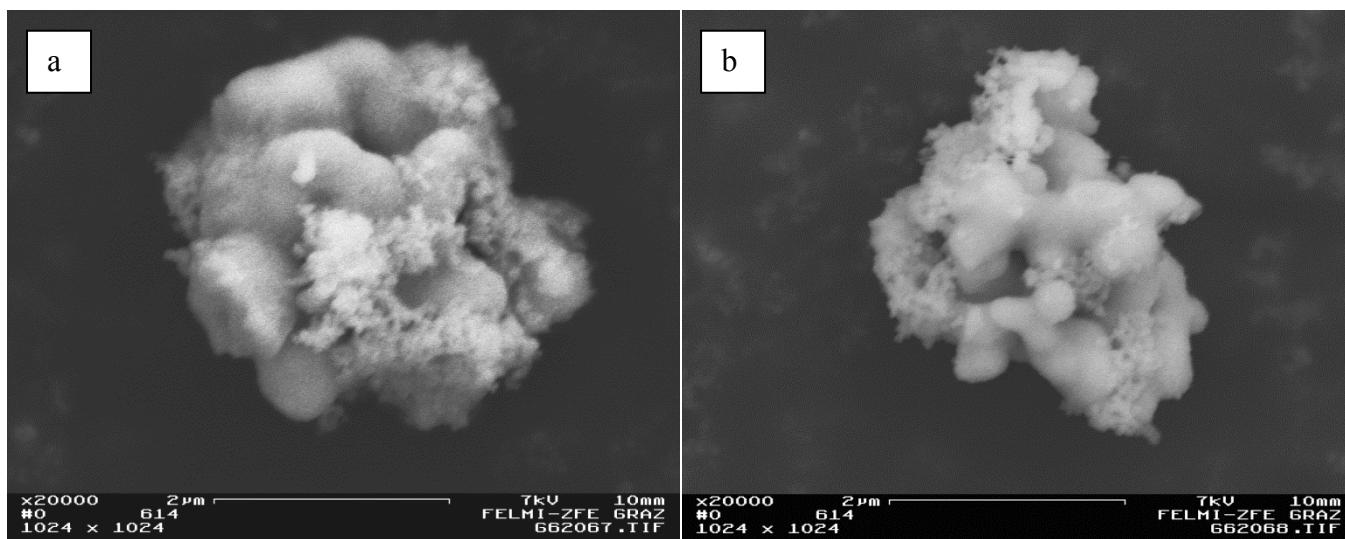


Figure 4-11. SEM images of nanoparticles obtained from the thermal decomposition of tris(trimethylsilyl)germane (**3**) without dicobalt octacarbonyl in *n*-dodecane in presence of TOPO at 142 °C. Sample contains irregular sub 500 nm particles as well as very fine nanoparticles.

In fact it can be concluded that dicobalt octacarbonyl increases the size of big particles and makes them spherical and lack of that decreases the size and increases irregularity. Formation of more spherical particles in presence of cobalt could be related to higher surface tension within the microscale particles due to presence of cobalt atoms. Table 4-5 provides the chemical composition of the sample according to EDS analysis which relates to Figure 4-11a and shows that particles are composed of germanium.

Table 4-5. Chemical composition of the sample prepared without dicobalt octacarbonyl related to figure 4-11a

	Germanium (Wt %)	Cobalt (Wt %)	Silicon (Wt %)
Point 1 (nanoscale particles)	99.2	-	0.8

4.2.2 In *n*-hexadecane without dicobalt octacarbonyl at 252 °C in presence of TOPO and oleylamine

As slow decomposition of precursor in presence of TOPO at low temperatures is along with formation of big particles, the synthesis temperature was increased to 252 °C and due to that *n*-hexadecane as solvent with higher boiling point was used instead of *n*-dodecane. To avoid formation of big particles at lower temperatures, the precursor was injected to a reaction flask once the reaction flask temperature was set to 252 °C. The whole reaction time was 20 minutes. As it is found that even at 252 °C, TOPO cannot control the particle size, oleylamine as another capping ligand was added to the reaction mixture.

Figure 4-12 shows the as prepared colloidal solution of germanium nanoparticles with brownish color. Figure 4-13 shows ^{29}Si NMR spectrum of reaction mixture after 20 minutes at $252\text{ }^\circ\text{C}$. According to NMR spectrum, precursor was completely consumed and only signals of by-products at 6.9 and 1.9 ppm were identified.

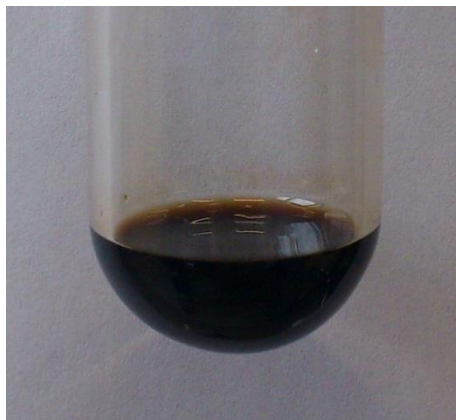


Figure 4-12. Colloidal solution of germanium nanoparticles as synthesized from tris(trimethylsilyl)germane (**3**) in presence of TOPO and oleylamine after 20 minutes heating at $252\text{ }^\circ\text{C}$.

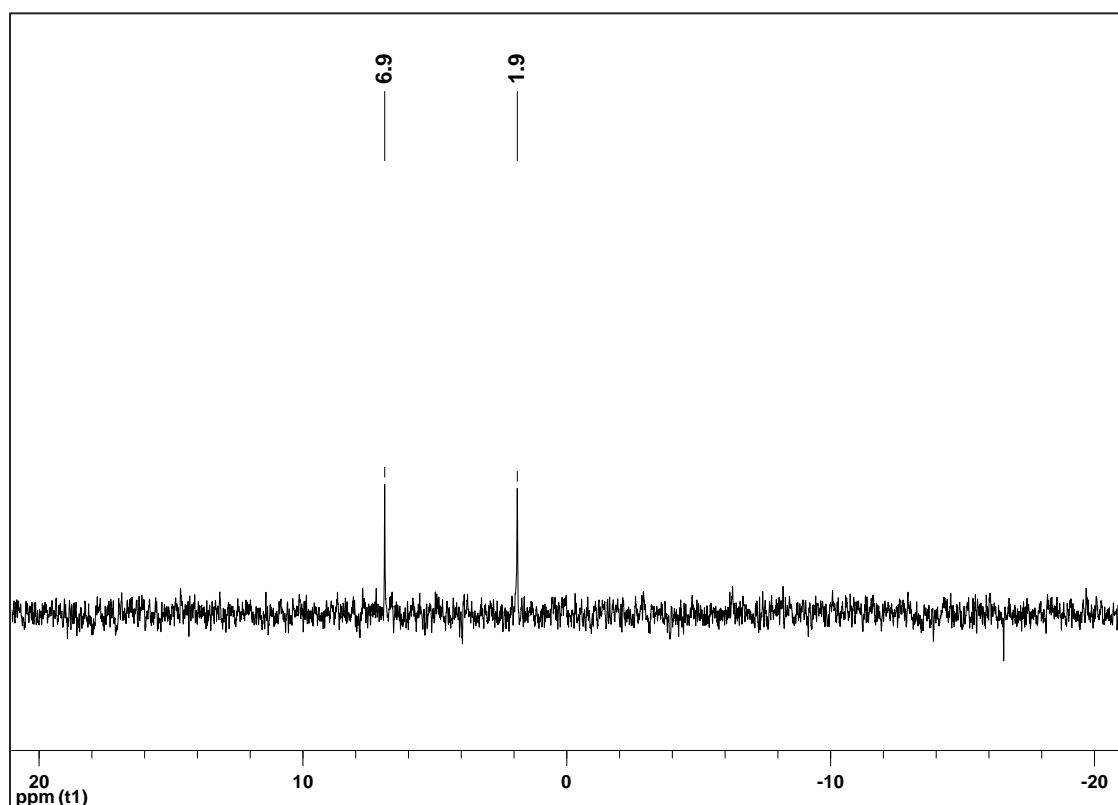


Figure 4-13. ^{29}Si NMR spectrum of colloidal solution of germanium nanoparticles synthesized from tris(trimethylsilyl)germane (**3**) in presence of TOPO and oleylamine after 20 minutes heating at $252\text{ }^\circ\text{C}$. (D_2O lock).

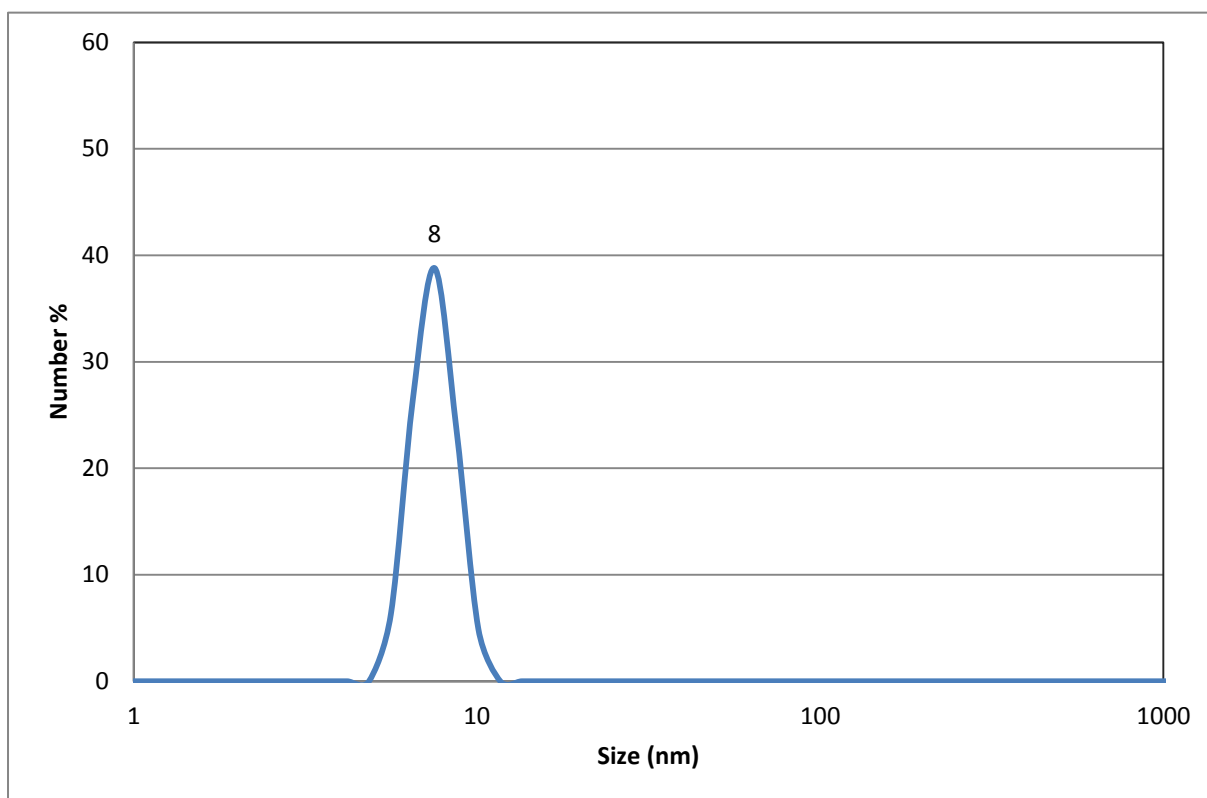


Figure 4-14. DLS number distribution of colloidal solution of germanium nanoparticles as synthesized from tris(trimethylsilyl)germane (**3**) in presence of TOPO and oleylamine after 20 minutes heating at 252 °C.

Figure 4-14 shows as synthesized DLS number distribution of germanium nanoparticles. Germanium nanoparticles have narrow size distribution from 5 to 11 nm with mean size of 8 nm. Although the sample is homogenous, immediately after dilution of the sample, a white precipitate forms which makes the DLS measurement impossible and incorrect. It seems that during the synthesis a polymerization might occur in the reaction mixture which makes the whole sample a single unite and any manipulation, disturbs the structure of this single unite and causes formation of a white precipitate.

4.3 Conclusion

This study confirmed that tris(trimethylsilyl)germane (**3**) has the potential to be used as a promising precursor for the synthesis of germanium containing nanostructures. Although germanium hydride **3** contains silicon atoms, these atoms do not participate in the structure of the final product due to the strong bonds between silicon and methyl groups.

In practice, initial assumption involving germanium dissociation from germanium hydride **3** by dicobalt octacarbonyl catalytic effect and formation of pure germanium particles has failed due to cobalt-carbonyl bond cleavage and formation of particles composed of germanium-cobalt alloy.

Reaction of germanium hydride **3** and dicobalt octacarbonyl without TOPO were involved formation of sub-micron particles of germanium-cobalt alloy while in presence of TOPO beside microscale particles, very fine nanoscale particles of germanium were formed.

However, without dicobalt octacarbonyl at 252 °C, colloidal solution of germanium nanoparticles with mean particle size of 8 nm was obtained.

In general it can be concluded that dicobalt octacarbonyl is responsible for formation of spherical microscale particles and higher amount of it is the reason for the formation of larger microscale particles, instead TOPO was responsible for the formation of very fine nanoscale particles. Without dicobalt octacarbonyl highly irregular sub-micron particles instead of spherical microscale particles are formed. Formation of more spherical particles in presence of cobalt could be due to higher surface tension within the microscale particles because of cobalt atoms.

Chapter 5

Colloidal synthesis of indium nanoparticles

5 Colloidal synthesis of indium nanoparticles

5.1 Synthesis of indium nanoparticles in polar medium followed by phase transfer to a non-polar medium

5.1.1 Indium nanoparticles capped tri-*n*-butylphosphine

One of the key points in the reduction synthesis of nanoparticles is the driving force. To increase the driving force upon a suitable reductant, also precursor's chemical composition is important.^{7,9} Due to that to obtain a high driving force for finer nanoparticles indium(III) chloride was chosen as a precursor to react with LiBH₄.

For dissolution of indium(III) chloride a polar solvent is required. Isobutylamine⁹ and diethylene glycol¹⁰ as polar solvents were previously used for the reduction synthesis of indium nanoparticles and here dimethylformamide (DMF) was used.

Different types of capping ligands have been reported to stabilize the colloidal solution of nanoparticles and to avoid the particles over growth during the synthesis. Capping ligands have two main characteristics. The first one is their ability to donate an electron pair to nanoparticles and the second one is their long aliphatic chain which makes them soluble in non-polar solvents. Capping ligands containing oxygen, nitrogen, phosphorous and sulfur can donate an electron to nanoparticles and bond to them.⁹⁸ The presence of a long aliphatic chain in the structure of the capping ligands increases the floatation of nanoparticles in non-polar solvents and avoids particles aggregation. Here tri-*n*-butylphosphine (TBP) with a short aliphatic chain is used instead of TOP with a long aliphatic chain as a capping ligand to find out the effect of TBP on the synthesis of indium nanoparticles. In the first step the effect of indium(III) chloride concentration on the average particle size was studied.

Figure 5-1 shows the relation between indium(III) chloride concentration in DMF and nanoparticles size distribution measured by dynamic light scattering method. The indium(III) chloride concentration increases according to Table 5-1. Although the mean particle size varies between samples, all of them have narrow size distribution of indium nanoparticles.

Table 5-1. Indium(III) chloride concentration change in DMF in different samples

	Sample A	Sample B	Sample C	Sample D
Concentration (mM)	18.3	27.4	36.5	45.6

By increasing the indium(III) chloride concentration from 18.3 mM to 27.4 mM and then to 36.5 mM the mean particle size decreases from 22 to 15 nm and finally to 8 nm respectively. But in contrast to this previous trend, by increasing the indium(III) chloride concentration to 45.6 mM the mean particle size increases to 20 nm. (Figure 5-2)

It seems that initially by increasing the precursor concentration, indium embryos formation increases and consequently the indium(0) inside the solution divides to more embryos, therefore the particle size decreases. But in sample D the presence of a high amount of indium(0) even after the formation of embryos is responsible for particles over growth.

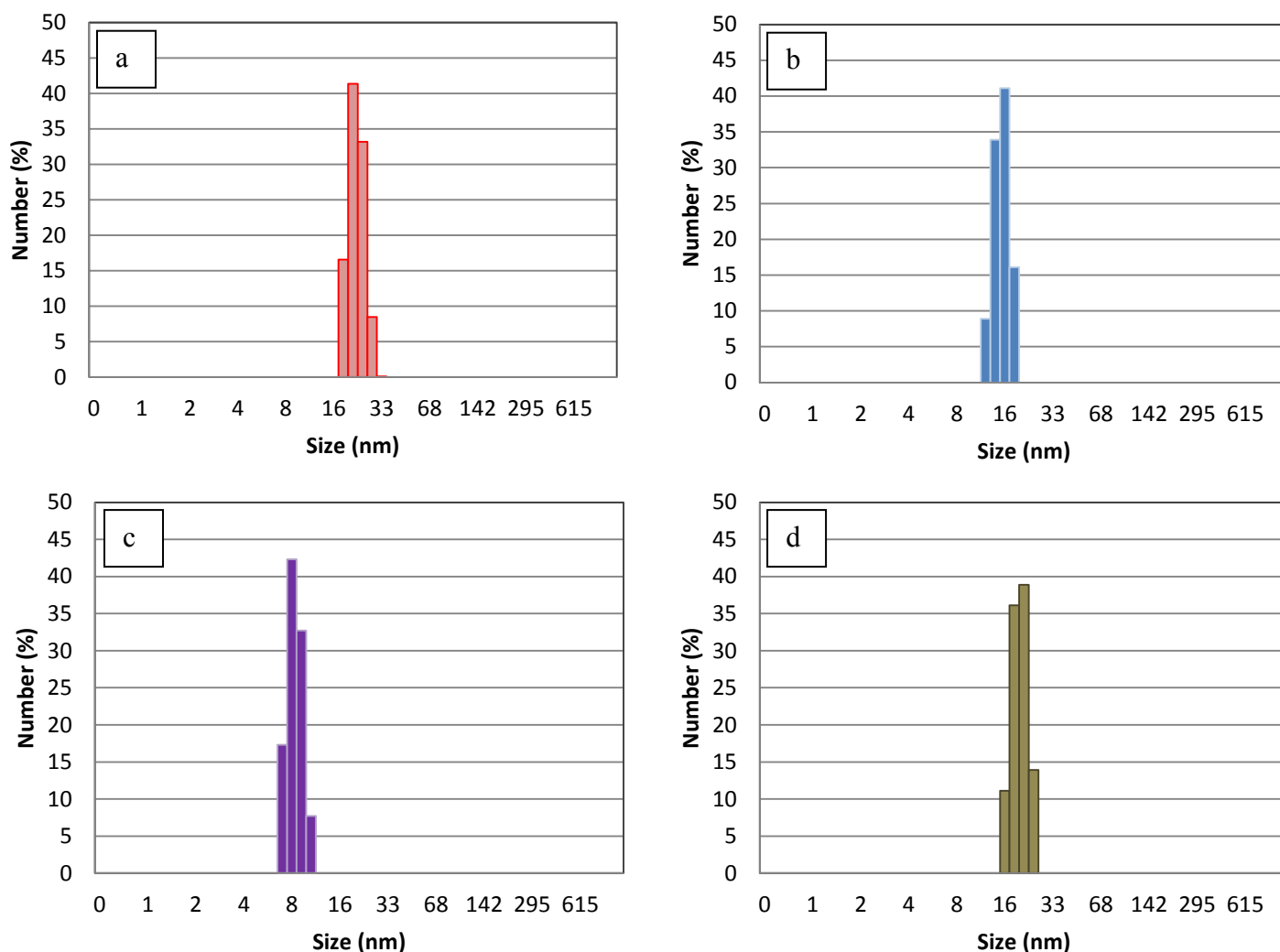


Figure 5-1. DLS analysis of Indium nanoparticles capped TBP with different InCl_3 concentration in DMF. Down is InCl_3 concentration related to each sample.

Sample a) 18.3 mM, Sample b) 27.4 mM, Sample c) 36.5 mM, Sample d) 45.6 mM.

Figure 5-3 shows bright field TEM image of indium nanoparticles of sample C. It shows sub 10 nm spherical nanoparticles in accordance with the DLS result. The TEM sample is prepared by dropping two drops of the in situ synthesized colloidal solution of indium nanoparticles on the TEM grid. The TEM grid containing indium nanoparticles was kept under nitrogen to preserve the nanoparticles from moisture.

Figure 5-3b shows the high resolution TEM image of two indium nanoparticles. Inset shows an area with crystalline order and atomic planes. Figure 5-4 which is a fast Fourier transformation of particles in Figure 5-3b contains some rings and dots which shows partial crystallinity. However Figure 5-5 which is SAED pattern of particles in Figure 5-3b shows amorphous nanoparticles.

Figure 5-6 provides the X-ray diffraction (XRD) pattern of indium nanoparticles. Due to the presence of a large peak at the beginning of the spectrum the sample contains mainly amorphous compound. However, presence of some small peaks in the spectrum shows that crystalline compound(s) exist in the sample but due to weakness of peaks it was not possible to

determine the crystalline compound(s). The highest possibility for the peak at 30 degree could be indium oxide due to oxidation of indium nanoparticles during the sample transfer to the XRD instrument.

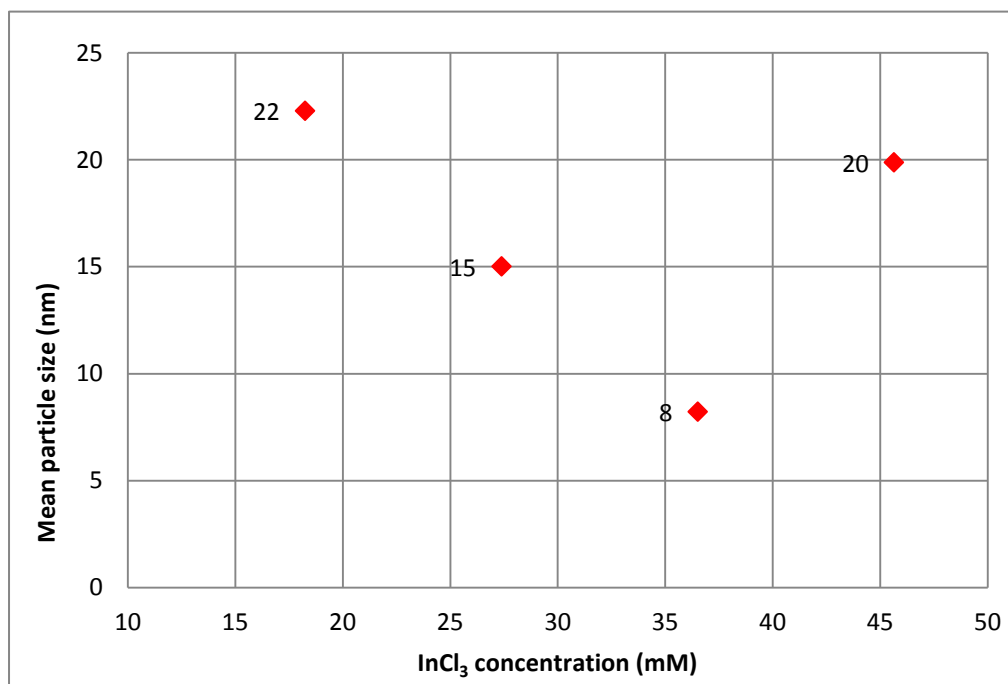


Figure 5-2. Relation between InCl₃ concentration in DMF and mean particle size diameter measured by DLS technique. Numbers on the left side of the squares show mean particle size.

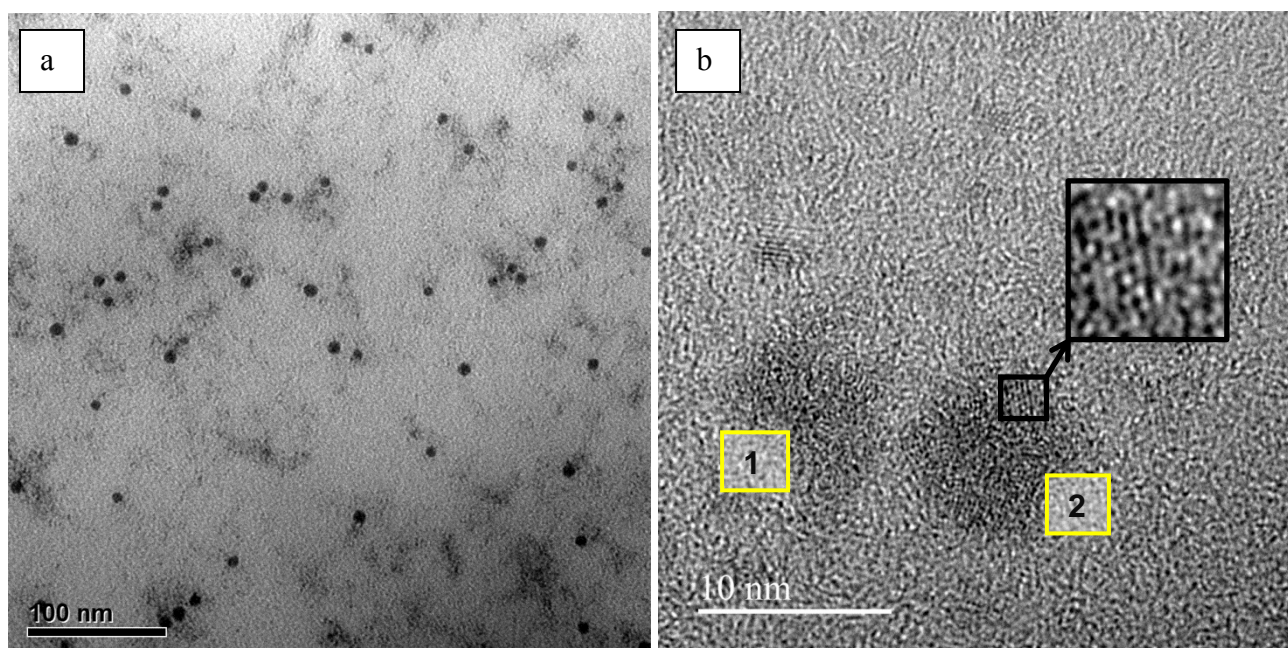


Figure 5-3. a) Bright filed TEM image of indium nanoparticles of sample C. b) Bright filed high resolution TEM image of two indium nanoparticles of sample C. Inset shows part of indium nanoparticle with crystalline order and atomic planes.

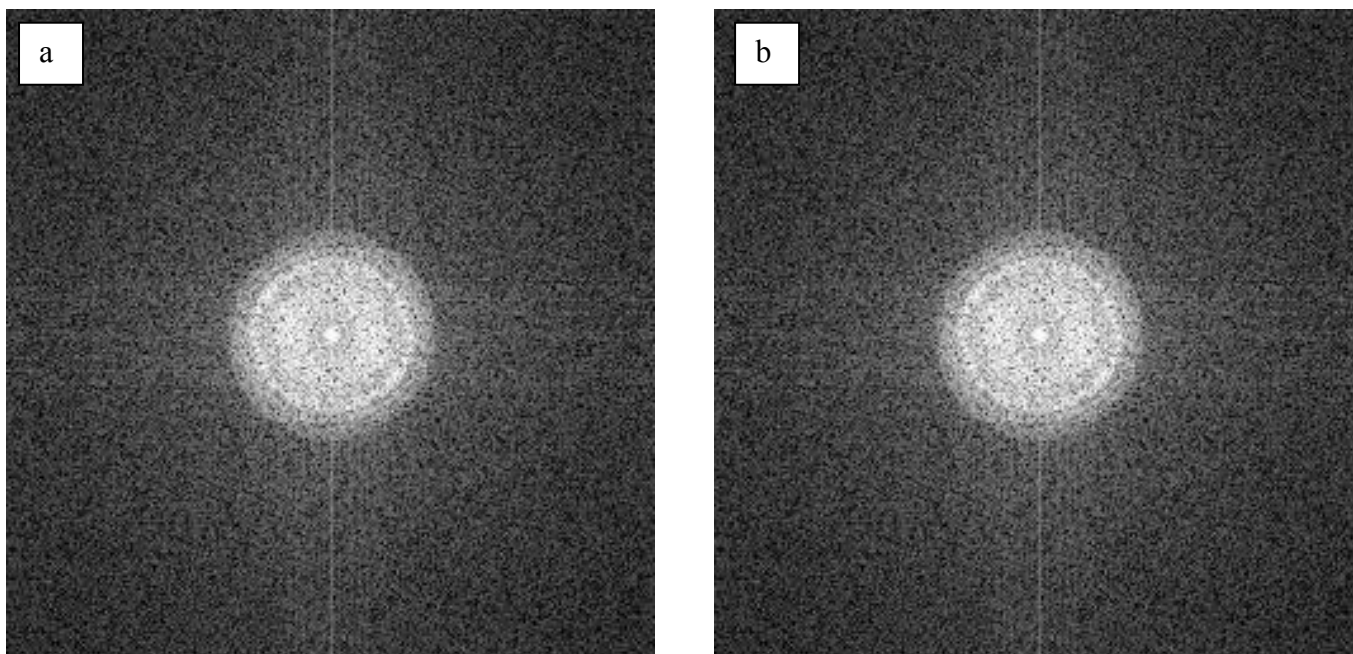


Figure 5-4. Fast Fourier transformation of two particles shows faint rings and dots which is a sign for partial crystallinity of particles, a) Particle 1 in Figure 5-3b, b) Particle 2 in Figure 5-3b.

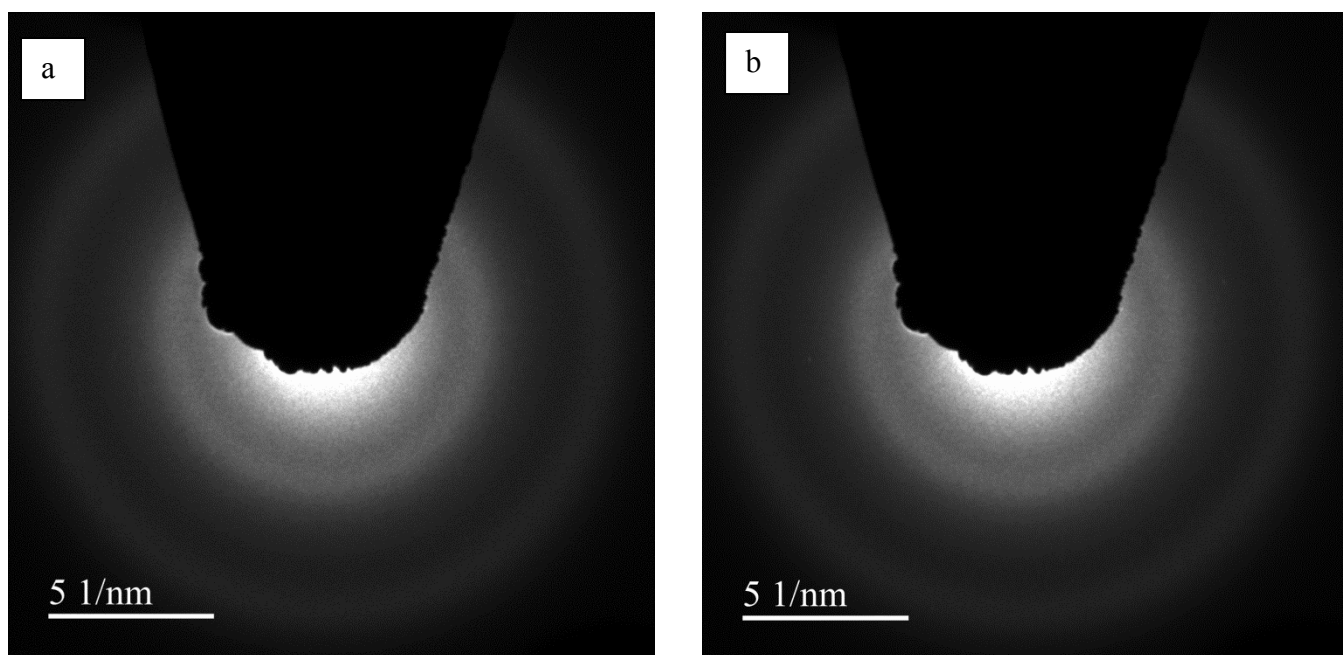


Figure 5-5. SAED patterns of two indium nanoparticles in Figure 5-3 show amorphous structures.

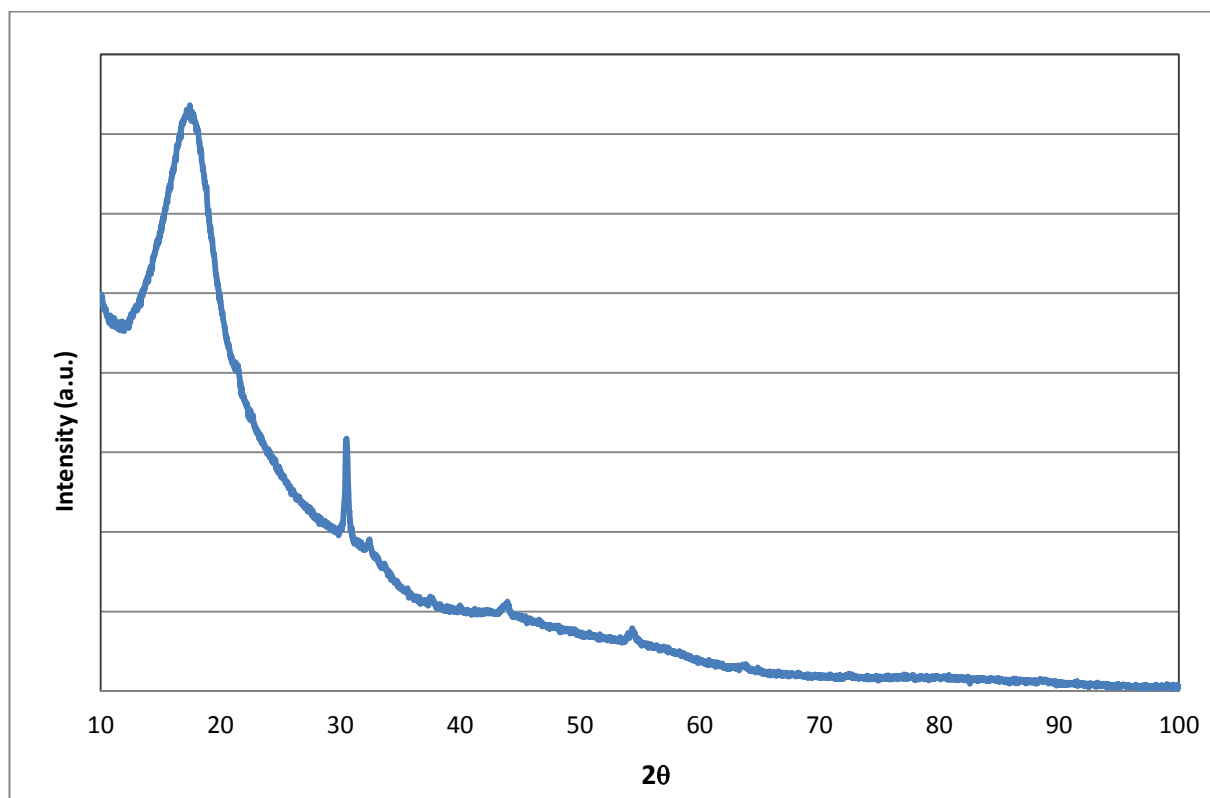


Figure 5-6. X-ray diffraction pattern of indium nanoparticles. A large peak at the beginning of XRD pattern shows amorphous structure of nanoparticles. Due to weakness of peaks it is not possible to determine the crystalline compound(s). The peak at 30 degree could relate to indium oxide caused by surface oxidation during sample transfer to XRD instrument.

5.1.2 Indium nanoparticles capped tri-*n*-butylphosphine phase transfer reaction

Phase transfer of nanoparticles from polar to non-polar solvents or reverse is important for several reasons. For instance synthesis of noble metal nanoparticles in non-polar organic media is limited due to the poor solubility of the corresponding metal ion precursors. As a result these metal ion precursors should dissolve primarily in a polar media and after nanoparticles formation, for some special functionalization they should transfer to non-polar media.⁹⁹

Another important factor of nanoparticles phase transfer is the longer stability without significant variation in the particle size over a time in non-polar organic media in comparison to polar organic media.¹⁰

For the mentioned reason indium nanoparticles capped with TBP in DMF were mixed with *n*-dodecane and left under vigorous stirring to study the possibility of indium nanoparticles phase transfer from DMF to *n*-dodecane with TBP. But it was observed that TBP could not act as phase transfer agent and *n*-dodecane remained completely colorless. Due to that indium nanoparticles capped with TBP in DMF were mixed with a mixture of *n*-dodecane and oleylamine and left for two hours under vigorous stirring. According to Figure 5-7 the phase transfer of indium nanoparticles in this mixture occurred and the DMF became completely colorless while the mixture of *n*-dodecane-oleylamine became dark brown. According to ³¹P NMR spectroscopic analysis TBP exists in both DMF and *n*-dodecane-oleylamine mixture after phase transfer reaction.

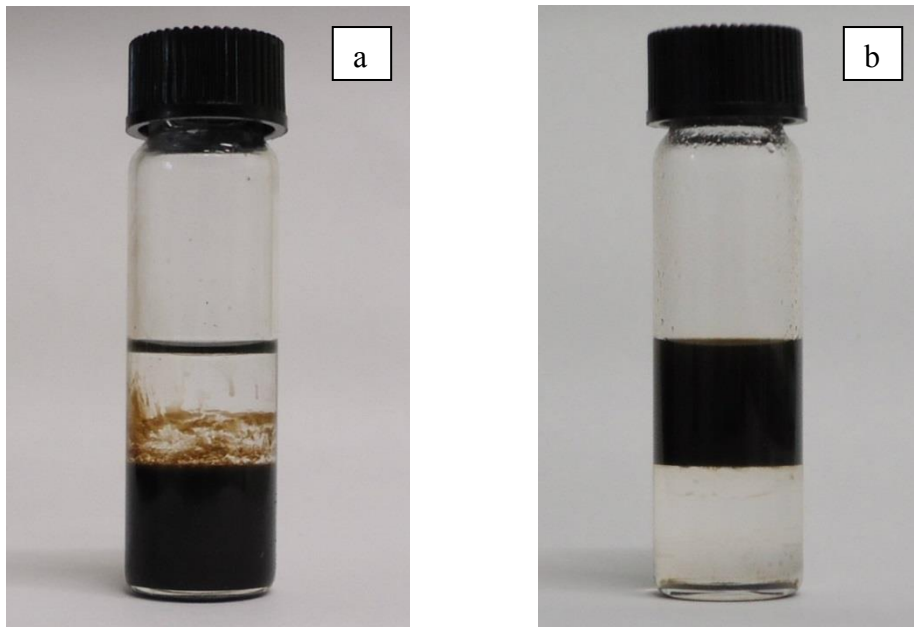


Figure 5-7. a) Indium nanoparticles in DMF at the bottom of vial, the top transparent solution is a mixture of dodecane and oleylamine,
b) Indium nanoparticles after phase transfer. The bottom transparent solution is DMF and the top layer is a mixture of dodecane, oleylamine and indium nanoparticles.

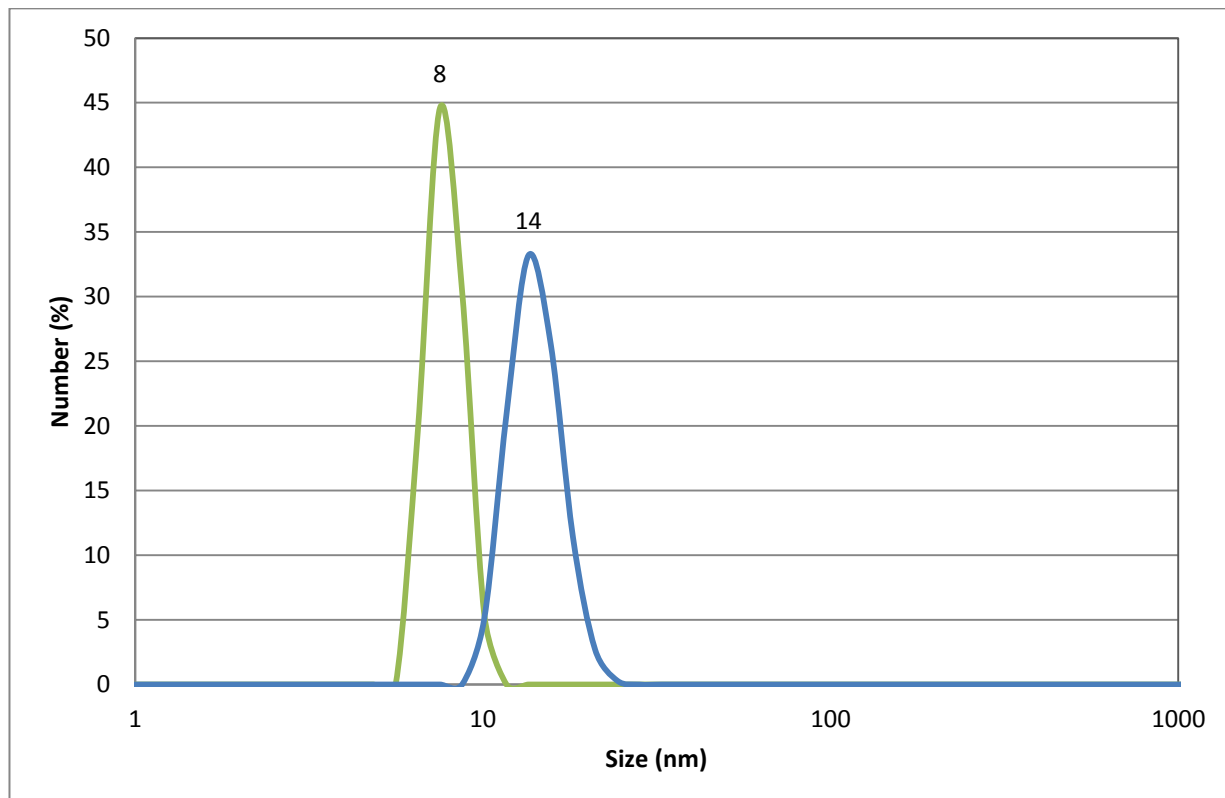


Figure 5-8. DLS number distribution of: Blue curve) indium nanoparticles after phase transfer to *n*-dodecane/oleylamine mixture with average diameter of 14 nm. Green curve) as prepared indium nanoparticles in DMF with average diameter of 8 nm.

Figure 5-8 shows the DLS number distribution of the in situ prepared colloidal solution of indium nanoparticles in DMF (green curve), and indium nanoparticles after phase transfer to a *n*-dodecane-oleylamine mixture (blue curve). Although the in situ prepared sample of indium nanoparticles in DMF has a mean particle size of 8nm, the mean particle size increases to 14 nm after phase transfer. This in fact is due to agglomeration of nanoparticles during phase transfer. This phenomenon is in accordance with the DLS result of indium nanoparticles transferred from diethylene glycol to dodecane or pentane with somehow increase in the mean particle size and formation of 40 nm particles as the biggest particles in the colloidal solution of indium nanoparticles reported by Hammarberg et al.¹⁰

5.1.3 FT-IR confirmation of ligand exchange during phase transfer reaction

Hammarberg et al.¹⁰ have reported complete transfer of indium nanoparticles from polar diethylene glycol to non-polar pentane or dodecane in 2 hours. As initially a colloidal solution of indium nanoparticles was synthesized in diethylene glycol in the presence of oleylamine, particles were easily transferred to an alkane solvents due to long aliphatic chain of oleylamine.¹⁰

As it is mentioned in section 5.2 phase transfer reaction of indium nanoparticles capped TBP from DMF to *n*-dodecane failed but took place in the presence of oleylamine, which strengthened the possibility of phase transfer reaction via a ligand exchange mechanism.

'In the ligand-exchange strategy, the molecules stabilizing the particles in the original first phase are replaced by other, more strongly binding ligands that allow the transfer to the second phase and provide colloidal stability there.'¹⁰⁰ Hatakeyama et al.¹⁰¹ have reported the two step ligand exchange reaction of magnetic nanoparticles which are primarily synthesized in oil to be then transferred to water for biomedical application. In first step the magnetic nanoparticles capped with fatty acids are treated with thiomalic acid which has the solubility in both oil and water to remove the primary fatty acid ligands and in the second step of ligand exchange the magnetic particles capped thiomalic acid treated with citric acid to obtain magnetic nanoparticles capped citrate which are highly soluble and dispersible in water.¹⁰¹

'For transfer of hydrophilic particles to the organic phase, the same concept is applied; this time, one chemical group has to bind strongly to the nanoparticle surface in order to replace the original ligand molecule and the other end has to have a hydrophobic character.'¹⁰⁰ Yang et al.¹⁰² show phase transfer reaction of citrate capped noble metals like Ru, Pt and Au in aqueous solution to toluene by nearly 100 percent efficiency. For this phase transfer citrate ligands are exchanged by dodecylamine.¹⁰²

Here to confirm phase transfer reaction of indium nanoparticles from DMF to *n*-dodecane occurs via ligand exchange strategy, both TBP capped indium nanoparticles and transferred indium nanoparticles to *n*-dodecane were studied by FT-IR spectroscopy.

First a colloidal solution of indium nanoparticles in DMF was centrifuged to separate nanoparticles from the solution, afterwards the solvent was removed and the residue redispersed in DMF and centrifuged again to remove free TBP. At the end the solution was removed and the residue was put under vacuum for a short period of time to remove volatiles. Figure 5-9 (red line), shows FT-IR spectrum of indium nanoparticles capped TBP and Figure 5-9 (blue line), shows FT-IR spectrum of pure TBP.

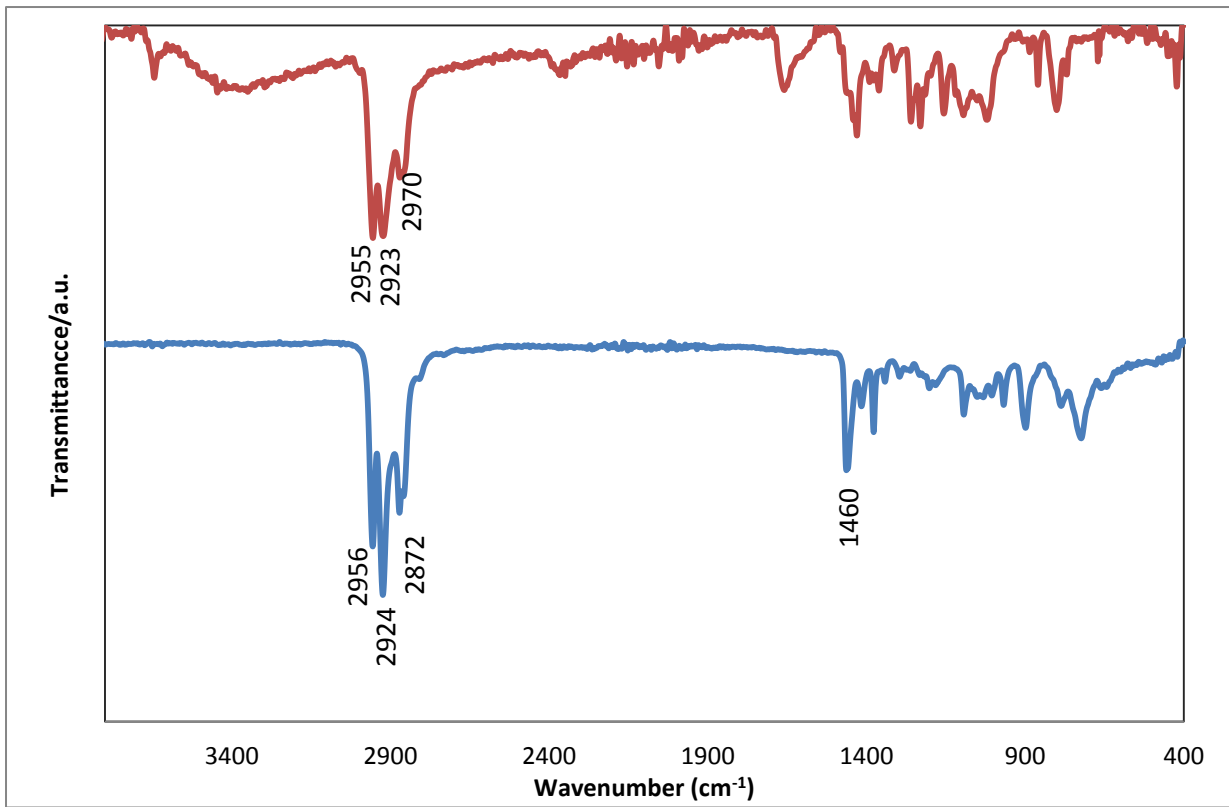


Figure 5-9. FT-IR spectra (red line) Indium nanoparticles capped TBP, (blue line) pure TBP.

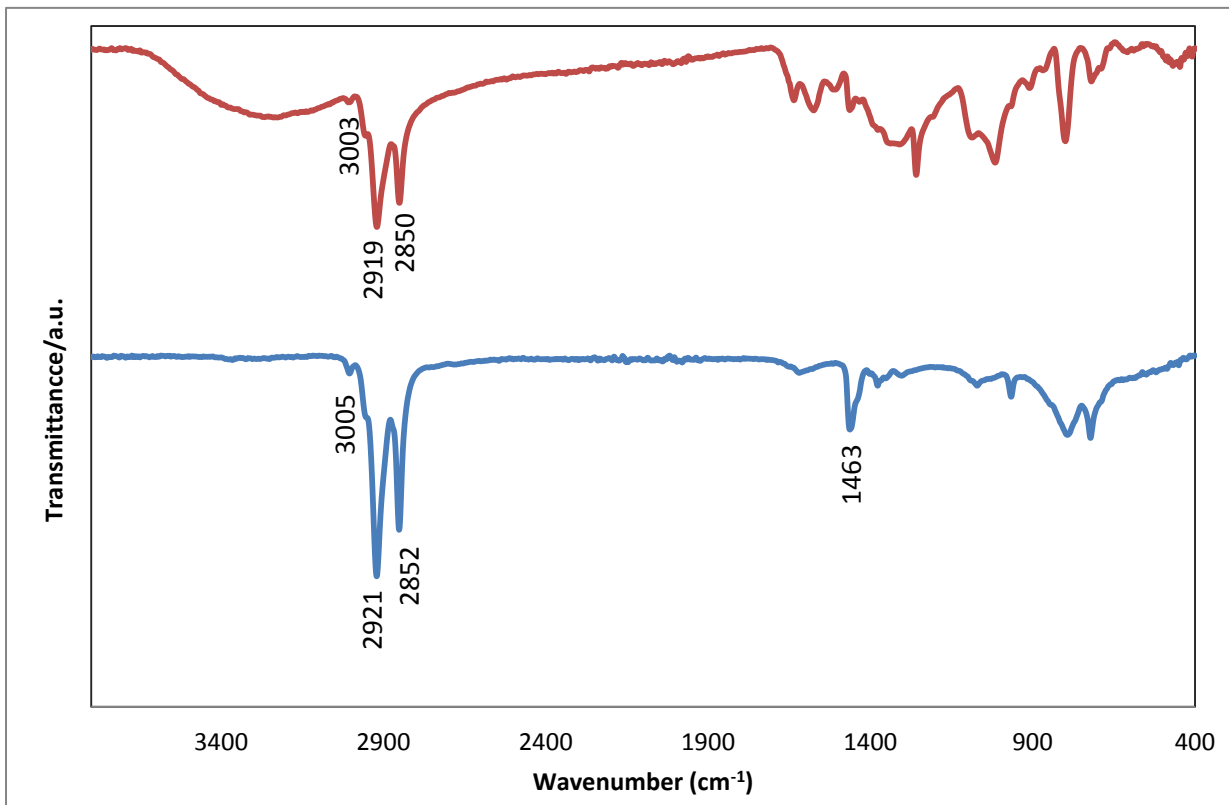


Figure 5-10. FT-IR spectra (red line) Indium nanoparticles after phase transfer with sign of oleylamine, (blue line) pure oleylamine.

According to Figure 5-9, the three identical alkyl chains at 2959, 2924 and 2872 cm^{-1} are in the same positions in both spectra but due to phosphine-indium interaction, peaks are not compatible in the right side of the spectra.

In case of phase transferred indium nanoparticles to the *n*-dodecane-oleylamine mixture, the sample was mixed first with THF and then DMF and centrifuged. Afterwards the solution was removed and the residue redispersed in DMF and centrifuged again to remove free capping ligands. Finally the solvent was removed and the residue was put under vacuum for a short period of time to remove volatiles. Figure 5-10 (red line) shows the FT-IR spectrum of the final residue and Figure 5-10 (blue line) shows the FT-IR spectrum of pure oleylamine. According to Figure 5-10 the three identical alkyl chains at 3005, 2921 and 2852 cm^{-1} are in the same positions in both spectra but due to amine-indium interaction, peaks are not comparable on the right side of the spectra.

Comparison between Figure 5-9 and 5-10 shows that TBP does not exist in the FT-IR spectrum of phase transferred indium nanoparticles. In fact presence of oleylamine and lack of TBP in Figure 5-10 (red line) confirms that phase transfer reaction occurs by ligand exchange strategy. This also shows that the amine-indium interaction is stronger than the phosphine-indium interaction.

5.2 One step synthesis of indium nanoparticles in a non-polar medium

5.2.1 Simultaneous phase transfer and ripening method

As the solubility of metal ion precursors in non-polar media is limited, primarily these precursors should be dissolved in polar media for nanoparticles synthesis.⁹⁹ Thereafter the phase transfer reaction is required to transfer the nanoparticles to a non-polar medium.

In contrast to the mentioned method, here due to the very slow nucleation of In(0) and as a result very slow formation of indium nanoparticles after reduction of indium(III) chloride by LiBH_4 in DMF, phase transfer of In(0) instead of indium nanoparticles from DMF to a non-polar medium in presence of a phase transfer agent is feasible. In fact formation of indium nanoparticles occurs in a non-polar medium instead of DMF.

Reduction of indium(III) chloride in DMF was performed in the presence of TBP because it was found that TBP can stabilize In(0). Without TBP, big silvery indium particles form instead of brown indium nanoparticles. After reduction of indium(III) chloride in DMF, In(0) stabilized TBP forms inside the solution. According to visual observation nucleation of In(0) and formation of pale yellow solution of DMF is a very slow reaction requires 30 minutes to initiate. In fact In(0) stabilized TBP in presence of oleylamine preferentially undergoes a very fast ligand exchange reaction instead of a very slow nucleation reaction. Newly formed In(0) stabilized oleylamine prefers migration from the non-polar medium to the polar DMF due to the long aliphatic chain of oleylamine. As In(0) transfer from DMF to non-polar medium happens continuously under vigorous stirring, indium nanoparticles nucleation and ripening occurs in non-polar medium.

Although according to visual observation nucleation of In(0) and formation of pale yellow DMF solution is a very slow reaction, color change in a non-polar medium is so quick. It seems that In(0) stabilized oleylamine in a non-polar medium rapidly nucleating to each other to form indium nanoparticles. At the end of the vigorous stirring to separate polar from non-polar

medium the solution mixture is kept immobile for a while. In this step the non-polar medium which is due to the formation of indium nanoparticles dark brown/black, forms the top layer and colorless DMF forms the lower layer.

For synthesis of colloidal solution of indium nanoparticles made by simultaneous phase transfer and ripening method the best *n*-dodecane to oleylamine volume ratio was 3:1 and the best *n*-dodecane to DMF solution mixture of In(0) stabilized TBP volume ratio was 1.5:1. Any deviation from these mentioned ratios causes the agglomeration of nanoparticles. In Figure 5-11 the blue line shows the DLS intensity distribution of the in situ prepared colloidal solution of indium nanoparticles in a *n*-dodecane-oleylamine mixture. Indium nanoparticles are monodispersed with narrow size distribution between 6 and 12 nm with an average diameter of 9 nm. In Figure 5-11 the red line shows the DLS intensity distribution of the same sample after 7 days. It shows that the sample is not stable and overtime agglomeration of indium nanoparticles occurs.

It was mentioned earlier that a monodispersed colloidal solution with mean particle size of 9 nm can only be obtained by certain ratios between different components of the reaction mixture. To decrease the mean particle size of colloidal solution of indium nanoparticles traces amounts of light amines like diphenylamine or 1-phenylethylamine were added to the *n*-dodecane/oleylamine mixture.

In Figure 5-12 the blue line shows the DLS intensity distribution of the in situ prepared colloidal solution of indium nanoparticles in a *n*-dodecane-oleylamine mixture in the presence of diphenylamine. Indium nanoparticles are monodispersed with narrow size distribution between 6 and 12 nm with average diameter of 9 nm. Comparison between the blue lines in Figure 5-11 and 5-12 which shows the samples without and with diphenylamine indicates that diphenylamine does not change the mean particle size of a colloidal solution. Although diphenylamine does not have any significant effect on the in situ prepared sample, but according to the red line in Figure 5-12 it increases the durability of colloidal solution of indium nanoparticles to 70 days.

DLS intensity distribution of the in situ prepared sample containing 1-phenylethylamine was similar to the sample containing diphenylamine but it lost its brown color within two days. Although it is difficult to explain this phenomenon precisely, it is possible that on those areas which oleylamine is substituted by 1-phenylethylamine the shielding effect of 1-phenylethylamine was not sufficient enough and indium nanoparticles react with traces of moisture in the solution mixture.

Figure 5-13 shows FT-IR spectra of indium nanoparticles synthesized in a *n*-dodecane/oleylamine-diphenylamine mixture (violet line) and *n*-dodecane-oleylamine mixture (blue line) and compares it with pure oleylamine (red line) and pure TBP (green line). Although initially In(0) stabilized TBP forms in DMF but after phase transfer reaction no traces of TBP is visible and instead oleylamine is present around indium nanoparticles (Figure 5-13 blue line). This is in agreement with the results obtained in section 5.3 showed that a phosphine-indium interaction is weaker than a oleylamine-indium interaction and due to that ligand exchange occurs in the reaction mixture.

As diphenylamine has a trace quantity in the colloidal solution of indium nanoparticles, it is not possible to prove or reject its presence as capping ligand beside oleylamine with FT-IR technique (Figure 5-13 violet line).

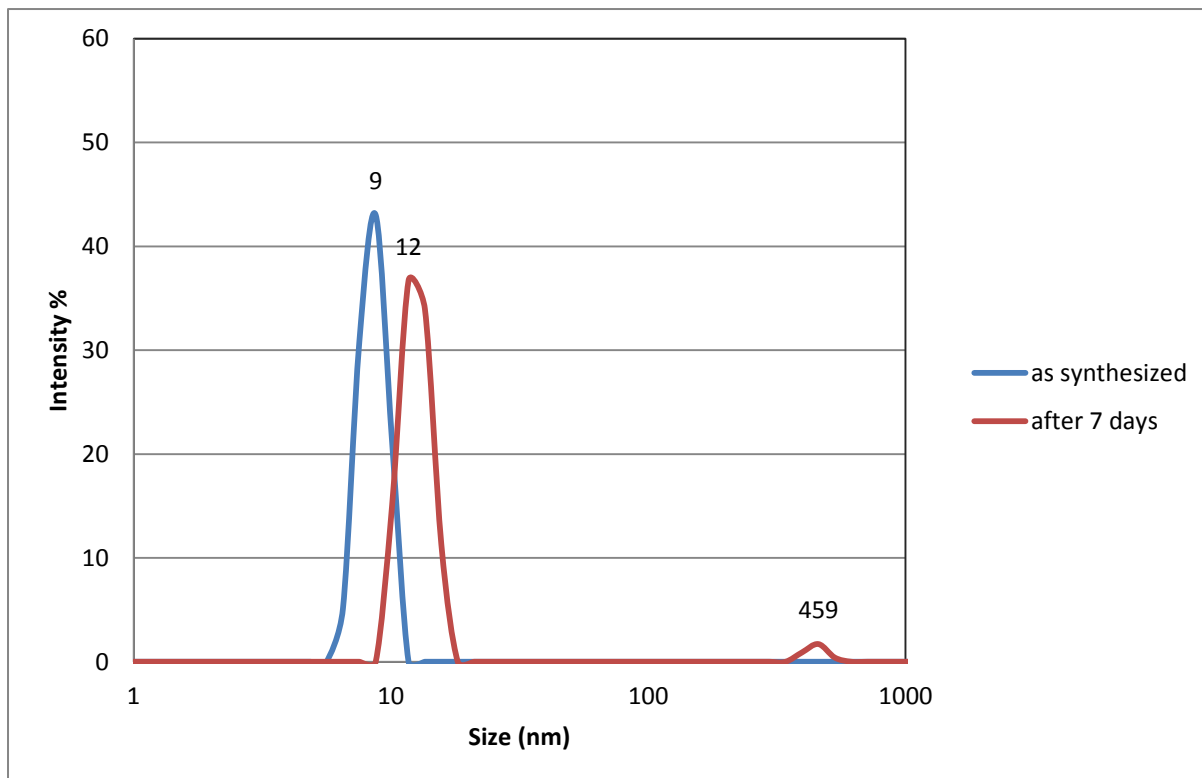


Figure 5-11. DLS intensity distribution of colloidal solution of indium nanoparticles with *n*-dodecane/oleylamine mixture. Blue line relates to as synthesized sample. Red line relates to the same sample after 7 days. Although as synthesized nanoparticles are mono-dispersed without any sign of agglomeration but sign of agglomeration appears in old sample.

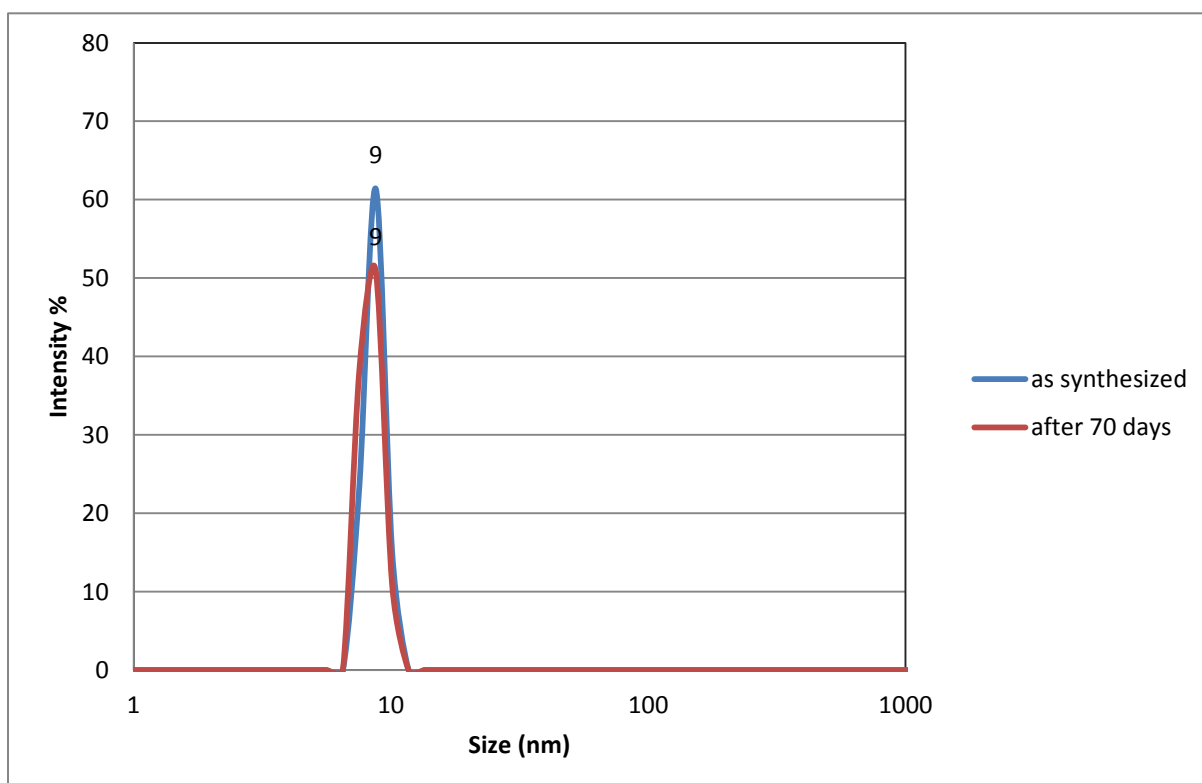


Figure 5-12. DLS intensity distribution of colloidal solution of indium nanoparticles with *n*-dodecane/oleylamine-diphenylamine mixture. Blue line relates to as synthesized sample. Red line relates to the same sample after 70 days. Nanoparticles are mono-dispersed without any sign of agglomeration in both as synthesized and old sample.

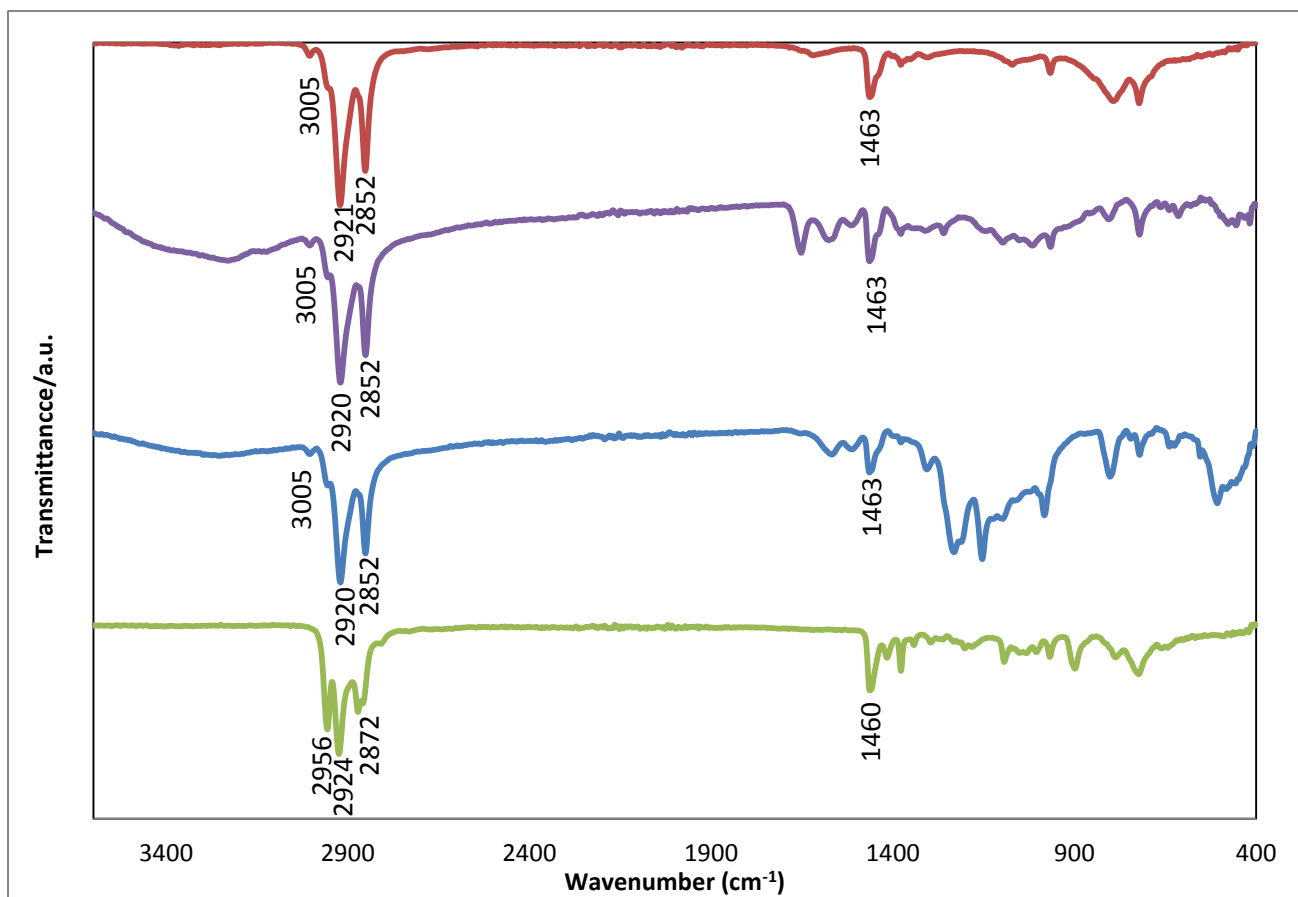


Figure 5-13. FT-IR spectra (red line) pure oleylamine, (violet line) indium nanoparticles from *n*-dodecane/oleylamine-diphenylamine, (blue line) indium nanoparticles from *n*-dodecane/oleylamine, (green line) pure TBP.

5.2.2 Small-angle X-ray scattering (SAXS) analysis of colloidal solution of indium nanoparticles

Figure 5-14 shows distance distribution function (related to the second moment of the histogram of distances within the particles) of the in situ prepared colloidal solution of indium nanoparticles. Blue line pertains to indium nanoparticles with oleylamine, red line to indium nanoparticles with oleylamine-diphenylamine and green line to a monodispersed sample with symmetrical bell shaped histogram. Both samples have mainly a mean particle diameter of 65 Å (radius between 30 and 35 Å) which is close to the result of DLS analysis with 8.7 nm (≈ 87 Å) but contain also a contribution of larger particle sizes (100 Å for sample with oleylamine/diphenylamine and 120 Å for sample with oleylamine). This difference of the mean particle diameter from both methods could be explained due to different measurement techniques between DLS and SAXS analysis with the X-ray scattering (SAXS) resulting particularly from the electron density contrast between sample and solvent. Higher values for DLS method in comparison to SAXS method have been reported by different studies; however, DLS method due to cheaper and faster response is more favorable.^{103,104}

According to Figure 5-14 colloidal solution of indium nanoparticles with only oleylamine exhibit a size distribution of nanoparticles with sizes up to 12 nm and colloidal solution of indium nanoparticles with oleylamine/diphenylamine up to 10 nm particles. Size distribution of

nanoparticles in sample with oleylamine is broader, whereas nanoparticles in the sample with oleylamine/diphenylamine show a more narrow distribution.

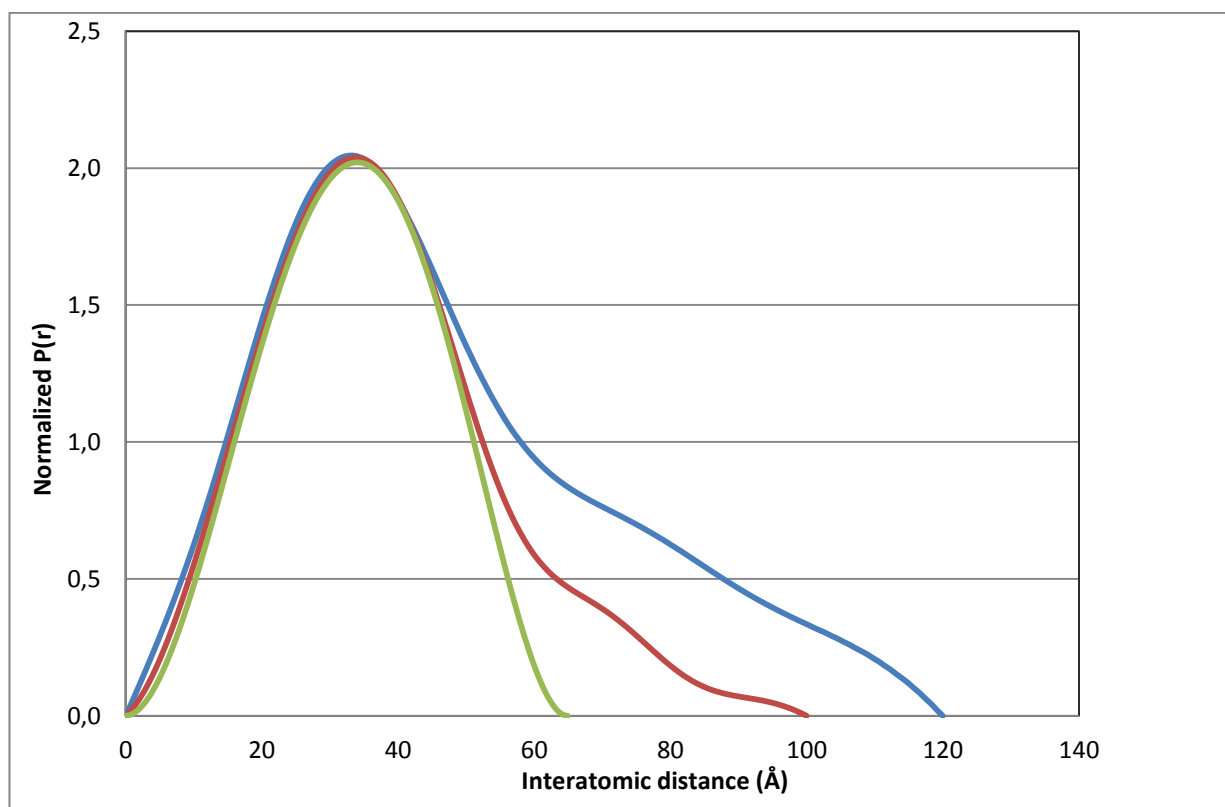


Figure 5-14. Distance distribution function $p(r)$ of as synthesized colloidal solution of indium nanoparticles. Red line: indium nanoparticles in presence of oleylamine/diphenylamine. Blue line: indium nanoparticles in presence of oleylamine. Green line: monodispersed sample with symmetrical bell shaped histogram. Sample with oleylamine/diphenylamine has a more narrow distance distribution and contains sub 10 nm particles, compared to sub 12 nm particles in the sample with only oleylamine.

5.3 Conclusion

Colloidal synthesis of indium nanoparticles from indium(III) chloride via LiBH_4 reduction in DMF in presence of TBP as capping ligand was studied. It is found that there is a direct relation between precursor concentration and particle size distribution. Only in a special concentration of the precursor, indium nanoparticles with mean diameter of 8 nm were formed and any deviation from that concentration increased the mean particle size.

XRD and SAED analysis of indium nanoparticles showed amorphous particles; however, fast Fourier transformation showed presence of low level of crystallinity which could relate to indium oxide due to partial oxidation of nanoparticles.

Although phase transfer of indium nanoparticles from DMF to a mixture of *n*-dodecane and oleylamine was successful, partial agglomeration of particles and mean particle size increase from 8 nm to 14 nm was observed according to DLS analysis. FTIR spectroscopy confirmed that phase transfer has occurred by ligand exchange mechanism.

In another approach named as simultaneous phase transfer and ripening method reduced solution of indium(III) chloride in DMF was mixed with a mixture of *n*-dodecane and oleylamine under vigorous stirring and formation of indium nanoparticles with mean particle size of 8 nm occurred directly in the non-polar medium.

It was found that a trace amount of diphenylamine beside oleylamine improved the durability of nanoparticles in comparison to oleylamine. FTIR spectroscopy showed that indium nanoparticles synthesized by this method with or without diphenylamine were capped only with oleylamine.

SAXS analysis showed that indium nanoparticles synthesized with the simultaneous phase transfer and ripening method in presence of diphenylamine had a more narrow distance distribution and contained sub 10 nm particles, compared to sub 12 nm particles in the sample with only oleylamine.

Chapter 6

Colloidal synthesis of germanium nanowires

6 Colloidal synthesis of germanium nanowires

Here in this research the synthesis of indium catalyzed germanium nanowires was performed in the presence of capping ligands such as TOPO and oleylamine in alkane solvents based on SLS mechanism in atmospheric pressure.

The synthesis of gold catalyzed germanium nanowires below the melting point of gold has been reported previously, that relates to the eutectic point in the binary phase diagram of gold-germanium.^{23,94,105} A eutectic point also exists in the binary phase diagram of bismuth-germanium, close to the melting point of bulk bismuth which has been exploited for synthesis of bismuth catalyzed germanium nanorods.²⁶

Similar to eutectic point in the binary phase diagram of bismuth-germanium, a eutectic point exist in the binary phase diagram of indium-germanium close to the melting point of bulk indium (Figure 6-1). Therefore indium nanoparticles were chosen as seeding agent for synthesis of germanium nanowires.

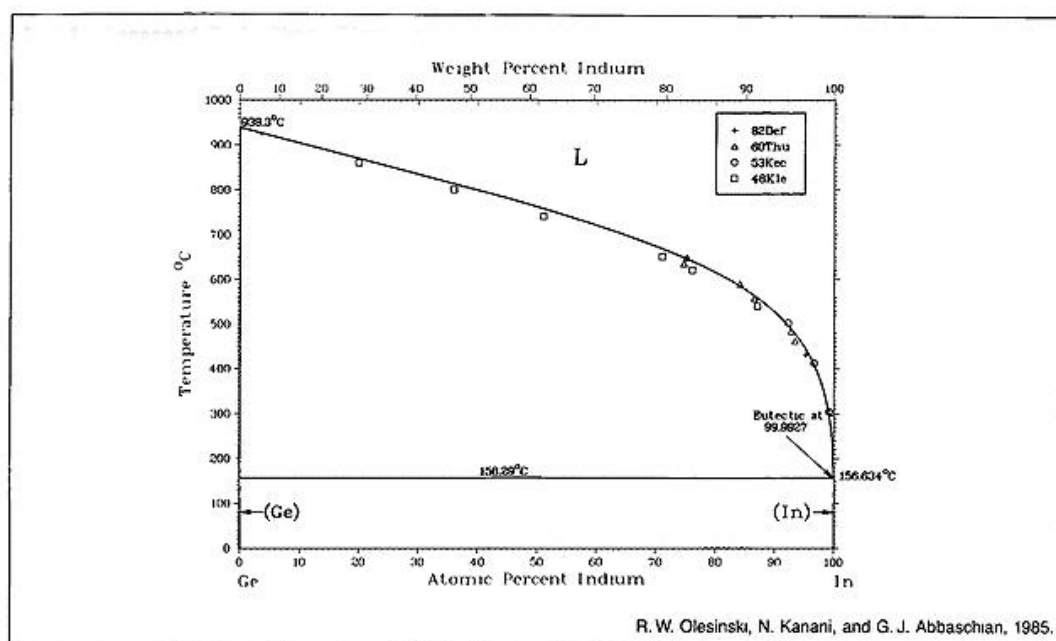


Figure 6-1. Indium-germanium phase diagram with a eutectic point at 99.98% indium at 156 °C.¹⁰⁶

Although DPG has been widely used as germanium precursor for synthesis of germanium nanowires,¹⁰⁷ it slowly decomposes at higher temperatures in the absence of seeding catalyst such as gold.²¹ In contrast to high thermally stable DPG, TGA analysis of pentakis(trimethylsilyl)digermene (**1**) has shown decomposition and sharp weight loss at 213 °C (see Chapter 3). Further analysis with GC-Mass spectrometry revealed that the sharp mass loss has been related to decomposition of germanium hydride **1** to volatile compounds such as germanium hydride **3** and oligosilylgermane **34**. With regard to unique low temperature decomposition of germanium hydride **1** even in the absence of seeding catalysts, an even more thermally sensitive oligosilylgermane 1,1,2,2-tetrakis(trimethylsilyl)digermene (**8**) was used as

germanium precursor for the synthesis of germanium nanowires at various temperatures from 180 °C to 350 °C.

6.1 Synthesis of germanium nanowires at 180 °C

6.1.1 In the presence of TOPO

Synthesis of germanium nanowires at 180 °C was performed in *n*-dodecane. Initially colloidal solution of indium nanoparticles capped oleylamine in *n*-dodecane was injected to the solution mixture of TOPO and *n*-dodecane at 180 °C, followed by injection of germanium hydride **8**. Upon the injection of germanium hydride **8** the color of the reaction mixture immediately turned black indicating very fast formation of germanium nanowires.

According to ²⁹Si NMR spectroscopy of the reaction mixture after formation of nanowires, the peak related to the precursor vanished indicating its complete consumption of precursor, and a peak at 6.9 ppm (with D₂O lock) appeared. The peak at 6.9 ppm relates to hexamethyldisiloxane and shows that the free trimethylsilyl groups of the precursor have reacted with oxygen atoms of TOPO and are trapped in the solution phase.

Figure 6-2 displays the SEM image of indium catalyzed germanium nanowires synthesized at 180 °C in presence of TOPO. Indium nanoparticles on tip of each germanium nanowire are clearly observed. According to EDS analysis the tips are composed of mainly indium and small quantity of germanium.

Due to polydispersity of initial colloidal solution of indium nanoparticles which was used for synthesis of nanowires both thick and thin nanowires have formed during the reaction, representing a direct relation between initial size of seed and final diameter of nanowire.

Figure 6-3 displays the bright field TEM image of germanium nanowires prepared with a monodispersed colloidal solution of indium nanoparticles. Curly and twisted nanowires have grown similar to the worm-like nanowires which has previously reported by Ryan and co-workers.⁵⁴ In addition, high resolution TEM images in Figure 6-4 clearly show that nanowires are mainly crystalline with numerous crystalline defects; however, amorphous regions (have been specified by a red box) also exist (Figure 6-4c).

In general the synthesis of germanium nanowires have been reported mostly above 300 °C and such a high temperature is required for several reasons such as the decomposition of the precursor, the melting of the seeding agents and finally the formation of crystalline nanowires. In contrast here due to advantages such as low temperature decomposition of germanium hydride **8** and low melting point of indium nanoparticles the growth temperature was chosen as low as 180 °C. However, the formation of defects as well as amorphous regions in the structures of germanium nanowires can be explained by the very low synthesis temperature.

Figure 6-5 displays EDS analysis and Table 6-1 shows related chemical composition of indium catalyzed germanium nanowires. Signals for copper, cobalt, iron and carbon relates to the TEM grid. The tip is composed of mainly indium and small quantity of germanium which confirms dissolution of germanium in indium nanoparticles and the formation of supersaturated solution of germanium in indium at elevated temperatures. Germanium nanowires are composed of approximately 98% of germanium and 2% of indium. Presence of high amount of indium in germanium nanowires shows high solubility of indium in germanium at 180 °C.

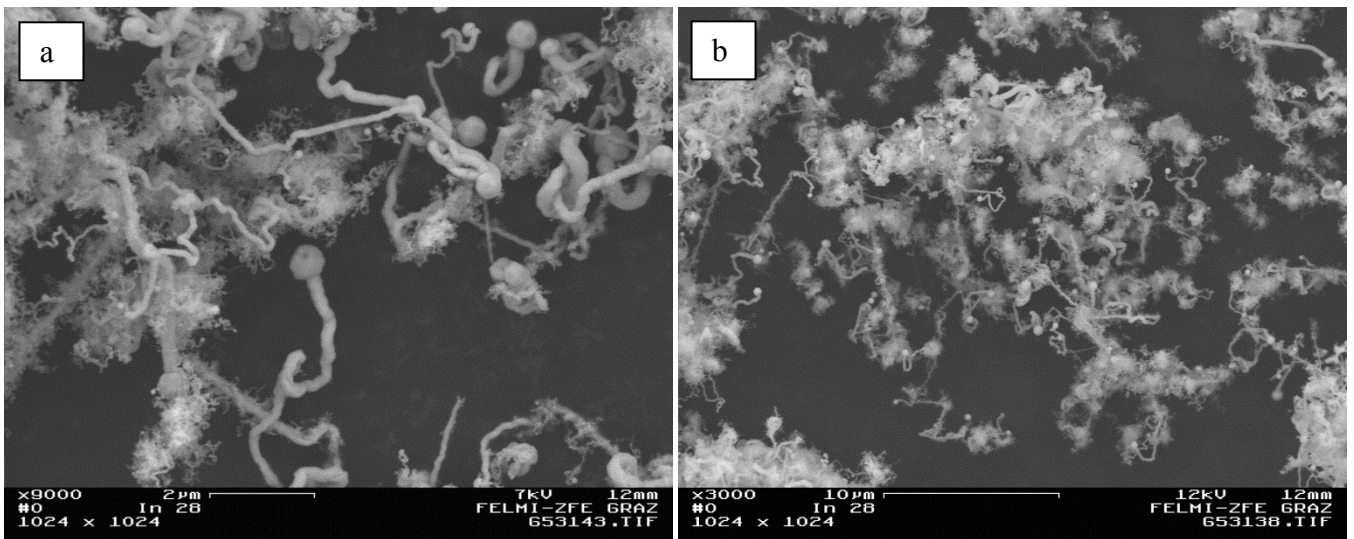


Figure 6-2. SEM image of indium catalyzed germanium nanowires synthesized at 180 °C in presence of TOPO with a polydispersed colloidal solution of indium nanoparticles. a) High yield of germanium nanowires. b) The spheres on tip of nanowires are indium nanoparticles. Due to polydispersity of colloidal solution of indium nanoparticles, numerous fine germanium nanowires have covered larger nanowires.

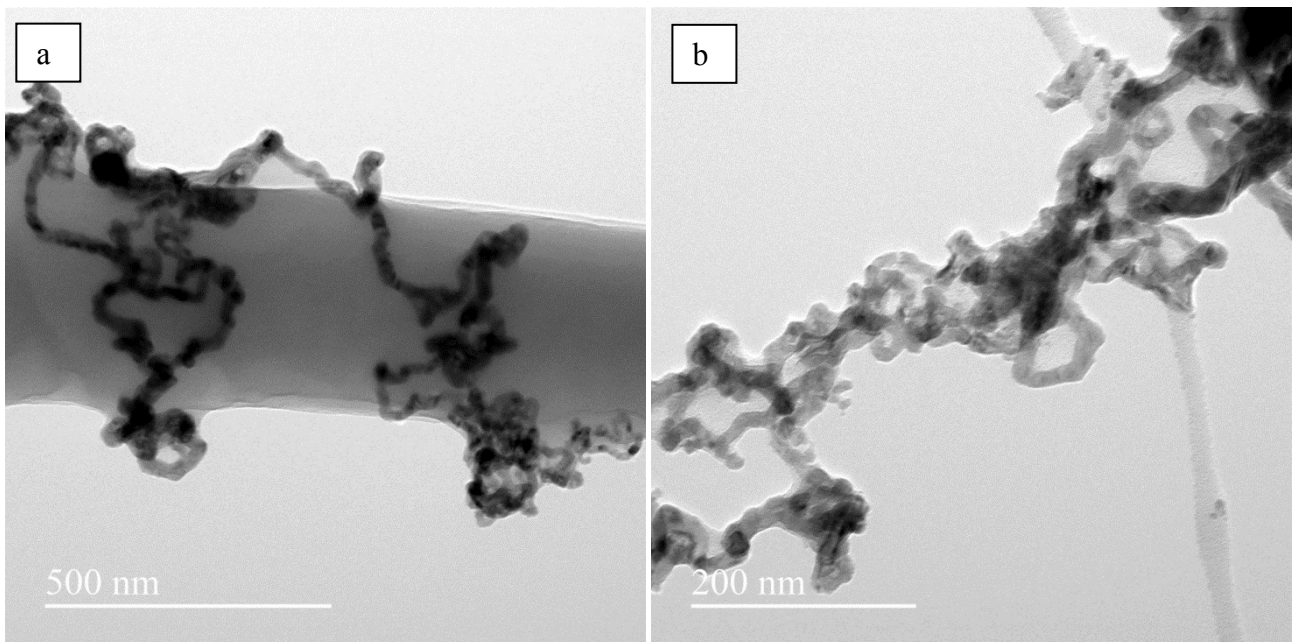


Figure 6-3. Bright field TEM images of germanium nanowires synthesized at 180 °C shows worm-like nanowires.

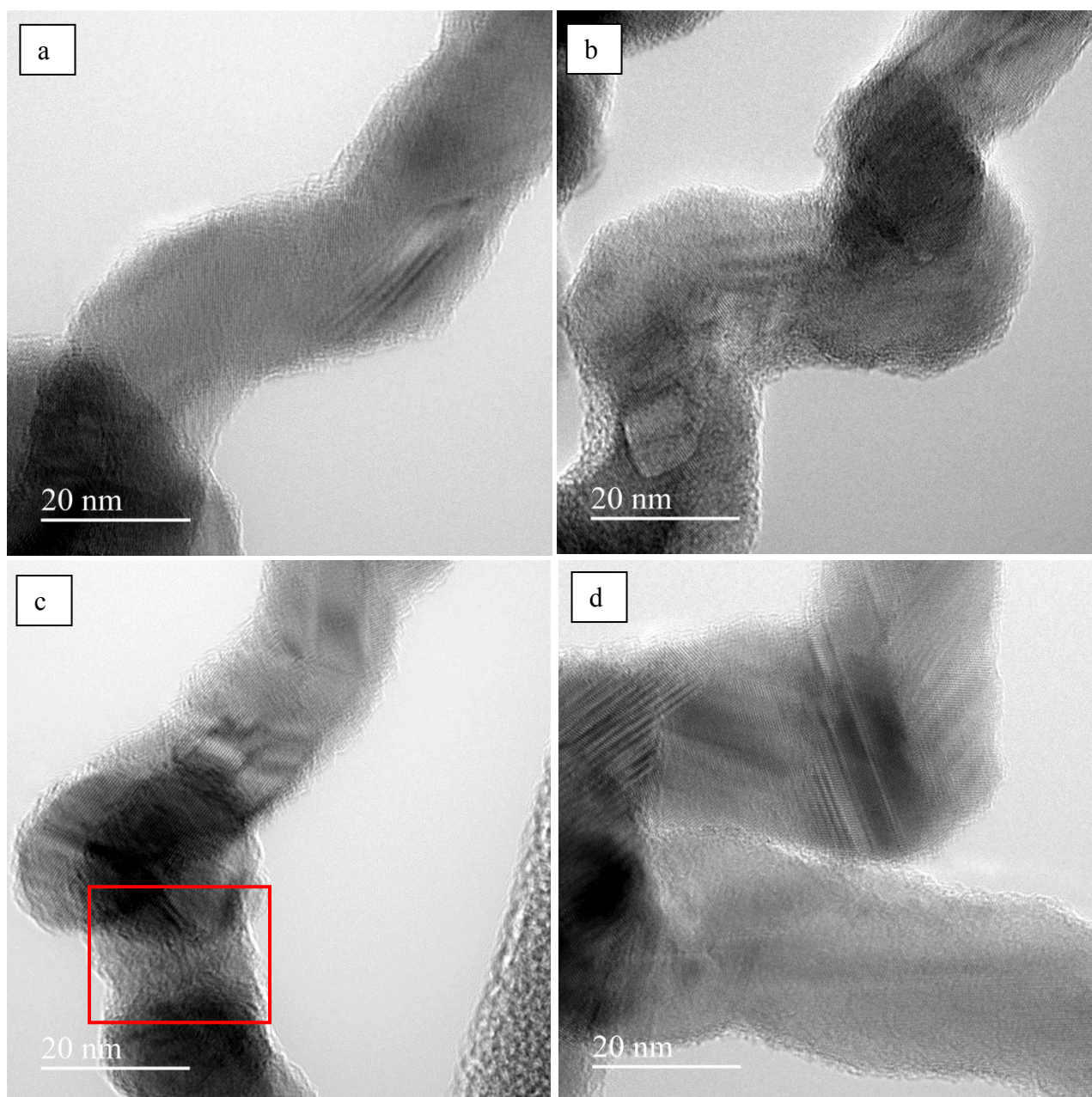


Figure 6-4. High resolution TEM images showing atomic planes and crystalline structure of germanium nanowires however due to crystalline faults they do not have a well-ordered crystalline structure.

^{29}Si NMR spectroscopy has shown that silicon atoms remain in the solution phase as hexamethyldisiloxane. In addition, EDS analysis of several nanowires even at twisted points revealed that silicon atoms do not incorporate in the germanium nanowires which confirms potential application of germanium hydride **8** as an appropriate germanium precursor. Similar reaction with DPG instead of germanium hydride **8** was performed at 180 °C and the reaction mixture after addition of DPG remained colorless. Furthermore, ^{13}C NMR spectroscopy of the reaction mixture showed presence of DPG after the reaction. This results show higher thermal stability of DPG in comparison to germanium hydride **8** and in contrast easier germanium atom liberation in germanium hydride **8**.

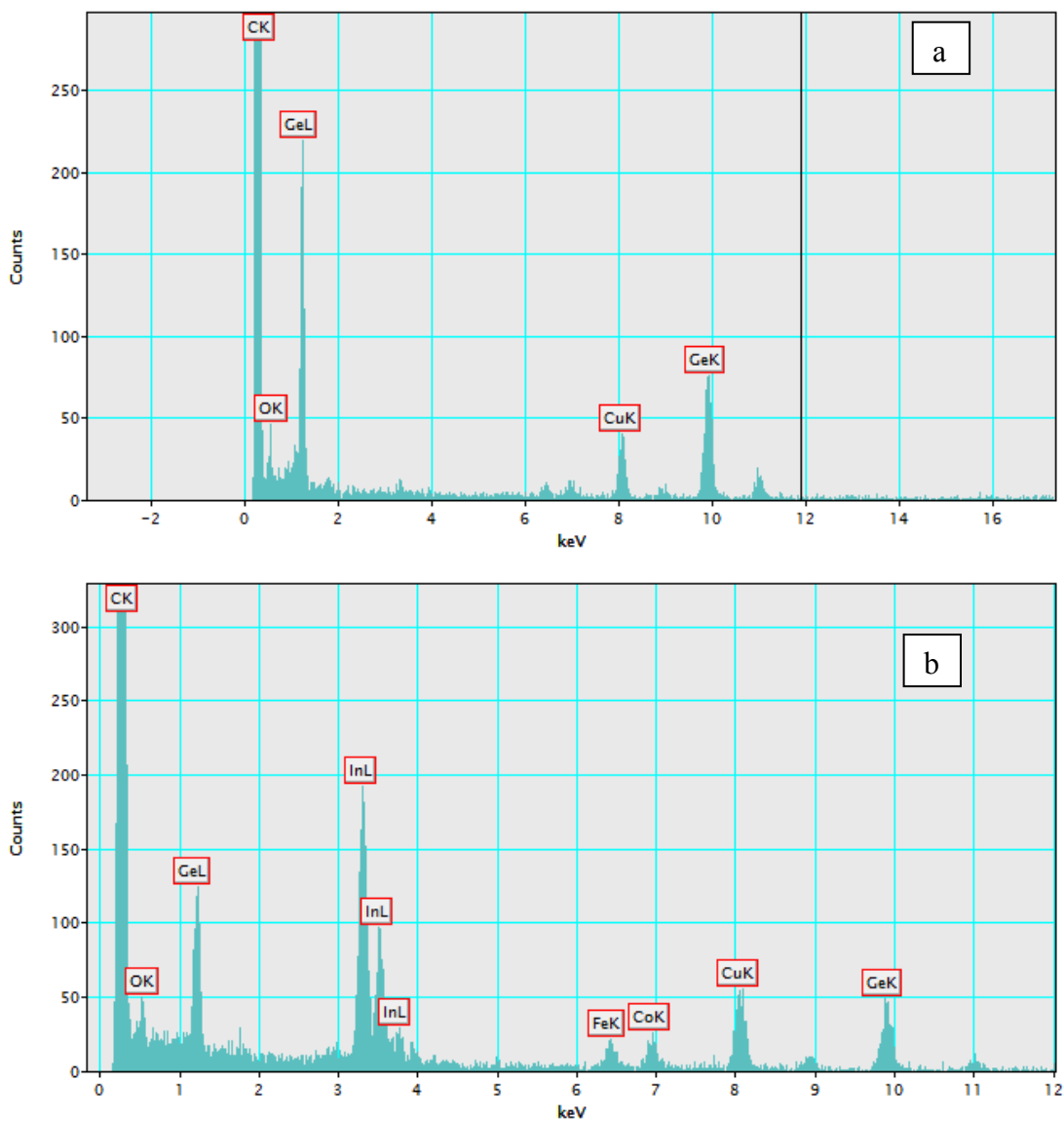


Figure 6-5. EDS analysis of indium catalyzed germanium nanowires synthesized at 180 °C (signals for Cu, Co, Fe and C relates to the TEM grid). a) Germanium nanowire. b) Indium nanoparticle at the tip of germanium nanowire.

Table 6-1. Provides a detail EDS analysis of indium catalyzed germanium nanowires grown at 180 °C.

	In wt%	Ge wt%
Tip	84	16
Ge NW point 1	1.9	98.1
Ge NW point 2	2.0	98.0
Ge NW point 3	2.3	97.7
Ge NW point 4	2.1	97.9

6.2 Synthesis of germanium nanowires at 300 °C

6.2.1 In the presence of TOPO or oleylamine

High level of defects as well as amorphous regions in the structure of germanium nanowires grown at 180 °C was presumed to be the result of low synthesis temperature. Therefore in this step, synthesis of germanium nanowires was performed in *n*-hexadecane at 300 °C. Indium nanoparticles as seeding agents were prepared in *n*-hexadecane instead of *n*-dodecane.

At 300 °C effect of TOPO and oleylamine was studied in two separate reactions on the morphology of germanium nanowires.

Figure 6-6 shows the bright field TEM image of indium catalyzed germanium nanowires formed at 300 °C in presence of TOPO. Similar to germanium nanowires formed at 180 °C they looked curly and twisted.

Figure 6-7 shows the high resolution TEM image of these germanium nanowires. Although germanium nanowires contain crystalline defects, amorphous regions do not exist in their structure due to the higher synthesis temperature.

In general it can be concluded that increasing synthesis temperature from 180 °C to 300 °C did not affect the curly structure of the germanium nanowires as in both cases highly twisted germanium nanowires were obtained.

Another sample of germanium nanowires was prepared in presence of oleylamine at 300 °C to compare the effect of different capping ligands to the morphology of nanowires. Figure 6-8 shows the SEM image and Figure 6-9 shows the bright field TEM image of germanium nanowires formed under this conditions. While in presence of oleylamine sub 200 nm diameter nanowires were grown, sub 50 nm diameter nanowires in presence of TOPO were formed. Different diameters in the two samples show that in early stage when a colloidal solution of indium nanoparticles was injected to the reaction vessel containing alkane solvent and capping ligands such as oleylamine or TOPO, coagulation of indium nanoparticles occurred in presence of oleylamine and as a result bigger nanowires were formed, while in presence of TOPO indium nanoparticles remained apart and therefore smaller nanowires were grown.

Another difference in morphology of two samples of nanowires caused by different capping ligands is occurrence of fewer twists in oleylamine capped nanowires than TOPO capped nanowires. In another words straighter nanowires were formed in presence of oleylamine in comparison to TOPO.

Figure 6-10 shows bright field and dark field TEM image as well as SAED pattern of two different germanium nanowires. Although the SAED patterns prove that straight germanium nanowires are crystalline, numerous planer defects (stacking faults), according to bright and dark field TEM images, exists parallel to the nanowires axis. Figure 6-10g shows the dark field TEM image of a germanium nanowire and Figure 6-10h displays the SAED parent of it. The brighter spots are not compatible with cubic crystal structure of bulk germanium. Incompatibility could be due to incorporation of indium atoms in the germanium matrix or high level of stacking faults.

Figure 6-11a and b show the dark field TEM images of a germanium nanowire under two different Bragg conditions. Numerous linear planes exist in both images parallel to the nanowire axis. The results from overlay of both Figure 6-11a and 6-11b shows that the linear

planes are not compatible with each other and do not overlap (Figure 6-11c) which confirms the presence of planar defects (stacking faults) in the structure of nanowires.

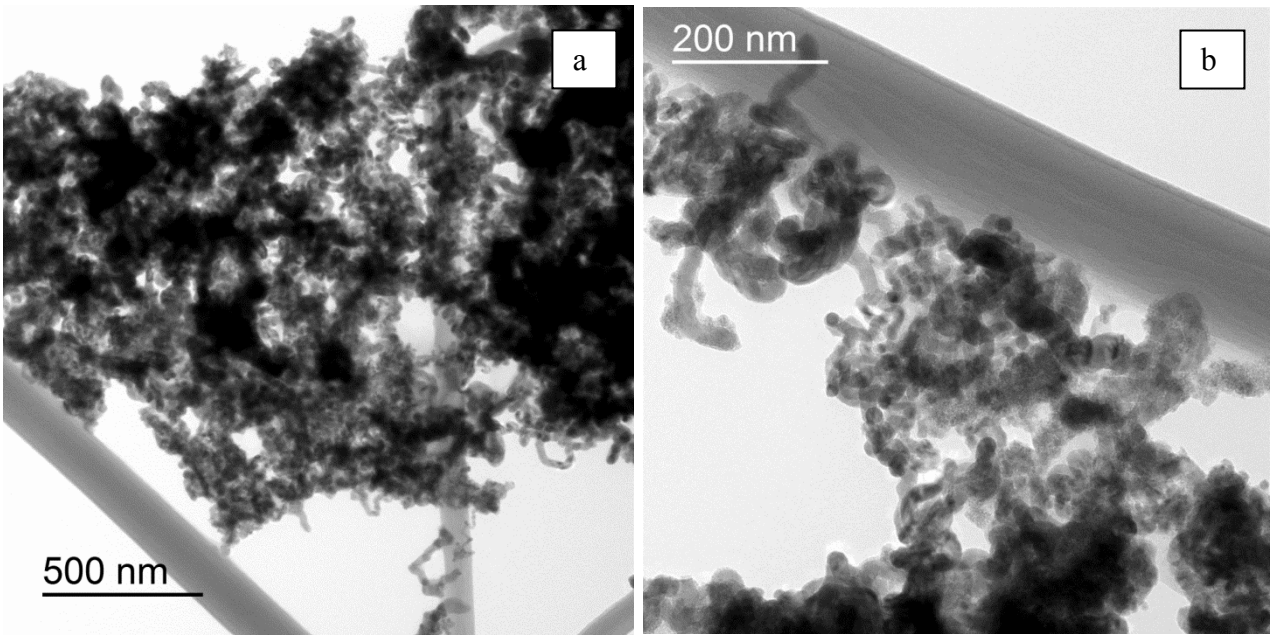


Figure 6-6. Bright field TEM image of indium catalyzed germanium nanowires synthesized at 300 °C in presence of TOPO. Nanowires are curly and highly twisted.

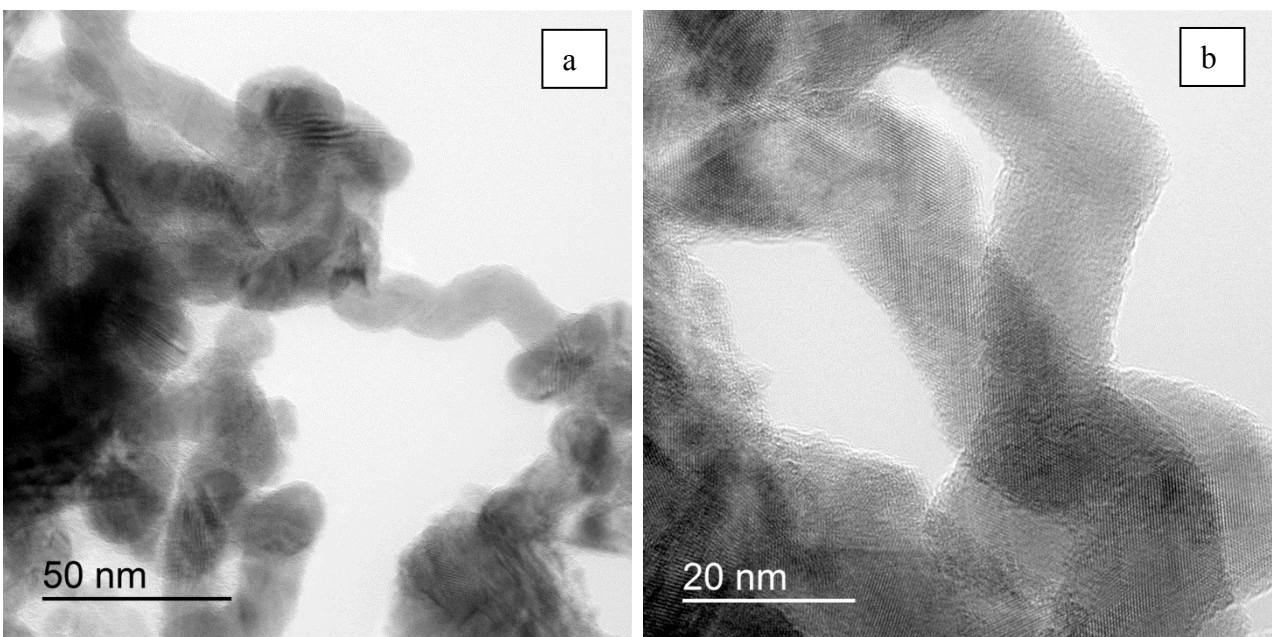


Figure 6-7. High resolution TEM images of indium catalyzed germanium nanowires synthesized at 300 °C in presence of TOPO, showing atomic planes and crystalline structure of germanium nanowires; however, due to crystalline faults they do not have a well-ordered crystalline structure.

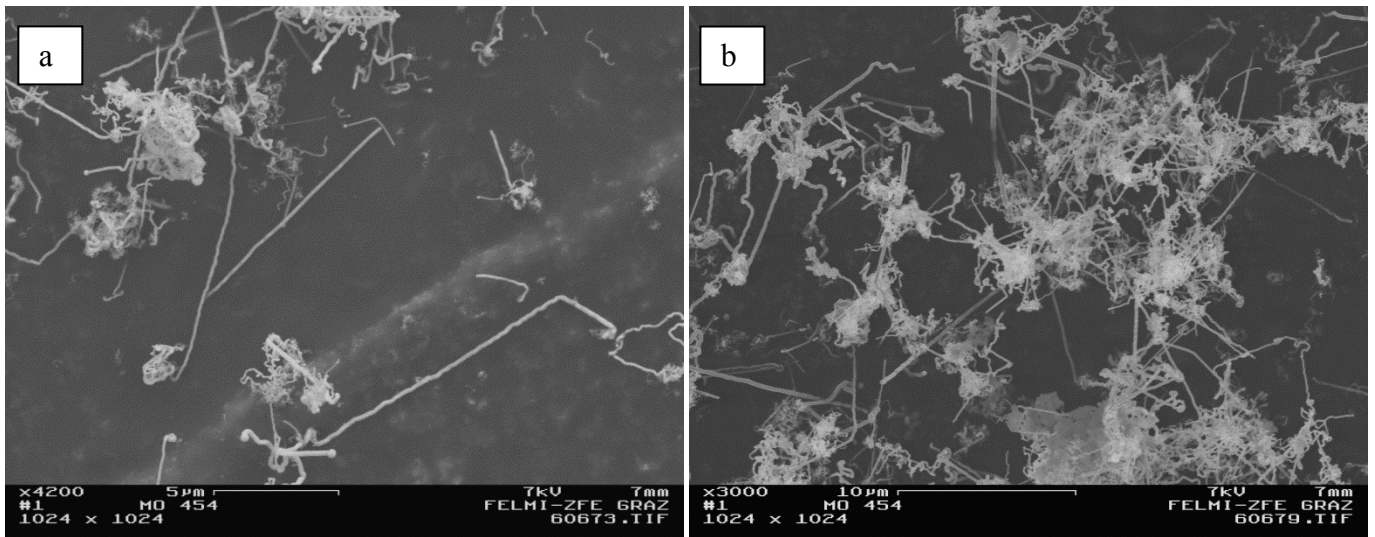


Figure 6-8. SEM image of indium catalyzed germanium nanowires synthesized at 300 °C in presence of oleylamine. More straight nanowires are present in this sample in comparison to the sample synthesized in presence of TOPO.

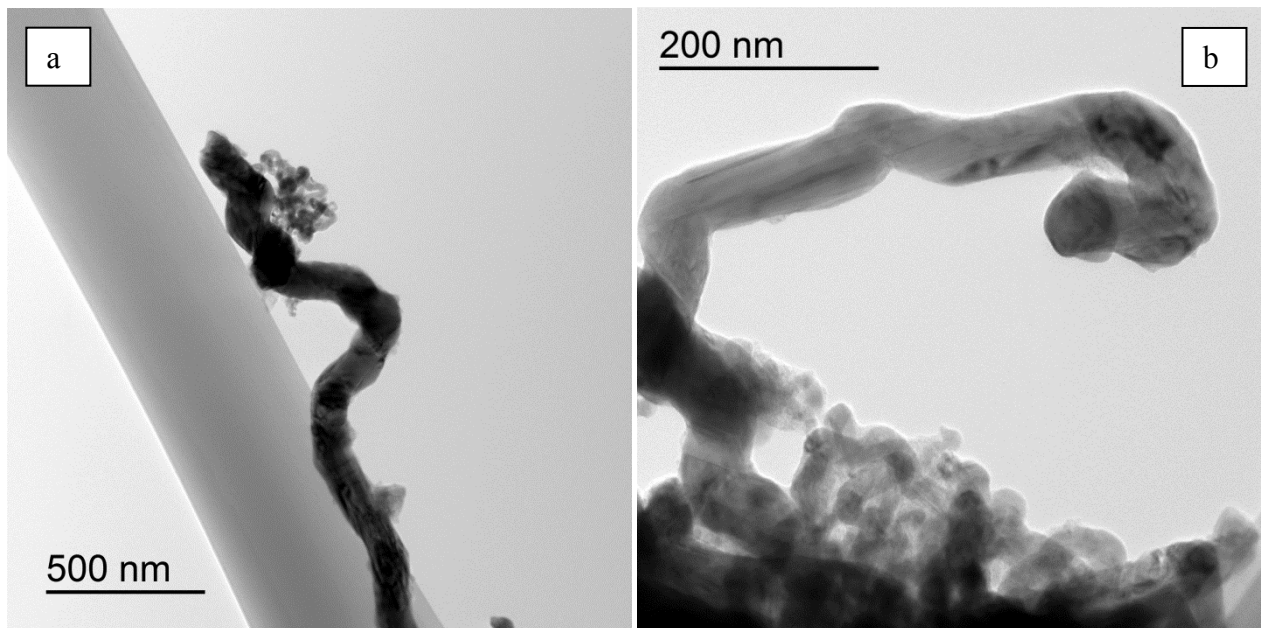


Figure 6-9. Bright field TEM image of indium catalyzed germanium nanowires synthesized at 300 °C in presence of oleylamine.

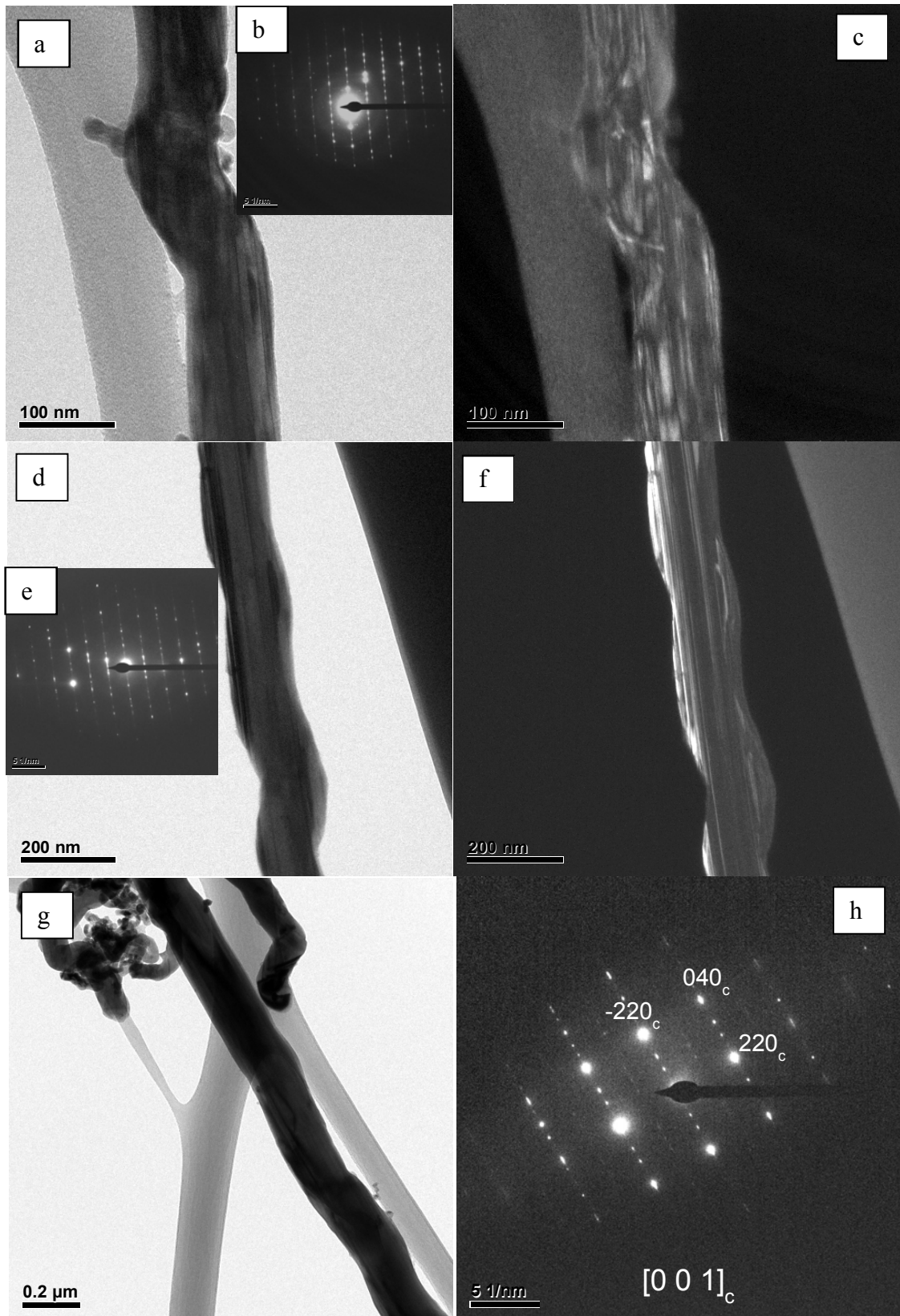


Figure 6-10. a) Bright field TEM image, b) SAED pattern, c) Dark field TEM image of same germanium nanowire. d) Bright field TEM image, e) SAED pattern, f) Dark field TEM image of another germanium nanowire. Although germanium nanowires are crystalline, numerous planar defects (stacking faults) exists parallel to the nanowires axis. g) dark field TEM image of a germanium nanowire and h) related SAED pattern of the nanowire with $[001]_c$ zone axis.

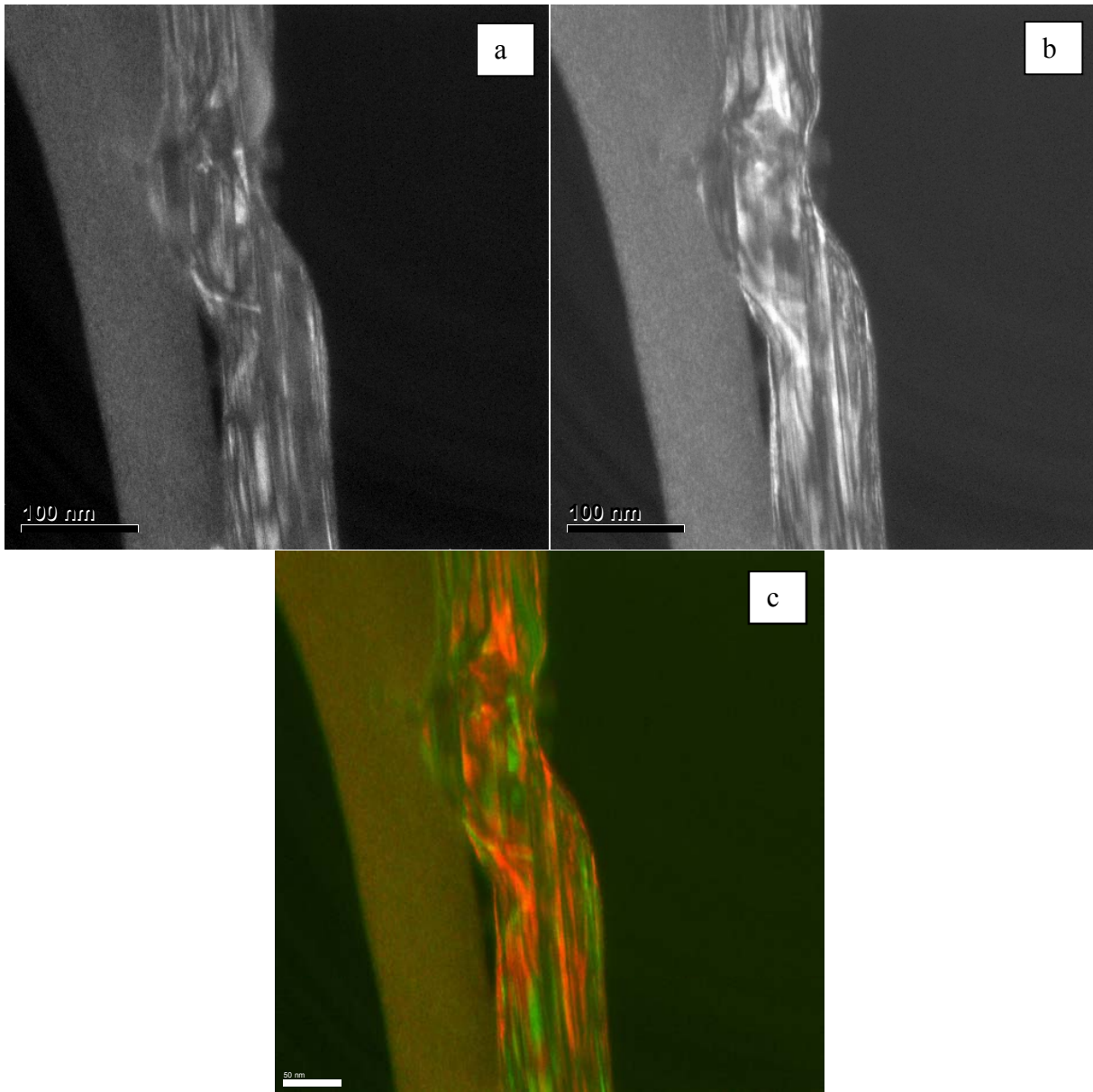


Figure 6-11. a & b) dark field TEM images of a germanium nanowire with different Bragg conditions. c) Overlay results of a (green) & b (red) shows presence of planner defects (stacking faults) in the structure.

Table 6-2. Provides a detail EDS analysis of indium catalyzed germanium nanowire grown at 300 °C.

	In wt%	Ge wt%
Ge NW point 1	2.5	97.5
Ge NW point 2	3.4	96.6
Ge NW point 3	2.7	97.3
Ge NW point 4	1.8	98.2

Although higher synthesis temperature did not change the curly structure of TOPO capped germanium nanowires straighter ones are formed in presence of oleylamine. Previously the effect of different solvents on the morphology of germanium nanowires and formation of different types of defects in the structure of them have reported by Ryan and co-workers⁵⁴ and it seems that different capping ligands could have similar effects on the morphology and the type of defects in germanium nanowires.

Table 6-2 provides a detail EDS analysis of germanium nanowires synthesized at 300 °C at various points of the nanowires. Comparison of EDS analysis in Table 6-1 and table 6-2 shows slight increase of indium in the structure of nanowires by increasing the synthesis temperature from 180 °C to 300 °C.

6.3 Synthesis of germanium nanowires at 350 °C

6.3.1 In the presence of oleylamine

Although crystalline and straight germanium nanowires were grown in presence of oleylamine at 300 °C, numerous stacking faults were formed in the structure of them. To reduce formation of stacking faults in the structure of germanium nanowires synthesis temperature was increased to 350 °C. Because of high synthesis temperature, squalane was substituted for *n*-hexadecane. A colloidal solution of indium nanoparticles as seeding agents was prepared in squalane instead of *n*-hexadecane.

Figure 6-12 shows the SEM image of indium catalyzed germanium nanowires formed in the presence of oleylamine at 350 °C. The sample contains mainly irregular and coagulated germanium nanoparticles along with a few number of curly germanium nanowires. Also some spherical microscale particles of germanium form under this condition. As mentioned above the synthesis of nanowires here had two differences in comparison to previous synthesis condition in presence of oleylamine. First, the temperature was increased from 300 °C to 350 °C and second, squalane was used as solvent instead of *n*-hexadecane.

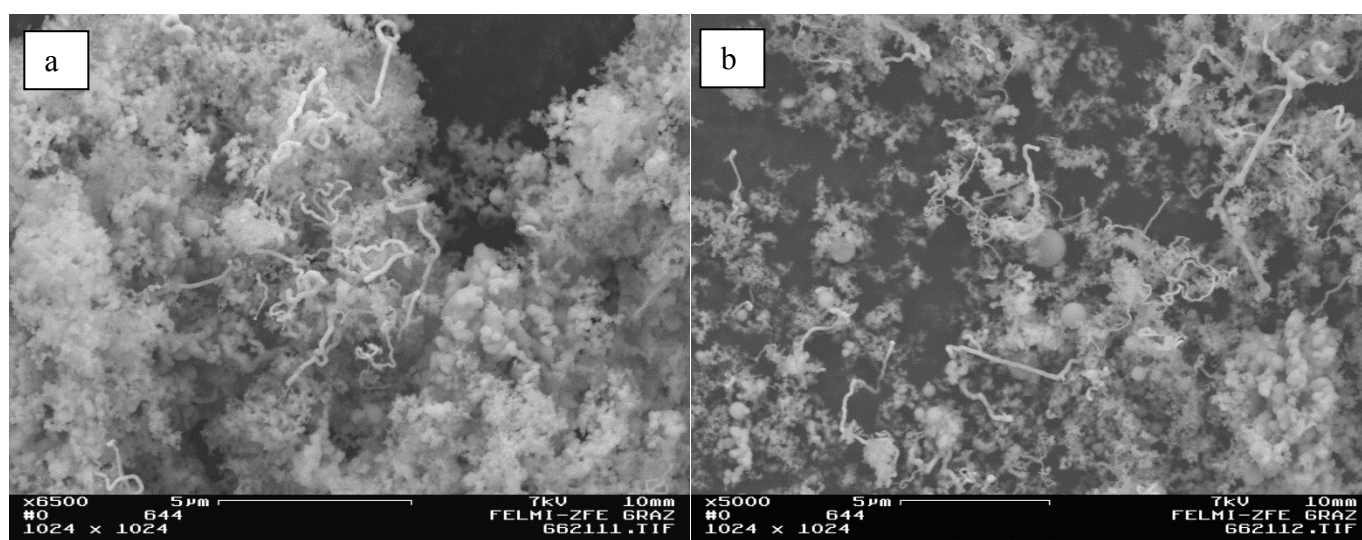


Figure 6-12. SEM image of indium catalyzed germanium nanowires synthesized at 350 °C in presence of oleylamine. a) Irregular and coagulated germanium nanoparticles along with a few curly germanium nanowires present in the sample. b) Spherical micro scale particles.

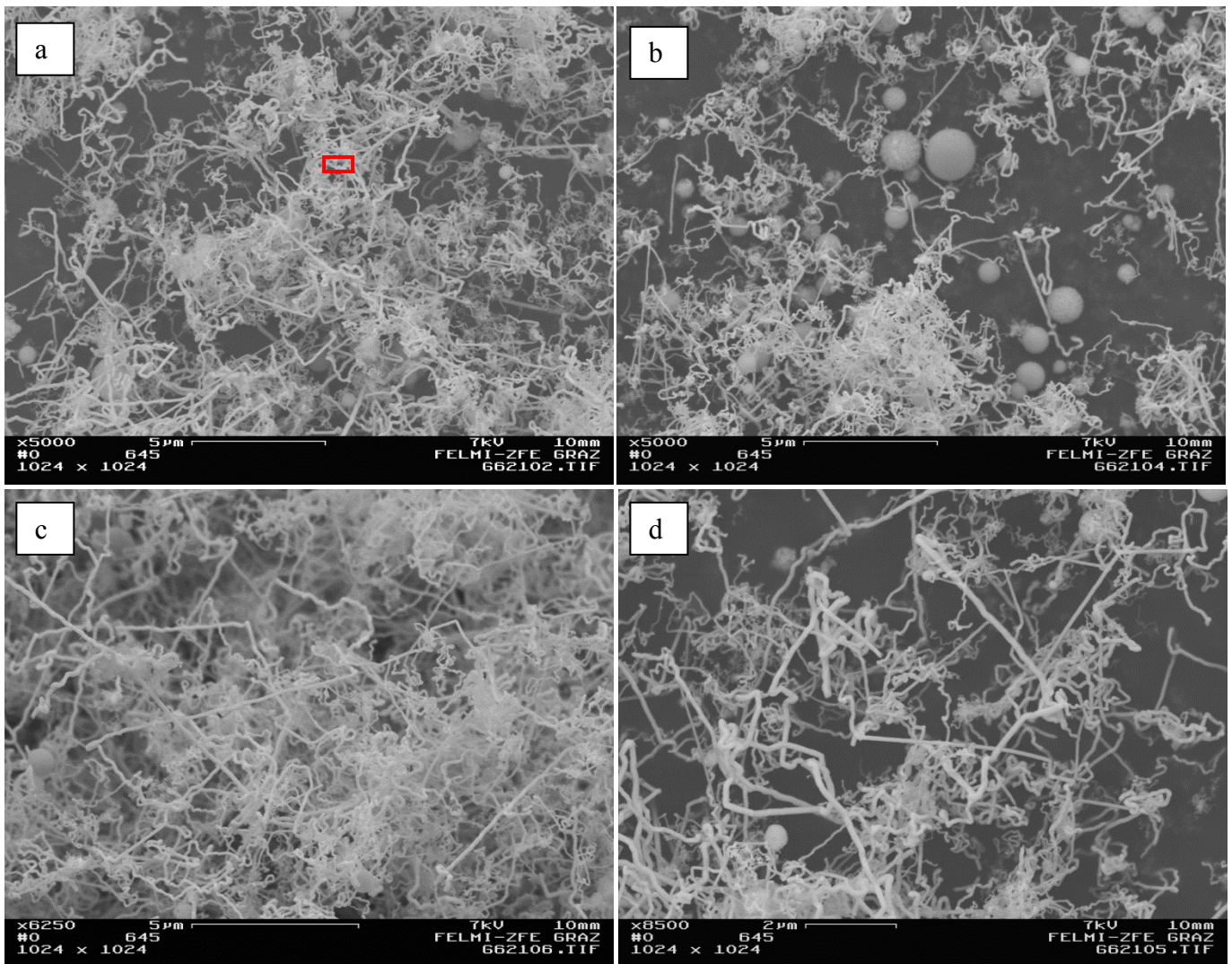


Figure 6-13. SEM image of indium catalyzed germanium nanowires synthesized at 350 °C in presence of oleylamine. a) EDS analysis of table 6-3 relates to the red box. b) Presence of spherical microscale germanium particles among nanowires. c, d) high yield of germanium nanowires.

Table 6-3. Provides a detail EDS analysis of indium catalyzed germanium nanowire grown at 350 °C related to the red box in figure 6-13a .

	In wt%	Ge wt%
Ge NWs in red box	2.9	97.1

In fact, the suppression of germanium nanowire growth and instead promotion of nanoparticle formation under this new condition is related to either squalane as a new solvent or higher synthesis temperature. To find the answer, another sample of indium catalyzed germanium nanowires was prepared at 350 °C with lower volume of squalane and higher volume of oleylamine. The reason for that was to keep the total volume of the liquid phase which nanowires need to grow equal in both samples and just study the effect of squalane to oleylamine ratio on the morphology of nanowires.

Figure 6-13 shows the SEM image of indium catalyzed germanium nanowires synthesized at 350 °C with lower volume of squalane. Instead of previously coagulated germanium nanoparticles in high volume of squalane, here the sample contains mainly germanium nanowires. However a number of spherical microscale particles of germanium are also present (Figure 6-13b). Formation of more nanowires with smaller squalane to oleylamine ratio illustrates that the synthesis of nanowires in squalane requires a higher amount of capping ligand in comparison to *n*-hexadecane.

According to Figure 6-13 even at 350 °C nanowires are slightly curly and very similar to the nanowires which were synthesized at 300 °C in presence of oleylamine. SEM analysis also displayed that sub 200 nm diameter nanowires were obtained in this sample.

Table 6-3 provides a detail EDS analysis of germanium nanowires synthesized at 350 °C related to the red box in Figure 6-13. Similar to the sample synthesized at 300 °C, approximately 3 wt% of nanowires are composed of indium.

6.3.2 In pure oleylamine

A further sample of indium catalyzed germanium nanowires was prepared at 350 °C in pure oleylamine to figure out the effect of pure oleylamine onto the morphology of nanowires.

Figure 6-14 shows the SEM image of these nanowires synthesized at 350 °C in pure oleylamine. Similar to the sample with higher volume of oleylamine to squalane, high yields of nanowires as well as few spherical microscale particles of germanium were obtained.

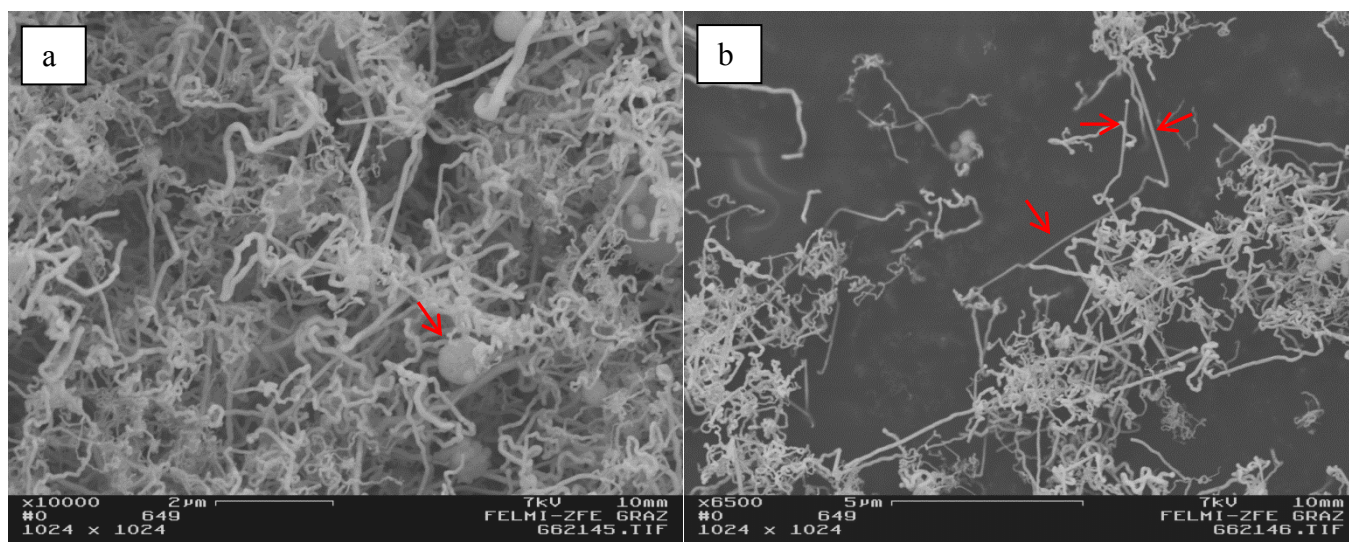


Figure 6-14. SEM image of indium catalyzed germanium nanowires synthesized at 350 °C in pure oleylamine. a) Presence of some spherical microscale particles among nanowires. b) Some of germanium nanowires are straight.

Although the morphology of nanowires synthesized in pure oleylamine is similar to the morphology of slightly curly nanowires synthesized in a mixture of oleylamine and squalane, several straight nanowires are shown in Figure 6-14b. SEM analysis displayed the formation of sub 200 nm diameter nanowires in pure oleylamine. Due to morphological similarities of nanowires at 300 °C and 350 °C, it can be concluded that higher synthesis temperatures cannot improve the morphology of nanowires and the formation of worm-like nanowires with numerous stacking faults could be related to the presence of indium atoms within the nanowires.

²⁹Si NMR spectroscopy of the solution mixture after the reaction showed a big signal at 1.9 ppm and a smaller signal at 6.9 ppm (with D₂O capillary). The signal at 1.9 ppm is related to a trimethylsilyl group bonded to a nitrogen atom¹⁰⁸ and the signal at 6.9 ppm is related to hexamethyldisiloxane.⁹⁶ Presence of oxygen in these samples which was prepared with oleylamine instead of TOPO is related to the trace amount of oxygen within the technical graded oleylamine (70 percent purity).

6.3.3 In a mixture of oleylamine and TOPO

Addition of small quantity of TOPO to oleylamine at 350 °C made a great difference to the morphology of the final product (Figure 6-15). The sample mainly contains of spherical microscale particles of germanium and a few number of germanium nanowires.

Thermal decomposition of tris(trimethylsilyl)germane (**3**) in the presence of TOPO has been studied previously in Chapter 4. It was found that reaction of trimethylsilyl groups of precursor with the oxygen in TOPO has an effect on the formation of germanium nanoparticles. In a similar pathway but more vigorously due to extremely higher temperatures, trimethylsilyl groups of germanium hydride **8** react with the oxygen in TOPO, cause a very fast release of a huge number of reactive Ge(0) species into the solution. As a result, the reactive Ge(0) species rapidly accumulate around each other and form spherical microscale particles instead of slow diffusion into the indium nanoparticles and subsequent formation of nanowires.

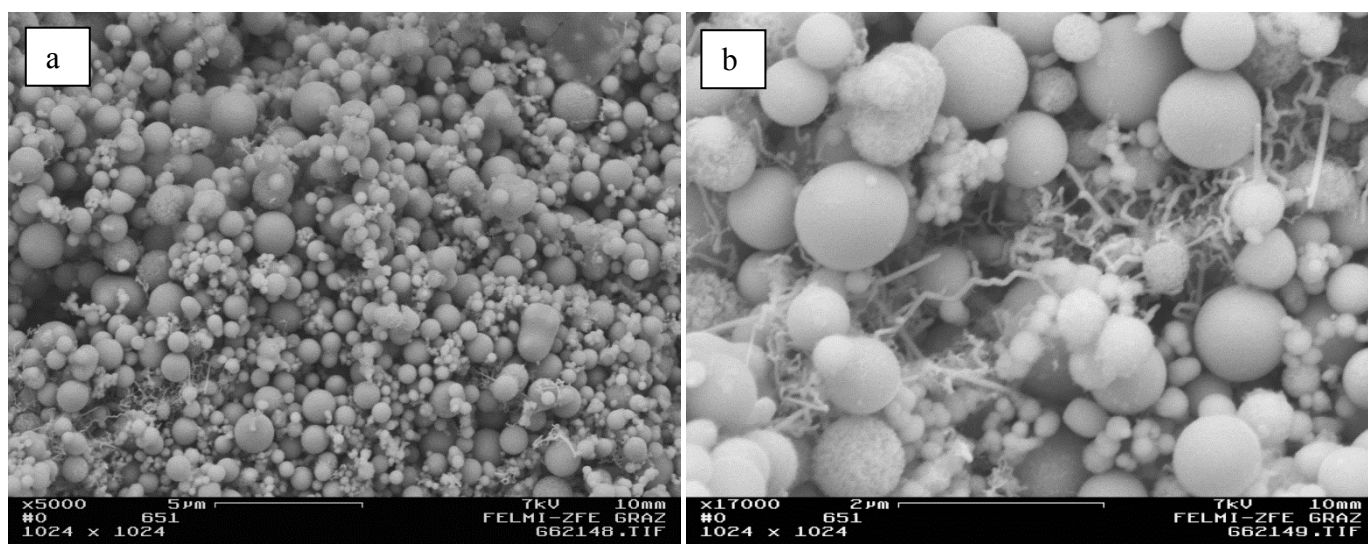


Figure 6-15. SEM image of indium catalyzed germanium nanowires synthesized at 350 °C in a mixture of oleylamine and TOPO. a) A large number of spherical microscale particles of germanium were formed in presence of TOPO. b) A few number of germanium nanowires are in between of spherical microscale particles of germanium.

According to the EDS analysis, spherical microscale particles of germanium has less than one percent of silicon impurity.

6.4 Synthesis of germanium nanowires at 380 °C

6.4.1 In the presence of TOPO

Previously in section 6.1 curly germanium nanowires were synthesized in *n*-dodecane in presence of TOPO at 180 °C. Here the synthesis temperature was increased to 380°C and squalane substituted *n*-dodecane to improve the morphology and crystallinity of nanowires. But at 380°C agglomerated germanium nanoparticles instead of germanium nanowires were obtained (Figure 6-16). It can be concluded that in the same pathway as it is explained in Section 6.3.3, trimethylsilyl groups of germanium hydride **8** react rapidly with the oxygen in TOPO at very high temperatures and again causes formation of germanium nanoparticles instead of nanowires.

The difference in the size distribution of germanium nanoparticles in this sample with the previous sample which was produced in a mixture of oleylamine and TOPO can be related to the different types of media that were used in these two reactions.

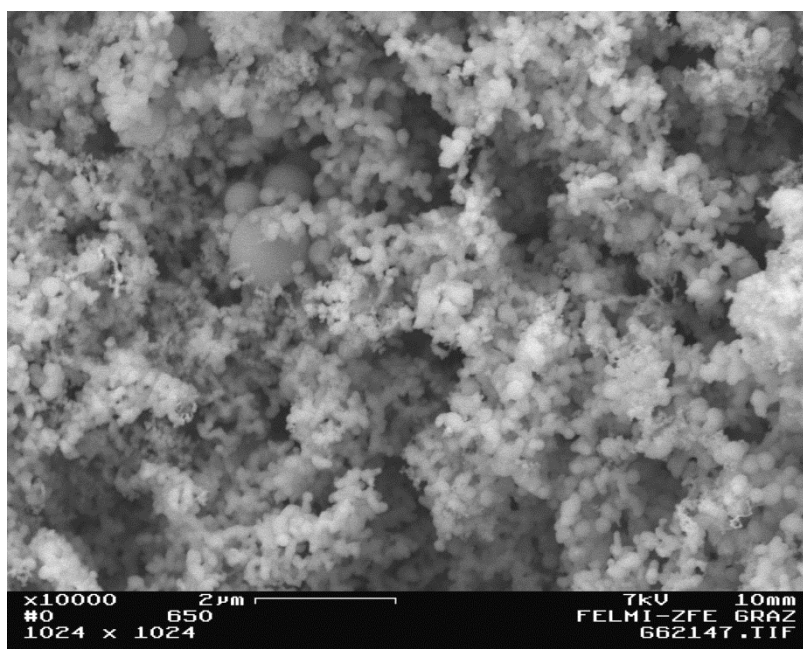


Figure 6-16. SEM image of indium catalyzed germanium nanowires synthesized at 380 °C in squalane in presence of TOPO. Instead of germanium nanowires, agglomerated germanium nanoparticles were formed.

6.5 Conclusion

Indium catalyzed synthesis of germanium nanowires via SLS mechanism in different alkane media was performed under atmospheric pressure and various temperatures with 1,1,2,2-tetrakis(trimethylsilyl)digermane (**8**) as a new germanium precursor. Due to the high thermal

sensitivity of **8** and ease of germanium release even at low temperatures, germanium nanowires were successfully synthesized at 180 °C in presence of TOPO capping ligand. However because of the low synthesis temperature, curly nanowires with crystalline defects were obtained.

Synthesis in *n*-hexadecane at 300 °C with TOPO capping ligand did not affect the quality of nanowires significantly, capping ligand such as oleylamine improved morphology and straightness of nanowires at the same temperature. Furthermore the synthesis was performed in squalane at 350 °C in the presence of oleylamine, but mainly coagulated germanium nanoparticles and only a few nanowire-like structures were obtained instead of the desired germanium nanowires. To improve the quality of the product in squalane at 350 °C, the oleylamine to squalane ratio was increase. In this case high yield of germanium nanowires similar in the morphology to the sample which was synthesized at 300 °C in *n*-hexadecane was obtained. Also similar nanowires in the case of morphology and yield were obtained in pure oleylamine at 350 °C.

EDS analysis displayed that nanowires are composed of germanium and approximately 2 to 3 wt% of indium without any silicon impurity. In fact according to ²⁹Si NMR spectroscopy, silicon atoms remain in the solution mixture as hexamethyldisiloxane and do not incorporate into the structure of nanowires.

Synthesis at temperatures above 300 °C in the presence of TOPO causes formation of germanium micro- and nanoparticles instead of nanowires which is related to the very fast reaction of trimethylsilyl groups of the precursor with the oxygen in TOPO and very fast release and accumulation of the reactive Ge(0) species in the form of particles instead of slow diffusion into the indium nanoparticles and formation of nanowires.

SAED pattern of the sample synthesized at 300 °C in presence of oleylamine revealed that crystalline structure of germanium nanowires are not anymore compatible with cubic structure and it contains numerous planer defects (stacking faults). Worm-like morphology of nanowires and high level of planer defects in the structure of them could be due to incorporation of indium atoms in the germanium matrix. However further analysis with HRTEM needs to be performed to precisely answer it in detail.

This study shows that 1,1,2,2-tetrakis(trimethylsilyl)digermane (**8**) as a new germanium precursor has the potential to release pure germanium atoms at a wide range of temperatures suitable for the synthesis of nanomaterials.

Chapter 7

Oligosilanylsilatrane

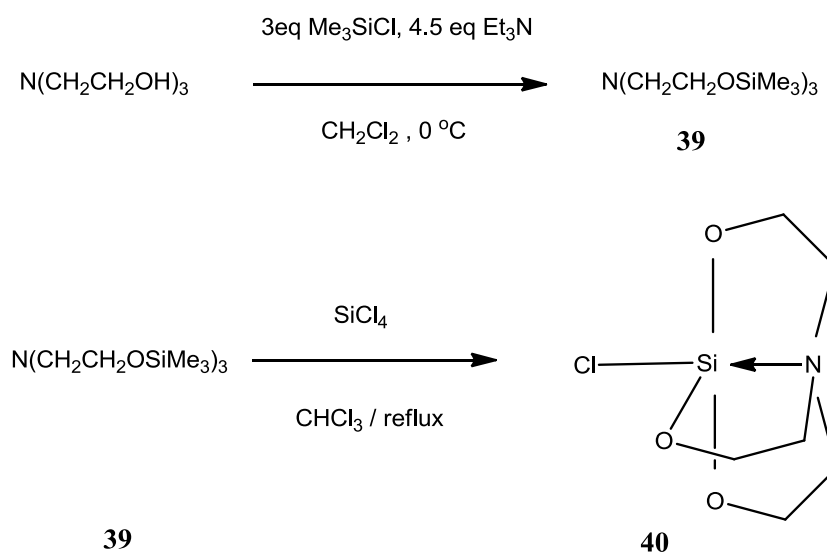
7 Oligosilanylsilatrane

7.1 Synthesis of primary silatrane units

For the synthesis of oligosilanylsilatrane a suitable way appears to be the reaction of a silatrane with an appropriate leaving group with a silanyl anion. It is known that among anionic leaving groups triflate CF_3SO_2 (OTf) is one of the best.¹⁰⁹ Due to that initially silatrane with different leaving groups ($\text{X} = \text{Cl}, \text{Br}, \text{OTf}$) were synthesized and in the second step the reaction of silatrane with silanyl anion was studied.

7.1.1 Synthesis of 1-chlorosilatrane (40)

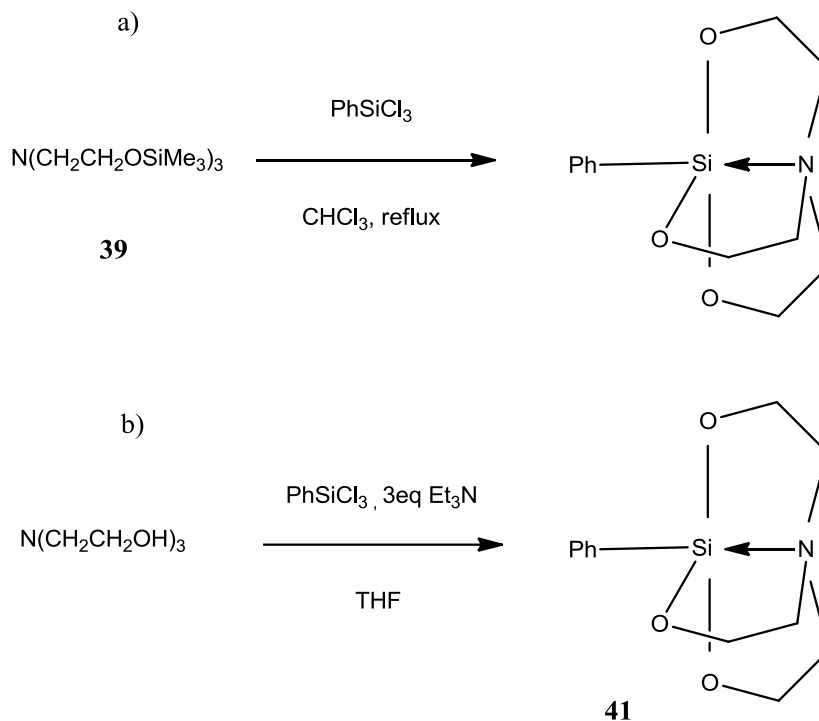
Synthesis of 1-chlorosilatrane (**40**) was performed according to literature procedure reported by Voronkov and co-workers⁷⁷ by reaction of $\text{N}(\text{CH}_2\text{CH}_2\text{OSiMe}_3)_3$ (**39**) with SiCl_4 under reflux (Scheme 7-1). During reflux a brownish polymeric compound forms in the reaction mixture which is highly soluble in chloroform. Insoluble 1-chlorosilatrane (**40**) in chloroform should be separated from brownish polymeric compound by a frit funnel as soon as the reaction flask comes to room temperature.



Scheme 7-1. Synthesis of 1-chlorosilatrane **40** from reaction of $\text{N}(\text{CH}_2\text{CH}_2\text{OSiMe}_3)_3$ (**39**) with SiCl_4 under reflux condition.

7.1.2 Synthesis of phenylsilatrane (41)

Synthesis of phenylsilatrane (**41**) was performed with two different methods which have been introduced both by Voronkov and co-workers.^{77,79} The first method was reaction of $\text{N}(\text{CH}_2\text{CH}_2\text{OSiMe}_3)_3$ (**39**) with PhSiCl_3 under reflux (Scheme 7-2a)⁷⁷ and the second one was reaction of trialkanolamine with PhSiCl_3 in presence of alkylamine (Scheme 7-2b).⁷⁹ The first method gave better yield.

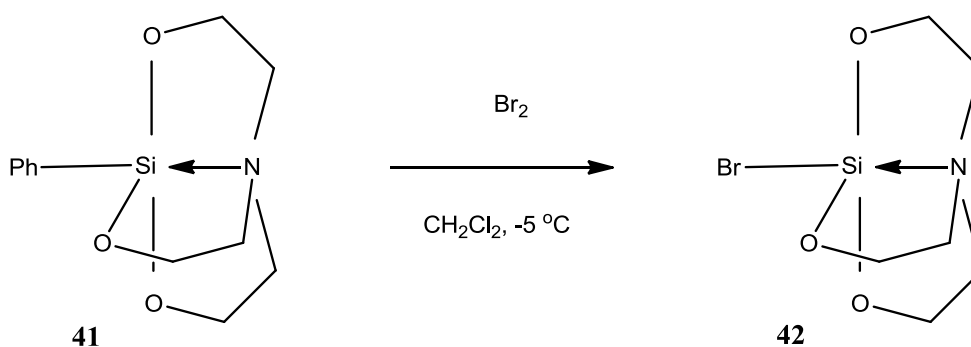


Scheme 7-2. a) Reaction of $N(\text{CH}_2\text{CH}_2\text{OSiMe}_3)_3$ (**39**) with phenyltrichlorosilane for synthesis of **41**. b) Reaction of phenyltrichlorosilane with triethanolamine for synthesis of **41**.

7.1.3 Synthesis of 1-bromosilatrane (**42**)

Synthesis of 1-bromosilatrane (**42**) was performed according to literature procedure reported by Voronkov et al.¹¹⁰ In this case a solution of bromine in CH_2Cl_2 was added to the solution of 1-phenylsilatrane in CH_2Cl_2 at -5°C (Scheme 7-3). It is found that in contrast to 1-chlorosilatrane (**40**), 1-bromosilatrane (**42**) is sensitive to air and it should be kept under an inert atmosphere.

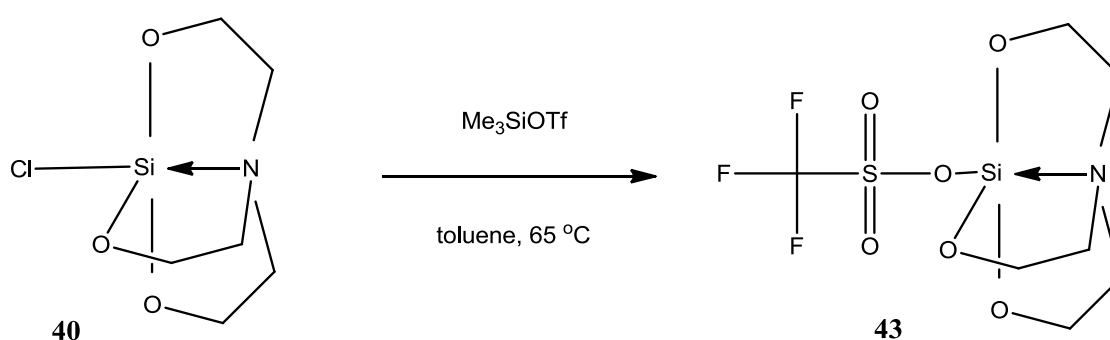
Selina et al.¹¹¹ has reported the selective cleavage of the Si-Br bond in reaction between $\text{PhC}\equiv\text{CLi}$ and 1-bromosilatrane (**42**) and formation of corresponding silatrane¹¹¹ which is promising for reaction between oligosilylpotassium and 1-bromosilatrane (**42**).



Scheme 7-3. Synthesis of 1-bromosilatrane (**42**) from bromination of phenylsilatrane (**41**)

7.1.4 Synthesis of 1-silatranyltriflate (43)

Synthesis of 1-germatranyltriflate (**44**) was reported by reaction of $N(\text{CH}_2\text{CH}_2\text{O})_3\text{GeOSiMe}_3$ with Me_3SiOTf in xylene.⁸³ In this reaction $-\text{OSiMe}_3$ was substituted by $-\text{OTf}$ at ambient temperature. Similarly Me_3SiOTf was reacted with 1-chlorosilatrane (**40**) to synthesize silatrane **43** (Scheme 1.5). Although the substitution of $-\text{OSiMe}_3$ with $-\text{OTf}$ occurs at ambient temperature over 12 hours, but complete substitution of $-\text{Cl}$ with $-\text{OTf}$ occurs only at 65°C over 72 hours. As the reaction reaches to equilibrium point, 2 equivalent amount of Me_3SiOTf to precursor **40** is required for complete conversion. Progress of reaction was monitored by ^1H NMR spectroscopic analysis of the peaks of Me_3SiOTf and the formed trimethylchlorosilane. It seems that formation of Me_3SiCl as a stable product is the driving force of this reaction and finally formation of silatrane **43**.

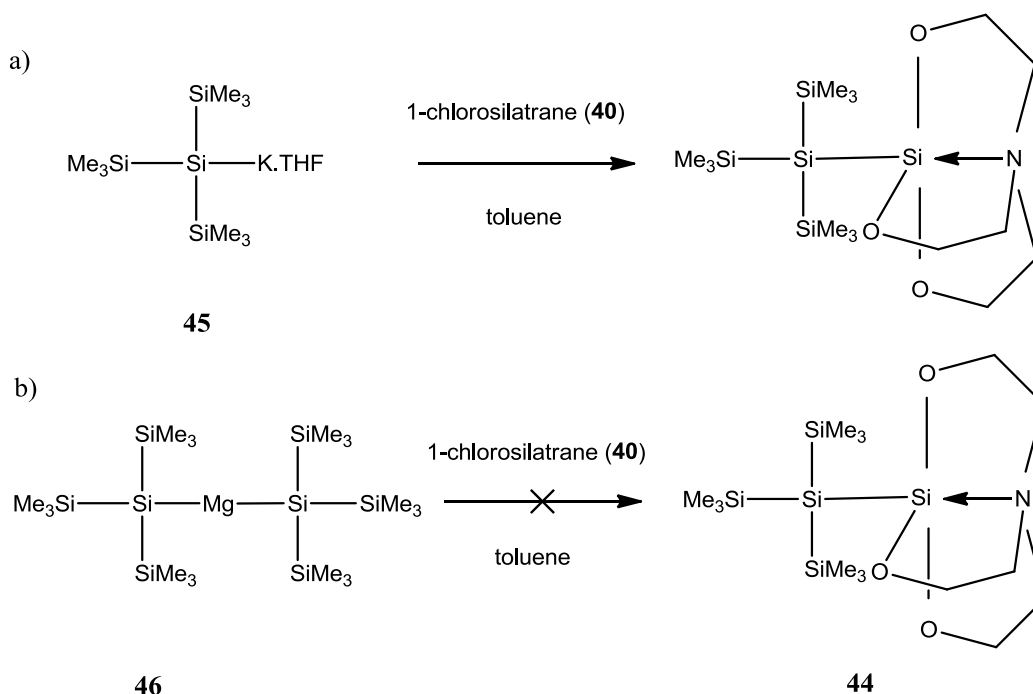


Scheme 7-4. Synthesis of 1-silatranyltriflate (**43**) from 1-chlorosilatrane (**40**)

7.2 Synthesis of oligosilanylsilatrane

7.2.1 Synthesis of tris(trimethylsilyl)silatranylsilane (**44**)

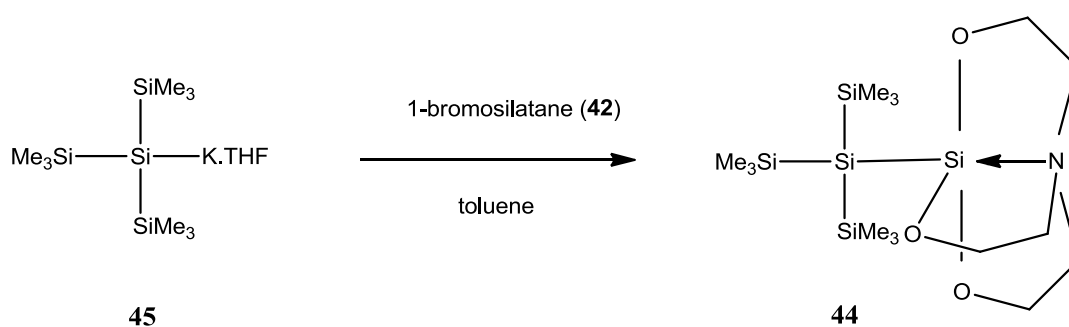
1-Chlorosilatrane (**40**) was reacted with both silanyl anion tris(trimethylsilyl)silylpotassium (**45**) and bis[tris(trimethylsilyl)silyl]magnesium (**46**) in separate reactions according to Scheme 7-5a and 7-5b, respectively. According to NMR spectroscopic analysis in case of reaction with oligosilylpotassium **45** a mixture of tetrakis(trimethylsilyl)silane (**47**), tris(trimethylsilyl)silane (**48**) and target silatrane **44** was obtained (Figure 7-1) and in case of reaction with oligosilylmagnesium **46** just silicon hydride **48** was formed and no sign of target silatrane **44** was observed (Figure 7-2). Similar to this, Cerveau et al.⁸¹ reported on the low reactivity of the Si-Cl bond of 1-chlorosilatrane (**40**) which is the consequence of the unusual molecular geometry and the Si-Cl short bond length of (2.12 Å) which is very close to that of the Si-Cl bond in tetracoordinate silicon compounds (2.05 Å).⁸¹



Scheme 7-5. a) Reaction of tris(trimethylsilyl)silylpotassium (**45**) with 1-chlorosilatane (**40**),
 b) Reaction of bis[tris(trimethylsilyl)silyl]magnesium (**46**) with 1-chlorosilatane (**40**).

As Selina et al.¹¹¹ have reported the selective cleavage of Si-Br bond in reaction between $\text{PhC}\equiv\text{CLi}$ and 1-bromosilatane (**42**) and formation of corresponding silatran in diethylether under reflux,¹¹¹ reaction of 1-bromosilatane (**42**) with oligosilylpotassium was performed (Scheme 7-6). According to NMR spectroscopic analysis (Figure 7-3) the final product is a mixture of oligosilane **47**, silicon hydride **48**, hexakis(trimethylsilyl)disilane (**49**) and target silatran **44**.

In this reaction potassium-bromide fast exchange leads to the formation of tris(trimethylsilyl)silylbromide (**50**). In the next step remaining oligosilylpotassium **45** reacts with **50** and oligosilane **49** forms. Formation of oligosilane **49** decreases the yield and makes the isolation of the target silatran **44** more difficult in comparison to the reaction of oligosilylpotassium with 1-chlorosilatane (**40**).



Scheme 7-6. Reaction of oligosilylpotassium **45** and 1-bromosilatane (**42**) for synthesis of tris(trimethylsilyl)silatranesilane (**44**).

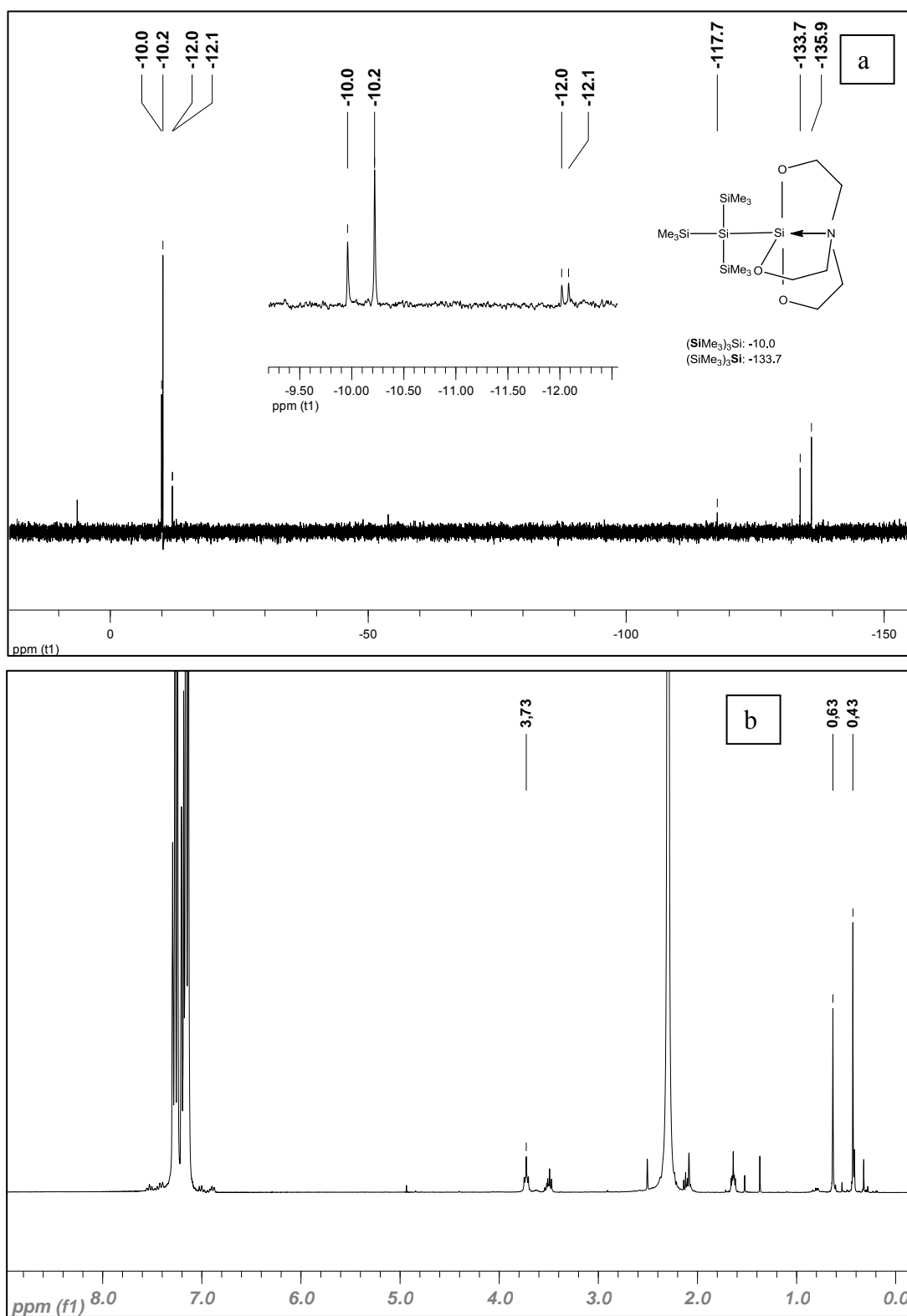


Figure 7-1. a) ^{29}Si NMR, b) ^1H NMR spectrum of reaction between tris(trimethylsilyl)silylpotassium (**45**) and 1-chlorosilatrane (**40**). A mixture of tetrakis(trimethylsilyl)silane (**47**), tris(trimethylsilyl)silane (**48**) and tris(trimethylsilyl)silatranysilane (**44**) was obtained. NMR is performed in toluene with D_2O lock.

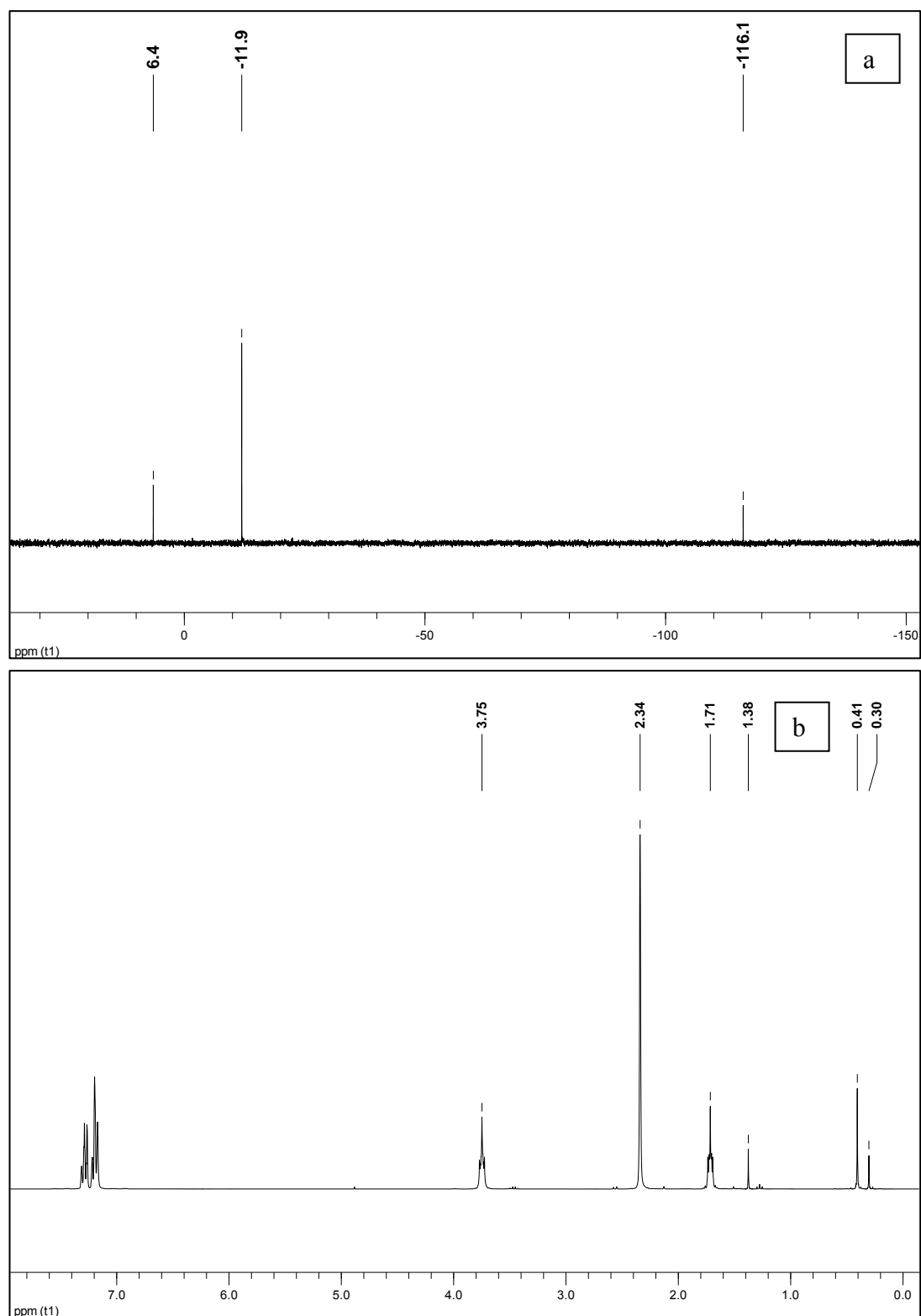


Figure 7-2. a) ^{29}Si NMR, b) ^1H NMR spectrum of reaction between bis[tris(trimethylsilyl)silyl]magnesium (**46**) and 1-chlorosilatrane (**40**). Instead of tris(trimethylsilyl)silatranylsilane (**44**) just tris(trimethylsilyl)silane (**48**) formed. NMR is performed in toluene with D_2O lock.

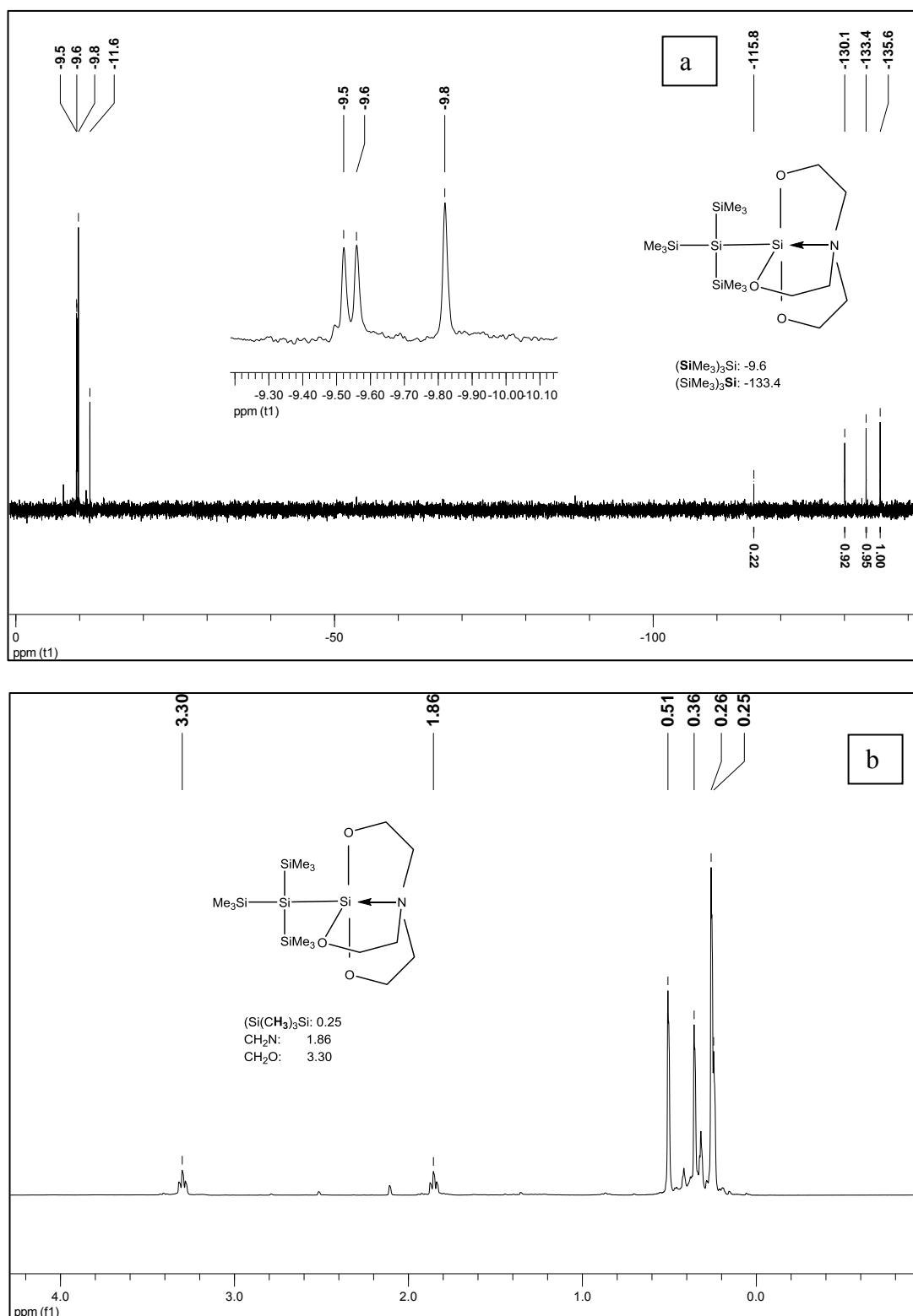
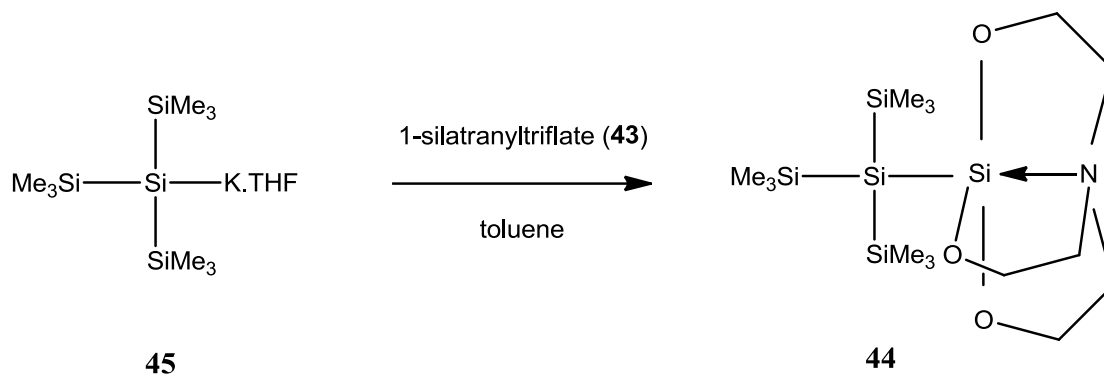


Figure 7-3. a) ^{29}Si NMR, b) ^1H NMR spectrum of synthesis of silatran **44** via the reaction of tris(trimethylsilyl)silylpotassium (**45**) and 1-bromosilatran. The final product is a mixture of tetrakis(trimethylsilyl)silane (**47**), hexakis(trimethylsilyl)disilane (**48**) and tris(trimethylsilyl)silane(**49**). NMR is performed in benzene with D_2O lock.

Zaitsev et al.⁸⁴ have reported the reaction of 1-germatranyltriflate with oligosilylgermylpotassium $[(\text{Me}_3\text{Si})_3\text{Si}]_3\text{GeK.THF}$ (**51**) to synthesize germatrane $\text{N}(\text{CH}_2\text{CH}_2\text{O})_3\text{Ge-Ge}(\text{SiMe}_3)_3$ (**52**) in 34% yield. Similar reaction of 1-silatranyltriflate with oligosilylpotassium **45** resulted in the synthesis of silatrane **44** in a clean reaction with 51% yield (Scheme 7-7). In contrast to the reaction of oligosilylpotassium **45** with 1-chloro- (**40**) and 1-bromosilatranes (**42**) which resulted in the formation of several compounds, reaction of oligosilylpotassium **45** with 1-silatranyltriflate (**43**) resulted in a clean reaction with high yield. Figure 7-4 shows the NMR spectroscopic analysis of this reaction.



*Scheme 7-7. Reaction of organosilylpotassium **45** and 1-silatranyltriflate (**43**) for synthesis of tris(trimethylsilyl)silatranylsilane (**44**).*

A different route is to first introduce the silicon atom of the silatrane into the polysilane structure and afterwards attach the triethanolamine unit to the silicon atom of the silatrane (Scheme 7-5). Due to less reactivity and more selectivity of organosilylmagnesium compounds over organosilyllithium and potassium compounds,¹¹² bis[tris(trimethylsilyl)silyl]magnesium (**45**) was reacted with silicon tetrachloride to obtain $(\text{Me}_3\text{Si})_3\text{SiSiCl}_3$ (**46**) as a pure product. Then **46** was reacted with triethanolamine in presence of triethylamine as a mild Lewis base to react with HCl generated during the reaction of silicon tetrachloride with the alcohol group of triethanolamine according to literature procedure reported by Zaitsev et al.⁸⁴

It is found that the yield of the reaction by this method is 16% which is far less than the reaction of oligosilylpotassium with 1-silatranyl triflate (**43**) with 51% yield.

As N-Si-C axial bond in simple silatranes with an electron withdrawing or donating groups like phenyl or methyl directly attached to hypercoordinated silicon atom is a four electron three center bonding unit, C-Si and Si-N bonds are in direct relation with each other. It means that longer C-Si bond length (implying a weaker C-Si bonding interaction) generally results in a shorter Si-N distance⁶⁷ (Table 7-1). In a similar way in oligosilanyl silatrane **44** the Si-Si-N axial bond is a four electron three center bond. As a result the Si-Si and the Si-N bonds are in direct relation with each other and longer Si-Si bond length (implying a weaker Si-Si bonding interaction) generally results in a shorter Si-N distance.

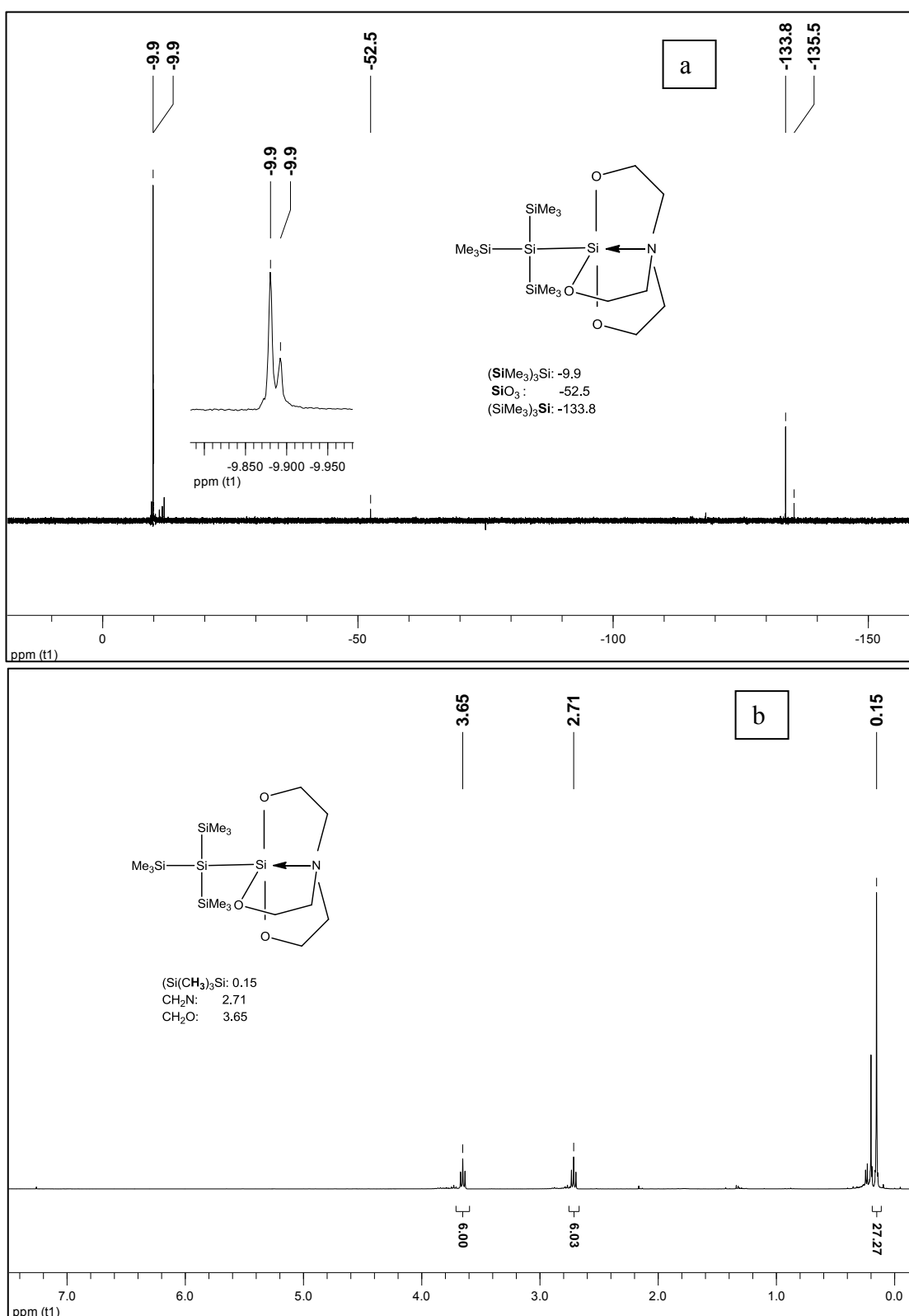
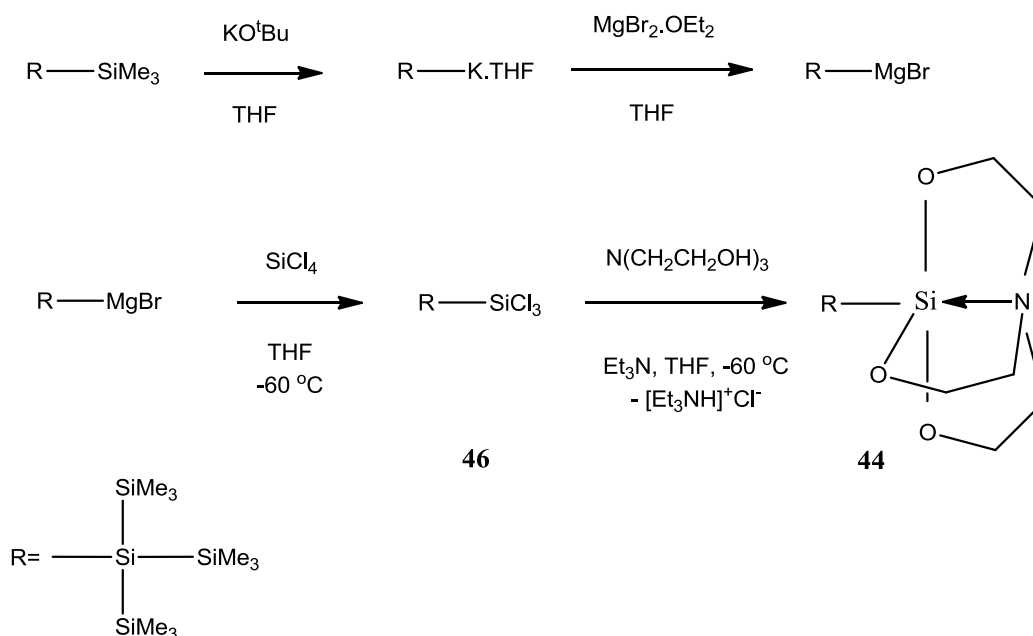


Figure 7-4. a) ²⁹Si NMR, b) ¹H NMR spectrum of synthesis of silatrane **44** via the reaction of tris(trimethylsilyl)silylpotassium (**45**) and 1-silatranyltriplate (**43**). Spectrum shows mostly the target silatrane **44** with small amount of tetrakis(trimethylsilyl)silane (**47**). NMR is performed in CDCl₃.



Scheme 7-5. Synthesis of tris(trimethylsilyl)silatranysilane (44).

Figure 7-5 shows the crystal structure and Table 7-2 shows selected bond lengths of oligosilanylsilatrane **44**. This molecule crystallizes in the triclinic space group P-1. The Si-N bond length of oligosilanylsilatrane **44** is with 2.292 Å between the Si-N bond length of 1-methyl-¹¹³ and 1-phenylsilatranes¹¹⁴ with 2.453 Å and 2.132 Å, respectively. The Si-SiO₃ bond length is with 2.3509 Å shorter than the Si-Si average bond length according to Cambridge crystallographic data center (CCDC)¹¹⁵ with 2.3721 Å which confirms that the structure of oligosilanylsilatrane **44** and mostly Si-SiO₃ should not be under a high level of stress. According to Table 7-1 the three O(x)-Si(1)-O(x') and the three C(x)-N(1)-C(x') angles are quite equal to each other which shows the symmetric trigonal bipyramidal structure of silatrane.

Table 7-1. Selected bond length of different silatranes.

Compound	Bond length (Å)		
	Si-N	Si-C	Si(1)-Si(2)
1-methylsilatrane ¹¹³	2.453	1.853	-
1-phenylsilatrane ¹¹⁴	2.132	1.894	-
N(CH ₂ CH ₂ O) ₃ SiSi(SiMe ₃) ₃ (44)	2.292	-	2.3509
Si-Si average bond length according to Cambridge crystallographic data center. ¹¹⁵	-	-	2.3721

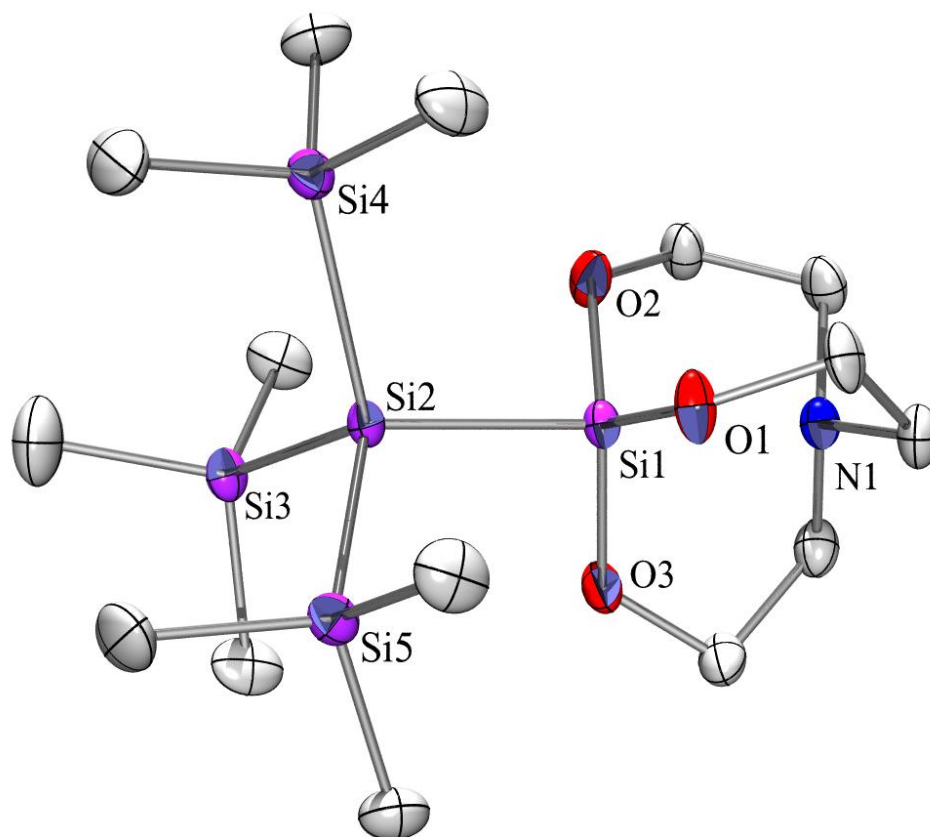


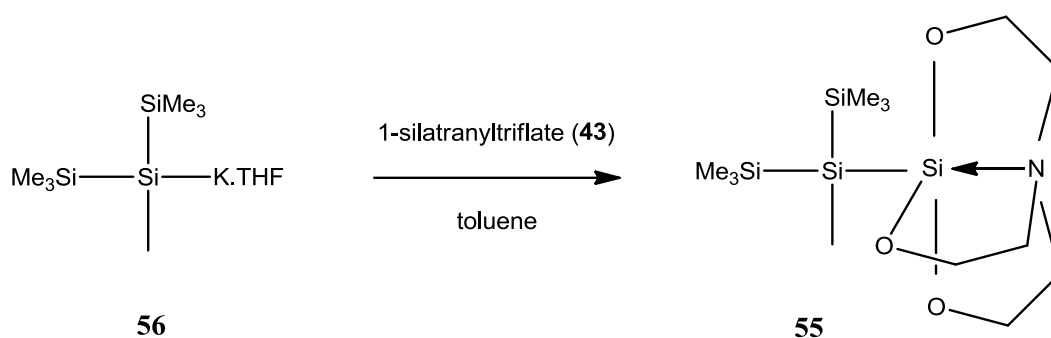
Figure 7-5. Crystal structure of tris(trimethylsilyl)silatranysilane (**44**).

Table 7-2. Selected bond lengths and angles of tris(trimethylsilyl)silatranysilane (**44**).

Bond Length	[Å]	Bond Angle	[°]
Si(1)-N(1)	2.292(4)	O(1)-Si(1)-O(2)	117.48(18)
Si(1)-O(3)	1.657(3)	O(1)-Si(1)-O(3)	117.02(18)
Si(1)-O(1)	1.650(3)	O(2)-Si(1)-O(3)	117.84(19)
Si(1)-O(2)	1.654(3)	C(1)-N(1)-C(5)	114.4(4)
Si(1)-Si(2)	2.3509(18)	C(1)-N(1)-C(3)	114.8(4)
		C(5)-N(1)-C(3)	114.9(4)

7.2.2 Synthesis of bis(trimethylsilyl)methylsilatranylsilane (55)

In previous section it is found that the synthesis of oligosilanylsilatrane is possible in two different routes. The first one is reaction of oligosilylpotassium with silatrane bearing a suitable leaving group like OTf and the second one is introduction of the silatrane-silicon atom into polysilane and then the triethanolamine unit. However, the first method is more appropriate because it provides better yields. Therefore the synthesis of oligosilanylsilatrane **55** was performed by reaction of bis(trimethylsilyl)methylsilylpotassium¹¹⁶ (**56**) with 1-silatranyltriflate (**43**) (Scheme 7-6). This reaction gave oligosilanylsilatrane **55** in a remarkable yield of 75% showing the better steric accessibility of the silanide.



Scheme 7-6. Reaction of bis(trimethylsilyl)methylsilylpotassium (56) with 1-silatranyltriflate (43) for synthesis of bis(trimethylsilyl)methylsilatranylsilane (55).

Figure 7-6 shows the crystal structure and Table 7-3 shows selected bond lengths of oligosilanylsilatrane **55**. In this compound Si-N bond length is 2.167 Å which is shorter than Si-N bond length of oligosilanylsilatrane **44** with 2.292 Å. In reverse Si-SiO₃ bond length for oligosilanylsilatrane **55** is 2.3523 Å which is longer than Si-SiO₃ bond length of oligosilanylsilatrane **44** with 2.3509 Å. This in fact is in accordance with the Gordon rule⁶⁷ that Si-Si-N axial bond is a four electron three center bonding unit and Si-Si and Si-N bonds are in direct relation with each other and longer Si-Si bond length (implying a weaker Si-Si bonding interaction) generally results in a shorter Si-N distance.

According to Table 7-2 and Table 7-3, in contrast to the crystal structure of oligosilanylsilatrane **44** with symmetric trigonal bipyramidal structure of silatrane, oligosilanylsilatrane **55** with three different O(x)-Si(1)-O(x') angle is quite asymmetric which could be due to substitution of trimethylsilyl group by methyl group and creation of an asymmetric forces around silatrane group.

7.2.3 Synthesis of bis(trimethylsilyl)ethylsilatranylsilane (57)

Synthesis of oligosilanylsilatrane **57** was performed by reaction of bis(trimethylsilyl)ethylsilylpotassium¹¹⁶ (**58**) with 1-silatranyltriflate (**43**) (Scheme 7-7). By this substitution of a methyl by an ethyl group, the yield of the reaction dropped from 75% to 25% due to lower steric accessibility of silanide.

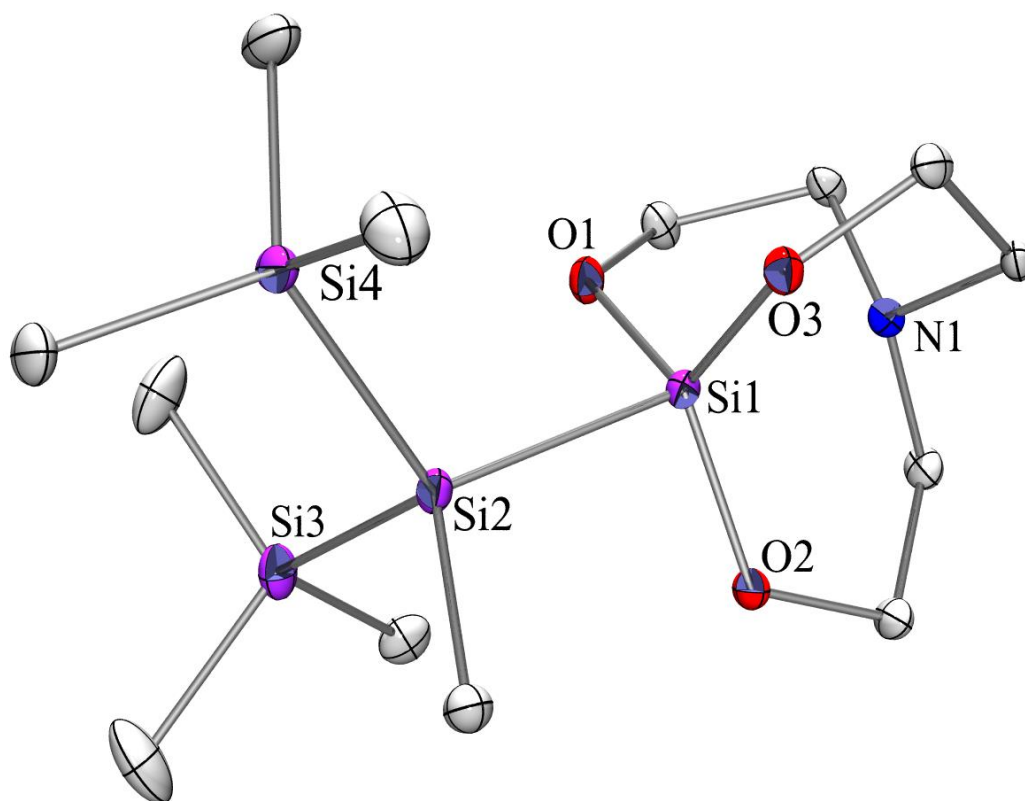
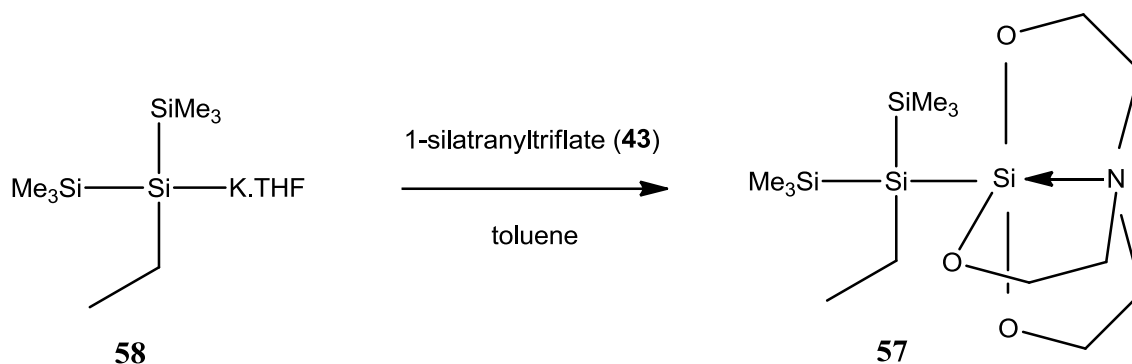


Figure 7-6. Crystal structure of bis(trimethylsilyl)methylsilatranyl silane (**55**).

Table 7-3. Selected bond lengths and angles of bis(trimethylsilyl)methylsilatranyl silane (**55**).

Bond Length	[Å]	Bond Angle	[°]
Si(1)-N(1)	2.167(3)	O(3)-Si(1)-O(1)	117.43(12)
Si(1)-O(3)	1.670(2)	O(3)-Si(1)-O(2)	117.76(12)
Si(1)-O(1)	1.673(2)	O(1)-Si(1)-O(2)	120.09(12)
Si(1)-O(2)	1.682(2)	C(1)-N(1)-C(6)	113.8(2)
Si(1)-Si(2)	2.3523(13)	C(1)-N(1)-C(4)	113.7(2)
		C(6)-N(1)-C(4)	113.7(2)

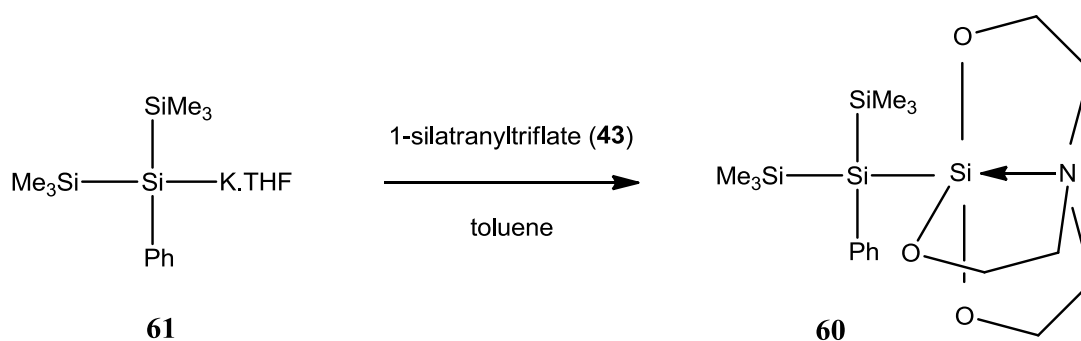


Scheme 7-7. Reaction of bis(trimethylsilyl)ethylsilylpotassium (58) and 1-silatranyl triflate (43) for synthesis of bis(trimethylsilyl)ethylsilatranylsilane (57).

Figure 7-7 shows the crystal structure and Table 7-4 shows selected bond lengths of oligosilanylsilatrane **57**. The Si-N bond length of this structure is with 2.182 Å longer than the Si-N bond length of oligosilanylsilatrane **55** with 2.167 Å. The Si-SiO₃ bond length of oligosilanylsilatrane **57** is 2.3443 Å which is shorter than the Si-SiO₃ bond length of oligosilanylsilatrane **55** with 2.3523 Å which again is in accordance with Gordon rule.⁶⁷ Similar to oligosilanylsilatrane **55** the three O(x)-Si(1)-O(x') angles are unequal which is due to presence of two trimethylsilyl group and one ethyl group around the silatrane group which produces an asymmetric forces.

7.2.4 Synthesis of bis(trimethylsilyl)phenylsilatranylsilane (60)

Synthesis of oligosilanylsilatrane **60** was performed by reaction of bis(trimethylsilyl)phenylsilylpotassium¹¹⁶ (**61**) with 1-silatranyl triflate (**43**) (Scheme 7-8). Due to the low steric accessibility of silanide caused by the phenyl group the yield in this reaction was only 27%. This yield is similar to the one for oligosilanylsilatrane **57** with an ethyl group instead of a phenyl group.



Scheme 7-8. Reaction of bis(trimethylsilyl)phenylsilylpotassium (61) and 1-silatranyl triflate (43) for synthesis of bis(trimethylsilyl)phenylsilatranylsilane (60).

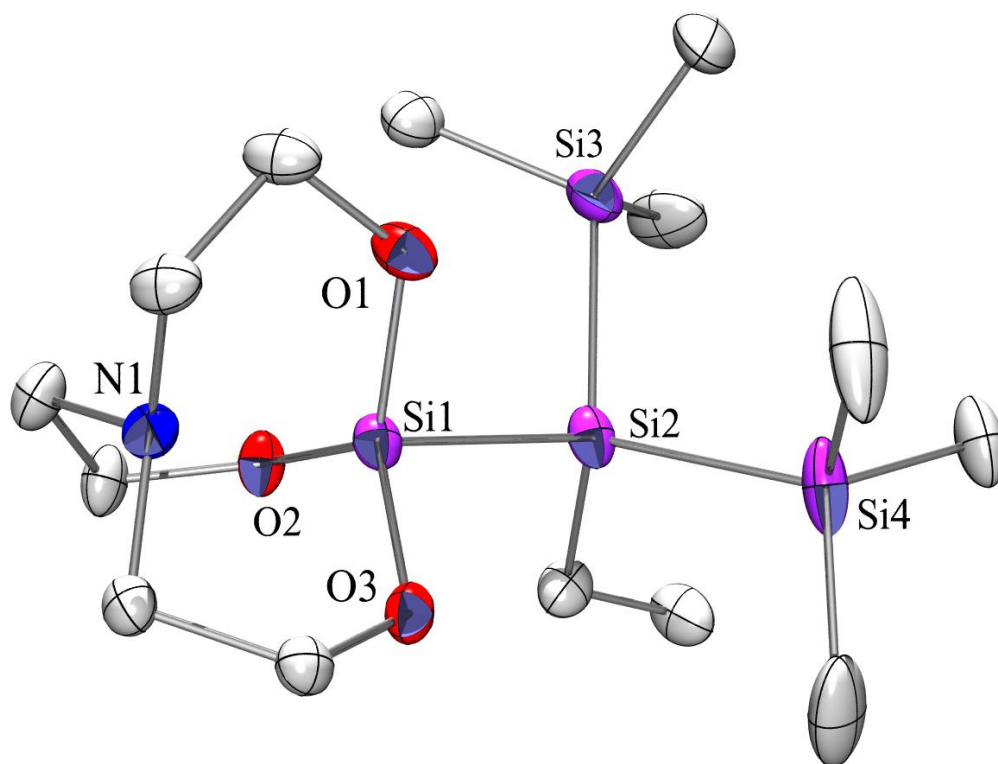


Figure 7-7. Crystal structure of bis(trimethylsilyl)ethylsilatranyl silane (**57**).

Table 7-4. Selected bond lengths and angles of bis(trimethylsilyl)ethylsilatranyl silane (**57**).

Bond Length	[Å]	Bond Angle	[°]
Si(1)-N(1)	2.182(3)	O(1)-Si(1)-O(3)	117.49(14)
Si(1)-O(3)	1.672(3)	O(1)-Si(1)-O(2)	120.03(15)
Si(1)-O(1)	1.671(3)	O(3)-Si(1)-O(2)	117.38(14)
Si(1)-O(2)	1.676(3)	C(6)-N(1)-C(4)	114.1(3)
Si(1)-Si(2)	2.3443(15)	C(6)-N(1)-C(2)	113.5(3)
		C(4)-N(1)-C(2)	113.7(3)

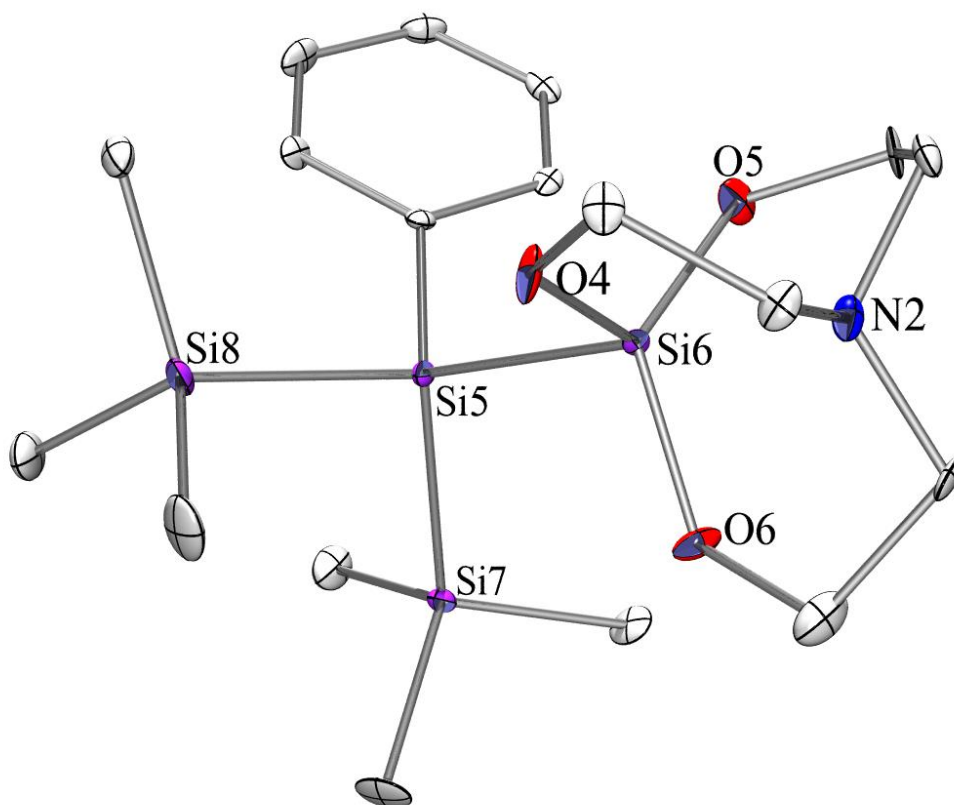


Figure 7-8. Crystal structure of bis(trimethylsilyl)phenylsilatranyl silane (**60**).

Table 7-5. Selected bond lengths and angles of bis(trimethylsilyl)phenylsilatranyl silane (**60**).

Bond Length	[Å]	Bond Angle	[°]
Si(6)-N(2)	2.176(6)	O(4)-Si(6)-O(6)	119.7(3)
Si(6)-O(4)	1.662(5)	O(4)-Si(6)-O(5)	118.4(3)
Si(6)-O(5)	1.682(5)	O(6)-Si(6)-O(5)	117.3(3)
Si(6)-O(6)	1.674(5)	C(28)-N(1)-C(30)	115.1(5)
Si(5)-Si(6)	2.383(2)	C(28)-N(1)-C(26)	113.9(6)
		C(30)-N(1)-C(26)	112.3(5)
Bond Length	[Å]	Bond Angle	[°]
Si(3)-N(1)	2.162(5)	O(2)-Si(3)-O(1)	119.4(3)
Si(3)-O(1)	1.674(5)	O(2)-Si(3)-O(3)	118.1(3)
Si(3)-O(2)	1.650(5)	O(1)-Si(3)-O(3)	118.3(3)
Si(3)-O(3)	1.676(5)	C(34)-N(2)-C(36)	113.6(5)
Si(1)-Si(3)	2.364(2)	C(34)-N(2)-C(32)	112.7(5)
		C(36)-N(2)-C(32)	114.2(5)

Figure 7-8 shows the crystal structure and Table 7-5 shows selected bond lengths of oligosilanylsilatrane **60**.

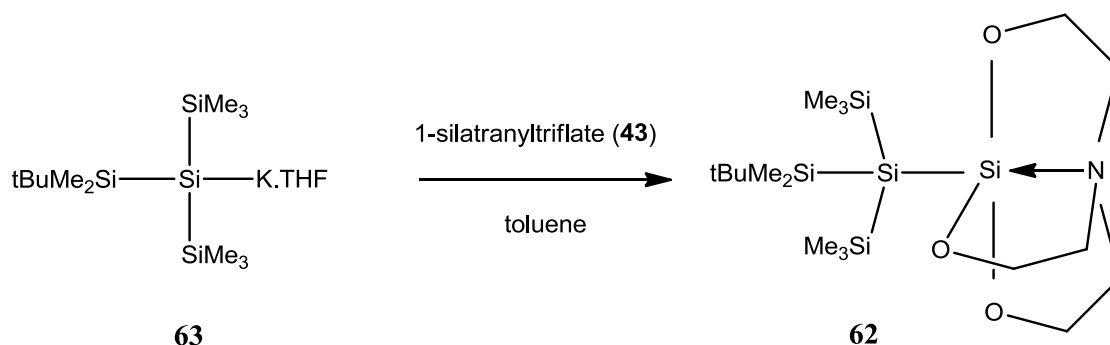
According to crystallographic data two molecules of oligosilanylsilatrane **60** are in the asymmetric condition in solid state. Due to that two different values for each bond length and bond angle are observed in this structure according to Table 7-5. Si-N bonds with 2.176 Å and 2.162 Å length exist in structure of oligosilanylsilatrane **60**. Si-N bond with 2.162 Å is the shortest Si-N bond among oligosilanylsilatrane **44**, **55** and **57**. The Si-N bond length in oligosilanylsilatrane **60** is so close to the Si-N bond length of 1-phenylsilatrane (**41**) with 2.132 Å which shows the effect of an electron withdrawal group like phenyl to the vicinal bond.

The Si-SiO₃ bonds with 2.364 Å and 2.383 Å lengths are the longest Si-SiO₃ bond among oligosilanylsilatrane **44**, **55** and **57**. Shortest Si-N and longest Si-SiO₃ bond in this structure in comparison to oligosilanylsilatrane **44**, **55** and **57** is in accordance with Gordon rule.⁶⁷

Similar to oligosilanylsilatrane **55** and **57** the three O(x)-Si(1)-O(x') angles are not equal which shows presence of unequal forces from two trimethylsilyl and one phenyl group to the silatrane group.

7.2.5 Synthesis of (*tert*-butyldimethylsilyl)bis(trimethylsilyl)silatranylsilane (**62**)

Synthesis of oligosilanylsilatrane **62** was performed by reaction of (*tert*-butyldimethylsilyl)bis(trimethylsilyl)silylpotassium¹¹⁶ (**63**) with 1-silatranyl triflate (**43**) (Scheme 7-9). For this reaction a yield of 42% was obtained which is higher than the 25% for oligosilanylsilatrane **57** or 27% for **60** but lower than the 51% for oligosilanylsilatrane **44**. This result shows that the steric accessibility of the silanide in presence of a *tert*-butyldimethylsilyl group is lower than a trimethylsilyl group and is higher than a phenyl or an ethyl group.



Scheme 7-9. Reaction of (*tert*-butyldimethylsilyl)bis(trimethylsilyl)silylpotassium (**63**) and 1-silatranyl triflate (**43**) for synthesis of (*tert*-butyldimethylsilyl)bis(trimethylsilyl)silatranylsilane (**62**).

Figure 7-9 shows the crystal structure and Table 7-6 shows selected bond lengths of oligosilanylsilatrane **62**.

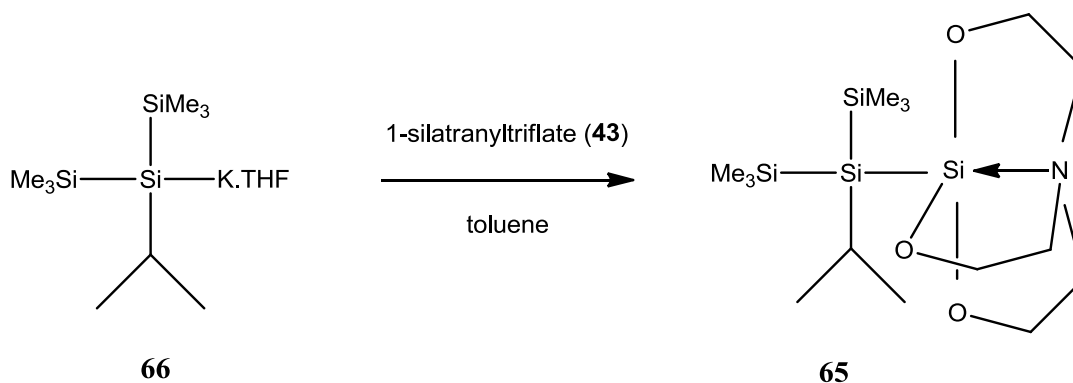
The Si-N and Si-SiO₃ bond lengths in this structure are with 2.283 Å and 2.3462 Å very close to the Si-N and Si-SiO₃ bond lengths of oligosilanylsilatrane **44** with 2.292 Å and 2.3509 Å. Despite the similarity of these two structures, relation between Si-N and Si-SiO₃ bonds in N-Si-

Si axial bond is not in accordance with Gordon rule⁶⁷. It means that by Si-N decrease from 2.292 Å in oligosilanylsilatrane **44** to 2.283 Å in oligosilanylsilatrane **62** and Si-SiO₃ also decrease instead of increase from 2.3509 Å in oligosilanylsilatrane **44** to 2.3462 Å in oligosilanylsilatrane **62**.

According to Table 7-6 the three O(x)-Si(1)-O(x') angles are very close to each other and the difference between them is less than one degree. In contrast to the previous oligosilanylsilatrane structures, there is a large distortion in the C(x)-N(1)-C(x') angles of oligosilanylsilatrane **62** as there is 7 degree difference between C(5)-N(1)-C(3) and C(3)-N(1)-C(1) angles by values of 117.7° and 110.7° respectively.

7.2.6 Synthesis of bis(trimethylsilyl)isopropylsilatranylsilane (**65**)

Synthesis of oligosilanylsilatrane **65** was achieved by reaction of bis(trimethylsilyl)isopropylsilylpotassium¹¹⁶ (**66**) with 1-silatranyltriflate (**43**) (Scheme 7-10). The yield of oligosilanylsilatrane **65** (56%) is slightly higher yield than for oligosilanylsilatrane **44** (51%). It shows that the steric accessibility of the silanide containing the isopropyl group is higher than the one with a trimethylsilyl group.



*Scheme 7-10. Reaction of bis(trimethylsilyl)isopropylsilylpotassium (**66**) and 1-silatranyltriflate (**43**) for synthesis of bis(trimethylsilyl)isopropylsilatranylsilane (**65**).*

7.2.7 Synthesis of 1,1-bis(trimethylsilyl)-1-silatranyl-pentamethyltrisilane (**67**)

Synthesis of oligosilanylsilatrane **67** was performed by reaction of 1,1-bis(trimethylsilyl)-1-potassium-pentamethyltrisilane (**68**) with 1-silatranyltriflate (**43**) (Scheme 7-11).

Oligosilanylsilatrane **67** with 58% yield has slightly higher yield than oligosilanylsilatrane **44** with 51% yield. It shows that steric accessibility of silanide in presence of pentamethyldisilane group is higher than trimethylsilyl group.

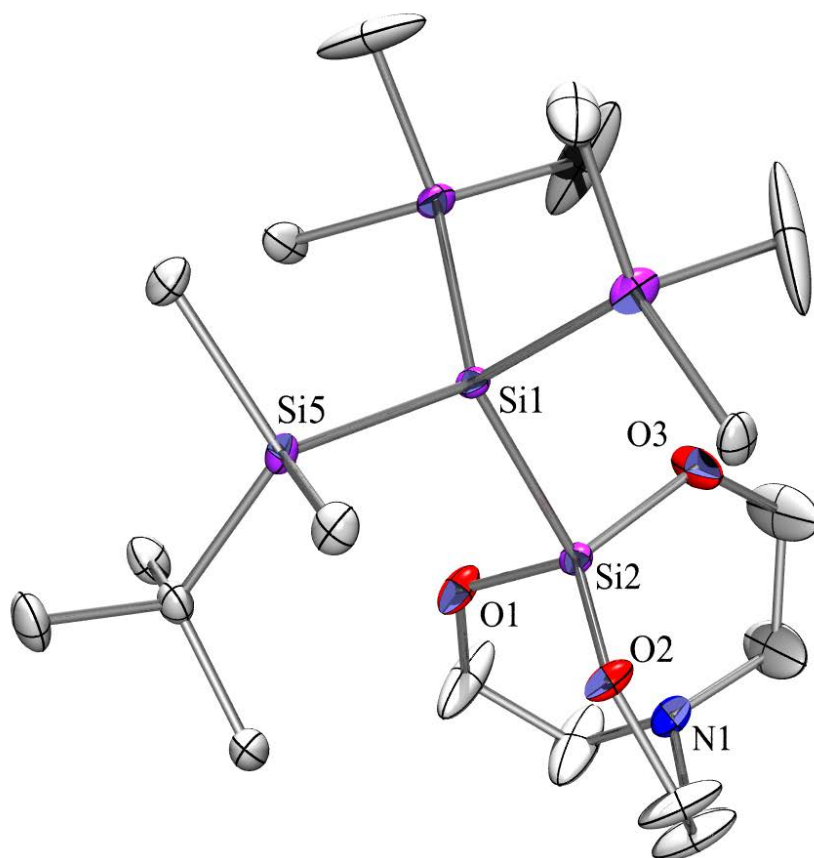
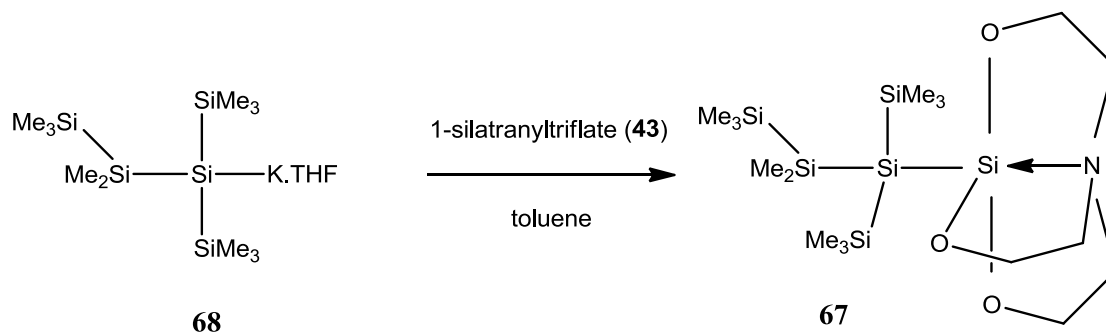


Figure 7-9. Crystal structure of (*tert*-butyldimethylsilyl)bis(trimethylsilyl)silatranyl silane (**62**).

Table 7-6. Selected bond lengths and angles of (*tert*-butyldimethylsilyl)bis(trimethylsilyl)silatranyl silane (**62**).

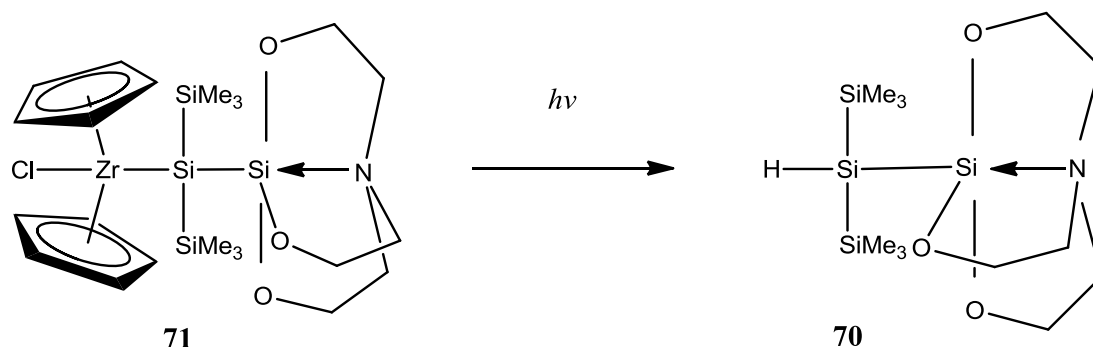
Bond Length	[Å]	Bond Angle	[°]
Si(2)-N(1)	2.283(3)	O(3)-Si(2)-O(2)	117.55(15)
Si(2)-O(1)	1.661(2)	O(3)-Si(2)-O(1)	116.97(15)
Si(2)-O(2)	1.660(2)	O(2)-Si(2)-O(1)	117.83(12)
Si(2)-O(3)	1.651(2)	C(5)-N(1)-C(3)	117.7(4)
Si(1)-Si(2)	2.3462(11)	C(5)-N(1)-C(1)	114.4(4)
		C(3)-N(1)-C(1)	110.7(4)



Scheme 7-11. Reaction of 1,1-bis(trimethylsilyl)-1-potassium-pentamethyltrisilane (**68**) and 1-silatranyl triflate (**43**) for synthesis of 1,1-bis(trimethylsilyl)-1-silatranyl-pentamethyltrisilane (**67**).

7.2.8 Synthesis of bis(trimethylsilyl)silatranylsilane (**70**)

Oligosilanylsilatrane **70** was synthesized by simple daylight decomposition of dicyclopentadienyl[bis(trimethylsilyl)silatranylsilyl]zirconiumchloride (**71**) (Scheme 7-12). The synthesis of oligosilatranylsilylzirconium **71** has been explained later in Section 7.4.3.



Scheme 7-12. Formation of bis(trimethylsilyl)silatranylsilane (**70**) by daylight decomposition of dicyclopentadienyl[bis(trimethylsilyl)silatranylsilyl]zirconiumchloride (**71**)

Figure 7-10 shows the crystal structure and Table 7-7 shows selected bond lengths of oligosilanylsilatrane **70**.

According to Gordon rule in N-Si-Si axial bond with a short Si-N bond, a long Si-SiO₃ bond should be observed⁶⁷. Si-N bond in **70** with 2.153 Å has the shortest bond among all previously discussed oligosilanylsilatrane; however, Si-SiO₃ bond with 2.3568 Å is not the longest Si-SiO₃ bond among the previously discussed oligosilanylsilatrane. This example shows that due to complexity of oligosilanylsilatrane in comparison to simple silatranes, Gordon rule⁶⁷ can be affected by other reasons like small size or electropositive nature of hydrogen atom.

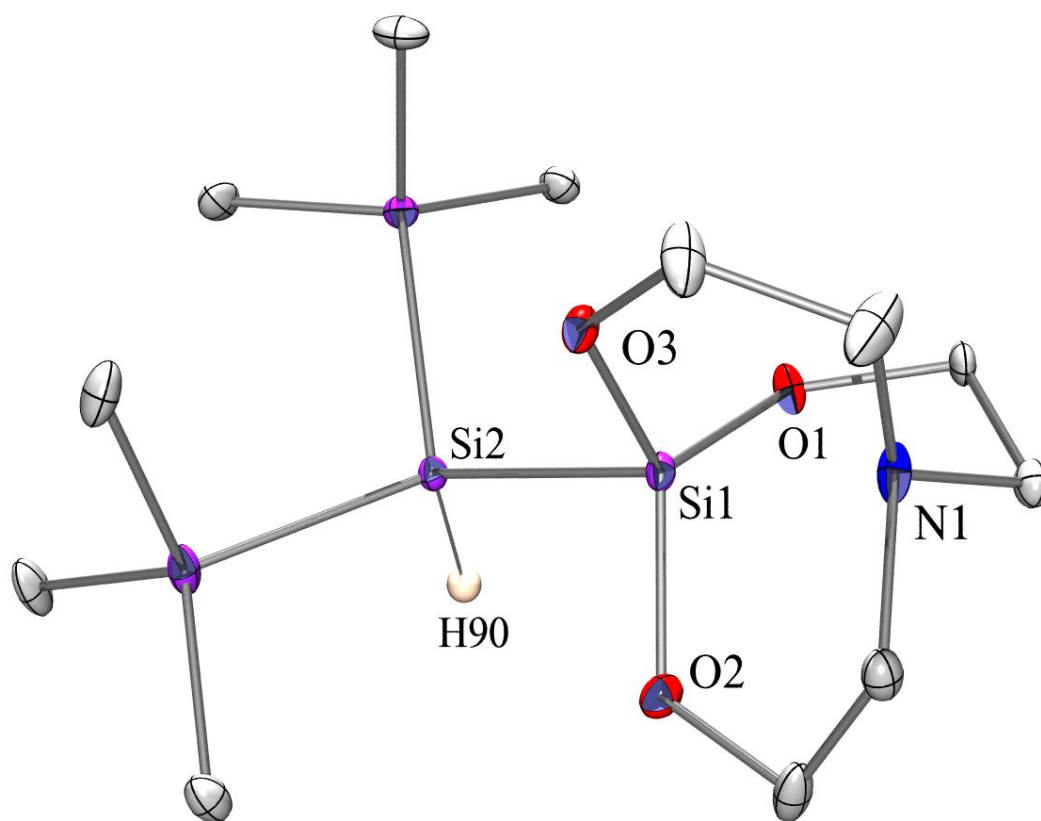


Figure 7-10. Crystal structure of bis(trimethylsilyl)silatranylsilane (**70**)

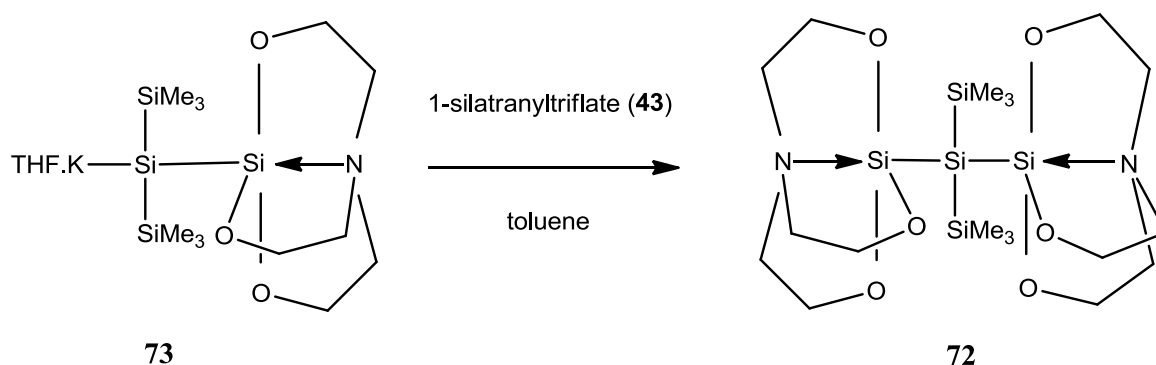
Table 7-7. Selected bond lengths and angles of bis(trimethylsilyl)silatranylsilane (**70**)

Bond Length	[Å]	Bond Angle	[°]
Si(1)-N(1)	2.153(3)	O(1)-Si(1)-O(2)	120.43(15)
Si(1)-O(3)	1.677(3)	O(1)-Si(1)-O(3)	118.68(14)
Si(1)-O(1)	1.674(3)	O(2)-Si(1)-O(3)	116.61(15)
Si(1)-O(2)	1.676(3)	C(6)-N(1)-C(2)	126.5(4)
Si(1)-Si(2)	2.3568(16)	C(6)-N(1)-C(4)	104.4(4)
		C(2)-N(1)-C(4)	109.2(4)

Because of the asymmetric forces on the silatrane group created by the two bulky trimethylsilyl groups and a small single hydrogen atom, the silatrane group loses its symmetry. Due to that three O(x)-Si(1)-O(x') angles are unequal. For the same reason the three C(x)-N(1)-C(x') angles are unequal too. This phenomenon can not be observed in oligosilanylsilatrane **44** due to the three equal trimethylsilyl groups.

7.2.9 Synthesis of disilatranyl-bis(trimethylsilyl)silane (**72**)

Synthesis of oligosilanylsilatrane **72** was performed by reaction of bis(trimethylsilyl)silatranyl.silyl.potassium (**73**) with 1-silatranyltriflate (**43**) (Scheme 7-13). Due to presence of a bulky silatrane group on oligosilatranyltrimethylpotassium **73** and very low accessibility of silanide, oligosilanylsilatrane **70** formed beside the target oligosilanylsilatrane. Via crystallization from pentane oligosilanylsilatrane **72** was obtained with 23% yield.



Scheme 7-13. Reaction of bis(trimethylsilyl)silatranyl.silyl.potassium (**73**) and 1-silatranyltriflate (**43**) for synthesis of disilatranyl-bis(trimethylsilyl)silane (**72**).

Figure 7-11 shows the crystal structure and Table 7-8 shows selected bond lengths of oligosilanylsilatrane **72**. Due to similarity of oligosilanylsilatrane **44** and **72** the existence of Gordon rule⁶⁷ was studied between these two molecular structures. In N-Si-Si axial bond Si-N bond length increases from 2.292 Å in oligosilanylsilatrane **44** to 2.421 Å in oligosilanylsilatrane **72** and in reverse Si-SiO₃ bond length decreases from 2.3509 Å in oligosilanylsilatrane **44** to 2.3416 Å in oligosilanylsilatrane **72** which is in accordance with Gordon rule.⁶⁷

Although each individual silatrane group is surrounded by unequal groups and it causes asymmetric forces around each silatrane group, but the distortion of three O(x)-Si(2)-O(x') angles and their differences is not significant.

7.2.10 Synthesis of 2-silatranyl-2,5,5-tris(trimethylsilyl)decamethylhexasilane (**75**)

Synthesis of 1-chloro-3,3-bis(trimethylsilyl)heptamethyltetrasilane (**76**) was performed according to literature procedure¹¹⁷ and the synthesis of **75** was done by reaction of oligosilatranyltrimethylpotassium **73** and chlorosilane **76** in toluene (Scheme 7-14).

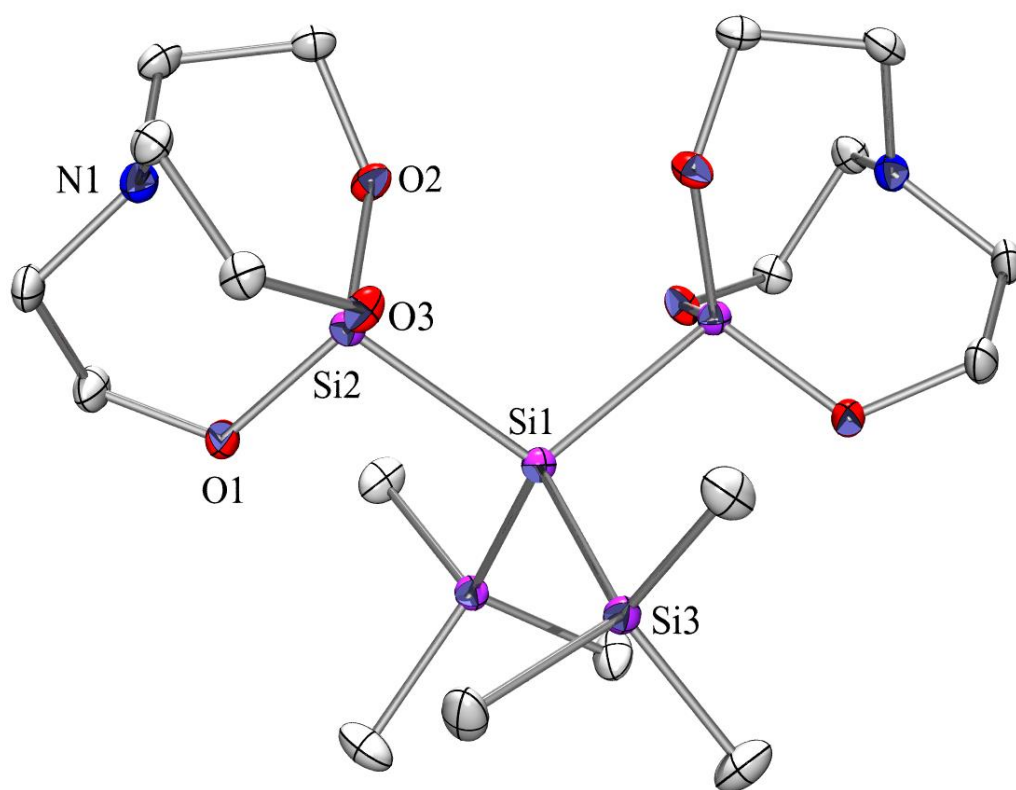
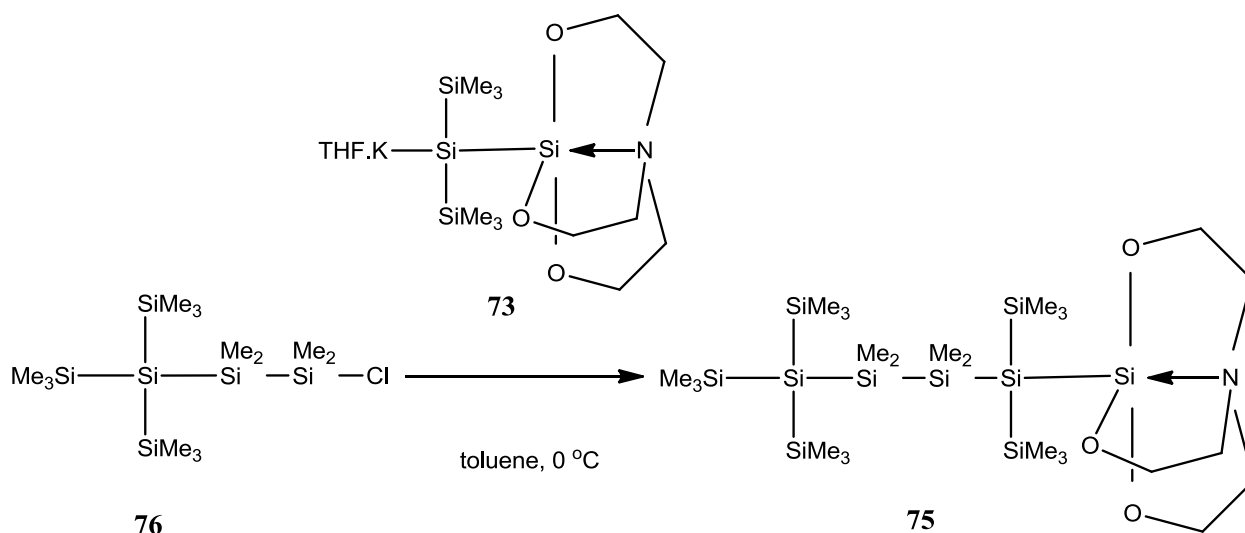


Figure 7-11. Crystal structure of disilatranyl-bis(trimethylsilyl)silane (**72**).

Table 7-8. Selected bond lengths and angles of disilatranyl-bis(trimethylsilyl)silane (**72**).

Bond Length	[Å]	Bond Angle	[°]
Si(2)-N(1)	2.421	O(3)-Si(2)-O(1)	115.03(5)
Si(2)-O(1)	1.6639(10)	O(2)-Si(2)-O(1)	116.40(5)
Si(2)-O(2)	1.6512(10)	O(2)-Si(2)-O(3)	116.47(5)
Si(2)-O(3)	1.6607(10)	C(6)-N(1)-C(2)	115.79(12)
Si(1)-Si(2)	2.3416(5)	C(6)-N(1)-C(4)	115.73(11)
Si(1)-Si(3)	2.3343(5)	C(2)-N(1)-C(4)	116.37(11)

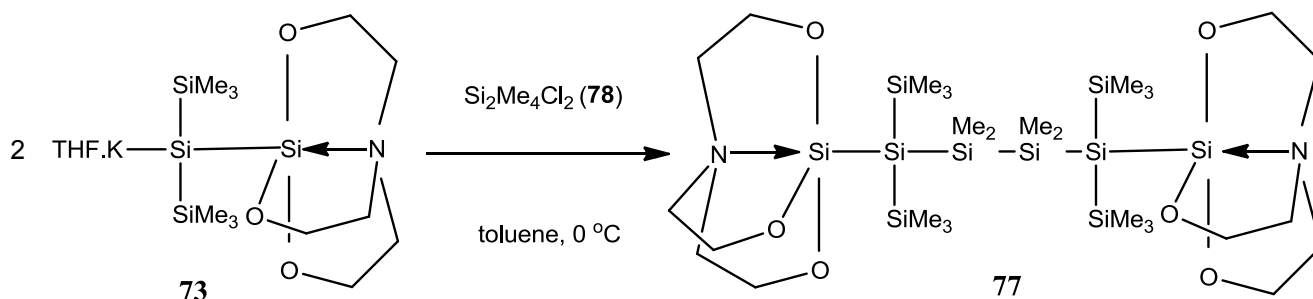
Oligosilanylsilatrane **75** was crystallized from a mixture of diethylether/acetonitrile 1:1 but due to presence of crystalline faults in single crystals, interpretation was not possible.



*Scheme 7-14. Reaction of bis(trimethylsilyl)silatranylsilyl.potassium (**73**) and 1-chloro-3,3-bis(trimethylsilyl)heptamethyltetrasilane (**76**) for synthesis of 2-silatranyl-2,5,5-tris(trimethylsilyl)decamethylhexasilane (**75**).*

7.2.11 Synthesis of 2,5-disilatranyl-2,5-bis(trimethylsilyl)decamethylhexasilane (**77**)

Synthesis of oligosilanylsilatrane **77** was performed similar to literature procedure reported by Whittaker et al.¹¹⁸ by reaction of two equivalent of oligosilatranylsilylpotassium **73** with 1,2-dichlorotetramethyldisilane (**78**) (Scheme 7-15).



*Scheme 7-15. Reaction of bis(trimethylsilyl)silatranylsilyl.potassium (**73**) and 1,2-dichlorotetramethyldisilane (**78**) for the synthesis of 2,4-disilatranyl-2,5-tris(trimethylsilyl)decamethylhexasilane (**77**).*

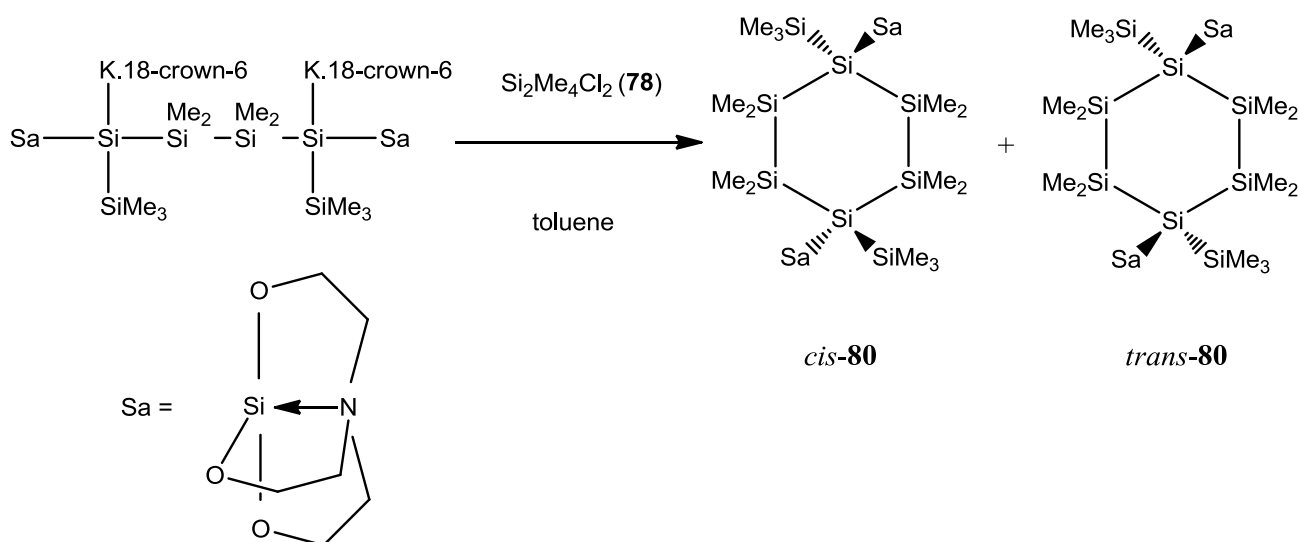
Figure 7-12 shows the crystal structure and Table 7-9 shows selected bond lengths of oligosilanylsilatrane **77**. Si-N and Si-SiO₃ bond lengths in oligosilanylsilatrane **77** are very close to Si-N and Si-SiO₃ bond lengths in oligosilanylsilatrane **44** according to Table 7-2. Due to asymmetric forces around silatrane group the three O(x)-Si(2)-O(x') angles are not equal in this structure as they are in oligosilanylsilatrane **44**. The same phenomenon is responsible for inequality of three C(x)-N(1)-C(x') angles.

Crystal structure of 2,2,5,5-tetrakis(trimethylsilyl)decamethylhexasilane (**79**) has been studied by Whittaker et al.¹¹⁸ which is suitable to be compared with oligosilanylsilatrane **77**.

According to Table 7-9, Si(1)-Si(5) bond length in oligosilanylsilatrane **77** is 2.3693 Å which is longer than the same Si-Si bond in oligosilane **79** with 2.345 Å. The presence of a bulky silatrane group could be responsible for Si-Si bond length increase in oligosilanylsilatrane **77**.

7.2.12 Synthesis of *cis/trans* 1,4-disilatranyl-1,4-bis(trimethylsilyl)octamethylcyclohexasilane (**80**)

Synthesis of cyclohexasilanylsilatrane **80** was done according to literature procedure¹¹⁹ by reaction of 2,5-disilatranyl-decamethylhexasilyl-2,5-dipotassium.18-crown-6 (**96**) with dichlorotetramethyldisilane (**78**) (Scheme 7-16).



Scheme 7-16. Synthesis of *cis/trans* 1,4-disilatranyl-1,4-bis(trimethylsilyl)octamethylcyclohexasilane (**80**) by reaction of 2,5-disilatranyl-decamethylhexasilyl-2,5-dipotassium.18-crown-6 (**96**) with dichlorotetramethyldisilane (**78**).

Figure 1.13 and 1.14 show crystal structure of the *cis* and *trans* isomer of cyclohexasilanylsilatrane **80**. According to NMR spectroscopy the ratio between the two isomers is 1:1. The *trans*-isomer is less soluble than *cis*-isomer. Due to the primary crystallization of *trans*-isomer from benzene, it is possible to separate both isomers from each other.

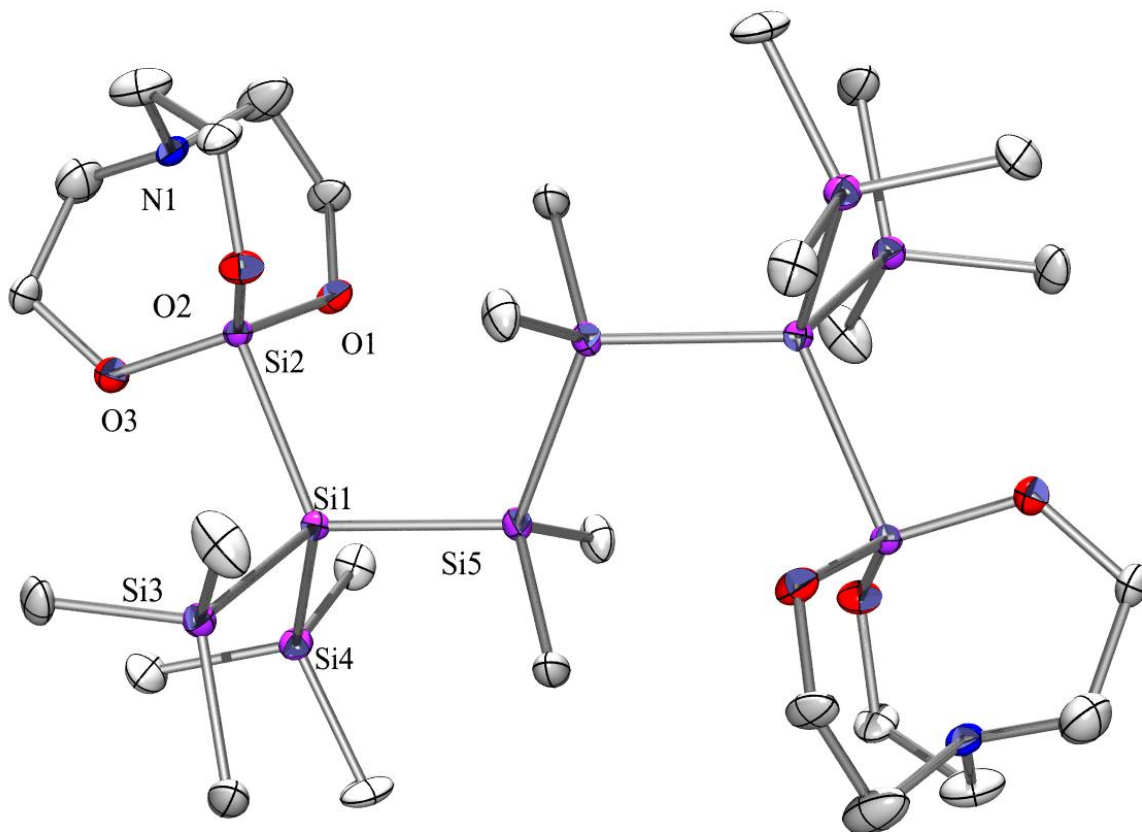


Figure 7-12. Crystal structure of 2,5-disilatranyl-2,5-bis(trimethylsilyl)decamethylhexasilane (77).

Table 7-9. Selected bond lengths and angles of 2,5-disilatranyl-2,5-bis(trimethylsilyl)decamethylhexasilane (77)

Bond Length	[Å]	Bond Angle	[°]
Si(2)-N(1)	2.223(4)	O(1)-Si(2)-O(2)	119.5(2)
Si(2)-O(3)	1.664(4)	O(1)-Si(2)-O(3)	116.8(2)
Si(2)-O(1)	1.657(4)	O(2)-Si(2)-O(3)	117.5(2)
Si(2)-O(2)	1.663(4)	C(4)-N(1)-C(2)	115.2(6)
Si(1)-Si(2)	2.3504(18)	C(4)-N(1)-C(6)	115.7(6)
Si(1)-Si(5)	2.3693(19)	C(2)-N(1)-C(6)	111.0(6)
Si(7)-N(2)	2.208(4)	O(6)-Si(7)-O(5)	116.5(2)
Si(7)-O(4)	1.671(4)	O(6)-Si(7)-O(4)	119.4(2)
Si(7)-O(5)	1.666(4)	O(5)-Si(7)-O(4)	118.6(2)
Si(7)-O(6)	1.665(4)	C(61)-N(2)-C(60)	115.1(11)
Si(6)-Si(7)	2.3417(18)	C(61)-N(2)-C(62)	114.3(12)
Si(6)-Si(9)	2.3585(19)	C(60)-N(2)-C(62)	109.2(11)

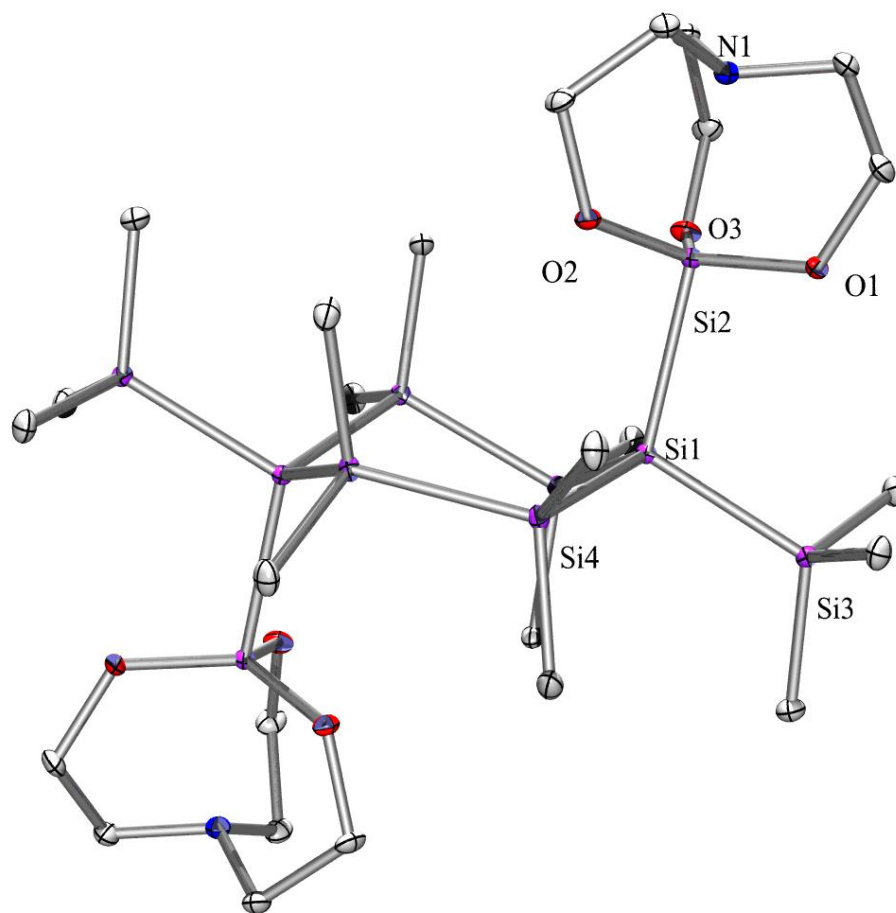


Figure 7-13. Crystal structure of *trans*-1,4-disilatranyl-1,4-bis(trimethylsilyl)octamethylcyclohexasilane (*trans*-**80**). The ring is engaging a chair conformation.

Table 7-10. Selected bond lengths and angles of *trans*-1,4-disilatranyl-1,4-bis(trimethylsilyl)octamethylcyclohexasilane (*trans*-**80**)

Bond Length	[Å]	Bond Angle	[°]
Si(2)-N(1)	2.194(2)	O(3)-Si(2)-O(1)	116.54(10)
Si(2)-O(3)	1.6703(19)	O(3)-Si(2)-O(2)	120.30(10)
Si(2)-O(1)	1.6731(18)	O(1)-Si(2)-O(2)	117.68(10)
Si(2)-O(2)	1.6740(18)	C(4)-N(1)-C(2)	114.5(2)
Si(1)-Si(2)	2.3639(10)	C(4)-N(1)-C(6)	113.3(2)
		C(2)-N(1)-C(6)	114.5(2)

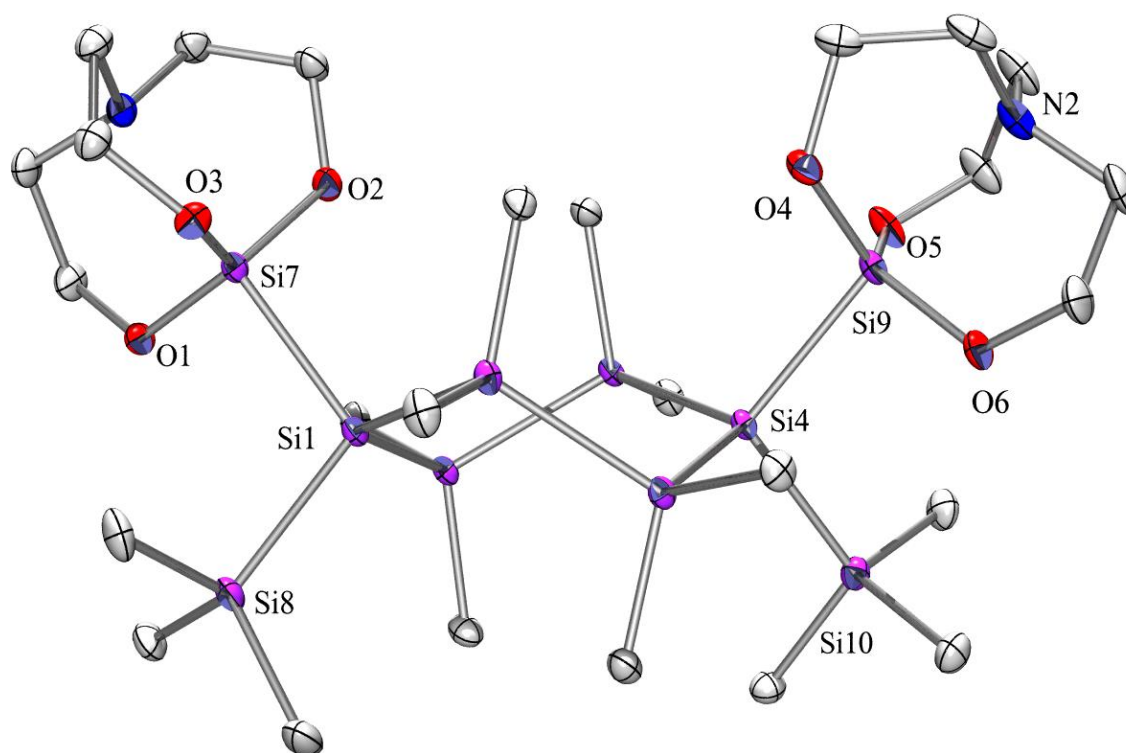


Figure 7-14. Crystal structure of *cis*-1,4-disilatranyl-1,4-bis(trimethylsilyl)octamethylcyclohexasilane (*cis*- **80**) with a twisted boat conformation of the six membered ring.

Table 7-11. Selected bond lengths and angles of *cis*-1,4-disilatranyl-1,4-bis(trimethylsilyl)octamethylcyclohexasilane (*cis*- **80**)

Bond Length	[Å]	Bond Angle	[°]
Si(7)-N(1)	2.2912(15)	O(2)-Si(7)-O(1)	117.62(6)
Si(9)-N(2)	2.3326(15)	O(3)-Si(7)-O(1)	116.66(6)
Si(1)-Si(7)	2.3447(8)	O(3)-Si(7)-O(2)	117.57(6)
Si(4)-Si(9)	2.3429(7)	O(4)-Si(9)-O(5)	115.53(7)
Si(7)-O(1)	1.6676(12)	O(4)-Si(9)-O(6)	116.64(7)
Si(7)-O(2)	1.6639(12)	O(5)-Si(9)-O(6)	118.80(7)
Si(7)-O(3)	1.6605(12)	C(16)-N(1)-C(20)	114.92(14)
Si(9)-O(4)	1.6572(12)	C(16)-N(1)-C(18)	114.20(13)
Si(9)-O(5)	1.6591(13)	C(20)-N(1)-C(18)	114.52(14)
Si(9)-O(6)	1.6602(13)	C(21)-N(2)-C(24)	115.26(16)
		C(21)-N(2)-C(25)	115.43(17)
		C(24)-N(2)-C(25)	115.01(17)

Once the crystals of *trans*-isomer formed, they have to be sonicated for further dissolution. In contrast the *cis*-isomer is highly soluble in alkane solvents and it crystallizes from pentane. Although the *cis*-isomer has two polar silatranyl groups in one side which decreases the solubility of the molecule but accumulation of methyl groups on the opposite side increase the solubility of the methylated side and in general increases the solubility of the *cis*-isomer while the presence of two bulky silatranyl groups in *trans*-isomer on opposite sides of the molecule makes the molecule totally solvent inaccessible.

According to Figure 1.13 and 1.14 the cyclohexasilane ring of the *trans*-isomer has chair and of the *cis*-isomer twisted boat conformation.

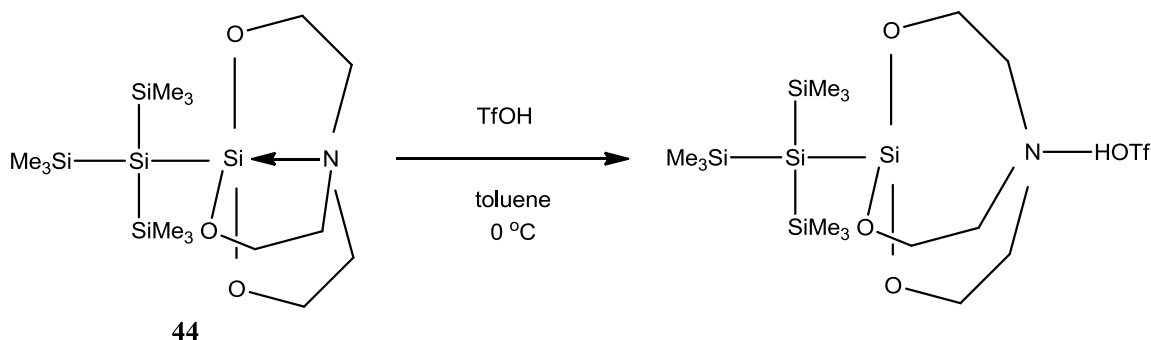
According to Table 7-10 and 7-11 endocyclic Si-Si bond angle attached to silatranyl group in *trans*-isomer is 111.74° while the same angle in *cis*-isomer is 112.60°. The Si-N bond in *trans*-isomer with 2.194 Å is shorter than the same bond in *cis*-isomer with 2.2912 and 2.3326 Å length. In reverse the Si-SiO₃ bond in *trans*-isomer with 2.3639 Å is longer than Si-SiO₃ bond in *cis*-isomer with 2.3447 and 2.3429 Å length. This in fact is in accordance with Gordon rule⁶⁷ and also shows that the Si-N interaction in *trans*-isomer is stronger than the *cis*-isomer.

The difference between the three O(x)-Si(x'')-O(x') angles in the *trans*-isomer is close to 4° which is higher than the *cis*-isomer with 1° and 3° depending on different orientations of the silatranyl groups. Although O(x)-Si(x'')-O(x') angles in both isomers are slightly different from each other, C(x)-N(1)-C(x') angles are mainly between 113° to 115° and are so close to each other.

7.2.13 Protonation of tris(trimethylsilyl)silatranylsilane (44) with trifluoromethanesulfonic acid

Alkylation or protonation of the transannular Si-N bond within the silatranyl group has been reported when this group undergoes a reaction with MeI or trifluoromethanesulfonic acid respectively.¹²⁰ In the case of methylation the initial Si-N bond length of the silatranyl group in silatranylosmium(II) complex {Cl(CO)(PPh₃)₂O_s[Si(OCH₂CH₂)₃N]} with bond length of 3.000 Å increases to 3.564 Å. Protonation with trifluoromethanesulfonic acid also occurs but the crystallographic data has not been reported.¹²⁰

Although theoretical calculations predict that protonation of silatranes with electronegative substituents is kinetically more favorable at the oxygen than at the nitrogen atom, but protonation of the nitrogen atom is more preferential in case of silylated silatranes.¹²¹



Scheme 7-17. Protonation of tris(trimethylsilyl)silatranylsilane (44) with trifluoromethanesulfonic acid.

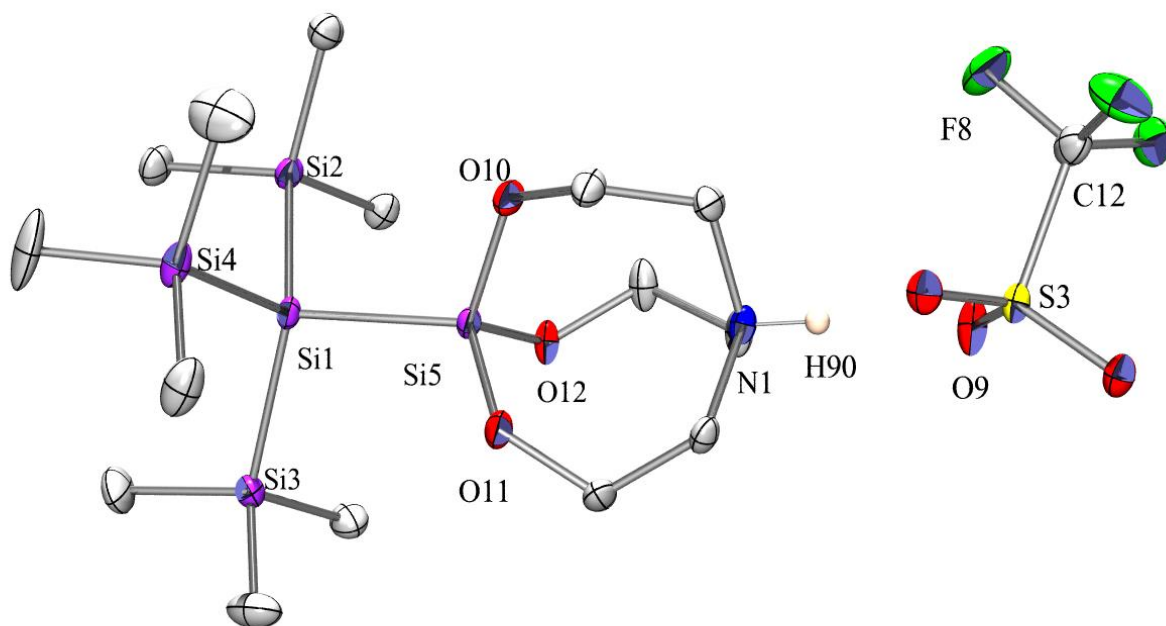


Figure 7-15. Crystal structure of Protonated tris(trimethylsilyl)silatranyl silane (**44**) with trifluoromethanesulfonic acid.

Table 7-12. Selected bond lengths and angles of Protonated tris(trimethylsilyl)silatranyl silane (**44**) with trifluoromethanesulfonic acid

Bond Length	[Å]	Bond Angle	[°]
Si(5)-N(1)	3.389	O(10)-Si(5)-O(12)	106.23(12)
Si(5)-N(1)	3.394	O(11)-Si(5)-O(12)	106.44(12)
Si(5)-O(10)	1.640(2)	O(11)-Si(5)-O(10)	106.94(12)
Si(5)-O(11)	1.637(2)	C(18)-N(1)-C(16)	116.8(3)
Si(5)-O(12)	1.645(2)	C(18)-N(1)-C(14)	115.3(3)
Si(1)-Si(5)	2.3072(12)	C(16)-N(1)-C(14)	115.8(2)

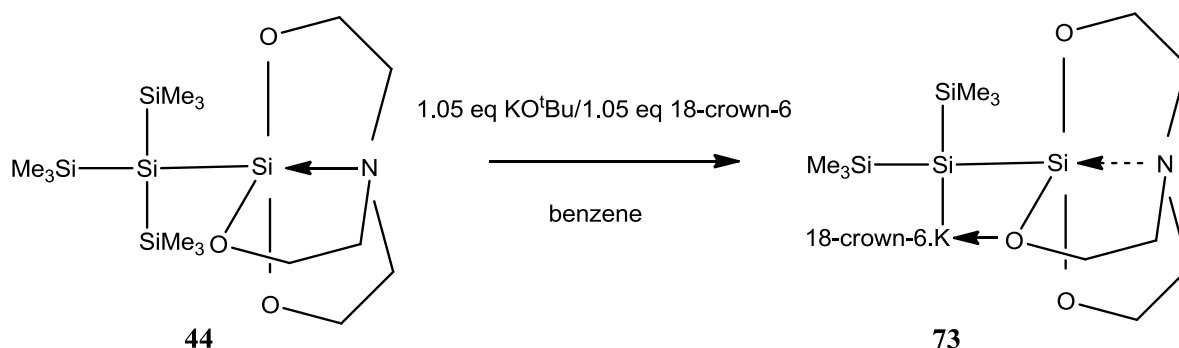
To estimate the degree of the nitrogen donation, oligosilanylsilatrane **44** was reacted with MeI and other protonating compounds. In presence of one equivalent of MeI or weak acids such as acetic acid and trichloroacetic acid no reaction was observed. By increasing the amount of weak acids to 5 equivalents in case of acetic acid no reaction was observed, but with trichloroacetic acid protonation of nitrogen atom was observed. In the case of strong acids like trifluoromethanesulfonic acid, protonation of the nitrogen atom occurs with only 1 equivalent of acid (Scheme 7-17). Reactivity of silatranylosmium(II) complex and non-reactivity of oligosilanylsilatrane **44** with MeI relates to the weak interaction of Si-N bond in silatranylosmium(II) complex and strong interaction of Si-N bond in oligosilanylsilatrane **44**. Also non-reactivity of nitrogen atom of silatrane group in oligosilanylsilatrane **44** with weak acids shows the strong electron donation of nitrogen to silicon atom.

Figure 7-15 shows the crystal structure and Table 7-12 the selected bond lengths of protonated oligosilanylsilatrane **44**. According to crystallographic data three molecules are in asymmetric unit. The Si-N bond increases to 3.389 Å in the protonated oligosilanylsilatrane **44** from 2.292 Å in oligosilanylsilatrane **44**. In reverse the Si-SiO₃ bond length decrease to 2.3072 Å from 2.3509 Å in oligosilanylsilatrane **44**. This phenomenon is in agreement with Gordon rule.⁶⁷ The long Si-N distance shows that the Si-N interaction is switches off by protonation of nitrogen atom. Due to presence of three trimethylsilyl groups around the silatranyl group and partial symmetry of the molecule the three O(x)-Si(5)-O(x') angles are very close to each other. The same condition is responsible for close values of three C(x)-N(1)-C(x') angles.

7.3 Synthesis of silatranylsilylanions

7.3.1 Synthesis of bis(trimethylsilyl)silatranylsilylpotassium.18-crown-6 (**73**)

Synthesis of oligosilatranylsilylpotassium **73** was performed by reaction of oligosilanylsilatrane **44** with one equivalent of each KO^tBu and 18-crown-6 in benzene (Scheme 7-18). The attack of the KO^tBu was selective at a trimethylsilyl group. It is found that the oligosilatranylsilylpotassium also forms in THF without 18-crown-6.



Scheme 7-18. Reaction of tris(trimethylsilyl)silatranylsilane (**44**), KO^tBu and 18-crown-6 in benzene for synthesis of bis(trimethylsilyl)silatranyl.silyl.potassium.18-crown-6 (**73**)

Figure 7-16 shows the crystal structure and Table 7-13 the selected bond lengths of oligosilatranylsilylpotassium **73**. According to the crystal structure the potassium atom coordinates with one oxygen atom of silatrane group with the bond length of 3.197 Å. Distinct

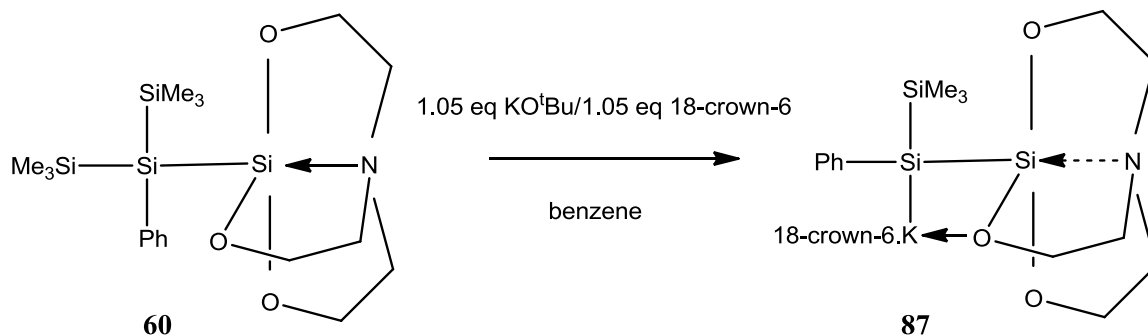
changes occurs in the trigonal bipyramidal structure of silatrane group as well as N-Si-Si axial bond of oligosilatranylsilylpotassium **73** in comparison to the neutral oligosilanylsilatrane **44**. The Si-N bond length increases from 2.292 Å in oligosilanylsilatrane **44** to 3.134 Å in oligosilatranylsilylpotassium **73** and in reverse axial Si-SiO₃ bond length decreases from 2.3509 Å in oligosilanylsilatrane **44** to 2.3080 Å in oligosilatranylsilylpotassium **73**. Simultaneous increase in Si-N bond length and decrease in Si-SiO₃ bond length shows the direct relation of these two bonds in accordance with Gordon rule.⁶⁷ Long Si-N distance shows that the Si-N interaction switches off by potassium silanide formation.

The Si-K distance of oligosilatranylsilylpotassium **73** is 3.3634 Å which is only slightly shorter than 3.447 Å Si-K distance of (Me₃Si)₃SiK·18-crown-6 (**45**).¹²² Also the distance between potassium and the silatranyl oxygen with 3.197 Å is elongated compared to K-O distances of the crown ether range from 2.787 to 2.926 Å.¹²²

Asymmetric structure and potassium-oxygen coordination in oligosilatranylsilylpotassium **73**, causes distortion of trigonal bipyramidal structure of silatranyl group and three unequal O(x)-Si(1)-O(x') angles as well as three unequal C(x)-N(1)-C(x') angles.

7.3.2 Synthesis of trimethylsilylphenylsilatranylsilylpotassium.18-crown-6 (**87**)

Synthesis of oligosilatranylsilylpotassium **87** was performed by reaction of oligosilanylsilatrane **60** with one equivalent of each KO^tBu and 18-crown-6 in benzene (Scheme 7-19). In this case also the attack of the KO^tBu was selective at one trimethylsilyl group. It is found that the oligosilatranylsilylpotassium **87** also forms in THF without 18-crown-6.



Scheme 7-19. Reaction of bis(trimethylsilyl)phenylsilatranylsilane (**60**), KO^tBu and 18-crown-6 in benzene for synthesis of trimethylsilylphenylsilatranyl.silyl.potassium.18-crown-6 (**87**)

Figure 7-17 shows the crystal structure and Table 7-14 the selected bond lengths of oligosilatranylsilylpotassium **87**. According to crystal structure potassium coordinates with oxygen of silatrane group with the bond length of 2.9983 Å.

Similar to oligosilatranylsilylpotassium **73** significant changes occurs in the structure of oligosilatranylsilylpotassium **87** in comparison to neutral oligosilanylsilatrane **60**. The Si-N bond length from increases from 2.182 Å in oligosilanylsilatrane **60** to 3.103 Å in oligosilatranylsilylpotassium **87** decrease in the Si-SiO₃ bond length from 2.364 Å and 2.383 Å in oligosilanylsilatrane **60** to 2.3080 Å in oligosilatranylsilylpotassium **87** occurs. Here also formation of potassium silanide switches off the Si-N interaction.

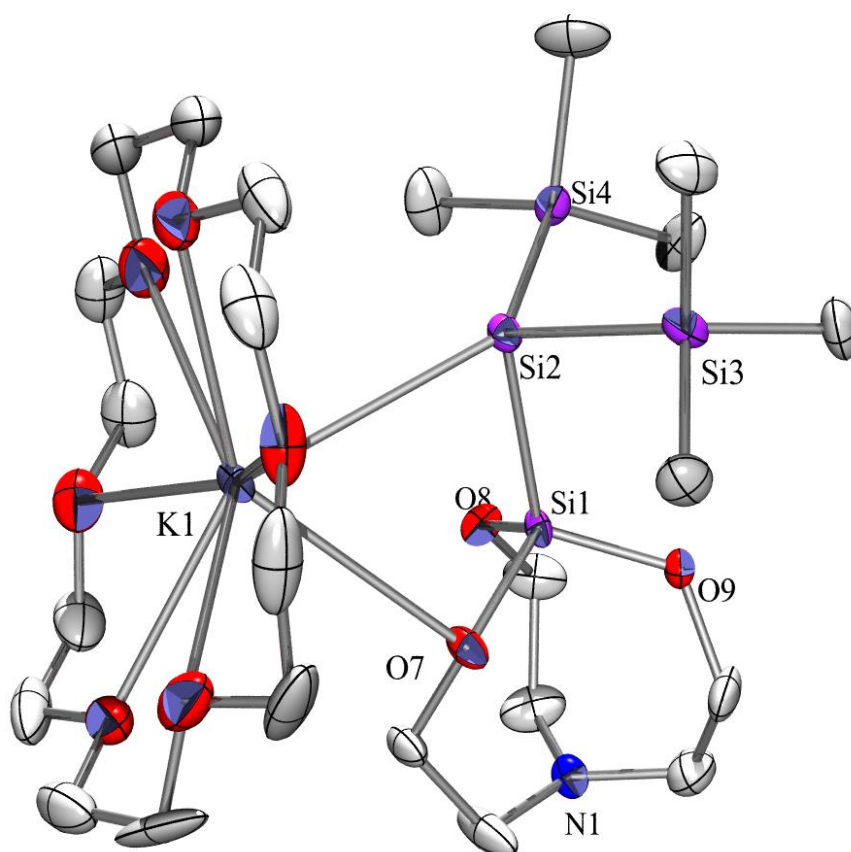


Figure 7-16. Crystal structure of bis(trimethylsilyl)silatranyl silyl potassium.18-crown-6 (**73**).

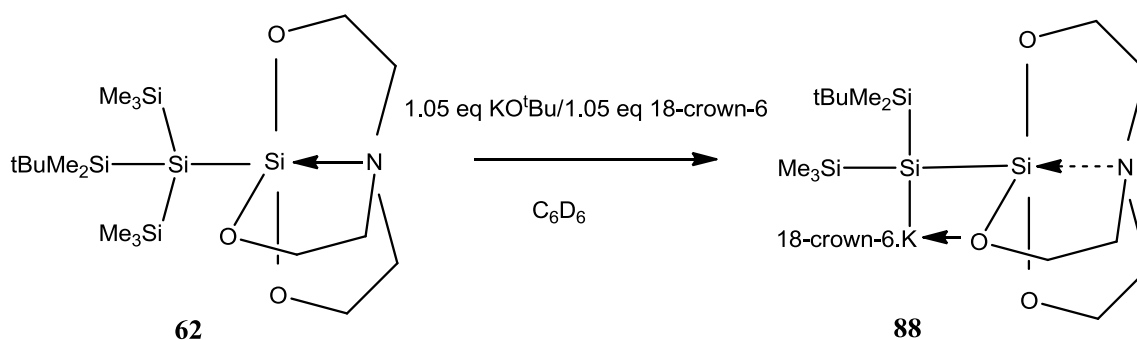
Table 7-13. Selected bond lengths and angles of bis(trimethylsilyl)silatranyl silyl potassium.18-crown-6 (**73**).

Bond Length	[Å]	Bond Angle	[°]
Si(1)-N(1)	3.134	O(9)-Si(1)-Si(2)	115.15(16)
Si(1)-O(7)	1.659(4)	O(8)-Si(1)-Si(2)	110.72(16)
Si(1)-O(8)	1.684(4)	O(7)-Si(1)-Si(2)	110.21(17)
Si(1)-O(9)	1.648(4)	C(14)-N(1)-C(16)	119.9(6)
Si(1)-Si(2)	2.3080(18)	C(14)-N(1)-C(17)	122.1(6)
Si(2)-K(1)	3.3634(16)	C(16)-N(1)-C(17)	117.4(5)
K(1)-O(7)	3.197(5)	Si(1)-Si(2)-K(1)	81.85(5)
		O(7)-Si(1)-O(8)	105.3(3)
		O(9)-Si(1)-O(8)	107.1(2)
		O(9)-Si(1)-O(7)	107.8(2)

Unequal three O(x)-Si(3)-O(x') angles as well as unequal three C(x)-N(1)-C(x') angles are due to the asymmetric structure of the molecule and the presence of asymmetric forces from surrounding groups of silatranyl group.

7.3.3 Synthesis of *(tert*-butyldimethylsilyl)(trimethylsilyl)silatranylsilylpotassium.18-crown-6 (**88**)

Synthesis of oligosilatranylsilylpotassium **88** was performed by reaction of oligosilanylsilatrane **62** with one equivalent of each KO^tBu and 18-crown-6 in benzene (Scheme 7-20). In this case also the attack of the KO^tBu was selective at one trimethylsilyl group.



Scheme 7-20. Reaction of *(tert*-butyldimethylsilyl)bis(trimethylsilyl)silatranylsilane (**62**), KO^tBu and 18-crown-6 in benzene for synthesis of *(tert*-butyldimethylsilyl)(trimethylsilyl)silatranyl.silyl.potassium.18-crown-6 (**88**)

Figure 7-18 shows the crystal structure and Table 7-15 the selected bond lengths of oligosilatranylsilylpotassium **88**. According to the crystal structure the potassium atom coordinates with one oxygen atom of the silatranyl group with a bond length of 2.936 Å. Increase in the N-Si bond length from 2.283 Å in oligosilanylsilatrane **62** to 3.184 Å in oligosilatranylsilylpotassium **88** decrease in the Si-SiO₃ bond length from 2.3462 Å in oligosilanylsilatrane **62** to 2.2947 Å in oligosilatranylsilylpotassium **88** is observed. Long Si-N distance shows that the Si-N interaction switches off by potassium silanide formation.

7.3.4 Synthesis of trimethylsilylmethylsilatranylsilylpotassium.18-crown-6 (**90**)

Synthesis of oligosilatranylsilylpotassium **90** was performed by reaction of oligosilanylsilatrane **55** with one equivalent of each KO^tBu and 18-crown-6 in benzene (Scheme 7-21). In this reaction the KO^tBu attack was not selectively to one trimethylsilyl group and attack also was observed at the silicon atom of the silatranyl unit. As a result the final product was a mixture of oligosilatranylsilylpotassium **90**, bis(trimethylsilyl)methylsilyl potassium.18-crown-6 (**56**) with 2:1 ration and N(CH₂CH₂O)₃Si^tBu (**92**). The separation of these compounds was impossible due to the oily nature of them.

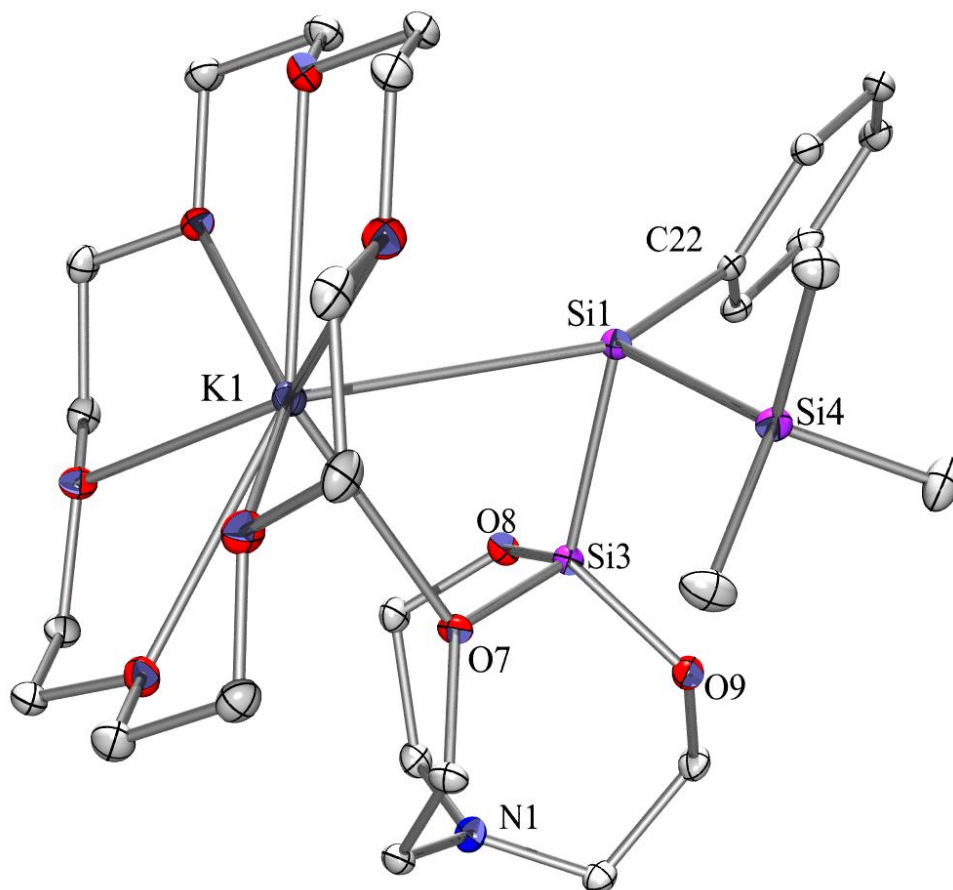
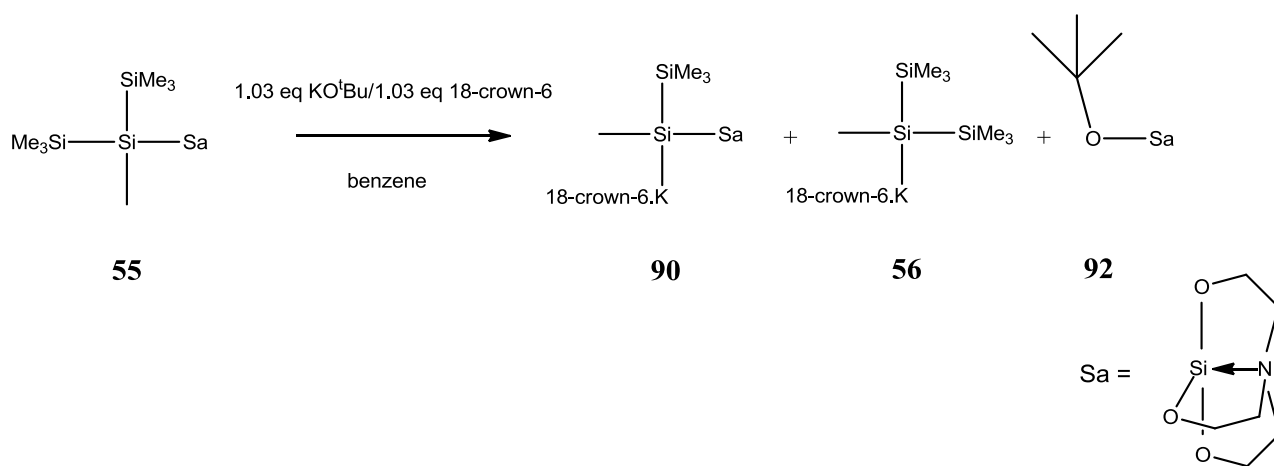


Figure 7-17. Crystal structure of trimethylsilylphenylsilatranyl silyl potassium.18-crown-6 (**87**)

Table 7-14. Selected bond lengths and angles of trimethylsilylphenylsilatranyl silyl potassium.18-crown-6 (**87**)

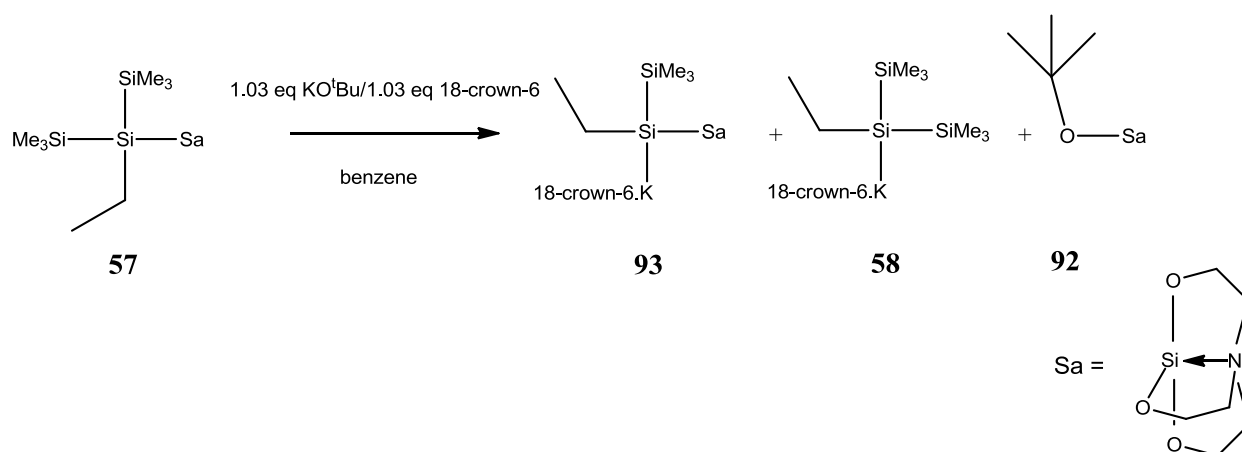
Bond Length	[Å]	Bond Angle	[°]
Si(1)-N(1)	3.103	O(7)-Si(3)-Si(1)	103.60(4)
Si(3)-O(7)	1.6716(12)	O(8)-Si(3)-Si(1)	113.62(5)
Si(3)-O(8)	1.6721(12)	O(9)-Si(3)-Si(1)	118.06(5)
Si(3)-O(9)	1.6642(12)	C(16)-N(1)-C(18)	120.35(14)
Si(1)-Si(3)	2.3087(7)	C(16)-N(1)-C(13)	119.81(14)
Si(1)-K(1)	3.5722(9)	C(18)-N(1)-C(13)	119.59(14)
K(1)-O(7)	2.9983(12)	Si(3)-Si(1)-K(1)	81.018(18)
		O(7)-Si(3)-O(8)	107.44(6)
		O(9)-Si(3)-O(8)	105.49(6)
		O(9)-Si(3)-O(7)	108.11(6)



Scheme 7-21. Reaction of bis(trimethylsilyl)methylsilatranyl silane (55), KO^tBu and 18-crown-6 in benzene for synthesis of trimethylsilylmethylsilatranyl.silyl.potassium.18-crown-6 (90)

7.3.5 Synthesis of trimethylsilylethylsilatranyl silyl potassium.18-crown-6 (93)

Synthesis of oligosilatranyl silyl potassium **93** was performed by reaction of oligosilanyl silatrane **57** with one equivalent of each KO^tBu and 18-crown-6 in benzene (Scheme 7-22). Similar to methylated substrate **55** also in this reaction the KO^tBu attack was not selectively at one trimethylsilyl group and attack also was observed at the silicon atom of the silatranyl unit. As a result the final product was a mixture of oligosilatranyl silyl potassium **93**, bis(trimethylsilyl)ethylsilyl potassium.18-crown-6 (**58**) and silatranyl ether **92**. In this case for the better sterically shielded ethylated oligosilanyl silatrane **57** the ratio between oligosilatranyl silyl potassium **93** and the silatranyl ether **92** was about 8:1.



Scheme 7-22. Reaction of bis(trimethylsilyl)ethylsilatranyl silane (57), KO^tBu and 18-crown-6 in benzene for synthesis of trimethylsilylmethylsilatranyl.silyl.potassium.18-crown-6 (93)

7.3.6 Synthesis of 2,5-disilatranyl-decamethylhexasilyl-2,5-dipotassium.18-crown-6 (96)

Synthesis of oligosilatranyl silyl potassium **96** was performed by reaction of oligosilanyl silatrane **77** with two equivalents of each KO^tBu and 18-crown-6 in benzene (Scheme 7-23). In this reaction the attack of the KO^tBu was selective at one trimethylsilyl group. According to NMR spectroscopic analysis reaction in THF proceeds in the initial step but finally a mixture of several unidentified compounds forms in the solution mixture.

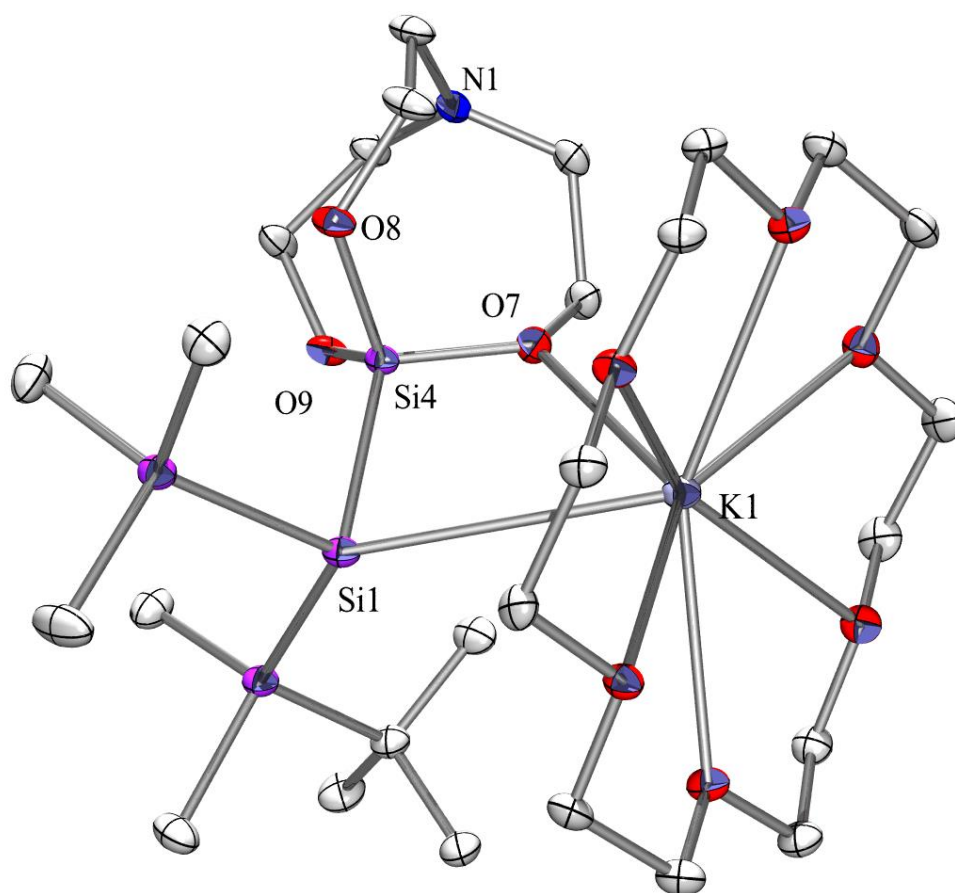
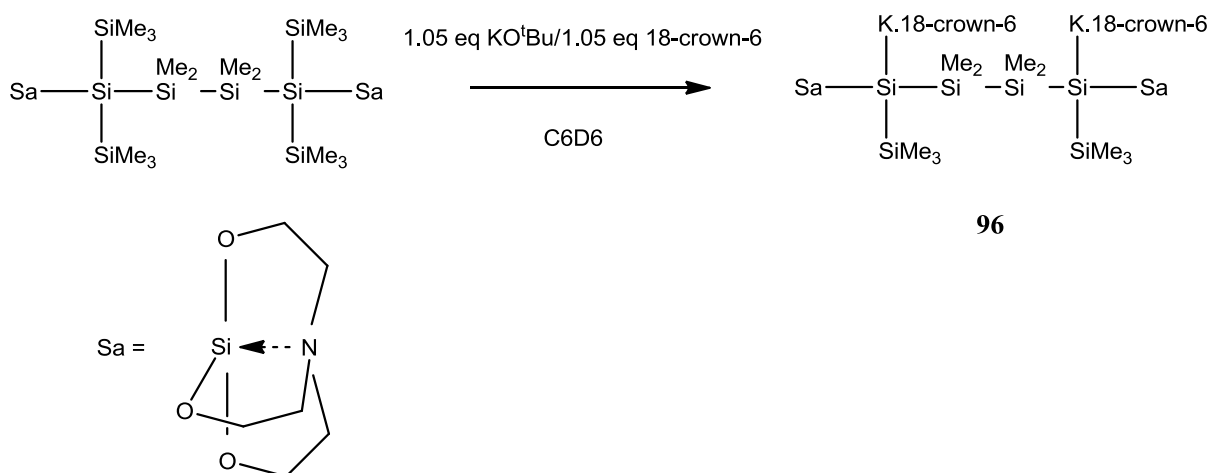


Figure 7-18. Crystal structure (*tert*-butyldimethylsilyl)(trimethylsilyl)silatranyl silyl potassium.18-crown-6 (**88**)

Table 7-15. Selected bond lengths and angles of (*tert*-butyldimethylsilyl)(trimethylsilyl)silatranyl silyl potassium.18-crown-6 (**88**)

Bond Length	[Å]	Bond Angle	[°]
Si(1)-N(1)	3.184	O(9)-Si(4)-Si(1)	118.44(8)
Si(4)-O(8)	1.656(2)	O(8)-Si(4)-Si(1)	112.19(9)
Si(4)-O(9)	1.660(2)	O(7)-Si(4)-Si(1)	108.55(9)
Si(4)-O(7)	1.670(2)	C(18)-N(1)-C(14)	119.8(3)
Si(1)-Si(4)	2.2947(12)	C(18)-N(1)-C(16)	119.3(3)
Si(1)-K(1)	3.6321(13)	C(14)-N(1)-C(16)	119.3(3)
K(1)-O(7)	2.936(2)	Si(4)-Si(1)-K(1)	77.72(4)
		O(8)-Si(4)-O(9)	105.61(12)
		O(8)-Si(4)-O(7)	106.14(12)
		O(9)-Si(4)-O(7)	105.07(11)

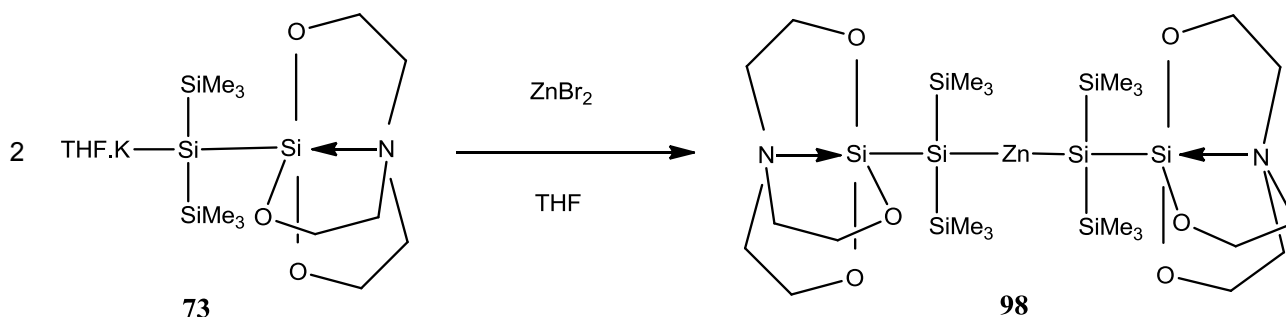


Scheme 7-23. Reaction of 2,4-disilatranyl-2,5-tris(trimethylsilyl)decamethylhexasilane (77), KO^tBu and 18-crown-6 in benzene for synthesis of 2,5-disilatranyl-decamethylhexasilyl-2,5-dipotassium.18-crown-6 (96)

7.4 Transmetalation reactions

7.4.1 Synthesis of bis[bis(trimethylsilyl)silatranyl]zinc (98)

Synthesis of oligosilatranylsilylzinc **98** was performed according to literature procedure¹²³ by reaction of two equivalent of oligosilatranylsilylpotassium **73** with one equivalent of ZnBr_2 (Scheme 7-24).



Scheme 7-24. Reaction of 2 equivalent of bis(trimethylsilyl)silatranyl.silyl.potassium (73) with ZnBr_2 for synthesis of bis[bis(trimethylsilyl)silatranyl]zinc (98)

Figure 7-19 shows the crystal structure and Table 7-16 the selected bond lengths of oligosilatranylsilylzinc **98**. This molecule crystallizes in the monoclinic space group C2/c .

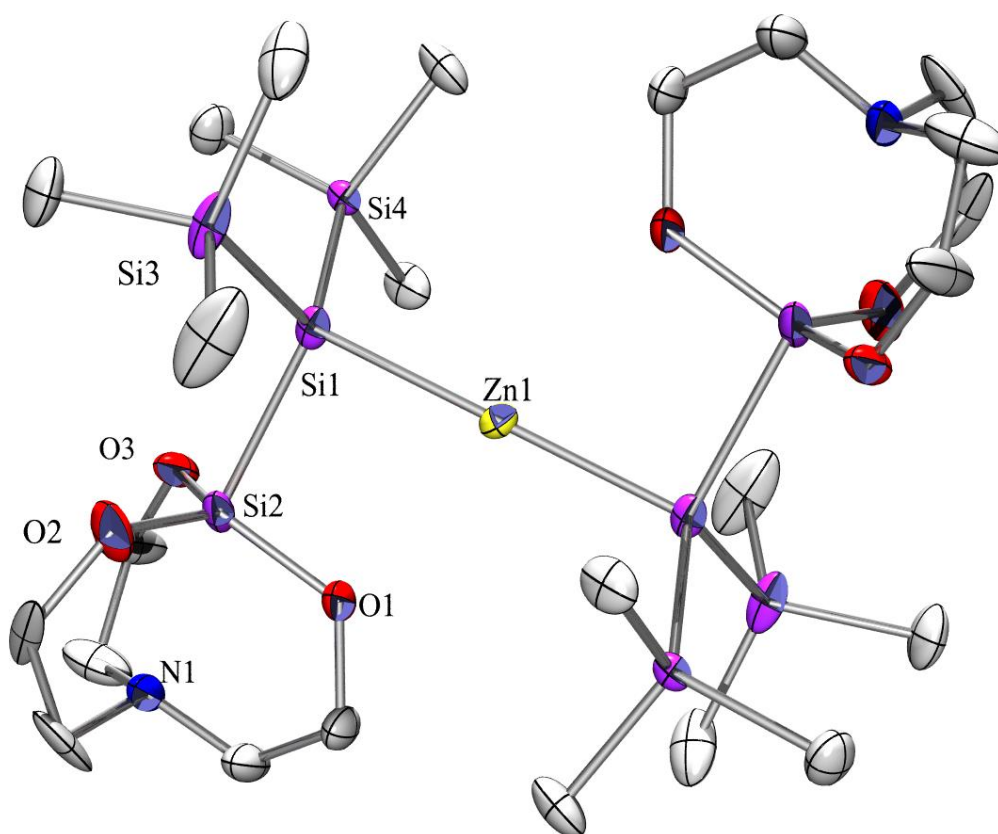


Figure 7-19. Crystal structure of bis[bis(trimethylsilyl)silatranylsilanyl]zinc (**98**)

7-16. Selected bond lengths and angles of bis[bis(trimethylsilyl)silatranylsilanyl]zinc (**98**)

Bond Length	[Å]	Bond Angle	[°]
Si(2)-N(1)	2.265(2)	O(2)-Si(2)-O(3)	117.03(19)
Si(2)-O(1)	1.679(3)	O(2)-Si(2)-O(1)	118.00(19)
Si(2)-O(2)	1.658(4)	O(3)-Si(2)-O(1)	117.4(2)
Si(2)-O(3)	1.664(3)	C(6)-N(1)-C(4)	115.0(5)
Si(1)-Si(2)	2.3489(18)	C(6)-N(1)-C(2)	101.9(5)
Zn(1)-Si(1)	2.3500(12)	C(4)-N(1)-C(2)	121.2(7)
		Si(1)-Zn(1)-Si(1)	180.0
		Si(2)-Si(1)-Zn(1)	97.18(5)

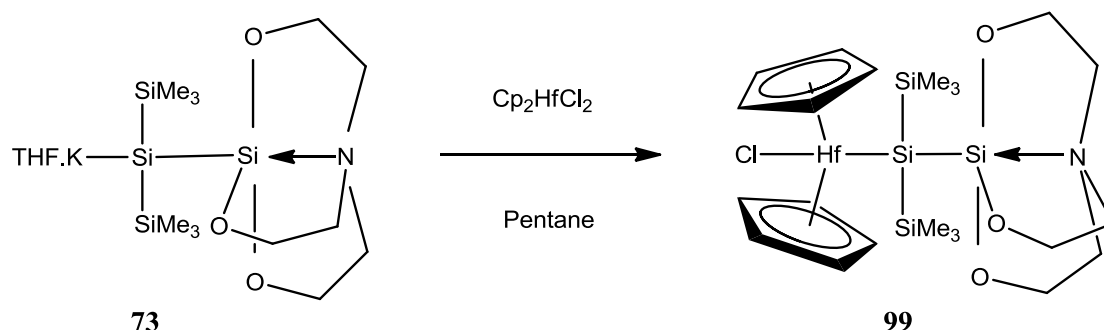
In contrast to oligosilatranylsilylpotassium compounds with potassium-oxygen coordination, oligosilatranylsilylzinc does not show any zinc-oxygen coordination.

Values for Si-Si-N axial bond with Si-N bond length of 2.265 Å and Si-SiO₃ bond length of 2.3489 Å in this molecule are so close to oligosilylsilatrane **44** with Si-N bond length of 2.292 Å and Si-SiO₃ bond length of 2.3509 Å than oligosilatranylsilylpotassium **73** with Si-N bond length of 3.134 Å and Si(1)-Si(2) bond length of 2.3080 Å. In fact no annihilation of Si-N interaction was observed for oligosilatranylsilylzinc **98**.

The Zn-Si distance of oligosilatranylsilylzinc **98** with 2.3500 Å is only slightly longer than Zn-Si distance of the structurally similar Zn[Si(SiMe₃)₃]₂ with 2.342 Å.¹²⁴

7.4.2 Synthesis of dicyclopentadienyl[bis(trimethylsilyl)silatranylsilyl]hafniumchloride (**99**)

Synthesis of light sensitive oligosilatranylsilylhafnium **99** was performed by reaction of one equivalent of oligosilatranylsilylpotassium **73** with one equivalent of hafnocene dichloride according to literature procedure¹²⁵ (Scheme 7-25). Orange crystals of the product were subjected to single crystal XRD analysis.



*Scheme 7-25. Reaction of one equivalent of bis(trimethylsilyl)silatranyl.silyl.potassium (**73**) with one equivalent of hafnocene dichloride for synthesis of dicyclopentadienyl[bis(trimethylsilyl)silatranylsilyl]hafniumchloride (**99**)*

Figure 7-20 shows the crystal structure and Table 7-17 the selected bond lengths of oligosilatranylsilylhafnium **99**. This molecule crystallizes in the monoclinic space group P2(1)/c.

In contrast to previously discussed oligosilatranylsilylpotassium compounds with potassium-oxygen coordination, oligosilatranylsilylhafnium does not show any hafnium-oxygen coordination.

Values for Si-Si-N axial bond with Si-N bond length of 2.347 Å and Si-SiO₃ bond length of 2.361 Å in this molecule are so close to oligosilylsilatrane **44** with Si-N bond length of 2.292 Å and Si-SiO₃ bond length of 2.3509 Å than oligosilatranylsilylpotassium **73** with Si-N bond length of 3.134 Å and Si(1)-Si(2) bond length of 2.3080 Å. In fact similar to oligosilatranylsilylzinc **98** no annihilation of Si-N interaction was observed for oligosilatranylsilylhafnium **99**.

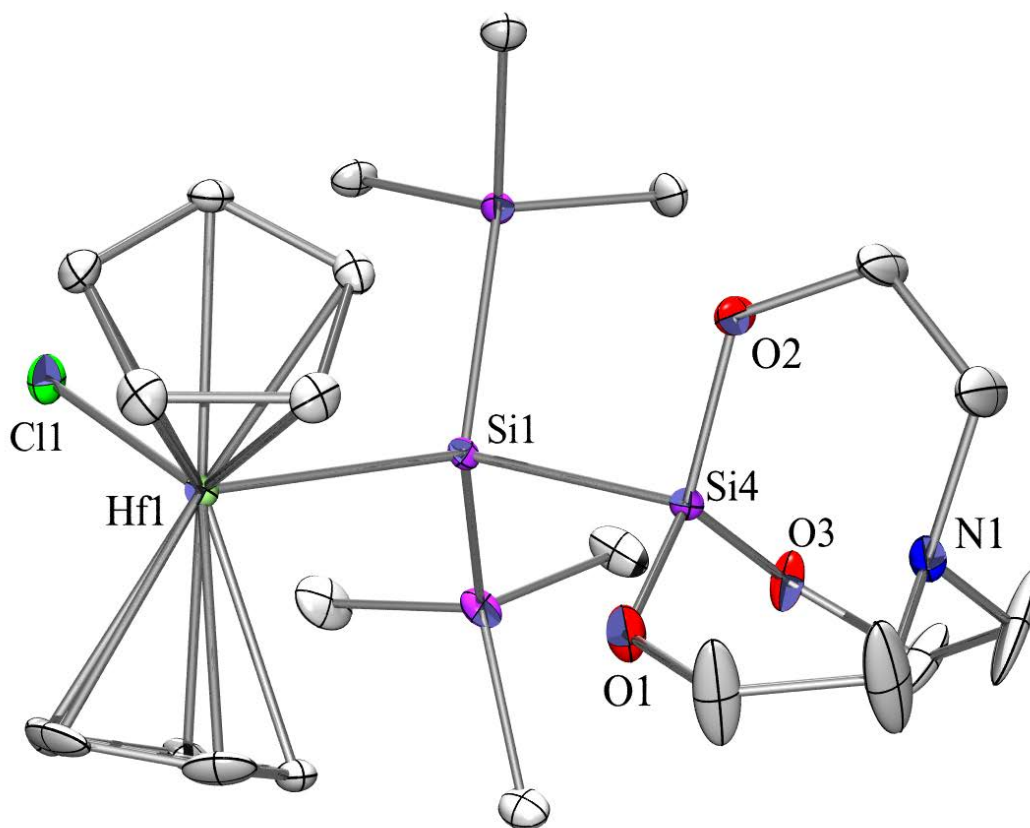


Figure 7-20. Crystal structure of dicyclopentadienyl[bis(trimethylsilyl)silatranyl]hafniumchloride (**99**)

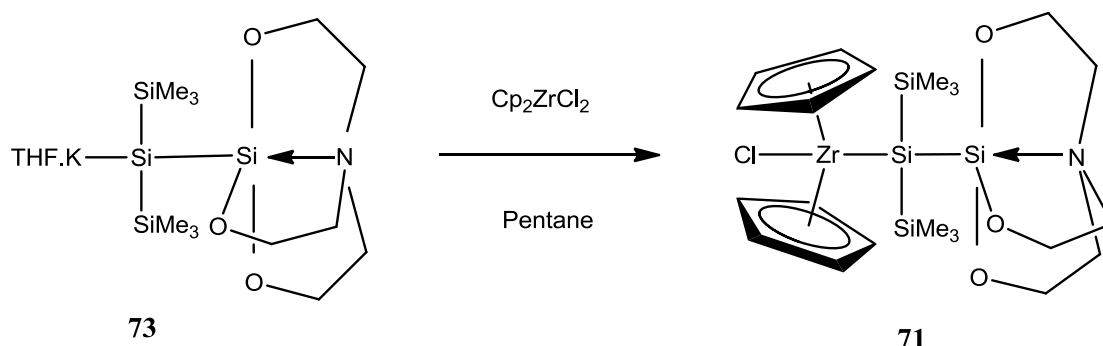
Table 7-17. Selected bond lengths and angles of dicyclopentadienyl[bis(trimethylsilyl)silatranyl]hafniumchloride (**99**)

Bond Length	[Å]	Bond Angle	[°]
Si(4)-N(1)	2.347	O(3)-Si(4)-O(1)	116.7(2)
Si(4)-O(3)	1.659(4)	O(3)-Si(4)-O(2)	116.5(2)
Si(4)-O(1)	1.662(4)	O(1)-Si(4)-O(2)	115.8(2)
Si(4)-O(2)	1.665(4)	C(22)-N(1)-C(18)	114.9(8)
Si(1)-Si(4)	2.361(2)	C(22)-N(1)-C(20)	114.6(7)
Hf(1)-Si(1)	2.7774(14)	C(18)-N(1)-C(20)	115.2(8)
Hf(1)-Cl(1)	2.4114(15)	Si(4)-Si(1)-Hf(1)	111.91(6)

Several compounds containing zirconocene unit have been studied previously in detail among which $\text{CpCp}^*\text{Hf}[\text{Si}(\text{SiMe}_3)_3]\text{Cl}$ ¹²⁶ (**100**) and $\text{Cp}_2\text{Hf}[\text{Si}(\text{SiMe}_3)_3]_2\text{Cl}$ ¹²⁷ (**101**) have structural similarities with oligosilatranyl silylhafnium **99**. The Si-Hf distance in oligosilatranyl silylhafnium **99** with 2.7774 Å is slightly shorter than Si-Hf distance in **100** and **101** with 2.881 Å and 2.850 Å, respectively. Elongated Si-Hf bond length in compound **100** and **101** is related to the presence of the bulky Cp* or two bulky Si(SiMe₃)₃ groups, respectively.

7.4.3 Synthesis of dicyclopentadienyl[bis(trimethylsilyl)silatranyl silyl]zirconium chloride (**71**)

Synthesis of light sensitive oligosilatranyl silyl zirconium **71** was performed by reaction of one equivalent of oligosilatranyl silyl potassium **73** with one equivalent of zirconocene dichloride according to literature procedure¹²⁵ (Scheme 7-26). Red crystals of the product were subjected to single crystal XRD analysis. However due to crystal defects it was not possible to solve the crystal structure in detail but no interaction between zirconium with oxygens of silatranyl group was observed.



*Scheme 7-26. Reaction of one equivalent of bis(trimethylsilyl)silatranyl silyl potassium (**73**) with one equivalent of zirconocene dichloride for synthesis of dicyclopentadienyl[bis(trimethylsilyl)silatranyl silyl]zirconium chloride (**71**)*

7.5 Conclusion

Synthesis of oligosilanyl silatranes was performed by reaction of different silatranes having different leaving groups (X= Cl, Br, CF₃SO₂) with silanyl anion. It is found that the reaction with CF₃SO₂ is the cleanest one with the highest yield. In another approach, the silicon atom of the silatrane was first introduced into the polysilane structure and afterwards the triethanolamine unit was added to the silicon atom of the silatrane. However the yield of the second method was one third of the first method.

Single crystal XRD analysis revealed that axial three-center four-electron Si-Si-N bond in oligosilanyl silatranes is in accordance with Gordon rule⁶⁷ and any change in polysilane part and subsequently Si-Si bond length, can directly affect Si-N bond length.

Synthesis of silanide from obtained oligosilanylsilatrane by reaction with potassium *tert*-butoxide was feasible. Formation of potassium silanides paved the way for further synthesis of oligosilanylsilatrane with long silicon chain or silicon ring suitable for UV-vis study.

It is found that formation of potassium silanide occurred by trimethylsilyl group cleavage switches off the Si-N interaction. The same Si-N interaction switch off, was also observed by protonation of the nitrogen atom of silatranyl group with acids such as trichloroacetic acid or trifluoromethanesulfonic acid.

Transmetallation reaction of oligosilanylsilylpotassium compounds was successfully performed in the presence of transition metal halides but in contrast to potassium silanides with K-O coordination no interaction between transition metal-oxygen was observed.

Multinuclear NMR spectroscopy was used to study the new synthesized oligosilanylsilatrane. It is found that the Si-N interaction or annihilation is recognizable mostly by ^{29}Si NMR spectroscopy. Annihilation of Si-N interaction shifts the ^{29}Si NMR signal of silatranyl silicon atom to down field by magnitude of approximately 40 ppm.

Chapter 8

Synthesis of oligosilanylsilatranes with other types of ligands

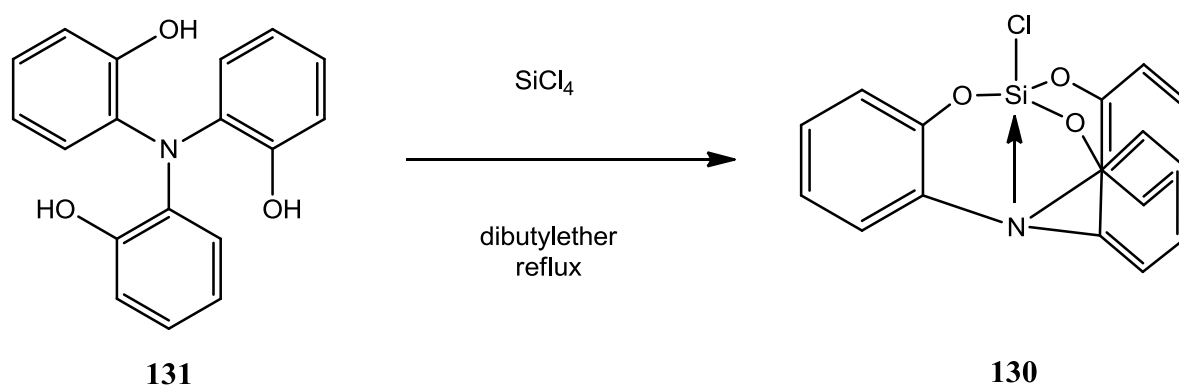
8 Oligosilanylsilatrane with other types of ligands

8.1 Synthesis of primary silatrane units

According to previous experiments in chapter 7 it is found that for the attachment of the silatrane unit to polysilane the best way is to react a silatrane with a suitable leaving group with silanyl anion. Due to that initially the silatrane unites with chloride leaving group were synthesized and then they were reacted with silanyl anions.

8.1.1 Synthesis of aminotris(phenyl-2'-oxy)silylchloride (**130**)

Tris(2-hydroxyphenyl)amine (**131**) and chlorosilatrane **130** were prepared following the procedure reported by Frye et al.⁷⁰ (Scheme 8-1).



*Scheme 8-1. Synthesis of aminotris(phenyl-2'-oxy)silylchloride (**130**) from the reaction of tris(2-hydroxyphenyl)amine (**131**) with SiCl_4 in reflux condition*

Figure 8-1 shows the crystal structure and Table 8-1 the selected bond lengths of chlorosilatrane **130**. This molecule crystallizes in the monoclinic space group $P 2(1)/n$.

Although the structure of chlorosilatrane **130** due to presence of phenyl groups is not flexible as the structure of silatrane with alkylamine, the Si-N bond length in chlorosilatrane **130** with 2.2125 Å is shorter than the Si-N bond of 1-chlorosilatrane (**40**) with 2.579 Å¹²⁸. This in fact shows to some extent the mobility of Si-N bond even in presence of three phenyl groups in the structure of the silatrane. Another difference between the structure of 1-chlorosilatrane (**40**) and chlorosilatrane **130** is the Si-Cl bond length. Si-Cl Bond length in chlorosilatrane **130** is 2.0707 Å which is shorter than Si-Cl bond in 1-chlorosilatrane (**40**) with 2.12 Å.⁸¹ Also in chlorosilatrane **130** three Si-O bonds with 1.65 Å length are shorter than three Si-O bonds in 1-chlorosilatrane (**40**) with 1.76 Å.

Although chlorosilatrane **130** has a symmetry axis along Si-N bond, the three $\text{O}(x)\text{-Si}(1)\text{-O}(x')$ angles are not equal.

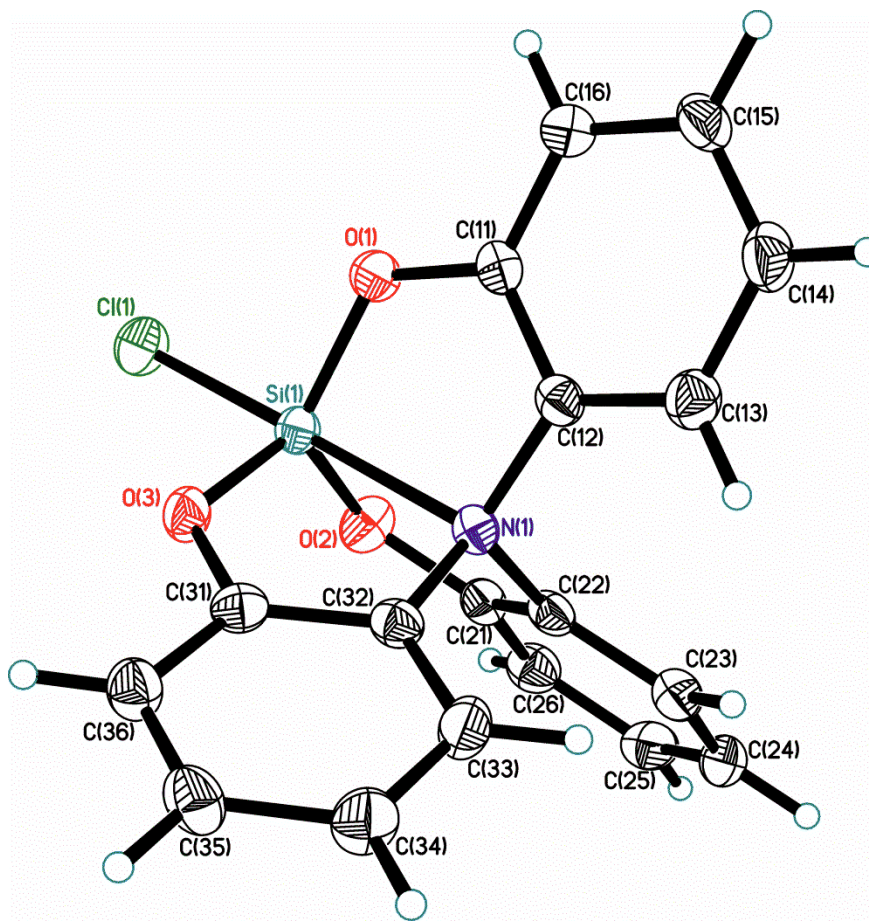


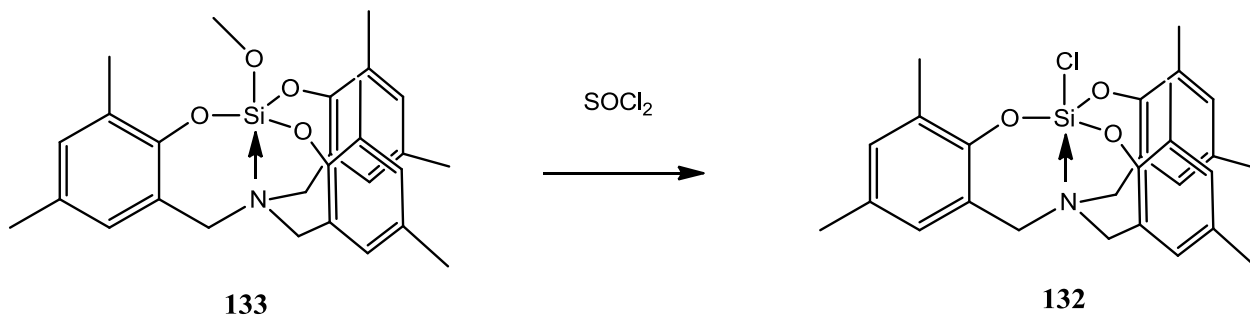
Figure 8-1. Crystal structure of aminotris(phenyl-2'-oxy)silylchloride (**130**)

Table 8-1 Selected bond lengths and angles of aminotris(phenyl-2'-oxy)silylchloride (**130**)

Bond Length	[Å]	Bond Angle	[°]
Si(1)-N(1)	2.2125(17)	O(3)-Si(1)-O(2)	117.74(9)
Si(1)-O(3)	1.6514(16)	O(3)-Si(1)-O(1)	119.18(9)
Si(1)-O(1)	1.6526(17)	O(1)-Si(1)-O(2)	119.23(9)
Si(1)-O(2)	1.6544(17)	C(12)-N(1)-C(32)	115.62(17)
Si(1)-Cl(1)	2.0707(8)	C(12)-N(1)-C(22)	114.49(17)
		C(32)-N(1)-C(22)	114.27(17)

8.1.2 Synthesis of aminotris(-3',5'-dimethylbenzyl-2'-oxy)silylchloride (**132**)

Synthesis of aminotris(-3',5'-dimethylbenzyl-2'-oxy)silylmethoxide (**133**) was performed according to literature procedure reported by Chandrasekaran et al.⁷¹ Following the procedure reported by Szpakolski et al.¹²⁹, methoxysilatrane **133** was reacted with excess thionylchloride under nitrogen for 18 hours to obtain chlorosilatrane **132** (Scheme 8-2).



*Scheme 8-2. Synthesis of aminotris(-3',5'-dimethylbenzyl-2'-oxy)silylchloride (**132**) by reaction of aminotris(-3',5'-dimethylbenzyl-2'-oxy)silylmethoxide (**133**) with thionylchloride*

Due to sensitivity of chlorosilatrane **132** to moisture during the crystallization in chloroform the hydrochloride derivative **134** of the ligand was formed (Figure 8-2).

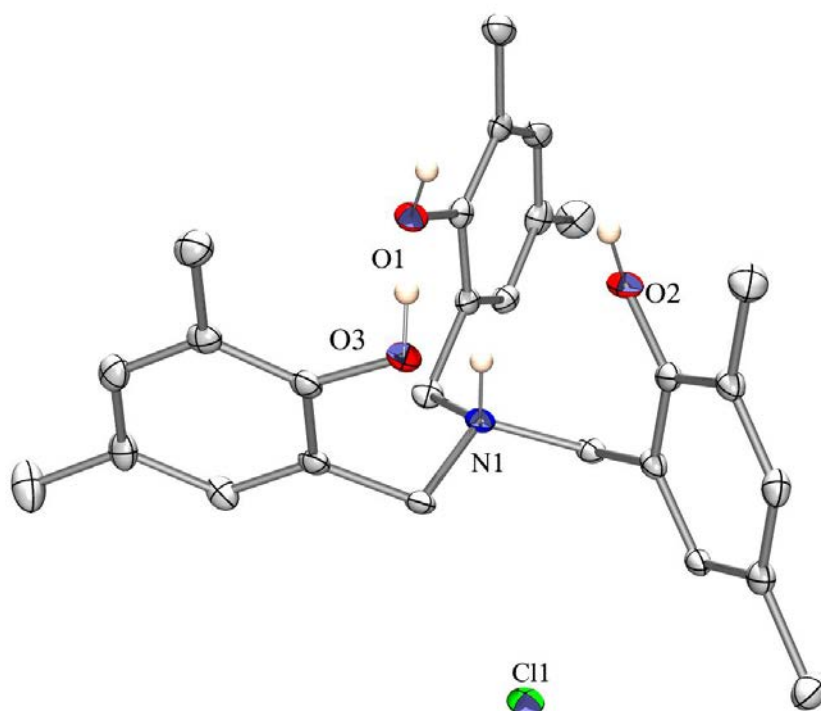


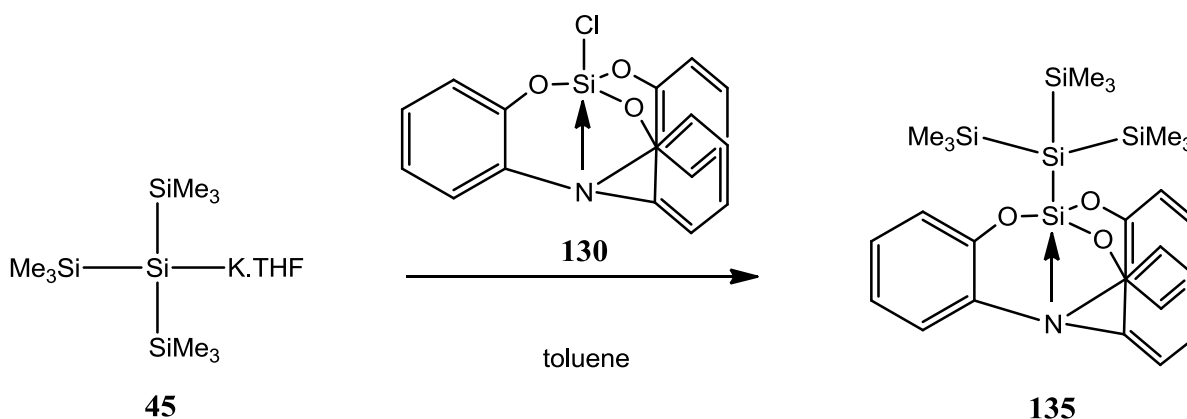
Figure 8-2. Crystal structure of tris(2-hydroxy-4,6-dimethylbenzyl)amine hydrochloride (**134**)

8.2 Synthesis of oligosilanylsilatrane

8.2.1 Synthesis of 1,1,1-aminotris(phenyl-2'-oxy)-2,2-bis(trimethylsilyl)trimethyltrisilane (135)

Oligosilanylsilatrane **135** was prepared by reaction of oligosilylpotassium **45** with chlorosilatrane **130** (Scheme 8-3).

Although the Si-Cl bond in chlorosilatrane **130** is shorter than 1-chlorosilatrane (**40**), it is more reactive. NMR spectroscopy only showed formation of oligosilanylsilatrane **135** without formation of any silicon hydride **48**. In contrast the reaction of oligosilylpotassium **45** with 1-chlorosilatrane was not clean (section 7-2-1) due to low reactivity of 1-chlorosilatrane (**40**) related to its unusual structural geometry.⁸² One of the differences between 1-chlorosilatrane (**40**) and chlorosilatrane **130** which could explain the higher reactivity of chlorosilatrane **130** over 1-chlorosilatrane (**40**) is the shorter Si-O distances in chlorosilatrane **130** which increases the accessibility of the silicon atom for nucleophilic attack in S_N2 reactions.



Scheme 8-3. Synthesis of 1,1,1-aminotris(phenyl-2'-oxy)-2,2-bis(trimethylsilyl)trimethyltrisilane (**135**) by reaction of oligosilylpotassium **45** with aminotris(phenyl-2'-oxy)silylchloride (**130**)

Figure 8-3 shows the crystal structure and Table 8-2 the selected bond lengths of oligosilanylsilatrane **135**. According to the crystallographic data two molecules of oligosilanylsilatrane **135** are in the asymmetric unit in the monoclinic space group C2/c. Due to this fact two different bond lengths are observed for this structure according to Table 9-2.

Si-N distance increases from 2.2125 Å in chlorosilatrane **130** to 2.455 Å and 2.509 Å in oligosilanylsilatrane **135** which shows the flexibility of the silatrane cage and mobility of nitrogen atom even in presence of three rigid phenyl groups.

In comparison to oligosilanylsilatrane **44** with alkylamine ligand and with Si-N bond length of 2.292 Å, the Si-N bond length increases to 2.455 Å and 2.509 Å in oligosilanylsilatrane **135**. In reverse Si-SiO₃ bond length decreases from 2.3509 Å in oligosilanylsilatrane **44** to 2.3096 Å and 2.3245 Å in oligosilanylsilatrane **135**. This fact could be explained by electron withdrawal character of phenyl groups. Unequal values of three O(x)-Si(1)-O(x') angles in spite of symmetry in the structure along Si-SiO₃ bond is due to torsion in silatranyl group which is created by three rigid phenyl groups.

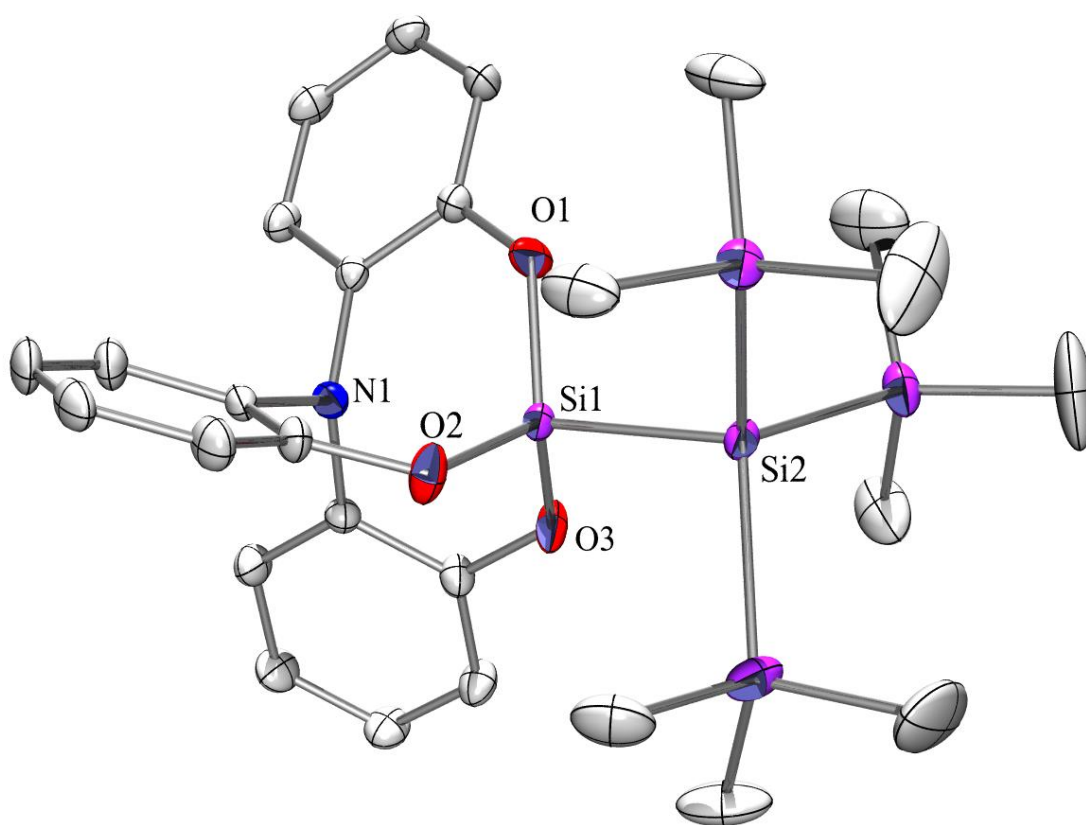


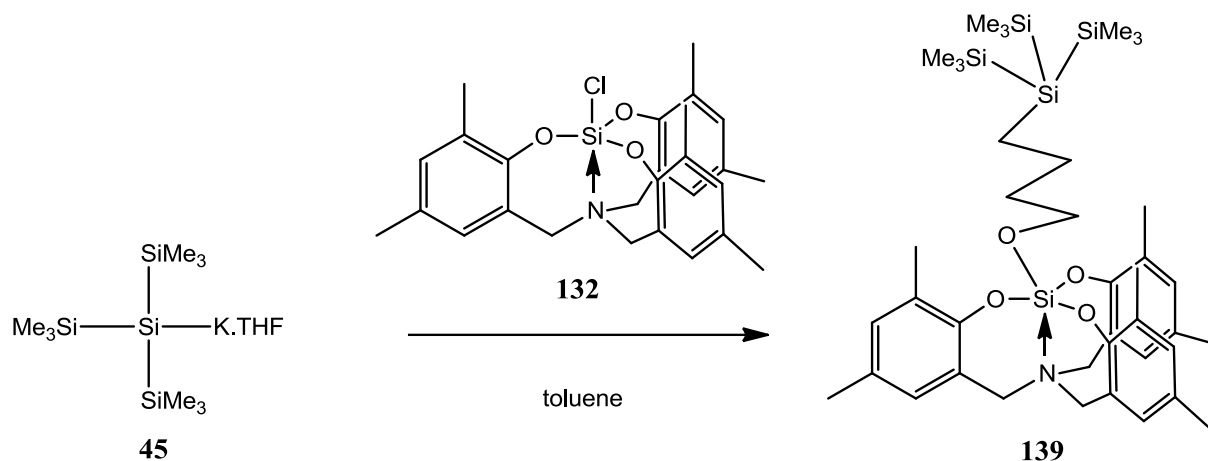
Figure 8-3. Crystal structure of 1,1,1-aminotris(phenyl-2'-oxy)-2,2-bis(trimethylsilyl)trimethyltrisilane (**135**)

Table 8-2. Selected bond lengths and angles of 1,1,1-aminotris(phenyl-2'-oxy)-2,2-bis(trimethylsilyl)trimethyltrisilane (**135**)

Bond Length	[Å]	Bond Angle	[°]
Si(1)-N(1)	2.455	O(3)-Si(1)-O(1)	115.53(10)
Si(1)-N(1)	2.509	O(3)-Si(1)-O(2)	113.71(10)
Si(1)-O(1)	1.6500(17)	O(1)-Si(1)-O(2)	114.48(10)
Si(1)-O(2)	1.6583(17)	C(6)-N(1)-C(14)	118.21(17)
Si(1)-O(3)	1.6487(16)	C(6)-N(1)-C(8)	116.38(16)
Si(1)-Si(2)	2.3096(9)	C(14)-N(1)-C(8)	119.11(17)
Si(6)-Si(7)	2.3245(9)		

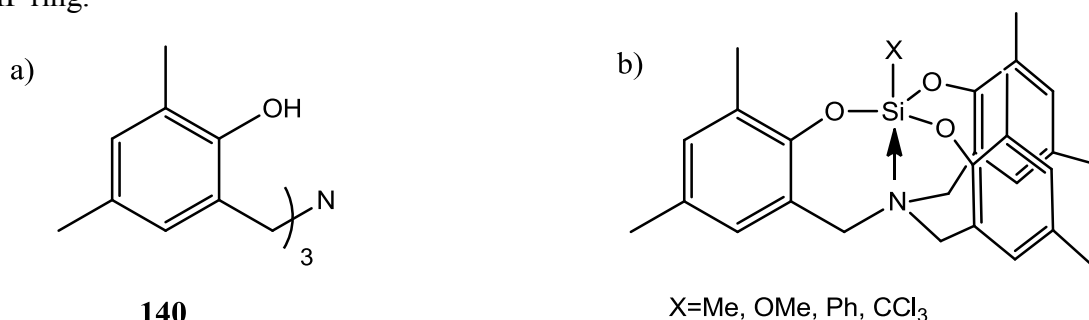
8.2.2 Synthesis of 1,1,1-aminotris(-3',5'-dimethylbenzyl-2'-oxy)-(4''-tris(trimethylsilyl)silyl)butanyloxysilane (139)

Oligosilanylsilatrane **139** was prepared by reaction of oligosilylpotassium **45** with chlorosilatrane **132** (Scheme 8-4). According to crystal structure of oligosilanylsilatrane **139** in Figure 8-4 a THF ring opening occurs and the oxygen atom of the THF reacts with the hypervalent silicon atom and the carbon atom of the THF reacts with the silylation of **45**.



Scheme 8-4. Synthesis of 1,1,1-aminotris(-3',5'-dimethylbenzyl-2'-oxy)-(4''-tris(trimethylsilyl)silyl)butanyloxysilane (**139**) by reaction of oligosilylpotassium **45** with aminotris(-3',5'-dimethylbenzyl-2'-oxy)silylchloride (**132**)

Two possible explanations exist for THF ring opening and formation of oligosilanylsilatrane **139**. The first one is due to presence of a trace amount of thionylchloride derived from the synthesis of chlorosilatrane **132**. The sulfur atom of the thionylchloride has a vacant *d* orbital and act as a Lewis acid. The second explanation relates to the acidic nature of chlorosilatrane **132**. Holmes and co-workers have reported a new class of silatranes with a tris(2-hydroxy-4,6-dimethylbenzyl)amine (**140**) ligand (Scheme 8-5).⁷¹ Depending on the increase in electron withdrawing capability of the X atom or group (Scheme 8-5b) an upfield shift in ²⁹Si NMR occurs indicating the more acidic character of the silatrane.⁷² X= methyl with ²⁹Si NMR shift of -74.5 is the least acidic and X= CCl₃ with ²⁹Si NMR shift of -140.8 is the most acidic group.⁷¹ Chlorosilatrane **132** with ²⁹Si NMR shift of -124.5 can act as an acidic compound and opens the THF ring.



Scheme 8-5 a) Tris(2-hydroxy-4,6-dimethylbenzyl)amine (**140**) ligand. b) silatrane with different groups in X position

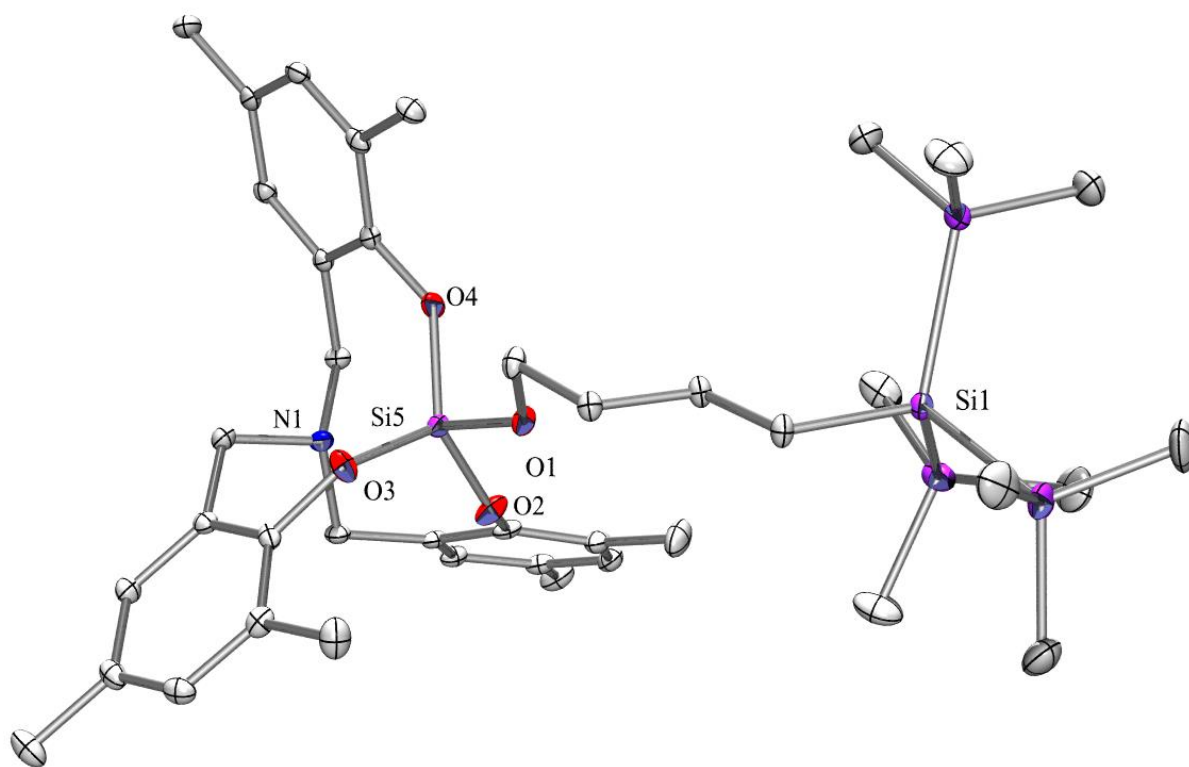


Figure 8-4. Crystal structure of $N[CH_2(Me_2C_6H_2)O]_3SiOCH_2CH_2CH_2CH_2Si(SiMe_3)_3$ (**139**)

Table 8-3. Selected bond lengths and angles of $N[CH_2(Me_2C_6H_2)O]_3SiOCH_2CH_2CH_2CH_2Si(SiMe_3)_3$ (**139**)

Bond Length	[Å]	Bond Angle	[°]
Si(5)-N(1)	2.529	O(2)-Si(5)-O(3)	116.16(17)
Si(5)-O(2)	1.625(3)	O(2)-Si(5)-O(4)	122.72(17)
Si(5)-O(3)	1.633(3)	O(3)-Si(5)-O(4)	113.78(16)
Si(5)-O(4)	1.635(3)	C(30)-N(1)-C(20)	109.1(3)
Si(5)-O(1)	1.645(3)	C(30)-N(1)-C(39)	110.5(3)
Si(1)-C(11)	1.909(4)	C(20)-N(1)-C(39)	110.0(3)

Bond Length	[Å]	Bond Angle	[°]
Si(10)-N(2)	2.719	O(8)-Si(10)-O(6)	116.72(16)
Si(10)-O(6)	1.628(3)	O(8)-Si(10)-O(7)	117.33(16)
Si(10)-O(7)	1.634(3)	O(6)-Si(10)-O(7)	111.69(15)
Si(10)-O(8)	1.622(3)	C(69)-N(2)-C(63)	111.8(3)
Si(10)-O(5)	1.622(3)	C(69)-N(2)-C(81)	110.8(3)
Si(6)-C(50)	1.909(5)	C(63)-N(2)-C(81)	110.9(3)

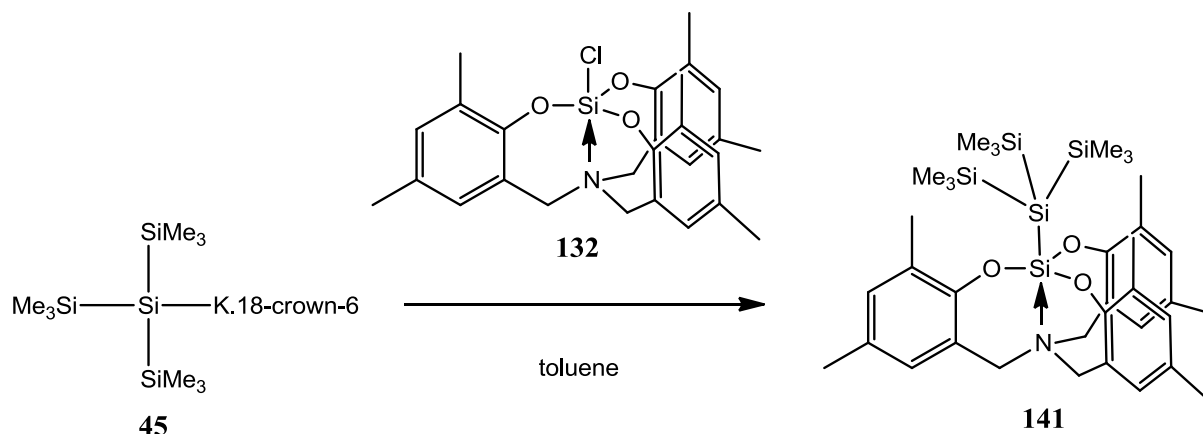
Figure 8-4 shows the crystal structure and Table 8-3 the selected bond lengths and angles of oligosilanylsilatrane **139**. According to the crystallographic data two molecules of oligosilanylsilatrane **139** are in the asymmetric unit in the triclinic space group P-1.

For Si-N bond with 2.529 Å and 2.719 Å length, O-SiO₃ bond is 1.645 Å and 1.622 Å respectively which means that the structure with shorter Si-N bond has longer O-SiO₃ bond and in reverse structure with longer Si-N bond has shorter O-SiO₃ bond. This in fact is in accordance with Gordon rule.⁶⁷

Unequal values of three O(x)-Si(5)-O(x') angles with close to 10° difference is mainly caused by the hydrocarbon chain of THF which is between silatranyl and (Me₃Si)₃Si- groups. In contrast to three unequal O(x)-Si(5)-O(x'), three C(x)-N(1)-C(x') angles are very close to each other. Although the O(x)-Si(5)-O(x') are under steric force, the torsion does not transfer to the three C(x)-N(1)-C(x') angles due to flexibility of silatranyl ligand.

8.2.3 Synthesis of 1,1,1-aminotris(-3',5'-dimethylbenzyl-2'-oxy)-2,2-bis(trimethylsilyl)trimethyltrisilane (**141**)

Oligosilanylsilatrane **141** was prepared by reaction of tris(trimethylsilyl)silylpotassium.18-crown-6 (**45**) with chlorosilatrane **132** (Scheme 8-6). In fact due to THF ring opening in previous reaction, oligosilylpotassium **45** was prepared in toluene in presence of 18-crown-6.



*Scheme 8-6. Synthesis of 1,1,1-aminotris(-3',5'-dimethylbenzyl-2'-oxy)-2,2-bis(trimethylsilyl)trimethyltrisilane (**141**) by reaction of tris(trimethylsilyl)silylpotassium.18-crown-6 (**45**) with aminotris(-3',5'-dimethylbenzyl-2'-oxy)silylchloride (**132**)*

Figure 8-5 shows the crystal structure and Table 8-4 the selected bond lengths and angles of oligosilanylsilatrane **141**. This molecule crystallizes in the hexagonal space group P-3c1.

Due to presence of a symmetry axis along the N-Si-Si bond three O(x)-Si(1)-O(x') angles as well as three C(x)-N(1)-C(x') angles are equal to each other. However the oligosilanylsilatrane **44** with trialkylamine ligand or oligosilanylsilatrane **135** with triphenylamine ligand are symmetric molecules but a symmetric crystal structure was not observed in their case.

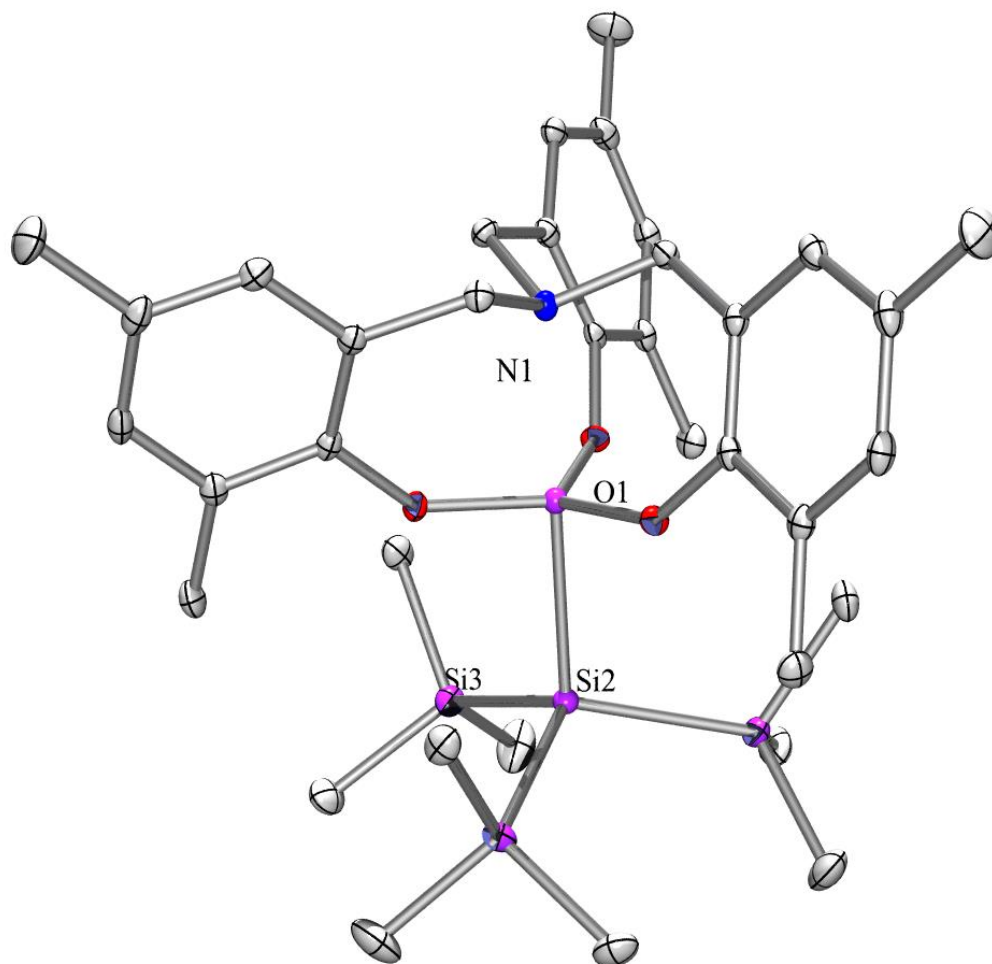


Figure 8-5. Crystal structure of 1,1,1-aminotris(-3',5'-dimethylbenzyl-2'-oxy)-2,2-bis(trimethylsilyl)trimethyltrisilane (**141**)

Table 8-4. Selected bond lengths and angles of 1,1,1-aminotris(-3',5'-dimethylbenzyl-2'-oxy)-2,2-bis(trimethylsilyl)trimethyltrisilane (**141**)

Bond Length	[Å]	Bond Angle	[°]
Si(1)-N(1)	2.237(4)	O(1)-Si(1)-O(1)	119.20(2)
Si(1)-O(3)	1.6669(18)	C(9)-N(1)-C(9)	109.11(17)
Si(1)-Si(2)	2.3770(17)		
Si(2)-Si(3)	2.3818(9)		

Although the Si-N bond of oligosilanylsilatrane **141** with 2.237 Å is slightly shorter than Si-N bond of oligosilanylsilatrane **135** with 2.455 Å and 2.509 Å, Si-SiO₃ bond with 2.3770 Å is highly longer than Si-SiO₃ bond of oligosilanylsilatrane **135** with 2.3096 Å and 2.3245 Å. It worth to mention that such a long Si-SiO₃ bond was only observed in oligosilanylsilatrane **60** with one phenyl group instead of trimethylsilyl group with 2.383 Å. Shorter Si-N and longer Si-SiO₃ bonds in oligosilanylsilatrane **141** in comparison to oligosilanylsilatrane **135** could be due to the following reasons. Less likely higher flexibility of silatranyl cage and more likely presence of electron donating groups like methyl in the silatranyl cage of oligosilanylsilatrane **141** in comparison to oligosilanylsilatrane **135** which reduces the electron withdrawing effect of the phenyl groups.

8.3 Conclusion

Synthesis of oligosilanylsilatrane with ligands containing aromatic rings instead of alkylamine ligands was studied. Synthesis was based on reaction of silatrane having a chloride as a leaving group with silanyl anion.

In chapter 7 it is found that reaction of 1-chlorosilatrane (**40**) with silanyl anion was not clean due to unreactivity of 1-chlorosilatrane (**40**) related to its unusual structural geometry.⁸² In contrast high reactivity and clean reaction of silatrane containing aromatic ligand and chloride living group with silanyl anions was observed.

Single crystal XRD analysis showed that Si-N distance in silatrane with aromatic ring varies similar to Si-N distance in silatrane with alkylamine ligand relating to the substituents on hypervalent silicon atom which means that silatrane with rigid aromatic rings still show some level of flexibility.

THF ring opening and insertion of opened THF ring between hypervalent silicon atom of silatrane and (Me₃Si)₃Si- group was observed during the reaction between chlorosilatrane **132** and silanyl anion coordinated THF. THF ring opening can occur because of two different reasons: First presence of trace amount of thionylchloride alongside chlorosilatrane **132**, or due to intrinsic acidity of chlorosilatrane **132**.

Chapter 9

Oligosilanylsilocanes

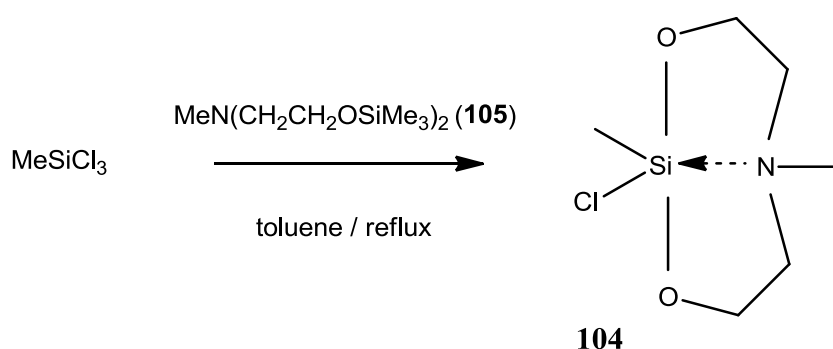
9 Oligosilanylsilocanes

9.1 Synthesis of primary silocane unites

According to previous experiments in chapter 7 it is found that for the attachment of the silatrane unit to polysilane the best way is to react a silatrane with a suitable leaving group with silanyl anion. Due to that initially the silocane unites with chloride leaving group were synthesized and then they were reacted with silanyl and germanyl anions.

9.1.1 Synthesis of $\text{MeN}(\text{CH}_2\text{CH}_2\text{O})_2\text{SiMeCl}$ (**104**)

Similar to reaction of $\text{N}(\text{CH}_2\text{CH}_2\text{OSiMe}_3)_3$ (**39**) with SiCl_4 reported by Voronkov and co-workers,⁷⁸ $\text{MeN}(\text{CH}_2\text{CH}_2\text{OSiMe}_3)_2$ (**105**) was reacted with MeSiCl_3 to synthesize chlorosilocane **104** under reflux (Scheme 9-1).



*Scheme 9-1. Synthesis of $\text{MeN}(\text{CH}_2\text{CH}_2\text{O})_2\text{SiMeCl}$ (**104**) by reaction of MeSiCl_3 and $\text{MeN}(\text{CH}_2\text{CH}_2\text{OSiMe}_3)_2$ (**105**) under reflux condition*

Figure 9-1 shows the crystal structure and Table 9-1 the selected bond lengths of chlorosilocane **104**. This molecule crystallizes in the monoclinic space group $\text{P2}(1)/n$.

Si-Cl bond in chlorosilocane **104** with length of 2.23 Å is slightly longer than Si-Cl bond in 1-chlorosilatrane (**40**) with 2.12 Å⁸¹. Due to presence of an electronegative atom like chloride the Si-N bond length shortens to 2.1168 Å.

In contrast to unusual geometry of 1-chlorosilatrane (**40**) that hinders the backside attack in $\text{S}_{\text{N}}2$ type reactions; in chlorosilocane **104** more reactivity is expected due to presence of more free space around the silicon atom which facilitates reactions based on $\text{S}_{\text{N}}2$ mechanism. Longer Si-Cl bond in comparison to 1-chlorosilatrane (**40**) could be also effective.

9.1.2 Synthesis of $(\text{MeO})_2\text{Si}(\text{OCH}_2\text{CH}_2)_2\text{NMe}$ (**106**)

Transesterification of alkoxy silane and alkylalcohols in the presence of a base has been reported previously.⁶⁶ In a similar reaction, $\text{Si}(\text{OMe})_4$ was reacted with N -methyl diethanolamine in presence of tetraethylammonium fluoride hydride as a strong base to synthesize dimethoxysilocane **106** (Scheme 9-2).

Depending on type of solvent ammonium fluoride can generate F^- or $[\text{OH}]^-$. Manning and co-workers reported formation of F^- in THF and CH_2Cl_2 while formation of $[\text{OH}]^-$ in acetonitrile in presence of traces amount of water.¹³⁰

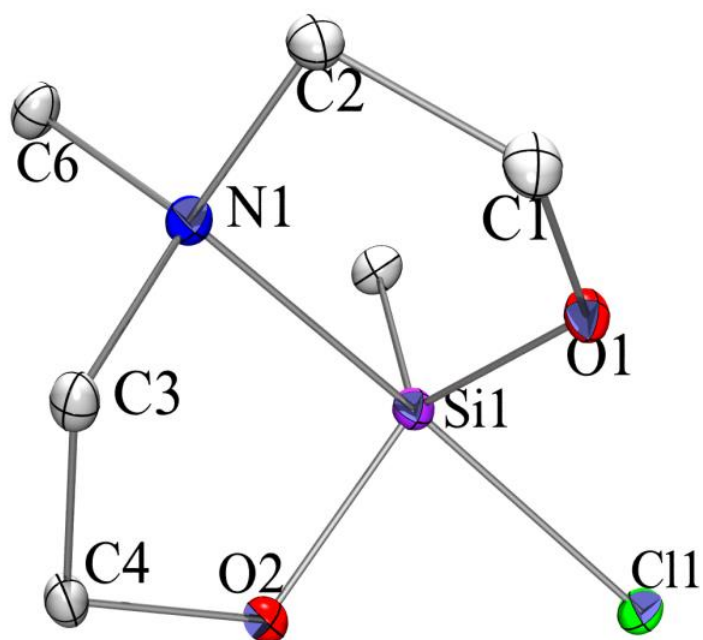
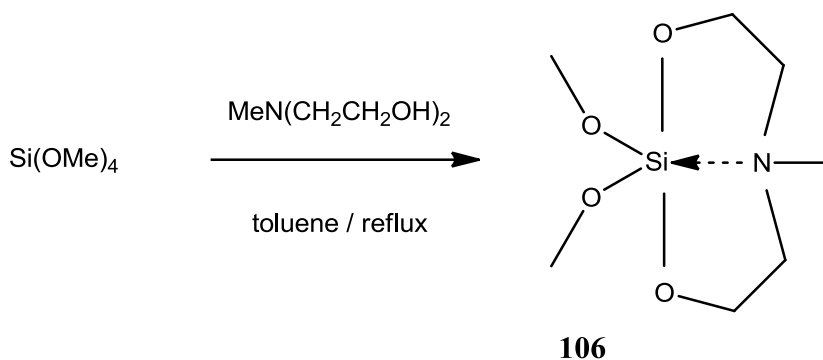


Figure 9-1. Crystal structure of MeClSi(OCH₂CH₂)₂NMe (**104**)

Table 9-1. Selected bond lengths and angles of MeClSi(OCH₂CH₂)₂NMe (**104**)

Bond Length	[Å]	Bond Angle	[°]
Si(1)-N(1)	2.1168(11)	O(1)-Si(1)-O(2)	121.69(5)
Cl(1)-Si(1)	2.2297(5)	C(2)-N(1)-C(3)	112.88(10)
Si(1)-O(1)	1.6553(9)	N(1)-Si(1)-Cl(1)	169.95(3)
Si(1)-O(2)	1.6563(10)	C(6)-N(1)-Si(1)	119.61(8)
Si(1)-C(5)	1.8600(14)	O(1)-Si(1)-Cl(1)	89.12(4)
N(1)-C(6)	1.4854(16)	O(2)-Si(1)-Cl(1)	90.87(4)
N(1)-C(2)	1.4850(17)		
N(1)-C(3)	1.4904(16)		

While the synthesis of dimethoxysilocane **106** in toluene proceeded, the reaction in acetonitrile did not work. Beside the higher reflux temperature in toluene that could be responsible for the synthesis of dimethoxysilocane **106**, formation of different types of anions during the synthesis in different solvents could be another reason for the successful formation in toluene.

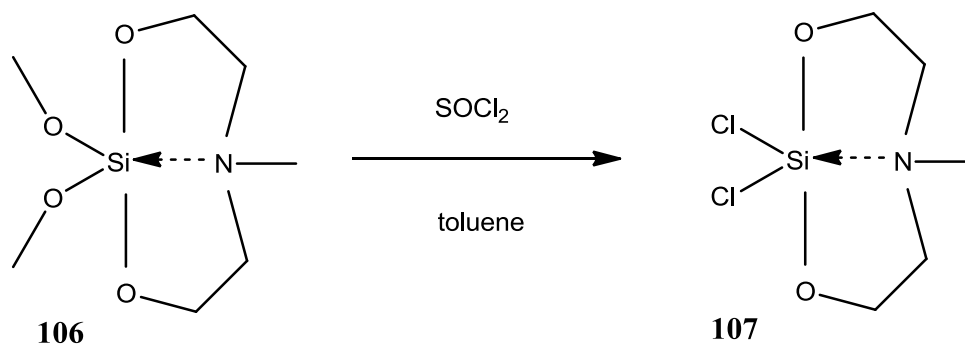


*Scheme 9-2. Synthesis of $(\text{MeO})_2\text{Si}(\text{OCH}_2\text{CH}_2)_2\text{NMe}$ (**106**) by reaction of *N*-methyldiethanolamine and $\text{Si}(\text{OMe})_4$ under reflux condition*

Due to the oily nature of the **106** and its sensitivity to traces amount of moisture, no further purification like distillation was performed and it was directly used for synthesis of $\text{Cl}_2\text{Si}(\text{OCH}_2\text{CH}_2)_2\text{NMe}$ (**107**).

9.1.3 Synthesis of $\text{Cl}_2\text{Si}(\text{OCH}_2\text{CH}_2)_2\text{NMe}$ (**107**)

Dichlorosilocane **107** was prepared according to literature procedure reported by Szpakolski et al.¹²⁹ Dimethoxysilocane **106** was reacted with an excess thionylchloride under nitrogen within 18 hours followed by decantation of the residue to remove sticky polymer which was forming during the reaction probably due to impurities of dimethoxysilocane **106** (Scheme 9-3).

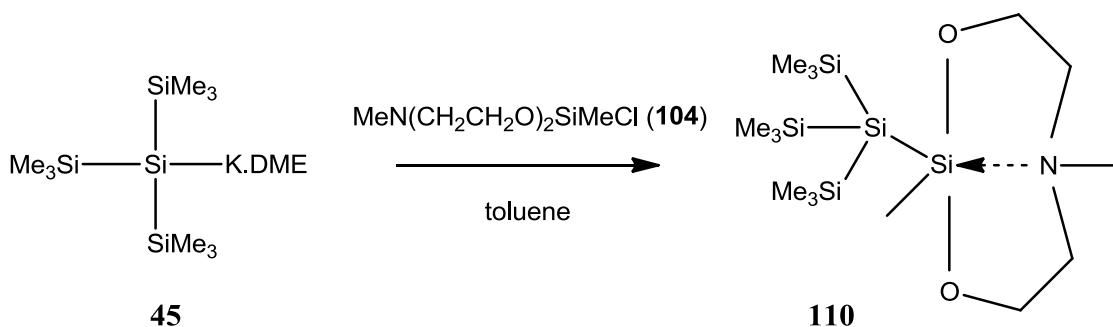


*Scheme 9-3. Synthesis of $\text{Cl}_2\text{Si}(\text{OCH}_2\text{CH}_2)_2\text{NMe}$ (**107**) by reaction of $(\text{MeO})_2\text{Si}(\text{OCH}_2\text{CH}_2)_2\text{NMe}$ (**106**) with thionylchloride*

9.2 Synthesis of oligosilanylsilocanes

9.2.1 Synthesis of 2'-(2',6'-dimethyl-1',3',6',2'-dioxazasilocanyl)-tris(trimethylsilyl)silane (110)

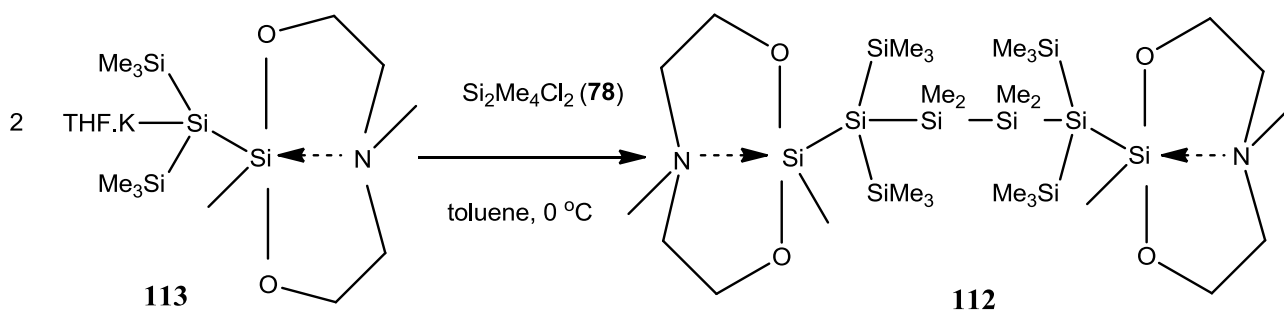
Synthesis of oligosilanylsilocane **110** was performed by reaction of tris(trimethylsilyl)silylpotassium.DME (**45**) with chlorosilocane **104** (Scheme 9-4). NMR spectroscopy only showed the formation of oligosilocanylsilane **110** without the formation of any silicon hydride **48**. As it is mentioned earlier in section 7-2-1 silicon hydride **48** forms in reaction between oligosilylpotassium **45** with 1-chloro (**40**) and 1-bromosilatrane (**42**) due to the steric hindrance of the bulky silatranyl group but the absence of silicon hydride **48** in this reaction confirms the higher reactivity of chlorosilocane **104** in reactions based on S_N2 mechanism in comparison to 1-chloro (**40**) and 1-bromosilatrane (**42**).



Scheme 9-4. Reaction of oligosilylpotassium **45** and chlorosilocane **104** for synthesis of 2'-(2',6'-dimethyl-1',3',6',2'-dioxazasilocanyl)-tris(trimethylsilyl)silane (**110**)

9.2.2 Synthesis of 1,4-bis-2'-(2',6'-dimethyl-1',3',6',2'-dioxazasilocanyl)-1,1,4,4-tetrakis(trimethylsilyl)tetramethyltetrasilane (112)

Synthesis of oligosilanylsilocane **112** was performed similar to the literature procedure reported by Whittaker et al.¹¹⁸ by reaction of two equivalent of 2'-(2',6'-dimethyl-1',3',6',2'-dioxazasilocanyl)bis(trimethylsilyl)silanylpotassium.THF (**113**) with silylhalide **78** (Scheme 9-5).



Scheme 9-5. Synthesis of 1,4-bis-2'-(2',6'-dimethyl-1',3',6',2'-dioxazasilocanyl)-1,1,4,4-tetrakis(trimethylsilyl)tetramethyltetrasilane (**112**) by reaction of respective oligosilocanylsilylpotassium (**113**) with 1,2-dichlorotetramethyldisilane (**78**)

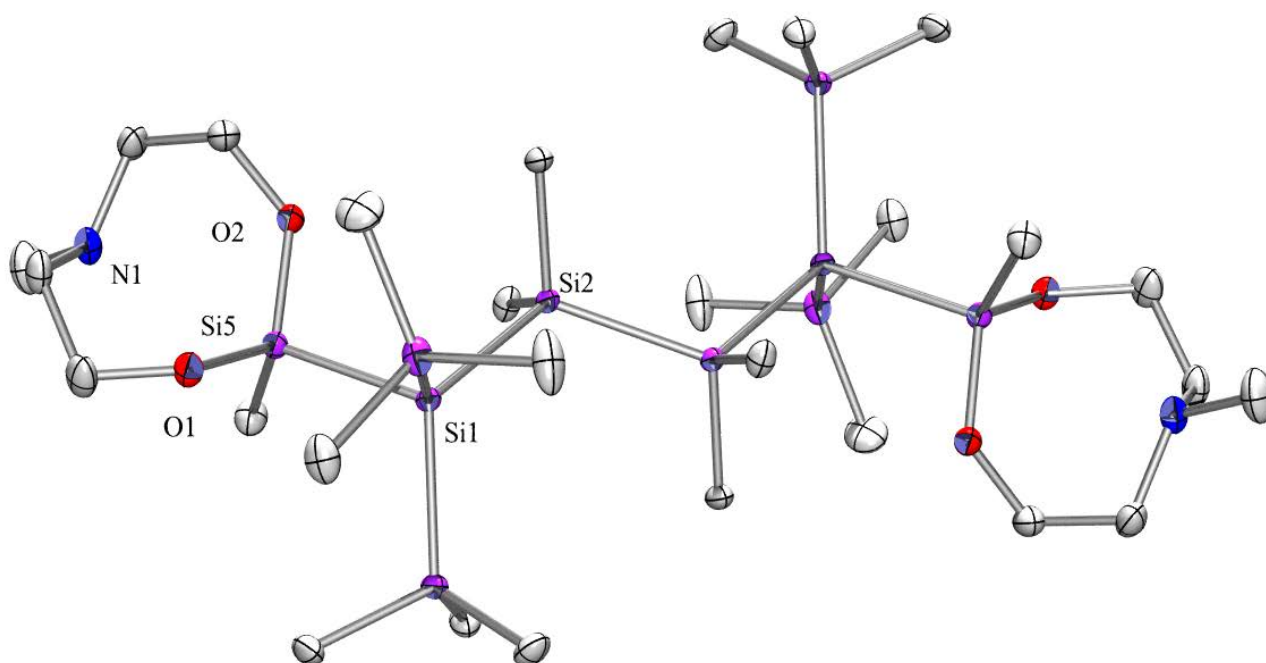


Figure 9-2. Crystal structure of 1,4-bis-2'-(2',6'-dimethyl-1',3',6',2'-dioxazasilocanyl)-1,1,4,4-tetrakis(trimethylsilyl)tetramethyltetrasilane (**112**)

Table 9-2. Selected bond lengths and angles of 1,4-bis-2'-(2',6'-dimethyl-1',3',6',2'-dioxazasilocanyl)-1,1,4,4-tetrakis(trimethylsilyl)tetramethyltetrasilane (**112**)

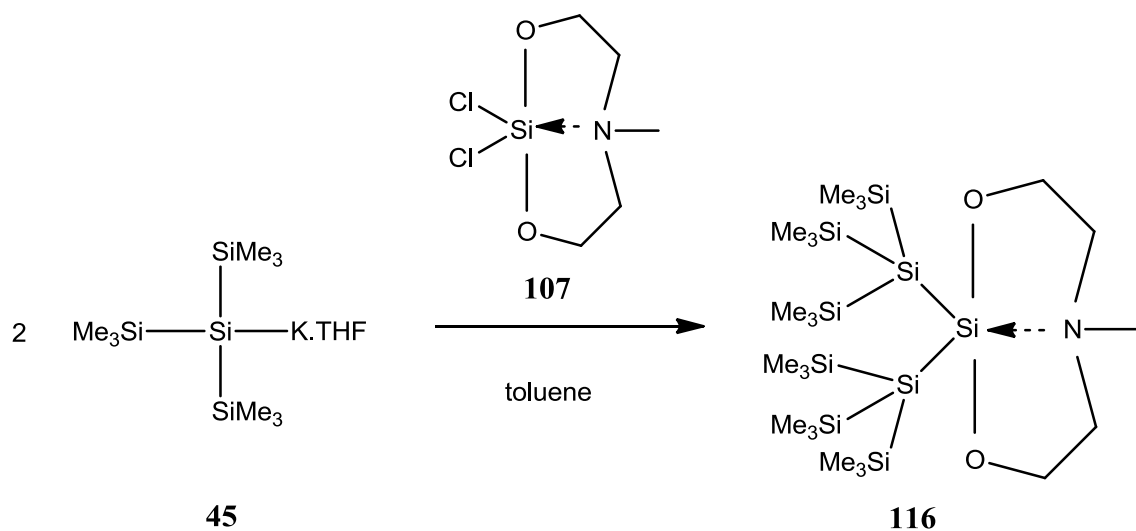
Bond Length	[Å]	Bond Angle	[°]
Si(1)-N(1)	2.934	O(1)-Si(5)-O(2)	113.50(10)
Si(5)-O(1)	1.6474(17)	C(13)-N(1)-C(11)	114.7(2)
Si(5)-O(2)	1.6456(17)	Si(5)-Si(1)-Si(2)	104.52(3)
Si(1)-Si(5)	2.3564(9)		
Si(1)-Si(2)	2.3643(9)		

Figure 9-2 shows the crystal structure and Table 9-2 the selected bond lengths and angles of oligosilanylsilocane **112**. Although in Si-Si-N axial bond Si-SiO₂ bond with 2.3564 Å is approximately close to Si-SiO₃ bond length of previously discussed oligosilanylsilatrane **77** in chapter 7-2 with Si-SiO₃ bond length of 2.3504 Å and 2.3417 Å, the Si-N bond length of 2.934 Å in oligosilanylsilocane **112** is longer than Si-N bond of oligosilanylsilatrane **77** with length of 2.223 Å and 2.208. Another difference between oligosilanylsilocane **112** and oligosilylsilatrane **77** is shorter Si-O bond with average length of 1.64 Å in comparison to Si-O bond of oligosilylsilatrane **77** with average length of 1.66 Å.

The transannular Si-N interaction depending on the substituents on silicon and nitrogen and in general it is less strong in silocanes than in silatranes⁷⁴, here according to Si-N, Si-SiO₂ and Si-SiO₃ bonds length in both silocanyl and silatranyl groups, it can be concluded that the Si-N interaction in silocanyl group of oligosilanylsilocane **112** is weaker than silatranyl group of oligosilylsilatrane **77**.

9.2.3 Synthesis of [(Me₃Si)₃Si]₂Si(OCH₂CH₂)₂NMe (**116**)

Oligosilocanylsilane **116** was synthesized by reaction of 2 equivalent of oligosilylpotassium **45** with dichlorosilocane **107** (Scheme 9-6). Although (Me₃Si)₃Si- is bulky but NMR spectroscopy of the reaction mixture after reaction showed mainly oligosilocanylsilane **116** and small quantity of oligosilane **47**.



Scheme 9-6. Synthesis of [(Me₃Si)₃Si]₂Si(OCH₂CH₂)₂NMe (**116**) by reaction of oligosilylpotassium **45** with Cl₂Si(OCH₂CH₂)₂NMe (**107**)

Figure 9-3 shows the crystal structure and Table 9-3 the selected bond lengths and angles of oligosilocanylsilane **116**. This molecule crystallizes in the orthorhombic space group Pccn. Si-N bond with 3.625 Å is even longer than Si-N bond of protonated oligosilanylsilatrane **44** with 3.389 Å (section 7-2-13). This shows that no interaction exist between Si-N in oligosilocanylsilane **116**. O-Si-O angle with 110.67 degree in oligosilocanylsilane **116** is slightly narrower than O-Si-O angle with 113.50 degree in oligosilanylsilocane **112** and highly

narrower than O-Si-O angle with 121.69 degree in chlorosilocane **104**. Very high Si-N distance and narrow O-Si-O angle in oligosilocanylsilane **116** is related to presence of two bulky hypersilyl groups around the silocanyl group.

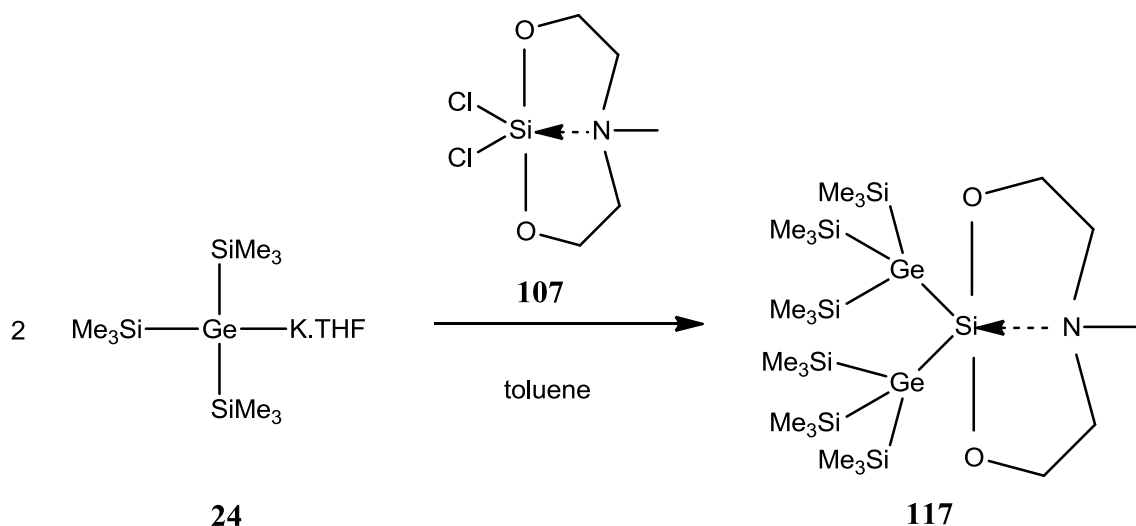
Si-SiO₂ bonds with 2.3881 Å and 2.3811 Å are longer than Si-Si average bond with 2.3721 Å according to Cambridge crystallographic data center.¹¹⁵

In contrast to silocane compounds which are sensitive to hydrolysis, oligosilocanylsilane **116** is stable in air. The high stability of this compound is related to the shielding effect of two bulky (Me₃Si)₃Si- groups around the silicon atom of the silocanyl group.

9.2.4 Synthesis of [(Me₃Si)₃Ge]₂Si(OCH₂CH₂)₂NMe (**117**)

Oligosilocanylsilylgermane **117** was synthesized by reaction of 2 equivalent of tris(trimethylsilyl)germylpotassium.THF (**24**) with dichlorosilocane **107** (Scheme 9-7).

In contrast to the clean reaction of oligosilocanylsilane **116**, NMR spectroscopy showed the presence of both oligosilylgermane **34** and oligosilocanylsilylgermane **117** in the reaction mixture which could be explained by the bigger size of (Me₃Si)₃Ge- in comparison to (Me₃Si)₃Si-.



*Scheme 9-7. Synthesis of [(Me₃Si)₃Ge]₂Si(OCH₂CH₂)₂NMe (**117**) by reaction of oligosilylgermylpotassium **24** with Cl₂Si(OCH₂CH₂)₂NMe (**107**)*

Figure 9-4 shows the crystal structure and Table 9-4 the selected bond lengths and angles of oligosilocanylsilylgermane **117**. This molecule crystallizes in the triclinic space group P-1.

Si-N bond with 3.501 Å is close to Si-N bond of oligosilocanylsilane **116** with 3.625 Å. The O-Si-O angle with 112.30 degree in oligosilocanylsilylgermane **117** is slightly wider than O-Si-O angle in oligosilocanylsilane **116** with 110.67 degree. As a result due to high Si-N distance and still narrow O-Si-O angle similar to oligosilocanylsilane **116** no interaction exist between Si-N in oligosilocanylsilylgermane **117**.

It is found that similar to oligosilocanylsilane **116**, oligosilocanylsilylgermane **117** is also stable in air which is related to shielding effect of two bulky (Me₃Si)₃Ge- groups around the silicon atom of silocanyl group.

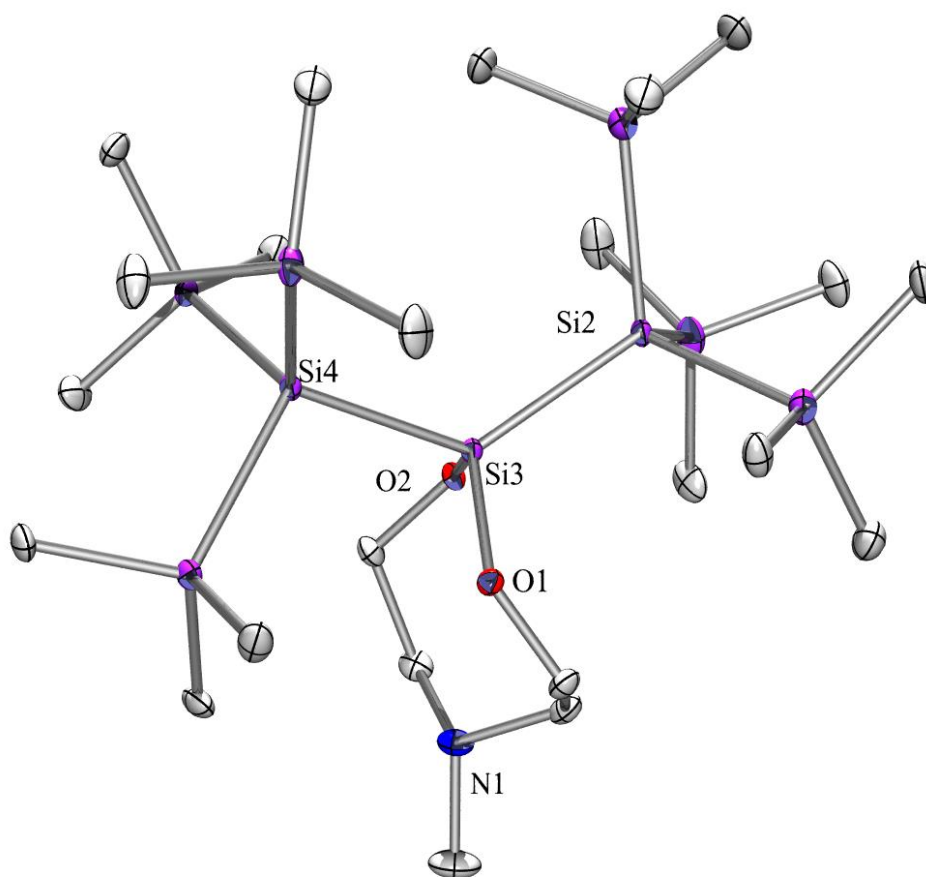


Figure 9-3. Crystal structure of $[(\text{Me}_3\text{Si})_3\text{Si}]_2\text{Si}(\text{OCH}_2\text{CH}_2)_2\text{NMe}$ (**116**)

Table 9-3. Selected bond lengths and angles of $[(\text{Me}_3\text{Si})_3\text{Si}]_2\text{Si}(\text{OCH}_2\text{CH}_2)_2\text{NMe}$ (**116**)

Bond Length	[Å]	Bond Angle	[°]
Si(1)-N(1)	3.625	O(1)-Si(3)-O(2)	110.67(12)
Si(3)-O(1)	1.652(2)	C(4)-N(1)-C(2)	114.2(3)
Si(3)-O(2)	1.660(2)	Si(4)-Si(3)-Si(2)	126.77(5)
Si(3)-Si(2)	2.3881(13)		
Si(3)-Si(4)	2.3811(12)		

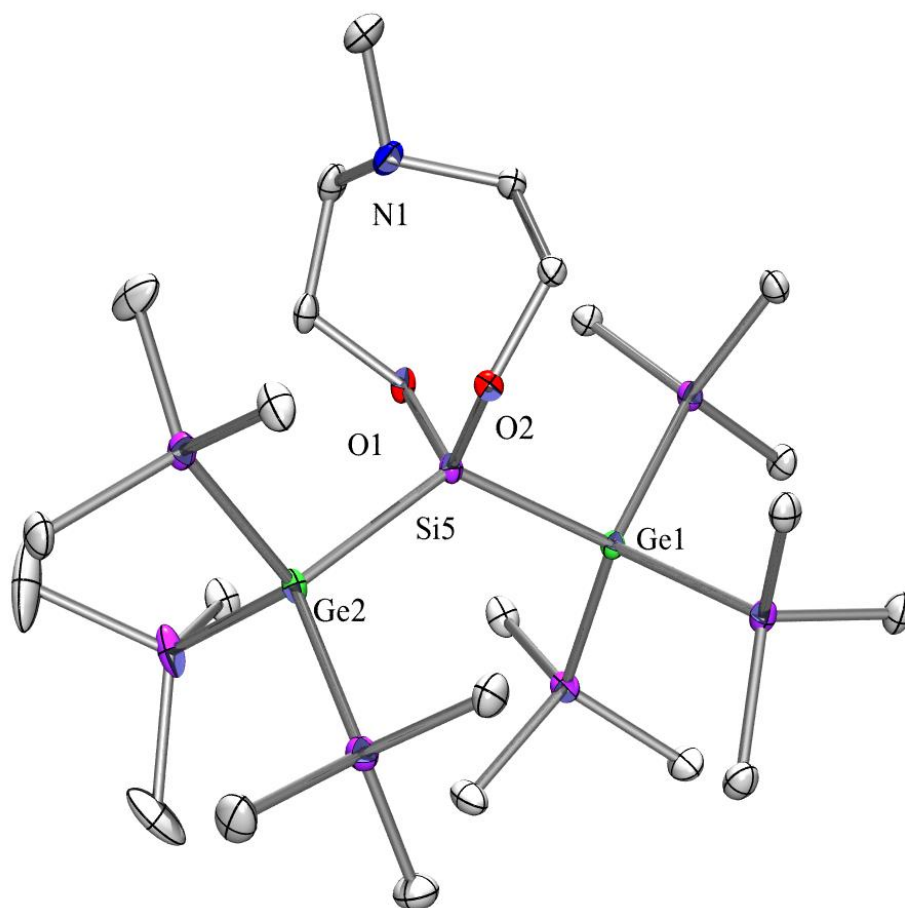


Figure 9-4. Crystal structure of $[(\text{Me}_3\text{Si})_3\text{Ge}]_2\text{Si}(\text{OCH}_2\text{CH}_2)_2\text{NMe}$ (**117**)

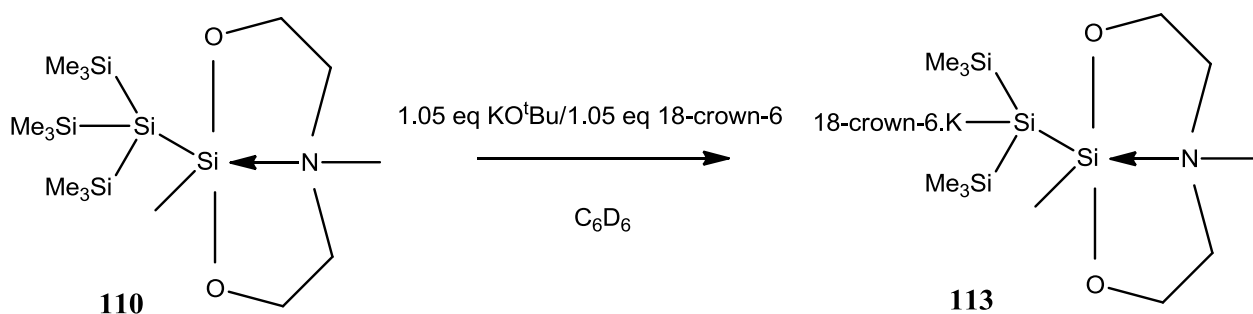
Table 9-4. Selected bond lengths and angles of $[(\text{Me}_3\text{Si})_3\text{Ge}]_2\text{Si}(\text{OCH}_2\text{CH}_2)_2\text{NMe}$ (**117**)

Bond Length	[Å]	Bond Angle	[°]
Si(1)-N(1)	3.501	O(1)-Si(5)-O(2)	112.30(6)
Si(5)-O(1)	1.6544(12)	C(2)-N(1)-C(4)	113.13(14)
Si(5)-O(2)	1.6501(12)	Ge(1)-Si(5)-Ge(2)	126.99(2)
Ge(1)-Si(5)	2.4105(6)		
Ge(2)-Si(5)	2.4177(5)		
Ge(1)-Si(2)	2.3863(6)		
Ge(2)-Si(8)	2.4162(6)		

9.3 Synthesis of silocanylsilylanions

9.3.1 Synthesis of 2'-(2',6'-dimethyl-1',3',6',2'-dioxasilocanyl)bis(trimethylsilyl)silylpotassium.18-crown-6 (113)

Synthesis of oligosilocanylsilylpotassium **113** was performed by reaction of oligosilocanylsilane **110** with one equivalent of each KO^tBu and 18-crown-6 in benzene (Scheme 9-8). In this case attack of the KO^tBu was selective at a trimethylsilyl group. It is found that the oligosilocanylsilylpotassium also forms in THF without 18-crown-6.



*Scheme 9-8. Reaction of 2'-(2',6'-dimethyl-1',3',6',2'-dioxasilocanyl)-tris(trimethylsilyl)silane (**110**), KO^tBu and 18-crown-6 in C₆D₆ for synthesis of 2'-(2',6'-dimethyl-1',3',6',2'-dioxasilocanyl)bis(trimethylsilyl)silylpotassium.18-crown-6 (**113**)*

9.4 Conclusion

The synthesis of oligosilanylsilocanes was studied by reaction of silocanes bearing a chloride atom as a leaving group with silanyl anion. Although it is found that chloride is not a good leaving group in the reaction of 1-chlorosilatrane (**40**) with silanyl anion due to unusual structural geometry of 1-chlorosilatrane (**40**)⁸², it is a suitable leaving group in the reaction of the mentioned chlorosilocanes with silanyl anions.

Single crystal XRD analysis revealed that transannular Si-N interaction in oligosilanylsilocanes is not as strong as in oligosilanylsilatrane and can be easily affected by bulky substituents on the silicon atom of silocanyl group.

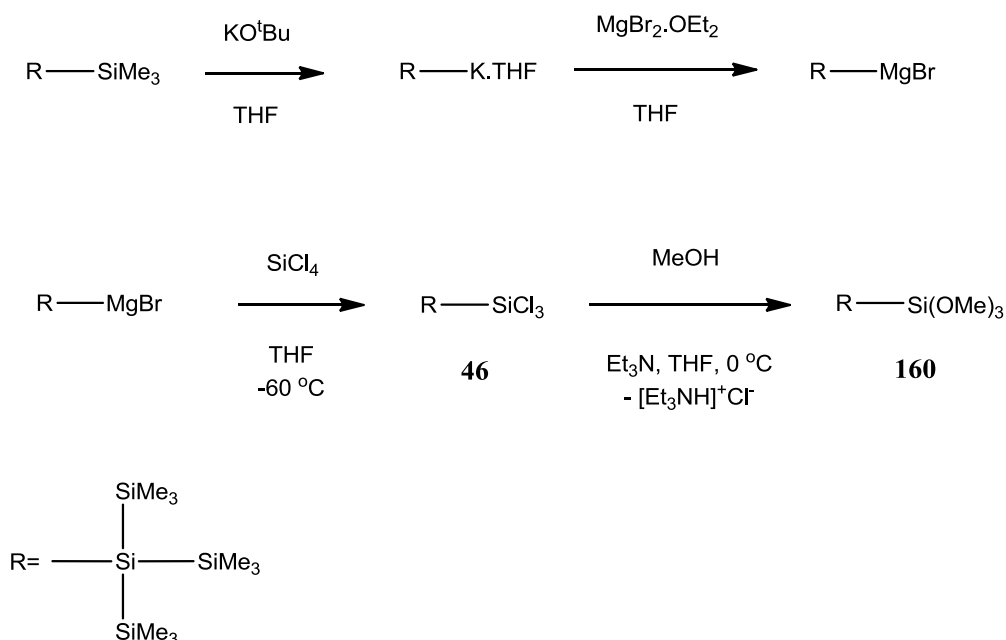
Chapter 10

Synthesis of methoxysilanes

10 Synthesis of methoxysilanes

10.1 Synthesis of tris(trimethylsilyl)[trimethoxysilyl]silane (**160**)

Synthesis of $(\text{Me}_3\text{Si})_3\text{SiSiCl}_3$ (**46**) was described earlier in section 7-2-1. Respective silylmethoxide was synthesized via alcoholysis of chlorosilane **46** in presence of a Lewis base like triethylamine to neutralize the HCl, the byproduct of the alcoholysis reaction.

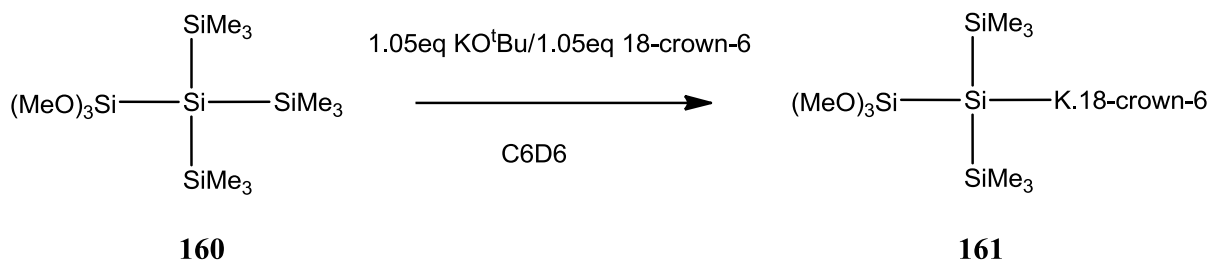


Scheme 10-1. Synthesis of tris(trimethylsilyl)[trimethoxysilyl]silane (**160**) via the alcoholysis of $(\text{Me}_3\text{Si})_3\text{SiSiCl}_3$ (**46**) with methanol

Oligosilylmethoxide **160** is partially similar to oligosilanylsilatrane **44**; however due to the absence of a nitrogen atom it has only a four valent silicon atom instead of a hypervalent silicon atom. As a result by comparing the characteristics of oligosilylmethoxide **160** with oligosilanylsilatrane **44**, it is possible to recognize the effect of the hypervalent silicon atom to oligosilanes and polysilanes. Although due to the oily nature of oligosilylmethoxide **160**, it was not possible to characterize it by single crystal XRD analysis.

10.2 Synthesis of bis(trimethylsilyl)[trimethoxysilyl]silylpotassium.18-crown-6 (**161**)

Synthesis of methoxysilylpotassium **161** was performed by reaction of oligosilylmethoxide **160** with one equivalent of each KO^tBu and 18-crown-6 in benzene (Scheme 10-2). In this case the attack of the KO^tBu was selective at a trimethylsilyl group. The methoxysilylpotassium also forms in THF without 18-crown-6 and because of the potassium-oxygen coordination a polymeric compound occurs.



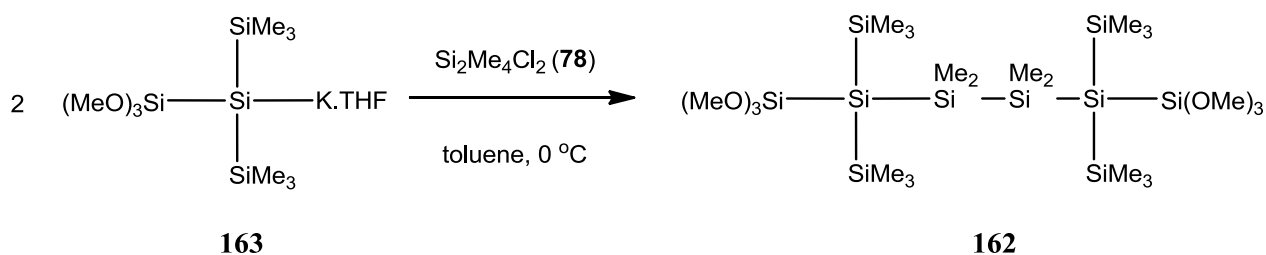
Scheme 10-2. Reaction of tris(trimethylsilyl)[trimethoxysilyl]silane (160), KO^tBu and 18-crown-6 in C₆D₆ for the synthesis of bis(trimethylsilyl)[trimethoxysilyl]silylpotassium. 18-crown-6 (161)

Figure 10-1 shows the crystal structure and Table 10-1 the selected bond lengths and angles of methoxysilylpotassium **161**. This molecule crystallizes in the orthorhombic space group Pbca. Potassium coordinates with both the oxygen atoms of 18-crown-6 and the methoxy groups. In both cases the potassium-oxygen bond lengths are around 2.9 Å. It is worth to mention that in this case a separation of the ionic pair is observed due to coordination of potassium to the oxygen atom of two methoxy groups. Notably the distance between potassium and the methoxy substituted silicon atom with 3.5694 Å is similar to K-Si bond length of oligosilatranylsilylpotassium **73**, **87** and **88** with 3.3634 Å, 3.5722 Å and 3.6321 Å respectively.

In methoxysilylpotassium **161** Si-O bond lengths are similar to Si-O bond lengths of oligosilanylsilatrane which was previously observed in chapter 7. Si-SiO₃ bond length with 2.313 Å is close to Si-SiO₃ bond length of oligosilatranylsilylpotassium **73**, **87** and **88** with 2.3080 Å, 2.3087 Å and 2.2947 Å respectively.

10.3 Synthesis of 2,5-bis(trimethoxysilyl)-2,5-bis(trimethylsilyl)decamethylhexasilane (162)

Synthesis of oligosilylmethoxide **162** was performed similar to literature procedure reported by Whittaker et al.¹¹⁸ by reaction of two equivalent of bis(trimethylsilyl)[trimethoxysilyl]silylpotassium.THF (**163**) with Cl₂Si₂Me₄ (Scheme 10-3). The UV absorption spectrum of this compound was prepared to be compared with oligosilanylsilatrane.



Scheme 10-3. Synthesis of 2,5-bis(trimethoxysilyl)-2,5-bis(trimethylsilyl)decamethylhexasilane (162) by reaction of bis(trimethylsilyl)[trimethoxysilyl]silylpotassium.THF (163) with Cl₂Si₂Me₄

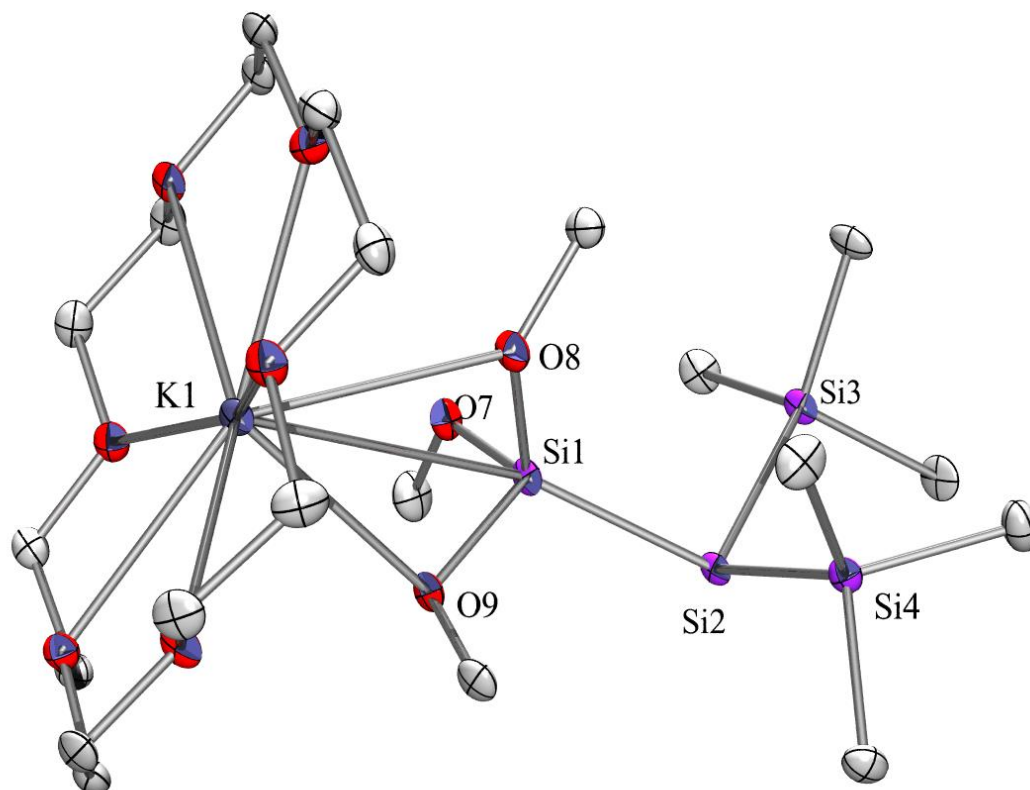


Figure 10-1. Crystal structure of bis(trimethylsilyl)[trimethoxysilyl]silylpotassium.18-crown-6 (**161**)

Table 10-1. Selected bond lengths and angles of bis(trimethylsilyl)[trimethoxysilyl]silylpotassium.18-crown-6 (**161**)

Bond Length	[Å]	Bond Angle	[°]
Si(1)-O(7)	1.658(4)	O(7)-Si(1)-O(8)	101.6(2)
Si(1)-O(8)	1.659(4)	O(7)-Si(1)-O(9)	103.19(19)
Si(1)-O(9)	1.679(4)	O(8)-Si(1)-O(9)	99.28(18)
Si(2)-Si(1)	2.313(2)	O(9)-K(1)-O(8)	51.66(10)
Si(2)-Si(3)	2.3386(19)	Si(1)-Si(2)-Si(3)	103.68(7)
Si(2)-Si(4)	2.350(2)	Si(1)-Si(2)-Si(4)	103.97(7)
K(1)-Si(1)	3.5694(19)	Si(3)-Si(2)-Si(4)	104.33(7)
K(1)-O(3)	2.805(4)		
K(1)-O(6)	2.954(4)		
K(1)-O(8)	2.984(4)		
K(1)-O(9)	2.847(4)		

10.4 Conclusion

Synthesis of oligosilylmethoxide was performed to be compared with oligosilanylsilatrane. In fact oligosilylmethoxide are structurally similar to oligosilanylsilatrane; however without the presence of a hypervalent silicon atom in their structure. Crystal structure of methoxysilylpotassium **161** showed K-O coordination similar to K-O coordination in oligosilatranyl-silylpotassium compounds; however due to absence of a bulky trialkylamine ligand, the potassium atom coordinates to silicon atom of the silylmethoxide group instead of central silicon atom of the molecule. Si-SiO₃ bond length in methoxysilylpotassium **161** with 2.313 Å is close to mean Si-SiO₃ bond length in oligosilatranyl-silylpotassium **73**, **87** and **88** with 2.304 Å. Mean Si-O bond length in all methoxysilylpotassium **161**, oligosilatranyl-silylpotassium **73**, **87** and **88** is equal to 1.66 Å. Comparison of UV absorption spectrum of oligosilylmethoxide **162** with oligosilanylsilatrane **75** and **77** will be discussed in chapter 11.

Chapter 11

UV-Vis study of oligosilanes containing hypervalent silicon atoms

11 UV-Vis study of oligosilanes containing a hypervalent silicon atom

11.1 Oligosilanes containing a silatranyl substituent

Figure 11-1 shows the UV absorption spectra of different oligosilanes with different substituents. The green line relates to oligosilane **79**¹¹⁸ with a peak at 257 nm.⁶³ Substitution of a SiMe₃ group with a silatranyl group in oligosilanyl silatrane **75** shifts the UV absorption to 254 nm. Moreover substitution of two SiMe₃ groups by two silatranyl groups in oligosilanyl silatrane **77** shifts the UV absorption further to blue region and the UV-Vis spectrum of this compound shows a peak at 252 nm. Oligosilanyl silacate **162** with six methoxy groups but without a nitrogen and a hypervalent silicon atom is partially similar to oligosilanyl silatrane **77**. It is found that the UV absorption spectrum of oligosilanyl silacate **162** with a peak at 253 nm is close to UV absorption spectrum of oligosilanyl silatrane **77** with a peak at 252 nm. Similarity of UV absorption spectra of these two oligosilanes shows that the hypervalent silicon atom does not have a significant influence on the UV absorption of the oligosilanyl silatrane **75** and **77** and mainly the oxygen atoms are responsible for hypsochromic shift in these compounds.

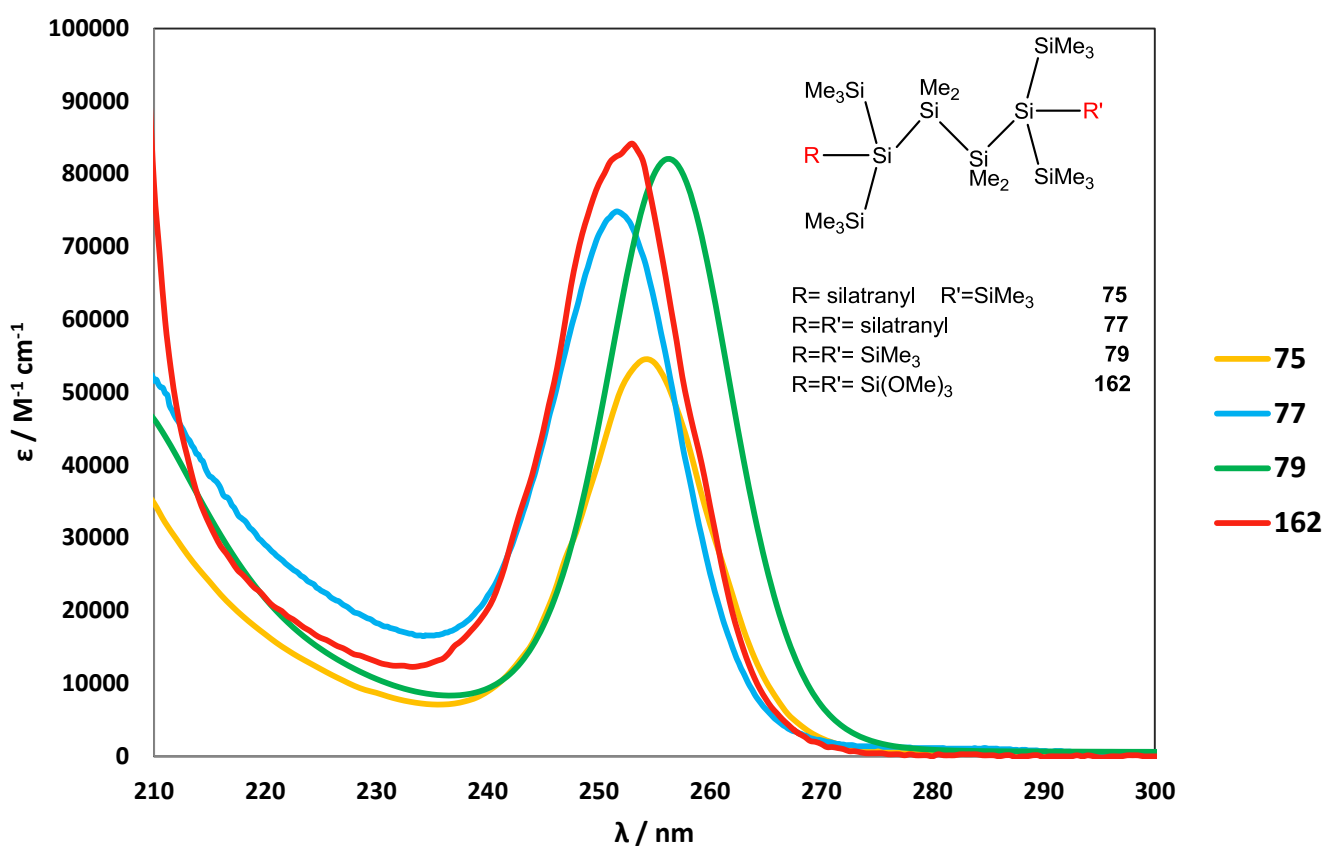


Figure 11-1. UV-Vis spectra of different oligosilanes with SiMe₃, silatranyl and methoxy substituents.

Yellow: 2-silatranyl-2,5,5-tris(trimethylsilyl)decamethylhexasilane (**75**)

Blue: 2,5-disilatranyl-2,5-bis(trimethylsilyl)decamethylhexasilane (**77**)

Green: 2,2,5,5-tetrakis(trimethylsilyl)decamethylhexasilane (**79**)

Red: 2,5-bis(trimethoxysilyl)-2,5-bis(trimethylsilyl)decamethylhexasilane (**162**)

11.2 Cyclohexasilane containing silatranyl substituent

Single crystal XRD studies in chapter 7 showed that the six membered ring in the *cis*-cyclohexasilanylsilatrane **80** and the previously reported cyclohexasilane **165**¹¹⁹ engaged a twisted boat conformation in both⁶³ in contrast to the *trans*-cyclohexasilanylsilatrane **80** with a chair conformation.

It has been reported that alkylated cyclosilanes $[(R_2Si)_n, n = 3-7]$ with smaller ring size exhibit hypsochromic shift in UV absorption spectrum while by further increase in the ring size the absorption behavior resembles more to linear compounds with bathochromic shift.¹³¹

Figure 11-2 shows the UV absorption spectra of cyclohexasilanes with different substituents. The green line relates to cyclohexasilane **165** with two peaks at 246 and 268 nm,⁶³ the blue line relates to *cis*-cyclohexasilanylsilatrane **80** with a peak at 242 nm and the *trans*-cyclohexasilanylsilatrane **80** with red spectrum does not have any distinct peak. Similar to UV absorption spectra of mentioned oligosilanylsilatranes with hypsochromic shift, *cis*-cyclohexasilanylsilatrane **80** also shows hypsochromic shift with magnitude of 4 nm and in case of *trans*-isomer the peak completely disappears.

Silatranyl substituents on cyclohexasilane slightly increase the molar extinction coefficient of these compounds in comparison to cyclohexasilane **165**.

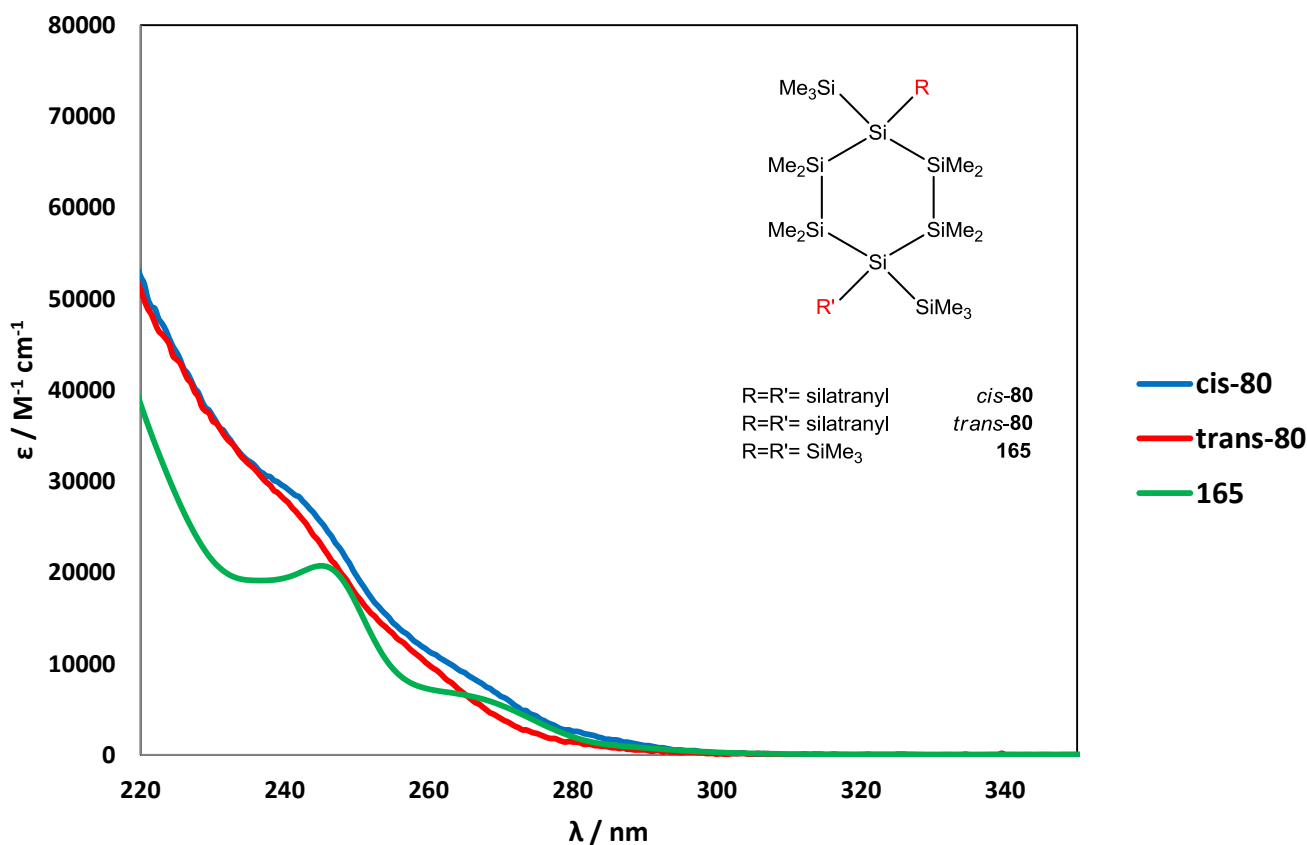


Figure 11-2. UV-Vis spectra of cyclohexasilanes with SiMe₃ and silatranyl substituents.

Blue: *cis* 1,4-disilatranyl-1,4-bis(trimethylsilyl)octamethylcyclohexasilane (**80**)
 Red: *trans* 1,4-disilatranyl-1,4-bis(trimethylsilyl)octamethylcyclohexasilane (**80**)
 Green: 1,1,4,4-tetrakis(trimethylsilyl)octamethylcyclohexasilane (**165**)

11.3 Oligosilane containing silocanyl substituent

Figure 11-3 shows the UV absorption spectra of different oligosilanes with silocanyl substituents. Green line relates to oligosilanyl silocane **112** with a peak at 254 nm. Comparison of the UV absorption spectrum of oligosilane **79**¹¹⁸ in Figure 11-1 with UV absorption spectrum of the oligosilanyl silocane **112** shows a blue shift with magnitude of 3 nm by substitution of SiMe₃ groups by silocanyl groups. Although according to UV absorption results in Figure 11-1 and 11-3 oligosilanes with silatranyl or silocanyl groups as terminal groups show hypsochromic shift, oligosilocanyl silane **116** and oligosilocanyl silylgermane **117** with a silocanyl group in the middle of the silicon chain show a bathochromic shift. It is worth to mention that the number of silicon atoms in **116** with bathochromic shifted UV spectrum is 9 while the number of silicon atoms in oligosilanes with silatranyl or silocanyl groups as terminal groups is 10.

The absence of a hypervalent silicon atom in **116** and **117** according to crystallographic data which is due to the presence of bulky groups like (Me₃Si)₃Si- and (Me₃Si)₃Ge- was studied in chapter 9. Although the absence of a hypervalent silicon atom in **116** and **117** and its presence in oligosilanes with silatranyl or silocanyl groups as terminal groups is one of the main important differences between these structures, it cannot be the reason for bathochromic behavior of **116** and **117** as the oligosilyl methoxide **162** without hypervalent silicon atom showed hypsochromic shift (Figure 11-1, red line).

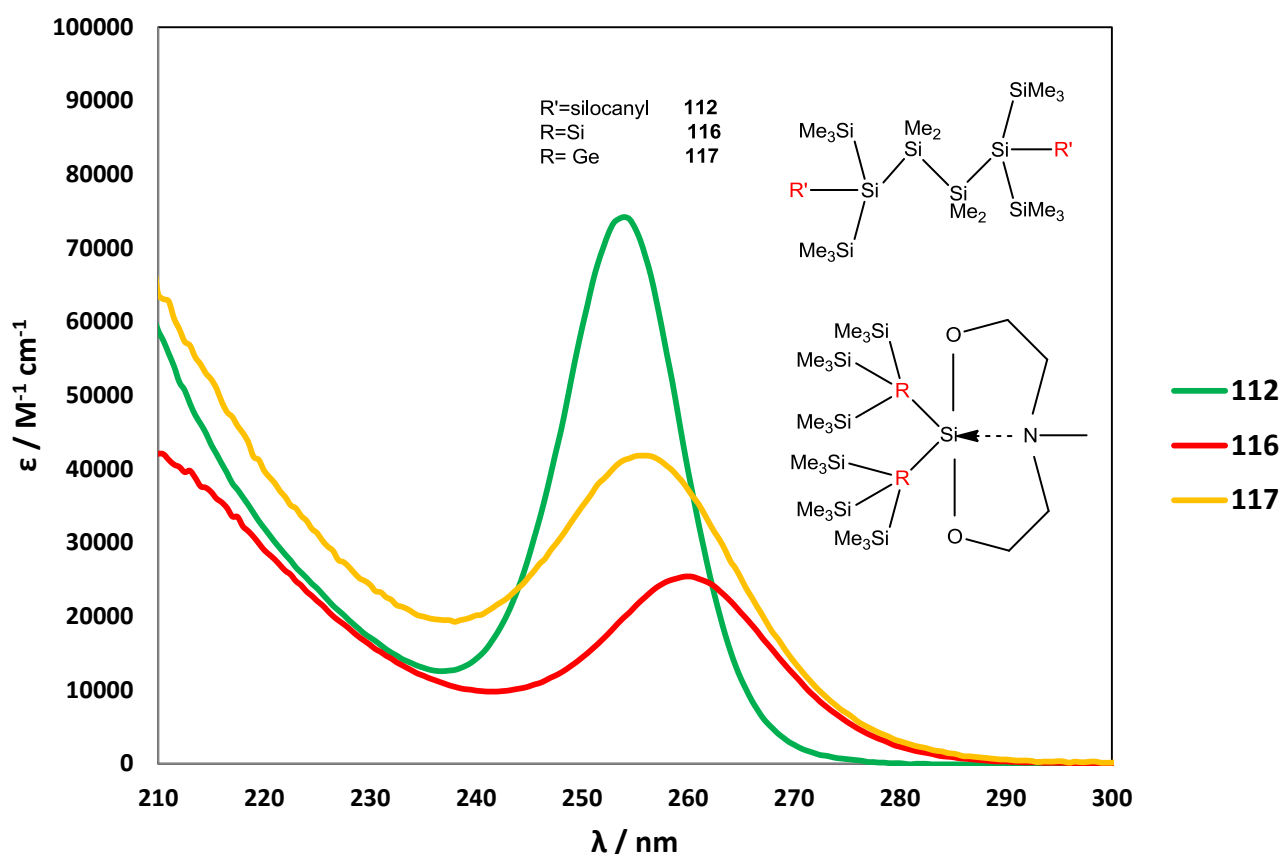


Figure 11-3. UV-Vis spectra of different oligosilanes with silocanyl substituent.

Green: 1,4-bis-2'--(2',6'-dimethyl-1',3',6',2'-dioxazasilocanyl)-1,1,4,4-tetrakis(trimethylsilyl)tetramethyltetrasilane (**112**)

Red: [(Me₃Si)₃Si]₂Si(OCH₂CH₂)₂NMe (**116**)

Yellow: [(Me₃Si)₃Ge]₂Si(OCH₂CH₂)₂NMe (**117**)

In general bathochromic shift mainly in **116** can be explained by the special spatial structure of this compound.

11.4 Conclusion

UV absorption spectra revealed that a substitution of trimethylsilyl group with a silatranyl group in oligosilanes with linear silicon backbone decreases the σ -bond electron delocalization and causes hypsochromic shift. The same hypsochromic shift can be observed by substitution of trimethylsilyl group with silocanyl group in oligosilane with linear silicon backbone. UV absorption spectrum of oligosilylmethoxide with six methoxy groups and without nitrogen and hypervalent silicon atom which is structurally similar to oligosilanylsilatrane in the absence of a nitrogen atom showed a similar hypsochromic shift.

In general similar hypsochromic shifts in UV absorption spectra of oligosilanylsilatrane and oligosilanylsilocane with hypervalent silicon atom and oligosilylmethoxide without hypervalent silicon atom show that the nitrogen lone pair donation to the silicon chain does not affect the UV absorption spectra significantly.

In contrast to oligosilanylsilatrane and oligosilanylsilocane with silatranyl or silocanyl groups as terminal groups, UV absorption spectra of oligosilanylsilocane with a silocanyl group in the middle of the silicon chain showed bathochromic shift. It is worth to mention that according to crystallographic data no hypervalent silicon atom exist in these type of compounds due to presence of bulky $(\text{Me}_3\text{Si})_3\text{M}$ - $[\text{M}=\text{Si}, \text{Ge}]$ groups. Bathochromic shift can be explained by special spatial structure of these compounds.

Chapter 12

Experimental section

12 Experimental section

12.1 General Experimental

12.1.1 Chemical substances

All manipulations involving air or moisture sensitive compounds were either performed under nitrogen atmosphere by employing standard Schlenk techniques or were carried out in a nitrogen filled glove box (Innovative Technology, Inc).

A column solvent purification system by Innovative Technologies was used for THF, DME, diethylether, toluene, benzene, pentane and heptane.

In case of medium boiling solvents like *n*-dodecane and *n*-hexadecane nitrogen gas was bubbled through them and in case of high boiling solvents like oleylamine and squalane, solvents were put under vacuum to remove oxygen.

DMF and *p*-xylene were first stirred with sodium sulfate under nitrogen for 24 hours and afterwards under nitrogen purging were transferred with cannula equipped with filter paper to another flask.

Acetonitrile was first treated with CaH₂ and then distilled under nitrogen and kept in a flask containing molecular sieve 3 Å.

Chemical substances used as starting materials like diphenylgermane,¹³² tetrakis(trimethylsilyl)silane (47),¹³³ tetrakis(trimethylsilyl)germane (7),¹³⁴ tris(trimethylsilyl)germane (3),⁸⁷ hexakis(trimethylsilyl)digermane (6),⁸⁷ tris(trimethylsilyl)[tris(trimethylsilyl)silyl]germane (17),⁸⁷ pentakis(trimethylsilyl)digermyl-potassium.18-crown-6 (4),⁸⁷ tetrakis(trimethylsilyl)digermyl-1,2-dipotassium 2×18-crown-6 (9),⁸⁷ bis(trimethylsilyl)[tris(trimethylsilyl)silyl]germyl-potassium.18-crown-6 (12),⁸⁷ [tris(trimethylsilyl)silyl]trimethylgermane (33),¹³⁵ 1-chlorosilatrane (40),⁷⁷ phenylsilatran (41),⁷⁷ 1-bromosilatrane (42),¹¹⁰ methyltris(trimethylsilyl)silane,¹³⁶ ethyltris(trimethylsilyl)silane,¹³⁷ phenyltris(trimethylsilyl)silane,¹³⁸ (*tert*-butyldimethylsilyl)tris(trimethylsilyl)silane,¹³⁹ isopropyltris(trimethylsilyl)silane,¹¹⁶ 2,2-bis(trimethylsilyl)octamethyltetrasilane,¹³⁹ 1-chloro-3,3-bis(trimethylsilyl)heptamethyltetrasilane (76),¹¹⁷ tris(2-methoxyphenyl)amine,⁷⁰ tris(2-hydroxyphenyl)amine (131),⁷⁰ aminotris(phenyl-2'-oxy)silylchloride (130),⁷⁰ 1,2-dichlorotetramethyldisilane (78),¹⁴⁰ tris(2-hydroxy-4,6-dimethylbenzyl)amine,⁷¹ were prepared according to literature procedures.

Otherwise they were purchased from chemical suppliers like potassium *tert*-butoxide (MERCK, 98%), oleylamine (Aldrich, technical grade, 70%), tri-*n*-butylphosphine (Aldrich, 93.5%), N,N-dimethylformamide (MERCK, 99%), indium(III) chloride (ABCR, 98%), tri-*n*-octylphosphine oxide (ABCR, 99%), *n*-dodecane (Sigma-Aldrich, 99%), *n*-hexadecane (Amresco, technical grade), squalane (Alfa Aesar, 98%), tetramethoxysilane (ACROS, 99%), triethanolamine (Sigma-Aldrich, 99%), *n*-methyldiethanolamine (Aldrich, 99%), thionyl chloride (ACROS, 99.5%), silicon tetrachloride (Riedel-de Haen, 99%), trimethylsilyltrifluoromethanesulphonate (Sigma-Aldrich, 98%), *tert*-butylchlorodiphenylsilane (Aldrich, 98%), dicobalt octacarbonyl (Fluka, 90-95% Co).

12.2 Analytical methods

12.2.1 Nuclear magnetic resonance (NMR) spectroscopy

NMR spectra were recorded on a Varian INOVA 300 (^1H 299.95 MHz, ^{13}C 75.43 MHz, ^{29}Si 59.59 MHz, ^{31}P 121.4 MHz and ^{19}F 282.17 MHz) spectrometer.

Samples were dissolved in chloroform- d_1 , benzene- d_6 , DMSO- d_6 or in the case of a non-deuterated solvent using a capillary filled with D_2O for deuterium lock. Shifts are reported in ppm downfield from TMS (tetramethylsilane) and are referenced to solvent residual signals.

12.2.2 Gas chromatography

GC analyses were carried out on an Agilent 7890A (capillary column HP-5MS; 30 m \times 0.250 mm; Film 0.25 μm) with mass spectrometer Agilent 5975C.

12.2.3 Mass spectroscopy

Mass spectra were obtained with an Agilent 5975C coupled to an Agilent 7890A gas chromatograph. Assignment of peaks was either accomplished by comparison to data from a database or for mass spectra not covered by the library identified by standard techniques for their interpretation.¹⁴¹

12.2.4 Direct insertion electron impact mass spectrometry (DI-EI)

It was performed by mass spectrometer GCT premier from Waters Company with electron impact ionization of 70eV and ion source temperature of 200 °C.

12.2.5 Transmission electron microscope (TEM)

TEM images were taken by T12 microscope from FEI, operated at 120kV with LaB_6 cathode or a monochromated TF20 microscope from FEI operated at 200kV with a Schottky cathode. TF20 microscope for X-ray spectroscopy equipped with a SiLi detector with ultrathin window and for electron energy loss spectroscopy with a high resolution Gatan imaging filter (GIF). The EFTEM images were recorded with the CCD camera integrated within the GIF and processed with Gatan's Digital Micrograph being corrected for dark current and gain variations. In order to optimize the signal to noise ratio, 150 μm aperture which is the largest possible condenser aperture on the microscope and the 70 μm objective aperture were used.

12.2.6 Scanning electron microscope (SEM)

SEM images were taken by Zeiss DSM 982 Gemini with field emission gun. The images were mainly recorded with the Everhart-Thornley detector (secondary electron images), some were recorded with the solid state detector (backscattered electrons images).

Energy dispersive x-ray spectroscopic (EDS) analysis was carried out with Noran Voyager.

In case of sensitive samples to oxygen and moisture, samples were transferred to the specimen holder inside the glove box under nitrogen and the specimen holder was transferred to the sealed chamber under nitrogen. Before analysis the sealed chamber was attached to the SEM

microscope and the specimen holder was transferred into the microscope with a screw handle without any contact to air.

12.2.7 Dynamic light scattering (DLS) analysis

DLS analyses of colloidal solution of nanoparticles were performed on a Malvern Zetasizer Nano ZS instrument equipped with He-Ne laser operating at 633 nm. The scattered light is registered at scattering angle of 173°, known as backscattered detection. Temperature equilibration lasted for 60 seconds at 25 °C and the measurement was carried out at 25 °C. Control of the instrument parameters such as cuvette position, temperature, measurement time and repetitions as well as data acquisition and analysis was attained via the Zetasizer Software V.6.12.

Fluorescence quartz cuvette of 10 × 10 × 48 mm size (Hellma Analytics) was used for measurement of colloidal solution of nanoparticles. Sample volume per measurement was about 2 mL.

12.2.8 X-ray crystal structure analysis

Data were recorded with a BRUKER-AXS SMART APEX CCD diffractometer employing graphite-monochromated Mo- K_{α} radiation ($\lambda=0.71073$ Å), equipped with a Kryoflex low temperature cooling unit for routine data collection at temperatures as low as 90 K (standard is 100 K). The data were reduced to F^2 and corrected for absorption effects with SAINT¹⁴² and SADABS,¹⁴³ respectively. The structures were solved by direct methods and refined by full-matrix least-squares method (SHELXL97).¹⁴⁴

12.2.9 X-ray powder diffraction (XRD) analysis

X-Ray Powder diffraction measurement was performed with a BRUKER D8 Advance diffractometer, Bragg-Brentano geometry with Cu K-alpha radiation, 2 theta angle ranges from 10 to 100 degree with an increment of 0.02 degree and measuring time of 10 seconds per step.

12.2.10 Thermogravimetric analysis (TGA)

Thermogravimetric analysis was performed with STA 449C Jupiter simultaneous TGA-DSC analyzer from NETZSCH. The thermal effect on mass change was studied in temperatures between 20 °C to 550 °C with a heating rate of 10 °C/min under helium atmosphere.

12.2.11 UV-Visible spectroscopy

UV-Visible analyses were performed with UV-1800 from Shimadzu and Cary 60 UV-Vis from Agilent Technologies and the absorbance wavelengths of samples were measured.

12.2.12 Elemental analysis

Elemental analyses were carried on a VARIO EL by HERAEUS Elementar.

12.2.13 Fourier-transform infrared spectroscopy (FT-IR)

FT-IR spectra were recorded on a Bruker Alpha FT-IR spectrometer. Precipitated indium nanoparticles capped with different types of ligands were directly subjected to analysis.

12.2.14 Small angle X-ray scattering (SAXS)

SAXS analysis was performed with a high-flux SAXSess camera (Anton Paar, Graz, Austria) connected to a DebyeFlex 3003 X-ray generator (GE-Electric, Germany), operating at 40 kV and 50 mA with a sealed-tube Cu anode. The Goebel-mirror focused and Kratky-slit collimated X-ray beam was line shaped (17 mm horizontal dimension at the sample) and scattered radiation from the phase transfer system (I) and (II) measured in the transmission mode was recorded by a one-dimensional MYTHEN-1k microstrip solid-state detector (Dectris Switzerland), within a q-range (with q being the magnitude of the scattering vector) of 0.1 to 5 nm⁻¹. Using CuK_α radiation of wavelength 0.154 nm and a sample-to-detector distance of 309 mm this corresponds to a total 2θ region of 0.14 ° to 7 °, applying the conversion $q \text{ [nm}^{-1}] = 4\pi(\sin\theta)/\lambda$ with 2θ being the scattering angle with respect to the incident beam and λ the wavelength of the X-rays.

Samples were filled into a 1mm (diameter) reusable quartz capillary with vacuum-tight sealing screw-caps at both ends. All measurements - of the sample and blank - were done in with the capillary in vacuum and at 20 °C, with an exposure time of 10 min each. The scattering of the blank (dodecane) were subtracted from the scattering of the samples (dispersed in dodecane, concentration= 0.2 mM) after normalizing both spectra to same transmission.

Background corrected scattering data of the samples were analyzed applying the Indirect Fourier Transformation method, which evaluates the particle distance distribution function p(r) in real space by using the program GIFT.^{145,146}

12.2.15 Melting point

Melting point determination was carried out on melting point apparatus with microscope from Mueller Optronic equipped with JM628 digital thermometer with Pt-100 thermocouple.

12.3 Other equipment

12.3.1 Tube furnace

Synthesis of indium catalyzed nanowires was performed with LOSA model tube furnace from HTM Reetz GmbH which was tilted 90 degree to place a Schlenk tube vertically inside it.

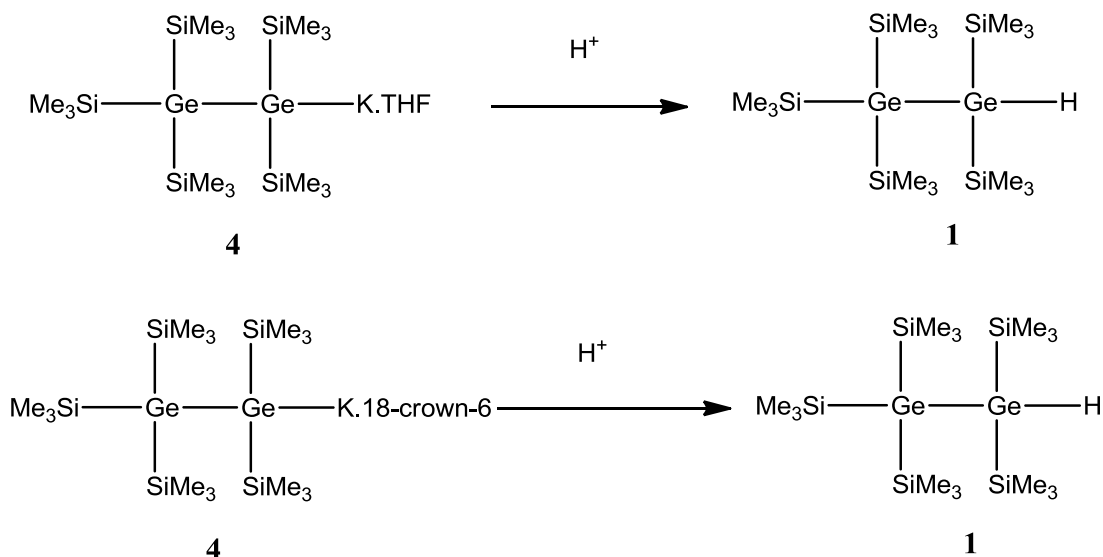
12.3.2 Centrifuge

Germanium nanowires were separated from liquid phase via Avanti J-20XP centrifuge from Beckman Coulter.

Germanium nanoparticles were separated from liquid phase via 5415C centrifuge from Eppendorf.

12.4 Synthesis of chemical compounds

12.4.1 Pentakis(trimethylsilyl)digermane (1)



1. A mixture of 100 mg (0.171 mmol) of hexakis(trimethylsilyl)digermane (**6**) and 20 mg (0.178 mmol) of KO^tBu and 47 mg (0.178 mmol) of 18-crown-6 was added to 1 mL of benzene and stirred for 90 minutes. Afterwards the obtained orange solution of oligosilylgermylpotassium was checked with NMR spectroscopy. Then the oligosilylgermylpotassium solution was added dropwise during 10 seconds to a mixture of 5 mL of degassed diethylether and 20 mL of 2M sulfuric acid under vigorous stirring.
2. A mixture of 100 mg (0.171 mmol) of hexakis(trimethylsilyl)digermane (**6**) and 20 mg (0.178 mmol) of KO^tBu was added to 1 mL of THF and stirred for 2 hours. Afterwards the obtained orange solution of oligosilylgermylpotassium was checked with NMR spectroscopy. Then the oligosilylgermylpotassium solution was added dropwise during 10 seconds to a flask containing 5 mL of degassed diethylether and 20 mL of degassed 2 M sulfuric acid under vigorous stirring.

In both experiments after 5 minutes the organic phase was transferred with cannula to another flask containing sodium sulfate to dry the organic phase. Afterwards the organic phase was transferred with cannula to another flask. After removal of the volatile colorless greasy **1** (79 mg, 90%) was obtained.

NMR (δ in ppm):

¹H(C₆D₆): 2.49 (s, 1H, GeH); 0.37 (s, 18H); 0.36 (s, 27H).

¹³C(C₆D₆): 3.74 ((Me₃Si)₃Ge); 3.63 ((Me₃Si)₂Ge).

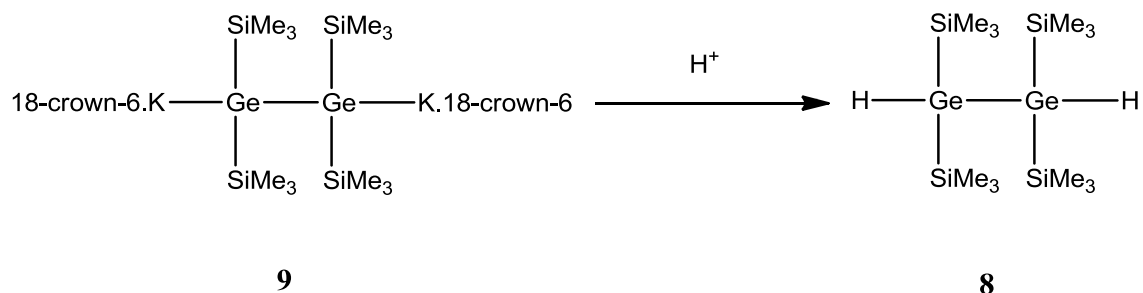
²⁹Si(C₆D₆): -4.9 ((Me₃Si)₃Ge); -5.7 ((Me₃Si)₂Ge).

MS (70eV) m/z (%):

512(2)[M-H₂]; 439 (4)[C₁₂H₃₅Ge₂Si₄⁺]; 364(17)[C₉H₂₄Ge₂Si₃⁺]; 293(9)[C₆H₁₇Ge₂Si₂⁺]; 220(9)[GeSi₂Me₆⁺]; 207(57)[C₅H₁₇GeSi₂⁺]; 131(9) [C₂H₅GeSi⁺]; 73(100)[SiMe₃⁺].

Elemental analysis: Calculated for: C₁₅H₄₆Ge₂Si₅: C, 35.17; H, 9.05. Found: C, 35.88; H, 8.81.

12.4.2 1,1,2,2-Tetrakis(trimethylsilyl)digermane (**8**)



A mixture of 100 mg (0.171 mmol) of hexakis(trimethylsilyl)digermane (**6**) and 40 mg (0.359 mmol) of KO^tBu and 94 mg (0.359 mmol) of 18-crown-6 was added to 1 mL of benzene and stirred for 4 hours. Slowly red crystals of oligosilylgermyldipotassium precipitated from the solution mixture. After decantation, pure crystals were dissolved in benzene and the solution mixture was added dropwise during 10 seconds to an ice cooled flask containing 5 mL of dry diethylether and 20 mL of degassed 2 M sulfuric acid. After 5 minutes the organic phase was transferred with cannula to another flask contained sodium sulfate to dry the organic phase. Then the organic phase was transferred with a cannula to another flask. After removal of the volatile colorless greasy **8** (53 mg, 70%) was obtained.

NMR (δ in ppm):

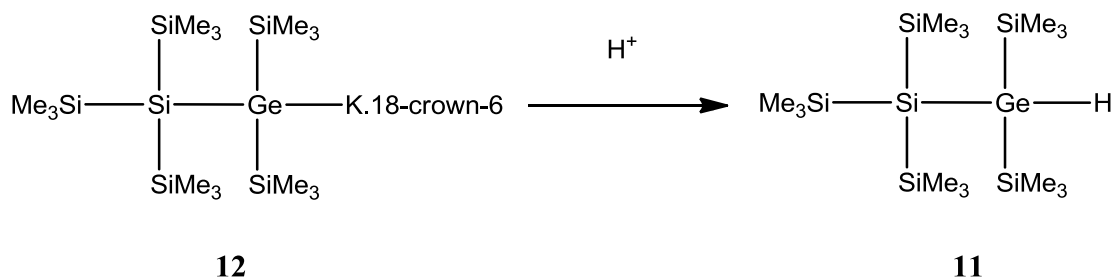
$^1\text{H}(\text{C}_6\text{D}_6)$: 2.46 (s, 2H, Ge**H**); 0.33 (s, 36H, (**CH**₃)₃Si).

$^{13}\text{C}(\text{C}_6\text{D}_6)$: 2.32 (**Me**₃Si).

$^{29}\text{Si}(\text{C}_6\text{D}_6)$: -5.7 (**Me**₃**Si**).

Elemental analysis: Calculated for: C₁₂H₃₈Ge₂Si₄: C, 32.75; H, 8.70. Found: C,34.39; H,8.66.

12.4.3 Bis(trimethylsilyl)[tris(trimethylsilyl)silyl]germane (**11**)



A mixture of 100 mg (0.185 mmol) of tris(trimethylsilyl)[tris(trimethylsilyl)silyl]germane and 22 mg (0.194 mmol) KO^tBu and 52 mg (0.194 mmol) of 18-crown-6 was dissolved in 1 mL of benzene and stirred for 90 minutes. After which the conversion was quantitative according to NMR spectroscopy, the orange solution of oligosilylgermylpotassium was added dropwise during 10 seconds to a flask containing 5 mL of dry diethylether and 20 mL of degassed 2 M sulfuric acid. After 5 minutes the organic phase was transferred with cannula to another flask contained sodium sulfate to dry the organic phase. Then the organic phase transferred with cannula to another flask. After removal of the volatile colorless greasy **11** (67 mg, 77%) was obtained.

NMR (δ in ppm):

$^1\text{H}(\text{C}_6\text{D}_6)$: 2.32 (s, 1H, GeH); 0.36 (s, 18H, (CH₃)₃Si-Ge); 0.32 (s, 27H, (CH₃)₃Si-Si).

$^{13}\text{C}(\text{C}_6\text{D}_6)$: 3.78 (Me₃Si-Ge); 3.18 (Me₃Si-Si).

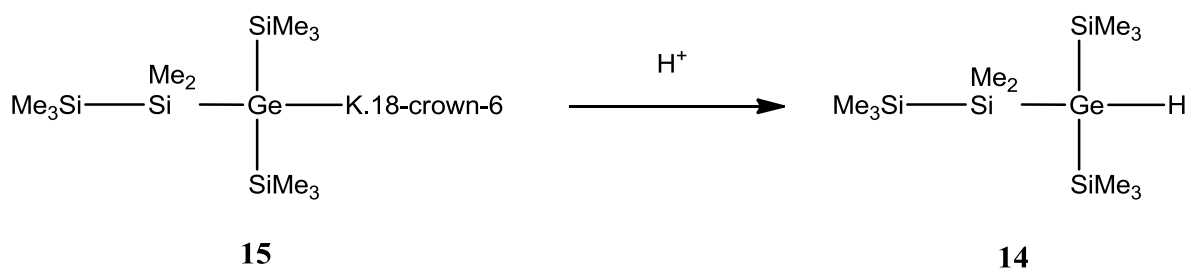
$^{29}\text{Si}(\text{C}_6\text{D}_6)$: -5.5 (Me₃Si-Ge); -9.9 (Me₃Si-Si); -123.4 (Me₃Si-Si).

MS (70eV) m/z (%):

394(31)[C₁₂H₃₆GeSi₅⁺]; 305(6)[C₈H₂₃GeSi₄⁺]; 245(15)[C₉H₂₅Si₄⁺]; 206(10)[C₅H₁₆GeSi₂⁺]; 171(14)[C₆H₁₅Si₃⁺]; 147(3)[GeSiMe₃⁺]; 73(100)[SiMe₃⁺].

Elemental analysis: Calculated for: C₁₅H₄₆GeSi₆: C, 38.52; H, 9.91. Found: C, 39.17; H, 9.78.

12.4.4 Bis(trimethylsilyl)pentamethyldisilanylgermane (14)



A mixture of 205 mg (0.484 mmol) of (pentamethyldisilyl)tris(trimethylsilyl)germane (**16**) with 57 mg (0.508 mmol, 1.05 eq) of KO^tBu and 134 mg (0.508 mmol, 1.05 eq) 18-crown-6 was dissolved in 2 mL of benzene and stirred for 2 hours. After which the conversion was quantitative according to NMR spectroscopy, the yellow solution of oligosilylgermylpotassium was added dropwise during 10 seconds to a flask containing 10 mL of dry diethylether and 20 mL of degassed 2 M sulfuric acid. After 5 minutes the organic phase was transferred with cannula to another flask contained sodium sulfate to dry the organic phase. Then the organic phase transferred with cannula to another flask. After removal of the volatile colorless greasy **14** (158 mg, 93%) was obtained.

NMR (δ in ppm):

¹H(C₆D₆): 2.21 (s, 1H, GeH); 0.35 (s, 6H, (CH₃)₂Si); 0.30 (s, 18H, (CH₃)₃Si-Ge); 0.18 (s, 9H, (CH₃)₃Si).

¹³C(C₆D₆): 3.05 (Me₃Si-Ge); -1.61 (Me₃Si); -1.66 (Me₂Si).

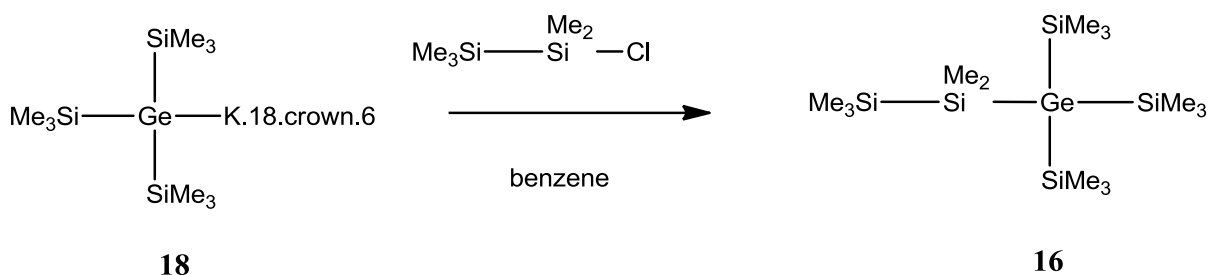
²⁹Si(C₆D₆): -5.7 (Me₃Si-Ge); -16.2 (Me₃Si); -34.4 (Me₂Si).

MS (70eV) m/z (%):

335(2)[GeSi₄C₁₀H₂₉⁺]; 278(27)[GeSi₃C₈H₂₄⁺]; 263(2)[GeSi₃C₇H₂₁⁺]; 218(2)[GeSi₂C₆H₁₆⁺];
 203(13)[GeSi₂C₅H₁₃⁺]; 189(10)[GeSi₂C₄H₁₁⁺]; 173(2)[GeSi₂C₃H₇⁺]; 159(2)[GeSi₂C₂H₅⁺];
 145(9)[GeSi₂CH₃⁺]; 131(24)[Si₂C₅H₁₅⁺]; 115(14)[Si₂C₄H₁₁⁺]; 99(4)[Si₂C₃H₇⁺];
 73(100)[SiMe₃⁺]; 59(8)[SiC₂H₇⁺].

Elemental analysis: Calculated for: C₁₁H₃₄GeSi₄: C, 37.60; H, 9.75. Found: C, 38.85; H, 9.41.

12.4.5 (Pentamethyldisilanyl)tris(trimethylsilyl)germane (16)



A mixture of 500 mg (1.368 mmol) of tetrakis(trimethylsilyl)germane (**7**) and 158 mg (1.409 mmol, 1.03 eq) of KO^tBu and 372 mg (1.409 mmol, 1.03 eq) of 18-crown-6 was dissolved in 3 mL of benzene and stirred for 3 hours. After NMR spectroscopy confirmed complete formation of oligosilylgermylpotassium, the yellow solution of the oligosilylgermylpotassium was added in 2 minutes to a solution of 251 mg (1.505 mmol, 1.1 eq) of chloropentamethyldisilane in 3 mL of benzene. After 5 hours the solution mixture was quenched with 1M sulfuric acid and the organic phase was extracted with pentane and dried over sodium sulfate. 508 mg crude compound was obtained after removal of organic phase by vacuum. Colorless crystals of **16** (423 mg, 73%) were obtained by crystallization from methanol/diethyleter 1:2.

Melting point: 128-155 °C.

NMR (δ in ppm):

¹H(C₆D₆): 0.35(s, 6H, (CH₃)₂Si); 0.30 (s, 27H, (CH₃)₃Si-Ge); 0.17 (s, 9H, (CH₃)₃Si).

¹³C(C₆D₆): 3.98 (Me₃Si-Ge); -0.38; -0.76.

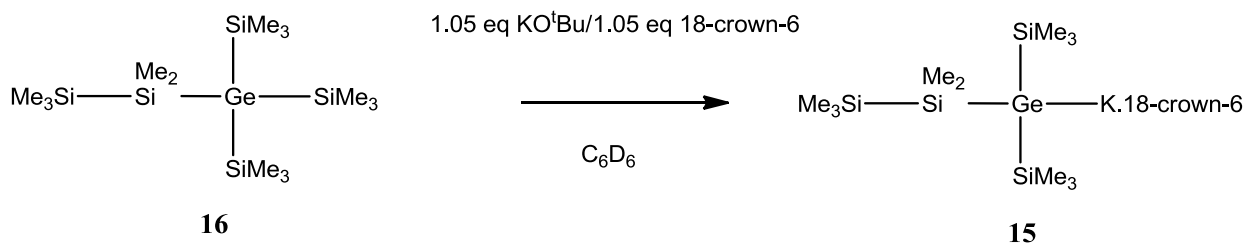
²⁹Si(C₆D₆): -5.2 (Me₃Si-Ge); -15.5 (Me₃Si); -34.0 (Me₂Si).

MS (70eV) m/z (%):

424(1)[M]; 408(1)[GeSi₅C₁₃H₃₈⁺]; 351(3)[M⁺-Me]; 332(2)[GeSi₄C₁₀H₂₆⁺]; 278(10)[M⁺-2SiMe₃]; 259(1)[GeSi₃C₇H₁₇⁺]; 243(1)[GeSi₃C₆H₁₃⁺]; 219(3)[GeSi₂C₆H₁₇⁺]; 203(11)[GeSi₂C₅H₁₃⁺]; 187(8)[GeSi₂C₄H₉⁺]; 171(7)[GeSi₂C₄H₉⁺]; 147(7)[GeSiC₃H₉⁺]; 131(35)[Si₂C₅H₁₅⁺]; 115(5)[Si₂C₄H₁₁⁺]; 99(2)[Si₂C₃H₇⁺]; 73(100)[SiMe₃⁺]; 57(4)[SiC₂H₅⁺].

Elemental analysis: Calculated for: C₁₄H₄₂GeSi₅: C, 39.70; H, 9.99. Found: C, 39.33; H, 9.50.

12.4.6 Bis(trimethylsilyl)pentamethyldisilanylgermyl-potassium.18-crown-6 (15)



A mixture of 205 mg (0.484 mmol) of (pentamethyldisilyl)tris(trimethylsilyl)germane (**16**) and 57 mg (0.508 mmol, 1.05 eq) of KO^tBu and 134 mg (0.508 mmol, 1.05 eq) 18-crown-6 was dissolved in 2 mL of C₆D₆. The solution color turned yellow immediately. After 2 hours the conversion was quantitative according to NMR spectroscopic analysis. Yield: (316 mg, 100%)

NMR (δ in ppm):

¹H(C₆D₆): 3.20 (s, 24H, CH₂O); 0.59 (s, 6H, (CH₃)₂Si); 0.53 (s, 18H, (CH₃)₃Si-Ge); 0.34 (s, 9H, (CH₃)₃Si).

¹³C(C₆D₆): 70.03 (CH₂O); 8.57 (Me₃Si-Ge); 3.49 (Me₃Si); 2.84 (Me₂Si).

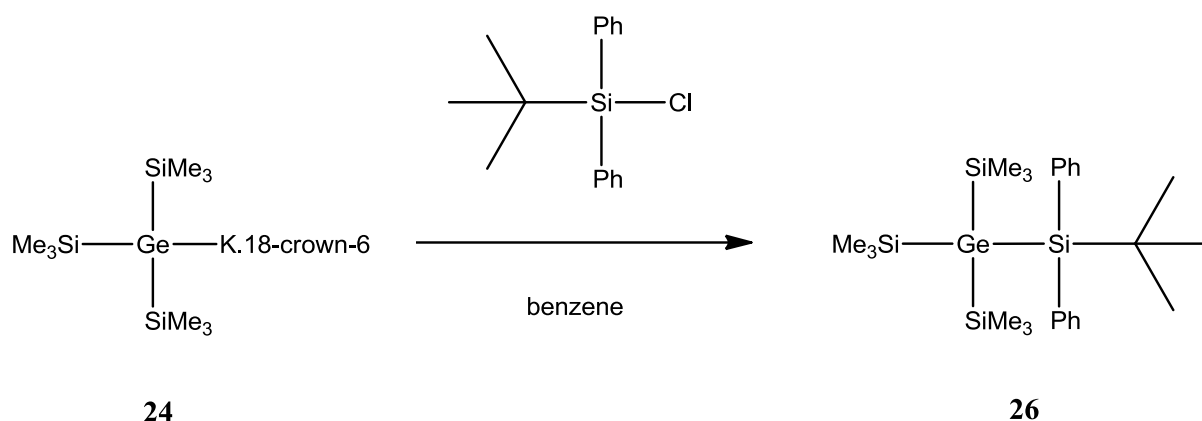
²⁹Si(C₆D₆): -3.4 (Me₃Si-Ge); -16.6 (Me₃Si); -33.0 (Me₂Si).

Ethylbromide derivatization:

MS (70eV) m/z (%):

380(1)[M]; 365(1)[M⁺-Me]; 350(3)[M⁺-Et]; 307(1)[M⁺-SiMe₃]; 292(1)[GeSi₃C₉H₂₆⁺];
 277(3)[GeSi₃C₈H₂₃⁺]; 262(1)[GeSi₃C₇H₂₀⁺]; 234(3)[GeSi₂C₇H₂₀⁺]; 219(8)[GeSi₂C₆H₁₇⁺];
 203(17)[GeSi₂C₅H₁₃⁺]; 187(6)[GeSi₂C₄H₉⁺]; 173(5)[GeSi₂C₃H₇⁺]; 159(4)[GeSiC₄H₉⁺];
 145(10)[GeSiC₃H₇⁺]; 131(33)[GeSiC₂H₅⁺]; 115(9)[GeSiCH⁺]; 73(100)[SiMe₃⁺];
 59(6)[SiC₂H₇⁺].

12.4.7 (*tert*-Butyldiphenylsilyl)tris(trimethylsilyl)germane (**26**)



A mixture of 500 mg (1.37 mmol) of tetrakis(trimethylsilyl)germane (**7**), 161 mg (1.43 mmol) of KO^tBu and 379 mg (1.43 mmol) of 18-crown-6 was dissolved in 4 mL of benzene. After 2 hours the yellow solution mixture was added dropwise over 1 hour to a solution of 412 mg (1.50 mmol) of *tert*-butylchlorodiphenylsilane in 10 mL of benzene at room temperature. The reaction mixture was stirred for another 2 hours. Afterwards the reaction mixture was quenched with 1M sulfuric acid and the aqueous layer was extracted with pentane and the combined organic phases were dried over sodium sulfate. 580 mg of a crude product was obtained after removal of solvent. Colorless crystals of **26** (325 mg, 44%) were obtained by crystallization from acetone.

Melting point: 346-358 °C.

NMR (δ in ppm):

$^1\text{H}(\text{CDCl}_3)$: 7.64 to 7.62 (m, 4H, *Ar*); 7.36 to 7.28 (m, 6H, *Ar*); 1.10 (s, 9H, (CH_3)₃-C); 0.15 (s, 27H, (CH_3)₃Si).

$^{13}\text{C}(\text{CDCl}_3)$: 137.53 (*ipso*); 136.98 (*ortho*); 128.62 (*para*); 127.21 (*meta*); 29.24 (*Me*₃-C); 20.23 (*Me*₃-C); 3.93 (*Me*₃Si).

$^{29}\text{Si}(\text{CDCl}_3)$: 7.9 (*t*-butyldiphenyl-Si); -4.7 (*Me*₃Si).

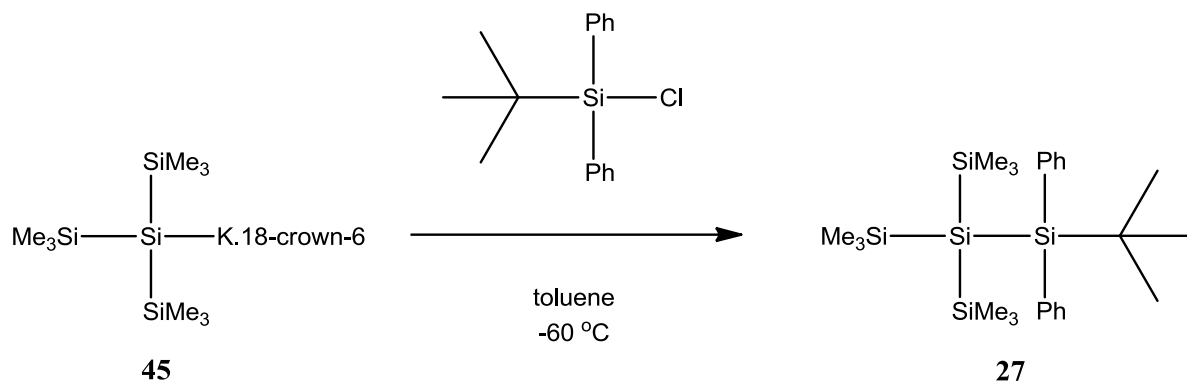
MS (70eV) *m/z* (%):

517(1)[*M*⁺-Me]; 475(19)[*M*⁺-*t*Bu]; 397(3)[C₁₅H₃₁GeSi₄⁺]; 278(26)[GeSi₃Me₈⁺];
 239(8)[*t*BuPh₂Si⁺]; 209(17)[C₁₄H₁₃Si⁺]; 197(31)[Ph₂SiMe⁺]; 135(100)[PhMe₂Si⁺];
 73(44)[SiMe₃⁺].

Elemental analysis: Calculated for: C₂₅H₄₆GeSi₄: C, 56.48; H, 8.72. Found: C, 56.70; H, 8.47.

Absorption: $\lambda = 240$ nm ($\epsilon = 1.33 \times 10^4$ M⁻¹cm⁻¹).

12.4.8 1-(*tert*-Butyl)-3,3,3-trimethyl-1,1-diphenyl-2,2-bis(trimethylsilyl)trisilane (**27**)



A mixture of 2.00 g (6.23 mmol) of tetrakis(trimethylsilyl)silane (**47**), 721 mg (6.41 mmol, 1.03 eq) of KO^tBu and 1.69 g (6.41 mmol, 1.03 eq) of 18-crown-6 was dissolved in 20 mL of toluene. After NMR showed complete formation of oligosilylpotassium, the orange solution of oligosilylpotassium was added dropwise to a -60 °C solution of 1.88 g (6.85 mmol, 1.1 eq) of *tert*-butylchlorodiphenylsilane in 10 mL of toluene. After final drop the reaction mixture was allowed to warm to room temperature and stirring was continued for another 6 hours. Afterwards the reaction mixture was quenched with 1M sulfuric acid and the aqueous layer was extracted with pentane and the combined organic phases were dried over sodium sulfate. 3.25 g of a crude product was obtained after removal of solvent. Colorless crystals of **27** (2.10 g, 69%) were obtained by crystallization from acetone.

Melting point: 342-355 °C.

NMR (δ in ppm):

¹H(CDCl₃): 7.66 to 7.62 (m, 4H, *Ar*); 7.38 to 7.29 (m, 6H, *Ar*); 1.10 (s, 9H, (CH₃)₃-C); 0.12 (s, 27H, (CH₃)₃Si).

¹³C(CDCl₃): 137.23 (*ipso*); 137.07 (*ortho*); 128.66 (*para*); 127.23 (*meta*); 29.37 (**Me**₃-C); 20.21 (**Me**₃-C); 3.57 (**Me**₃Si).

²⁹Si(CDCl₃): 3.7 (*t*-butyldiphenyl-Si); -9.4 (**Me**₃Si); -134.1 ((**Me**₃Si)₃Si).

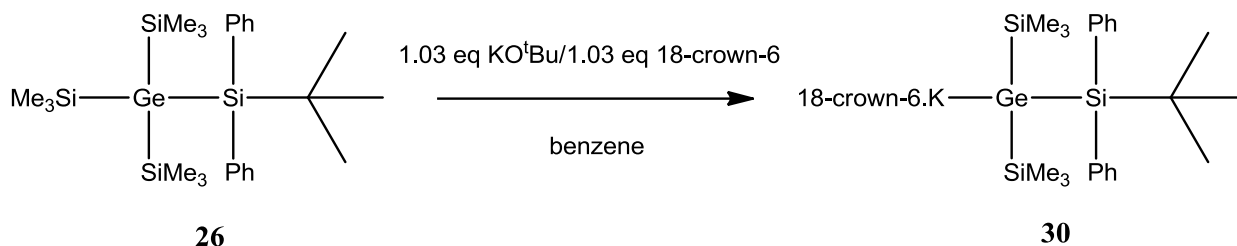
MS (70eV) m/z (%):

471(2)[M⁺-Me]; 429(73)[M⁺-^tBu]; 351(8)[C₁₅H₃₁Si₅⁺]; 281(14)[Ph₂Si₃C₃H₇⁺]; 232(26)[(SiMe₃)₂Si₂Me₂⁺]; 197(27)[Ph₂SiMe⁺]; 177 (10) [C₇H₉Si₃⁺]; 135(100)[PhMe₂Si⁺]; 73(55)[SiMe₃⁺].

Elemental analysis: Calculated for: C₂₅H₄₆Si₅: C, 61.65; H, 9.52. Found: C, 60.93; H, 9.38.

Absorption: $\lambda = 239$ nm ($\epsilon = 1.22 \times 10^4$ M⁻¹cm⁻¹).

12.4.9 ((*tert*-Butyldiphenylsilyl)bis(trimethylsilyl)germyl)potassium.18-crown-6 (30)



A mixture of 200 mg (0.37 mmol) of (*tert*-butyldiphenylsilyl)tris(trimethylsilyl)germane (**26**), 43 mg (0.39 mmol, 1.03 eq) of KO^tBu and 102 mg (0.39 mmol, 1.03 eq) of 18-crown-6 was dissolved in 2 mL of benzene without stirring the solution mixture. The solution color turned yellow immediately. Yellow crystals of the product precipitated from benzene after 14 hours. After decantation, clean product was put under vacuum to remove residual of benzene. The dried crystals were dissolved in C₆D₆ and subjected to NMR spectroscopic analysis.

NMR (δ in ppm):

¹H(C₆D₆): 8.22 to 8.19 (d, 4H, *Ar*); 7.34 to 7.23 (m, 6H, *Ar*); 3.14 (s, 24H, CH₂O); 1.53 (s, 9H, (CH₃)₃-C); 0.56 (s, 18H, (CH₃)₂Si).

¹³C(C₆D₆): 146.08 (*ipso*); 137.90 (*ortho*); 126.68 (*para*); 126.66 (*meta*); 69.99 (CH₂O); 30.89 (Me₃-C); 20.79 (Me₃-C); 8.24 (Me₃Si).

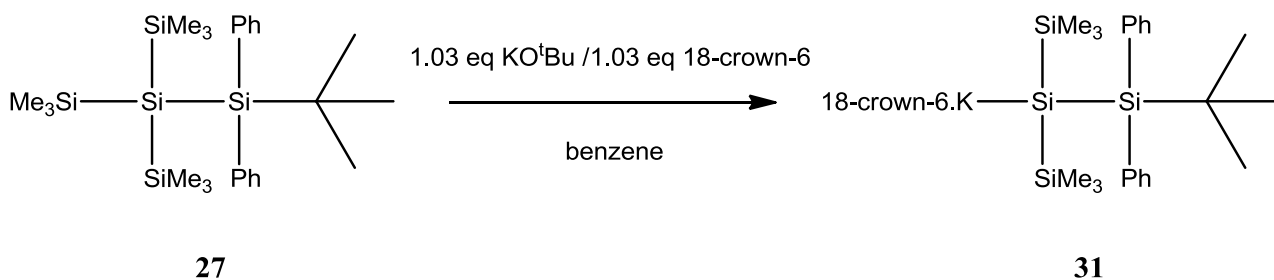
²⁹Si(C₆D₆): 14.4 (*t*-butyldiphenyl-Si); -5.1 (Me₃Si).

Ethylbromide derivatization:

MS (70eV) m/z (%):

488(1)[M]; 459(2)[M⁺-Et]; 431(24)[M⁺-^tBu]; 327(4)[C₁₂H₂₅GeSi₃⁺]; 267(6)[PhGeSi₂Me₄⁺]; 239(7)[^tBuPh₂Si⁺]; 219(4)[C₆H₁₇GeSi₂⁺]; 197(32)[C₁₃H₁₃Si⁺]; 177(30)[C₅H₁₅GeSi⁺]; 135(100)[PhMe₂Si⁺]; 73(38)[SiMe₃⁺].

12.4.10 2-*tert*-Butyl-2,2-diphenyl-1,1-bis(trimethylsilyl)disilanyl)potassium.18-crown-6 (31)



A mixture of 200 mg (0.41 mmol) of 1-(*tert*-butyl)-3,3,3-trimethyl-1,1-diphenyl-2,2-bis(trimethylsilyl)trisilane (**27**), 47 mg (0.42 mmol, 1.03 eq) of KO^{*t*}Bu and 112 mg (0.42 mmol, 1.03 eq) of 18-crown-6 was dissolved in 2 mL of benzene without stirring the solution mixture. The solution color turned yellow immediately. Yellow crystals of the product precipitated from benzene after 14 hours. After decantation, clean product was put under vacuum to remove residual of benzene. The dried crystals were dissolved in C₆D₆ and subjected to NMR spectroscopic analysis.

NMR (δ in ppm):

¹H(C₆D₆): 8.22 to 8.20 (d, 4H, *Ar*); 7.34 to 7.26 (m, 6H, *Ar*); 3.13 (s, 24H, CH₂O); 1.53 (s, 9H, (CH₃)₃-C); 0.54 (s, 18H, (CH₃)₂Si).

¹³C(C₆D₆): 145.85 (*ipso*); 137.98 (*ortho*); 126.71 (*para*); 126.63 (*meta*); 69.95 (CH₂O); 30.95 (Me₃-C); 20.75 (Me₃-C); 8.08 (Me₃Si).

²⁹Si(C₆D₆): 12.7 (*t*-butyldiphenyl-Si); -6.4 (Me₃Si); -186.1 ((Me₃Si)₂Si).

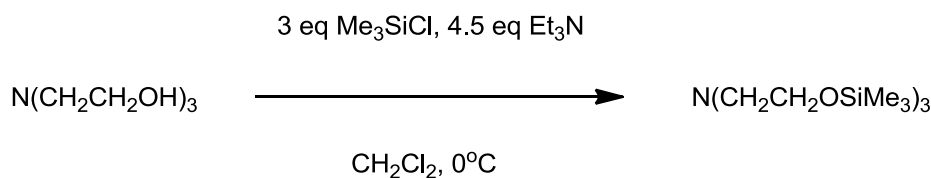
Ethylbromide derivatization:

MS (70eV) m/z (%):

385(89)[M⁺-^{*t*}Bu]; 357(14)[C₁₈H₂₉Si₄⁺]; 281(7)[Ph₂Si₃C₃H₇⁺]; 239(7)[Ph₂Si₃H⁺]; 197(35)[Ph₂SiMe⁺]; 177 (11) [C₇H₉Si₃⁺]; 135(100)[PhMe₂Si⁺]; 105(16)[PhSi⁺]; 73(37)[SiMe₃⁺]; 57(11)[^{*t*}Bu⁺].

12.5 Synthesis of oligosilanylsilatrane

12.5.1 Synthesis of N(CH₂CH₂OSiMe₃)₃ (**39**)



39

10.0 g (0.067 mol, 1 eq) of triethanolamine was dissolved in 100 mL of dichloromethane in 500 mL two neck flask under nitrogen. 30.0 g (0.301 mol, 4.5 eq) of triethylamine was added to the flask and the mixture was cooled down to 0 °C with ice bath. 25.5 g (0.234 mol, 3.5 eq) of trimethylchlorosilane was added dropwise to the flask via septum within 1 hour. Afterwards the ice bath was removed and the reaction mixture was left to come to room temperature while stirring. Then the reaction mixture was added slowly to 100 mL of water. The organic phase was separated from aqueous phase via separating funnel and the combined organic phase was dried over sodium sulfate. After removal of the volatile a pale yellow oil N(CH₂CH₂OSiMe₃)₃ (**39**) (18.0 g, 73%) was obtained.

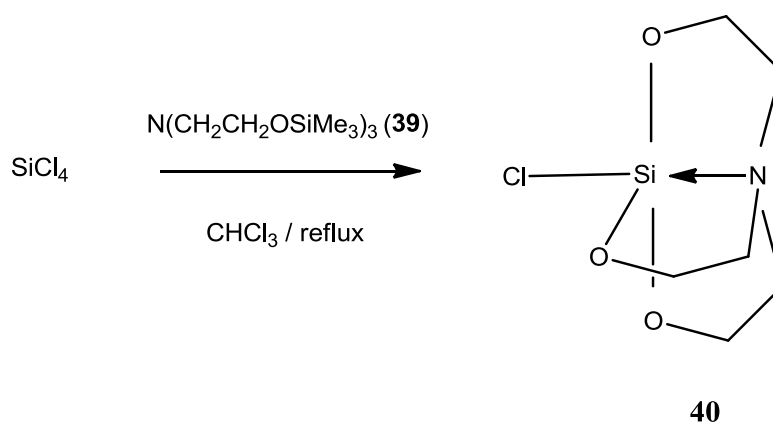
NMR (δ in ppm):

¹H(CDCl₃): 3.51 (t, J = 6.8 Hz, 6H, OCH₂); 2.59 (t, J =6.8 Hz, 6H, NCH₂); 0.00 (s, 27H, Si(CH₃)₃).

¹³C(CDCl₃): 61.05 (OCH₂); 57.59 (NCH₂); -0.69 (Me₃Si).

²⁹Si(CDCl₃): 17.6 (SiMe₃).

12.5.2 1-Chlorosilatrane⁷⁷ (**40**)



A mixture of 14.0 g (0.0383 mol) of $\text{N}(\text{CH}_2\text{CH}_2\text{OSiMe}_3)_3$ (**39**) and 7.0 g (0.0412 mol) of SiCl_4 was dissolved in 40 mL of chloroform in a 250 mL three neck flask equipped with condenser under nitrogen. The flask was left for 6 hours under reflux while stirring with stir bar. Afterwards the volatile was removed by vacuum and the residue put into frit funnel and washed with chloroform. 7.1 g of 1-chlorosilatrane (**40**) was obtained as a white powder.

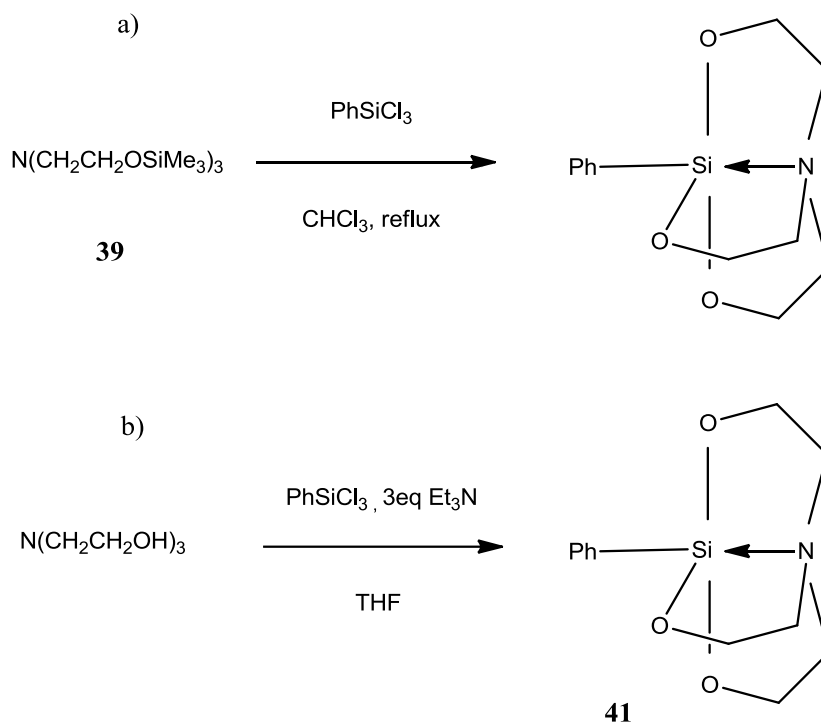
NMR (δ in ppm):

$^1\text{H}(\text{CDCl}_3)$: 3.97 (t, $J= 6.0$ Hz, 6H, OCH_2); 3.01 (t, $J= 6.0$ Hz, 6H, NCH_2).

$^{13}\text{C}(\text{CDCl}_3)$: 58.10 (OCH_2); 51.40 (NCH_2).

$^{29}\text{Si}(\text{CDCl}_3)$: -85.9 (SiCl).

12.5.3 Phenylsilatrane^{77,79} (**41**)



Procedure a:

A mixture of 20.0 g (0.0547 mol, 1 eq) of $\text{N}(\text{CH}_2\text{CH}_2\text{OSiMe}_3)_3$ (**39**) and 12.0 g (0.0567 mol, 1.04 eq) of PhSiCl_3 was dissolved in 50 mL of chloroform in a 250 mL three neck flask equipped with condenser under nitrogen. The flask was left for 6 hours under reflux while stirring with stir bar. Afterwards the volatile was removed by vacuum and the residue was dissolved in dichloromethane. Colorless crystals of **41** (6.0 g, 44%) was obtained from dichloromethane.

Procedure b:

A mixture of 2.82 g (0.0189 mol) triethanolamine and 5.74 g (0.0567 mol) of triethylamine in 10 mL of THF under nitrogen was cooled to 0 °C with ice bath. 4.00 g (0.0189 mol) of PhSiCl_3 was added dropwise to the solution mixture. Afterwards the ice bath was removed and the solution was left to come to room temperature. The reaction mixture which contains white precipitate of $[\text{Et}_3\text{NH}]^+\text{Cl}^-$ was passed through filter paper and the residue was washed with THF. After removal of the volatile white powder **41** (1.3 g, 27%) was obtained.

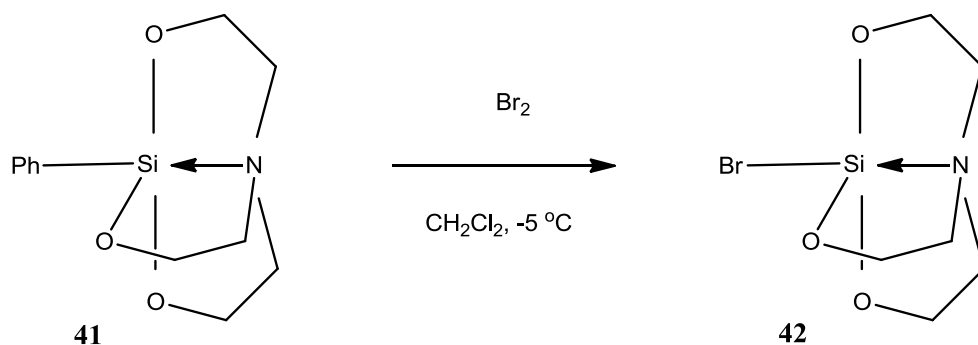
NMR (δ in ppm):

$^1\text{H}(\text{CDCl}_3)$: 7.74 to 7.22 (m, 5H, (**Ph**-Si)); 3.90 (t, $J= 5.8$ Hz, 6H, OCH_2); 2.92 (t, $J= 5.8$ Hz, 6H, NCH_2).

$^{13}\text{C}(\text{CDCl}_3)$: 142.30 (aryl); 134.00 (aryl); 127.40 (aryl); 126.90 (aryl); 57.60 (OCH_2); 50.80 (NCH_2).

$^{29}\text{Si}(\text{CDCl}_3)$: -80.4.

12.5.4 1-Bromosilatrane¹¹⁰ (42)



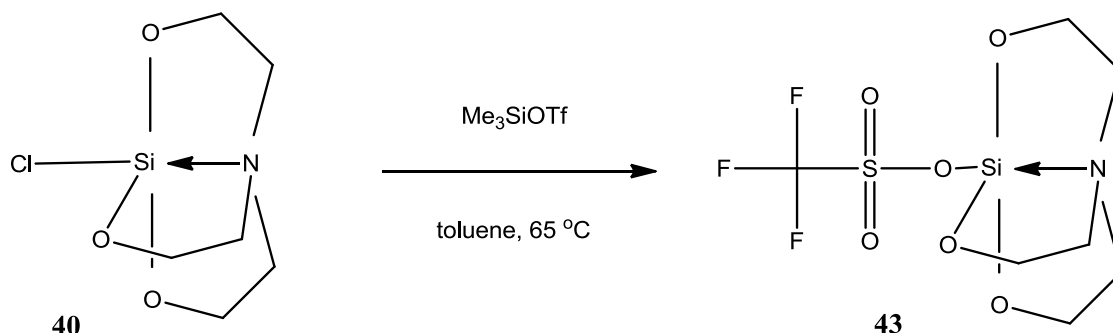
3.0 g (0.0119 mol, 1 eq) phenylsilatrane was dissolved in 15 mL of CH_2Cl_2 in a two neck flask equipped with a dropping funnel under nitrogen purging. The flask was cooled down to $-5\text{ }^\circ\text{C}$ and 2.0 g (0.0125 mol, 1.05 eq) of bromine in 10 mL of CH_2Cl_2 in dropping funnel was added dropwise to the flask over 90 minutes. Afterward the reaction mixture left to come to room temperature while stirring. After removal of the volatile yellow air sensitive powder **42** (3.4 g) was obtained.

NMR (δ in ppm):

^1H (DMSO- d_6): 3.78 (t, $J= 6.0$ Hz, 6H, OCH_2); 3.04 (t, $J= 6.0$ Hz, 6H, NCH_2).

^{29}Si (DMSO- d_6): -88.7 (SiBr).

12.5.5 1-Silatranyltriflate (43)



Slurry of 2.00 g (9.54 mmol, 1 eq) of 1-chlorosilatran (**40**) and 4.24 g (19.07 mmol, 2 eq) of trimethylsilyltrifluoromethanesulfonate in 1mL of toluene was heated for 72 hours at $65\text{ }^\circ\text{C}$ while stirring strongly with stir bar. Progress of reaction was monitored by ^1H NMR spectroscopic analysis of the peaks of trimethylsilyltriflate and the formed trimethylchlorosilane. After removal of the volatile white air sensitive powder **43** (2.92 g, 97%) was obtained.

NMR (δ in ppm):

^1H (DMSO- d_6): 3.84 (t, $J=5.9$ Hz, 6H, OCH_2); 3.13 (t, $J=5.9$ Hz, 6H, NCH_2).

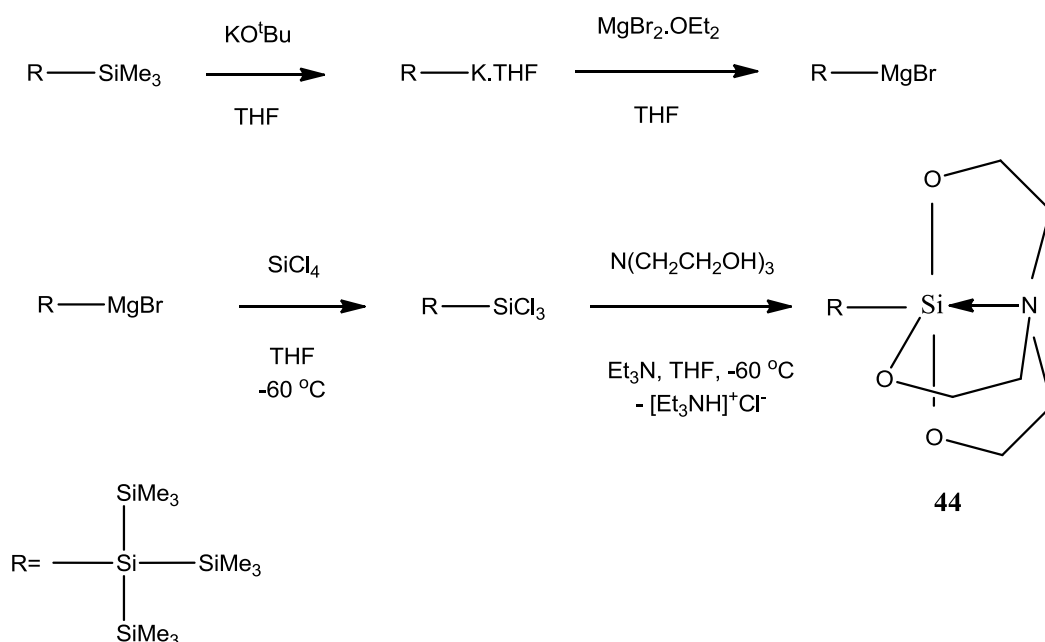
^{13}C (DMSO- d_6): 118.33 (q, $J_{\text{C-F}}=318$ Hz, CF_3); 57.52 (OCH_2); 50.69 (NCH_2).

^{29}Si (DMSO- d_6): -97.1.

^{19}F (DMSO- d_6): -77.45.

Elemental analysis: Calculated for: $\text{C}_7\text{H}_{12}\text{F}_3\text{NO}_6\text{SSi}$: C, 26.00; H, 3.74; N, 4.33; S, 9.92.
Found: C, 25.73; H, 2.54; N, 4.20; S, 9.69.

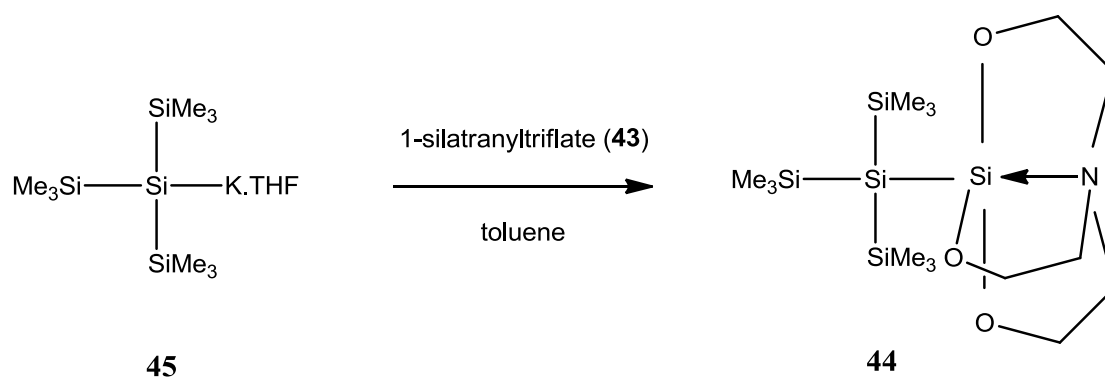
12.5.6 Tris(trimethylsilyl)silatranyl silane (**44**)



Route 1:

A mixture of 4.00 g (12.47 mmol, 1 eq) of tetrakis(trimethylsilyl)silane (**47**) with 1.47 g (12.84 mmol, 1.03 eq) of KO^tBu was dissolved in 20 mL of THF. The solution color turned orange immediately. After NMR spectroscopy confirmed formation of oligosilylpotassium, 1.66 g (6.42 mmol, 0.51 eq) of magnesium bromide ethyl etherate was added to the solution while stirring.

The oligosilylmagnesium solution in THF was added dropwise to the -60 °C solution of 4.24 g (24.93 mmol, 2 eq) of SiCl₄ in 10 mL of THF. The reaction mixture was left while stirring to come to 10 °C. Afterwards the solvent was removed by vacuum. The residue was dissolved in pentane and was transferred to another flask under nitrogen with cannula equipped with filter paper. After removal of pentane the product was dissolved in THF and was added dropwise to the solution mixture of 3.72 g (24.93 mmol, 2 eq) of triethanolamine and 7.57 g (74.8 mmol, 6 eq) of triethylamine in 15 mL of THF at -60 °C. The solution mixture was left while stirring to come to room temperature. Afterwards the volatiles were removed by vacuum and the residue was dissolved in pentane and filtered. Then the solution mixture was quenched with distilled water and afterwards the organic phase was separated by separating funnel and the combined organic phase was dried over sodium sulfate. After removal of the volatiles 2 g of crude compound was obtained. Colorless crystals of **44** (830 mg, 16%) was obtained from *n*-hexane.



Route2:

A mixture of 2.000 g (6.23 mmol, 1 eq) of tetrakis(trimethylsilyl)silane (**47**) with 734 mg (6.54 mmol, 1.05 eq) of KO^tBu was dissolved in 6 mL of THF. The solution color turned orange immediately. After NMR spectroscopy confirmed formation of oligosilyl potassium, THF was removed by putting the sample under vacuum. Afterwards the oligosilyl potassium was dissolved in 6 mL of toluene and was added dropwise over 2 hours to the slurry of 2.217 g (6.85 mmol, 1.1 eq) of 1-silatranyl triflate (**43**) in 2 mL of toluene while stirring. After 12 hours the solution mixture was filtered and the filter paper was washed with pentane. After removal of the volatiles 2.2 g of crude compound was obtained. After sublimation at 40 °C at 1 mbar 2.0 g of solid compound was obtained. Colorless crystals of **44** (1.35 g, 51%) was obtained from *n*-hexane.

Melting point: 144-146 °C.

NMR (δ in ppm):

$^1\text{H}(\text{CDCl}_3)$: 3.65 (t, $J=5.6$ Hz, 6H, OCH_2); 2.72 (t, $J=5.6$ Hz, 6H, NCH_2); 0.15 (s, 27H, $(\text{CH}_3)_3\text{Si}$).

$^{13}\text{C}(\text{CDCl}_3)$: 58.56 (OCH_2); 52.15 (NCH_2); 2.20 ($\text{Me}_3\text{Si-Si}$).

$^{29}\text{Si}(\text{CDCl}_3)$: -9.9 (Me_3Si); -52.6 (SiO_3); -133.9 ($(\text{Me}_3\text{Si})_3\text{Si}$).

$^1\text{H}(\text{C}_6\text{D}_6)$: 3.30 (t, $J=5.6$ Hz, 6H, OCH_2); 1.83 (t, $J=5.6$ Hz, 6H, NCH_2); 0.53 (s, 27H, $(\text{CH}_3)_3\text{Si}$).

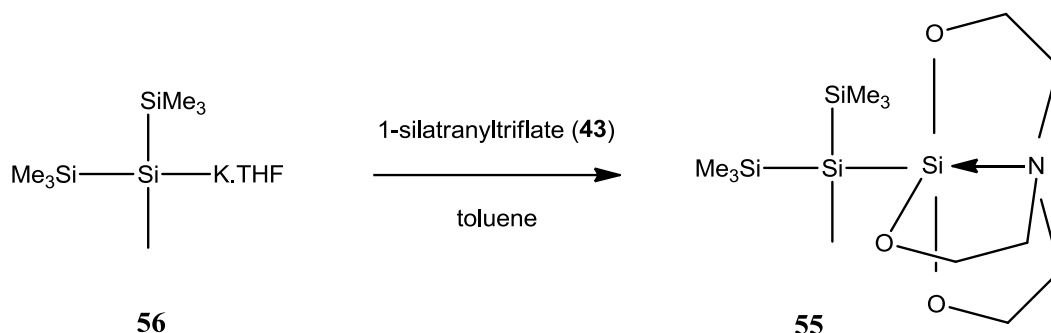
$^{13}\text{C}(\text{C}_6\text{D}_6)$: 58.55 (OCH_2); 51.53 (NCH_2); 2.77 ($\text{Me}_3\text{Si-Si}$).

MS (70eV) m/z (%):

423(3)[$\text{M}^+ + \text{H}$]; 406(4)[$\text{M}^+ - \text{Me}$]; 278(3)[$(\text{SiMe}_3)_3\text{SiSiH}_3^+$]; 249(1)[$(\text{SiMe}_3)_3\text{SiH}$]; 232(2)[Si_4Me_8^+]; 174(100)[$\text{N}(\text{CH}_2\text{CH}_2\text{O})_3\text{Si}^+$]; 147(1)[$\text{N}(\text{CH}_2\text{CH}_2\text{O})_3^+$]; 73(13)[SiMe_3^+].

Elemental analysis: Calculated for: $\text{C}_{15}\text{H}_{39}\text{NO}_3\text{Si}_5$: C, 42.70; H, 9.32; N, 3.32. Found: C, 43.29; H, 8.62; N, 3.25.

12.5.7 Bis(trimethylsilyl)methylsilatranyl silane (**55**)



A mixture of 1.500 g (5.70 mmol, 1 eq) of methyltris(trimethylsilyl)silane with 672 mg (5.98 mmol, 1.05 eq) of KO^tBu was dissolved in 5 mL of THF. The solution color turned orange immediately. After NMR spectroscopy confirmed formation of oligosilyl potassium, THF was removed by putting the sample under vacuum. Afterwards the oligosilyl potassium was dissolved in 5 mL of toluene and was added dropwise over 2 hours to the slurry of 2.027 g (6.27 mmol, 1.1 eq) of 1-silatranyl triflate (**43**) in 2 mL of toluene while stirring. After 12 hours the solution mixture was filtered and the filter paper was washed with pentane. After removal of the volatiles 1.50 g of crude compound was obtained. After sublimation at 34 °C at 1 mbar 1.40 g of solid compound was obtained. Colorless crystals of **55** (1.155 g, 75%) was obtained from *n*-hexane.

Melting point: 109-111 °C.

NMR (δ in ppm):

¹H(CDCl₃): 3.69 (t, *J*=5.6 Hz, 6H, OCH₂); 2.74 (t, *J*=5.6 Hz, 6H, NCH₂); 0.09 (s, 18H, ((CH₃)₃Si)₂-Si); 0.03 (s, 3H, (CH₃)Si).

¹³C(CDCl₃): 58.33 (OCH₂); 51.79 (NCH₂); -0.03 ((Me₃Si)₂-Si); -12.66 (MeSi).

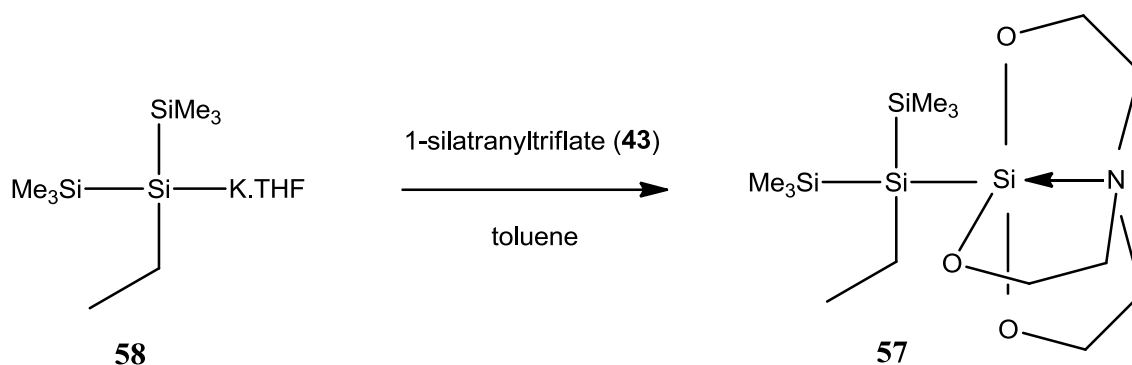
²⁹Si(CDCl₃): -12.9 (Me₃Si); -57.8 (SiO₃); -88.0 ((Me₃Si)₂Si).

MS (70eV) *m/z* (%):

364(4)[M]; 348(5)[M⁺-Me]; 309(39)[Me(SiMe₃)₂SiSiO₃C₃H₈⁺];
 294(13)[Me(SiMe₃)₂SiSiO₃C₂H₅⁺]; 279(10)[Me(SiMe₃)₂SiSiO₃CH₂⁺];
 260(3)[N(CH₂CH₂O)₃SiSi₂Me₂⁺]; 193(5)[Me₄Si₃O₃H⁺]; 174(100)[N(CH₂CH₂O)₃Si⁺];
 132(3)[Si₃O₃⁺]; 73(9)[SiMe₃⁺].

Elemental analysis: Calculated for: C₁₃H₃₃NO₃Si₄: C, 42.93; H, 9.14; N, 3.85. Found: C, 43.20; H, 8.56; N, 3.72.

12.5.8 Bis(trimethylsilyl)ethylsilatranyl silane (**57**)



A mixture of 600 mg (2.17 mmol, 1 eq) of ethyltris(trimethylsilyl)silane with 255 mg (2.27 mmol, 1.05 eq) of KO^tBu was dissolved in 2 mL of THF. The solution color turned orange immediately. After NMR spectroscopy confirmed formation of oligosilyl potassium, THF was removed by putting the sample under vacuum. Afterwards the oligosilyl potassium was dissolved in 2 mL of toluene and was added dropwise over 3 hours to the slurry of 772 mg (2.39 mmol, 1.1 eq) of 1-silatranyl triflate (**43**) in 1 mL of toluene while stirring. After 12 hours the solution mixture was filtered and the filter paper was washed with pentane. After removal of the volatiles 560 mg of crude compound was obtained. After sublimation at 38 °C at 1 mbar 280 mg of solid compound was obtained. Colorless crystals of **57** (205 mg, 25%) was obtained from *n*-hexane.

Melting point: 109-111 °C.

NMR (δ in ppm):

¹H(CDCl₃): 3.66 (t, $J=5.6$ Hz, 6H, OCH₂); 2.71 (t, $J=5.6$ Hz, 6H, NCH₂); 1.05 (t, $J=7.9$ Hz, 3H); 0.72 (q, $J=7.3$ Hz, 2H); 0.10 (s, 18H, ((CH₃)₃Si)₂-Si).

¹³C(CDCl₃): 58.34 (OCH₂); 51.86 (NCH₂); 12.79 (CH₃-CH₂); 0.73 ((Me₃Si)₂-Si); -0.02 (CH₃-CH₂).

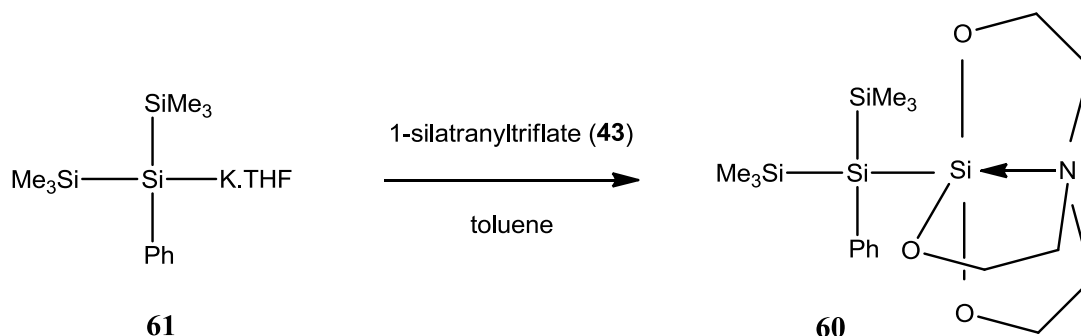
²⁹Si(CDCl₃): -13.2 (Me₃Si); -56.6 (SiO₃); -78.4 ((Me₃Si)₂Si).

MS (70eV) m/z (%):

377(5)[M]; 362(7)[M⁺-Me]; 309(13)[Et(SiMe₃)₂SiSiO₃C₂H₆⁺]; 294(4)[Et(SiMe₃)₂SiSiO₃CH₃⁺]; 279(3)[Et(SiMe₃)₂SiSiO₃⁺]; 193(3)[Me₄Si₃O₃H⁺]; 174(100)[N(CH₂CH₂O)₃Si⁺]; 130(3)[NC₆H₁₂O₂⁺]; 73(7)[SiMe₃⁺].

Elemental analysis: Calculated for: C₁₄H₃₅NO₃Si₄: C, 44.51; H, 9.34; N, 3.71. Found: C, 44.96; H, 9.08; N, 3.57.

12.5.9 Bis(trimethylsilyl)phenylsilatranyl silane (60)



A mixture of 2.000 g (6.158 mmol, 1 eq) of phenyltris(trimethylsilyl)silane with 712 mg (6.343 mmol, 1.03 eq) of KO^tBu was dissolved in 5 mL of THF. The solution color turned orange immediately. After NMR spectroscopy confirmed formation of oligosilyl potassium, THF was removed by putting the sample under vacuum.

Afterwards the oligosilyl potassium was dissolved in 5 mL of toluene and was added dropwise over 2 hours to the slurry of 2.190 g (6.774 mmol, 1.1 eq) of 1-silatranyl triflate (**43**) in 1 mL of toluene while stirring. After 12 hours the solution mixture was filtered and the filter paper was washed with pentane. After removal of the volatiles 1.80 g of crude compound was obtained. Colorless crystals of **60** (700 mg, 27%) was obtained from *n*-hexane.

Melting point: 161-163 °C.

NMR (δ in ppm):

^1H (CDCl_3): 7.66 to 7.64 (m, 2H); 7.26 to 7.20 (m, 3H); 3.75 (t, $J=5.6$ Hz, 6H, OCH_2); 2.76 (t, $J=5.6$ Hz, 6H, NCH_2); 0.17 (s, 18H, $(\text{CH}_3)_3\text{Si}$).

^{13}C (CDCl_3): 136.91 (*ortho*); 129.07 (*ipso*); 127.03 (*meta*); 126.40 (*para*); 58.14 (OCH_2); 51.62 (NCH_2); 0.54 ($\text{Me}_3\text{Si-Si}$).

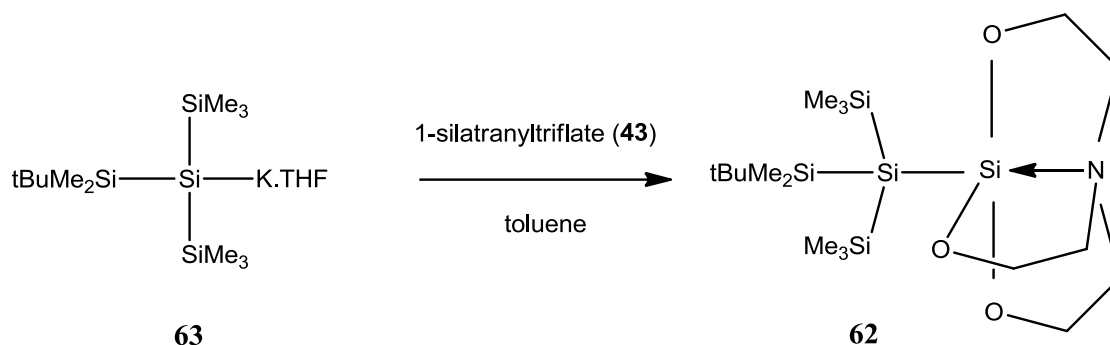
^{29}Si (CDCl_3): -13.1 (Me_3Si); -56.6 (SiO_3); -76.2 ($(\text{Me}_3\text{Si})_2\text{Si}$).

MS (70eV) m/z (%):

425(4)[M]; 410(4)[M^+-Me]; 352(2)[M^+-SiMe_3]; 309(11)[$(\text{SiMe}_3)_2\text{SiSiO}_3\text{C}_4\text{H}_{11}^+$];
279(3)[$(\text{SiMe}_3)_2\text{SiSiO}_3\text{C}_2\text{H}_5^+$]; 253(4)[$(\text{SiMe}_3)_2\text{SiSiO}_3\text{H}_3^+$]; 193(2)[$\text{Me}_4\text{Si}_3\text{O}_3\text{H}^+$];
174(100)[$\text{N}(\text{CH}_2\text{CH}_2\text{O})_3\text{Si}^+$]; 135(6)[$\text{Si}_3\text{O}_3\text{H}_3^+$]; 73(3)[SiMe_3^+].

Elemental analysis: Calculated for: $\text{C}_{18}\text{H}_{35}\text{NO}_3\text{Si}_4$: C, 50.77; H, 8.28; N, 3.29. Found: C, 49.84; H, 7.86; N, 3.19.

12.5.10 (*tert*-Butyldimethylsilyl)bis(trimethylsilyl)silatranylsilane (**62**)



A mixture of 500 mg (1.38 mmol, 1 eq) of (*tert*-butyldimethylsilyl)tris(trimethylsilyl)silane with 162 mg (1.45 mmol, 1.05 eq) of KO^tBu was dissolved in 2 mL of THF. The solution color turned orange immediately. After NMR spectroscopy confirmed formation of oligosilylpotassium, THF was removed by putting the sample under vacuum. Afterwards the oligosilylpotassium was dissolved in 2 mL of toluene and was added dropwise over 2 hours to the slurry of 490 mg (1.51 mmol, 1.1 eq) of 1-silatranyltriflate (**43**) in 1 mL of toluene while stirring. After 12 hours the solution mixture was filtered and the filter paper was washed with pentane. After removal of the volatiles 380 mg of crude compound was obtained. Colorless crystals of **62** (268 mg, 42%) was obtained from *n*-hexane.

Melting point: 124-126 °C.

NMR (δ in ppm):

¹H(CDCl₃): 3.65 (t, *J*=5.4 Hz, 6H, OCH₂); 2.72 (t, *J*=5.4 Hz, 6H, NCH₂); 0.93 (s, 9H, (CH₃)₃C); 0.18 (s, 18H, (CH₃)₂Si); 0.12 (s, 6H, (CH₃)₂Si).

¹³C(CDCl₃): 58.68 (OCH₂); 52.09(NCH₂); 27.98 (Me₃C); 18.43(Me₃C); 2.77((Me₃Si)₂-Si); -1.61 (Me₂Si-Si).

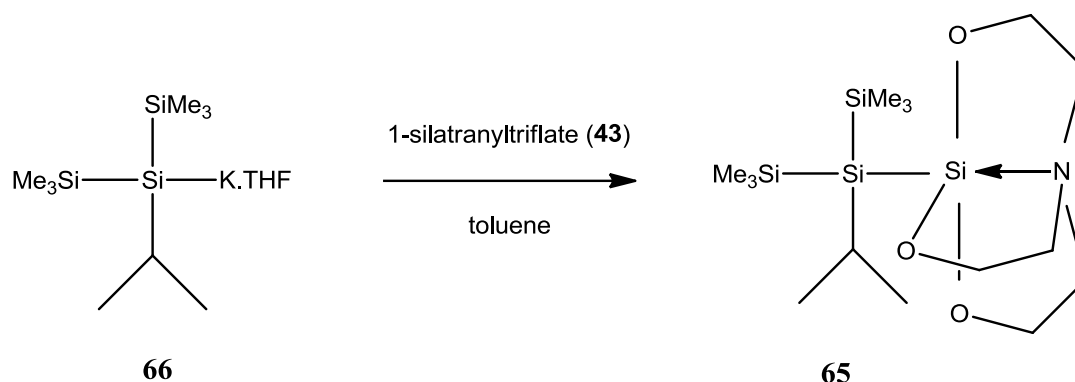
²⁹Si(CDCl₃): 4.0 (^tBuMe₂Si); -9.7 (Me₃Si); -51.5 (SiO₃); -136.8 ((Me₃Si)₂Si).

MS (70eV) *m/z* (%):

463(3)[M]; 448(8)[M⁺-Me]; 406(15)[M⁺-^tBu]; 290(2)[^tBuSi₄Me₈H]; 174(100)[N(CH₂CH₂O)₃Si⁺]; 73(10)[SiMe₃⁺].

Elemental analysis: Calculated for: C₁₈H₄₅NO₃Si₅: C, 46.60; H, 9.78; N, 3.02. Found: C, 46.78; H, 8.99; N, 3.05.

12.5.11 Bis(trimethylsilyl)isopropylsilatranyl silane (**65**)



A mixture of 500 mg (1.276 mmol, 1 eq) of isopropyltris(trimethylsilyl)silane with 147 mg (1.314 mmol, 1.03 eq) of KO^tBu was dissolved in 2 mL of THF. The solution color turned orange immediately. After NMR spectroscopy confirmed formation of oligosilyl potassium, THF was removed by putting the sample under vacuum. Afterwards the oligosilyl potassium was dissolved in 2 mL of toluene and was added dropwise over 2 hours to the slurry of 453 mg (1.404 mmol, 1.1 eq) of 1-silatranyl triflate (**43**) in 1 mL of toluene while stirring. After 12 hours the solution mixture was filtered and the filter paper was washed with pentane. After removal of the volatiles 420 mg of crude compound was obtained. Colorless crystals of **65** (283 mg, 56%) was obtained from *n*-hexane.

Melting point: 118-120 °C.

NMR (δ in ppm):

^1H (CDCl₃): 3.67 (t, $J=5.6$ Hz, 6H, OCH₂); 2.73 (t, $J=5.6$ Hz, 6H, NCH₂); 1.34 to 1.18 (m, 1H, Me₂CH); 1.12 (d, $J=6.4$ Hz, 6H, (CH₃)₂CH); 0.14 (s, 18H, (CH₃)₃Si).

^{13}C (CDCl₃): 58.48 (OCH₂); 52.03 (NCH₂); 23.30 (Me₂CH); 11.05 (Me₂CH); 1.40 (Me₃Si-Si).

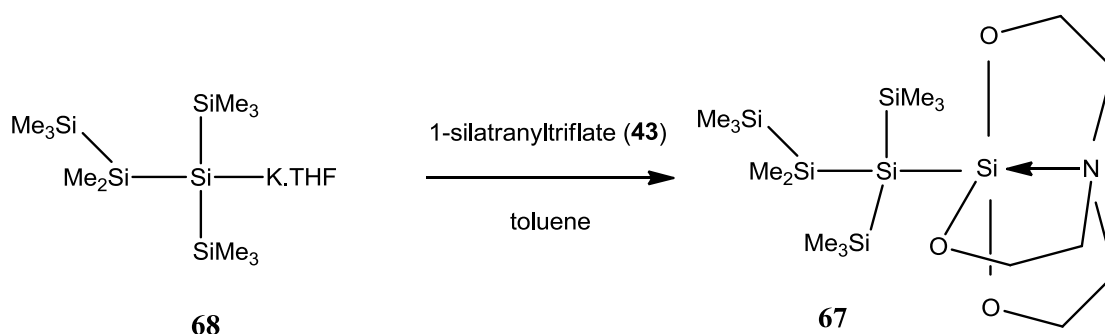
^{29}Si (CDCl₃): -13.5 (Me₃Si); -56.6 (SiO₃); -69.6 ((Me₃Si)₂Si).

MS (70eV) m/z (%):

391(5)[M]; 376(7)[M⁺-Me]; 202(2)[^tPrSi₃Me₅⁺]; 174(100)[N(CH₂CH₂O)₃Si⁺]; 130(2)[NC₆H₁₂O₂⁺]; 73(8)[SiMe₃⁺].

Elemental analysis: Calculated for: C₁₅H₃₇NO₃Si₄: C, 45.98; H, 9.52; N, 3.57. Found: C, 45.22; H, 8.89; N, 3.52.

12.5.12 1,1-Bis(trimethylsilyl)-1-silatranyl-pentamethyltrisilane (67)



A mixture of 435 mg (1.148 mmol, 1 eq) of 2,2-bis(trimethylsilyl)octamethyltetrasilane with 135 mg (1.205 mmol, 1.05 eq) of KO^tBu was dissolved in 2 mL of THF. The solution color turned yellow immediately. After NMR spectroscopy confirmed formation of oligosilylpotassium, THF was removed by putting the sample under vacuum. Afterwards the oligosilylpotassium was dissolved in 2 mL of toluene and was added dropwise over 2 hours to the slurry of 408 mg (1.262 mmol, 1.1 eq) of 1-silatranyltriflate (**43**) in 1 mL of toluene while stirring. After 12 hours the solution mixture was filtered and the filter paper was washed with pentane. After removal of the volatiles 530 mg of crude compound was obtained. Colorless crystals of **67** (320 mg, 58%) was obtained from a mixture of diethylether and acetonitrile 1:1.

Melting point: 78-79 °C.

NMR (δ in ppm):

¹H(CDCl₃): 3.66 (t, $J=5.6$ Hz, 6H, OCH₂); 2.73 (t, $J=5.6$ Hz, 6H, NCH₂); 0.19 (s, 6H, (CH₃)₂Si); 0.17 (s, 18H, ((CH₃)₃Si)₂Si); 0.09 (s, 9H, (CH₃)₃Si).

¹³C(CDCl₃): 58.41 (OCH₂); 51.85 (NCH₂); 2.60 ((Me₃Si)₂-Si); -1.24 (Me₃Si); -2.01 (Me₂Si).

²⁹Si(CDCl₃): -9.3 ((Me₃Si)₂Si); -15.0 (Me₃Si-SiMe₂); -40.0 (Me₃Si-SiMe₂); -54.0 (SiO₃); -132.2 ((Me₃Si)₂Si).

MS (70eV) m/z (%):

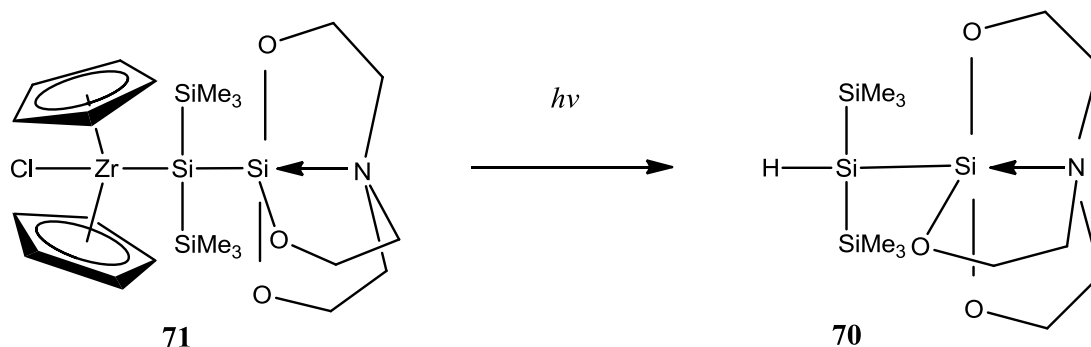
464(10)[M⁺-Me]; 406(100)[M⁺-SiMe₃]; 290(3)[Si₅C₁₀H₃₀⁺]; 174(50)[N(CH₂CH₂O)₃Si⁺];

131(3)[NC₆H₁₃O₂⁺]; 73(10)[SiMe₃⁺].

Elemental analysis: Calculated for: C₁₇H₄₅NO₃Si₆: C, 42.53; H, 9.45; N, 2.92. Found: C, 42.43; H, 8.94; N, 2.70.

UV absorption: $\lambda = 223$ nm ($\epsilon = 1.85 \times 10^4$ M⁻¹cm⁻¹).

12.5.13 Bis(trimethylsilyl)silatranylsilane (**70**)



A mixture of 100 mg (0.236 mmol, 1 eq) of tris(trimethylsilyl)silatranylsilane (**44**) and 27 mg (0.0247 mmol, 1.05 eq) of KO^tBu was dissolved in 1 mL of THF and left for 14 hours. The solution color turned orange immediately. After NMR spectroscopy confirmed formation of oligosilatranylsilylpotassium, THF was removed by putting the sample under vacuum. Afterwards the oligosilatranylsilylpotassium was dissolved in 2 mL of toluene and was added dropwise over 30 minutes to the slurry of 76 mg (0.260 mmol) of Cp₂ZrCl₂ in pentane while stirring. After complete decomposition of the product, volatiles were removed and the residue was dissolved in pentane and filtered with filter paper. Colorless crystals of **70** (53 mg, 64%) was obtained from pentane at -55 °C.

Melting point: 83-93 °C.

NMR (δ in ppm):

¹H(C₆D₆): 3.31 (t, $J=5.8$ Hz, 6H, OCH₂); 2.85 (s, 1H, SiH); 1.83 (t, $J=5.8$ Hz, 6H, NCH₂); 0.52 (s, 18H, (CH₃)₃Si).

¹³C(C₆D₆): 58.13 (OCH₂); 51.03 (NCH₂); 2.03 (Me₃Si-Si).

²⁹Si(C₆D₆): -12.0 (Me₃Si); -60.9 (SiO₃); -117.4 ((Me₃Si)₃Si).

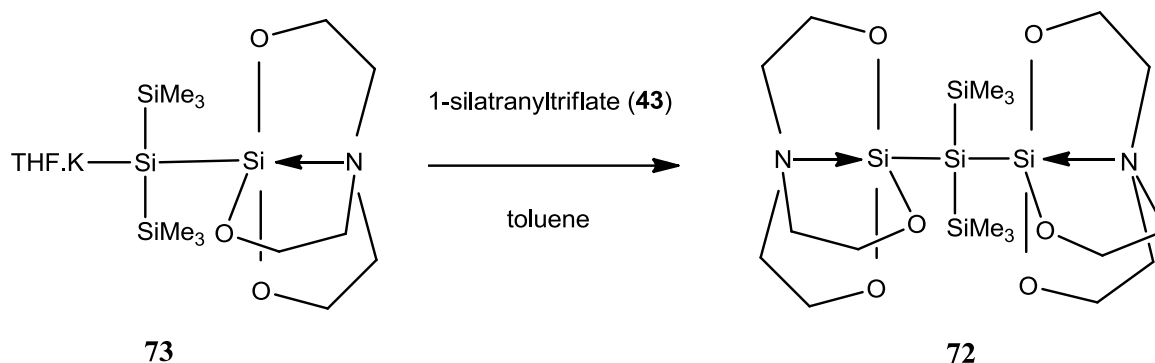
MS (70eV) m/z (%):

349(2)[M]; 334(7)[M⁺-Me]; 309(3)[(SiMe₃)₂SiSiO₃C₄H₁₁⁺]; 174(100)[N(CH₂CH₂O)₃Si⁺]; 131(2)[NC₆H₁₃O₂⁺]; 73(5)[SiMe₃⁺].

Elemental analysis: Calculated for: C₁₂H₃₁NO₃Si₄: C, 41.21; H, 8.93; N, 4.01. Found: C, 42.89; H, 8.15; N, 3.58.

IR (ATR, neat) $\nu_{\text{Si-H}} = 2044.84 \text{ cm}^{-1}$

12.5.14 Disilatranyl-bis(trimethylsilyl)silane (72)



A mixture of 310 mg (0.734 mmol, 1 eq) of tris(trimethylsilyl)silatranylsilane (**44**) and 85 mg (0.756 mmol, 1.03 eq) of KO^tBu was dissolved in 2 mL of THF and left for 14 hours. After NMR spectroscopy confirmed formation of oligosilatranylsilylpotassium in pale beige solution, THF was removed by putting the sample under vacuum. Afterwards the oligosilatranylsilylpotassium was dissolved in 2 mL of toluene and was added dropwise over 1 hour to the slurry of 261 mg (0.808 mmol, 1.1 eq) of 1-silatranyltriflate (**43**) in 0.5 mL of toluene while stirring. After 14 hours the solution mixture was filtered and the filter paper was washed with pentane and then the volatiles were removed with vacuum. Colorless crystals of **72** (90 mg, 23%) was obtained from pentane.

Melting point: 138-140 °C.

NMR (δ in ppm):

$^1\text{H}(\text{CDCl}_3)$: 3.68 (t, $J=5.4$ Hz, 12H, OCH_2); 2.71 (t, $J=5.4$ Hz, 12H, NCH_2); 0.17 (s, 18H, $(\text{CH}_3)_3\text{Si}$).

$^{13}\text{C}(\text{CDCl}_3)$: 59.38 (OCH_2); 52.71 (NCH_2); 1.72 ($\text{Me}_3\text{Si-Si}$).

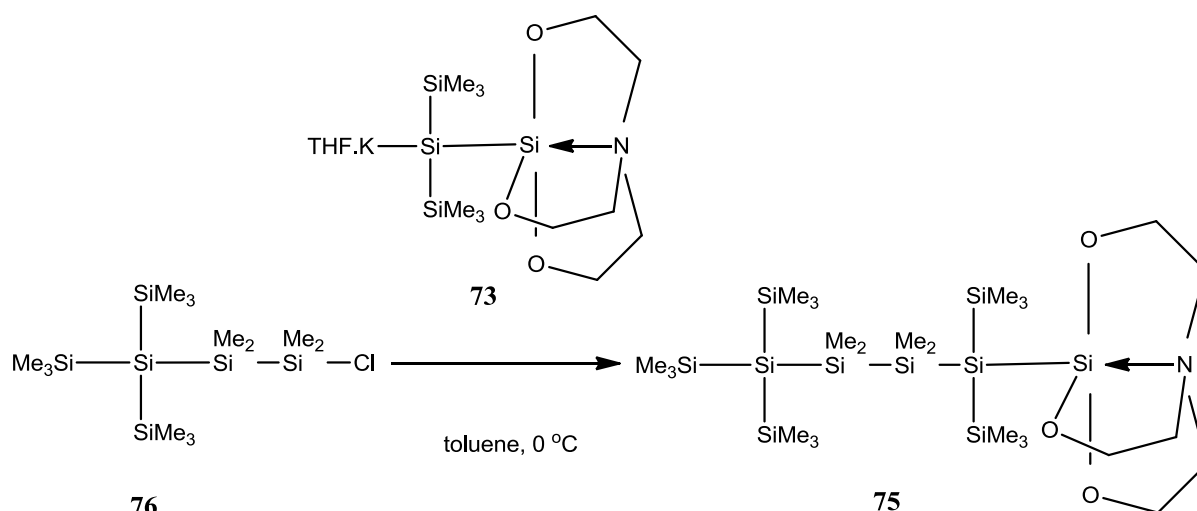
$^{29}\text{Si}(\text{CDCl}_3)$: -9.5 (Me_3Si); -46.8 (SiO_3); -135.5 ($(\text{Me}_3\text{Si})_2\text{Si}$).

MS (70eV) m/z (%):

522(3)[M]; 507(6)[M^+-Me]; 449(6)[M^+-SiMe_3]; 393(1)[$\text{N}(\text{CH}_2\text{CH}_2\text{O})_3\text{SiSi}_3\text{O}_3\text{C}_6\text{H}_{15}^+$];
 347(17)[$\text{N}(\text{CH}_2\text{CH}_2\text{O})_3\text{SiSi}_3\text{C}_6\text{H}_{17}^+$]; 309(13)[$(\text{SiMe}_3)_2\text{SiSiO}_3\text{C}_4\text{H}_{11}^+$];
 279(3)[$(\text{SiMe}_3)_2\text{SiSiO}_3\text{C}_2\text{H}_5^+$]; 248(3)[$\text{Si}_4\text{O}_3\text{C}_6\text{H}_{16}^+$]; 218(11)[$\text{Si}_4\text{O}_3\text{C}_4\text{H}_{10}^+$];
 174(100)[$\text{N}(\text{CH}_2\text{CH}_2\text{O})_3\text{Si}^+$]; 130(6)[$\text{NC}_6\text{H}_{12}\text{O}_2^+$]; 73(5)[SiMe_3^+].

Elemental analysis: Calculated for: $\text{C}_{18}\text{H}_{42}\text{N}_2\text{O}_6\text{Si}_5$: C, 41.34; H, 8.09; N, 5.36. Found: C, 42.56; H, 7.38; N, 5.28.

12.5.15 2-Silatranyl-2,5,5-tris(trimethylsilyl)decamethylhexasilane (75)



A mixture of 350 mg (0.751 mmol, 1 eq) of tris(trimethylsilyl)silatranylsilane (**44**) and 87 mg (0.774 mmol, 1.03 eq) of KO^tBu was dissolved in 2 mL of THF and left for 14 hours while stirring. After NMR spectroscopy confirmed formation of oligosilatranylsilylpotassium in pale beige solution, THF was removed by putting the sample under vacuum. Afterwards the oligosilatranylsilylpotassium was dissolved in 3 mL of benzene and was added dropwise over 1 hour to the ice cooled solution of 300 mg (0.751 mmol, 1 eq) of 1-chloro-3,3-bis(trimethylsilyl)heptamethyltetrasilane (**76**) in toluene. After 12 hours volatiles were removed by vacuum at 25 °C and the residue was dissolved in pentane and passed through filter paper. After removal of the volatiles 530 mg of crude compound was obtained. Colorless crystals of **75** (354 mg, 66%) was obtained from a mixture of diethylether and acetonitrile 1:1.

Melting point: 130-136 °C.

NMR (δ in ppm):

^1H (CDCl_3): 3.66 (t, $J=5.6$ Hz, 6H, OCH_2); 2.73 (t, $J=5.6$ Hz, 6H, NCH_2); 0.39 (s, 6H, $(\text{CH}_3)_2\text{Si}$); 0.35 (s, 6H, $(\text{CH}_3)_2\text{Si}$); 0.24 (s, 27H, $(\text{CH}_3)_3\text{Si-Si}$); 0.20 (s, 18H, $(\text{CH}_3)_2\text{Si-Si}$).

^{13}C (CDCl_3): 58.50 (OCH_2); 51.84 (NCH_2); 3.52 ($(\text{Me}_3\text{Si})_3\text{-Si}$); 2.97 ($(\text{Me}_3\text{Si})_2\text{-Si}$); 0.53 (Me_2Si); 0.40 (Me_2Si).

^{29}Si (CDCl_3): -9.2 ($(\text{Me}_3\text{Si})_2\text{Si}$); -9.6 ($(\text{Me}_3\text{Si})_3\text{Si}$); -30.6 ; -30.8; -53.8 (SiO_3); -128.6 ($(\text{Me}_3\text{Si})_3\text{Si}$); -129.3 ($(\text{Me}_3\text{Si})_2\text{Si}$).

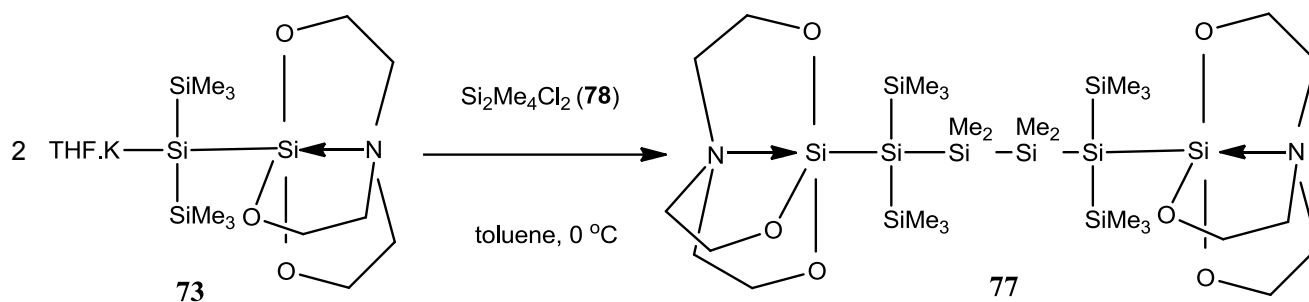
MS (70eV) m/z (%):

696(3)[$\text{M}^+ - \text{Me}$]; 638(1)[$\text{M}^+ - \text{SiMe}_3$]; 464(7)[$\text{M}^+ - \text{Si}(\text{SiMe}_3)_3$]; 406(100)[$\text{M}^+ - \text{Me}_2\text{SiSi}(\text{SiMe}_3)_3$]; 290(1)[$\text{Si}_5\text{C}_{10}\text{H}_{30}^+$]; 231(2)[$\text{Si}_4\text{C}_8\text{H}_{23}^+$]; 174(18)[$\text{N}(\text{CH}_2\text{CH}_2\text{O})_3\text{Si}^+$]; 131(2)[$\text{NC}_6\text{H}_{13}\text{O}_2^+$]; 73(5)[SiMe_3^+].

Elemental analysis: Calculated for: $\text{C}_{25}\text{H}_{69}\text{NO}_3\text{Si}_{10}$: C, 42.13; H, 9.76; N, 1.97. Found: C, 41.66; H, 9.65; N, 1.73.

UV absorption: $\lambda = 254$ nm ($\epsilon = 5.45 \times 10^4 \text{ M}^{-1}\text{cm}^{-1}$).

12.5.16 2,5-Disilatranyl-2,5-bis(trimethylsilyl)decamethylhexasilane (77)



A mixture of 500 mg (1.185 mmol, 1 eq) of tris(trimethylsilyl)silatranyl silane (**44**) and 137 mg (1.2206 mmol, 1.03 eq) of KO^tBu was dissolved in 3 mL of THF and left for 14 hours while stirring. After NMR spectroscopy confirmed formation of oligosilatranyl silyl potassium in pale beige solution, THF was removed by putting the sample under vacuum. Afterwards the oligosilatranyl silyl potassium was dissolved in 4 mL of benzene and was added dropwise over 1 hour to the ice cooled solution of 116 mg (0.622 mmol, 0.55 eq) of 1,2-dichlorotetramethyldisilane (**78**) in toluene. After 12 hours the volatile part was removed by vacuum at 25 °C and the residue was dissolved in benzene and filtered with filter paper. After removal of the volatiles 440 mg crude compound was obtained. Colorless crystals of **77** (200 mg, 41%) was obtained from a mixture of diethylether and acetonitrile 1:1.

Melting point: 244-248 °C.

NMR (δ in ppm):

$^1\text{H}(\text{C}_6\text{D}_6)$: 3.36 (t, $J=5.6$ Hz, 12H, OCH₂); 1.90 (t, $J=5.6$ Hz, 12H, NCH₂); 0.84 (s, 12H, (CH₃)₂Si); 0.61 (s, 36H, (CH₃)₃Si-Si).

$^{13}\text{C}(\text{C}_6\text{D}_6)$: 58.75 (OCH₂); 51.49 (NCH₂); 3.54 ((Me₃Si)₂-Si); 0.56 (Me₂Si).

$^{29}\text{Si}(\text{C}_6\text{D}_6)$: -9.2 ((Me₃Si)₃Si); -31.2 (Me₂Si); -53.2 (SiO₃); -129.5 ((Me₃Si)₃Si).

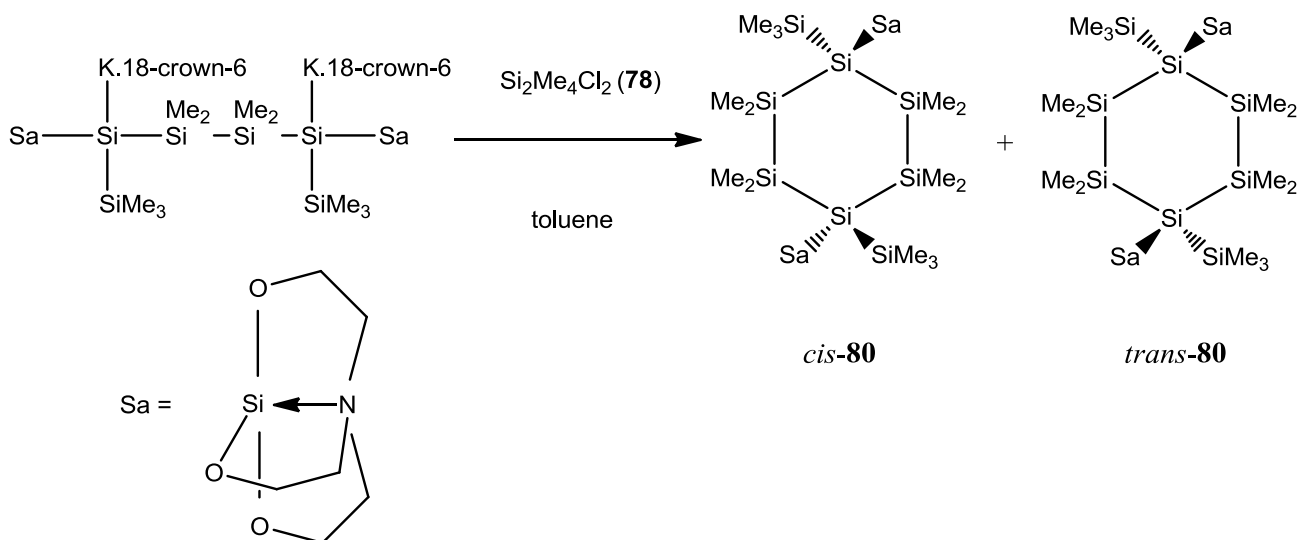
MS (70eV) m/z (%):

799(1)[M⁺-Me]; 640(1)[N(CH₂CH₂O)₃SiSi₈O₃C₁₃H₃₈⁺]; 464(11)[N(CH₂CH₂O)₃SiSi₅C₁₀H₃₀⁺];
 406(100)[N(CH₂CH₂O)₃SiSi₄C₈H₂₄⁺]; 362(3)[N(CH₂CH₂O)₃SiSi₄C₅H₁₆⁺];
 278(3)[(SiMe₃)₂SiSiO₃C₂H₄⁺]; 246(2)[Si₄O₃C₆H₁₄⁺]; 207(7)[Si₄O₃C₃H₁₁⁺];
 174(32)[N(CH₂CH₂O)₃Si⁺]; 117(3)[NC₅H₁₁O₂⁺]; 73(10)[SiMe₃⁺].

Elemental analysis: Calculated for: C₂₈H₇₂N₂O₆Si₁₀: C, 41.33; H, 8.92; N, 3.44. Found: C, 41.27; H, 8.22; N, 3.28.

UV absorption: $\lambda = 252$ nm ($\epsilon = 7.48 \times 10^4$ M⁻¹cm⁻¹) in diethylether.

12.5.17 *cis/trans* 1,4-Disilatranyl-1,4-bis(trimethylsilyl)octamethylcyclohexasilane (**80**)



A mixture of 100 mg (0.123 mmol, 1 eq) of 2,5-disilatranyl-2,5-bis(trimethylsilyl)decamethylhexasilane (**77**) with 28 mg (0.253 mmol, 2.03 eq) of KO^tBu and 68 mg (0.253 mmol, 2.03 eq) of 18-crown-6 was dissolved in 1 mL of benzene. After NMR spectroscopy confirmed formation of oligosilatranylsilylpotassium, the colorless solution was added dropwise over 15 minutes to the solution of 25 mg (0.135 mmol, 1.1 eq) of 1,2-dichlorotetramethyldisilane (**78**) in toluene. After 5 hours the volatile was removed by vacuum and the residue was dissolved in benzene and filtered with filter paper. 16 mg of colorless *trans*-isomer was first obtained by crystallization from benzene. In the second step 15 mg of milky *cis*-isomer was obtained by crystallization from a mixture of acetonitrile/diethylether 1:2. Yield: 32%.

Trans-isomer

Melting point: at 150 °C turned black, at 302 °C some liquid droplets appeared without further change to 340 °C.

NMR (δ in ppm):

$^1\text{H}(\text{C}_6\text{D}_6)$: 3.37 (t, $J=5.6$ Hz, 12H, OCH₂); 1.90 (t, $J=5.6$ Hz, 12H, NCH₂); 0.76 (s, 12H, (CH₃)₂Si); 0.75 (s, 12H, (CH₃)₂Si); 0.67 (s, 18H, (CH₃)₃Si-Si).

$^{13}\text{C}(\text{C}_6\text{D}_6)$: 58.88 (OCH₂); 51.65 (NCH₂); 3.85 ((Me₃Si)₂-Si); -1.09 (Me₂Si), -1.26 (Me₂Si).

$^{29}\text{Si}(\text{C}_6\text{D}_6)$: -6.4 ((Me₃Si)₃Si); -36.2 (Me₂Si); -52.3 (SiO₃); -130.3 ((Me₃Si)₃Si).

UV absorption: Start point $\lambda = 298$ nm,

Shoulder $\lambda = 242$ nm ($\epsilon = 2.62 \times 10^4 \text{ M}^{-1}\text{cm}^{-1}$) in THF

Cis-isomer

Melting point: 172-201°C.

NMR (δ in ppm):

$^1\text{H}(\text{C}_6\text{D}_6)$: 3.40 (t, $J=5.3$ Hz, 12H, OCH_2); 1.92 (t, $J=5.3$ Hz, 12H, NCH_2); 0.78 (s, 12H, $(\text{CH}_3)_2\text{Si}$); 0.71 (s, 12H, $(\text{CH}_3)_2\text{Si}$); 0.62 (s, 18H, $(\text{CH}_3)_3\text{Si-Si}$).

$^{13}\text{C}(\text{C}_6\text{D}_6)$: 58.95 (OCH_2); 51.88 (NCH_2); 3.67 ($(\text{Me}_3\text{Si})_2\text{-Si}$); -0.91 (Me_2Si), -1.05 (Me_2Si).

$^{29}\text{Si}(\text{C}_6\text{D}_6)$: -7.8($(\text{Me}_3\text{Si})_3\text{Si}$); -37.5 (Me_2Si); -50.7 (SiO_3); -129.9 ($(\text{Me}_3\text{Si})_3\text{Si}$).

UV absorption: Start point $\lambda = 303$ nm,

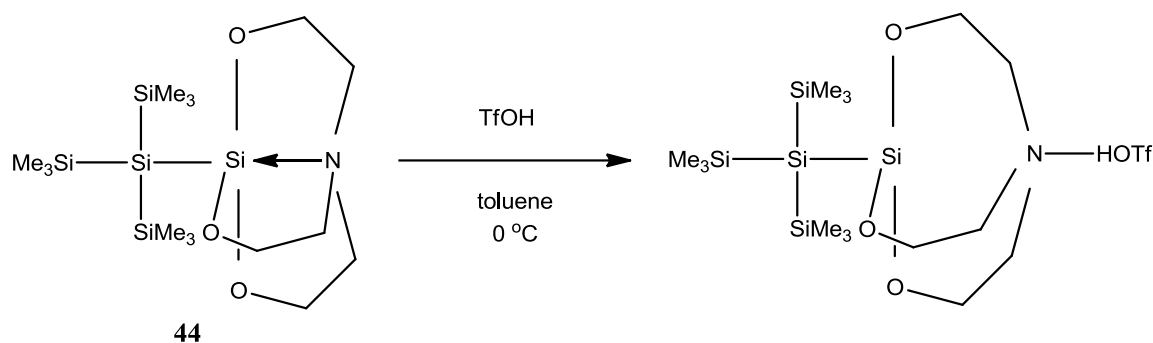
Shoulder $\lambda = 242$ nm ($\epsilon = 2.84 \times 10^4 \text{ M}^{-1}\text{cm}^{-1}$) in THF.

EI/MS (70eV) m/z (%):

782(3)[M]; 767(1)[$\text{M}^+ - \text{Me}$]; 754(1)[$\text{Si}_{10}\text{C}_{25}\text{H}_{64}\text{NO}_6^+$]; 709(2)[$\text{M}^+ - \text{SiMe}_3$];
681(1)[$\text{Si}_9\text{C}_{22}\text{H}_{55}\text{NO}_6^+$]; 653(1)[$\text{Si}_9\text{C}_{20}\text{H}_{51}\text{NO}_6^+$]; 608(1)[$\text{Si}_9\text{C}_{20}\text{H}_{54}\text{NO}_3^+$];
593(3)[$\text{Si}_9\text{C}_{19}\text{H}_{51}\text{NO}_3^+$]; 520(1)[$\text{Si}_8\text{C}_{16}\text{H}_{42}\text{NO}_3^+$]; 492(1)[$\text{Si}_8\text{C}_{15}\text{H}_{40}\text{O}_3^+$]; 450(1)[$\text{Si}_8\text{C}_{12}\text{H}_{34}\text{O}_3^+$];
436(1)[$\text{Si}_8\text{C}_{14}\text{H}_{44}^+$]; 420(1)[$\text{Si}_8\text{C}_{13}\text{H}_{40}^+$]; 404(1)[$\text{Si}_8\text{C}_{12}\text{H}_{36}^+$]; 390(2)[$\text{Si}_8\text{C}_{11}\text{H}_{34}^+$];
376(2)[$\text{Si}_5\text{C}_{12}\text{H}_{30}\text{NO}_3^+$]; 362(2)[$\text{Si}_5\text{C}_{11}\text{H}_{28}\text{NO}_3^+$]; 346(2)[$\text{Si}_7\text{C}_{10}\text{H}_{30}^+$]; 333(1)[$\text{Si}_4\text{C}_{11}\text{H}_{27}\text{NO}_3^+$];
290(5)[$\text{Si}_6\text{C}_8\text{H}_{26}^+$]; 248(3)[$\text{Si}_3\text{C}_8\text{H}_{20}\text{O}_3^+$]; 232(7)[$\text{Si}_3\text{C}_7\text{H}_{16}\text{O}_3^+$]; 174(100)[$\text{N}(\text{CH}_2\text{CH}_2\text{O})_3\text{Si}^+$];
144(3)[$\text{SiC}_5\text{H}_{10}\text{NO}_2^+$]; 130(6)[$\text{NC}_6\text{H}_{12}\text{O}_2^+$]; 73(21)[SiMe_3^+].

Elemental analysis: Calculated for: $\text{C}_{26}\text{H}_{66}\text{N}_2\text{O}_6\text{Si}_{10}$: C, 39.85; H, 8.49; N, 3.57. Found: C, 44.93; H, 8.44; N, 3.00.

12.5.18 Protonated tris(trimethylsilyl)silatranylsilane (**44**) with trifluoromethanesulfonic acid



31 mg (0.210 mmol, 0.95 eq) of TfOH in 1 mL of toluene was added dropwise over 30 minutes to the ice cooled solution of 93 mg (0.220 mmol, 1 eq) of tris(trimethylsilyl)silatranylsilane (**44**) in 1 mL of toluene while stirring. After 3 hours the volatiles were removed by vacuum. Colorless crystals of the protonated **44** (84 mg, 67%) was obtained from benzene.

Melting point: 156-160 °C.

NMR (δ in ppm):

$^1\text{H}(\text{C}_6\text{D}_6)$: 10.68 (s, 1H, TfOH); 3.34 (t, $J=4.50$ Hz, 6H, OCH₂); 2.64 (s, 6H, NCH₂); 0.25 (s, 27H, (CH₃)₃Si).

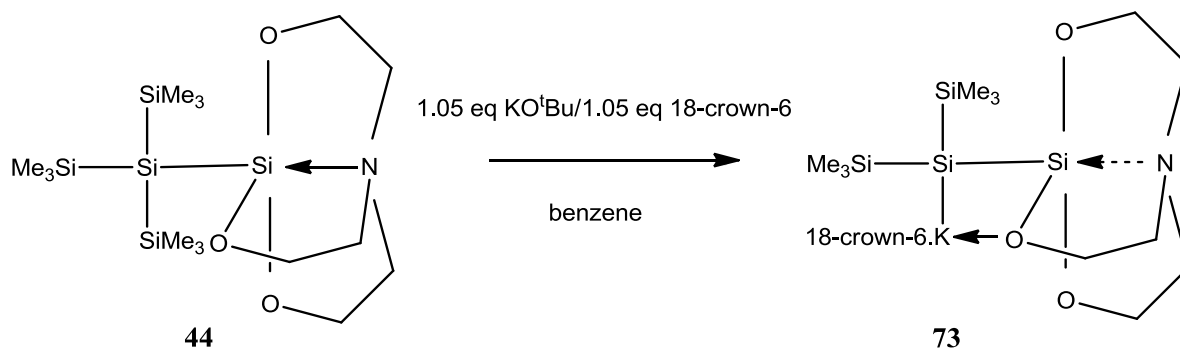
$^{13}\text{C}(\text{C}_6\text{D}_6)$: 121.52 (q, $J=319$ Hz, CF₃); 56.44 (OCH₂); 53.13 (NCH₂); 2.11 (Me₃Si-Si).

$^{29}\text{Si}(\text{C}_6\text{D}_6)$: -9.7 (Me₃Si); -22.8 (SiO₃); -141.4 ((Me₃Si)₂Si).

$^{19}\text{F}(\text{C}_6\text{D}_6)$: -77.85.

Elemental analysis: Calculated for: C₁₆H₄₀F₃NO₆SSi₅: C, 33.60; H, 7.05; N, 2.45; S, 5.61. Found: C, 34.54; H, 5.94; N, 2.35; S, 4.33.

12.5.19 Bis(trimethylsilyl)silatranyl potassium.18-crown-6 (73)



A mixture of 50 mg (0.118 mmol, 1 eq) of tris(trimethylsilyl)silatranyl silane (**44**) and 14 mg (0.124 mmol, 1.05 eq) of KO^tBu and 33 mg (0.124 mmol, 1.05 eq) of 18-crown-6 was dissolved in 1 mL of C₆D₆ and left for 14 hours. After NMR spectroscopy confirmed formation of oligosilatranyl silyl potassium, the pale yellow solution mixture was left for crystallization in a vial. Pale orange crystals were obtained on the walls of the vial. Yield: (77mg, 100%).

NMR (δ in ppm):

¹H(C₆D₆): 3.86 (t, $J=5.1$ Hz, 6H, OCH₂); 3.30 (s, 24H, CH₂O); 2.84 (t, $J=5.1$ Hz, 6H, NCH₂); 0.78 (s, 18H, (CH₃)₃Si).

¹³C(C₆D₆): 70.23 (CH₂O); 60.96 (OCH₂); 54.26 (NCH₂); 7.18 (Me₃Si-Si).

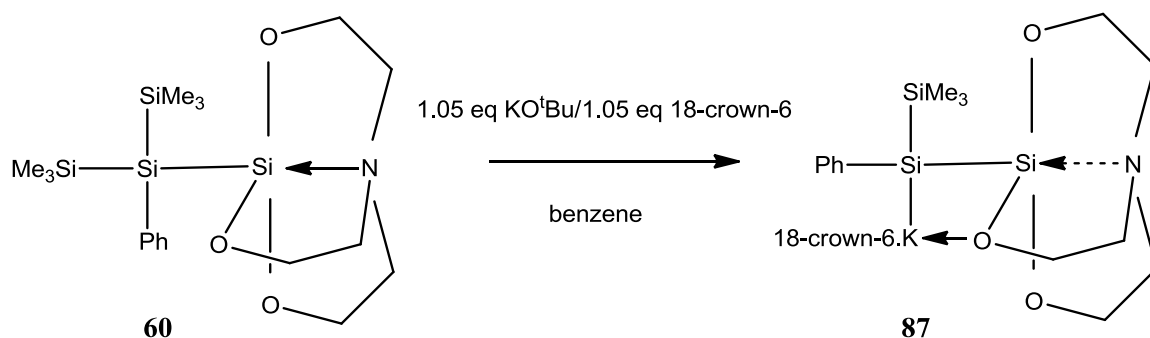
²⁹Si(C₆D₆): -3.2 (Me₃Si); -11.8 (SiO₃); -210.5 ((Me₃Si)₃Si).

Ethylbromide derivatization:

MS (70eV) m/z (%):

377(6)[M]; 362(8)[M⁺-Me]; 304(3)[M⁺-SiMe₃]; 174(100)[N(CH₂CH₂O)₃Si⁺];
130(3)[NC₆H₁₂O₂⁺]; 73(6)[SiMe₃⁺].

12.5.20 Trimethylsilylphenylsilatranyl silatranyl potassium.18-crown-6 (87)



A mixture of 50 mg (0.117 mmol, 1 eq) of bis(trimethylsilyl)phenylsilatranyl silane (**60**) and 14 mg (0.123 mmol, 1.05 eq) of KO^tBu and 32 mg (0.123 mmol, 1.05 eq) of 18-crown-6 was dissolved in 1 mL of C₆D₆ and left for 14 hours. After NMR spectroscopy confirmed formation of oligosilatranyl silatranyl potassium, the pale orange solution mixture was left for crystallization in a vial. Yellow crystals were obtained on the walls of the vial. Yield: (77mg, 100%).

NMR (δ in ppm):

¹H(C₆D₆): 8.14 to 8.11 (d, 2H); 7.13 to 6.91 (m, 3H); 3.84 (t, $J=5.0$ Hz, 6H, OCH₂); 3.20 (s, 24H, CH₂O); 2.81 (t, $J=5.0$, Hz 6H, NCH₂); 0.69 (s, 9H, (CH₃)₃Si).

¹³C(C₆D₆): 157.75 (*ipso*); 137.61 (*ortho*); 126.19 (*meta*); 121.69 (*para*); 70.15 (CH₂O); 61.14 (OCH₂); 54.17 (NCH₂); 4.58 (Me₃Si-Si).

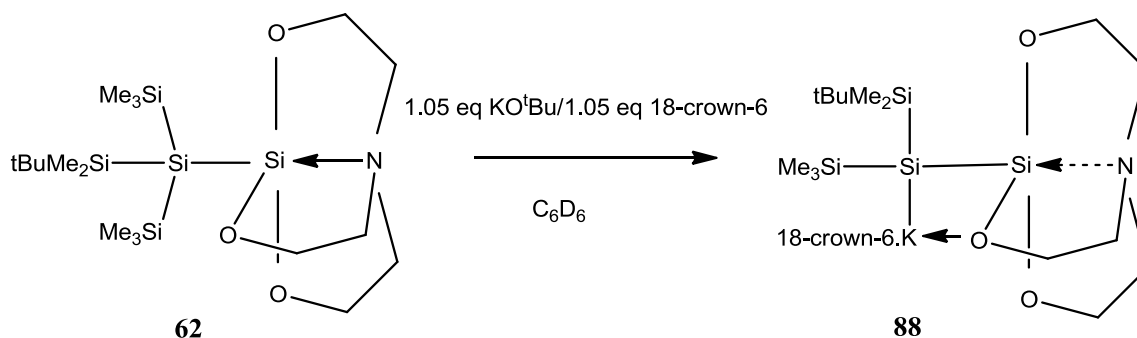
²⁹Si(C₆D₆): -7.7 (Me₃Si); -19.4 (SiO₃); -113.0 ((Me₃Si)Si).

Ethylbromide derivatization:

MS (70eV) m/z (%):

366(5)[M⁺-Me]; 308(10)[M⁺-SiMe₃]; 280(31)[N(CH₂CH₂O)₃SiSiPhH⁺];
 253(4)[PhSi₃O₃C₃H₈⁺]; 174(100)[N(CH₂CH₂O)₃Si⁺]; 135(7)[Si₃O₃H₃⁺]; 73(3)[SiMe₃⁺].

12.5.21 (*tert*-Butyldimethylsilyl)(trimethylsilyl)silatranyl potassium.18-crown-6 (**88**)



A mixture of 50 mg (0.107 mmol, 1 eq) of (*tert*-butyldimethylsilyl)bis(trimethylsilyl)silatranyl silane (**62**) and 13 mg (0.113 mmol, 1.05 eq) of KO^tBu and 30 mg (0.113 mmol, 1.05 eq) of 18-crown-6 was dissolved in 1 mL of C₆D₆ and left for 14 hours. After NMR spectroscopy confirmed formation of oligosilatranyl silyl potassium, the pale yellow solution mixture was left for crystallization in a vial. Pale yellow crystals were obtained on the walls of the vial. Yield: (74mg, 100%).

NMR (δ in ppm):

¹H(C₆D₆): 3.81 (t, *J*=5.0 Hz, 6H, OCH₂); 3.28 (s, 24H, CH₂O); 2.82 (t, *J*=5.0 Hz, 6H, NCH₂); 1.19 (s, 9H, (CH₃)₃C); 0.71 (s, 9H, (CH₃)₃Si); 0.70 (s, 6H, (CH₃)₂Si).

¹³C(C₆D₆): 70.06 (CH₂O); 60.97 (OCH₂); 54.23 (NCH₂); 29.22 (Me₃C); 19.22 (Me₃C); 7.37 ((Me₃Si)Si); 1.95 ((Me₂Si)Si).

²⁹Si(C₆D₆): 11.3 (^tBuMe₂Si); -3.0 (Me₃Si); -11.0 (SiO₃); -215.7 ((Me₃Si)Si).

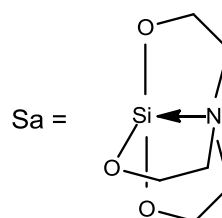
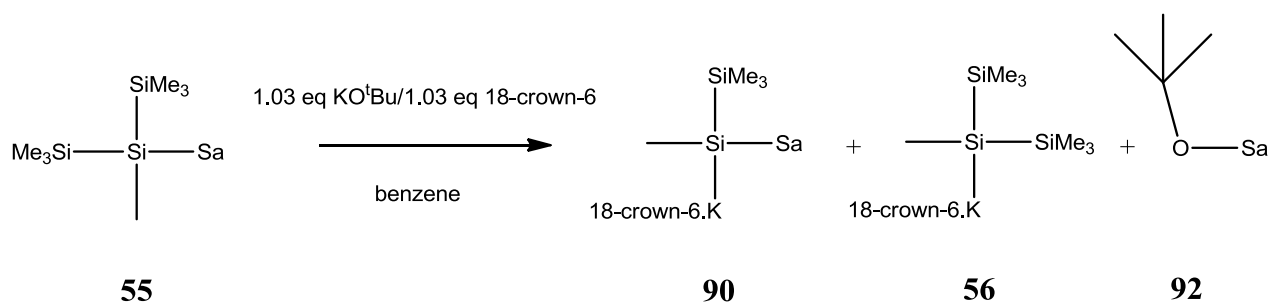
Ethylbromide derivatization:

MS (70eV) m/z (%):

419(3)[M]; 404(6)[M⁺-Me]; 362(22)[M⁺-^tBu]; 246(3)[Si₃C₁₁H₃₀⁺];

174(100)[N(CH₂CH₂O)₃Si⁺]; 130(3)[NC₆H₁₂O₂⁺]; 73(8)[SiMe₃⁺].

12.5.22 Trimethylsilylmethylsilatranylilpotassium.18-crown-6 (90)



A mixture of 200 mg (0.550 mmol, 1 eq) of bis(trimethylsilyl)methylsilatranyl silane (**55**) and 63 mg (0.566 mmol, 1.03 eq) of KO^tBu and 150 mg (0.566 mmol, 1.03 eq) of 18-crown-6 was dissolved in 2 mL of C₆D₆ and left for 14 hours. NMR spectroscopy showed a mixture of three products: trimethylsilylmethylsilatranylilpotassium.18-crown-6 (**90**), bis(trimethylsilyl)methylsilylpotassium.18-crown-6 (**56**) and N(CH₂CH₂O)₃SiO^tBu (**92**) in an orange solution. Yield: (260 mg, 80%).

NMR (δ in ppm):

¹H(C₆D₆): 3.76 (t, *J*=4.4 Hz, 6H, OCH₂); 3.26 (s, 24H, CH₂O); 2.80 (t, *J*=4.4 Hz, 6H, NCH₂); 0.52 (s, 9H, (CH₃)₃Si-Si); 0.45 (s, 3H, CH₃-Si).

¹³C(C₆D₆): 70.03 (CH₂O); 60.91 (OCH₂); 54.17 (NCH₂); 4.06 (Me₃Si-Si); -9.24 (CH₃-Si).

²⁹Si(C₆D₆): -5.1 (Me₃Si); -14.9 (SiO₃); -144.0 ((Me₃Si)Si).

Ethylbromide derivatization:

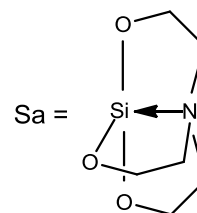
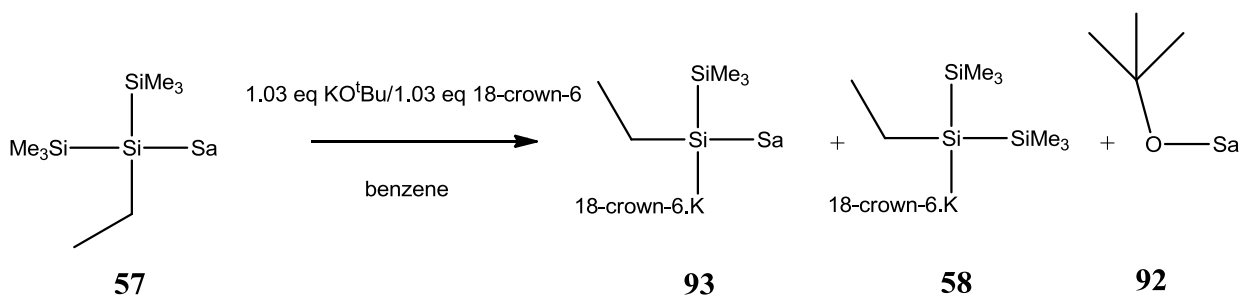
MS (70eV) m/z (%):

318(1)[M⁺-H]; 304(10)[M⁺-Me]; 290(3)[M⁺-Et]; 276(3)[N(CH₂CH₂O)₃SiSi₂C₃H₁₀⁺];

246(10)[M⁺-SiMe₃]; 218(41)[N(CH₂CH₂O)₃SiSiCH₄⁺]; 193(8)[Me₄Si₃O₃H⁺];

174(100)[N(CH₂CH₂O)₃Si⁺]; 149(4)[NC₆H₁₅O₃⁺]; 130(4)[NC₆H₁₂O₂⁺]; 73(7)[SiMe₃⁺].

12.5.23 Trimethylsilylethylsilatranyl silylpotassium.18-crown-6 (93)



A mixture of 50 mg (0.132 mmol, 1 eq) of bis(trimethylsilyl)ethylsilatranyl silane (**57**) and 15 mg (0.138 mmol, 1.05 eq) of KO^tBu and 36 mg (0.138 mmol, 1.05 eq) of 18-crown-6 was dissolved in 1 mL of C₆D₆ and left for 14 hours. NMR spectroscopy showed a mixture of three products as trimethylsilylethylsilatranyl silylpotassium.18-crown-6 (**93**), bis(trimethylsilyl)ethylsilyl potassium.18-crown-6 (**58**) and N(CH₂CH₂O)₃SiO^tBu (**92**) in an orange solution. Yield: (71mg, 89%).

NMR (δ in ppm):

¹H(C₆D₆): 3.88 (t, $J=5.2$ Hz, 6H, OCH₂); 3.27 (s, 24H, CH₂O); 2.88 (t, $J=5.2$ Hz, 6H, NCH₂); 1.68 (t, $J=7.5$ Hz, 3H); 1.41 (q, $J=7.8$ Hz, 2H); 0.74 (s, 9H, (CH₃)₃Si-Si).

¹³C(C₆D₆): 70.08 (CH₂O); 60.95 (OCH₂); 54.29 (NCH₂); 19.42 (CH₃-CH₂); 4.85 (Me₃Si-Si); 2.68 (CH₃-CH₂).

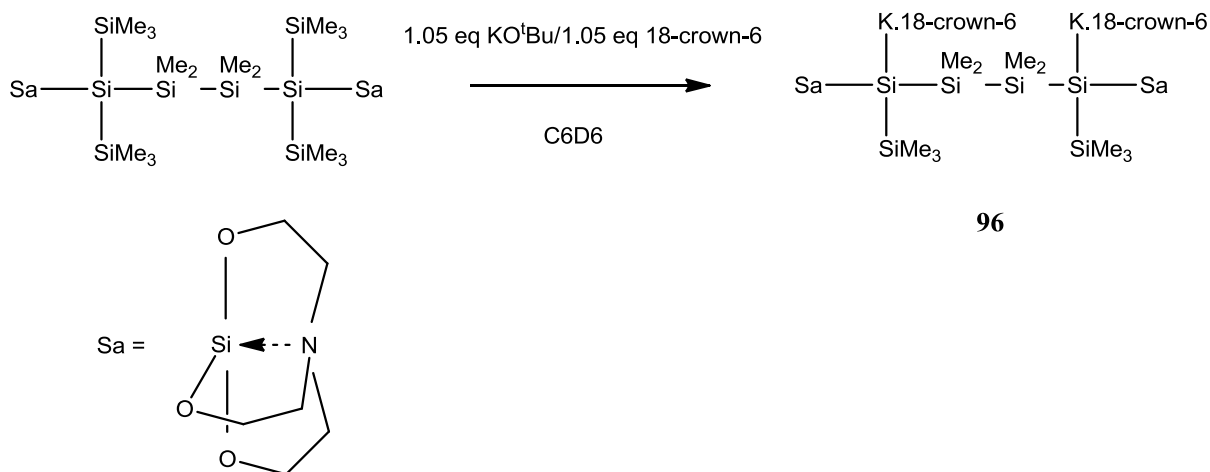
²⁹Si(C₆D₆): -6.2 (Me₃Si); -15.0 (SiO₃); -125.1 ((Me₃Si)Si).

Ethylbromide derivatization:

MS (70eV) m/z (%):

333(1)[M]; 318(8)[M⁺-Me]; 304(4)[M⁺-Et]; 290(3)[N(CH₂CH₂O)₃SiSi₂Me₄⁺];
 276(3)[N(CH₂CH₂O)₃SiSi₂C₃H₁₀⁺]; 260(11)[M⁺-SiMe₃]; 246(3)[N(CH₂CH₂O)₃SiSiC₃H₈⁺];
 232(42)[N(CH₂CH₂O)₃SiSiC₂H₆⁺]; 218(2)[N(CH₂CH₂O)₃SiSiCH₄⁺];
 204(3)[N(CH₂CH₂O)₃SiSiH₂⁺]; 174(100)[N(CH₂CH₂O)₃Si⁺]; 130(4)[NC₆H₁₂O₂⁺];
 73(5)[SiMe₃⁺].

12.5.24 2,5-Disilatranyl-decamethylhexasilyl-2,5-dipotassium.18-crown-6 (96)



A mixture of 50 mg (0.061 mmol, 1 eq) of 2,5-disilatranyl-2,5-bis(trimethylsilyl)decamethylhexasilane (**77**) and 14 mg (0.129 mmol, 2.05 eq) of KO^tBu and 34 mg (0.129 mmol, 2.05 eq) of 18-crown-6 was dissolved in 1 mL of C₆D₆ and left for 14 hours, after which NMR spectroscopic confirmed formation of oligosilatranylsilyldipotassium in a color less solution. Yield: (77mg, 100%).

NMR (δ in ppm):

¹H(C₆D₆): 3.92 (t, $J=4.4$ Hz, 12H, OCH₂); 3.35 (s, 48H, CH₂O); 2.91 (t, $J=5.0$ Hz, 12H, NCH₂); 0.88 (s, 12H, (CH₃)₂Si); 0.80 (s, 18H, (CH₃)₃Si-Si).

¹³C(C₆D₆): 70.10 (CH₂O); 60.95 (OCH₂); 54.53 (NCH₂); 7.99 ((Me₃Si)₂-Si); 2.76 (Me₂Si).

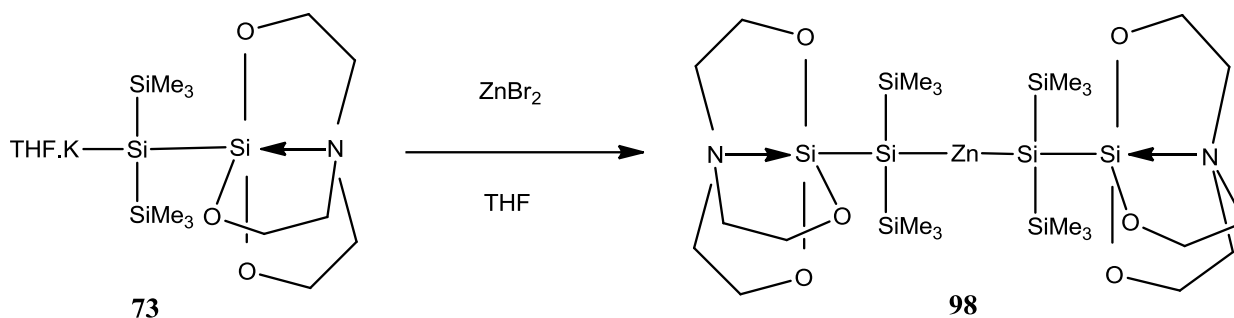
²⁹Si(C₆D₆): -2.3 ((Me₃Si)₃Si); -9.9 (SiO₃); -24.1 (Me₂Si); -209.0 ((Me₃Si)₃Si).

Ethylbromide derivatization:

EI/MS (70eV) m/z (%):

723(1)[M⁺-H]; 709(1)[M⁺-Me]; 695(1)[M⁺-Et]; 651(1)[M⁺-SiMe₃]; 550(1)[Si₇C₂₀H₅₂NO₃⁺];
 420(10)[Si₅C₁₅H₃₈NO₃⁺]; 362(100)[Si₄C₁₃H₃₂NO₃⁺]; 318(2)[Si₄C₁₀H₂₄NO₃⁺];
 290(2)[Si₃C₁₀H₂₄NO₃⁺]; 248(2)[Si₃C₈H₂₀O₃⁺]; 174(44)[N(CH₂CH₂O)₃Si⁺]; 133(9)[Si₃HO₃⁺];
 114(4)[C₈H₄N⁺]; 101(4)[Si₂C₃H₉⁺]; 89(27)[SiC₂H₅O₂⁺]; 73(27)[SiMe₃⁺].

12.5.25 Bis[bis(trimethylsilyl)silatranylsilanyl]zinc (98)



A mixture of 100 mg (0.237 mmol, 1 eq) of tris(trimethylsilyl)silatranylsilane (**44**) and 27 mg (0.0244 mmol, 1.03 eq) of KO^tBu was dissolved in 1 mL of THF and left for 14 hours. Formation of oligosilatranylsilylpotassium was monitored by NMR spectroscopic analysis. Afterwards 27 mg (0.118 mmole, 0.5 eq) of ZnBr₂ in 2 mL of THF was added dropwise to the pale beige solution of oligosilatranylsilylpotassium while stirring. After 6 hours the volatiles were removed by vacuum and the compound was extracted with pentane. Pale yellow crystals were obtained from a mixture of diethylether and pentane 1:1 inside the glovebox.

Melting point: 59-78 °C.

NMR (δ in ppm):

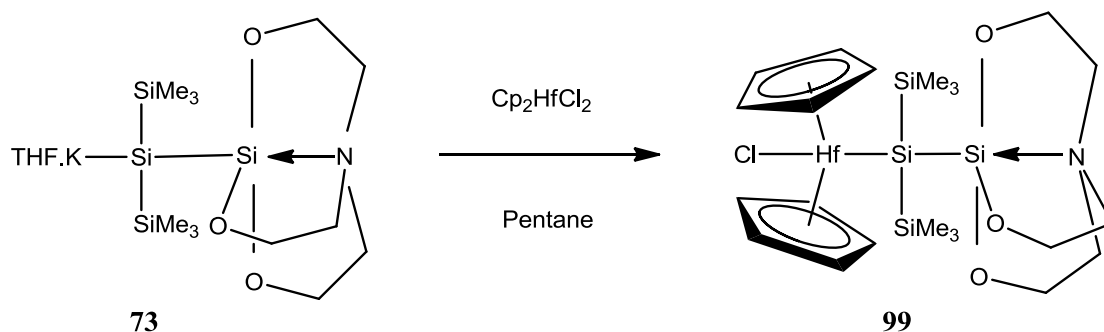
¹H(C₆D₆): 3.45 (t, $J=5.7$ Hz, 12H, OCH₂); 1.97 (t, $J=5.7$ Hz, 12H, NCH₂); 0.64 (s, 36H, (CH₃)₃Si).

¹³C(C₆D₆): 59.10 (OCH₂); 51.55 (NCH₂); 4.27 (Me₃Si-Si).

²⁹Si(C₆D₆): -7.2 (Me₃Si); -48.1 (SiO₃); -133.8 ((Me₃Si)₂Si).

Elemental analysis: Calculated for: C₂₄H₆₀N₂O₆Si₈Zn: C, 37.79; H, 7.93; N, 3.67. Found: C, 38.63; H, 7.08; N, 3.80.

12.5.26 Dicyclopentadienyl[bis(trimethylsilyl)silatranylsilyl]hafniumchloride (99)



A mixture of 80 mg (0.189 mmol, 1 eq) of tris(trimethylsilyl)silatranylsilane (**44**) and 22 mg (0.199 mmol, 1.03 eq) of KO^tBu was dissolved in 1 mL of THF and left for 14 hours. The solution color turned pale beige immediately. After NMR spectroscopy confirmed formation of oligosilatranylsilylpotassium, THF was removed by putting the sample under vacuum. Afterwards the oligosilatranylsilylpotassium was dissolved in 2 mL of benzene and was added dropwise over 20 minutes to the slurry of Cp₂HfCl₂ in pentane while stirring. After 3 hours the volatile compounds were removed by vacuum and the residue dissolved in diethylether/benzene 20:1. Orange crystals were obtained on the walls of a vial at room temperature.

Melting point: 137-172 °C.

NMR (δ in ppm):

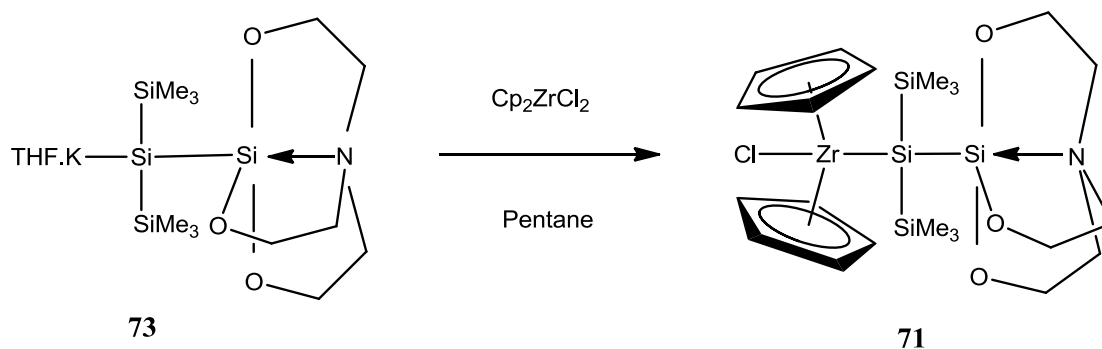
¹H(C₆D₆): 6.15 (s, 10H, **CH**); 3.44 (t, *J*=5.2 Hz, 6H, **OCH₂**); 2.16 (t, *J*=5.2 Hz, 6H, **NCH₂**); 0.57 (s, 18H, (**CH₃**)₃Si).

¹³C(C₆D₆): 110.62 (**CH**); 60.02 (**OCH₂**); 52.37 (**NCH₂**); 4.56 (**Me₃Si-Si**).

²⁹Si(C₆D₆): -4.5 (**Me₃Si**); -35.9 (**SiO₃**); -79.0 (**(Me₃Si)₂Si**).

Elemental analysis: Calculated for: C₂₂H₄₀ClHfNO₃Si₄: C, 38.14; H, 5.82; N, 2.02. Found: C, 37.52; H, 5.41; N, 2.00.

12.5.27 Dicyclopentadienyl[bis(trimethylsilyl)silatranysilyl]zirconiumchloride (71)



A mixture of 100 mg (0.237 mmol, 1 eq) of tris(trimethylsilyl)silatranysilane (**44**) and 27 mg (0.0244 mmol, 1.03 eq) of KO^tBu was dissolved in 1 mL of THF and left for 14 hours. The solution color turned pale beige immediately. After NMR spectroscopy confirmed formation of oligosilatranysilylpotasium, THF was removed by putting the sample under vacuum and then the oligosilatranysilylpotasium was dissolved in 2 mL of benzene and was added dropwise over 10 minutes to the slurry of Cp₂ZrCl₂ in pentane while stirring. After 3 hours the volatile compounds were removed by vacuum and the residue dissolved in toluene. Red micro crystals were obtained by crystallization from toluene at -50 °C.

Melting point: 145-168 °C.

NMR (δ in ppm):

¹H(C₆D₆): 6.24 (s, 10H, **CH**); 3.44 (t, *J*=5.4 Hz, 6H, **OCH₂**); 2.12 (t, *J*=5.4 Hz, 6H, **NCH₂**); 0.59 (s, 18H, (**CH₃**)₃Si).

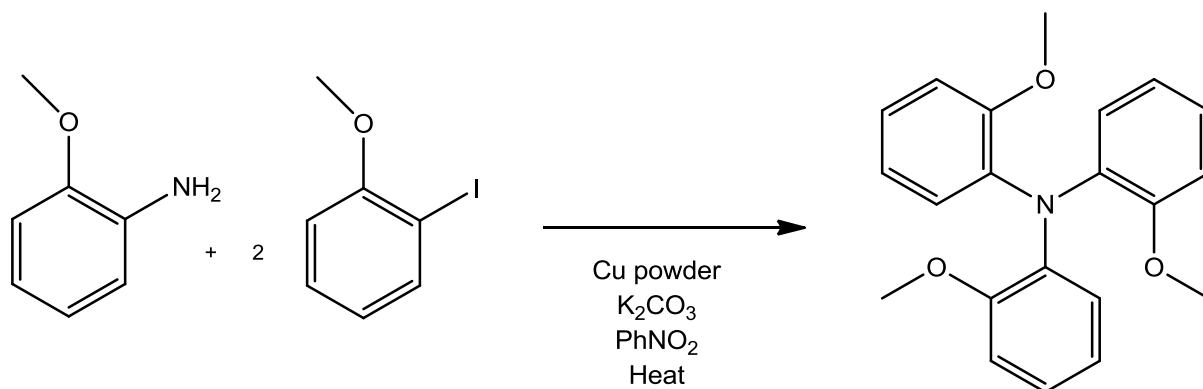
¹³C(C₆D₆): 111.40 (**CH**); 59.97 (**OCH₂**); 52.32 (**NCH₂**); 4.32 (**Me₃Si-Si**).

²⁹Si(C₆D₆): -5.7 (**Me₃Si**); -39.3 (**SiO₃**); -82.9 (**(Me₃Si)₂Si**).

Elemental analysis: Calculated for: C₂₂H₄₀ClNO₃Si₄Zr: C, 43.63; H, 6.66; N, 2.31. Found: C, 43.51; H, 6.38; N, 2.55.

12.6 Synthesis of oligosilanylsilatrane with other types of ligands

12.6.1 Tris(2-methoxyphenyl)amine⁷⁰



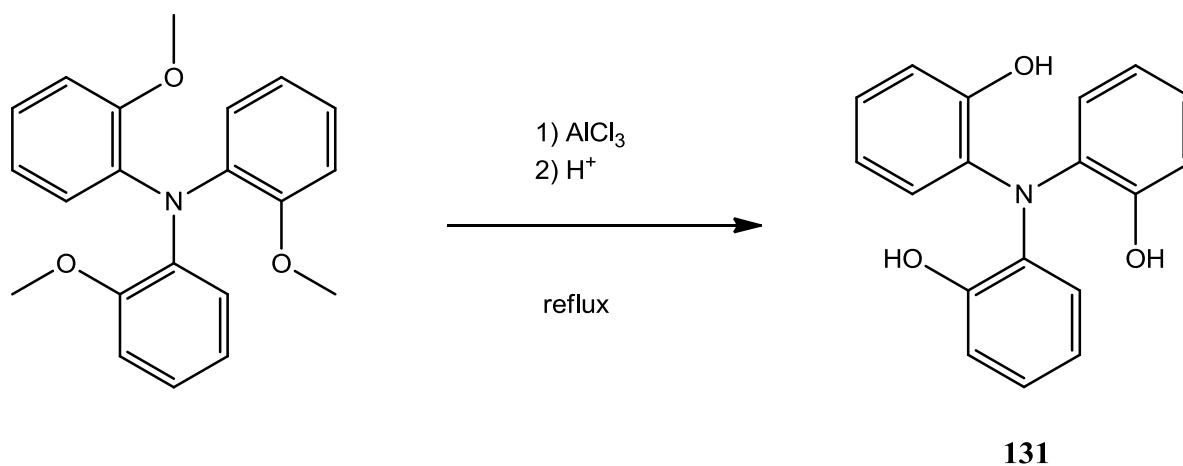
To a three necked flask equipped with a reflux condenser, Dean-Stark trap and stir bar was added 4.96 g (40.27 mmol) of *o*-anisidine, 18.30 g (78.19 mmol) of *o*-iodoanisole, 23.50 g of K₂CO₃ powder, 5.0 g of spongy copper powder and 15 g of nitrobenzene. The flask was then heated for 3 hours at reflux with flashes of nitrogen to remove the water from the reaction mixture and collect it in Dean-Stark trap. The reaction mixture was then cooled and the product was extracted with hot chloroform and filtered with filter paper. Chloroform was removed by vacuum. Nitrobenzene was distilled off at 55 °C, 1mbar. The residue was dissolved in ethylacetate and mixed with 100 mg of activated carbon and passed the silica gel column. Afterwards ethylacetate was removed by vacuum. The residue was dissolved in 10 mL of hot chloroform and then 5 mL of petroleum ether 100-120 °C was added to it and left for crystallization. Colorless crystals of the tris(2-methoxyphenyl)amine (8.53 g, 65%) were obtained by filtering the solution mixture with frit filter.

NMR (δ in ppm):

¹H(CDCl₃): 7.05 to 7.01 (m, 3H, aryl); 6.87 to 6.78 (m, 9H, aryl); 3.57 (s, 9H, OCH₃).

¹³C(CDCl₃): 153.06 (aryl); 137.69 (aryl); 124.44 (aryl); 123.69 (aryl); 120.57 (aryl); 112.47 (aryl); 55.68 (OMe).

12.6.2 Tris(2-hydroxyphenyl)amine⁷⁰ (**131**)



In a three necked flask with condenser a mixture of 1.000 g (2.98 mmol, 1 eq) of tris(2-methoxyphenyl)amine and 910 mg (6.82 mmol, 2.3 eq) AlCl₃ in 5 mL toluene was refluxed for 90 minutes. After cooling the mixture to room temperature, 20 mL of 10% HCl was added to the mixture and stirred for 2 hours. Organic phase was extracted with ethylacetate and dried over sodium sulfate. 1.040 g crude compound was obtained after volatile was removed by vacuum.

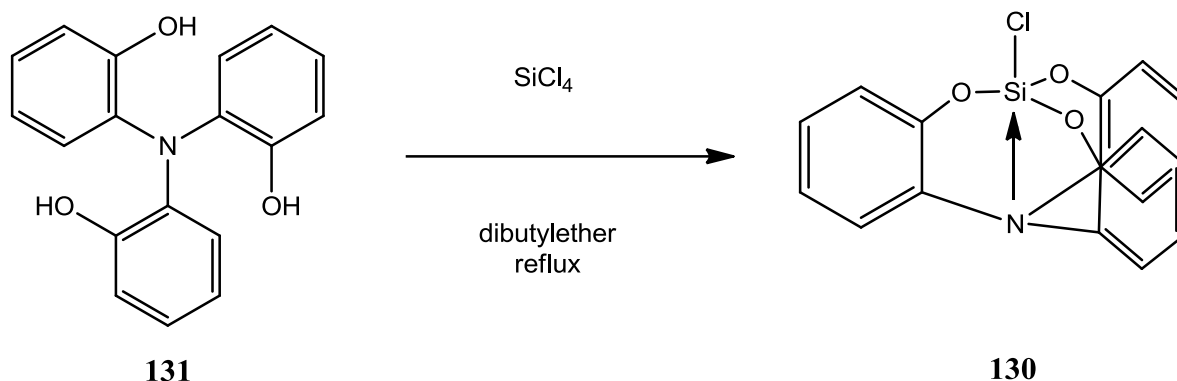
The crude compound was dissolved in a mixture of diethylether and pentane with ratio 1:2 and filtered with filter paper. Filter paper was washed with the same solution mixture. 900 mg compound was obtained after volatile was removed by vacuum. Colorless crystals of **131** (480 mg, 55%) was obtained from dichloromethane.

NMR (δ in ppm):

¹H(CDCl₃): 7.11 to 7.07 (t, 3H, aryl); 6.94 to 6.85 (m, 9H, aryl); 5.71 (s, 3H, OH).

¹³C(CDCl₃): 149.77 (aryl); 133.45 (aryl); 126.68 (aryl); 125.37 (aryl); 121.53 (aryl); 117.29 (aryl).

12.6.3 Aminotris(phenyl-2'-oxy)silylchloride⁷⁰ (**130**)



In a three necked flask equipped with condenser a mixture of 348 mg (1.18 mmol) of tris(2-hydroxyphenyl)amine (**131**) and 222 mg (1.30 mmol/ 1.1 eq) of SiCl₄ in 5 mL of dibutylether was refluxed for 3 hours. After removal of the volatile beige powdery **130** (412 mg, 71%) was obtained.

Melting point: 260-275 °C.

NMR (δ in ppm):

¹H(DMSO-d₆): 8.42 to 8.39 (d, 3H, aryl), 7.29 to 7.23 (t, 3H, aryl), 7.14 to 7.04 (m, 6H, aryl).

¹³C (DMSO-d₆): 151.97 (aryl); 136.15 (aryl); 129.66 (aryl); 126.34 (aryl); 122.54 (aryl); 116.88 (aryl).

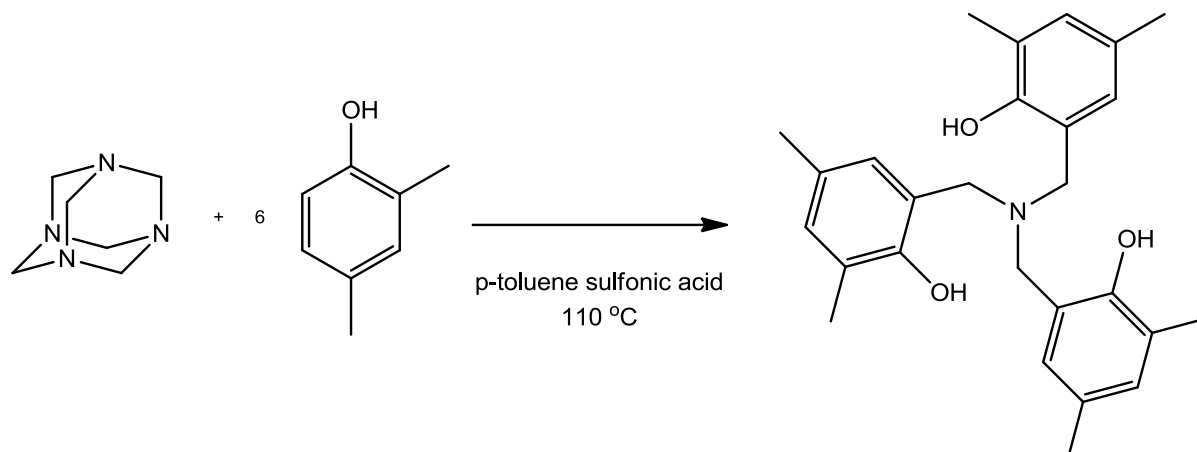
²⁹Si(DMSO-d₆): -97.8.

EI/MS (70eV) m/z (%):

353(100)[M]; 337(3)[M⁺-O]; 324(15)[SiC₁₇H₁₁ClNO₂⁺]; 318(27)[M⁺-Cl];
300(3)[SiC₁₅H₁₁ClNO₂⁺]; 288(3)[SiC₁₇H₁₀NO₂⁺]; 261(15)[SiC₁₂H₈ClNO₂⁺];
243(1)[SiC₁₂H₉NO₃⁺]; 225(2)[SiC₁₂H₇NO₂⁺]; 206(2)[SiC₉H₅ClNO⁺]; 176(3)[SiC₅H₇ClNO₂⁺];
166(2)[C₁₂H₈N⁺]; 153(2)[C₁₁H₇N⁺]; 139(2)[C₁₀H₅N⁺]; 128(1)[C₉H₆N⁺]; 105(1)[C₇H₇N⁺];
91(1)[C₆H₅N⁺]; 77(3)[C₆H₅⁺]; 63(7)[SiCl⁺].

Elemental analysis: Calculated for: C₁₈H₁₂ClNO₃Si: C, 61.10; H, 3.42; N, 3.96. Found: C, 62.22; H, 3.11; N, 3.72.

12.6.4 Tris(2-hydroxy-4,6-dimethylbenzyl)amine⁷¹



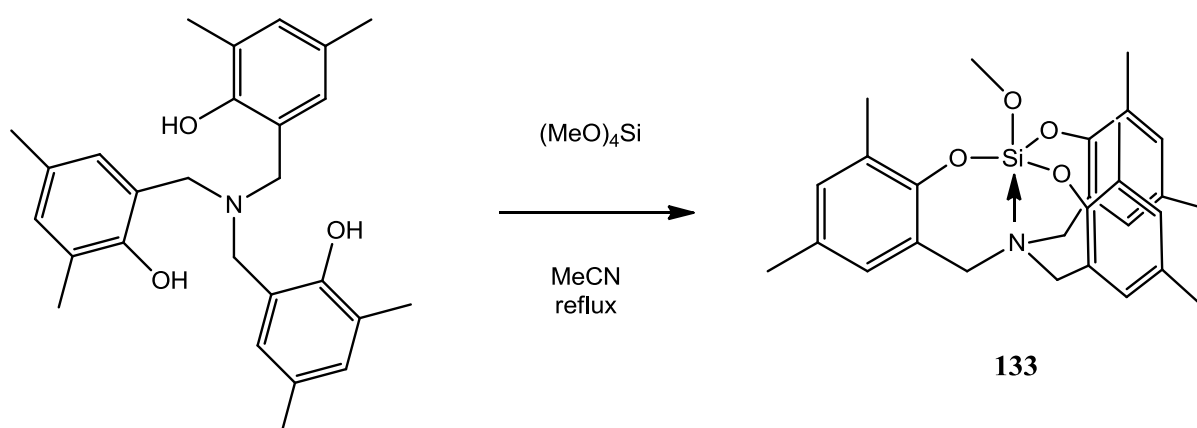
A mixture of hexamethylenetetramine (22.8 g, 0.162 mol), 2,4-dimethylphenol (90.0 mL, 0.744 mol) and *p*-toluenesulfonic acid hydrate (0.6 g) was stirred and heated with an oil bath at 110 °C for 20 h. Then an additional quantity of 2,4-dimethylphenol (30.0 mL, 0.248 mol) was added and heated for a further period of 20 h. White powder of tris(2-hydroxy-4,6-dimethylbenzyl)amine (26.0 g, 38%) was obtained from isopropanol.

NMR (δ in ppm):

¹H(CDCl₃): 6.85 (s, 3H, aryl); 6.73 (s, 3H, aryl); 6.51 (s, 3H, OH); 3.63 (s, 6H, NCH₂); 2.21 (s, 9H, aryl-CH₃); 2.19 (s, 9H, aryl-CH₃).

¹³C(CDCl₃): 151.10 (aryl); 131.29 (aryl); 129.08 (aryl); 128.82 (aryl); 124.57 (aryl); 121.75 (aryl); 56.49 (NCH₂); 20.36 (aryl-Me); 15.88 (aryl-Me).

12.6.5 Aminotris(-3',5'-dimethylbenzyl-2'-oxy)silylmethoxide⁷¹ (**133**)



A solution of tetramethoxysilane (399 mg, 2.62 mmol, 1.1 eq), tris(2-hydroxy-4,6-dimethylbenzyl)amine (1.000 g, 2.38 mmol), and tetraethylammonium fluoride hydrate (50 mg) in acetonitrile (25 mL) was heated to reflux for 16 hours. 1.30 g white residue obtained after the volatiles were removed by vacuum. The white residue was dissolved in diethylether. Colorless crystals of **133** (995 mg, 88%) was obtained from diethylether. According to NMR spectroscopy it is found that diethylether co-crystallizes with the **133**.

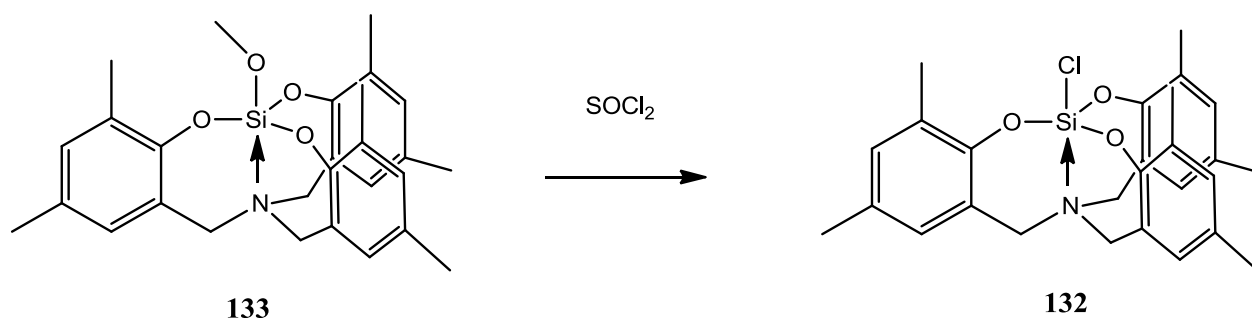
NMR (δ in ppm):

$^1\text{H}(\text{CDCl}_3)$: 6.89 (s, 3H, aryl); 6.66 (s, 3H, aryl); 3.90 (s, 3H, OCH_3); 3.50 (s, 6H, NCH_2); 2.31 (s, 9H, aryl- CH_3); 2.21 (s, 9H, aryl- CH_3).

$^{13}\text{C}(\text{CDCl}_3)$: 148.44 (aryl); 131.08 (aryl); 130.73 (aryl); 128.96 (aryl); 127.39 (aryl); 124.67 (aryl); 57.04 (NCH_2); 51.83 (SiOMe); 20.46 (aryl- Me); 16.65 (aryl- Me).

$^{29}\text{Si}(\text{CDCl}_3)$: -121.9.

12.6.6 Aminotris(-3',5'-dimethylbenzyl-2'-oxy)silylchloride (**132**)



5 mL of thionyl chloride was added to 703 mg of aminotris(-3',5'-dimethylbenzyl-2'-oxy)silylmethoxide (**133**) and stirred for 20 hours. After removal of the volatile white powdery **132** (692 mg, 69%) was obtained.

Melting point: decomposition at 175 °C without melting till 350 °C.

NMR (δ in ppm):

$^1\text{H}(\text{CDCl}_3)$: 6.94 (s, 3H, aryl); 6.63 (s, 3H, aryl); 3.66 (s, 6H, NCH_2); 2.31 (s, 9H, aryl- CH_3); 2.22 (s, 9H, aryl- CH_3).

$^{13}\text{C}(\text{CDCl}_3)$: 147.96 (aryl); 131.59 (aryl); 131.28 (aryl); 129.20 (aryl); 126.21 (aryl); 121.23 (aryl); 58.02 (NCH_2); 20.52 (aryl- Me); 16.41 (aryl- Me).

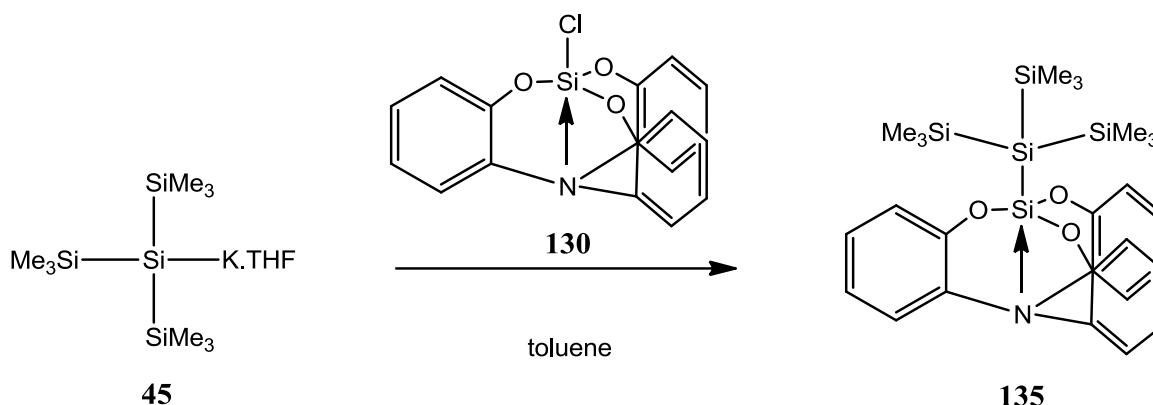
$^{29}\text{Si}(\text{CDCl}_3)$: -124.5.

EI/MS (70eV) m/z (%):

479(26)[M]; 463(2)[$\text{SiC}_{26}\text{H}_{26}\text{ClNO}_3^+$]; 444(100)[M^+-Cl]; 360(2)[$\text{SiC}_{18}\text{H}_{19}\text{ClNO}_3^+$]; 344(63)[$\text{SiC}_{18}\text{H}_{19}\text{ClNO}_2^+$]; 330(19)[$\text{SiC}_{17}\text{H}_{17}\text{ClNO}_2^+$]; 317(9)[$\text{SiC}_{16}\text{H}_{16}\text{ClNO}_2^+$]; 309(5)[$\text{SiC}_{18}\text{H}_{19}\text{NO}_2^+$]; 287(4)[$\text{SiC}_{15}\text{H}_{17}\text{NO}_3^+$]; 281(2)[$\text{C}_{18}\text{H}_{19}\text{NO}_2^+$]; 237(3)[$\text{SiC}_{10}\text{H}_8\text{ClNO}_2^+$]; 221(3)[$\text{C}_{16}\text{H}_{15}\text{N}^+$]; 183(3)[$\text{C}_{13}\text{H}_{13}\text{N}^+$]; 134(13)[$\text{C}_8\text{H}_8\text{NO}^+$]; 118(16)[$\text{C}_9\text{H}_{10}^+$]; 105(10)[C_8H_9^+]; 77(6)[C_6H_5^+].

Elemental analysis: Calculated for: $\text{C}_{27}\text{H}_{30}\text{ClNO}_3\text{Si}$: C, 67.55; H, 6.30; N, 2.92. Found: C, 66.42; H, 5.70; N, 2.81.

12.6.7 1,1,1-Aminotris(phenyl-2'-oxy)-2,2-bis(trimethylsilyl)trimethyltrisilane (135)



A mixture of 100 mg (0.312 mmol, 1 eq) of tetrakis(trimethylsilyl)silane (**47**) with 36 mg (0.321 mmol, 1.03 eq) of KO^tBu was dissolved in 1 mL of THF. The solution color turned orange immediately. After NMR spectroscopy confirmed formation of oligosilylpotassium, THF was removed by putting the sample under vacuum. Afterwards the oligosilylpotassium was dissolved in 2 mL of toluene and was added dropwise over 1 hour to the slurry of 110 mg (0.312 mmol, 1 eq) of aminotris(phenyl-2'-oxy)silylchloride (**130**) in 1 mL of toluene while stirring. After 12 hours the volatile was removed by vacuum and the residue was dissolved in benzene and filtered with filter paper. 110 mg crude compound was obtained. Colorless crystals of **135** (105 mg, 60%) was obtained from diethylether.

Melting point: 253-257 °C.

NMR (δ in ppm):

¹H(CDCl₃): 7.72 to 7.69 (d, 3H, aryl), 7.15 to 7.10 (t, 3H, aryl), 7.00 to 6.91 (m, 6H, aryl); 0.35 (s, 27H, (CH₃)₃Si).

¹³C(CDCl₃): 154.36 (aryl); 136.47 (aryl); 128.55 (aryl); 127.90 (aryl); 121.94 (aryl); 118.11 (aryl); 2.16 (SiMe₃).

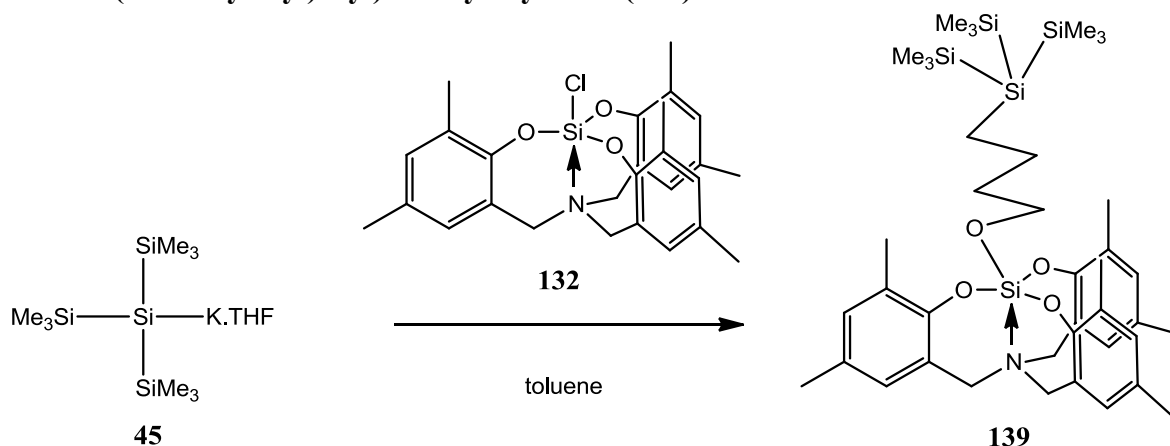
²⁹Si(CDCl₃): -9.4 (Me₃Si); -45.9 (SiO₃); -135.3 ((Me₃Si)₃Si).

EI/MS (70eV) m/z (%):

565(21)[M]; 550(8)[M⁺-Me]; 492(6)[M⁺-SiMe₃]; 434(2)[Si₄C₂₀H₂₀NO₃⁺];
 407(8)[Si₃C₂₀H₂₁NO₃⁺]; 392(31)[Si₄C₁₆H₂₆NO₃⁺]; 376(14)[Si₄C₁₆H₂₆NO₂⁺];
 335(5)[Si₄C₁₃H₂₁NO₂⁺]; 318(100)[SiC₁₈H₁₂NO₃⁺]; 305(7)[SiC₁₇H₁₁NO₃⁺];
 300(6)[Si₃C₁₃H₁₄NO₂⁺]; 267(4)[SiC₁₄H₉NO₃⁺]; 232(73)[Si₄C₈H₂₄⁺]; 217(2)[Si₄C₇H₂₁⁺];
 174(31)[Si₃C₆H₁₈⁺]; 159(26)[Si₃C₅H₁₅⁺]; 131(15)[C₈H₅NO⁺]; 115(11)[C₈H₅N⁺];
 91(8)[C₆H₅N⁺]; 73(100)[SiMe₃⁺].

Elemental analysis: Calculated for: C₂₇H₃₉NO₃Si₅: C, 57.29; H, 6.94; N, 2.47. Found: C, 56.95; H, 6.79; N, 2.50.

12.6.8 1,1,1-Aminotris(-3',5'-dimethylbenzyl-2'-oxy)-(4''-tris(trimethylsilyl)silyl)butanyloxysilane (**139**)



A mixture of 280 mg (0.873 mmol, 1 eq) of tetrakis(trimethylsilyl)silane (**47**) with 101 mg (0.899 mmol, 1.03 eq) of KO^tBu was dissolved in 3 mL of THF. The solution color turned orange immediately. After NMR spectroscopy confirmed formation of oligosilylpotassium, THF was removed by putting the sample under vacuum. Afterwards the oligosilylpotassium was dissolved in 5 mL of toluene and was added dropwise over 10 minutes to the slurry of 419 mg (0.873 mmol, 1 eq) of aminotris(-3',5'-dimethylbenzyl-2'-oxy)silylchloride (**132**) in 3 mL of toluene while stirring. After 12 hours the volatile was removed by vacuum and the residue was dissolved in benzene and filtered with filter paper. 610 mg crude compound was obtained after removal of the volatiles. Colorless crystals of **139** (425 g, 64%) was obtained from a mixture of acetonitrile and diethylether 1:2.

Melting point: 144-153 °C.

NMR (δ in ppm):

¹H(CDCl₃): 6.90 (s, 3H, aryl); 6.70 (s, 3H, aryl); 4.19 (t, $J=6.6$ Hz, 2H, OCH₂); 3.47 (s, 6H, NCH₂); 2.32 (s, 9H, aryl-CH₃); 2.23 (s, 9H, aryl-CH₃); 1.83 (quintet, $J=7$ Hz, 2H, CH₂); 1.67 to 1.57 (m, 2H, CH₂); 0.93 to 0.87 (m, 2H, SiCH₂); 0.22 (s, 27H, (CH₃)₃Si).

¹³C(CDCl₃): 148.61 (aryl); 130.97 (aryl); 130.83 (aryl); 129.14 (aryl); 127.89 (aryl); 126.28 (aryl); 63.03 (CH₂); 56.65 (NCH₂); 37.48 (CH₂); 25.62 (CH₂); 20.47 (aryl-Me); 16.87 (aryl-Me); 7.79 (CH₂); 1.20 (Me₃Si-Si).

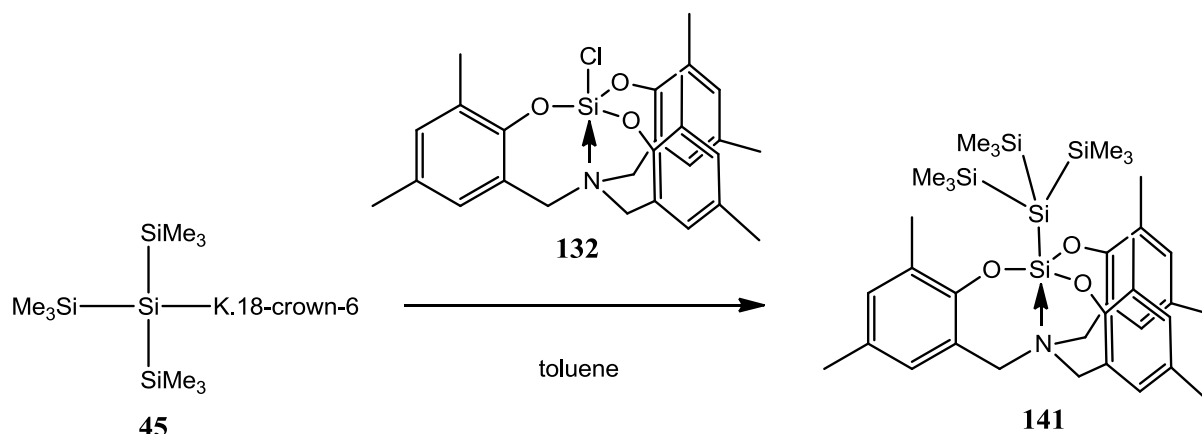
²⁹Si(CDCl₃): -12.8 (Me₃Si); -82.1 ((Me₃Si)₃Si); -117.1 (SiO₃).

EI/MS (70eV) m/z (%):

763(2)[M]; 690(1)[M⁺-SiMe₃]; 628(37)[Si₅C₃₁H₅₄NO₃⁺]; 556(3)[Si₄C₂₈H₄₆NO₃⁺];
 500(20)[Si₃C₂₅H₃₈NO₄⁺]; 444(100)[SiC₂₇H₃₀NO₃⁺]; 417(4)[Si₃C₂₀H₃₁NO₃⁺];
 382(15)[Si₃C₁₆H₂₈NO₄⁺]; 326(5)[SiC₁₈H₂₀NO₃⁺]; 263(4)[Si₂C₁₃H₁₉O₂⁺]; 247(13)[Si₄C₉H₂₇⁺];
 231(34)[Si₄C₈H₂₃⁺]; 191(6)[SiC₁₀H₁₃NO⁺]; 175(59)[Si₃C₆H₁₉⁺]; 147(7)[SiC₈H₇O⁺];
 131(22)[C₈H₅NO⁺]; 119(18)[C₈H₇O⁺]; 91(9)[C₇H₇⁺]; 73(93)[SiMe₃⁺].

Elemental analysis: Calculated for: Si₅C₄₀H₆₅NO₄: C, 62.85; H, 8.57; N, 1.83. Found: C, 62.84; H, 8.38; N, 1.92.

12.6.9 1,1,1-Aminotris(-3',5'-dimethylbenzyl-2'-oxy)-2,2-bis(trimethylsilyl)trimethyltrisilane (141)



A mixture of 400 mg (1.25 mmol, 1 eq) of tetrakis(trimethylsilyl)silane (**47**) with 144 mg (1.29 mmol, 1.03 eq) of KO^tBu and 340 mg (1.29 mmol, 1.03 eq) of 18-crown-6 was dissolved in 5 mL of toluene. After NMR spectroscopy confirmed formation of oligosilylpotassium, the orange solution of oligosilylpotassium was added dropwise over 5 minutes to the slurry of 600 mg (1.25 mmol, 1 eq) of aminotris(-3',5'-dimethylbenzyl-2'-oxy)silylchloride (**132**) in 2 mL of toluene while stirring. After 12 hours the solution mixture was quenched with distilled water and then the organic phase was separated by separating funnel and the combined organic phase was dried over sodium sulphate. After removal of the volatiles 770 mg of crude compound was obtained. Colorless crystals of **141** (635 g, 73%) was obtained from diethylether.

Melting point: 185-190 °C.

NMR (δ in ppm):

At -40 °C:

¹H(CDCl₃): 6.94 (s, 3H, aryl); 6.58 (s, 3H, aryl); 4.44 (d, *J*=14.4 Hz, 3H, NCH₂); 2.94 (d, *J*=14.7 Hz, 3H, NCH₂); 2.26 (s, 9H, aryl-CH₃); 2.22 (s, 9H, aryl-CH₃); 0.22 (s, 27H, (CH₃)₃Si).

At room temperature:

¹H(CDCl₃): 6.91 (s, 3H, aryl); 6.56 (s, 3H, aryl); 3.67 (s, 6H, NCH₂); 2.28 (s, 9H, aryl-CH₃); 2.22 (s, 9H, aryl-CH₃); 0.26 (s, 27H, (CH₃)₃Si).

¹³C(CDCl₃): 148.91 (aryl); 131.11 (aryl); 129.76 (aryl); 127.61 (aryl); 126.01 (aryl); 120.36 (aryl); 58.31 (NCH₂); 20.38 (aryl-Me); 18.00 (aryl-Me); 4.61 (Me₃Si-Si).

²⁹Si(CDCl₃): -10.4 (Me₃Si); -107.7 ((Me₃Si)₃Si); -123.6 (SiO₃).

EI/MS (70eV) m/z (%):

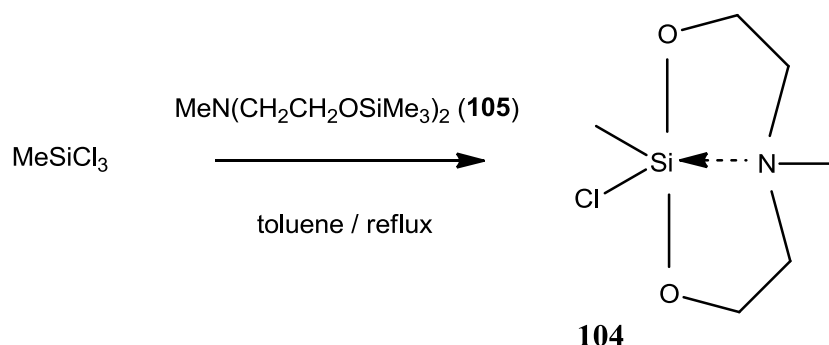
676(1)[M⁺-Me]; 557(21)[Si₅C₂₇H₄₇NO₂⁺]; 542(14)[Si₅C₂₆H₄₄NO₂⁺]; 484(55)[Si₄C₂₄H₃₈NO₂⁺];
 444(100)[SiC₂₇H₃₀NO₃⁺]; 410(7)[Si₃C₂₀H₂₄NO₃⁺]; 382(31)[Si₄C₁₆H₃₂NO₂⁺];
 366(3)[Si₄C₁₅H₂₈NO₂⁺]; 352(4)[Si₄C₁₄H₂₆NO₂⁺]; 322(15)[Si₄C₁₃H₂₄NO⁺];
 310(21)[SiC₁₈H₂₀NO₂⁺]; 292(6)[Si₅C₉H₂₈O⁺]; 248(4)[Si₄C₉H₂₈⁺]; 235(6)[Si₄C₆H₁₉O₂⁺];

221(6)[SiC₁₀H₁₁NO₃⁺]; 207(6)[SiC₉H₉NO₃⁺]; 174(15)[Si₃C₆H₁₈⁺]; 159(10)[Si₃C₅H₁₅⁺];
134(43)[C₉H₁₀O⁺]; 119(9)[C₈H₇O⁺]; 105(19)[C₇H₅O⁺]; 73(80)[SiMe₃⁺].

Elemental analysis: Calculated for: Si₅C₃₆H₅₇NO₃: C, 62.46; H, 8.30; N, 2.02. Found: C, 61.52;
H, 8.14; N, 2.11.

12.7 Synthesis of oligosilanylsilocanes

12.7.1 Synthesis of MeN(CH₂CH₂O)₂SiMeCl (104)



A mixture of 1.155 g (4.32 mmol) of $\text{MeN}(\text{CH}_2\text{CH}_2\text{OSiMe}_3)_2$ (**105**) and 679 mg (4.54 mmol, 1.05 eq) of MeSiCl_3 was dissolved in 6 mL of toluene in a 100 mL three necked flask equipped with condenser under nitrogen. The reaction mixture was left for 20 hours under reflux while stirring with stir bar. Colorless crystals were formed right after removal of the heating mantel. Colorless crystals of **104** (563 g, 69%) was obtained by decantation.

Melting point: 128-131 °C.

NMR (δ in ppm):

$^1\text{H}(\text{CDCl}_3)$: 3.96 to 3.81 (m, 4H); 2.90 to 2.82 (quintet, $J=6.1$ Hz, 2H); 2.70 to 2.62 (quintet, $J=6.1$ Hz, 2H); 2.46 (s, 3H, NCH_3); 0.55 (s, 3H, SiCH_3).

$^{13}\text{C}(\text{CDCl}_3)$: 59.66 (OCH_2); 54.60 (NCH_2); 43.56 (MeN); 3.89 (MeSi).

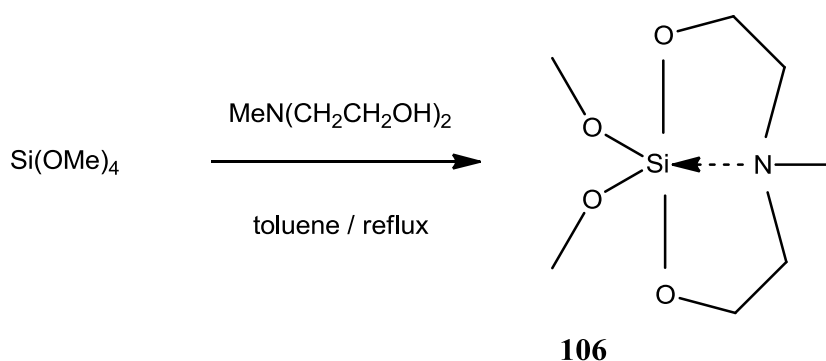
$^{29}\text{Si}(\text{CDCl}_3)$: -56.3 (SiO_2).

EI/MS (70eV) m/z (%):

195(65)[M]; 180(53)[$\text{M}^+ - \text{Me}$]; 166(4)[$\text{SiC}_4\text{H}_9\text{ClNO}_2^+$]; 160(18)[$\text{M}^+ - \text{Cl}$];
152(49)[$\text{SiC}_4\text{H}_9\text{ClO}_2^+$]; 137(100)[$\text{SiC}_3\text{H}_6\text{ClO}_2^+$]; 122(5)[$\text{SiC}_3\text{H}_7\text{ClO}^+$]; 116(7)[$\text{SiC}_4\text{H}_{10}\text{NO}^+$];
109(50)[$\text{SiCH}_2\text{ClO}_2^+$]; 95(22)[SiClO_2^+]; 79(10)[SiClO^+]; 70(19)[$\text{C}_4\text{H}_8\text{N}^+$]; 63(9)[SiCl^+].

Elemental analysis: Calculated for: $\text{C}_6\text{H}_{14}\text{ClNO}_2\text{Si}$: C, 36.82; H, 7.21; N, 7.16. Found: C, 37.16; H, 7.12; N, 7.25.

12.7.2 (MeO)₂Si(OCH₂CH₂)₂NMe (106)



A mixture of 1.000 g (8.390 mmol) of N-methyldiethanolamine and 1.405 g (9.230 mmol, 1.1 eq) of tetramethoxysilane and 31 mg (0.208 mmol) tetraethylammonium fluoride hydride was dissolved in 9 mL of toluene in a 100 mL three necked flask equipped with condenser under nitrogen. The reaction mixture was left for 24 hours under reflux while stirring with stir bar. After removal of the volatile colorless oily **106** (1.685 g) with some impurities according to NMR spectroscopy was obtained.

NMR (δ in ppm):

¹H(C₆D₆): 3.67 (s, 6H, OCH₃); 3.54 to 3.48 (m, 4H); 2.74 to 2.63 (m, 1H); 2.31 to 2.21 (m, 1H); 2.11 to 2.07 (m, 2H); 2.04 (s, 3H, NCH₃).

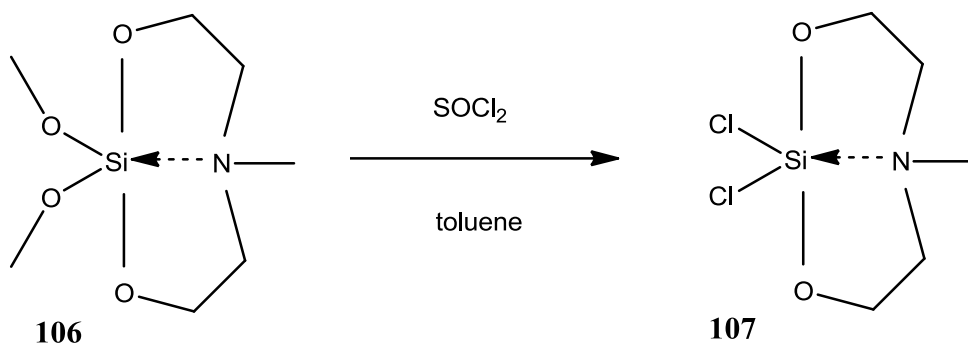
¹³C(C₆D₆): 60.23 (OCH₂); 55.27 (NCH₂); 51.45 (SiOMe); 43.08 (MeN).

²⁹Si(C₆D₆): -90.7.

EI/MS (70eV) m/z (%):

207(35)[M]; 176(70)[M-OMe⁺]; 164(11)[SiC₅H₁₂O₄⁺]; 149(58)[SiC₄H₉O₄⁺];
 145(21)[SiC₅H₁₁NO₂⁺]; 132(16)[SiC₄H₁₀NO₂⁺]; 121(41)[SiC₃H₉O₃⁺]; 107(6)[SiC₂H₇O₃⁺];
 87(100)[C₄H₉NO⁺]; 77(11)[SiHO₃⁺]; 71(86)[C₄H₉N⁺]; 61(10)[SiHO₂⁺].

12.7.3 Cl₂Si(OCH₂CH₂)₂NMe (107)



(MeO)₂Si(OCH₂CH₂)₂NMe (**106**) without further purification was dissolved in 5 mL of toluene and afterwards 4 mL of thionylchloride was added dropwise over 30 minutes to the reaction mixture. A greenish precipitate was formed during the dropping of thionylchloride but the solution mixture was left while stirring for 14 hours. By decantation a pale green residue was obtained. The residue was mixed with 5 ml of toluene and 5 ml of thionylchloride and again decanted. After removal of the volatile by vacuum pale green-orange powder of **107** (1.716 g) was obtained. Without decantation a sticky layer forms on the surface of the powders of **107** which prevents it from further reaction.

NMR (δ in ppm):

At 0 °C:

¹H(CDCl₃): 4.03 (t, J = 6.0 Hz, 4H, OCH₂); 3.13 to 3.05 (quintet, J = 6.0 Hz, 2H); 2.96 to 2.88 (quintet, J = 6.0 Hz, 2H); 2.68 (s, 3H, CH₃N).

At room temperature:

¹H(CDCl₃): 4.03 (t, J = 6.0 Hz, 4H, OCH₂); 3.12 to 2.84 (broad peak, 4H); 2.67 (s, 3H, CH₃N).

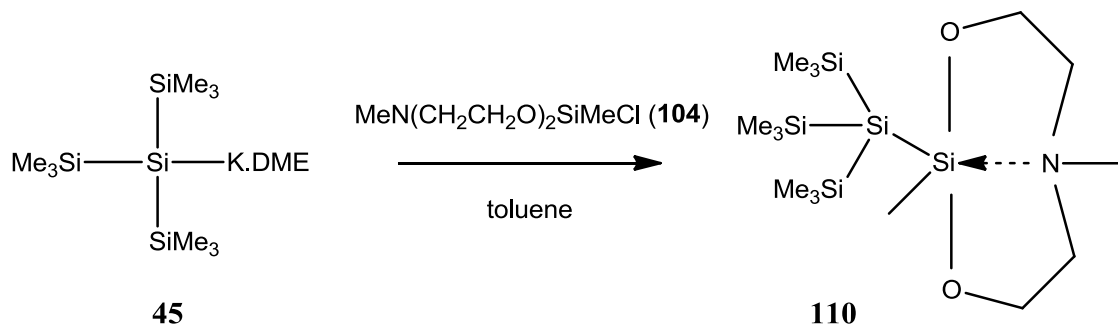
¹³C (CDCl₃): 58.92 (OCH₂); 53.77 (NCH₂); 44.94 (MeN).

²⁹Si(CDCl₃): -89.4.

EI/MS (70eV) m/z (%):

215(55)[M]; 200(7)[M⁺-Me]; 180(100)[M⁺-Cl]; 172(37)[SiC₃H₆Cl₂O₂⁺];
 157(40)[SiC₂H₃Cl₂O₂⁺]; 136(21)[SiC₃H₅ClO₂⁺]; 129(12)[SiCH₃Cl₂O⁺]; 115(25)[SiHCl₂O⁺];
 106(18)[SiC₂H₃ClO⁺]; 99(7)[SiC₃H₅NO⁺]; 81(5)[SiH₂ClO⁺]; 70(22)[C₄H₈N⁺]; 63(9)[SiCl⁺].

12.7.4 2'-(2',6'-dimethyl-1',3',6',2'-dioxazasilocanyl)-tris(trimethylsilyl)silane (**110**)



A mixture of 500 mg (1.558 mmol, 1 eq) of tetrakis(trimethylsilyl)silane (**47**) with 180 mg (1.605 mmol, 1.03 eq) of KO^tBu was dissolved in 3 mL of DME. The solution color turned orange immediately. After NMR spectroscopy confirmed formation of oligosilylpotassium, DME was removed by putting the sample under vacuum. Afterwards the oligosilylpotassium was dissolved in 5 mL of toluene and was added very fast to the slurry of 315 mg (1.605 mmol, 1.03 eq) of MeN(CH₂CH₂O)₂SiMeCl (**104**) in 1 mL of toluene while stirring. After 5 hours the solution mixture was filtered and the filter paper was washed with pentane. 405 mg of crude compound was obtained. Colorless crystals of **110** (373 mg, 61%) was obtained from pentane at -57 °C.

Melting point: 45-50 °C.

NMR (δ in ppm):

¹H(CDCl₃): 3.78 to 3.64 (m, 4H); 2.56 (t, *J* = 4.5 Hz, 4H); 2.41 (s, 3H, CH₃N); 0.31 (s, 3H, SiCH₃); 0.19 (s, 27H, (CH₃)₃Si).

¹³C(CDCl₃): 62.25 (OCH₂); 58.34 (NCH₂); 44.32 (MeN); 3.70 (MeSi); 2.40 ((Me₃Si)₃-Si).

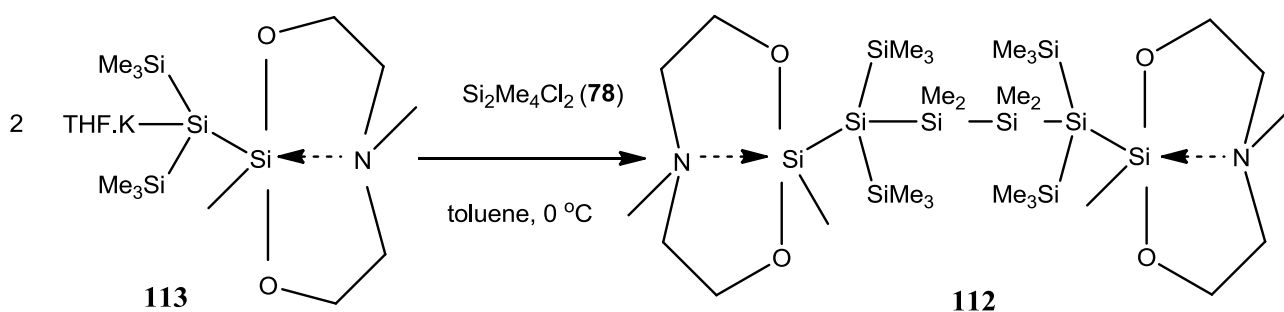
²⁹Si(CDCl₃): 3.5 (SiO₂); -10.1 (Me₃Si); -134.8 ((Me₃Si)₃Si).

MS (70eV) *m/z* (%):

392(1)[M⁺-Me]; 334(1)[M⁺-SiMe₃]; 247(1)[Si₄C₉H₂₇⁺]; 233(1)[Si₄C₈H₂₅⁺];
 189(1)[Si₂C₆H₁₅NO₂⁺]; 175(2)[Si₂C₅H₁₃NO₂⁺]; 160(100)[Si₂C₆H₁₄NO₂⁺];
 145(1)[SiC₅H₁₁NO₂⁺]; 131(2)[NC₆H₁₃O₂⁺]; 116(13)[NC₅H₁₀O₂⁺]; 101(1)[NC₅H₁₁O⁺];
 87(1)[NC₄H₉O⁺]; 73(16)[SiMe₃⁺].

Elemental analysis: Calculated for: C₁₅H₄₁NO₂Si₅: C, 44.17; H, 10.13; N, 3.43. Found: C, 44.24; H, 9.63; N, 3.41.

12.7.5 1,4-Bis-2'-(2',6'-dimethyl-1',3',6',2'-dioxazasilocanyl)-1,1,4,4-tetrakis(trimethylsilyl)tetramethyltetrasilane (112)



A mixture of 221 mg (0.542 mmol, 1 eq) of 2'-(2',6'-dimethyl-1',3',6',2'-dioxazasilocanyl)-tris(trimethylsilyl)silane (**110**) with 62 mg (0.558 mmol, 1.03 eq) of KO^tBu was dissolved in 3 mL of THF. The solution color turned yellow immediately. After NMR spectroscopy confirmed formation of oligosilocanylsilylpotassium, THF was removed by putting the sample under vacuum.

Afterwards the oligosilocanylsilylpotassium was dissolved in 3 mL of toluene and was added dropwise over 15 minutes to the ice cooled solution of 56 mg (0.298 mmol, 0.6 eq) of 1,2-dichlorotetramethyldisilane (**78**) in toluene. After 12 hours the volatile part was removed by vacuum and the residue was dissolved in benzene and passed through filter paper. 197 mg crude compound was obtained after benzene removal. Colorless crystals of **112** (150 mg, 70%) was obtained from a mixture of diethylether and acetonitrile 2:1.

Melting point: 128-137 $^\circ\text{C}$.

NMR (δ in ppm):

^1H (CDCl_3): 3.75 to 3.63 (m, 8H); 2.57 (t, $J=4.4$ Hz, 8H); 2.41 (s, 6H, CH_3N); 0.36 (s, 12H, $\text{Si}(\text{CH}_3)_2$); 0.34 (s, 6H, SiCH_3); 0.22 (s, 36H, $(\text{CH}_3)_3\text{Si}$).

^{13}C (CDCl_3): 62.32 (OCH_2); 58.65 (NCH_2); 43.91 (MeN); 3.63 (MeSi); 3.11 ($(\text{Me}_3\text{Si})_3\text{Si}$); 0.18 (Me_2Si).

^{29}Si (CDCl_3): 2.5 (SiO_2); -9.6 (Me_3Si); -31.0 (Me_2Si); -129.6 ($(\text{Me}_3\text{Si})_3\text{Si}$).

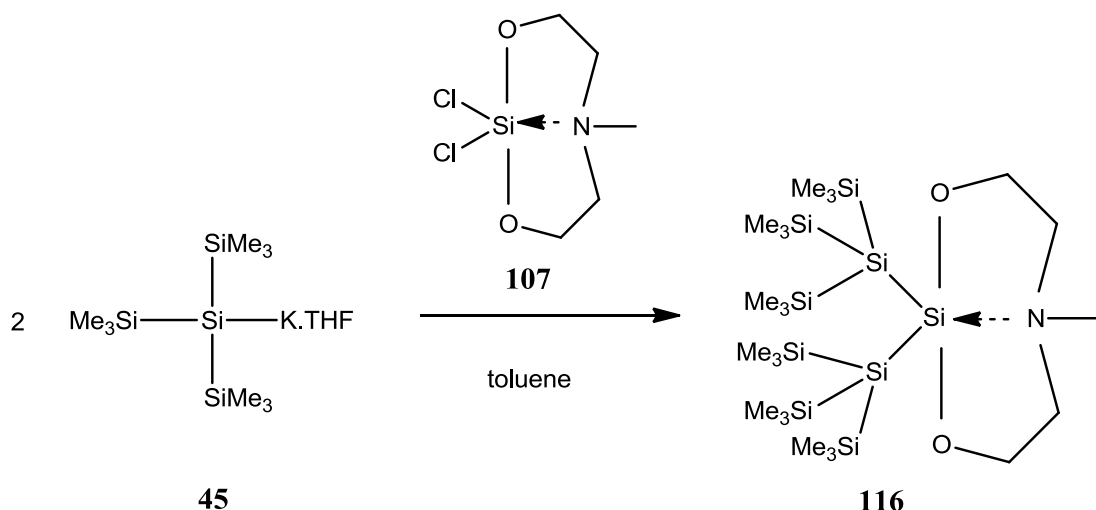
EI/MS (70eV) m/z (%):

784(1)[M^+]; 769(3)[M^+-Me]; 711(1)[M^+-SiMe_3]; 624(1)[$\text{C}_{22}\text{H}_{62}\text{NO}_2\text{Si}_9^+$]; 465(1)[$\text{C}_{16}\text{H}_{49}\text{Si}_8^+$]; 450(3)[$\text{C}_{16}\text{H}_{44}\text{NO}_2\text{Si}_6^+$]; 392(4)[$\text{C}_{14}\text{H}_{38}\text{NO}_2\text{Si}_5^+$]; 318(1)[$\text{C}_{10}\text{H}_{30}\text{Si}_6^+$]; 275(1)[$\text{C}_9\text{H}_{27}\text{Si}_5^+$]; 243(1)[$\text{C}_7\text{H}_{19}\text{Si}_5^+$]; 217(2)[$\text{C}_7\text{H}_{21}\text{Si}_4^+$]; 173(1)[$\text{C}_6\text{H}_{17}\text{Si}_3^+$]; 160(100)[$\text{C}_6\text{H}_{14}\text{NO}_2\text{Si}^+$]; 131(3)[$\text{NC}_6\text{H}_{13}\text{O}_2^+$]; 116(27)[$\text{NC}_5\text{H}_{10}\text{O}_2^+$]; 84(6)[$\text{NC}_5\text{H}_{10}^+$]; 73(16)[SiMe_3^+].

Elemental analysis: Calculated for: $\text{C}_{28}\text{H}_{76}\text{N}_2\text{O}_4\text{Si}_{10}$: C, 42.80; H, 9.75; N, 3.57. Found: C, 42.45; H, 9.41; N, 3.43.

Absorption: $\lambda = 254\text{nm}$ ($\epsilon = 7.42 \times 10^4 \text{ M}^{-1}\text{cm}^{-1}$) in *n*-hexane.

12.7.6 [(Me₃Si)₃Si]₂Si(OCH₂CH₂)₂NMe (116)



A mixture of 200 mg (0.624 mmol, 1 eq) of tetrakis(trimethylsilyl)silane (**47**) with 72 mg (0.642 mmol, 1.03 eq) of KO^tBu was dissolved in 3 mL of THF. The solution color turned orange immediately. After NMR spectroscopy confirmed formation of oligosilylpotassium, THF was removed by putting the sample under vacuum. Afterwards the oligosilylpotassium was dissolved in 5 mL of toluene and was added very fast to the slurry of 114 mg (0.530 mmol, 0.82 eq) of Cl₂Si(OCH₂CH₂)₂NMe (**107**) in 1 mL of toluene while stirring. After 6 hours the volatile was removed and the residue was dissolved in benzene and filtered with filter paper. 161 mg of crude compound was obtained after removal of the volatiles by vacuum. Colorless crystals of **116** (132 mg, 66%) was obtained from a mixture of diethylether and acetonitrile 2:1.

Melting point: 192-208 °C.

NMR (δ in ppm):

¹H(CDCl₃): 3.82 (t, *J*=4.6 Hz, 4H, OCH₂); 2.66 (t, *J*=4.7 Hz, 4H, NCH₂); 2.37 (s, 3H, CH₃N); 0.28 (s, 54H, (CH₃)₃Si).

¹³C(CDCl₃): 66.37 (OCH₂); 59.33 (NCH₂); 47.34 (MeN); 4.01 ((Me₃Si)₃-Si).

²⁹Si(CDCl₃): 19.6 (SiO₂); -9.6 (Me₃Si); -121.0 ((Me₃Si)₃Si).

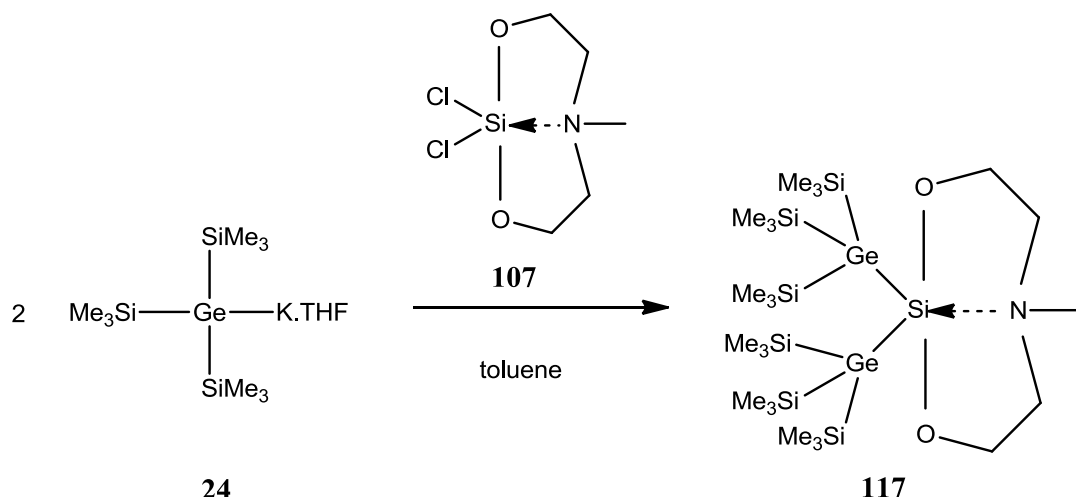
EI/MS (70eV) m/z (%):

638(1)[M⁺-H]; 624(3)[M⁺-Me]; 392(100)[M⁺-Si(SiMe₃)₃]; 320(2)[C₁₁H₃₀NO₂Si₄⁺];
 291(1)[C₉H₂₅NO₂Si₄⁺]; 233(1)[C₈H₂₅Si₄⁺]; 217(2)[C₇H₂₁Si₄⁺]; 173(7)[C₆H₁₇Si₃⁺];
 160(31)[C₅H₁₆Si₃⁺]; 131(5)[C₆H₁₃NO₂⁺]; 116(4)[C₅H₁₀NO₂⁺]; 84(5)[C₅H₁₀N⁺];
 73(25)[SiMe₃⁺].

Elemental analysis: Calculated for: C₂₃H₆₅NO₂Si₉: C, 43.13; H, 10.23; N, 2.19. Found: C, 43.89; H, 8.62; N, 2.12.

Absorption: λ = 260 nm (ε = 2.54 × 10⁴ M⁻¹cm⁻¹) in diethylether.

12.7.7 [(Me₃Si)₃Ge]₂Si(OCH₂CH₂)₂NMe (**117**)



A mixture of 400 mg (1.095 mmol, 1 eq) of tetrakis(trimethylsilyl)germane (**7**) with 126 mg (1.128 mmol, 1.03 eq) of KO^tBu was dissolved in 3 mL of THF. The solution color turned yellow immediately. After NMR spectroscopy confirmed formation of oligogermylpotassium, THF was removed by putting the sample under vacuum. Afterwards the oligogermylpotassium was dissolved in 5 mL of toluene and was added very fast to the slurry of 200 mg (0.925 mmol, 0.84 eq) of Cl₂Si(OCH₂CH₂)₂NMe (**107**) in 1 mL of toluene while stirring. After 6 hours the volatile was removed and the residue was dissolved in benzene and filtered with filter paper. 321 mg crude compound was obtained after removal of the volatiles. After sublimation of the formed tetrakis(trimethylsilyl)germane at 45 °C/ 0 mbar, 220 mg white powder was obtained. Colorless crystals of **117** (153 mg, 38%) was obtained from a mixture of diethylether and acetonitrile 2:1.

Melting point: 139-148 °C.

NMR (δ in ppm):

¹H(CDCl₃): 3.81 (t, $J=4.4$ Hz, 4H, OCH₂); 2.66 (t, $J=4.4$ Hz, 4H, NCH₂); 2.37 (s, 3H, CH₃N); 0.31 (s, 54H, (CH₃)₃Si).

¹³C(CDCl₃): 66.14 (OCH₂); 59.28 (NCH₂); 47.37 (MeN); 4.43 ((Me₃Si)₃).

²⁹Si(CDCl₃): 17.7 (SiO₂); -4.6 (Me₃Si).

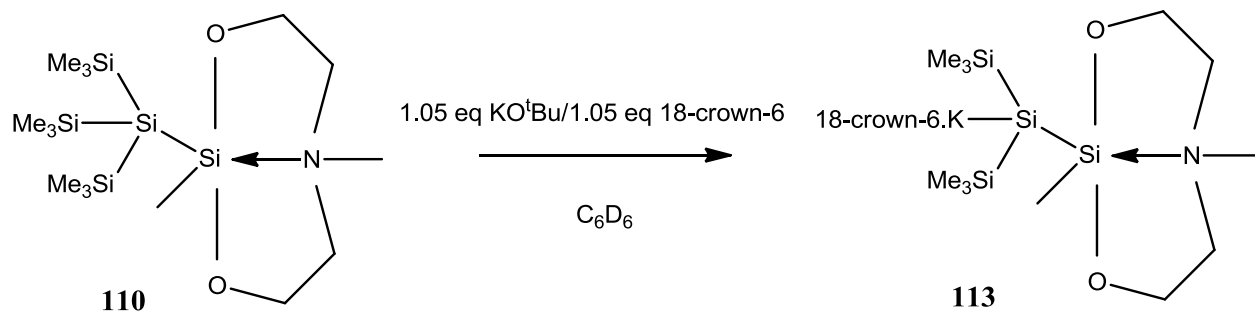
EI/MS (70eV) m/z (%):

730(1)[M]; 714(1)[C₂₂H₆₀Ge₂NO₂Si₇⁺]; 656(1)[C₂₀H₅₄Ge₂NO₂Si₆⁺];
 438(54)[C₁₄H₃₈GeNO₂Si₄⁺]; 365(2)[C₁₁H₂₉GeNO₂Si₃⁺]; 293(1)[C₉H₂₇GeSi₃⁺];
 261(1)[C₆H₁₃GeNO₂Si₂⁺]; 218(6)[C₆H₁₆GeSi₂⁺]; 205(2)[C₅H₁₅GeSi₂⁺]; 191(2)[C₄H₁₃GeSi₂⁺];
 160(42)[C₂H₆GeSi₂⁺]; 147(9)[GeSiMe₃⁺]; 131(8)[C₆H₁₃NO₂⁺]; 116(5)[C₅H₁₀NO₂⁺];
 84(3)[C₃H₁₀N⁺]; 75(100)[CH₃O₂Si⁺]; 73(33)[SiMe₃⁺].

Elemental analysis: Calculated for: C₂₃H₆₅Ge₂NO₂Si₇: C, 37.86; H, 8.98; N, 1.92. Found: C, 38.66; H, 7.70; N, 1.86.

Absorption: $\lambda = 256$ nm ($\epsilon = 4.18 \times 10^4$ M⁻¹cm⁻¹) in diethylether.

12.7.8 2'-(2',6'-dimethyl-1',3',6',2'-dioxazasilocanyl)bis(trimethylsilyl)-silanylpotassium.18-crown-6 (113)



A mixture of 48 mg (0.117 mmol, 1 eq) of 2'-(2',6'-dimethyl-1',3',6',2'-dioxazasilocanyl)-tris(trimethylsilyl)silane (**110**) and 14 mg (0.123 mmol, 1.05 eq) of KO^tBu and 32 mg (0.123 mmol, 1.05 eq) of 18-crown-6 was dissolved in 1 mL of C₆D₆ and left for 14 hours. Afterwards NMR spectroscopy confirmed formation of oligosilocanylsilylpotassium in a yellow solution. Yield: (74mg, 100%).

NMR (δ in ppm):

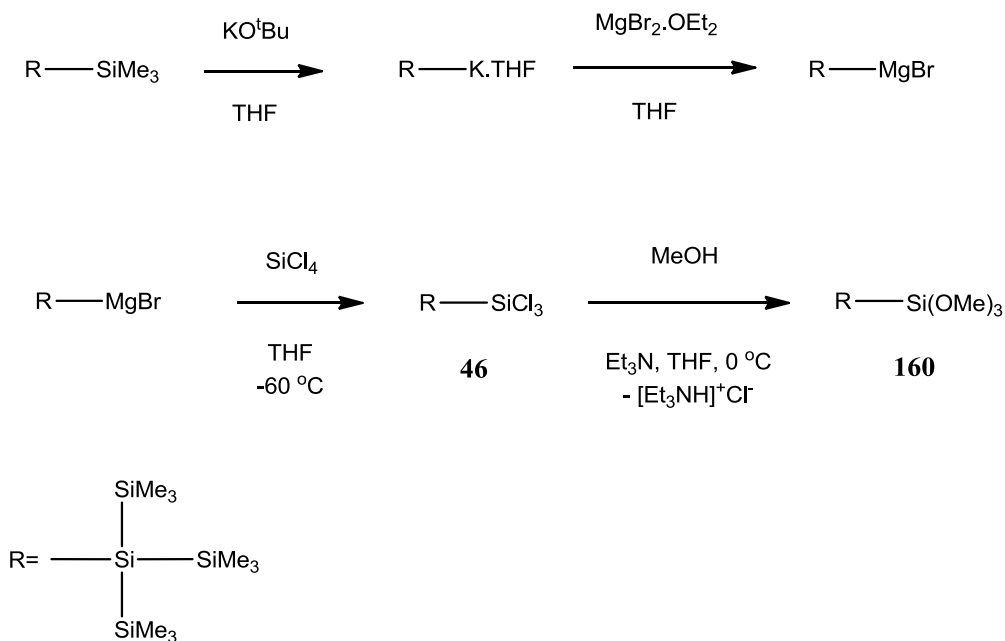
¹H(C₆D₆): 4.18 to 4.10 (m, 2H); 4.05 to 3.98 (m, 2H); 3.28 (s, 24H, CH₂O); 2.94 to 2.86 (m, 2H); 2.76 to 2.68 (m, 2H); 2.42 (s, 3H, CH₃N); 0.77 (s, 3H, SiCH₃); 0.71 (s, 18H, (CH₃)₃Si).

¹³C(C₆D₆): 70.14 (CH₂O); 63.00 (OCH₂); 60.74 (NCH₂); 46.22 (MeN); 7.54 ((Me₃Si)₃-Si) 6.40 (MeSi).

²⁹Si(C₆D₆): 30.7 (SiO₂); -4.8 (Me₃Si); -202.9 ((Me₃Si)₃Si).

12.8 Synthesis of methoxysilanes

12.8.1 Tris(trimethylsilyl)[trimethoxysilyl]silane (**160**)



A mixture of 1.000 g (3.12 mmol, 1 eq) of tetrakis(trimethylsilyl)silane (**47**) with 360 mg (3.21 mmol, 1.03 eq) of KO^tBu was dissolved in 6 mL of THF. After NMR confirmed formation of organosilylanion 450 mg (1.74 mmol, 0.55 eq) of magnesium bromide ethyl etherate was added to the solution while stirring.

The organosilylmagnesium anion solution in THF was added dropwise to the -60 °C solution of 1.590 g (9.36 mmol, 3 eq) of SiCl₄ in 6 mL of THF.

The reaction mixture was left while stirring to come to 10 °C. Afterwards the solvent was removed by vacuum. The residue was dissolved in pentane and was transferred to another flask under nitrogen by cannula. After removal of pentane, 1.045 g of white powder as product was obtained.

The 1.045 g (2.75 mmol, 1 eq) of tris(trimethylsilyl)trichlorosilylsilane (**46**) was dissolved in THF and was added dropwise to the solution mixture of 529 mg (16.50 mmol, 6 eq) of methanol and 1.110 g (10.97 mmol, 4 eq) of triethylamine in 10 mL of THF at 0 °C while stirring. Afterwards the reaction mixture was left to come to room temperature. Then the volatile was removed and the residue was dissolved in pentane and filtered with filter paper. 995 mg crude compound was obtained after removal of volatile by vacuum. Colorless crystals of **160** (823 mg, 81%) were obtained from a mixture of diethylether and acetonitrile 2:1 at -55 °C.

Melting point: 135-142 °C.

NMR (δ in ppm):

$^1\text{H}(\text{C}_6\text{D}_6)$: 3.46 (s, 9H, OCH_3); 0.35 (s, 27H, $\text{Si}(\text{CH}_3)_3$).

$^{13}\text{C}(\text{C}_6\text{D}_6)$: 50.01 (OMe); 2.60 (SiMe_3).

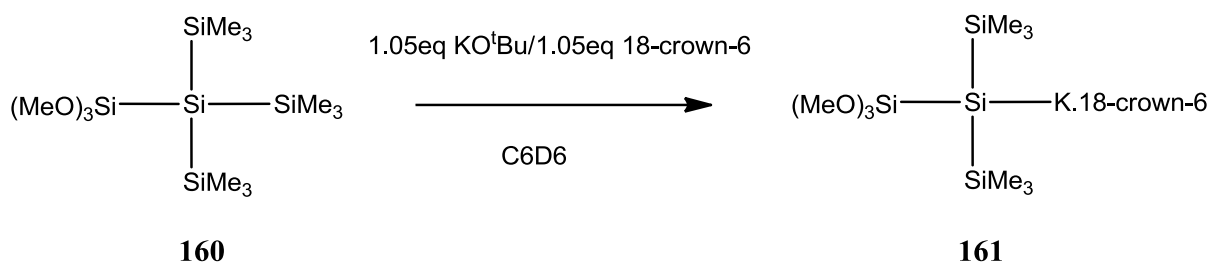
$^{29}\text{Si}(\text{C}_6\text{D}_6)$: -9.8 ($\text{Si}(\text{SiMe}_3)_3$); -32.2 ($\text{Si}(\text{OMe})_3$); -141.1 ($\text{Si}(\text{SiMe}_3)_3$).

MS (70eV) m/z (%):

368(1)[M]; 353(1)[$\text{M}^+ - \text{Me}$]; 264(6)[$\text{Si}_4\text{C}_8\text{H}_{24}\text{O}_2^+$]; 249(2)[$\text{Si}_4\text{C}_7\text{H}_{21}\text{O}_2^+$]; 235(1)[$\text{Si}_4\text{C}_6\text{H}_{19}\text{O}_2^+$];
219(2)[$\text{Si}_4\text{C}_6\text{H}_{19}\text{O}^+$]; 205(5)[$\text{Si}_4\text{C}_4\text{H}_{13}\text{O}_2^+$]; 189(1)[$\text{Si}_4\text{C}_3\text{H}_9\text{O}_2^+$]; 175(4)[$\text{Si}_3\text{C}_6\text{H}_{19}^+$];
161(2)[$\text{Si}_3\text{C}_5\text{H}_{17}^+$]; 147(2)[$\text{Si}_2\text{C}_3\text{H}_7\text{O}_3^+$]; 131(6)[$\text{Si}_3\text{C}_3\text{H}_{11}^+$]; 117(5)[$\text{Si}_2\text{C}_2\text{H}_5\text{O}_2^+$];
91(5)[$\text{SiC}_2\text{H}_7\text{O}_2^+$]; 73(100)[SiMe_3^+].

Elemental analysis: Calculated for: $\text{C}_{12}\text{H}_{36}\text{O}_3\text{Si}_5$: C, 39.08; H, 9.84. Found: C, 39.43; H, 9.49.

12.8.2 Bis(trimethylsilyl)[trimethoxysilyl]silylpotassium.18-crown-6 (161)



A mixture of 50 mg (0.135 mmol, 1 eq) of tris(trimethylsilyl)[trimethoxysilyl]silane (**160**) and 16 mg (0.142 mmol, 1.05 eq) of KO^tBu and 38 mg (0.098 mmol, 1.05 eq) of 18-crown-6 was dissolved in 1 mL of C₆D₆ and left for 14 hours. After NMR spectroscopy confirmed formation of methoxysilylpotassium in a pale beige solution, C₆D₆ was removed by putting the sample under vacuum and afterwards the residue was dissolved in diethylether. Pale beige crystals were obtained on the walls of the vial. Yield: (80mg, 100%).

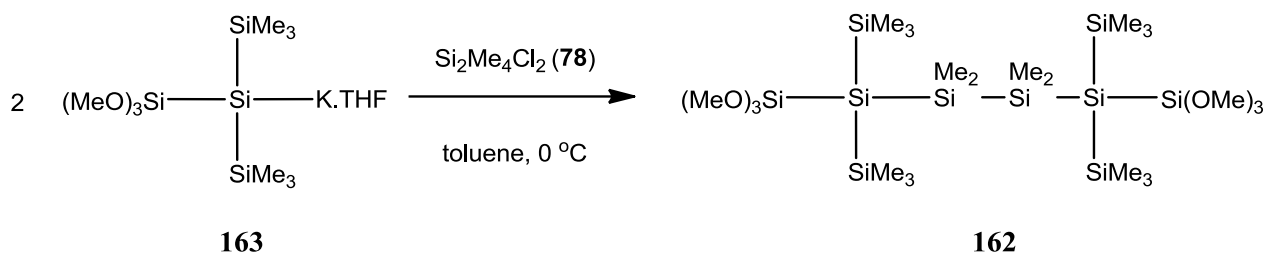
NMR (δ in ppm):

¹H(C₆D₆): 3.74 (s, 9H, OCH₃); 3.24 (s, 24H, CH₂O); 0.68 (s, 18H, Si(CH₃)₃).

¹³C(C₆D₆): 70.08 (CH₂O); 50.08 (OMe); 7.67 (SiMe₃).

²⁹Si(C₆D₆): 0.9 (Si(OMe)₃); -4.3 (Si(SiMe₃)₃); -220.9 (Si(SiMe₃)₃).

12.8.3 2,5-Bis(trimethoxysilyl)-2,5-bis(trimethylsilyl)decamethylhexasilane (162)



A mixture of 100 mg (0.272 mmol, 1 eq) of tris(trimethylsilyl)[trimethoxysilyl]silane (**160**) with 32 mg (0.285 mmol, 1.05 eq) of KO^tBu was dissolved in 1.5 mL of THF. The solution color turned beige immediately. After NMR spectroscopy confirmed formation of methoxysilylpotassium, it was added dropwise over 15 minutes to the ice cooled solution of 27 mg (0.142 mmol, 0.55 eq) of 1,2-dichlorotetramethyldisilane (**78**) in 5 mL of toluene and left to come to room temperature slowly while stirring. Afterwards the volatile was removed by vacuum and the residue dissolved in pentane and filtered with filter paper in air. 90 mg crude compound was obtained after removal of the volatiles. Colorless crystals of **162** (67 mg, 69%) were obtained from a mixture of diethylether and acetonitrile 2:1.

Melting point: 134-143°C.

NMR (δ in ppm):

¹H(C₆D₆): 3.48 (s, 18H, OCH₃); 0.71 (s, 12H, Si(CH₂)₂); 0.46 (s, 36H, Si(CH₃)₃).

¹³C(C₆D₆): 50.26 (OMe); 3.27 (SiMe₃); 0.37 (SiMe₂).

²⁹Si(C₆D₆): -9.2 (Si(SiMe₃)₃); -30.5 (SiMe₂); -32.7 (Si(OMe)₃); -135.7 (Si(SiMe₃)₃).

MS (70eV) m/z (%):

691(3)[M⁺-Me]; 644(1)[M⁺-2(OMe)]; 411(17)[Si₆C₁₃H₃₉O₃⁺]; 353(95)[Si₅C₁₁H₃₃O₃⁺]; 337(2)[Si₅C₁₀H₂₉O₃⁺]; 321(6)[Si₅C₁₀H₂₉O₂⁺]; 295(2)[Si₄C₉H₂₇O₃⁺]; 279(4)[Si₄C₈H₂₃O₃⁺]; 263(18)[Si₄C₈H₂₃O₂⁺]; 233(6)[Si₄C₈H₂₅⁺]; 205(12)[Si₄C₆H₂₁⁺]; 189(9)[Si₄C₅H₁₇⁺]; 175(7)[Si₃C₆H₁₉⁺]; 159(6)[Si₃C₄H₁₁O⁺]; 147(7)[Si₃C₄H₁₅⁺]; 131(11)[Si₃C₃H₁₁⁺]; 117(13)[Si₂C₄H₁₃⁺]; 89(14)[SiC₂H₅O₂⁺]; 73(100)[SiMe₃⁺].

Elemental analysis: Calculated for: C₂₂H₆₆O₆ Si₁₀: C, 37.34; H, 9.40. Found: C, 38.48; H, 9.00.

Absorption: $\lambda = 253$ nm ($\epsilon = 8.42 \times 10^4$ M⁻¹cm⁻¹) in n-hexane.

12.9 Nanomaterials' synthesis

12.9.1 Synthesis of germanium nanoparticles

12.9.1.1 In *n*-heptane with precursor to dicobalt octacarbonyl ratio 20:1 at 90 °C

A mixture of 164 mg (0.57 mmol) of tris(trimethylsilyl)germane and 10 mg (0.028 mmol) of dicobaltoctacarbonyl (5 mol % with respect to tris(trimethylsilyl)germane) was added to 1 mL of *n*-heptane and transferred to an NMR tube containing D₂O capillary. The NMR tube was completely sealed with parafilm and transferred to a Schlenk tube under nitrogen. A thermometer was put inside the Schlenk tube to measure the exact temperature of the sample. Oil bath was used to heat up the Schlenk tube to 90 °C.

12.9.1.2 In *n*-heptane with precursor to dicobalt octacarbonyl ratio 20:1 at 142 °C

100 mg (0.34 mmol) of tris(trimethylsilyl)germane was dissolved in 1 mL of *n*-heptane inside a Schlenk tube, then 6 mg (0.017 mmol) of dicobaltoctacarbonyl (5 mol % with respect to tris(trimethylsilyl)germane) was dissolved in 1 mL of *n*-heptane in another flask and then the solution was transferred to the Schlenk tube. Afterwards the solution mixture was heated up to 142 °C for 24 hours.

12.9.1.3 In *n*-dodecane with precursor to dicobalt octacarbonyl ratio 20:1 at 142 °C in presence of TOPO

100 mg (0.34 mmol) of tris(trimethylsilyl)germane was dissolved in 1 mL of *n*-dodecane inside a Schlenk tube, then 6 mg (0.017 mmol) of dicobaltoctacarbonyl (5 mol % with respect to tris(trimethylsilyl)germane) was dissolved in 1 mL of *n*-dodecane in another flask and then the solution was transferred to the Schlenk tube. After 1 hour, 500 mg (1.29 mmol) of TOPO was dissolved in 2 mL of *n*-dodecane and then was transferred to the Schlenk tube. Afterwards the solution mixture was heated up to 142 °C for 42 hours while stirred at 400 rpm.

12.9.1.4 In *n*-dodecane with precursor to dicobalt octacarbonyl ratio 20:4 at 142 °C in presence of TOPO

100 mg (0.34 mmol) of tris(trimethylsilyl)germane was dissolved in 1 mL of *n*-dodecane inside a Schlenk tube, then 24 mg (0.070 mmol) of dicobaltoctacarbonyl (20 mol % with respect to tris(trimethylsilyl)germane) was dissolved in 1 mL of *n*-dodecane in another flask and then the solution was transferred to the Schlenk tube. After 1 hour, 500 mg (1.29 mmol) of TOPO was dissolved in 2 mL of dodecane and then was transferred to the Schlenk tube. Afterwards the solution mixture was heated up to 142 °C for 42 hours while stirred at 400 rpm.

12.9.1.5 In *p*-xylene with precursor to dicobalt octacarbonyl ratio 20:1 at 142 °C in presence of TOPO

100 mg (0.34 mmol) of tris(trimethylsilyl)germane was dissolved in 1 mL of dry *p*-xylene inside a Schlenk tube, then 6 mg (0.017 mmol) of dicobaltoctacarbonyl (5 mol % with respect

to tris(trimethylsilyl)germane) was dissolved in 1 mL of dry *p*-xylene in another flask and then the solution was transferred to the Schlenk tube. After 1 hour, 500 mg (1.29 mmol) of TOPO was dissolved in 2 mL of dry *p*-xylene and then was transferred to the Schlenk tube. Afterwards the solution mixture was heated up to 142 °C for 140 hours (6 days) while stirred at 400 rpm.

12.9.1.6 In *n*-dodecane without dicobalt octacarbonyl at 142 °C in presence of TOPO

500 mg (1.29 mmol) of TOPO was dissolved in 3 mL of *n*-dodecane inside a Schlenk tube and afterwards 100 mg (0.34 mmol) of tris(trimethylsilyl)germane was added to solution mixture. Afterwards the solution mixture was heated up to 142 °C for 42 hours while stirred at 400 rpm.

12.9.1.7 In *n*-hexadecane without dicobalt octacarbonyl at 252 °C in presence of TOPO and oleylamine

178 mg (0.460 mmol) of TOPO was dissolved in 2 mL of *n*-hexadecane in a Schlenk tube. Afterwards 0.3 mL of oleylamine was added to the mixture and heated up to 252 °C with oil bath. Then 20 mg (0.068 mmol) of tris(trimethylsilyl)germane was added rapidly to the Schlenk tube and immediately the Schlenk tube was closed and left for 20 minutes at 252 °C while stirred at 700 rpm. Afterwards the Schlenk tube brought out of the oil bath and left in air to come to room temperature.

12.9.2 Synthesis of indium nanoparticles

12.9.2.1 Indium nanoparticles capped tri-*n*-butylphosphine

For synthesis of indium nanoparticles of sample C, 40 mg (0.18 mmol) of anhydrous indium(III) chloride was dissolved in 4.5 mL of degassed dimethylformamid (DMF) in a Schlenk flask under nitrogen and was stirred for 15 min. (For synthesis of indium nanoparticles of sample A, B and D, 20, 30 and 50 mg of anhydrous indium(III) chloride was dissolved in the same amount of DMF respectively).

Then 450 µL of tri-*n*-butylphosphine was added to the mixture and was stirred for 30 min. Afterwards 220 µL of 2M solution of LiBH₄ in THF was added to the sample C through a septum dropwise with similar intervals between each drop to the solution mixture during 90 seconds while stirred at 1200 rpm (110 µL, 180 µL and 270 µL of 2M solution of LiBH₄ in THF was added to sample A, B and D respectively following the same procedure for sample C). The stirring of the solution mixture was continued for 30 min at 1200 rpm while the septum with a needle inside was in place to let hydrogen gas come out of the flask. Afterwards the flask was put on oil bath with initial temperature of 45 °C and then the temperature was increased to 50 °C in 6 minutes and then the flask was kept at 50 °C for 4 minutes (During heating the flask stirring speed was 800 rpm). Then the flask was left at room temperature while stirred at 1200 RPM for 3 hours and at this step was used for further analysis with DLS and TEM. The color of final solution containing indium nanoparticles was dark brown.

12.9.2.2 Indium nanoparticles capped tri-*n*-butylphosphine phase transfer to the mixture of *n*-dodecane and oleylamine

1.5 mL of degassed *n*-dodecane and 0.5 mL of degassed oleylamine were mixed in a Schlenk flask under nitrogen and put under vigorous stirring at 1200 rpm. 1 mL of as prepared indium nanoparticles in DMF was injected rapidly to the mixture and left under vigorous stirring for 2 hours. Afterwards the solution mixture was transferred to a vial under nitrogen for separation of polar and nonpolar phases.

12.9.2.3 Indium nanoparticles simultaneous phase transfer and ripening method

40 mg (0.18 mmol) of anhydrous indium(III) chloride was dissolved in 4.5 mL of degassed DMF in a Schlenk flask under nitrogen and was stirred for 15 min.

Then 450 μL of tri-*n*-butylphosphine was added to the mixture and was stirred for 30 min. Afterwards 220 μL of 2M solution of LiBH_4 in THF was added to the solution mixture through a septum drop-wise with similar intervals between each drop during 90 seconds while stirred at 1200 rpm. The stirring was continued for 12 min at 1200 rpm after last drop while the septum was in place with a needle inside to let hydrogen gas came out of the flask. Afterwards 1 mL of the solution mixture was syringed and was added to the mixture of 1.5 mL of *n*-dodecane and 0.5 mL of oleylamine under vigorous stirring at 1200 rpm. The vigorous stirring was continued for 90 minutes after which the solution mixture was left immobile for 3 hours for complete separation of polar and non-polar media. Non-polar phase containing indium nanoparticles as top layer was syringed and was transferred to another flask under nitrogen.

12.9.2.4 Indium nanoparticles simultaneous phase transfer and ripening method in presence of diphenylamine or 1-phenylethylamine

40 mg (0.18 mmol) of anhydrous indium(III) chloride was dissolved in 4.5 mL of degassed DMF in a Schlenk flask under nitrogen and was stirred for 15 min.

Then 450 μL of tri-*n*-butylphosphine was added to the mixture and was stirred for 30 min. Afterwards 220 μL of 2M solution of LiBH_4 in THF was added to the solution mixture through a septum drop-wise with similar intervals between each drop during 90 seconds while stirred at 1200 rpm. The stirring was continued for 12 min at 1200 rpm after last drop while the septum was in place with a needle inside to let hydrogen gas came out of the flask. Afterwards 1 mL of the solution mixture was syringed and was added to the mixture of 1.5 mL of *n*-dodecane and 0.5 mL of oleylamine and 56 mg (0.33 mmol) of diphenylamine or 46 mg (0.38 mmol) of 1-phenylethylamine under vigorous stirring at 1200 rpm. The stirring was continued for 90 minutes after which the solution mixture left immobile for 3 hours for complete separation of polar and non-polar media. Non-polar phase containing indium nanoparticles as top layer was syringed and was transferred to another flask under nitrogen.

12.9.3 Synthesis of germanium nanowires with 1,1,2,2-tetrakis(trimethylsilyl)digermane (8) precursor

12.9.3.1 Germanium nanowires synthesis at 180 °C in *n*-dodecane in presence of TOPO

250 mg (0.674 mmol) of TOPO was dissolved in 1.3 mL of *n*-dodecane inside a Schlenk tube with a stir bar inside and heated to 180 °C with an oil bath while stirred at 150 rpm. Afterwards 270 µL of colloidal solution of indium nanoparticles in *n*-dodecane with mean diameter of 9 nm was syringed and was transferred to the Schlenk tube. 30 seconds later a solution of 60 mg (0.136 mmol) of 1,1,2,2-tetrakis(trimethylsilyl)digermane (8) in 400 µL of *n*-dodecane was injected rapidly to the Schlenk tube. Then the Schlenk tube was closed and left for 5 minutes in oil bath while stirred at 150 rpm. Afterwards the Schlenk tube was brought out of the oil bath and left in air to cool down to room temperature. As soon as the Schlenk tube cooled down, 1 mL of dry and degassed toluene was added to it to prevent TOPO solidification.

Used molar ratio of Ge:In was 55:1

Weight of the black solid obtained: 14 mg

12.9.3.2 Germanium nanowires synthesis at 300 °C in *n*-hexadecane in presence of TOPO

200 mg (0.483 mmol) of TOPO was dissolved in 1.5 mL of *n*-hexadecane inside a Schlenk tube and the Schlenk tube was placed inside a vertical tube furnace and heated to 300 °C. Afterwards 200 µL of colloidal solution of indium nanoparticles in *n*-hexadecane with mean diameter of 9 nm was syringed and was transferred to the Schlenk tube. 30 seconds later a solution of 79 mg (0.179 mmol) of 1,1,2,2-tetrakis(trimethylsilyl)digermane (8) in 100 µL of *n*-hexadecane was injected rapidly to the Schlenk tube. Then the Schlenk tube was closed and left for 5 minutes at 300 °C. Afterwards the Schlenk tube was brought out of the furnace and left in air to cool down to room temperature. As soon as the Schlenk tube cooled down, 1 mL of dry and degassed toluene was added to it to prevent TOPO solidification.

Used molar ratio of Ge:In was 100:1

Weight of the black solid obtained: 21 mg

12.9.3.3 Germanium nanowires synthesis at 300 °C in *n*-hexadecane in presence of oleylamine

300 µL of oleylamine was added to 1.5 mL of *n*-hexadecane inside a Schlenk tube and the Schlenk tube was placed inside a vertical tube furnace and heated to 300 °C. Afterwards 200 µL of colloidal solution of indium nanoparticles in *n*-hexadecane with mean diameter of 9 nm was syringed and was transferred to the Schlenk tube. 30 seconds later a solution of 79 mg (0.179 mmol) of 1,1,2,2-tetrakis(trimethylsilyl)digermane (8) in 100 µL of *n*-hexadecane was injected rapidly to the Schlenk tube. Then the Schlenk tube was closed and left for 5 minutes at 300 °C. Afterwards the Schlenk tube was brought out of the furnace and left in air to cool down to room temperature.

Used molar ratio of Ge:In was 100:1

Weight of the black solid obtained: 20 mg

12.9.3.4 Germanium nanowires synthesis at 350 °C in presence of oleylamine

-With high squalane to oleylamine ratio

300 μ L of oleylamine was added to 1.5 mL of squalane inside a Schlenk tube and the Schlenk tube was placed inside a vertical tube furnace and heated to 350 °C. Afterwards 200 μ L of colloidal solution of indium nanoparticles in squalane with mean diameter of 9 nm was syringed and was transferred to the Schlenk tube. 15 seconds later 79 mg (0.179 mmol) of 1,1,2,2-tetrakis(trimethylsilyl)digermane (**8**) was injected rapidly to the Schlenk tube. Then the Schlenk tube was closed and left for 6 minutes at 350 °C. Afterwards the Schlenk tube was brought out of the furnace and left in air to cool down to room temperature.

Used molar ratio of Ge:In was 100:1

Weight of the black solid obtained: 24 mg

-With low squalane to oleylamine ratio

1 mL of oleylamine was added to 800 μ L of squalane inside a Schlenk tube and the Schlenk tube was placed inside a vertical tube furnace and heated to 350 °C. Afterwards 200 μ L of colloidal solution of indium nanoparticles in squalane with mean diameter of 9 nm was syringed and was transferred to the Schlenk tube. 15 seconds later 79 mg (0.179 mmol) of 1,1,2,2-tetrakis(trimethylsilyl)digermane (**8**) was injected rapidly to the Schlenk tube. Then the Schlenk tube was closed and left for 6 minutes at 350 °C. Afterwards the Schlenk tube was brought out of the furnace and left in air to cool down to room temperature.

Used molar ratio of Ge:In was 100:1

Weight of the black solid obtained: 20 mg

-With pure oleylamine without any squalane

1.5 mL of oleylamine was added to a Schlenk tube and the Schlenk tube was placed inside a vertical tube furnace and heated to 350 °C. Afterwards 200 μ L of colloidal solution of indium nanoparticles in squalane with mean diameter of 9 nm was syringed and was transferred to the Schlenk tube. 15 seconds later 79 mg (0.179 mmol) of 1,1,2,2-tetrakis(trimethylsilyl)digermane (**8**) was injected rapidly to the Schlenk tube. Then the Schlenk tube was closed and left for 6 minutes at 350 °C. Afterwards the Schlenk tube was brought out of the furnace and left in air to cool down to room temperature.

Used molar ratio of Ge:In was 100:1

Weight of the black solid obtained: 23 mg

-With a mixture of oleylamine and TOPO

200 mg (0.483 mmol) of TOPO was dissolved in 900 μ L of oleylamine inside a Schlenk tube and the Schlenk tube was placed inside a vertical tube furnace and heated to 350 °C. Afterwards 150 μ L of colloidal solution of indium nanoparticles in squalane with mean diameter of 9 nm was syringed and was transferred to the Schlenk tube. 15 seconds later 59 mg (0.134 mmol) of 1,1,2,2-tetrakis(trimethylsilyl)digermane (**8**) was injected rapidly to the Schlenk tube. Then the Schlenk tube was closed and left for 6 minutes at 350 °C. Afterwards the Schlenk tube was brought out of the furnace and left in air to cool down to room temperature.

Used molar ratio of Ge:In was 96:1

Weight of the black solid obtained: 14 mg

12.9.3.5 Germanium nanowires synthesis at 380 °C in squalane in presence of TOPO

300 mg (0.776 mmol) of TOPO was dissolved in 1.3 mL of squalane inside a Schlenk tube and the Schlenk tube was placed inside a vertical tube furnace and heated to 380 °C. Afterwards 200 μ L of colloidal solution of indium nanoparticles in squalane with mean diameter of 9 nm was syringed and was transferred to the Schlenk tube. 15 seconds later 79 mg (0.179 mmol) of 1,1,2,2-tetrakis(trimethylsilyl)digermane (**8**) was injected rapidly to the Schlenk tube. Then the Schlenk tube was closed and left for 6 minutes at 380 °C. Afterwards the Schlenk tube was brought out of the furnace and left in air to cool down to room temperature. As soon as the Schlenk tube cooled down, 1 mL of dry and degassed toluene was added to it to prevent TOPO solidification.

Used molar ratio of Ge:In was 100:1

Weight of the black solid obtained: 21 mg

12.10 Preparation of analytical samples of nanomaterials

12.10.1 Germanium nanoparticles separation from solution for SEM analysis

0.7 mL of the reaction mixture of germanium nanoparticles was mixed with 0.8 mL of dry and degassed methanol inside a polypropylene vial under nitrogen and was centrifuged for 10 min at 6000 rpm. Afterwards the solution mixture was decanted; the residue was mixed with 1.5 mL of methanol and was redispersed with ultrasonic bath. Again the vial containing germanium nanoparticles in methanol was centrifuged for 10 min at 6000 rpm; the solution phase was decanted and finally the residue was put under vacuum to remove volatiles. To avoid oxidation of the black residue, it was transferred to a SEM sample holder in a special sealed chamber inside a glovebox before SEM analysis.

12.10.2 Indium nanoparticles sample preparation for TEM analysis

A pre-carbon coated copper TEM grid was put on a filter paper, 2 drops of colloidal solution of indium nanoparticles in DMF was dropped on the grid and immediately the grid was transferred to a vial and put under vacuum for 10 minutes to remove volatile compounds. Afterwards the vial was refilled with nitrogen and to avoid indium nanoparticles oxidation the grid was kept under nitrogen until TEM analysis.

12.10.3 Indium nanoparticles capped ligands sample preparation for FT-IR spectroscopy

To avoid oxidation of indium nanoparticles the whole work up was performed under nitrogen and the samples were brought out to air right before FT-IR analysis.

- *indium nanoparticles capped tri-*n*-butylphosphine in DMF*

2 mL of as prepared colloidal solution of indium nanoparticles capped tri-*n*-butylphosphine in DMF was centrifuged for 10 minutes at 6000 rpm. Afterwards the solution phase was decanted; the residue was mixed with 5 mL of dry DMF and was redispersed with ultrasonic bath. Again the vial containing indium nanoparticles in DMF was centrifuged for 5 min at 2000 rpm; the solution phase was decanted and finally the residue was put under vacuum for 15 minutes to remove volatiles. The residue was directly subjected to FT-IR spectroscopy.

- *Indium nanoparticles in non-polar media*

2 mL of colloidal solution of indium nanoparticles in non-polar media was mixed with 14 mL of dry DMF and 6 mL of dry THF and the mixture was stirred for 2 minutes. Then the solution mixture was centrifuged for 5 minutes at 2000 rpm. Afterwards the solution phase was decanted; the residue was mixed with 10 mL of dry DMF and was redispersed with ultrasonication. The sample containing redispersed particles in DMF was centrifuged for 6 minutes at 2000; the solution phase was decanted and finally the residue was put under vacuum for 15 minutes to remove volatiles. The residue was directly subjected to FT-IR spectroscopy.

12.10.4 Germanium nanowires separation from solution for SEM and TEM analysis

The solution mixture of indium catalyzed germanium nanowires was mixed with 10 mL of methanol in a 20 mL glass vial and was centrifuged for 5 minutes at 3000 rpm to remove the capping ligand on the surface of nanowires. Afterwards the solution mixture was decanted; the black residue was mixed with 15 mL of pentane and was redispersed via shaking the vial in hand. The sample containing redispersed nanowires in pentane was centrifuged for 5 minutes at 3000 rpm; the solution phase was decanted and the vial containing the black residue was transferred into a glass chamber under low flow of nitrogen to evaporate the residue of pentane. Finally the sample was put under vacuum for 30 minutes for complete removal of the volatiles. Sample kept inside the glovebox for further SEM and TEM analysis.

13 References

- (1) Zaitseva, N.; Dai, Z. R.; Grant, C. D.; Harper, J.; Saw, C. *Chem. Mater.* **2007**, *19*, 5174–5178.
- (2) Vaughn, D. D.; Bondi, J. F.; Schaak, R. E. *Chem. Mater.* **2010**, *22*, 6103–6108.
- (3) Chiu, H. W.; Chervin, C. N.; Kauzlarich, S. M. *Chem. Mater.* **2005**, *17*, 4858–4864.
- (4) Heath, J. R.; Shiang, J. J.; Alivisatos, A. P. *J. Chem. Phys.* **1994**, *101*, 1607–1615.
- (5) Taylor, B. R.; Kauzlarich, S. M.; Delgado, G. R.; Lee, H. W. H. *Chem. Mater.* **1999**, *11*, 2493–2500.
- (6) Tsai, K. L.; Dye, J. L. *J. Am. Chem. Soc.* **1991**, *113*, 1650–1652.
- (7) Liu, Q.; Zhou, D.; Nishio, K.; Ichino, R.; Okido, M. *Mater. Trans.* **2010**, *51*, 1386–1389.
- (8) Dang, T. M. D.; Le, T. T. T.; Fribourg-Blanc, E.; Dang, M. C. *Adv. Nat. Sci: Nanosci. Nanotechnol.* **2011**, *2*, 025004.
- (9) Lim, T. H.; Ingham, B.; Kamarudin, K. H.; Etchegoin, P. G.; Tilley, R. D. *Cryst. Growth Des.* **2010**, *10*, 3854–3858.
- (10) Hammarberg, E.; Feldmann, C. *Chem. Mater.* **2009**, *21*, 771–774.
- (11) Neogy, S.; Savalia, R. T.; Tewari, R.; Srivastava, D.; Dey, G. K. *Indian J. Pure Appl. Phys.* **2006**, *44*, 119–124.
- (12) Wang, Z. L. *Adv. Mater.* **2003**, *15*, 1497–1514.
- (13) Zhou, W.; Greer, H. F. *Int. J. Nanotechnol.* **2012**, *9*, 69.
- (14) Bendersky, L. A.; Gayle, F. W. *Electron diffraction using transmission electron microscopy*; National Institute of Standards and Technology, 2001.
- (15) Hunter, D.; Osborn, W.; Wang, K.; Kazantseva, N.; Hattrick-Simpers, J.; Suchoski, R.; Takahashi, R.; Young, M. L.; Mehta, A.; Bendersky, L. A.; Lofland, S. E.; Wuttig, M.; Takeuchi, I. *Nat. Commun.* **2011**, *2*, 518.
- (16) Carrado, A.; Pelletier, H.; Rol, T. In *Biomedical Engineering - From Theory to Applications*; Fazel, R., Ed.; InTech, 2011.
- (17) Hassan, P. A.; Rana, S.; Verma, G. *Langmuir* **2015**, *31*, 3–12.
- (18) Kätzel, Uwe. *Dynamic Light Scattering for the Characterization of Polydisperse Fractal Systems by the Example of*. Unpublished PhD dissertation, Dresden University of Technology; Dresden, Germany, 2007.
- (19) Schnablegger, Heimo; Singh, Yashveer. *The SAXS Guide*; Anton Paar GmbH, 2013.
- (20) Wang, D. *Pure Appl. Chem.* **2007**, *79*, 55–65.
- (21) Chockla, A. M.; Korgel, B. A. *J. Mater. Chem.* **2009**, *19*, 996–1001.
- (22) Lu, X.; Fanfair, D. D.; Johnston, K. P.; Korgel, B. A. *J. Am. Chem. Soc.* **2005**, *127*, 15718–15719.
- (23) Hanrath, T.; Korgel, B. A. *J. Am. Chem. Soc.* **2002**, *124*, 1424–1429.
- (24) Wang, D.; Dai, H. *Angew. Chem. Int. Ed.* **2002**, *41*, 4783–4786.
- (25) Biswas, S.; Singha, A.; Morris, M. A.; Holmes, J. D. *Nano Lett.* **2012**, *12*, 5654–5663.
- (26) Chockla, A. M.; Harris, J. T.; Korgel, B. A. *Chem. Mater.* **2011**, *23*, 1964–1970.
- (27) Geaney, H.; Mullane, E.; Ryan, K. M. *J. Mater. Chem. C* **2013**, *1*, 4996–5007.
- (28) Wang, F.; Dong, A.; Sun, J.; Tang, R.; Yu, H.; Buhro, W. E. *Inorg. Chem.* **2006**, *45*, 7511–7521.
- (29) Okamoto, H.; Massalski, T. B. *Bull. Alloy Phase Diagr.* **1984**, *5*, 601–610.
- (30) Olesinski, R. W.; Abbaschian, G. J. *Bull. Alloy Phase Diagr.* **1986**, *7*, 535–540.
- (31) Yang, H.-J.; Tuan, H.-Y. *J. Mater. Chem.* **2012**, *22*, 2215–2225.
- (32) Holmes, J. D.; Johnston, K. P.; Doty, R. C.; Korgel, B. A. *Science* **2000**, *287*, 1471–1473.
- (33) Hanrath, T.; Korgel, B. *Adv. Mater.* **2003**, *15*, 437–440.
- (34) Park, J.-H.; Sudarshan, T. S. *Chemical Vapor Deposition*; ASM International, 2001.

- (35) Pei, L. Z.; Cai, Z. Y. *Recent Pat. Nanotechnol.* **2012**, *6*, 44–59.
- (36) Zahedifar, M.; Farangi, M.; Pakzamid, M. H. *J. NanoStructures* **2013**, *3*, 103–108.
- (37) Li, C.; Mizuta, H.; O, S. In *Nanowires - Implementations and Applications*; Hashim, A., Ed.; InTech, 2011.
- (38) Morales, A. M.; Lieber, C. M. *Science* **1998**, *279*, 208–211.
- (39) Hiruma, K.; Murakoshi, H.; Yazawa, M.; Katsuyama, T. *J. Cryst. Growth* **1996**, *163*, 226–231.
- (40) Zhang, Y. F.; Tang, Y. H.; Wang, N.; Lee, C. S.; Bello, I.; Lee, S. T. *Phys. Rev. B* **2000**, *61*, 4518–4521.
- (41) Franchi, S. In *Molecular Beam Epitaxy*; Henini, M., Ed.; Elsevier: Oxford, 2013; pp. 1–46.
- (42) Omi, H.; Ogino, T. *Appl. Phys. Lett.* **1997**, *71*, 2163–2165.
- (43) Carim, A. I.; Collins, S. M.; Foley, J. M.; Maldonado, S. *J. Am. Chem. Soc.* **2011**, *133*, 13292–13295.
- (44) Gu, J.; Collins, S. M.; Carim, A. I.; Hao, X.; Bartlett, B. M.; Maldonado, S. *Nano Lett.* **2012**, *12*, 4617–4623.
- (45) Hobbs, R. G.; Barth, S.; Petkov, N.; Zirngast, M.; Marschner, C.; Morris, M. A.; Holmes, J. D. *J. Am. Chem. Soc.* **2010**, *132*, 13742–13749.
- (46) Lotty, O.; Hobbs, R.; O'Regan, C.; Hlina, J.; Marschner, C.; O'Dwyer, C.; Petkov, N.; Holmes, J. D. *Chem. Mater.* **2013**, *25*, 215–222.
- (47) Yang, Z.; Veinot, J. G. C. *J. Mater. Chem.* **2011**, *21*, 16505–16509.
- (48) Yi, G.-C. *Semiconductor Nanostructures for Optoelectronic Devices: Processing, Characterization and Applications*; Springer Science & Business Media, 2012.
- (49) Claeys, C.; Simoen, E. *Germanium-Based Technologies: From Materials to Devices*; Elsevier, 2011.
- (50) Dunlap, W. C. *Phys. Rev.* **1954**, *94*, 1531–1540.
- (51) Jeon, N.; Dayeh, S. A.; Lauhon, L. J. *Nano Lett.* **2013**, *13*, 3947–3952.
- (52) Lopez, F. J.; Hemesath, E. R.; Lauhon, L. J. *Nano Lett.* **2009**, *9*, 2774–2779.
- (53) Morris, J. W. In *Materials science*; 2014; pp. 76–107.
- (54) Geaney, H.; Dickinson, C.; Weng, W.; Kiely, C. J.; Barrett, C. A.; Gunning, R. D.; Ryan, K. M. *Cryst. Growth Des.* **2011**, *11*, 3266–3272.
- (55) Barth, S.; Boland, J. J.; Holmes, J. D. *Nano Lett.* **2011**, *11*, 1550–1555.
- (56) Kipping, F. S.; Sands, J. E. *J. Chem. Soc., Trans.* **1921**, *119*, 830–847.
- (57) Miller, R. D.; Michl, J. *Chem. Rev.* **1989**, *89*, 1359–1410.
- (58) Wesson, J. P.; Williams, T. C. *J. Polym. Sci. Polym. Chem. Ed.* **1980**, *18*, 959–965.
- (59) Marschner, C. In *Functional Molecular Silicon Compounds I*; Scheschkewitz, D., Ed.; Structure and Bonding; Springer International Publishing, 2013; pp. 163–228.
- (60) Plitt, H. S.; Downing, J. W.; Raymond, M. K.; Balaji, V.; Michl, J. *J. Chem. Soc., Faraday Trans.* **1994**, *90*, 1653–1662.
- (61) Bande, A.; Michl, J. *Chem. – Eur. J.* **2009**, *15*, 8504–8517.
- (62) Gilman, H.; Atwell, W. H.; Schwebke, G. L. *J. Organomet. Chem.* **1964**, *2*, 369–371.
- (63) Marschner, C.; Baumgartner, J.; Wallner, A. *Dalton Trans.* **2006**, 5667–5674.
- (64) Stueger, H.; Fuerpass, G.; Baumgartner, J.; Mitterfellner, T.; Flock, M. *Z. Naturforsch., B: Chem. Sci* **2009**, *64*, 1598–1606.
- (65) Fujiki, M.; Koe, J. R.; Terao, K.; Sato, T.; Teramoto, A.; Watanabe, J. *Polym J* **2003**, *35*, 297–344.
- (66) Voronkov, M. G. *Pure Appl. Chem.* **1966**, *13*, 35–59.
- (67) Gordon, M. S.; Carroll, M. T.; Jensen, J. H.; Davis, L. P.; Burggraf, L. W.; Guidry, R. M. *Organometallics* **1991**, *10*, 2657–2660.
- (68) Schmidt, M. W.; Windus, T. L.; Gordon, M. S. *J. Am. Chem. Soc.* **1995**, *117*, 7480–7486.

- (69) Trofimov, A. B.; Zakrzewski, V. G.; Dolgounitcheva, O.; Ortiz, J. V.; Sidorkin, V. F.; Belogolova, E. F.; Belogolov, M.; Pestunovich, V. A. *J. Am. Chem. Soc.* **2005**, *127*, 986–995.
- (70) Frye, C. L.; Vincent, G. A.; Hauschildt, G. L. *J. Am. Chem. Soc.* **1966**, *88*, 2727–2730.
- (71) Chandrasekaran, A.; Day, R. O.; Holmes, R. R. *J. Am. Chem. Soc.* **2000**, *122*, 1066–1072.
- (72) Puri, J. K.; Singh, R.; Chahal, V. K. *Chem. Soc. Rev.* **2011**, *40*, 1791–1840.
- (73) Wagler, J.; Gerlach, D.; Roewer, G. *Chem. Heterocycl. Compd.* **2006**, *42*, 1557–1567.
- (74) Shatz, V. D.; Belikov, V. A.; Urtane, I. P.; Zelchan, G. I.; Lukevics, E. *J. Chromatogr. A* **1982**, *237*, 57–63.
- (75) Kemme, A.; Bleidelis, J.; Urtane, I.; Zelchan, G.; Lukevics, E. *J. Organomet. Chem.* **1980**, *202*, 115–121.
- (76) Karlov, S. S.; Selina, A. A.; Chernyshova, E. S.; Oprunenko, Y. F.; Merkulov, A. A.; Tafeenko, V. A.; Churakov, A. V.; Howard, J. A. K.; Zaitseva, G. S. *Inorg. Chim. Acta* **2007**, *360*, 563–578.
- (77) Voronkov, M. G.; Kuznetsova, G. A.; Baryshok, V. P. *Russ. J. Gen. Chem.* **2010**, *80*, 1926–1928.
- (78) Adamovich, S. N.; Prokopyev, V. Y.; Rakhlin, V. I.; Mirskov, R. G.; Voronkov, M. G. *Synth. React. Inorg. Met.-Org. Chem.* **1991**, *21*, 1261–1264.
- (79) Voronkov, M. G.; Kuznetsova, G. A. *Russ. J. Gen. Chem.* **2009**, *79*, 925–927.
- (80) Chuit, C.; Corriu, R. J. P.; Reye, C.; Young, J. C. *Chem. Rev.* **1993**, *93*, 1371–1448.
- (81) Cerveau, G.; Chuit, C.; Corriu, R. J. P.; Nayyar, N. K.; Reye, C. *J. Organomet. Chem.* **1990**, *389*, 159–168.
- (82) Voronkov, M. G.; Dyakov, V. M.; Kirpichenko, S. V. *J. Organomet. Chem.* **1982**, *233*, 1–147.
- (83) Karlov, S. S.; Shutov, P. L.; Akhmedov, N. G.; Seip, M. A.; Lorberth, J.; Zaitseva, G. S. *J. Organomet. Chem.* **2000**, *598*, 387–394.
- (84) Zaitsev, K. V.; Churakov, A. V.; Poleshchuk, O. K.; Oprunenko, Y. F.; Zaitseva, G. S.; Karlov, S. S. *Dalton Trans.* **2014**, *43*, 6605–6609.
- (85) Hall, L. H. *J. Electrochem. Soc.* **1972**, *119*, 1593–1596.
- (86) Woelk, E.; Shenai-Khatkhate, D. V.; DiCarlo Jr., R. L.; Amamchyan, A.; Power, M. B.; Lamare, B.; Beaudoin, G.; Sagnes, I. *J. Cryst. Growth* **2006**, *287*, 684–687.
- (87) Fischer, J.; Baumgartner, J.; Marschner, C. *Organometallics* **2005**, *24*, 1263–1268.
- (88) Hlina, J.; Mechtler, C.; Wagner, H.; Baumgartner, J.; Marschner, C. *Organometallics* **2009**, *28*, 4065–4071.
- (89) Fischer, Jelena. Synthesis of Complex Polysilanes. PhD dissertation, Graz University of Technology: Graz, Austria, 2005.
- (90) Marschner, C. *Eur. J. Inorg. Chem.* **1998**, *1998*, 221–226.
- (91) Bock, H.; Meuret, J.; Ruppert, K. *Angew. Chem.* **1993**, *105*, 413–415.
- (92) Fischer, Roland. Oligosilylanions: Syntheses and Properties. PhD dissertation, Graz University of Technology: Graz, Austria, 2003.
- (93) Pandurangan, A.; Morin, C.; Qian, D.; Andrews, R.; Crocker, M. *Carbon* **2009**, *47*, 1708–1714.
- (94) Arnold, D. C.; Hobbs, R. G.; Zirngast, M.; Marschner, C.; Hill, J. J.; Ziegler, K. J.; Morris, M. A.; Holmes, J. D. *J. Mater. Chem.* **2009**, *19*, 954–961.
- (95) Zirngast, M.; Marschner, C.; Baumgartner, J. *Organometallics* **2006**, *25*, 4897–4908.
- (96) Rohde, M.; Müller, L. O.; Himmel, D.; Scherer, H.; Krossing, I. *Chem. Eur. J.* **2014**, *20*, 1218–1222.
- (97) Lloyd, G. E. *Mineral. Mag.* **1987**, *51*, 3–19.
- (98) Cookson, J. *Platin. Met. Rev.* **2012**, *56*, 83–98.
- (99) Yang, J.; Lee, J. Y.; Ying, J. Y. *Chem. Soc. Rev.* **2011**, *40*, 1672–1696.

- (100) Sperling, R. A.; Parak, W. J. *Philos. Trans. R. Soc. London, Ser. A* **2010**, *368*, 1333–1383.
- (101) Hatakeyama, M.; Kishi, H.; Kita, Y.; Imai, K.; Nishio, K.; Karasawa, S.; Masaïke, Y.; Sakamoto, S.; Sandhu, A.; Tanimoto, A.; Gomi, T.; Kohda, E.; Abe, M.; Handa, H. *J. Mater. Chem.* **2011**, *21*, 5959–5966.
- (102) Yang, J.; Lee, J. Y.; Deivaraj, T. C.; Too, H. P. *J. Colloid Interface Sci.* **2004**, *277*, 95–99.
- (103) Pabisch, S.; Feichtenschlager, B.; Kickelbick, G.; Peterlik, H. *Chem. Phys. Lett.* **2012**, *521*, 91–97.
- (104) Chen, Z. H.; Kim, C.; Zeng, X.; Hwang, S. H.; Jang, J.; Ungar, G. *Langmuir* **2012**, *28*, 15350–15361.
- (105) Collins, G.; Kolešnik, M.; Krstić, V.; Holmes, J. D. *Chem. Mater.* **2010**, *22*, 5235–5243.
- (106) Olesinki, R. W.; Kanani, N.; Abbaschian, G. J. *Bull. Alloy Phase Diagr.* **1985**, *6*, 536–539.
- (107) O'Regan, C.; Biswas, S.; Petkov, N.; Holmes, J. D. *J. Mater. Chem. C* **2013**, *2*, 14–33.
- (108) Wrackmeyer, B.; Stader, C.; Zhou, H. *Spectrochim. Acta Part Mol. Spectrosc.* **1989**, *45*, 1101–1111.
- (109) Smith, M. B.; March, J. *Marche's Advanced Organic Chemistry 6th ed.*; John Wiley & Sons, Inc., 2006.
- (110) Voronkov, M. G.; Baryshok, V. P.; Lazareva, N. F. *Russ. Chem. Bull.* **1996**, *45*, 1970–1972.
- (111) Selina, A. A.; Karlov, S. S.; Gauchenova, E. V.; Churakov, A. V.; Kuz'mina, L. G.; Howard, J. A. K.; Lorberth, J.; Zaitseva, G. S. *Heteroat. Chem.* **2004**, *15*, 43–56.
- (112) Gaderbauer, W.; Zirngast, M.; Baumgartner, J.; Marschner, C.; Tilley, T. D. *Organometallics* **2006**, *25*, 2599–2606.
- (113) Shen, Q.; Hilderbrandt, R. L. *J. Mol. Struct.* **1980**, *64*, 257–262.
- (114) Párkányi, L.; Nagy, J.; Simon, K. *J. Organomet. Chem.* **1975**, *101*, 11–18.
- (115) Conquest, version 1.16 was used. Bruno, I. J.; Edgington, P. R.; Kessler, M.; Macrae, C. F.; McCabe, P.; Pearson, J.; Ta.
- (116) Kayser, C.; Fischer, R.; Baumgartner, J.; Marschner, C. *Organometallics* **2002**, *21*, 1023–1030.
- (117) Wallner, A.; Wagner, H.; Baumgartner, J.; Marschner, C.; Rohm, H. W.; Köckerling, M.; Krempner, C. *Organometallics* **2008**, *27*, 5221–5229.
- (118) Whittaker, S. M.; Brun, M.-C.; Cervantes-Lee, F.; Pannell, K. H. *J. Organomet. Chem.* **1995**, *499*, 247–252.
- (119) Fischer, R.; Konopa, T.; Ullly, S.; Baumgartner, J.; Marschner, C. *J. Organomet. Chem.* **2003**, *685*, 79–92.
- (120) Attar-Bashi, M. T.; Rickard, C. E. F.; Roper, W. R.; Wright, L. J.; Woodgate, S. D. *Organometallics* **1998**, *17*, 504–506.
- (121) Yoshikawa, A.; Gordon, M. S.; Sidorkin, V. F.; Pestunovich, V. A. *Organometallics* **2001**, *20*, 927–931.
- (122) Jenkins, D. M.; Teng, W.; English, U.; Stone, D.; Ruhlandt-Senge, K. *Organometallics* **2001**, *20*, 4600–4606.
- (123) Gaderbauer, W.; Balatoni, I.; Wagner, H.; Baumgartner, J.; Marschner, C. *Dalton Trans.* **2010**, *39*, 1598–1603.
- (124) Arnold, J.; Tilley, T. D.; Rheingold, A. L.; Geib, S. J. *Inorg. Chem.* **1987**, *26*, 2106–2109.
- (125) Kayser, C.; Marschner, C. *Monatsh. Chem.* **1999**, *130*, 203–206.
- (126) Woo, H. G.; Heyn, R. H.; Tilley, T. D. *J. Am. Chem. Soc.* **1992**, *114*, 5698–5707.

- (127) Kayser, C.; Frank, D.; Baumgartner, J.; Marschner, C. *J. Organomet. Chem.* **2003**, *667*, 149–153.
- (128) Csonka, G. I.; Hencsei, P. *J. Comput. Chem.* **1996**, *17*, 767–780.
- (129) Szpakolski, K.; Latham, K.; Rix, C.; Rani, R. A.; Kalantar-zadeh, K. *Polyhedron* **2013**, *52*, 719–732.
- (130) Cox, M. G.; Manning, A. R.; Soye, P.; McArdle, P.; Cunningham, D. *Journal of Organometallic Chemistry* **1994**, *484*, 97–106.
- (131) West, R. *Pure Appl. Chem.* **1982**, *54*.
- (132) Johnson, O. H.; Harris, D. M. *J. Am. Chem. Soc.* **1950**, *72*, 5564–5566.
- (133) Gilman, H.; Smith, C. L. *J. Organomet. Chem.* **1967**, *8*, 245–253.
- (134) Brook, A. G.; Abdesaken, F.; Söllradl, H. *J. Organomet. Chem.* **1986**, *299*, 9–13.
- (135) Wagner, H.; Baumgartner, J.; Müller, T.; Marschner, C. *J. Am. Chem. Soc.* **2009**, *131*, 5022–5023.
- (136) Kollegger, G.; Hassler, K. *J. Organomet. Chem.* **1995**, *485*, 233–236.
- (137) Marschner, C. *Eur. J. Inorg. Chem.* **1998**, *1998*, 221–226.
- (138) Herzog, U.; Roewer, G. *J. Organomet. Chem.* **1997**, *544*, 217–223.
- (139) Apeloig, Y.; Yuzefovich, M.; Bendikov, M.; Bravo-Zhivotovskii, D.; Klinkhammer, K. *Organometallics* **1997**, *16*, 1265–1269.
- (140) Ishikawa, M.; Kumada, M.; Sakurai, H. *J. Organomet. Chem.* **1970**, *23*, 63–69.
- (141) McLafferty, F. W. *Interpretation of Mass Spectra*; University science books, Mill valley, Ca, 1980.
- (142) SAINTPLUS: Software Reference Manual, Version 6.45; BrukerAXS: Madison, WI, 1997–2003.
- (143) Sheldrick, G. M. SADABS. Version 2.10; Bruker AXS, Madison, WI, 2003.
- (144) Sheldrick, G. M. *Acta Crystallographica Section A Foundations of Crystallography* **2008**, *64*, 112–122.
- (145) Glatter, O.; Kratky, O. *Small Angle X-ray Scattering*; Academic Press, 1982.
- (146) Guinier, A.; Fournet, G. *Small-angle scattering of X-rays*; Wiley, 1955.

14 Appendix

14.1 X-ray crystallographic tables

14.1.1 (*tert*-Butyldiphenylsilyl)tris(trimethylsilyl)germane (26)

Empirical formula	C ₂₅ H ₄₆ Ge Si ₄	
Formula weight	531.57	
Temperature	100(2) K	
Wavelength	0.71073 Å	
Crystal system, space group	monoclinic, P2(1)/c	
Unit cell dimensions	a = 10.088(2) Å	α = 90 deg.
	b = 31.046(6) Å	β = 117.24(3) deg.
	c = 10.690(2) Å	γ = 90 deg.
Volume	2976.7(10) Å ³	
Z, Calculated density	4, 1.186 Mg/m ³	
Absorption coefficient	1.201 mm ⁻¹	
F(000)	1136	
Crystal size	0.38 x 0.26 x 0.14 mm	
Theta range for data collection	1.31 to 26.38 deg.	
Limiting indices	-12 ≤ h ≤ 12, -37 ≤ k ≤ 38, -13 ≤ l ≤ 13	
Reflections collected / unique	22422 / 6057 [R(int) = 0.0872]	
Completeness to theta = 26.38	99.4 %	
Absorption correction	SADABS	
Max. and min. transmission	0.8499 and 0.6583	
Refinement method	Full-matrix least-squares on F ²	
Data / restraints / parameters	6057 / 0 / 283	
Goodness-of-fit on F ²	1.078	
Final R indices [I > 2σ(I)]	R1 = 0.0703, wR2 = 0.1826	
R indices (all data)	R1 = 0.0849, wR2 = 0.1883	
Largest diff. peak and hole	3.146 and -1.348 e.Å ⁻³	

14.1.2 1-(*tert*-Butyl)-3,3,3-trimethyl-1,1-diphenyl-2,2-bis(trimethylsilyl)trisilane (27)

Empirical formula	C ₂₅ H ₄₆ Si ₅	
Formula weight	487.07	
Temperature	100(2) K	
Wavelength	0.71073 Å	
Crystal system, space group	monoclinic, P2(1)/c	
Unit cell dimensions	a = 10.594(2) Å	α = 90 deg.
	b = 18.139(4) Å	β = 95.11(3) deg.
	c = 15.919(3) Å	γ = 90 deg.
Volume	3046.8(11) Å ³	
Z, Calculated density	4, 1.062 Mg/m ³	
Absorption coefficient	0.245 mm ⁻¹	
F(000)	1064	
Crystal size	0.28 x 0.24 x 0.12 mm	
Theta range for data collection	1.71 to 26.37 deg.	
Limiting indices	-13 ≤ h ≤ 13, -22 ≤ k ≤ 22, -19 ≤ l ≤ 19	
Reflections collected / unique	24118 / 6202 [R(int) = 0.0679]	
Completeness to theta = 26.37	99.5 %	
Absorption correction	SADABS	
Max. and min. transmission	0.9712 and 0.9346	
Refinement method	Full-matrix least-squares on F ²	
Data / restraints / parameters	6202 / 0 / 283	
Goodness-of-fit on F ²	0.981	
Final R indices [I > 2 σ (I)]	R1 = 0.0480, wR2 = 0.1079	
R indices (all data)	R1 = 0.0731, wR2 = 0.1164	
Largest diff. peak and hole	0.420 and -0.254 e.Å ⁻³	

14.1.3 ((*tert*-Butyldiphenylsilyl)bis(trimethylsilyl)germyl)potassium.18-crown-6 (30)

Empirical formula	C ₃₄ H ₆₁ Ge K O ₆ Si ₄	
Formula weight	761.79	
Temperature	100(2) K	
Wavelength	0.71073 Å	
Crystal system, space group	monoclinic, P2(1)/c	
Unit cell dimensions	a = 9.6258(19) Å	α = 90 deg.
	b = 21.484(4) Å	β = 101.32(3) deg.
	c = 20.354(4) Å	γ = 90 deg.
Volume	4127.4(14) Å ³	
Z, Calculated density	4, 1.226 Mg/m ³	
Absorption coefficient	0.968 mm ⁻¹	
F(000)	1624	
Crystal size	0.28 x 0.18 x 0.18 mm	
Theta range for data collection	1.90 to 26.38 deg.	
Limiting indices	-12 ≤ h ≤ 12, -26 ≤ k ≤ 26, -25 ≤ l ≤ 25	
Reflections collected / unique	32766 / 8421 [R(int) = 0.0469]	
Completeness to theta = 26.38	99.9 %	
Absorption correction	SADABS	
Max. and min. transmission	0.8451 and 0.7734	
Refinement method	Full-matrix least-squares on F ²	
Data / restraints / parameters	8421 / 0 / 415	
Goodness-of-fit on F ²	1.039	
Final R indices [I > 2 σ (I)]	R1 = 0.0421, wR2 = 0.1019	
R indices (all data)	R1 = 0.0535, wR2 = 0.1067	
Largest diff. peak and hole	0.718 and -0.231 e.Å ⁻³	

**14.1.4 2-tert-Butyl-2,2-diphenyl-1,1-bis(trimethylsilyl)disilanyl)potassium.18-crown-6
(31)**

Empirical formula	C ₃₄ H ₆₁ K O ₆ Si ₄	
Formula weight	717.29	
Temperature	100(2) K	
Wavelength	0.71073 Å	
Crystal system, space group	monoclinic, P2(1)/n	
Unit cell dimensions	a = 9.5929(19) Å	α = 90 deg.
	b = 21.354(4) Å	β = 101.01(3) deg.
	c = 20.266(4) Å	γ = 90 deg.
Volume	4074.8(14) Å ³	
Z, Calculated density	4, 1.169 Mg/m ³	
Absorption coefficient	0.286 mm ⁻¹	
F(000)	1552	
Crystal size	0.36 x 0.32 x 0.24 mm	
Theta range for data collection	1.40 to 26.33 deg.	
Limiting indices	-11 ≤ h ≤ 11, -26 ≤ k ≤ 26, -25 ≤ l ≤ 25	
Reflections collected / unique	32093 / 8245 [R(int) = 0.0477]	
Completeness to theta = 26.33	99.5 %	
Absorption correction	SADABS	
Max. and min. transmission	0.9345 and 0.9040	
Refinement method	Full-matrix least-squares on F ²	
Data / restraints / parameters	8245 / 0 / 415	
Goodness-of-fit on F ²	1.053	
Final R indices [I > 2 σ (I)]	R1 = 0.0491, wR2 = 0.1188	
R indices (all data)	R1 = 0.0634, wR2 = 0.1256	
Largest diff. peak and hole	0.434 and -0.641 e.Å ⁻³	

14.1.5 Tris(trimethylsilyl)silatranysilane (44)

Empirical formula	C ₁₅ H ₃₉ N O ₃ Si ₅	
Formula weight	421.92	
Temperature	200(2) K	
Wavelength	0.71073 Å	
Crystal system, space group	triclinic, P-1	
Unit cell dimensions	a = 8.9914(18) Å	α = 90.30(3) deg.
	b = 10.914(2) Å	β = 90.05(3) deg.
	c = 13.856(3) Å	γ = 112.46(3) deg.
Volume	1256.5(4) Å ³	
Z, Calculated density	2, 1.115 Mg/m ³	
Absorption coefficient	0.297 mm ⁻¹	
F(000)	460	
Crystal size	0.26 x 0.18 x 0.12 mm	
Theta range for data collection	2.02 to 26.37 deg.	
Limiting indices	-11 ≤ h ≤ 11, -13 ≤ k ≤ 13, -17 ≤ l ≤ 17	
Reflections collected / unique	9262 / 4886 [R(int) = 0.0579]	
Completeness to theta = 26.37	95.0 %	
Absorption correction	SADABS	
Max. and min. transmission	0.9653 and 0.9268	
Refinement method	Full-matrix least-squares on F ²	
Data / restraints / parameters	4886 / 0 / 226	
Goodness-of-fit on F ²	1.069	
Final R indices [I > 2 σ(I)]	R1 = 0.0806, wR2 = 0.2198	
R indices (all data)	R1 = 0.1011, wR2 = 0.2331	
Largest diff. peak and hole	0.971 and -0.661 e.Å ⁻³	

14.1.6 Bis(trimethylsilyl)methylsilatranyl silane (55)

Empirical formula	C ₁₃ H ₃₃ N O ₃ Si ₄	
Formula weight	363.76	
Temperature	100(2) K	
Wavelength	0.71073 Å	
Crystal system, space group	orthorhombic, Pcca	
Unit cell dimensions	a = 26.403(5) Å	α = 90 deg.
	b = 12.048(2) Å	β = 90 deg.
	c = 12.972(3) Å	γ = 90 deg.
Volume	4126.5(14) Å ³	
Z, Calculated density	8, 1.171 Mg/m ³	
Absorption coefficient	0.296 mm ⁻¹	
F(000)	1584	
Crystal size	0.29 x 0.20 x 0.12 mm	
Theta range for data collection	1.54 to 26.37 deg.	
Limiting indices	-32 ≤ h ≤ 32, -15 ≤ k ≤ 15, -15 ≤ l ≤ 16	
Reflections collected / unique	31229 / 4226 [R(int) = 0.0563]	
Completeness to theta = 26.37	100.0 %	
Absorption correction	SADABS	
Max. and min. transmission	0.9653 and 0.9191	
Refinement method	Full-matrix least-squares on F ²	
Data / restraints / parameters	4226 / 0 / 197	
Goodness-of-fit on F ²	1.397	
Final R indices [I > 2 σ(I)]	R1 = 0.0753, wR2 = 0.1461	
R indices (all data)	R1 = 0.0793, wR2 = 0.1481	
Largest diff. peak and hole	0.514 and -0.358 e.Å ⁻³	

14.1.7 Bis(trimethylsilyl)ethylsilatranyl silane (57)

Empirical formula	C ₁₄ H ₃₅ N O ₃ Si ₄	
Formula weight	377.79	
Temperature	150(2) K	
Wavelength	0.71073 Å	
Crystal system, space group	orthorhombic, Pcca	
Unit cell dimensions	a = 26.703(5) Å	α = 90 deg.
	b = 12.277(3) Å	β = 90 deg.
	c = 13.290(3) Å	γ = 90 deg.
Volume	4356.7(15) Å ³	
Z, Calculated density	8, 1.152 Mg/m ³	
Absorption coefficient	0.283 mm ⁻¹	
F(000)	1648	
Crystal size	0.42 x 0.37 x 0.12 mm	
Theta range for data collection	1.53 to 26.38 deg.	
Limiting indices	-33 ≤ h ≤ 33, -15 ≤ k ≤ 15, -16 ≤ l ≤ 16	
Reflections collected / unique	32747 / 4467 [R(int) = 0.0533]	
Completeness to theta = 26.38	99.9 %	
Absorption correction	SADABS	
Max. and min. transmission	0.9669 and 0.8905	
Refinement method	Full-matrix least-squares on F ²	
Data / restraints / parameters	4467 / 1 / 225	
Goodness-of-fit on F ²	1.135	
Final R indices [I > 2 σ(I)]	R1 = 0.0811, wR2 = 0.1831	
R indices (all data)	R1 = 0.1009, wR2 = 0.1964	
Largest diff. peak and hole	0.573 and -0.413 e.Å ⁻³	

14.1.8 Bis(trimethylsilyl)phenylsilatranylsilane (60)

Empirical formula	C ₁₈ H ₃₅ N O ₃ Si ₄	
Formula weight	425.83	
Temperature	100(2) K	
Wavelength	0.71073 Å	
Crystal system, space group	orthorhombic, Pca2(1)	
Unit cell dimensions	a = 19.188(4) Å	α = 90 deg.
	b = 10.488(2) Å	β = 90 deg.
	c = 23.506(5) Å	γ = 90 deg.
Volume	4730.6(16) Å ³	
Z, Calculated density	8, 1.196 Mg/m ³	
Absorption coefficient	0.268 mm ⁻¹	
F(000)	1840	
Crystal size	0.19 x 0.17 x 0.12 mm	
Theta range for data collection	1.73 to 26.00 deg.	
Limiting indices	-23 ≤ h ≤ 23, -12 ≤ k ≤ 12, -28 ≤ l ≤ 28	
Reflections collected / unique	35342 / 9218 [R(int) = 0.0704]	
Completeness to theta = 26.00	100.0 %	
Absorption correction	SADABS	
Max. and min. transmission	0.9685 and 0.9508	
Refinement method	Full-matrix least-squares on F ²	
Data / restraints / parameters	9218 / 13 / 482	
Goodness-of-fit on F ²	1.217	
Final R indices [I > 2 σ(I)]	R1 = 0.0910, wR2 = 0.2092	
R indices (all data)	R1 = 0.0961, wR2 = 0.2124	
Absolute structure parameter	0.60(19)	
Largest diff. peak and hole	1.565 and -0.505 e.Å ⁻³	

14.1.9 (*tert*-Butyldimethylsilyl)bis(trimethylsilyl)silatranylsilane (62)

Empirical formula	C ₁₈ H ₄₅ N O ₃ Si ₅	
Formula weight	464.00	
Temperature	100(2) K	
Wavelength	0.71073 Å	
Crystal system, space group	trigonal, R-3	
Unit cell dimensions	a = 35.146(6) Å	α = 90 deg.
	b = 35.146(6) Å	β = 90 deg.
	c = 11.619(2) Å	γ = 120 deg.
Volume	12429(4) Å ³	
Z, Calculated density	18, 1.116 Mg/m ³	
Absorption coefficient	0.275 mm ⁻¹	
F(000)	4572	
Crystal size	0.25 x 0.15 x 0.08 mm	
Theta range for data collection	1.88 to 26.35 deg.	
Limiting indices	-43 ≤ h ≤ 43, -43 ≤ k ≤ 43, -14 ≤ l ≤ 14	
Reflections collected / unique	33094 / 5643 [R(int) = 0.0312]	
Completeness to theta = 26.35	100.0 %	
Absorption correction	SADABS	
Max. and min. transmission	0.9783 and 0.9343	
Refinement method	Full-matrix least-squares on F ²	
Data / restraints / parameters	5643 / 0 / 346	
Goodness-of-fit on F ²	1.022	
Final R indices [I > 2 σ (I)]	R1 = 0.0678, wR2 = 0.1673	
R indices (all data)	R1 = 0.0726, wR2 = 0.1712	
Largest diff. peak and hole	1.229 and -0.951 e.Å ⁻³	

14.1.10 Bis(trimethylsilyl)silatranyl silane (70)

Empirical formula	C ₁₂ H ₃₁ N O ₃ Si ₄	
Formula weight	349.74	
Temperature	100(2) K	
Wavelength	0.71073 Å	
Crystal system, space group	triclinic, P-1	
Unit cell dimensions	a = 7.679(3) Å	α = 88.725(6) deg.
	b = 11.337(4) Å	β = 87.958(6) deg.
	c = 12.014(5) Å	γ = 70.280(6) deg.
Volume	983.9(7) Å ³	
Z, Calculated density	2, 1.181 Mg/m ³	
Absorption coefficient	0.308 mm ⁻¹	
F(000)	380	
Crystal size	0.20 x 0.11 x 0.08 mm	
Theta range for data collection	1.70 to 25.50 deg.	
Limiting indices	-9 ≤ h ≤ 9, -13 ≤ k ≤ 13, -14 ≤ l ≤ 14	
Reflections collected / unique	7218 / 3571 [R(int) = 0.0266]	
Completeness to theta = 25.50	97.6 %	
Absorption correction	SADABS	
Max. and min. transmission	0.9758 and 0.9410	
Refinement method	Full-matrix least-squares on F ²	
Data / restraints / parameters	3571 / 0 / 210	
Goodness-of-fit on F ²	1.082	
Final R indices [I > 2 σ (I)]	R1 = 0.0697, wR2 = 0.1921	
R indices (all data)	R1 = 0.0749, wR2 = 0.1966	
Largest diff. peak and hole	1.006 and -0.422 e.Å ⁻³	

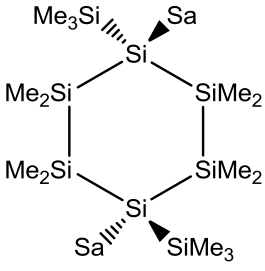
14.1.11 Disilatranyl-bis(trimethylsilyl)silane (72)

Empirical formula	C ₁₈ H ₄₂ N ₂ O ₆ Si ₅	
Formula weight	522.99	
Temperature	100(2) K	
Wavelength	0.71073 Å	
Crystal system, space group	monoclinic, C2/c	
Unit cell dimensions	a = 15.731(3) Å	α = 90 deg.
	b = 17.399(3) Å	β = 92.113(4) deg.
	c = 10.549(2) Å	γ = 90 deg.
Volume	2885.1(10) Å ³	
Z, Calculated density	4, 1.204 Mg/m ³	
Absorption coefficient	0.280 mm ⁻¹	
F(000)	1128	
Crystal size	0.44 x 0.22 x 0.17 mm	
Theta range for data collection	1.75 to 26.31 deg.	
Limiting indices	-19 ≤ h ≤ 19, -21 ≤ k ≤ 21, -13 ≤ l ≤ 13	
Reflections collected / unique	11303 / 2937 [R(int) = 0.0277]	
Completeness to theta = 26.31	99.7 %	
Absorption correction	SADABS	
Max. and min. transmission	0.9540 and 0.8868	
Refinement method	Full-matrix least-squares on F ²	
Data / restraints / parameters	2937 / 0 / 144	
Goodness-of-fit on F ²	1.066	
Final R indices [I > 2 σ (I)]	R1 = 0.0303, wR2 = 0.0803	
R indices (all data)	R1 = 0.0322, wR2 = 0.0817	
Largest diff. peak and hole	0.380 and -0.260 e.Å ⁻³	

14.1.12 2,5-Disilatranyl-2,5-tris(trimethylsilyl)decamethylhexasilane (77)

Empirical formula	C ₂₈ H ₇₂ N ₂ O ₆ Si ₁₀	
Formula weight	813.78	
Temperature	100(2) K	
Wavelength	0.71073 Å	
Crystal system, space group	monoclinic, P2(1)/c	
Unit cell dimensions	a = 25.410(6) Å	α = 90 deg.
	b = 10.481(3) Å	β = 90.779(4) deg.
	c = 17.482(4) Å	γ = 90 deg.
Volume	4655(2) Å ³	
Z, Calculated density	4, 1.161 Mg/m ³	
Absorption coefficient	0.318 mm ⁻¹	
F(000)	1768	
Crystal size	0.28 x 0.18 x 0.12 mm	
Theta range for data collection	0.80 to 26.36 deg.	
Limiting indices	-31 ≤ h ≤ 31, -13 ≤ k ≤ 13, -21 ≤ l ≤ 21	
Reflections collected / unique	35832 / 9429 [R(int) = 0.0521]	
Completeness to theta = 26.36	99.2 %	
Absorption correction	SADABS	
Max. and min. transmission	0.9628 and 0.9162	
Refinement method	Full-matrix least-squares on F ²	
Data / restraints / parameters	9429 / 0 / 459	
Goodness-of-fit on F ²	1.241	
Final R indices [I > 2 σ(I)]	R1 = 0.0907, wR2 = 0.2093	
R indices (all data)	R1 = 0.1011, wR2 = 0.2145	
Largest diff. peak and hole	1.299 and -0.423 e.Å ⁻³	

14.1.13 *trans*-1,4-Disilatranyl-1,4-bis(trimethylsilyl)octamethylcyclohexasilane (*trans*-80)

Empirical formula	C ₁₆ H ₃₆ N O ₃ Si ₅	
Formula weight	430.91	
Temperature	100(2) K	
Wavelength	0.71073 Å	
Crystal system, space group	monoclinic, C2/c	
Unit cell dimensions	a = 21.512(5) Å	α = 90 deg.
	b = 10.6939(19) Å	β = 115.423(6) deg.
	c = 22.770(4) Å	γ = 90 deg.
Volume	4730.8(16) Å ³	
Z, Calculated density	8, 1.210 Mg/m ³	
Absorption coefficient	0.317 mm ⁻¹	
F(000)	1864	
Crystal size	0.44 x 0.36 x 0.13 mm	
Theta range for data collection	1.98 to 26.25 deg.	
Limiting indices	-26 ≤ h ≤ 26, -13 ≤ k ≤ 13, -28 ≤ l ≤ 28	
Reflections collected / unique	18088 / 4767 [R(int) = 0.0328]	
Completeness to theta = 26.25	99.8 %	
Absorption correction	SADABS	
Max. and min. transmission	0.9600 and 0.8732	
Refinement method	Full-matrix least-squares on F ²	
Data / restraints / parameters	4767 / 0 / 233	
Goodness-of-fit on F ²	1.187	
Final R indices [I > 2 σ (I)]	R1 = 0.0526, wR2 = 0.1180	
R indices (all data)	R1 = 0.0585, wR2 = 0.1214	
Largest diff. peak and hole	0.559 and -0.506 e.Å ⁻³	

14.1.14 *cis*-1,4-Disilatranyl-1,4-bis(trimethylsilyl)octamethylcyclohexasilane (*cis*-80)

Empirical formula	C ₂₆ H ₆₆ N ₂ O ₆ Si ₁₀	
Formula weight	783.71	
Temperature	100(2) K	
Wavelength	0.71073 Å	
Crystal system, space group	triclinic, P-1	
Unit cell dimensions	a = 12.710(3) Å	α = 74.801(4) deg.
	b = 13.762(3) Å	β = 67.356(3) deg.
	c = 14.195(3) Å	γ = 80.458(4) deg.
Volume	2205.6(9) Å ³	
Z, Calculated density	2, 1.180 Mg/m ³	
Absorption coefficient	0.333 mm ⁻¹	
F(000)	848	
Crystal size	0.36 x 0.30 x 0.26 mm	
Theta range for data collection	1.54 to 26.20 deg.	
Limiting indices	-15 ≤ h ≤ 15, -17 ≤ k ≤ 17, -17 ≤ l ≤ 17	
Reflections collected / unique	17341 / 8677 [R(int) = 0.0240]	
Completeness to theta = 26.20	97.9 %	
Absorption correction	SADABS	
Max. and min. transmission	0.9184 and 0.8895	
Refinement method	Full-matrix least-squares on F ²	
Data / restraints / parameters	8677 / 0 / 411	
Goodness-of-fit on F ²	1.076	
Final R indices [I > 2 σ(I)]	R1 = 0.0358, wR2 = 0.0994	
R indices (all data)	R1 = 0.0392, wR2 = 0.1018	
Largest diff. peak and hole	0.714 and -0.307 e.Å ⁻³	

14.1.15 Protonated tris(trimethylsilyl)silatranylsilane (44) with Trifluoromethanesulfonic acid

Empirical formula	$C_{57} H_{129} F_9 N_3 O_{18} S_3 Si_{15}$	
Formula weight	1833.16	
Temperature	100(2) K	
Wavelength	0.71073 Å	
Crystal system, space group	monoclinic, P2(1)/c	
Unit cell dimensions	$a = 21.030(3) \text{ \AA}$	$\alpha = 90 \text{ deg.}$
	$b = 10.2241(16) \text{ \AA}$	$\beta = 92.743(3) \text{ deg.}$
	$c = 45.503(7) \text{ \AA}$	$\gamma = 90 \text{ deg.}$
Volume	$9773(3) \text{ \AA}^3$	
Z, Calculated density	4, 1.246 Mg/m ³	
Absorption coefficient	0.331 mm ⁻¹	
F(000)	3900	
Crystal size	0.34 x 0.22 x 0.16 mm	
Theta range for data collection	1.29 to 26.38 deg.	
Limiting indices	$-26 \leq h \leq 26, -12 \leq k \leq 12, -56 \leq l \leq 56$	
Reflections collected / unique	76582 / 19975 [R(int) = 0.0597]	
Completeness to theta = 26.38	99.9 %	
Absorption correction	SADABS	
Max. and min. transmission	0.9489 and 0.8957	
Refinement method	Full-matrix least-squares on F ²	
Data / restraints / parameters	19975 / 3 / 985	
Goodness-of-fit on F ²	1.065	
Final R indices [I > 2 σ (I)]	R1 = 0.0646, wR2 = 0.1392	
R indices (all data)	R1 = 0.0905, wR2 = 0.1508	
Largest diff. peak and hole	0.908 and -0.319 e.Å ⁻³	

14.1.16 Bis(trimethylsilyl)silatranlysilylpotassium.18-crown-6 (73)

Empirical formula	C ₂₄ H ₅₄ K N O ₉ Si ₄	
Formula weight	652.14	
Temperature	100(2) K	
Wavelength	0.71073 Å	
Crystal system, space group	monoclinic, P2(1)/n	
Unit cell dimensions	a = 11.342(2) Å	α = 90 deg.
	b = 20.852(4) Å	β = 98.962(3) deg.
	c = 15.232(3) Å	γ = 90 deg.
Volume	3558.5(12) Å ³	
Z, Calculated density	4, 1.217 Mg/m ³	
Absorption coefficient	0.327 mm ⁻¹	
F(000)	1408	
Crystal size	0.28 x 0.26 x 0.10 mm	
Theta range for data collection	1.67 to 26.00 deg.	
Limiting indices	-13 ≤ h ≤ 13, -25 ≤ k ≤ 25, -16 ≤ l ≤ 16	
Reflections collected / unique	26127 / 6593 [R(int) = 0.0379]	
Completeness to theta = 26.00	94.4 %	
Max. and min. transmission	0.9680 and 0.9139	
Refinement method	Full-matrix least-squares on F ²	
Data / restraints / parameters	6593 / 6 / 386	
Goodness-of-fit on F ²	1.080	
Final R indices [I > 2 σ (I)]	R1 = 0.0950, wR2 = 0.2282	
R indices (all data)	R1 = 0.1050, wR2 = 0.2357	
Largest diff. peak and hole	1.276 and -0.517 e.Å ⁻³	

14.1.17 Trimethylsilylphenylsilylanyltrimethylpotassium.18-crown-6 (87)

Empirical formula	C ₃₀ H ₅₃ K N O ₉ Si ₃	
Formula weight	695.10	
Temperature	100(2) K	
Wavelength	0.71073 Å	
Crystal system, space group	triclinic, P-1	
Unit cell dimensions	a = 10.790(2) Å	α = 93.348(3) deg.
	b = 10.863(2) Å	β = 105.422(3) deg.
	c = 16.420(3) Å	γ = 99.085(3) deg.
Volume	1821.8(6) Å ³	
Z, Calculated density	2, 1.267 Mg/m ³	
Absorption coefficient	0.293 mm ⁻¹	
F(000)	746	
Crystal size	0.22 x 0.12 x 0.10 mm	
Theta range for data collection	1.91 to 26.35 deg.	
Limiting indices	-13 ≤ h ≤ 13, -13 ≤ k ≤ 13, -20 ≤ l ≤ 20	
Reflections collected / unique	14615 / 7314 [R(int) = 0.0194]	
Completeness to theta = 26.35	98.3 %	
Absorption correction	SADABS	
Max. and min. transmission	0.9713 and 0.9383	
Refinement method	Full-matrix least-squares on F ²	
Data / restraints / parameters	7314 / 0 / 400	
Goodness-of-fit on F ²	1.037	
Final R indices [I > 2 σ (I)]	R1 = 0.0378, wR2 = 0.0901	
R indices (all data)	R1 = 0.0423, wR2 = 0.0928	
Largest diff. peak and hole	0.487 and -0.240 e.Å ⁻³	

14.1.18 (*tert*-Butyldimethylsilyl)(trimethylsilyl)silatranylsilylpotassium.18-crown-6 (88)

Empirical formula	C ₂₇ H ₆₀ K N O ₉ Si ₄	
Formula weight	694.22	
Temperature	100(2) K	
Wavelength	0.71073 Å	
Crystal system, space group	monoclinic, P2(1)/n	
Unit cell dimensions	a = 11.940(4) Å	α = 90 deg.
	b = 17.559(6) Å	β = 92.508(6) deg.
	c = 18.011(6) Å	γ = 90 deg.
Volume	3773(2) Å ³	
Z, Calculated density	4, 1.222 Mg/m ³	
Absorption coefficient	0.313 mm ⁻¹	
F(000)	1504	
Crystal size	0.44 x 0.40 x 0.17 mm	
Theta range for data collection	1.62 to 26.37 deg.	
Limiting indices	-14 ≤ h ≤ 14, -21 ≤ k ≤ 21, -22 ≤ l ≤ 22	
Reflections collected / unique	29281 / 7706 [R(int) = 0.0613]	
Completeness to theta = 26.37	99.8 %	
Absorption correction	SADABS	
Max. and min. transmission	0.9487 and 0.8746	
Refinement method	Full-matrix least-squares on F ²	
Data / restraints / parameters	7706 / 0 / 387	
Goodness-of-fit on F ²	1.078	
Final R indices [I > 2 σ(I)]	R1 = 0.0638, wR2 = 0.1461	
R indices (all data)	R1 = 0.0835, wR2 = 0.1550	
Largest diff. peak and hole	0.616 and -0.528 e.Å ⁻³	

14.1.19 Bis[bis(trimethylsilyl)silatranylsilanyl]zinc (98)

Empirical formula	C ₂₄ H ₆₀ N ₂ O ₆ Si ₈ Zn	
Formula weight	762.83	
Temperature	100(2) K	
Wavelength	0.71073 Å	
Crystal system, space group	monoclinic, C2/c	
Unit cell dimensions	a = 22.934(7) Å	α = 90 deg.
	b = 11.727(3) Å	β = 103.317(7) deg.
	c = 15.772(4) Å	γ = 90 deg.
Volume	4127.9(19) Å ³	
Z, Calculated density	4, 1.227 Mg/m ³	
Absorption coefficient	0.861 mm ⁻¹	
F(000)	1632	
Crystal size	0.18 x 0.12 x 0.05 mm	
Theta range for data collection	1.82 to 26.38 deg.	
Limiting indices	-28 ≤ h ≤ 28, -14 ≤ k ≤ 14, -19 ≤ l ≤ 19	
Reflections collected / unique	16118 / 4215 [R(int) = 0.0352]	
Completeness to theta = 26.38	99.7 %	
Absorption correction	SADABS	
Max. and min. transmission	0.9582 and 0.8604	
Refinement method	Full-matrix least-squares on F ²	
Data / restraints / parameters	4215 / 28 / 221	
Goodness-of-fit on F ²	1.079	
Final R indices [I > 2 σ(I)]	R1 = 0.0638, wR2 = 0.1394	
R indices (all data)	R1 = 0.0724, wR2 = 0.1443	
Largest diff. peak and hole	0.830 and -0.683 e.Å ⁻³	

14.1.20 Dicyclopentadienyl[bis(trimethylsilyl)silatranylsilyl]hafniumchloride (99)

Empirical formula	C ₂₂ H ₄₀ Cl Hf N O ₃ Si ₄	
Formula weight	692.85	
Temperature	100(2) K	
Wavelength	0.71073 Å	
Crystal system, space group	monoclinic, P2(1)/c	
Unit cell dimensions	a = 11.397(3) Å	α = 90 deg.
	b = 11.523(3) Å	β = 98.649(4) deg.
	c = 21.702(5) Å	γ = 90 deg.
Volume	2817.6(12) Å ³	
Z, Calculated density	4, 1.633 Mg/m ³	
Absorption coefficient	3.991 mm ⁻¹	
F(000)	1392	
Crystal size	0.24 x 0.14 x 0.09 mm	
Theta range for data collection	1.81 to 26.34 deg.	
Limiting indices	-14 ≤ h ≤ 14, -14 ≤ k ≤ 14, -27 ≤ l ≤ 27	
Reflections collected / unique	21898 / 5719 [R(int) = 0.0572]	
Completeness to theta = 26.34	99.5 %	
Absorption correction	SADABS	
Max. and min. transmission	0.7153 and 0.4476	
Refinement method	Full-matrix least-squares on F ²	
Data / restraints / parameters	5719 / 0 / 295	
Goodness-of-fit on F ²	1.132	
Final R indices [I > 2 σ(I)]	R1 = 0.0433, wR2 = 0.0959	
R indices (all data)	R1 = 0.0472, wR2 = 0.0980	
Largest diff. peak and hole	2.815 and -1.715 e.Å ⁻³	

14.1.21 MeN(CH₂CH₂O)₂SiMeCl (104)

Empirical formula	C ₆ H ₁₄ Cl N O ₂ Si	
Formula weight	195.72	
Temperature	100(2) K	
Wavelength	0.71073 Å	
Crystal system, space group	monoclinic, P2(1)/n	
Unit cell dimensions	a = 6.8840(13) Å	α = 90 deg.
	b = 11.800(2) Å	β = 92.907(3) deg.
	c = 11.154(2) Å	γ = 90 deg.
Volume	904.9(3) Å ³	
Z, Calculated density	4, 1.437 Mg/m ³	
Absorption coefficient	0.509 mm ⁻¹	
F(000)	416	
Crystal size	0.52 x 0.33 x 0.11 mm	
Theta range for data collection	2.51 to 26.28 deg.	
Limiting indices	-8 ≤ h ≤ 8, -14 ≤ k ≤ 14, -13 ≤ l ≤ 13	
Reflections collected / unique	7036 / 1833 [R(int) = 0.0169]	
Completeness to theta = 26.28	99.8 %	
Absorption correction	SADABS	
Max. and min. transmission	0.9462 and 0.7779	
Refinement method	Full-matrix least-squares on F ²	
Data / restraints / parameters	1833 / 0 / 102	
Goodness-of-fit on F ²	1.109	
Final R indices [I > 2 σ (I)]	R1 = 0.0258, wR2 = 0.0696	
R indices (all data)	R1 = 0.0265, wR2 = 0.0701	
Largest diff. peak and hole	0.386 and -0.195 e.Å ⁻³	

14.1.22 1,4-bis-2'-(2',6'-dimethyl-1',3',6',2'-dioxazasilocanyl)-1,1,4,4-tetrakis(trimethylsilyl)tetramethyltetrasilane (112)

Empirical formula	C ₂₈ H ₇₆ N ₂ O ₄ Si ₁₀	
Formula weight	785.81	
Temperature	100(2) K	
Wavelength	0.71073 Å	
Crystal system, space group	?, ?	
Unit cell dimensions	a = 9.773(2) Å	α = 90 deg.
	b = 18.507(4) Å	β = 103.801(3) deg.
	c = 13.604(3) Å	γ = 90 deg.
Volume	2389.6(10) Å ³	
Z, Calculated density	2, 1.092 Mg/m ³	
Absorption coefficient	0.305 mm ⁻¹	
F(000)	860	
Crystal size	0.33 x 0.23 x 0.18 mm	
Theta range for data collection	1.89 to 26.35 deg.	
Limiting indices	-12 ≤ h ≤ 12, -23 ≤ k ≤ 23, -16 ≤ l ≤ 16	
Reflections collected / unique	18794 / 4868 [R(int) = 0.0269]	
Completeness to theta = 26.35	99.9 %	
Absorption correction	SADABS	
Max. and min. transmission	0.9472 and 0.9062	
Refinement method	Full-matrix least-squares on F ²	
Data / restraints / parameters	4868 / 0 / 209	
Goodness-of-fit on F ²	1.139	
Final R indices [I > 2 σ (I)]	R1 = 0.0491, wR2 = 0.1225	
R indices (all data)	R1 = 0.0525, wR2 = 0.1247	
Largest diff. peak and hole	0.858 and -0.295 e.Å ⁻³	

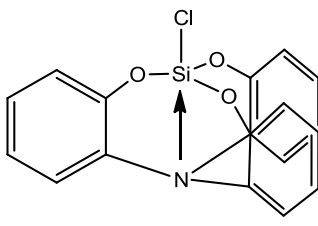
14.1.23 [(Me₃Si)₃Si]₂Si(OCH₂CH₂)₂NMe (116)

Empirical formula	C ₂₃ H ₆₅ N O ₂ Si ₉	
Formula weight	640.57	
Temperature	100(2) K	
Wavelength	0.71073 Å	
Crystal system, space group	orthorhombic, Pccn	
Unit cell dimensions	a = 43.341(8) Å	α = 90 deg.
	b = 12.833(2) Å	β = 90 deg.
	c = 14.389(3) Å	γ = 90 deg.
Volume	8003(2) Å ³	
Z, Calculated density	8, 1.063 Mg/m ³	
Absorption coefficient	0.318 mm ⁻¹	
F(000)	2816	
Crystal size	0.32 x 0.25 x 0.12 mm	
Theta range for data collection	0.94 to 26.37 deg.	
Limiting indices	-54 ≤ h ≤ 54, -16 ≤ k ≤ 15, -17 ≤ l ≤ 17	
Reflections collected / unique	55175 / 8159 [R(int) = 0.0448]	
Completeness to theta = 26.37	99.9 %	
Absorption correction	SADABS	
Max. and min. transmission	0.9629 and 0.9051	
Refinement method	Full-matrix least-squares on F ²	
Data / restraints / parameters	8159 / 0 / 335	
Goodness-of-fit on F ²	1.110	
Final R indices [I > 2 σ (I)]	R1 = 0.0716, wR2 = 0.1795	
R indices (all data)	R1 = 0.0781, wR2 = 0.1845	
Largest diff. peak and hole	2.971 and -0.540 e.Å ⁻³	

14.1.24 [(Me₃Si)₃Ge]₂Si(OCH₂CH₂)₂NMe (117)

Empirical formula	C ₂₃ H ₆₅ Ge ₂ N O ₂ Si ₇	
Formula weight	729.57	
Temperature	100(2) K	
Wavelength	0.71073 Å	
Crystal system, space group	triclinic, P-1	
Unit cell dimensions	a = 9.9517(18) Å	α = 101.476(3) deg.
	b = 12.433(2) Å	β = 92.764(3) deg.
	c = 17.836(3) Å	γ = 110.105(3) deg.
Volume	2014.6(6) Å ³	
Z, Calculated density	2, 1.203 Mg/m ³	
Absorption coefficient	1.719 mm ⁻¹	
F(000)	776	
Crystal size	0.34 x 0.22 x 0.17 mm	
Theta range for data collection	1.79 to 26.36 deg.	
Limiting indices	-12 ≤ h ≤ 12, -15 ≤ k ≤ 15, -22 ≤ l ≤ 21	
Reflections collected / unique	16140 / 8103 [R(int) = 0.0167]	
Completeness to theta = 26.36	98.4 %	
Absorption correction	SADABS	
Max. and min. transmission	0.7587 and 0.5925	
Refinement method	Full-matrix least-squares on F ²	
Data / restraints / parameters	8103 / 0 / 335	
Goodness-of-fit on F ²	1.054	
Final R indices [I > 2 σ (I)]	R1 = 0.0254, wR2 = 0.0661	
R indices (all data)	R1 = 0.0291, wR2 = 0.0676	
Largest diff. peak and hole	0.672 and -0.305 e.Å ⁻³	

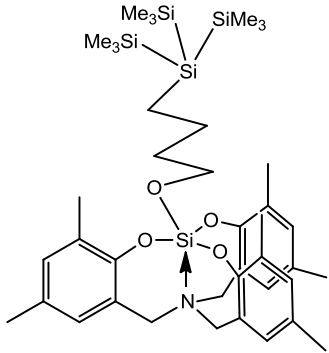
14.1.25 Aminotris(phenyl-2'-oxy)silylchloride (130)

Empirical formula	C ₁₈ H ₁₂ Cl N O ₃ Si	
Formula weight	353.83	
Temperature	183(2) K	
Wavelength	0.71073 Å	
Crystal system, space group	monoclinic, P 2(1)/n	
Unit cell dimensions	a = 9.2802(14) Å	α = 90 deg.
	b = 14.072(2) Å	β = 90.084(2) deg.
	c = 11.6193(18) Å	γ = 90 deg.
Volume	1517.4(4) Å ³	
Z, Calculated density	4, 1.549 Mg/m ³	
Absorption coefficient	0.348 mm ⁻¹	
F(000)	728	
Crystal size	0.35 x 0.35 x 0.15 mm	
Theta range for data collection	1.45 to 26.00 deg.	
Limiting indices	-11 ≤ h ≤ 11, -17 ≤ k ≤ 17, -14 ≤ l ≤ 14	
Reflections collected / unique	11824 / 2982 [R(int) = 0.0273]	
Completeness to theta = 26.00	99.6 %	
Absorption correction	Semi-empirical from equivalents	
Max. and min. transmission	0.9497 and 0.8879	
Refinement method	Full-matrix least-squares on F ²	
Data / restraints / parameters	2982 / 0 / 218	
Goodness-of-fit on F ²	1.044	
Final R indices [I > 2 σ(I)]	R1 = 0.0385, wR2 = 0.1008	
R indices (all data)	R1 = 0.0404, wR2 = 0.1023	
Largest diff. peak and hole	1.066 and -0.264 e.Å ⁻³	

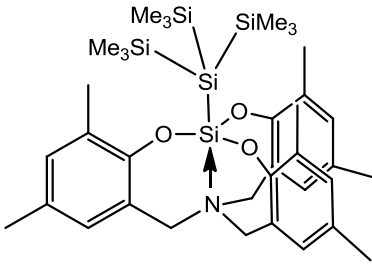
14.1.26 1,1,1-Aminotris(phenyl-2'-oxy)-2,2-bis(trimethylsilyl)trimethyltrisilane (135)

Empirical formula	C ₅₄ H ₇₈ N ₂ O ₆ Si ₁₀	
Formula weight	1132.08	
Temperature	200(2) K	
Wavelength	0.71073 Å	
Crystal system, space group	monoclinic, C2/c	
Unit cell dimensions	a = 60.459(13) Å	α = 90 deg.
	b = 12.913(3) Å	β = 100.080(6) deg.
	c = 16.786(4) Å	γ = 90 deg.
Volume	12903(5) Å ³	
Z, Calculated density	8, 1.166 Mg/m ³	
Absorption coefficient	0.248 mm ⁻¹	
F(000)	4832	
Crystal size	0.54 x 0.29 x 0.26 mm	
Theta range for data collection	1.61 to 26.37 deg.	
Limiting indices	-74 ≤ h ≤ 75, -16 ≤ k ≤ 16, -20 ≤ l ≤ 20	
Reflections collected / unique	50482 / 13161 [R(int) = 0.0358]	
Completeness to theta = 26.37	99.8 %	
Absorption correction	SADABS	
Max. and min. transmission	0.9383 and 0.8776	
Refinement method	Full-matrix least-squares on F ²	
Data / restraints / parameters	13161 / 0 / 667	
Goodness-of-fit on F ²	1.026	
Final R indices [I > 2 σ (I)]	R1 = 0.0513, wR2 = 0.1254	
R indices (all data)	R1 = 0.0672, wR2 = 0.1339	
Largest diff. peak and hole	0.439 and -0.221 e.Å ⁻³	

14.1.27 1,1,1-Aminotris(-3',5'-dimethylbenzyl-2'-oxy)-(4''-tris(trimethylsilyl)silyl)butanyloxysilane (139)

Empirical formula	C ₄₀ H ₆₄ N O ₄ Si ₅	
Formula weight	763.37	
Temperature	100(2) K	
Wavelength	0.71073 Å	
Crystal system, space group	triclinic, P-1	
Unit cell dimensions	a = 13.822(4) Å	α = 87.588(4) deg.
	b = 17.584(5) Å	β = 75.904(4) deg.
	c = 20.129(5) Å	γ = 70.969(4) deg.
Volume	4482(2) Å ³	
Z, Calculated density	4, 1.131 Mg/m ³	
Absorption coefficient	0.196 mm ⁻¹	
F(000)	1652	
Crystal size	0.33 x 0.27 x 0.06 mm	
Theta range for data collection	1.58 to 26.36 deg.	
Limiting indices	-17 ≤ h ≤ 17, -21 ≤ k ≤ 21, -25 ≤ l ≤ 25	
Reflections collected / unique	35561 / 17932 [R(int) = 0.0362]	
Completeness to theta = 26.36	97.9 %	
Absorption correction	SADABS	
Max. and min. transmission	0.9883 and 0.9380	
Refinement method	Full-matrix least-squares on F ²	
Data / restraints / parameters	17932 / 0 / 931	
Goodness-of-fit on F ²	1.002	
Final R indices [I > 2 σ(I)]	R1 = 0.0877, wR2 = 0.2219	
R indices (all data)	R1 = 0.1009, wR2 = 0.2301	
Largest diff. peak and hole	3.580 and -1.638 e.Å ⁻³	

14.1.28 1,1,1-Aminotris(-3',5'-dimethylbenzyl-2'-oxy)-2,2-bis(trimethylsilyl)trimethyltrisilane (141)

Empirical formula	C ₃₆ H ₅₇ N O ₃ Si ₅	
Formula weight	692.28	
Temperature	100(2) K	
Wavelength	0.71073 Å	
Crystal system, space group	hexagonal, P-3c1	
Unit cell dimensions	a = 14.3849(18) Å	α = 90 deg.
	b = 14.3849(18) Å	β = 90 deg.
	c = 22.169(4) Å	γ = 120 deg.
Volume	3972.8(10) Å ³	
Z, Calculated density	4, 1.157 Mg/m ³	
Absorption coefficient	0.213 mm ⁻¹	
F(000)	1496	
Crystal size	0.20 x 0.20 x 0.12 mm	
Theta range for data collection	1.63 to 26.36 deg.	
Limiting indices	-17 ≤ h ≤ 17, -17 ≤ k ≤ 17, -27 ≤ l ≤ 27	
Reflections collected / unique	29652 / 2696 [R(int) = 0.0351]	
Completeness to theta = 26.36	99.8 %	
Absorption correction	SADABS	
Max. and min. transmission	0.9749 and 0.9586	
Refinement method	Full-matrix least-squares on F ²	
Data / restraints / parameters	2696 / 0 / 141	
Goodness-of-fit on F ²	1.263	
Final R indices [I > 2 σ(I)]	R1 = 0.0599, wR2 = 0.1346	
R indices (all data)	R1 = 0.0611, wR2 = 0.1352	
Largest diff. peak and hole	0.451 and -0.299 e.Å ⁻³	

14.1.29 Bis(trimethylsilyl)[trimethoxysilyl]silylpotassium.18-crown-6 (161)

Empirical formula	C ₂₁ H ₅₁ K O ₉ Si ₄	
Formula weight	599.08	
Temperature	100(2) K	
Wavelength	0.71073 Å	
Crystal system, space group	orthorhombic, Pbc _a	
Unit cell dimensions	a = 17.927(6) Å	α = 90 deg.
	b = 18.514(7) Å	β = 90 deg.
	c = 19.920(7) Å	γ = 90 deg.
Volume	6612(4) Å ³	
Z, Calculated density	8, 1.204 Mg/m ³	
Absorption coefficient	0.346 mm ⁻¹	
F(000)	2592	
Crystal size	0.22 x 0.15 x 0.12 mm	
Theta range for data collection	1.88 to 25.25 deg.	
Limiting indices	-21 ≤ h ≤ 21, -22 ≤ k ≤ 21, -23 ≤ l ≤ 23	
Reflections collected / unique	43966 / 5979 [R(int) = 0.1054]	
Completeness to theta = 25.25	100.0 %	
Absorption correction	SADABS	
Max. and min. transmission	0.9597 and 0.9279	
Refinement method	Full-matrix least-squares on F ²	
Data / restraints / parameters	5979 / 0 / 325	
Goodness-of-fit on F ²	1.255	
Final R indices [I > 2 σ (I)]	R1 = 0.0932, wR2 = 0.2060	
R indices (all data)	R1 = 0.1081, wR2 = 0.2141	
Largest diff. peak and hole	1.252 and -0.472 e.Å ⁻³	

14.2 Curriculum Vitae

Personal data

Name: Mohammad Aghazadeh Meshgi
Date of birth: 1, Feb, 1982
Place of birth: Oroumieh, Iran
Nationality: Iranian
Parents: Hassan Aghazadeh Meshgi, Giti Faroughi

Education

1988 - 1992 15th-khordad primary school
1992 - 1993 Valfajr primary school

1993 - 1996 Mehdipoor secondary school

1996 - 1999 Tarbiat high school
1999 - 2000 Noor pre-university school

2001 - 2005 **BSc: Materials Engineering – Industrial Metallurgy**
Islamic Azad University, Science and Research Tehran Branch, Faculty of Materials Engineering, Tehran, Iran
Under supervision of Dr. Hossein Yoozbashizadeh

2007 - 2009 **MSc: Materials Engineering – Materials Identification, Selection & Manufacturing Method**
Islamic Azad University, South Tehran Branch, Faculty of Engineering, School of Materials Eng., Tehran, Iran
Under supervision of Prof. Farshad Akhlaghi

2012 - 2015 **PhD: Chemical Engineering – Inorganic Chemistry**
Graz University of Technology, Inorganic Chemistry Dept., Graz, Austria
Under supervision of Prof. Christoph Marschner

Work experiences

2006 - 2012 **Iranelco company, Tehran, Iran.**
Research engineer and laboratory manager

2014 - 2015 **Graz University of Technology**
Project assistant